



UNIVERSIDAD DE BURGOS  
FACULTAD DE CIENCIAS

Synthesis and characterization of Ru(II), Ir(III) and  
Rh(III) trischelate complexes with benzimidazole  
based ligands for photodynamic therapy and  
photocatalysis

The bright side of the chemistry

PhD Thesis

Igor Echevarría Poza

Burgos, September 2022





**Universidad de Burgos**

**Departamento de Química**

**Áreas de Química Inorgánica y Química Orgánica**

Los Drs. Gustavo Espino Ordóñez y Roberto Quesada Pato, Profesores Titulares del Departamento de Química de la Universidad de Burgos,

**Certifican:**

Que el trabajo de investigación incluido en la presente memoria que lleva por título **“Synthesis and characterization of Ru(II), Ir(III) and Rh(III) trischelate complexes with benzimidazole based ligands for photodynamic therapy and photocatalysis. The bright side of the chemistry”** ha sido realizado en el Departamento de Química de la Universidad de Burgos bajo su dirección por el graduado **Igor Echevarría Poza** y autorizan su presentación para que sea calificada como Tesis Doctoral.

Firma manuscrita en azul de Gustavo Espino Ordóñez.

Fdo.: Gustavo Espino Ordóñez

Firma manuscrita en azul de Roberto Quesada Pato.

Fdo.: Roberto Quesada Pato

Burgos, 24 de junio de 2022





*Life is not easy for any of us. But what of that? We must have perseverance  
and above all confidence in ourselves. We must believe that we are  
gifted for something and that this thing must be attained.*

**Marie Curie**



## Agradecimientos

Por todos esos momentos felices en los que te encuentras en una nube, y todos esos momentos difíciles y de frustración en los que parece que te encuentras en un pozo sin fondo. Porque al final es imposible valorar lo bueno si viene demasiado fácil, gracias por todos y cada uno de los momentos vividos.

Intentaré agradecer en estas líneas a todas las personas que han hecho posible este logro, porque sin todas ellas no lo hubiera logrado. Espero no olvidarme ninguna, porque son muchas.

Lo primero, quiero agradecer al Dr. Gustavo Espino por todos estos años, por hacer que me apasionara la investigación como para hacer un doctorado, por confiar en mí y por esa cercanía y buen rollo que transmite, que hace posible que lo que en principio sería la relación entre un director y su doctorando trascienda más allá. Y también por esa visión que tiene, que más que enfocarse en los logros de la actividad investigadora, se enfoca en el proceso de aprendizaje.

Al Dr. Roberto Quesada por confiar en mí y darme la oportunidad de llevar a cabo mi doctorado, lo cual no habría sido posible sin su ayuda. Además, también he podido aprender mucho de él, gracias a su gran perspectiva, capaz de ver de un simple vistazo cualquier detalle del trabajo del que tú ni siquiera te habías dado cuenta y también de enfocar las cosas de la manera más precisa.

A los Dres. Félix Jalón y Blanca Manzano, por haber podido colaborar con ellos, lo que me ha permitido aprender mucho y crecer como investigador. Pero, ante todo, han sido y son una verdadera fuente de inspiración y motivación. La verdad, me parece increíble como después de la gran carrera investigadora que han tenido y después de haberlo logrado todo, sigan con ese afán de conocimiento, esa vocación y ese espíritu de trabajo como si fuera su primer día. Espero que no cambiéis nunca.

Al Dr. José Vicente Cuevas por introducirme en el mundo de la química computacional, por la paciencia que siempre ha tenido y su disposición para echarme una mano por muy liado que estuviese. Y también por expandir mis horizontes en los cafés gracias a su gran capacidad para la argumentación y sentido del humor.

Al Dr. Gabriel García Herbosa, por enseñarme las bases de la electroquímica y despertar mi interés por el almacenamiento de energía, las baterías y el hidrógeno, temas que puede que desconociera si no fuera por él. Y por ser una inmensa fuente de conocimiento, ilustrándonos sobre los más diversos temas en cualquier momento, motivándome a seguir aprendiendo.

A la Dra. Arancha Carbayo, por preocuparse por mí en mis primeros pasos en el laboratorio y echarme una mano, y por estar siempre ahí por si se la necesita. Que, aunque a veces su trabajo dentro del grupo pueda quedar un tanto eclipsado, su labor es vital e insustituible.

A las Dras. Anna Massaguer, Sílvia Barrabés y María Ángeles Martínez, y a Elisenda Zafón y el resto de gente de la Universidad de Girona, por permitirnos colaborar con ellas, por su buen trato y por darnos siempre facilidades. Hacéis que colaborar con vosotras no sea sólo fructífero sino también agradable.

Sin olvidarme del técnico del área Félix Ausín, una de las mejores personas que he conocido, que siempre está ahí para ayudarnos con cualquier cosa del laboratorio, siempre con una sonrisa y sin ninguna queja por muy pesados que podamos ser.

Ni del resto de compañeros del área, pues todos me han ayudado de una u otra manera a lo largo de todos estos años. A estos hay que sumar todos los compañeros que han pasado, durante un mayor o menor tiempo, por el laboratorio: Oscar, Ana, Raúl, Marta, Jairo, Juan, Mónica, Daniel, Nacho, Dani, Cristina, Carmen, Iván, Alba, Víctor, Santi, Matteo y Larry. En especial, tengo que agradecer a la Dra. Marta Martínez, por ayudarme a dar mis primeros pasos en el laboratorio, y a la Dra. Mónica Vaquero, por ayudarme a dar el salto cualitativo que necesitaba y madurar como investigador.

También quiero destacar la labor de Jacinto, Marta, Pilar y el resto de técnicos del parque científico tecnológico (PCT), por hacernos caso siempre por muchas muestras que bajemos, por ayudarnos a llevar a cabo cualquier experimento que se nos ocurra y por tener siempre un trato amable con nosotros.

Y también dar las gracias al Fondo Social Europeo y Consejería de Educación de la Junta de Castilla y León (EDU/1100/2017) por hacer posible este doctorado mediante su financiación.

Pero, sobre todo, tengo que agradecerles a mis padres y mi hermano, y el resto de mi familia, que siempre han estado ahí para ayudarme y apoyarme, y aguantarme en mis malos momentos. Sin vosotros no hubiera sido posible, así que esta tesis en parte es vuestra también. Y tampoco me puedo olvidar de mis amigos, que han sabido aguantar mis quejas constantes y perdonar que a menudo estuviera ausente.

## Acknowledgements

For all those happy moments when you find yourself on a cloud, and all those difficult and frustrating moments when it seems that you are in a bottomless pit. Because in the end it is impossible to value the good if it comes too easy, thanks for each and every one of the moments lived.

I will try to thank in these lines all the people who have made this achievement possible, because without all of them I would not have succeeded. I hope I don't forget anyone, because there are many.

First of all, I want to thank Dr. Gustavo Espino for all these years, for making me passionate about research to do a PhD, for trusting me and for that closeness and good vibes that he transmits, which makes it possible that what would be the relationship between a director and his doctoral student transcends further. And also because of that vision that he has, which rather than focusing on the achievements of the research activity, focuses on the learning process.

To Dr. Roberto Quesada for trusting me and giving me the opportunity to complete my PhD, which would not have been possible without his help. In addition, I have also been able to learn a lot from him, thanks to his great perspective, able to see at a glance any detail of the work that you had not even noticed and also able to focus things in the most precise way.

To Drs. Félix Jalón and Blanca Manzano, for being able to collaborate with them, which has allowed me to learn a lot and grow as a researcher. But, above all, they have been and are a true source of inspiration and motivation. The truth is that it seems incredible to me how after the great research career they have had and after having achieved everything, they continue with that desire for knowledge, that vocation and that spirit of work as if it was their first day. I hope you both never change.

To Dr. José Vicente Cuevas for introducing me into the world of computational chemistry, for the patience he has always had and his willingness to lend me a hand no matter how busy he was. And also for expanding my horizons in the cafes thanks to his great capacity for argumentation and sense of humour.

To Dr. Gabriel García Herbosa, for teaching me the basics of electrochemistry and awakening my interest in energy storage, batteries and hydrogen, topics that I might not have known if it weren't for him. And for being an immense source of knowledge, enlightening us on the most diverse topics at any time, motivating me to continue learning.

To Dr. Arancha Carbayo, for caring about me in my first steps in the laboratory and lending me a hand, and for always being there if needed. Even if sometimes her work within the group may be somewhat overshadowed, her work is vital and irreplaceable.

To the Drs. Anna Massaguer, Sílvia Barrabés and María Ángeles Martínez, and to Elisenda Zafón and the rest of the people from the University of Girona, for allowing us to collaborate with them, for their good treatment and for always giving us facilities. You make collaborating with you not only fruitful but also enjoyable.

Without forgetting the area technician Félix Ausín, one of the best people I have ever met, who is always there to help us with anything in the laboratory, always with a smile and without any complaints, no matter how annoying we may be.

Neither the rest of the colleagues of the area, because all of them have helped me in one way or another throughout all these years. To these I have to add all the colleagues who have passed, for a longer or shorter time, through the laboratory: Óscar, Ana, Raúl, Marta, Jairo, Juan, Mónica, Daniel, Nacho, Dani, Cristina, Carmen, Iván, Alba, Víctor, Santi, Matteo and Larry. In particular, I have to thank Dr. Marta Martínez, for helping me to take my first steps in the laboratory, and Dr. Mónica Vaquero, for helping me to make the qualitative leap I needed and mature as a researcher.

I also want to highlight the work of Jacinto, Marta, Pilar and the rest of the technicians of the technological science park (PCT), for always paying attention to us no matter how many samples we bring to them, for helping us carry out any experiment that comes to our mind and for always having a friendly treatment with us.

And also I have to thank the European Social Fund and the Ministry of Education of the Junta de Castilla y León (EDU/1100/2017) for making this doctorate possible through its financing.

But, above all, I have to thank my parents and my brother, and the rest of my family, who have always been there to help me and support me, and put up with me in my bad times. Without you it would not have been possible, so this thesis is partly yours as well. And I can't forget my friends either, who have been able to put up with my constant complaints and forgive me for often being absent.

## Index

### Contenido

<b>Agradecimientos</b> .....	7
<b>Acknowledgements</b> .....	9
<b>Index of compounds</b> .....	19
<b>Abbreviations</b> .....	24
General abbreviations .....	24
NMR abbreviations.....	28
IR abbreviations.....	28
<b>The metals and the ligands</b> .....	29
<b>1. Metals</b> .....	31
1.1. Ruthenium .....	31
1.2. Rhodium .....	32
1.3. Iridium .....	32
<b>2. Ligands</b> .....	33
<b>Bibliography</b> .....	36
<b>Tris-chelate complexes: Synthesis, structure, properties and applications</b> .....	39
<b>1. Synthetic procedures</b> .....	39
1.1. Iridium and rhodium complexes .....	39
1.2. Ruthenium complexes.....	40
<b>2. Structure of the complexes</b> .....	41
2.1. Iridium and rhodium complexes .....	41
2.2. Ruthenium complexes.....	42
<b>3. A theoretical insight into luminescence</b> .....	43
3.1. Absorption spectra .....	43
3.2. Emission spectra.....	44
<b>4. Properties</b> .....	46

<b>5. Applications</b> .....	52
<b>Bibliography</b> .....	55
<b>Part 1. Ir(III) and Rh(III) tris-chelate complexes for photodynamic therapy (PDT)</b> ..	63
<b>Objectives</b> .....	63
<b>Cancer through the history, metals in medicine and photodynamic therapy (PDT)</b>	67
<b>0. Introduction to cancer</b> .....	67
<b>1. Cancer and treatment: a brief story</b> .....	68
1.1. From surgical treatments to radiotherapy .....	68
1.2. Chemotherapy .....	68
1.3. Targeted therapies .....	69
1.3.1. Monoclonal antibodies .....	70
1.3.2. Selective kinase inhibitors .....	70
1.3.3. Proteasome inhibitors .....	71
1.3.4. Molecular radiotherapy .....	72
1.4. Immune checkpoint inhibitors .....	72
1.5. New directions in cancer therapy .....	73
<b>2. Metals in medicine</b> .....	74
2.1. Properties of metal complexes .....	74
2.2. Imaging and Diagnosis .....	75
2.3. Metal complexes as therapeutic agents .....	77
2.3.1. Gold antiarthritic drugs .....	77
2.3.2. Antimicrobial and antiviral agents .....	78
2.3.3. Insulin mimetics .....	80
2.3.4. Cardiovascular system .....	82
2.3.5. Anticancer agents .....	82
2.3.5.1. Platinum anticancer agents .....	82
2.3.5.2. Other metal-based anticancer agents .....	82
<b>3. Photodynamic therapy (PDT)</b> .....	92



---

3.1. Historical development of photodynamic therapy .....	92
3.2. Cellular Mechanisms of PDT .....	94
3.3. Requirements for the photosensitizers (PS).....	95
3.4. PDT targets .....	97
3.4.1. Targets at the molecular level .....	97
3.4.2. Targets at the cellular level .....	99
3.5. Cell death pathways in PDT .....	100
3.6. Photosensitizers for PDT .....	101
3.6.1. First generation .....	101
3.6.2. Second generation.....	102
3.6.3. Third generation photosensitizers .....	106
3.7 Recent advances in PDT.....	112
3.7.1. Two-photon PDT.....	112
3.7.2. Upconverting nanoparticles (UCNPs) for PDT .....	113
3.7.3. Dual function PSs (theragnosis).....	115
3.7.4. Complexation of a BODIPY-based ligand.....	116
3.7.5. Use of nanocarriers .....	117
3.7.6. Use of targeting biomolecules.....	118
3.7.7. X-ray PDT .....	123
3.7.8. AIE (aggregation induced emission) .....	124
<b>Bibliography</b> .....	126
<b>Chapter 1. Thiabendazole-based Rh(III) and Ir(III) Biscyclometalated Complexes with Mitochondria-Targeted Anticancer Activity and Metal-Sensitive Photodynamic Activity .....</b>	<b>157</b>
<b>Authorship Statement</b> .....	<b>157</b>
<b>0. Abstract</b> .....	<b>157</b>
<b>1. Introduction</b> .....	<b>158</b>
<b>2. Results and discussion</b> .....	<b>160</b>
2.1. Synthesis of ligands and complexes .....	160

2.2. Characterization of complexes .....	161
2.3. Crystal structures.....	162
2.4. pH stability.....	163
2.5. Photophysical properties.....	164
2.6. Biological properties.....	165
2.6.1. In vitro cytotoxicity.....	165
2.6.2. Cellular uptake.....	165
2.6.3. Cell cycle arrest.....	166
2.6.4. Induction of apoptosis.....	167
2.6.5. Cellular localization .....	169
2.6.6. Effect on the Mitochondrial Membrane Potential.....	171
2.6.7. Intracellular ROS detection .....	171
2.6.8. Study of Cardiolipin oxidation .....	173
2.6.9. Photodynamic activity .....	173
2.7. Ir(III)-promoted singlet oxygen photo-generation and photooxidation of sulphides.....	175
2.7.1. Photo-stability of complexes <b>[Ir-a]Cl</b> and <b>[Ir-b]Cl</b> .....	175
2.7.2. Photo-oxidation of thioanisole.....	175
2.7.3. Photo-oxidation of L-cysteine and L-methionine .....	177
<b>3. Conclusions .....</b>	<b>178</b>
<b>4. Synthesis and characterization .....</b>	<b>178</b>
4.1. L <sup>2</sup> .....	178
4.2. Rh(III) and Ir(III)-complexes .....	179
<b>Bibliography.....</b>	<b>183</b>
<b>Chapter 2. Photodynamic Therapy with Mitochondria-targeted Biscyclometalated Ir(III) Complexes. Multi-action Mechanism and Strong influence of the Cyclometalating Ligand .....</b>	<b>189</b>
<b>Authorship Statement .....</b>	<b>189</b>
<b>0. Abstract.....</b>	<b>189</b>

---

<b>1. Introduction</b> .....	190
<b>2. Results and discussion</b> .....	192
2.1. Synthesis and general characterization.....	192
2.2. X-ray diffraction.....	194
2.3. Electrochemical measurements .....	196
2.4. Photophysical properties.....	197
2.5. $^1\text{O}_2$ generation .....	199
2.6. Phototoxicity studies and internalization kinetics .....	200
2.7. Internalization mechanism and intracellular distribution.....	202
2.8. Mitochondrial membrane damage .....	205
2.9. Photocatalytic oxidation of NADH.....	206
2.10. DNA interaction .....	207
2.11. Effect on cell cycle .....	208
2.12. Cell death mechanism .....	209
2.13. Clonogenic assays.....	211
<b>3. Conclusions</b> .....	212
<b>4. Synthesis and characterization</b> .....	214
4.1. Ligands.....	214
4.2. Ir(III)-complexes.....	215
<b>Bibliography</b> .....	219
<b>Chapter 3. Rational Design of Mitochondria Targeted Thiabendazole-based Ir(III) Biscyclometalated Complexes for a Multimodal Photodynamic Therapy of Cancer.</b> .....	229
<b>Authorship Statement</b> .....	229
<b>0. Abstract</b> .....	229
<b>1. Introduction</b> .....	230
<b>2. Results and discussion</b> .....	233
2.1. Synthesis of ligands and iridium(III) complexes .....	233
2.2. Characterization of the Ir(III)-compounds.....	234

2.3. Crystal structures by X-ray diffraction.....	235
2.4. Photostability experiments .....	237
2.5. Theoretical calculations.....	237
2.6. Electrochemical properties .....	239
2.7. Photophysical properties.....	242
2.8. Ability of <sup>1</sup> O <sub>2</sub> generation.....	244
2.9. Phototoxic activity and cellular uptake .....	245
2.10. Clonogenic assays.....	248
2.11. Internalization Mechanism and Intracellular Localization .....	249
2.12. Superoxide Production .....	252
2.13. Mitochondrial damage .....	253
2.14. Photocatalytic Oxidation of NADH .....	254
2.15. Reaction with DNA .....	256
2.16. Cell Death Mechanism.....	259
<b>3. Conclusions .....</b>	<b>260</b>
<b>4. Synthesis and characterization .....</b>	<b>261</b>
4.1. Bromides.....	261
4.2. Ligands.....	262
4.3. Ir(III)-complexes.....	265
<b>Bibliography.....</b>	<b>272</b>
<b>Part 2. Ru(II) and Ir(III) tris-chelate complexes for photocatalysis .....</b>	<b>281</b>
<b>Objectives.....</b>	<b>281</b>
<b>Photocatalysis.....</b>	<b>281</b>
<b>1. From catalysis to photocatalysis .....</b>	<b>285</b>
1.1. Catalysis.....	285
1.1.1. Historical development and definition.....	285
1.1.2. Main types of catalysis and applications.....	285
1.2. Photocatalysis.....	287
1.2.1. Historical development and definition.....	287

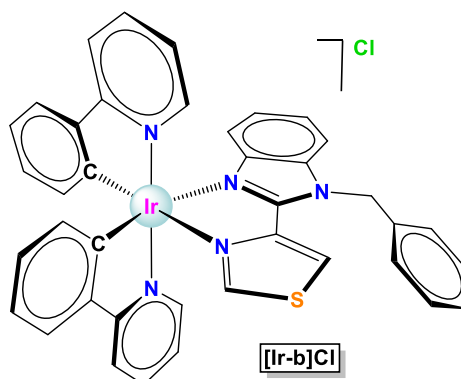
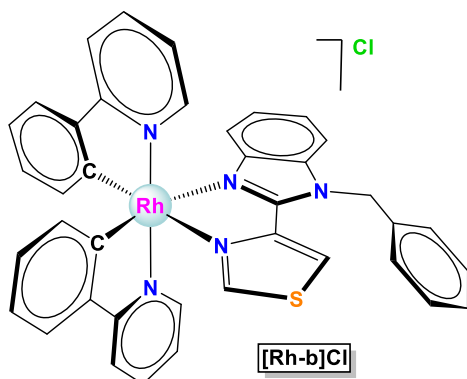
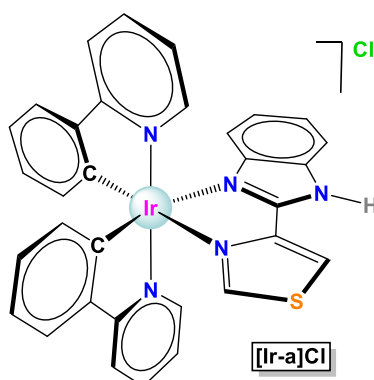
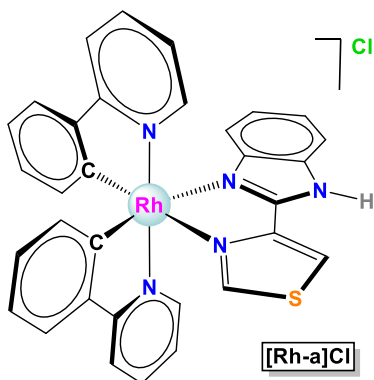
---

1.2.2. A brief view inside the mechanism .....	289
1.2.3. Main types of photocatalysis and applications .....	290
<b>2. Photocatalysis with Ir(III) and Ru(II) tris-chelate complexes .....</b>	<b>293</b>
<b>Bibliography .....</b>	<b>301</b>
<b>Chapter 4. Synthesis of <math>\alpha</math>-Amino Nitriles Through One-Pot Selective Ru-Photocatalyzed Oxidative Cyanation of Amines .....</b>	<b>311</b>
<b>0. Abstract .....</b>	<b>311</b>
<b>1. Introduction .....</b>	<b>312</b>
<b>2. Results and discussion .....</b>	<b>314</b>
2.1. Synthesis of ligands and ruthenium(II) complexes.....	314
2.2. Characterization of the Ru(II)-complexes.....	315
2.3. Crystal structure by X-ray diffraction .....	316
2.4. Photostability experiments .....	317
2.5. Theoretical calculations.....	318
2.6. Photophysical properties.....	320
2.7. Determination of singlet oxygen quantum yields .....	322
2.8. Electrochemical properties .....	323
2.9. Photooxidation of amines .....	325
2.10. One-Pot Photocatalytic Cyanation of Amines to produce $\alpha$ -amino nitriles...328	
2.11. Mechanism .....	330
<b>3. Conclusions .....</b>	<b>331</b>
<b>4. Synthesis and characterization .....</b>	<b>332</b>
4.1. Ru(II)-complexes.....	332
<b>Bibliography .....</b>	<b>336</b>
<b>Chapter 5. Photocatalytic Aerobic Dehydrogenation of N-Heterocycles with Ir(III) Photosensitizers Bearing the 2(2'-Pyridyl)benzimidazole Scaffold .....</b>	<b>343</b>
<b>0. Abstract .....</b>	<b>343</b>
<b>1. Introduction .....</b>	<b>344</b>

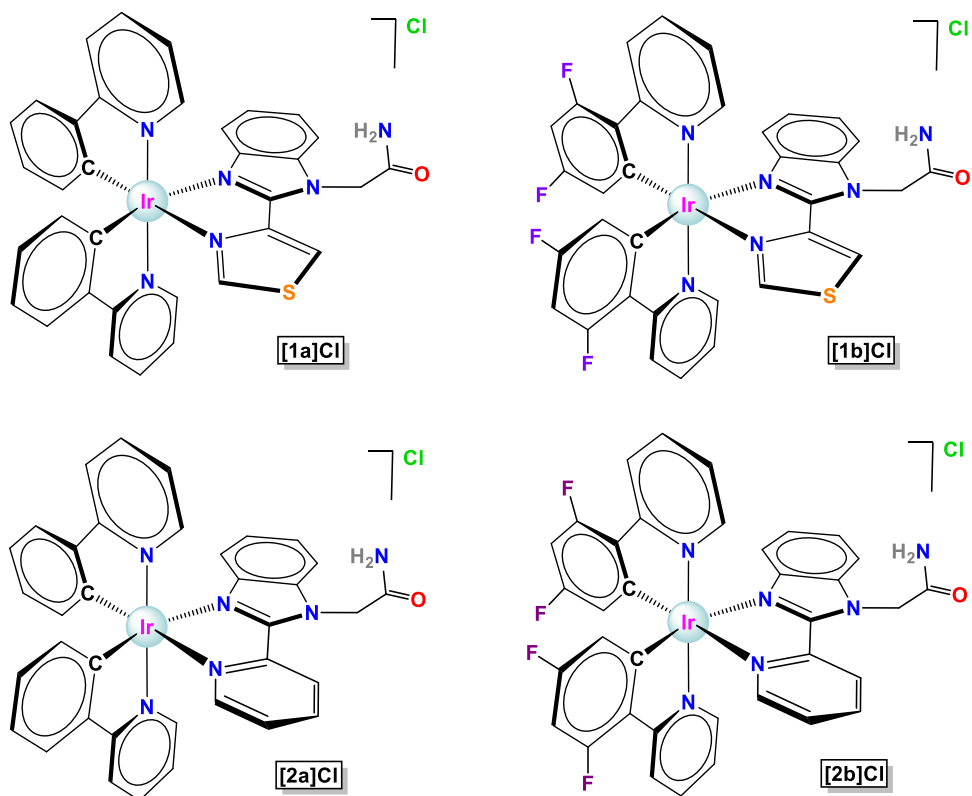
<b>2. Results and discussion</b> .....	345
2.1. Synthesis of Ligands and Iridium(III) Complexes .....	345
2.2. Characterization of the Ir(III) Complexes .....	347
2.3. Crystal Structure by X-ray Diffraction.....	347
2.4. Photostability Experiments .....	349
2.5. Theoretical Calculations .....	349
2.6. Photophysical Properties.....	352
2.7. Electrochemical Properties.....	354
2.8. Photocatalytic Activity in the Oxidation of Heterocycles .....	356
2.9. Mechanism .....	364
<b>3. Conclusions</b> .....	366
<b>4. Synthesis and characterization</b> .....	368
4.1. Ir(III)-complexes.....	368
<b>Bibliography</b> .....	373
<b>Final conclusions</b> .....	379
<b>Supporting information of the chapters</b> .....	USB flash drive

## Index of compounds

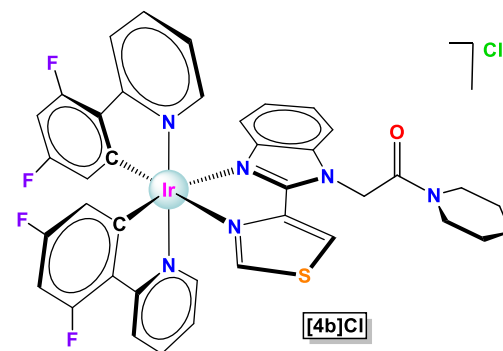
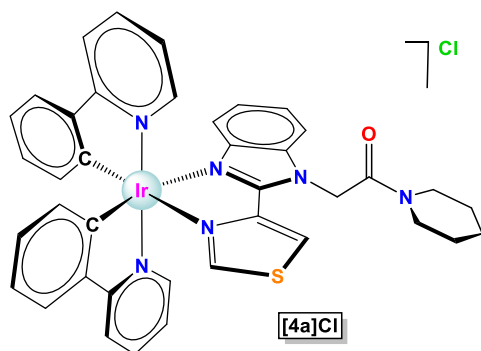
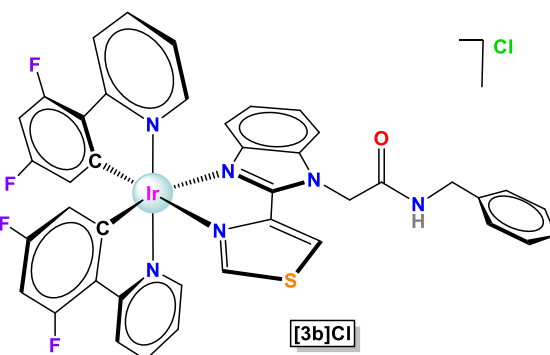
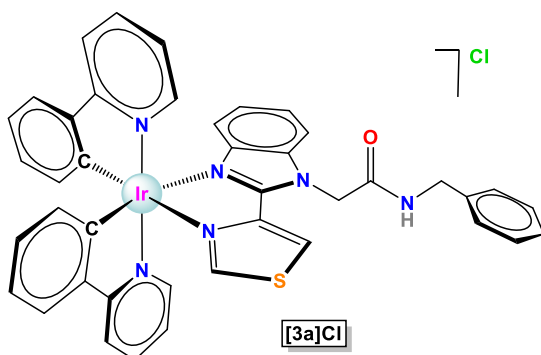
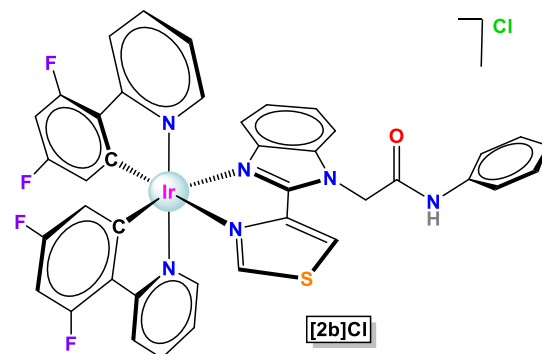
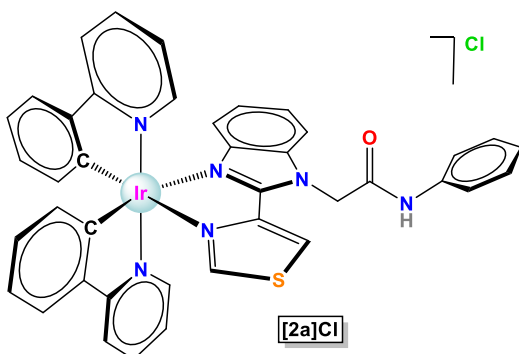
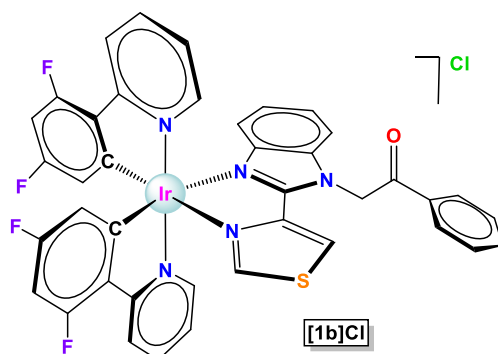
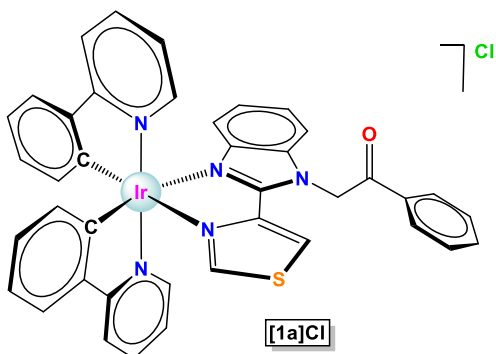
Chapter 1. Thiabendazole-based Rh(III) and Ir(III) Biscyclometalated Complexes with Mitochondria-Targeted Anticancer Activity and Metal-Sensitive Photodynamic Activity.



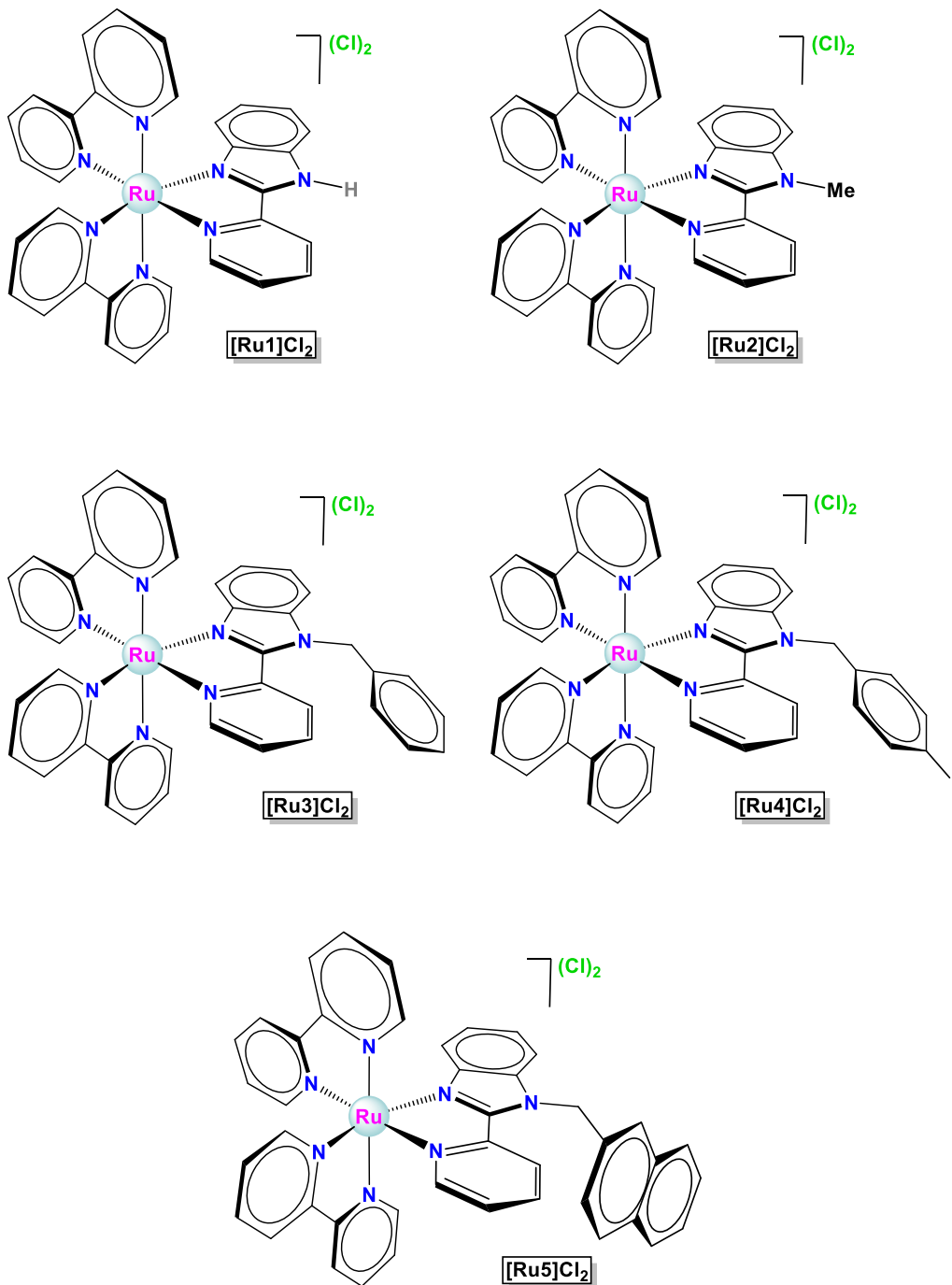
**Chapter 2. Photodynamic Therapy with Mitochondria-targeted Biscyclometalated Ir(III) Complexes. Multi-action Mechanism and Strong influence of the Cyclometalating Ligand.**

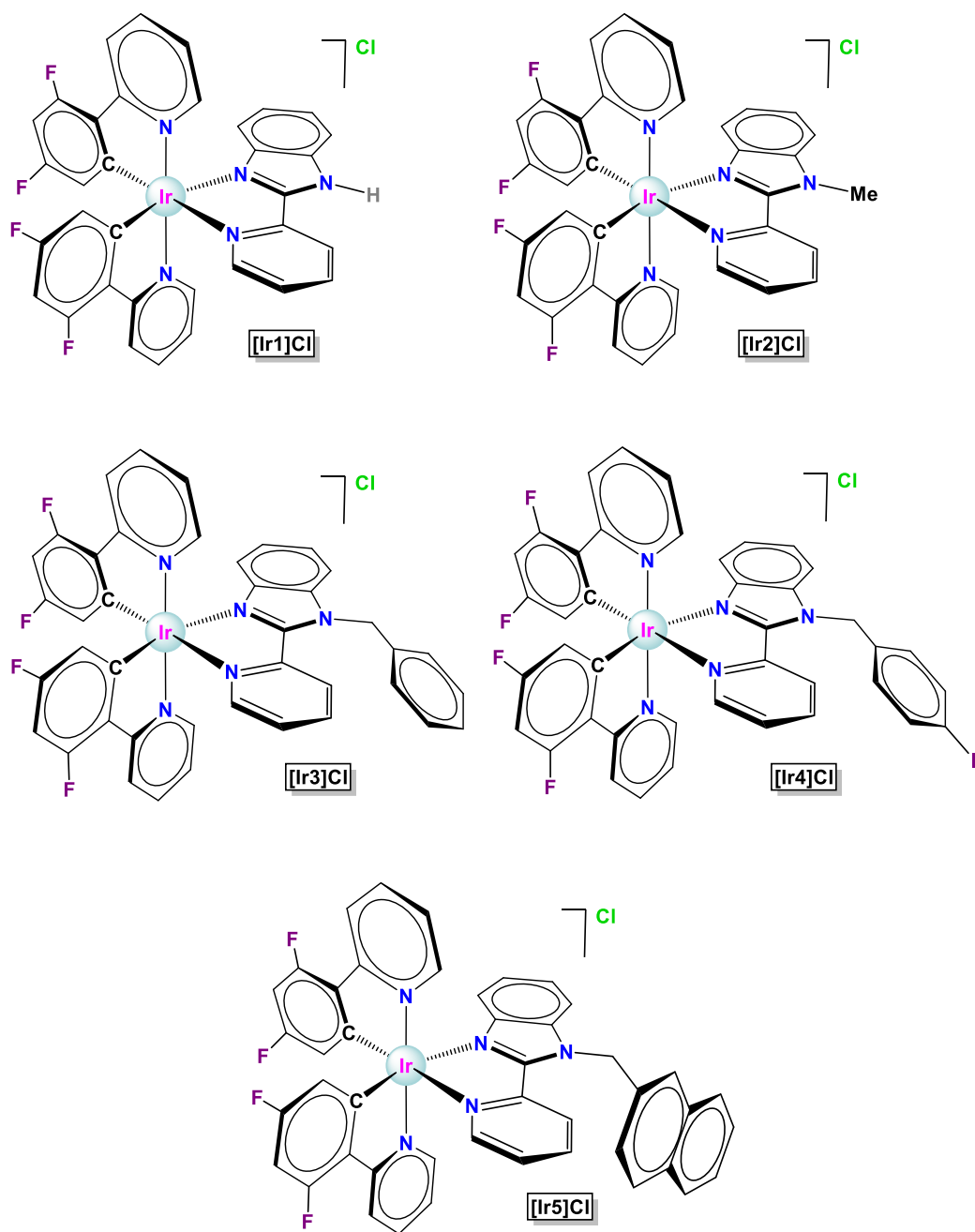




**Chapter 3. Rational Design of Mitochondria Targeted Thiabendazole-based Ir(III) Biscyclometalated Complexes for a Multimodal Photodynamic Therapy of Cancer.**

Chapter 4. Synthesis of  $\alpha$ -Amino Nitriles Through One-Pot Selective Ru-Photocatalyzed Oxidative Cyanation of Amines.



**Chapter 5. Photocatalytic Aerobic Dehydrogenation of N-Heterocycles with Ir(III) Photosensitizers Bearing the 2(2'-Pyridyl)benzimidazole Scaffold.**

## Abbreviations

### General abbreviations

**2-TQP** 5,10,15,20-Tetra(quinolin-2-yl)porphyrin

**5-PEP** 5-pyren-1-ylethynyl-1,10-phenanthroline

**A** Electron acceptor

**A** Adenine

**ABVD** Adriamycin, Bleomycin, Vinblastine and Dacarbazine

**acac** acetylacetonate

**AcOH** Acetic acid

**ACTB**  $\beta$ -actin

**AD** anno Domini

**ADCC** Antibody-Dependent Cell-Mediated Cytotoxicity

**ADH** Antidiuretic hormone

**ADH** Acceptorless dehydrogenation

**AIDS** Acquired immunodeficiency syndrome

**AIE** Aggregation Induced Emission

**AIQ** Aggregation Induced Quenching

**ALA** 5-Aminolaevulinic acid

**ALL** Acute lymphocytic leukemia / acute lymphoblastic leukemia

**AML** Acute myelogenous leukemia

**APL** Acute promyelocytic leukemia

**Asp** Asparagine

**ASS** Acetylsalicylic acid

**ATP** Adenosine triphosphate

**ATR** Attenuated Total Reflectance

**ATO** Arsenic trioxide

**Axi-cel** Axicabtagene ciloleucel

**BAs** Bile Acids

**BC** Before Christ

**Bcl-2** B-cell lymphoma 2

**Bcl-xL** B-cell lymphoma-extra large

**BDNF** Brain-derived neurotrophic factor

**BEOV** bis(ethylmaltolato)oxovanadium (IV)

**Bim** Benzimidazole

**BIOV**

bis(isopropylmaltolato)oxovanadium (IV)

**BMA** Bismethylamine

**BMOV** Bis(maltolato)oxovanadium (IV)

**Bn** Benzyl

**BODIPY** 4,4-difluoro-4-bora3a,4a-diaza-s-indacene

**bpz** 2,2'-bipyrazine

**bpy** 2,2'-bipyridine

**BQ** 1,4-Benzoquinone

**Bu** Butyl

**CAR-T** Chimeric-Antigen Receptor

**Cas9** CRISPR associated protein 9

**CB** Conduction band

**CBDCA** CycloButane DiCarboxylic Acid

**CBS** Colloidal bismuth subcitrate

**CCCP** carbonyl cyanide *m*-chlorophenyl hydrazone

**CCDC** Cambridge Crystallographic Data Centre

**CCR5** C-C chemokine receptor type 5

**CD4** Cluster of differentiation 4

**CD19** Cluster of differentiation 19

**CD80** Cluster of differentiation 80

**CD86** Cluster of differentiation 86

**CHOP** Cyclophosphamide, Hydroxydaunorubicin, Oncovin and Prednisone

**CHNS** Elemental Analysis

**cit** tetradeprotonated citric acid

**CLL** chronic lymphocytic leukemia

**CMF** Cyclophosphamide, Methotrexate, and Fluorouracil

**CML** Chronic myelogenous leukemia

**Cp** Cyclopentadienyl

<b>Cp*</b>	(1,2,3,4,5-Pentamethylcyclopentadiene)	<b>E</b>	Energy
<b>Cq</b>	Quantification cycle	<b>E</b>	Entgegen
<b>CRISPR</b>	Clustered regularly interspaced short palindromic repeats	<b>E</b>	Reduction potential
<b>CTL-4</b>	Cytotoxic T-lymphocyte-4	<b>EDTMP</b>	Ethylenediamine tetra(methylene phosphonic acid)
<b>CTLA4</b>	Cytotoxic T-lymphocyte-associated antigen 4	<b>Eg</b>	Energy gap
<b>Ctrl</b>	High affinity copper uptake protein 1	<b>EGFR</b>	epidermal growth factor receptor
<b>CV</b>	Cyclic voltammetry	<b>EMA</b>	European Medicines Agency
<b>CXCR-4</b>	C-X-C chemokine receptor type 4		en ethylenediamine
<b>Cys</b>	Cysteine	<b>EPR</b>	Enhanced permeability and retention
<b>D</b>	Electron donor	<b>ER</b>	Endoplasmic reticulum
<b>dab</b>	diaminobenzene	<b>ERK</b>	Extracellular signal-regulated kinase
<b>DABCO</b>	1,4-diazabicyclo[2.2.2]octane	<b>ESI</b>	Electrospray ionization
<b>dach</b>	1,2-diaminocyclohexane	<b>eT</b>	electron transfer
<b>DDQ</b>	2,3-Dichloro-5,6-dicyano-1,4-benzoquinone	<b>ET</b>	Energy transfer
<b>df(CF<sub>3</sub>)ppy</b>	2-(2,4-difluorophenyl)-5-(trifluoromethyl)pyridine	<b>ETC</b>	Electron transport chain
<b>DFMO</b>	α-difluoromethylornithine	<b>EY</b>	Eosin Y
<b>dfppy</b>	2-(2,4-difluorophenyl)pyridine)	<b>FA</b>	Folic Acid
<b>DFT</b>	Density functional theory	<b>FC</b>	Ferrocene
<b>DFX</b>	desferrioxamine	<b>FC<sup>+</sup></b>	Ferrocenium
<b>DHE</b>	dihematoporphyrin-ether	<b>FDA</b>	Food and Drug administration
<b>DHE</b>	Dihydroethidium	<b>FT-IR</b>	Fourier-transform infrared spectroscopy
<b>DLBCL</b>	Diffuse large B cell lymphoma	<b>G</b>	guanine
<b>DNA</b>	Deoxyribonucleic Acid	<b>GIST</b>	Gastrointestinal stromal tumour
<b>DO3A</b>	Tetraazacyclododecane triacetate	<b>Glu</b>	Glutamic acid
<b>DOTA</b>	Dodecane tetraacetic acid	<b>Gly</b>	Glycine
<b>Dp44mT</b>	di-2-pyridylketone-4,4,-dimethyl-3-thiosemicarbazone	<b>H2DCFDA</b>	2',7' dichlorodihydrofluorescein diacetate
<b>DPBF</b>	1,3-diphenylisobenzofuran	<b>HA</b>	Hyaluronic acid
<b>dppe</b>	1,2-diphenylphosphinoethane	<b>HDAC</b>	Histone deacetylases
<b>dpype</b>	1,2-dipyridylphosphinoethane	<b>HEDP</b>	1-Hydroxyethylidene-1,1-diphosphonic acid
<b>DSSC</b>	Dye-sensitized solar cell	<b>HER2/neu</b>	Human epidermal growth factor receptor 2
<b>dtbbpy</b>	4,4'-Di-tert-butyl-2,2'-bipyridine	<b>HMPAO</b>	Hexamethylpropylene amine oxime
<b>DTPA</b>	Diethylenetriaminepentaacetic acid	<b>HOMO</b>	Highest Occupied Molecular Orbital
		<b>HP</b>	Hydroxypropyl
		<b>Hp</b>	Hematoporphyrin

<b>HpD</b> Hematoporphyrin derivative	<b>MCTS</b> Multicellular spheroids
<b>HR</b> High Resolution	<b>MEK</b> Mitogen-activated protein kinase kinase
<b>MAG</b> Mercaptoacetyltriglycine	<b>Met</b> Methionine
<b>MFI</b> Mean Fluorescent Intensity	<b>MLCT</b> Metal to Ligand Charge Transfer
<b>MO</b> Molecular Orbital	<b>MMP</b> Matrix metalloproteinase
<b>HIV</b> Human immunodeficiency viruses	<b>MMP</b> Mitochondrial membrane potential
<b>HIV-1P</b> Human immunodeficiency viruses-1 protease	<b>MO</b> Molecular Orbital
<b>Hpybim</b> 2-pyridylbenzimidazole	<b>MOLs</b> Metal Organic Layers
<b>HSV</b> Herpes simplex virus	<b>MOPP</b> Mustargen, Oncovin, Procarbazine and Prednisone
<b>HVEM</b> Herpesvirus entry mediator	<b>MRI</b> Magnetic resonance imaging
<b>IC<sub>50</sub></b> Half maximal inhibitory concentration	<b>MRT</b> Molecular radiotherapy
<b>IgG</b> Immunoglobulin G	<b>MS</b> Mass Spectrometry
<b><sup>131</sup>I-MIBG</b> Metaiodo-benzylguanidine	<b>MT</b> Metallothionein
<b>IR</b> Infrared	<b>mtDNA</b> <b>mitochondrial</b> Deoxyribonucleic Acid
<b>Irr</b> Irreversible	<b>mTOR</b> Mammalian target of rapamycin
<b>ISC</b> Intersystem crossing	<b>NaCaC</b> Sodium Cacodylate
<b>iso</b> isonicotinate	<b>NAD (NADH/NAD<sup>+</sup>)</b> Nicotinamide adenine dinucleotide
<b>IUPAC</b> International Union of Pure and Applied Chemistry	<b>NAO</b> 10-N-nonyl acridine orange
<b>LC</b> Ligand Centred	<b>NBS</b> N-bromosuccinimide
<b>LEC</b> Light-Emitting Electrochemical Cell	<b>NHL</b> Non-Hodgkin's lymphoma
<b>LED</b> Light-Emitting Diode	<b>nic</b> nicotinate
<b>LFSE</b> Ligand-Field Splitting Energy	<b>NIR</b> Near infrared
<b>LLCT</b> Ligand to Ligand Charge Transfer	<b>NMR</b> Nuclear Magnetic Resonance
<b>LmACR2</b> Leishmania major ACR2	<b>NRD</b> Non-radiative decay
<b>LMCT</b> Ligand to Metal Charge Transfer	<b>NSCLC</b> Non-small cell lung carcinoma
<b>LMWCr</b> Low molecular weight chromium-binding substance	<b>OC</b> Open circular conformation
<b>LS</b> Low spin	<b>ODH</b> Oxidative dehydrogenation
<b>LUMO</b> Lowest Unoccupied Molecular Orbital	<b>OLED</b> Organic Light-Emitting Diode
<b>mAb</b> monoclonal antibody	<b>OPV</b> Organic photovoltaic devices
<b>madd</b> (1,12-bis((2-hydroxy-5-methoxybenzyl)-1,5,8,12-tetraazodecane))	<b>ORTEP</b> Oak Ridge Thermal Ellipsoid Plot
<b>MB</b> Methylene Blue	<b>OS</b> Oxidation state
<b>MC</b> Metal Centred	<b>Ox</b> oxidation
<b>MCF-7</b> Michigan Cancer Foundation-7	

<b>PAHs</b> polyaromatic hydrocarbons	<b>S</b> Substrate
<b>PC</b> Photocatalyst	<b>SBU</b> s Secondary Building Units
<b>PD1</b> Programmed cell death protein 1	<b>SC</b> Supercoiled conformation
<b>PDGFR</b> platelet-derived growth factor receptor	<b>SCE</b> Saturated calomel electrode
<b>PD-L1</b> Programmed death-ligand 1	<b>SCFR</b> Stem cell factor receptor
<b>PDT</b> Photodynamic Therapy	<b>SCLC</b> Small cell lung carcinoma
<b>PEG</b> Polyethylene glycol	<b>SCRf</b> Self-consistent reaction field
<b>PET</b> positron emission tomography	<b>sdAb</b> single-domain antibody
<b>Ph</b> phenyl	<b>SET</b> Single electron transfer
<b>Phen</b> (1,10-phenanthroline)	<b>SI</b> Supporting information
<b>PI</b> Photoindex	<b>SOC</b> Spin-Orbit Coupling
<b>PI</b> Propidium iodide	<b>SODIS</b> Solar water disinfection
<b>PLED</b> Polymer light-emitting diodes	<b>SPECT</b> Single-photon emission computed topography
<b>pLL</b> PEGylated liposomes	<b>SPI</b> Selective Phototoxicity Indexes
<b>PLQY</b> Photoluminescent quantum yield	<b>ssDNA</b> single-stranded DNA
<b>PMB</b> p-methoxybenzyl	<b>SSL</b> Solid-state Lighting
<b>PMT</b> Photomultiplier tube	<b>T</b> Triplet
<b>POMs</b> polyoxometalates	<b>T</b> T cell
<b>PPIX</b> Protoporphyrin IX	<b>TBZ</b> 2-(4'-thiazolyl)benzimidazole/thiabendazole
<b>ppy</b> 2-phenylpyridine	<b>TCSPC</b> Time-correlated single-photon counting
<b>prop</b> propionate	<b>TD-DFT</b> Time dependent density functional theory
<b>PS</b> Photosensitizer	<b>TEMPO</b> 2,2,6,6-Tetramethylpiperidin-1-yl)oxyl
<b>PSMA</b> Prostate-Specific Membrane Antigen	<b>Tf</b> Transferrin
<b>PTI</b> polyamine transport inhibitor	<b>TfR1</b> Transferrin receptor protein 1
<b>Py</b> Pyridine	<b>THQ</b> 1,2,3,4-tetrahydroquinoline
<b>Pybim</b> 2-(2-Pyridyl)benzimidazole	<b>TMRM</b> Tetramethylrhodamine
<b>QD</b> Quantum Dot	<b>TMSCN</b> Trimethylsilyl cyanide
<b>Q-TOF</b> Quadrupole Time of Flight	<b>TOF</b> Turn Over Frequency
<b>R</b> Reagent	<b>TON</b> Turn Over Number
<b>RB</b> Rose Bengal	<b>TPP</b> Tetraphenylporphyrin
<b>RBC</b> Ranitidine bismuth citrate	<b>UCNP</b> Upconverting nanoparticle
<b>Red</b> Reduction	<b>UV</b> Ultraviolet
<b>Rev</b> reversible	<b>UV-Vis</b> Ultraviolet-Visible
<b>RIGU</b> Rigid bond restraints	<b>VB</b> valence band
<b>RIM/RIR</b> Restriction of Intramolecular Motions/Rotations	<b>VEGF-A</b> Vascular endothelial growth factor A
<b>ROS</b> Reactive Oxygen Species	<b>v/v</b> Volume/volume
<b>RT</b> Room Temperature	<b><math>\Lambda_M</math></b> Molar Conductivity
<b>RT-qPCR</b> Real time quantitative polymerase chain reaction	
<b>S</b> Singlet	

**XEOL** X-ray Excited Optical  
Luminescence

**Z** zusammen

### NMR abbreviations

**{<sup>1</sup>H}** Decoupled Hydrogen

**br** broad

**COSY** Correlation Spectroscopy

**d** doublet

**HMBC** Heteronuclear Multiple  
Bond Correlation

**HSQC** Heteronuclear Single  
Quantum Correlation

**NOESY** Nuclear Overhauser Effect  
Spectroscopy

**q** quadruplet

**s** singlet

**sept** septuplet

**t** triplet

### IR abbreviations

**as** asymmetric

**br** broad

**ip** in plane

**m** medium

**oop** out of plane

**s** strong

**sym** symmetric

**vs** very strong

**w** weak

**δ** bending vibrational mode

**v** stretching vibrational mode





---

***The metals and the ligands***

---





## 1. Metals

For this work, three metals have been selected: ruthenium, rhodium and iridium. All of them are d-block transition metals, noble metals and belong to the platinum-group metals (Fig. 1), a group of six elements (ruthenium, rhodium, palladium, osmium, iridium, and platinum) which have similar physical and chemical properties and are usually found together in nature.<sup>1</sup>

**PERIODIC TABLE OF THE ELEMENTS**

The periodic table shows the following elements highlighted in green:

- Ruthenium (Ru, atomic number 44, atomic weight 101.07)
- Rhodium (Rh, atomic number 45, atomic weight 102.91)
- Iridium (Ir, atomic number 77, atomic weight 223.21)

Fig. 1. Periodic Table of the elements.

### 1.1. Ruthenium

Ruthenium (Ru) is a transition metal located in the group 8 and period 5 of the periodic table. It has an atomic number of 44 and an atomic weight of 101.07 u, and it is a silvery white solid at room temperature. Being the 74<sup>th</sup> most abundant element, is relatively rare, only about 12-30 tonnes are mined each year and the world reserves are estimated to be approximately 5,000 tonnes. In nature, ruthenium is found in ores with other platinum-group metals and is mostly obtained from the Ural Mountains and from North and South America. The main use for ruthenium is in the electronics industry for chip resistors and electrical contacts, close to 50% of the ruthenium extracted worldwide is used for this purpose.

The electronic configuration of ruthenium is  $[\text{Kr}]4d^75s^1$ . Naturally occurring ruthenium is composed of seven stable isotopes:  $^{96}\text{Ru}$  (5.52%),  $^{98}\text{Ru}$  (1.88%),  $^{99}\text{Ru}$  (12.7%),  $^{100}\text{Ru}$  (12.6%),  $^{101}\text{Ru}$  (17.0%),  $^{102}\text{Ru}$  (31.6%),  $^{104}\text{Ru}$  (18.7%). Additionally, 34 radioactive isotopes

have been discovered. Ruthenium displays a wide variety of oxidation states, from 0 to +8, and also -2, although the most common are +2, +3 and +4. In this introduction, we will focus on Ru(II), because it is the oxidation state of ruthenium in our complexes; ruthenium(II), with octahedral geometry, has a LS (low spin)  $d^6$  ( $t_{2g}^6$ ) electronic configuration, being diamagnetic, and hence, suitable to be characterized by NMR spectroscopy, which is very useful.<sup>2,3,4,5,6</sup>

## 1.2. Rhodium

Rhodium (Rh) is a transition metal located in the group 9 and period 5 of the periodic table. It has an atomic number of 45 and an atomic weight of 102.91 u, and it is a silvery white solid at room temperature. Rhodium is one of the rarest elements (only 0.0002 ppm in the Earth's crust), which affects its price, being the most expensive metal; only about 20-30 tonnes are mined each year and the world reserves are unknown. In nature, rhodium is usually found in ores with other metals such as palladium, silver, platinum, and gold, and it is mostly obtained from South Africa, the Ural Mountains and North America. The main use of this element is found in automobiles as a catalytic converter, around an 80% of the extracted rhodium is used for this application.

The electronic configuration of rhodium is  $[Kr]4d^85s^1$ . Naturally occurring rhodium is composed of only one stable isotope,  $^{103}\text{Rh}$  (100%). Additionally, 24 radioactive isotopes have been discovered, the most stable of which are  $^{99}\text{Rh}$ ,  $^{101}\text{Rh}$ ,  $^{102}\text{Rh}$ , and  $^{102m}\text{Rh}$ . Rhodium has a wide variety of oxidation states, going from 0 to +6, and also -1 and -3, being +2 and +3 the most common. We will focus on Rh(III), because it is the oxidation state of rhodium in our complexes. Rhodium(III), with octahedral geometry, has a LS  $d^6$  ( $t_{2g}^6$ ) electronic configuration, being diamagnetic, and hence, suitable to be characterized by NMR, which is very advantageous.<sup>2,3,4,5,6</sup>

## 1.3. Iridium

Iridium (Ir) is a transition metal located in the group 9 and period 6 of the periodic table. It has an atomic number of 77 and an atomic weight of 192.22 u, and it is a silvery white solid at room temperature. Iridium is one of the nine least abundant stable elements in Earth's crust (0.001 ppm in crustal rock; it is found in meteorites in higher abundance), only about 5-10 tonnes are mined each year and the world reserves are unknown. In the nature, iridium is usually found in ores with platinum and osmium, and is mostly obtained from South Africa, Alaska and Russia. The main use of iridium is in the manufacture of alloys (often combined with platinum) for special purposes: spark plugs used in helicopters, electrical contacts, special types of electrical wires, electrodes, etc.

The electronic configuration of iridium is  $[\text{Xe}]4f^{14}5d^76s^2$ . Naturally occurring iridium is composed of only two isotopes:  $^{191}\text{Ir}$  (37.3%) and  $^{193}\text{Ir}$  (62.7%). Additionally, 37 radioactive isotopes have been discovered, being  $^{192}\text{Ir}$  the most stable, with a half-life of 73.83 days. Iridium has a wide variety of oxidation states, going from 0 to +9, and also -1 and -3, although the oxidation states +3 and +4 are the most common. We will focus on Ir(III), because it is the oxidation state of the iridium in our complexes; iridium(III), with octahedral geometry, has a LS  $d^6$  ( $t_{2g}^6$ ) electronic configuration, being diamagnetic, and hence, also suitable to be characterized by NMR.<sup>2,3,4,5,6</sup>

## 2. Ligands

As ancillary ligands we have chosen benzimidazole (Fig. 2) based compounds because of their excellent coordination abilities and their bioactive properties. Benzimidazoles are aromatic heterocyclic compounds, which can be seen as a benzo derivatives of imidazole.<sup>7,8</sup>

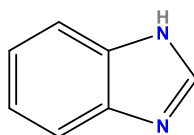


Fig. 2. Benzimidazole

The therapeutic potential of benzimidazole was first studied by Woolley in 1944, when he speculated that benzimidazole can act in a similar way to purines to elicit some biological responses. Over the years, benzimidazole has evolved and proved itself like an important pharmacophore due to its presence in a wide range of bioactive compounds. The optimization of its diverse pharmacological activities is usually accomplished through modification of the substituents around the benzimidazole scaffold. Indeed, this strategy has allowed to obtain a wide variety of drugs. Thus, benzimidazoles are found in drugs displaying a wide variety of activities: antimicrobial (albendazole), antiviral (envirodine, maribavir), antiparasitics (thiabendazole), antifungals (benzimidazole, thiabendazole), anticancer (nocodazole, veliparib), antiprotozoal (albendazole), analgesic (benitramide), antiulcer (omeprazole), antihistaminic (astemizole, lerisetron), antihypertensive (candesartan, telmisartan) and proton pump inhibitors (omeprazole, lansoprazole, pantoprazole) among others (Fig. 3).<sup>7,9,10</sup>

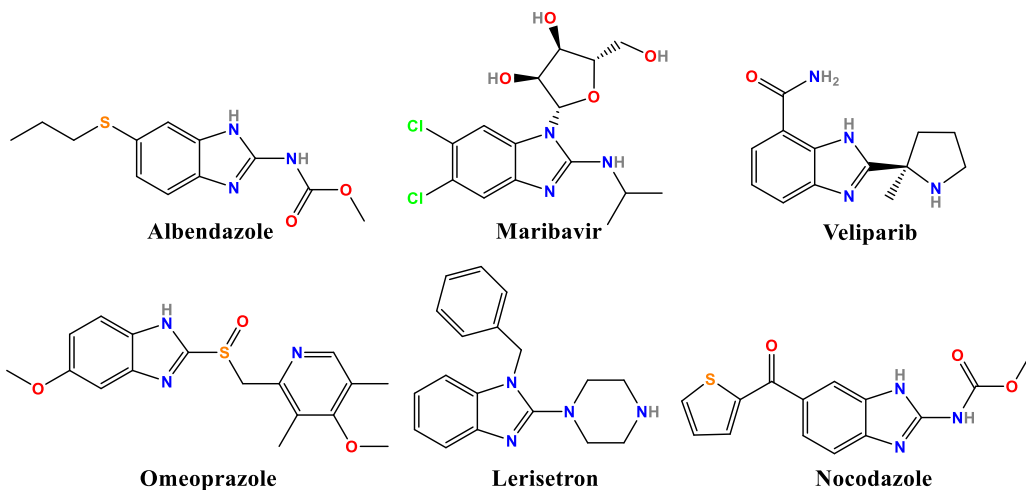


Fig. 3. Examples of drugs with a benzimidazole scaffold.

It is also worth mentioning that 5,6-dimethyl-benzimidazole is present in the structure of vitamin B12 (Fig. 4).<sup>7,10</sup>

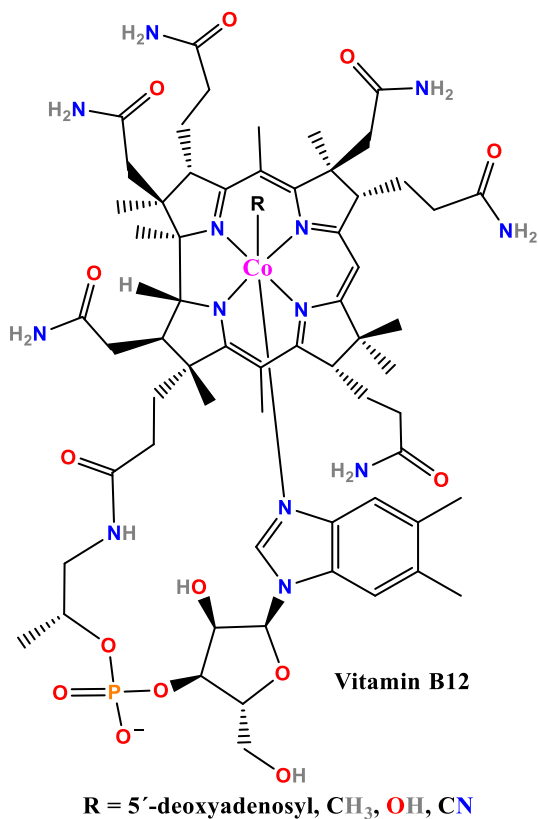
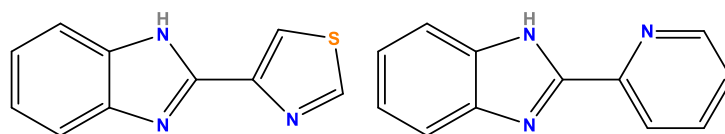


Fig. 4. Vitamin B12.

In order to produce bidentate ligands capable of coordinating to a metal centre by two donor atoms, benzimidazole can be linked to other suitable heterocycle scaffolds through the 2-position. Thus, thiazole and pyridine were selected yielding thiabendazole and pyridylbenzimidazole respectively (Fig. 5). Thiabendazole, 2-(4'-thiazolyl)benzimidazole (TBZ) is a colourless, odourless compound which was first discovered in the 1960s and exhibits fungicide, parasiticide and chelating properties, along with rapid absorption upon ingestion. It has wide applicability in several domains, from veterinary and human medicine, and also pharmaceutical sciences, to agriculture and food industry.<sup>11,12,13</sup>

Pyridylbenzimidazole, 2-(2'-pyridyl)benzimidazole (Pybim) is a white to brown compound which has several applications in medicine because of its nematocidal and phytotoxic activities, its analgesic activity and its urease inhibitory activity.<sup>14,15,16</sup>



*Fig. 5. Thiabendazole and pyridylbenzimidazole ligands.*

## Bibliography

1. M. L. Zientek, P. J. Loferski, H. L. Parks, R. F. Schulte, and R. R. Seal II, Platinum-group elements (No. 1802-N), *US Geological Survey*, 2017.
2. P. Atkins, and T. Overton, *Shriver and Atkins' inorganic chemistry*, Oxford University Press, USA, 2010.
3. C. E. Housecroft, and A. G. Sharpe, *Inorganic Chemistry*, Fourth edition, Pearson, 2012.
4. F.A. Cotton, and G. Wilkinson, *Advanced inorganic chemistry. A comprehensive text*. Estados Unidos, Wiley and sons Ltd, 1980.
5. N. N. Greenwood, and A. Earnshaw, *Chemistry of the Elements*, Second Edition, Butterworth Heinemann, 1997.
6. E. Constable, *Comprehensive coordination chemistry II: from biology to nanotechnology* Newnes, 2003.
7. a) I. M. Madawali, E. N. Gaviraj, N. V. Kalyane, and B. Shivakumar, A review on substituted benzimidazoles: biologically active compounds, *Am. J. Pharm. Tech. Res.*, 2019, **9**, 256-274. b) P. M. K. Prasad, A. Kanvinde, S. Raja, Potent biological agent benzimidazole—a review, *Int. j. pharm.*, 2016, **8**, 22-33.
8. T. Y. Fonkui, *Schiff Bases: Synthesis, Characterization and Antimicrobial Properties*. University of Johannesburg (South Africa), 2018.
9. Y. Bansal, and O. Silakari, The therapeutic journey of benzimidazoles: A review, *Bioorg. Med. Chem.*, 2012, **20**, 6208–6236.
10. Salahuddin, M. Shaharyar, and Avijit Mazumder, Benzimidazoles: A biologically active compounds, *Arab. J. Chem.*, 2017, **10**, S157–S173.
11. H. J. Robinson, H. F. Phares, and O. E. Graessle, The Toxicological and Antifungal Properties of Thiabendazole, *Ecotoxicol. Environ. Saf.*, 1978, **1**, 471-476.
12. a) A. M. Tabanez, B. A. Nogueira, A. Milani, M. E. S., Eusébio, et al., Thiabendazole and Thiabendazole-Formic Acid Solvate: A Computational, Crystallographic, Spectroscopic and Thermal Study, *Molecules*, 2020, **25**, 3083. b) R. Ouyang, W. Li, L. Wang, M. Yao, S. Du, and Y. Wang, Solubility measurement and data correlation of thiabendazole in 12 pure organic solvents from 283.15 to 323.15 K, *J. Chem. Eng. Data*, 2020, **65**, 5055-5061.
13. T. Fujitani, M. Yoneyama, A. Ogata, T. Ueta, K. Mori and H. Ichikawa, New metabolites of thiabendazole and the metabolism of thiabendazole by mouse embryo in vivo and in vitro, *Fd. Chem. Toxic.*, 1991, **29**, 265-274.
14. A. Kamil, S. Akhter, M. Ahmed3, G. H. Rizwani, et al., Chemical and Biological Studies of 2-(2'-pyridyl) Benzimidazole and Its Synthesized Derivatives, *VRI Biol. Med. Chem.*, 2013, **1**, 51-56.
15. A. Kamil, S. Akhtar, A. Khan, E. Farooq, U. Nishan, R. Uddin, and U. Farooq, Synthesis, structure–activity relationship and antinociceptive activities of some 2-(2'-pyridyl) benzimidazole derivatives, *Med. Chem. Res.*, 2016, **25**, 1216–1228.
16. Z. S. Saify, A. Kamil, S. Akhtar, M. Taha, et al., 2-(2'-Pyridyl) benzimidazole derivatives and their urease inhibitory activity, *Med. Chem. Res.*, 2014, **23**, 4447–4454.





---

***Tris-chelate complexes:  
Synthesis, structure,  
properties and applications***

---





# 1. Synthetic procedures

## 1.1. Iridium and rhodium complexes

There are two general types of cyclometalated tris-chelate Ir(III) and Rh(III) compounds: **(a) Neutral homoleptic complexes**, with three identical cyclometalated ligands, whose general formula is  $[M^{III}(C^{\wedge}N)_3]$  ( $M = Ir/Rh$ ), where  $C^{\wedge}N$  stands for the cyclometalated ligands, and **(b) Heteroleptic complexes**, with only two identical cyclometalated ligands, whose general formula is  $[M^{III}(C^{\wedge}N)_2(X^{\wedge}X)]^{n+}$  ( $M = Ir/Rh$ ), where  $C^{\wedge}N$  stands for the cyclometalated ligands and  $X^{\wedge}X$  for a variety of chelate ligands, such as N,N-donors, O,O-donors etc.<sup>1</sup> This work is focused in the latter, which are commonly called bis-cyclometalated Ir(III) or Rh(III) complexes.

For the synthesis of bis-cyclometalated Ir(III) and Rh(III) complexes of general formula  $[M^{III}(C^{\wedge}N)_2(N^{\wedge}N)]^+$  ( $M = Ir/Rh$ ;  $N^{\wedge}N =$  neutral N,N-donor ligand) we follow a two-steps procedure:

1. Synthesis of the chloride-bridged dimeric starting materials  $[(C^{\wedge}N)_2M^{III}(\mu-Cl)_2M^{III}(C^{\wedge}N)_2]$  ( $M = Ir, Rh$ ). As described by Nonoyama<sup>2</sup> and Sprouse,<sup>3</sup> the metal salt,  $IrCl_3 \cdot nH_2O$  or  $RhCl_3 \cdot nH_2O$  ( $n \approx 3$ ), is reacted with the cyclometalated pro-ligand ( $HC^{\wedge}N$ ), 2-phenylpyridine (ppy) or 2-(2,4-difluorophenyl)pyridine (dfppy), which suffers spontaneous deprotonation, in a solvent mixture of 2-ethoxyethanol and water (3:1; v/v) and refluxed for 24 hours under a nitrogen atmosphere to yield the product. In the case of 2-(2,4-Difluorophenyl)pyridine), reaction conditions change slightly: 2-methoxyethanol is used instead of 2-ethoxyethanol, and the reaction time is extended to 60 hours (Fig. 1).

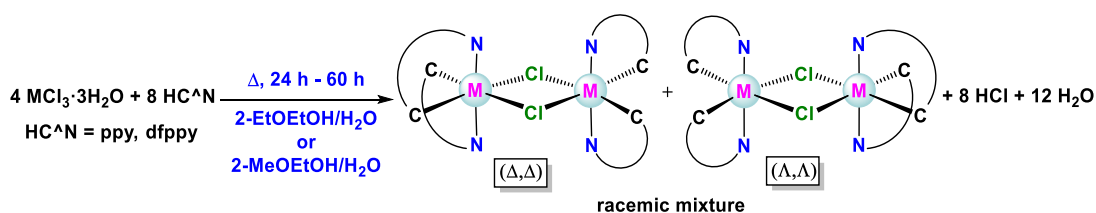


Fig. 1. Synthetic procedure for the dinuclear chlorido-bridged complexes ( $M = Ir, Rh$ ).

2. Synthesis of the bis-cyclometalated cationic compounds of formula  $[M^{III}(C^{\wedge}N)_2(N^{\wedge}N)]^+$  ( $M = Ir/Rh$ ). In the second step, the dimer obtained from the first step is reacted with an ancillary ligand of the diimine type ( $N^{\wedge}N$ ) in a mixture of dichloromethane and methanol (1:1.25; v/v) and refluxed for 24 hours under a nitrogen atmosphere to yield the desired product (Fig. 2).<sup>4</sup>

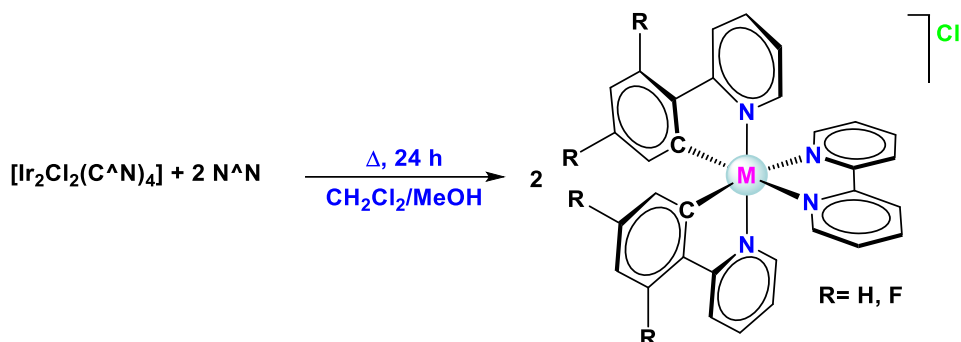


Fig. 2. Synthetic procedure for the bis-cyclometalated cationic compounds ( $M = \text{Ir}, \text{Rh}$ ).

## 1.2. Ruthenium complexes

There are two general types of Ru(II) trischelate compounds: (a) homoleptic complexes, with formula  $[\text{Ru}^{\text{II}}(\text{N}^{\wedge}\text{N})_3]^{2+}$ , where the three diimine  $\text{N}^{\wedge}\text{N}$  ligands are identical, and heteroleptic complexes, where two of the  $\text{N}^{\wedge}\text{N}$  ligands are the same and the third ligand is different ( $[\text{Ru}^{\text{II}}(\text{N}^{\wedge}\text{N})_2(\text{N}^{\wedge}\text{N}')]^{2+}$ ).<sup>5</sup> This work will be focused on heteroleptic derivatives.

For the synthesis of Ru(II) complexes of general formula  $[\text{Ru}^{\text{II}}(\text{N}^{\wedge}\text{N})_2(\text{N}^{\wedge}\text{N}')]^{2+}$ , where all the N,N ligands are neutral, we follow a two-steps procedure:

1. Synthesis of the bis-diimine dichloride starting materials  $[\text{Ru}^{\text{II}}(\text{N}^{\wedge}\text{N})_2\text{Cl}_2] \cdot 2\text{H}_2\text{O}$ . As described by Meyer<sup>6</sup> and Sprintschnik,<sup>7</sup> the metal salt,  $\text{RuCl}_3 \cdot n\text{H}_2\text{O}$  ( $n \approx 3$ ), is reacted with the diimine ligand ( $\text{N}^{\wedge}\text{N}$ ) of interest, for instance 2,2'-bipyridine (bpy), in dimethylformamide as solvent, in the presence of lithium chloride, and refluxed for 3 hours to yield the product after recrystallization in acetone (Fig. 3).

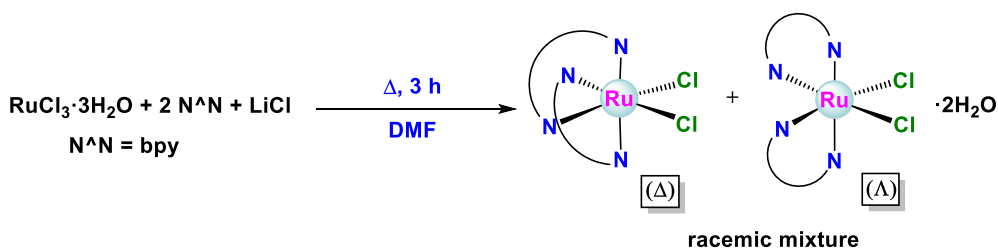


Fig. 3. Synthetic procedure for the ruthenium bis-diimine dichloride complexes.

2. Synthesis of the tris-chelate cationic compounds of general formula  $[\text{Ru}^{\text{II}}(\text{N}^{\wedge}\text{N})_2(\text{N}^{\wedge}\text{N}')]^{2+}$ . In the second step, the dichloro complex obtained in the first step is reacted with a diimine ancillary ligand ( $\text{N}^{\wedge}\text{N}'$ ) in ethanol and refluxed for 4-20 hours to yield the product (Fig. 4).<sup>6,7</sup>

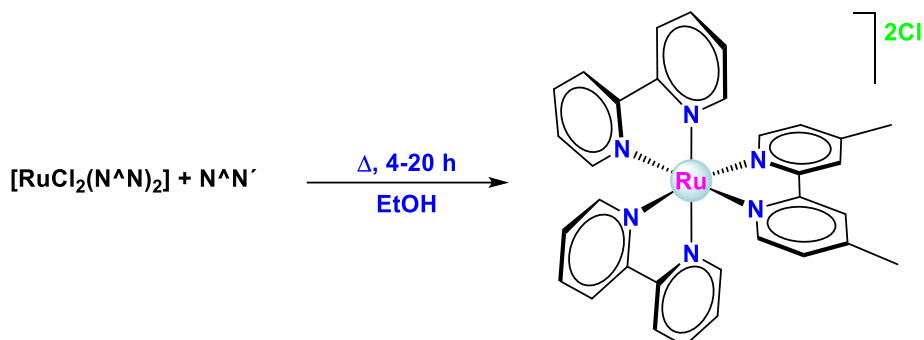


Fig. 4. Synthetic procedure for ruthenium tris-chelate dicationic compounds.

## 2. Structure of the complexes

All the products described above can present different configurations, depending on the disposition of the ligands and the type of product. So, they present stereoisomerism (*cis*- and *trans*-isomers) and/or enantiomerism ( $\Delta$  and  $\Lambda$  isomers), also known as optical isomerism.<sup>3,8,9,10,11</sup>

### 2.1. Iridium and rhodium complexes

Regarding stereoisomerism, both iridium and rhodium chloride-bridged dimeric starting materials, and iridium and rhodium bis-cyclometalated compounds present a *trans*-N,N *cis*-C,C configuration (Fig. 5). This is due to the strong *trans* effect of the C atoms bonded to the metal centre, which prevents the mutual *cis*-C,C coordination and favours the coordination of the N atoms *trans* to them.<sup>3,8,10</sup>

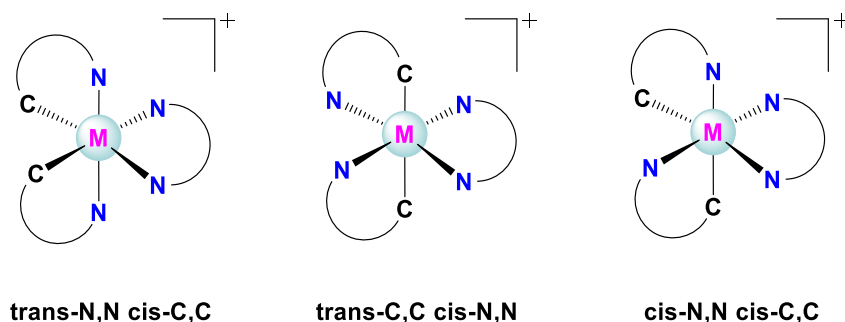


Fig. 5. Possible stereoisomers for iridium and rhodium compounds ( $M = Ir, Rh$ ).

Tris- and bis-chelate octahedral iridium and rhodium compounds present helical chirality (chirality derived from the geometry of a helix), where the metallic atom is considered as the stereocentre. This determines the presence of 2 enantiomers,  $\Delta$  and  $\Lambda$ , which are present in a racemic mixture (50:50). To assign the absolute configuration descriptors, the turning sense of the helix has to be taken into account.

If the turning is clockwise, the enantiomer is  $\Delta$ , and if it is anticlockwise, the enantiomer is  $\Lambda$  (Fig. 6).<sup>3,8,9,10</sup>

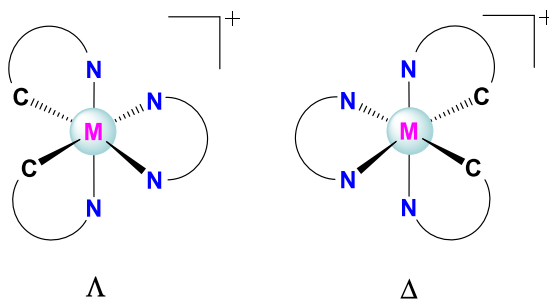


Fig. 6.  $\Lambda$  and  $\Delta$  enantiomers for iridium and rhodium tris-chelate complexes ( $M = Ir, Rh$ ).

The starting materials possess a structure based in 2 units with an octahedral coordination environment, with two cyclometalated ligands per unit and two chloride bridges, and therefore, they possess 2 stereogenic elements per molecule due to the helical chirality of each half of the molecule. So there are 3 possible isomers: the racemic mixture formed by the couple of enantiomers ( $\Delta, \Delta$ ) and ( $\Lambda, \Lambda$ ) and the meso form ( $\Delta, \Lambda$ ) (Fig. 7). Nevertheless, in the practice, the racemic mixture is favoured due to the internal steric hindrance between the  $C^{\wedge}N$  ligands associated to the meso form.<sup>3,8,9,10</sup>

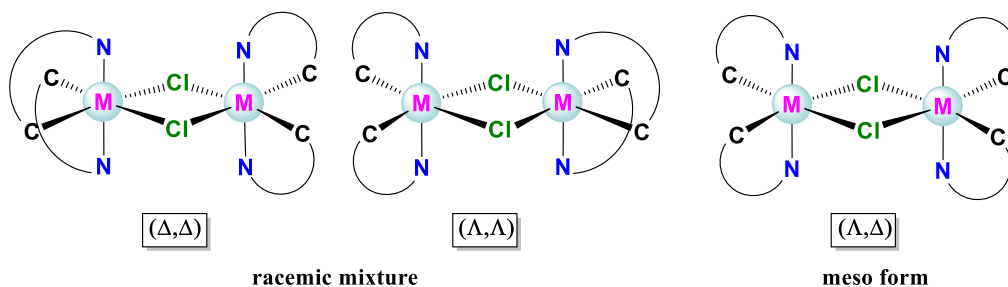


Fig. 7. Possible stereoisomers for the iridium and rhodium starting materials ( $M = Ir, Rh$ ).

## 2.2. Ruthenium complexes

In the case of the ruthenium derivatives, both the dicationic compounds and the neutral starting materials present helical chirality as well. Both present an octahedral coordination environment with 2 bipyridines, and an ancillary ligand for the dicationic compounds or 2 chloride anions for the starting materials. This provides helical chirality to the complexes, being the ruthenium atom the stereogenic centre, which leads to the presence of 2 enantiomers  $\Delta$  and  $\Lambda$ , that are present in a 1:1 ratio in the form of a racemic mixture (Fig. 8).<sup>9,10,11</sup>

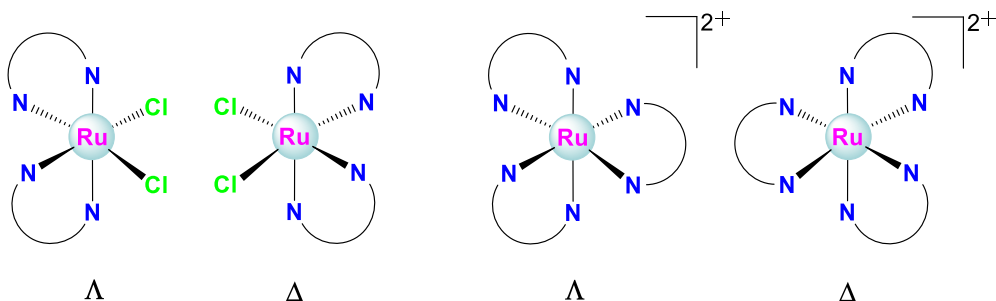


Fig. 8.  $\Delta$  and  $\Lambda$  enantiomers for ruthenium starting materials (left) and mononuclear compounds (right).

### 3. A theoretical insight into luminescence

Before starting the discussion of the properties of the tris-chelate complexes, I would like to present an introduction about the luminescence phenomenon.

#### 3.1. Absorption spectra

Many compounds of d-block metals can absorb light in the visible region of the electromagnetic spectrum. Thereby, the study of their absorbance spectra provides structural information. The interpretation of these spectra is not always straightforward, yet it is important to note that the different absorption bands correspond to electronic transitions between different energy levels (between different molecular orbitals (MOs)). These transitions can be of 2 types:<sup>9</sup>

- a) **d-d transitions:** electronic transitions between orbitals with essentially metallic character (d orbitals).
- b) **Charge transfer transitions:** electronic transitions between MOs centred in the metal and MOs centred in the ligands or vice versa. They imply a charge transfer from the metal to the ligand (MLCT) or vice versa (LMCT).

The absorbed energy corresponds to the energy consumed in the transition from a ground state to an electronically excited state, which is governed by the selection rules of electronic spectroscopy that establish the following:<sup>9</sup>

- a) **Spin selection rule:** the transitions between electronic states with different spin multiplicity are forbidden, in other words, only those electronic transitions that proceed without change in the spin of the excited electron are allowed (e.g.  $S_0 \rightarrow S_1$  or  $T_0 \rightarrow T_1$ ).
  - a. **Singlet state.** It is a molecular electronic state in which the electronic spins are paired. According to the Pauli Exclusion Principle, a pair of electrons that are in the same energy level must have opposite spins.

**b. Triplet state.** It is a molecular electronic state in which the electronic spins are not paired, that is, there are 2 electrons with parallel spins, or having the same spin.

- b) Laporte selection rule:** only electronic transitions involving  $\Delta l = \pm 1$  ( $s \rightarrow p$ ,  $p \rightarrow d$ ,  $d \rightarrow f$ ) are allowed; so that the electronic transitions involving  $\Delta l = 0$  (between orbitals of the same type:  $s \rightarrow s$ ,  $p \rightarrow p$ ,  $d \rightarrow d$ ,  $f \rightarrow f$ ); or  $\Delta l = \pm 2$  ( $s \rightarrow d$ ,  $p \rightarrow f$ ) are forbidden.

However, in practice there are two singular mechanisms that allow the observation of some forbidden transitions either by the spin selection rule or by the Laporte selection rule.<sup>9</sup>

- a) **Spin-orbit coupling (SOC).** This type of coupling causes the partial mixing of states with different spin multiplicities, and consequently makes possible some transitions between orbitals with different theoretical spin multiplicities. The resulting transitions are called intersystem crossing (ISC) processes.
- b) **Vibronic coupling.** In general, although some d-d transitions may be allowed by spin, they are forbidden by the Laporte selection rule. However, in complexes with octahedral geometry, which are centrosymmetric, the vibrations experienced by the molecules cause momentary loss of the centre of symmetry, which makes possible a transitory mixture of d and p orbitals. Since the lifetime of the vibrations ( $10^{-13}$  s) is longer than that of an electronic transition ( $10^{-18}$  s), it is possible to observe d-d transitions between orbitals that have a certain **pd** character, although the intensity of the absorption is weak. In non-centrosymmetric molecules (e.g. molecules with tetrahedral geometry) the mixing of p-d orbitals takes place to a greater extent and the probability of d-d transitions is higher, and therefore the absorption and colour are more intense.<sup>9</sup>

### 3.2. Emission spectra

The various processes of relaxation from an excited electronic state to another more stable state or to the ground state are represented in the adapted Jablonski diagram shown in Fig. 9:<sup>9,12,13,14</sup>

- a) **Deactivation by photochemical reactions**, which cause the degradation or decomposition of the original molecule.
- b) **Quenching by interaction with other species** present in solution. This type of deactivation may involve an energy transfer process ( $A^* + B \rightarrow A + B^*$ ) or an electron transfer process that causes the oxidation or the reduction of the excited molecule ( $A^* + B \rightarrow A^+ + B^-$  or  $A^* + B \rightarrow A^- + B^+$ ).
- c) **Radiative deactivation or luminescence:** This process involves the relaxation of an excited electronic state as a result of the emission of visible light (electromagnetic radiation). Two types of processes are distinguished depending on its particular mechanism.



- a. **Fluorescence.** Radiative relaxation process between 2 states with the same spin multiplicity. It is a process allowed by the spin selection rule and therefore it is fast (ns).
  - b. **Phosphorescence.** Radiative relaxation process between 2 states with different spin multiplicity. It is a process forbidden by the spin selection rule and therefore it is usually slow ( $\mu\text{s}$ ), and can even persist after the excitation has ended. This process implies a previous ISC process (see below).
- d) **Non-radiative deactivation:** these are decay processes between 2 electronic states that occur with loss of thermal energy and without the emission of photons. Two types are distinguished based on the spin multiplicity of the excited and ground states.
- a. **Internal conversion or deactivation by vibrational relaxation,** when the process takes place between states with the same state of molecular spin or multiplicity. The energy of the excited state is transferred to vibrational modes of the molecule and transformed into heat.
  - b. **Deactivation through intersystem crossing (ISC).** It is a non-radiative relaxation process that takes place between electronic states with different spin multiplicities. From a singlet state to a triplet state for example.

Therefore, the processes of fluorescence and internal conversion are spin-allowed, while phosphorescence and intersystem crossing are spin-forbidden. Each deactivation process is characterized by a rate constant and each excited state by a lifetime. In addition, for luminescent processes, a parameter called photoluminescent quantum yield (PLQY or  $\phi_{\text{PL}}$ ) can be defined, as the ratio between the photons emitted by luminescence and the photons absorbed, expressed as a percentage of one or one hundred. In other words, it represents the probability that an excited state is deactivated by a luminescent process (fluorescence or phosphorescence). All these processes compete with each other and are shown schematically in the following Jablonski diagram (Fig. 9).<sup>9,12,13,14</sup>

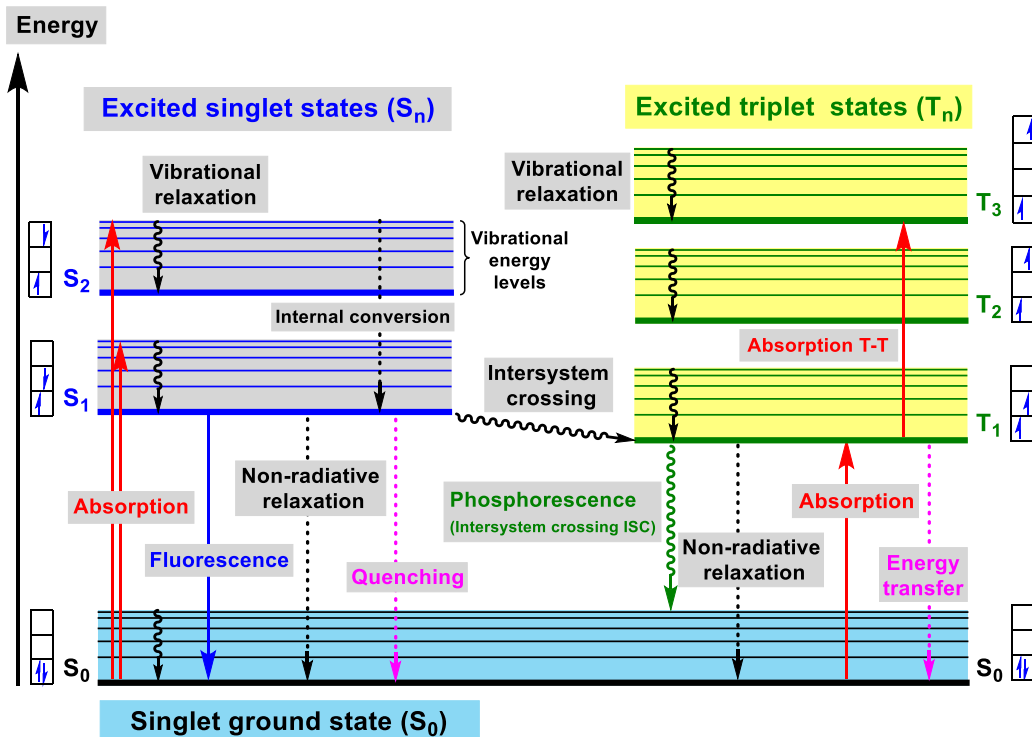


Fig. 9 Adapted Jablonski diagram. Time scale for the different processes: Absorbance ( $10^{-15}$  s), Vibrational relaxation and Internal conversion ( $10^{-11}$  to  $10^{-14}$  s); Non-radiative relaxation ( $10^{-5}$  to  $10^{-7}$  s); Fluorescence ( $10^{-7}$  to  $10^{-9}$  s); phosphorescence ( $10^{-3}$  to 100 s); Intersystem crossing ( $10^{-8}$  to  $10^{-10}$  s).

## 4. Properties

In complexes with octahedral geometry, as a result of the ligand field, the five d orbitals of the d-block transition metals are split into 2 sets of degenerate orbitals: three stabilized  $t_{2g}$  orbitals ( $d_{xy}$ ,  $d_{xz}$ ,  $d_{yz}$ ), and two destabilized  $e_g$  orbitals ( $d_{z^2}$ ,  $d_{x^2-y^2}$ ), with respect to the degenerate situation for the free ion in the gaseous state. The difference in energy between these two levels,  $\Delta_o$ , depends on several factors:<sup>15,16</sup>

- The size of the d orbitals:  $\Delta_o$  increases with the increasing size of the d orbitals ( $\Delta_o(3d) < \Delta_o(4d) < \Delta_o(5d)$ ).
- The oxidation state (EO) of the metal centre: the higher the EO, the greater the value of  $\Delta_o$ .
- The intensity of the ligands field according to the spectrochemical series (see below).

Ru(II), Rh(III) and Ir(III) possess a  $4d^6$ ,  $4d^6$  and  $5d^6$  electronic configurations respectively. So, in complexes with an octahedral geometry, like the tris-chelate complexes, they present a low spin electronic configuration,  $t_{2g}^6e_g^0$ , where all the  $t_{2g}$  orbitals are fully

occupied and the  $e_g$  orbitals are fully unoccupied due to high value of  $\Delta_o$  (see Fig. 10).<sup>15,16</sup>

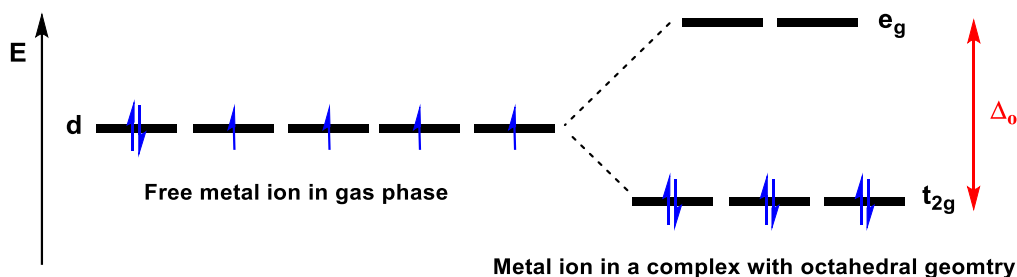


Fig. 10. Electronic configuration for a metal ion in gas phase and in a complex with octahedral geometry, according to the crystal field theory (CFT).

The spectrochemical series of both metals and ligands are very useful to get a qualitative idea of the value of  $\Delta_o$  for different compounds, due to the fact that they summarize in a rational way the 3 factors mentioned above (factors a and b are included in the spectrochemical series of the metals and factor c in the ligands series).

#### Spectrochemical series for ligands:<sup>17</sup>

$\text{CO} > \text{CN}^- > \text{PPh}_3 > \text{NO}_2^- > \text{SO}_3^{2-} > \text{phen} > \text{bpy} > \text{en} > \text{NH}_3 > \text{py} > \text{CH}_3\text{CN} > \text{ONO}^- > \text{NCS}^- > \text{OH}_2 > \text{C}_2\text{O}_4^{2-} > \text{ONO}_2^- > \text{OSO}_3^{2-} > \text{OCHO}^- > \text{OH}^- > \text{OCO}_2^{2-} > \text{OCOR}^- > \text{S}_2\text{O}_3^{2-} > \text{F}^- > \text{N}_3^- > \text{Cl}^- > \text{SCN}^- > \text{S}^{2-} > \text{Br}^- > \text{I}^-$

#### Spectrochemical series for metals:<sup>17</sup>

$\text{Pt}^{4+} > \text{Ir}^{3+} > \text{Pd}^{4+} > \text{Ru}^{3+} > \text{Rh}^{3+} > \text{Mo}^{3+} > \text{Mn}^{4+} > \text{Co}^{3+} > \text{Fe}^{3+} > \text{V}^{2+} > \text{Fe}^{2+} > \text{Co}^{2+} > \text{Ni}^{2+} > \text{Mn}^{2+}$

The 3 metals studied in this thesis have a high  $\Delta_o$ , being Ir(III) the one with a greater value of  $\Delta_o$  followed by Rh(III) and then by Ru(II) (even if Ru(II) does not appear in the series, it should have a  $\Delta_o$  value slightly lower than that for Rh(III), because both have a **4d** orbital, but Rh(III) exhibits a higher Oxidation State than Ru(II)). Regarding the ligands, it is more difficult to make a comparison, but it is clear that N^N ligands, as it can be seen for bpy (2,2'-Bipyridine) or phen (1,10-phenanthroline), have high values for  $\Delta_o$ , which is due to their strong  $\sigma$ -donor and  $\pi$ -acceptor properties that stabilize the electronic configurations. Moreover, even though C^N are not present in the series, they are very strong-field ligands and provide very high  $\Delta_o$  values for their respective complexes.<sup>15,16</sup> So, it can be rationally stated that the Ru(II), Rh(III) and Ir(III) tris-chelate complexes of this nature will possess high values of  $\Delta_o$ .

Possessing a high  $\Delta_o$  is an important feature regarding the photophysical properties because it implies that metal centred (MC) excited states are less accessible and are less populated than metal ligand charge transfer (MLCT) excited states, so non-radiative deactivation processes are less probable. The MC excited states in  $d^6$

octahedral complexes are strongly distorted along the vibrational coordinates of the M-ligand bond compared with the ground state. So, when the excited state of lowest energy is MC, the complex undergoes non-radiative deactivation processes to the ground state and/or ligand dissociation. Because of this, the lifetime of the excited state is very short and no luminescent processes are observed. On the contrary, if the lower energy excited states exhibit LC (ligand centred) or MLCT character, the geometric distortion is small, and the complexes do not undergo rapid non-radiative decay processes. In this case, it is possible to observe luminescent processes (except at high temperature, at which MC states are more populated).<sup>12,15</sup>

However, there are other factors that affect the photophysical properties. In the case of Ru(II) and Rh(III), even if their respective  $\Delta_o$  values are high and their excited state of lowest energy possess a MLCT nature, they usually have a MC excited state close to it in energy which is thermally accessible, so there is a non-radiative competitive deactivation mechanism which affects importantly, and negatively, the photophysical properties of the complexes of these metals.<sup>15,18,19</sup> Taking this into account, it is obvious that Ir(III), *a priori*, possesses the best photophysical properties, which are extraordinary, by far.<sup>20,21</sup> So, when discussing the properties below, we will focus mainly on those for Ir(III) biscyclometalated tris-chelate complexes.

Ir(III) biscyclometalated tris-chelate complexes possess a variety of extraordinary and advantageous physical and photophysical properties compared with organic fluorophores and other organometallic compounds which are:<sup>20,21</sup>

- a) **High thermal, chemical and photochemical stability.** This is due to the high strength of the Ir-L bonds, specially the Ir-C ones, thanks to their strong  $\sigma$ -donor character with a covalent nature. This remarkable stability, which is superior to that of its analogues of the 1<sup>st</sup> and 2<sup>nd</sup> transition series, makes these complexes stable after long periods of irradiation or several electrochemical cycles.<sup>16,20,21,22,23</sup>
- b) **Extraordinary internal quantum efficiency (luminescent efficiency)** thanks to several features:
  1. **High spin-orbit coupling (SOC):** The SOC of an electron is the electromagnetic interaction that occurs between the electronic spin and the magnetic field generated by the orbit of the electron around the nucleus.<sup>24</sup> Iridium has the highest SOC of all the elements of the d block ( $\xi_{Ir} = 3909 \text{ cm}^{-1}$ , compared to  $\xi_{Fe} = 431 \text{ cm}^{-1}$ ,  $\xi_{Ru} = 1042 \text{ cm}^{-1}$ ,  $\xi_{Os} = 3381 \text{ cm}^{-1}$ <sup>16</sup> and  $\xi_{Rh} = 1425 \text{ cm}^{-1}$ ),<sup>23</sup> which causes, as stated before, the partial mixing of states with different spin multiplicities, this in turn implies that when an iridium complex is promoted to one of the excited singlet states ( $S_n$ ), the ISC is so efficient that it can be considered unitary.<sup>15,16,23</sup>
  2. **High Stokes shifts:** The Stokes shift is the difference between the wavelength of the maximum of the absorption band and the wavelength of the maximum of the emission band. In other words, it is

the difference in energy between the photon absorbed and the photon emitted by a compound as a result of the loss of a certain amount of energy through vibrational relaxation processes (fluorescence) or ISC (phosphorescence), before the return to the ground state.<sup>21</sup> In the case of fluorogenic organic compounds the Stokes shifts are very small, since the excited state resulting from absorption and the excited state from which emission takes place are usually the same ( $S_1$ ). Hence, there is an important overlap between the absorption and emission spectra resulting in self-absorption processes (self-quenching) which involves a loss in emission intensity. However, in organometallic compounds, especially in Ir(III) compounds, the Stokes shifts are large, due to ISC (after absorption the excitation leads to a singlet state but the emission takes place from a triplet state) and therefore self-absorption processes are rare, yielding to small emission intensity losses, which translates into a higher luminescent efficiency.<sup>21,22</sup>

3. **High  $\Delta_0$ :** This implies as explained before, that MC excited states are less accessible and are less populated than MLCT excited states, so non-radiative deactivation processes are less probable.<sup>15</sup>
  4. **High molecular rigidity:** This feature is associated with the octahedral geometry, which reduces the molecular vibrations and thereby the possibilities of non-radiative transitions and collisional heat losses.<sup>25</sup>
- c) **Long lifetimes for emission processes.** Phosphorescent compounds are characterized by the long lifetimes of the emissive excited state ( $\mu\text{s}$ ), compared to the lifetimes of fluorescent molecules (ns).<sup>22</sup> This fact represents a significant advantage for the use of these compounds in Bioimaging techniques, since it allows to eliminate the background fluorescence produced by biological molecules, which is based in short-lived processes.<sup>21,23</sup> However, this feature can also have drawbacks, since long lifetimes make quenching of excited states more likely (e.g. triplet excited states of transition metal complexes can be efficiently quenched by molecular oxygen present in solution).<sup>23</sup>
- d) **Versatility in modulating the colour of the emitted light.** The modulation of the colour of the emitted light (the wavelength of the maximum of the emission band) is accomplished by varying the energy gap between the HOMO and the LUMO, which can be achieved easily in this type of complexes.<sup>15,20</sup> This happens thanks to the fact that the HOMO and the LUMO are located in different parts of the complex: the HOMO is located in the Ir(III) metal centre and the phenyl rings of the C<sup>^</sup>N ligands, and the LUMO in the ancillary ligand (usually the N<sup>^</sup>N ligand).<sup>15,16,21,26</sup> So, it is easy to tune the colour of the emitted light by independent chemical modifications in the different parts of the complex,<sup>15,21</sup> which can also affect other photophysical properties like the lifetimes and the quantum yields. The two general procedures employed to modify this type of compounds are: (a) Installation of electron-withdrawing groups within the C<sup>^</sup>N ligands to decrease the  $\sigma$ -donor character, which in turn decreases the

electronic density over the Ir(III) metal centre, leading to a net stabilization of the HOMO; and (b) addition of electron donating groups to the ancillary ligand (or use of electron-rich ancillary ligands) to destabilize the LUMO.<sup>15</sup> Regardless the method, an increase in the HOMO-LUMO bandgap is produced along with a blue-shift in the emission wavelength. Fig. 11 shows the effect on the emission wavelength caused by different biscyclometalated and ancillary ligands independently in typical Ir(III) complexes.<sup>15,27,28</sup>

Moreover, these complexes also present some other interesting properties associated with phosphorescence:

- **Mechanochromism:** is a phenomenon where the material shows changes in the emission colour in the presence of a mechanical stimuli like rubbing, grinding, shearing, etc. It is caused by the interruption of molecular interactions such as  $\pi$ - $\pi$  stacking and hydrogen bonds.<sup>26</sup>
- **Piezochromism:** in this case, the material manifests variations in the emission colour when pressure is applied, usually by a grinding process. It can be understood like a variant of mechanochromism where the external stimuli that triggers the change in the emission is pressure. It has been proposed that piezochromism is caused by crystalline-amorphous phase transformations that occur in the process of grinding. The process can be reversible by heat or solvent treatments.<sup>29,30</sup>
- **Electrochromism:** this property is associated to changes suffered by the material in the emission colour (or the opacity) when a voltage is applied. It is caused by a non-homogeneous distribution of the ions which leads to the formation of a strong internal electric field that can polarize some bonds of the material.<sup>26</sup>
- **Solvatochromism:** this event is associated with changes in the emission colour of the material depending on the solvent in which is dissolved. This occurs due to the different effects caused by different solvents on the electronic ground and excited states of the material, which ultimately affect the energy gap between them. The main solvent-related factors affecting the energy gap of the material are the hydrogen bonding capacity and the dielectric constant.<sup>31</sup>
- **Vapochromism:** it can be defined as the changes suffered by the material in its emission colour by exposure to volatile organic compounds or gases. It is closely related to solvatochromism.<sup>32</sup>
- **Halochromism:** this is a phenomenon where a material shows changes in the emission colour when pH changes occur. It is related with groups or motifs which can suffer protonation or deprotonation processes, which affects their electron donating or withdrawing capacity and consequently modifies the HOMO-LUMO band gap.<sup>33,34</sup>

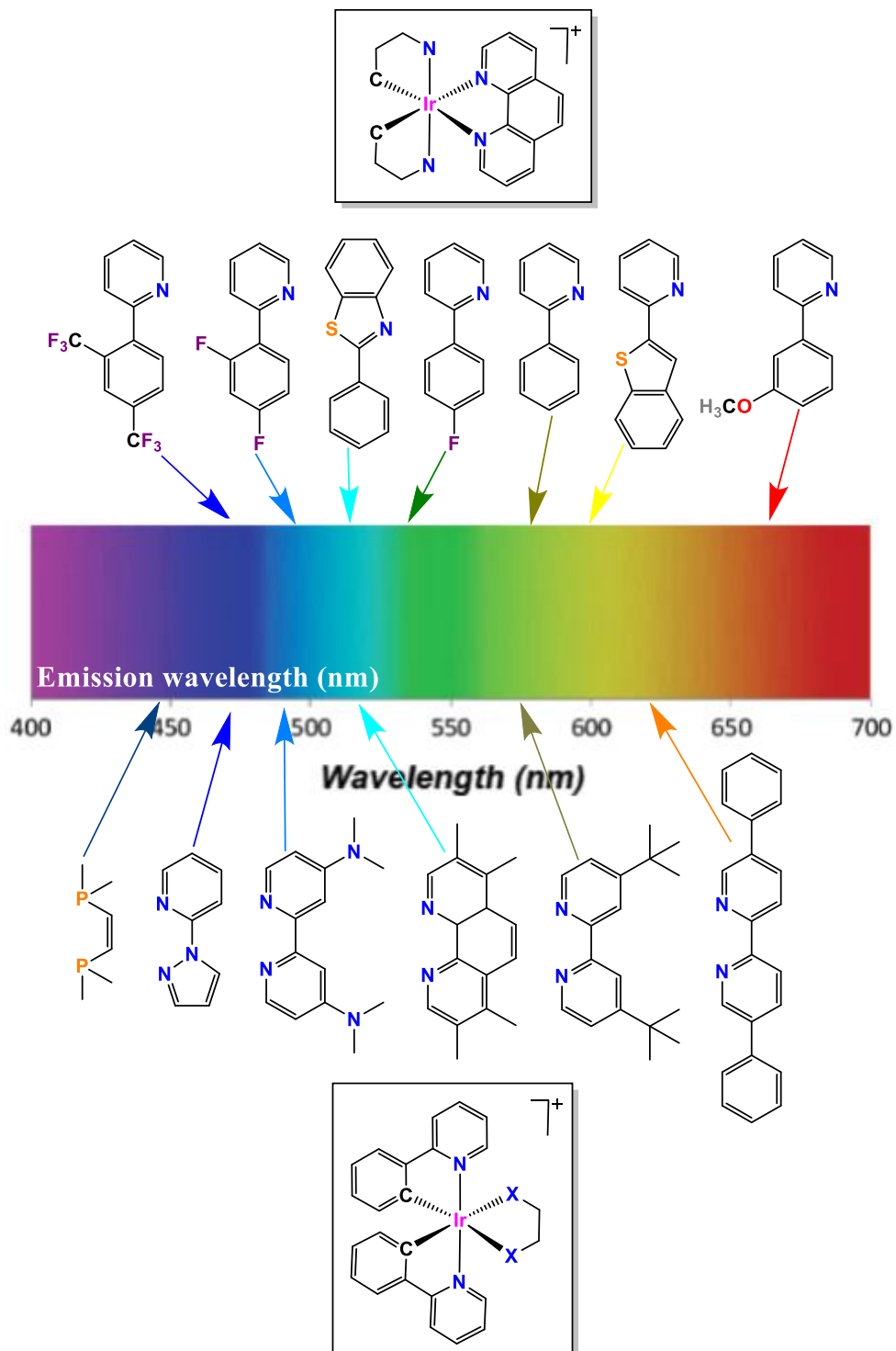


Fig. 11. Effect on the emission wavelength of several typical Ir(III) complexes depending on the electronic features of their ligands.

## 5. Applications

As expected from the outstanding properties of Ir(III), Rh(III) and Ru(II) tris-chelate complexes, they are suitable for a wide range of applications:

- **Photodynamic therapy (PDT).** PDT is a medical strategy used for the treatment of skin and ophthalmic diseases, and also in anticancer and antibacterial protocols. It has important benefits, since it is a minimally invasive treatment compared to surgery, it can be targeted specifically (minimizing of systemic toxicity) and it avoids long-term side effects that are common in other therapies.<sup>35,36</sup> PDT is based on the interaction of three elements: the photosensitizer (PS), the light source and oxygen. Its mechanism of action involves the following steps: under a suitable light irradiation, the PS (which ideally is non-toxic) absorbs one photon of light and is promoted to a singlet excited state ( $^1\text{PS}^*$ ), then it suffers a partial relaxation to a triplet excited state ( $^3\text{PS}^*$ ) by an intersystem crossing (ISC) process;  $^3\text{PS}^*$  can interact with  $\text{O}_2$  in its fundamental state, which is a triplet ( $^3\text{O}_2$ ), generating the superoxide radical anion  $\text{O}_2^{\cdot-}$  (type I mechanism), or alternatively singlet oxygen  $^1\text{O}_2$  (type II mechanism). These species belong to a class of very reactive oxygen derivatives, known as Reactive Oxygen Species (ROS), which are able to oxidize essential biomolecules like DNA and proteins and induce cellular damage and death in an efficient and selective way.<sup>37,38</sup> Indeed, Ir(III),<sup>39,40,41</sup> Rh(III)<sup>41</sup> and Ru(II)<sup>42,43</sup> tris-chelate complexes, have shown promising capacities for this purpose.
- **Photocatalysis.** Tris-chelate metal complexes can act as photoredox catalysts. They can absorb visible light to be promoted to electronic excited states which can act as excellent oxidants or reductants. Moreover, these complexes usually have long-lived excited states, and their properties are easily modified by varying the ligands attached to the metal core. This makes them suitable to act as photocatalysts in a variety of chemical transformations under very mild conditions (i. e. room temperature).<sup>23,44,45</sup> For example, Ir(III) and Ru(II) organometallic complexes can catalyse dehalogenations,<sup>46,47</sup> alkylations,<sup>47,48,49</sup> trifluoromethylations,<sup>23,47,50</sup> benzylations,<sup>51,52</sup> [2+2] cycloadditions,<sup>44,53,54</sup> photopolymerizations,<sup>55</sup>  $\text{CO}_2$  reduction.<sup>56,57</sup> In fact, photocatalysis is recognised as an useful tool for a greener organic synthesis, since it allows to employ light as endless energy source and to reduce side-products.<sup>47</sup>
- **Solid-state lightning (SSL).** It is a type of lightning that consists in using semiconductors to convert electricity into light in contrast with the conventional lightning devices, which create light either from electrically heated metal filaments (incandescence), or plasma and gases encased in a glass bulb with very low efficiency. In SSL, there are 3 main types of devices: light-



emitting diodes (LEDs), organic light-emitting diodes (OLEDs; they can also be converted into light-emitting electrochemical cells (LECs) by adding mobile ions to OLEDs), or polymer light-emitting diodes (PLED).<sup>58</sup> Ir(III) and Ru(II) tris-chelate complexes have found applicability as OLEDs<sup>59,60,61</sup> and LECs.<sup>59,62,63</sup> Moreover Ru(II) compounds can also be used in LEDs as phosphorescent dopants<sup>64</sup> and Ir(III) compounds as coating for light conversion.<sup>65</sup> It is also remarkable that Ir(III) compounds can also be used for PLEDs,<sup>66,67</sup> covering the whole range of lightning sources. In the case of Rh(III) compounds, their application is restricted to doped thin films for OLEDs.<sup>68</sup>

- **Fluorogenic probes.**

1. **pH sensors.** Ir(III) and Ru(II) polypyridine complexes containing an acidic or basic functional group on the ligands can be used as pH sensors due to the changes in the emission properties caused by the loss or the binding of a proton to the functional polypyridine ligand.<sup>69,70</sup>
2. **Cation sensors.** The main strategy for the development of these sensors involves the incorporation of a receptor, like a Lewis base or a crown ether into the Ir(III) or Ru(II) polypyridine complex. The complexes of these metals are able to detect a wide variety of cations like  $\text{Fe}^{2+}$ ,  $\text{Fe}^{3+}$ ,  $\text{Pb}^{2+}$ ,  $\text{Zn}^{2+}$ ,  $\text{Cu}^{2+}$ ,  $\text{Ni}^{2+}$ ,  $\text{Cd}^{2+}$ ,  $\text{Ca}^{2+}$ ,  $\text{Mg}^{2+}$ ,  $\text{Ba}^{2+}$ ,  $\text{Na}^+$ ,  $\text{Ag}^+$  and  $\text{Cu}^+$ .<sup>69,71</sup> They are also capable of detecting  $\text{Hg}^{2+}$  when adding sulphur atoms to the ligands by a soft-soft interaction between the sulphur atom and the  $\text{Hg}^{2+}$ .<sup>69,72</sup> The detection mechanism for cation sensors is based on the fact that the addition of these ions leads to a dramatic change in the absorption and/or emission properties (partial or total emission quenching and shifting of absorption or emission bands; more rarely emission intensity enhancement has also been observed).<sup>69</sup>
3. **Anion sensors.** In the case of using Ir(III) or Ru(II) complexes designed to detect anions, it is important to consider that the binding of anions to the ligands can significantly affect the emission properties of the complexes, giving place not only to quenching and shifting phenomena in the emission, but important colour changes in the solution due to both electronic effects and chemical reactions between the anion and the complex. In particular, different photosensitizers have been described for the detection of  $\text{CN}^-$ ,  $\text{F}^-$ ,  $\text{Cl}^-$ ,  $\text{Br}^-$ ,  $\text{I}^-$ ,  $\text{NO}_3^-$ ,  $\text{ClO}_4^-$ , and  $\text{HSO}_4^-$ .<sup>69,73</sup>
4. **Oxygen sensors.** The luminescence of the Ir(III) and Ru(II) polypyridine complexes is effectively quenched by oxygen, allowing them to act as oxygen sensors. This occurs due to the interaction between the triplet excited state of the photosensitizer and the triplet ground state of oxygen, through an energy transfer mechanism. For this purpose, Ir(III) complexes are of particular interest because they perfectly match the

criteria for oxygen sensors: high emission quantum yields, long emission lifetimes, high sensitivity, high reversibility and fast response time.<sup>69,74,75</sup>

5. **Biomolecule sensors.** Nucleotides, DNA, proteins and amino acids can be easily detected by tuning the functional groups in the ligands of Ir(III) and Ru(II) complexes. The binding of these biomolecules with the complexes can be readily followed by changes in the emission properties of the complexes.<sup>69,76</sup>

- **Bioimaging.** - Bioimaging is a non-invasive process that allows to visualize biological activity in a specific period of time, without inhibiting life processes. It is very helpful for the observation of subcellular structures and tissues. Ir(III) compounds are really interesting for this purpose, since they are able to stain a wide variety of targets/organelles through specific ligand tuning. The main targets described for Ir(III) compounds are: cytoplasm, mitochondria, perinuclear regions, nuclei, plasma membranes, lysosomes, Golgi apparatus.<sup>74,77,78,79,80</sup> For Ru(II) compounds, nuclei and plasma membrane are the main targets.<sup>74</sup>
- **Data recording and storage devices.** Luminescent materials that respond to external stimuli (mechanical, electrical, presence of some vapours...) and show a change in the emission colours, are very interesting for the design and construction of optical data recording and storage devices, which have a great significance in our society. Ir(III) complexes can be an interesting option in this field.<sup>26,81,82</sup>
- **Organic photovoltaic devices (OPV) and dye-sensitized solar cells (DSSC).** These devices convert solar energy to electrical energy, which is very interesting if we consider the current energy crisis and the environmental problems derived from the use of fossil fuels. Moreover, this type of devices possesses multiple benefits in comparison with silicon solar cells: they are flexible, ease to produce, with low manufacturing cost, and they have a high absorption coefficient. The main difference within OPVs and DSSCs is that DSSC is a hybrid technology as it involves organic and inorganic materials in the active layer, while in OPV this layer is purely composed by an organic electronic material that can be formed by either small molecules or polymers (small molecules can be organometallic).<sup>83,84,85</sup> Ir(III) compounds can be used in both systems,<sup>86,87,88</sup> but Ru(II) complexes are preferentially used for DSSC.<sup>89,90,91</sup>

## Bibliography

1. a) T. Karatsu, M. Takahashi, S. Yagai, and A. Kitamura, Photophysical Properties of Substituted Homoleptic and Heteroleptic Phenylimidazolinato Ir(III) Complexes as a Blue Phosphorescent Material, *Inorg. Chem.*, 2013, **52**, 12338–12350. b) R. Ibraimo Patia, Photophysical Properties of Imine Metal Complexes (Doctoral dissertation, University of Leicester), 2018.
2. M. Nonoyama, Benzo [h] quinolin-10-yl-N Iridium (III) Complexes, *Bull. Chem. Soc. Jpn.*, 1974, **47**, 767-768.
3. S. Sprouse, K. A. King, P. J. Spellane, and R. J. Watts, Photophysical Effects of Metal-Carbon Bonds in Ortho-Metalated Complexes of Ir(III) and Rh(III), *J. Am. Chem. Soc.*, 1984, **106**, 6647-6653.
4. L. Murphy, A. Congreve, L. O. Palsson, and J. A. Gareth Williams, The time domain in co-stained cell imaging: time-resolved emission imaging microscopy using a protonatable luminescent iridium complex, *Chem. Commun.*, 2010, **46**, 8743–8745.
5. L. Kohler, L. Nease, P. Vo, J. Garofolo, D. K. Heidary, R. P. Thummel, and E. C. Glazer, Photochemical and Photobiological Activity of Ru(II) Homoleptic and Heteroleptic Complexes Containing Methylated Bipyridyl-type Ligands, *Inorg. Chem.*, 2017, **56**, 20, 12214–12223
6. B. P. Sullivan, D. J. Salmon, and T. J. Meyer, Mixed phosphine 2, 2'-bipyridine complexes of ruthenium, *Inorg. Chem.*, 1978, **17**, 3334-3341.
7. G. Sprintschnik, H. W. Sprintschnik, P. P. Kirsch, and D. G. Whitten, Preparation and Photochemical Reactivity of Surfactant Ruthenium(II) Complexes in Monolayer Assemblies and at Water-Solid Interfaces 1-2, *J. Am. Chem. Soc.*, 1977, **99**, 4947–4954.
8. a) L. Chen, C. Yang, M. Li, J. Qin, J. Gao, H. You, and D. Ma, Supramolecular architectures, photophysics, and electroluminescence of 1, 3, 4-oxadiazole-based iridium (III) complexes: from  $\mu$ -dichloro bridged dimer to mononuclear complexes, *Cryst. Growth Des.*, 2007, **7**, 39-46. b) P. Brulatti, New luminescent iridium (III) complexes containing NCN cyclometallated ligands: synthesis, photophysical properties and emission tuning (Doctoral dissertation, Durham University), 2010.
9. C. E. Housecroft, and A. G. Sharpe, *Inorganic Chemistry*, Fourth edition, Pearson, 2012.
10. H. Amouri, and M. Gruselle, *Chirality in transition metal chemistry: molecules, supramolecular assemblies and materials*, John Wiley & Sons, 2008.
11. H. Sato, and A. Yamagishi, Application of the  $\Delta$ ,  $\Lambda$  isomerism of octahedral metal complexes as a chiral source in photochemistry, *J. Photochem. Photobiol. C: Photochem. Rev.*, 2007, **8**, 67–84.
12. a) A. Juris, V. Balzani, F. Barigelletti, S. Campagna, P. L. Belser, and A. V. von Zelewsky, Ru(II) polypyridine complexes: photophysics, photochemistry, electrochemistry, and chemiluminescence, *Coord. Chem. Rev.*, 1988, **84**, 85-277. b) K. Kalyanasundaram, and M. Grätzel, *Photosensitization and photocatalysis using inorganic and organometallic compounds (Vol. 14)*, Springer Science & Business Media, 1993.
13. J. R. Lakowicz, *Principles of fluorescence spectroscopy*, Third Edition, Boston, MA: springer US, 2006.
14. J. R. Albani, *Principles and Applications of Fluorescence Spectroscopy*, John Wiley & Sons, 2008.
15. R. D. Costa, E. Ortí, H. J. Bolink, F. Monti, G. Accorsi, and N. Armaroli, Luminescent Ionic Transition-Metal Complexes for Light-Emitting Electrochemical Cells, *Angew. Chem. Int. Ed.*, 2012, **51**, 8178 – 8211.

16. a) S. Ladouceur, and E. Zysman-Colman, A Comprehensive Survey of Cationic Iridium(III) Complexes Bearing Nontraditional Ligand Chelation Motifs, *Eur. J. Inorg. Chem.*, 2013, 2985–3007. b) A. Baschieri, New functionalized ligands for luminescent metal complexes: from design to applications, 2013.
17. T. Ishii, S. Tsuboi, G. Sakane, M. Yamashita, and B. K. Breedlove, Universal spectrochemical series of six-coordinate octahedral metal complexes for modifying the ligand field splitting, *Dalton Trans.*, 2009, **4**, 680–687.
18. F. Wei, S. L. Lai, S. Zhao, M. Ng, M. Y. Chan, V. W. W. Yam, and K. M. C. Wong, Ligand Mediated Luminescence Enhancement in Cyclometalated Rhodium(III) Complexes and Their Applications in Efficient Organic Light-Emitting Devices, *J. Am. Chem. Soc.*, 2019, **141**, 12863–12871.
19. F. Barigelletti, D. Sandrini, M. Maestri, V. Balzani, A. Von Zelewsky, L. Chassot, P. Jolliet, and U. Maeder, Temperature dependence of the luminescence of cyclometalated palladium (II), rhodium (III), platinum (II), and platinum (IV) complexes, *Inorg. Chem.*, 1988, **27**, 3644–3647.
20. S. Ladouceur, K. N. Swanick, S. Gallagher-Duval, Z. Ding, and E. Zysman-Colman, Strongly Blue Luminescent Cationic Iridium(III) Complexes with an Electron-Rich Ancillary Ligand: Evaluation of Their Optoelectronic and Electrochemiluminescence Properties, *Eur. J. Inorg. Chem.*, 2013, 5329–5343.
21. E. Baggaley, J. A. Weinstein, and J. A. G. Williams, Lighting the way to see inside the live cell with luminescent transition metal complexes, *Coord. Chem. Rev.*, 2012, **256**, 1762–1785.
22. V. Fernández-Moreira, F. L. Thorp-Greenwood, and M. P. Coogan, Application of  $d^6$  transition metal complexes in fluorescence cell imaging, *Chem. Commun.*, 2010, **46**, 186–202.
23. Y. You, and W. Nam, Photofunctional triplet excited states of cyclometalated Ir(III) complexes: beyond electroluminescence, *Chem. Soc. Rev.*, 2012, **41**, 7061–7084.
24. S. Majumdar, H.S. Majumdar, and R. Österbacka, *Comprehensive Nanoscience and Technology*, Volume 1, Academic Press, 2011.
25. H. Xu, R. Chen, Q. Sun, W. Lai, Q. Su, W. Huang, and X. Liu, Recent progress in metal–organic complexes for optoelectronic applications, *Chem. Soc. Rev.*, 2014, **43**, 3259.
26. H. Sun, S. Liu, W. Lin, K. Y. Zhang, et al., Smart responsive phosphorescent materials for data recording and security protection, *Nat. Commun.*, 2014, **5**, 3601.
27. Y. You, S. Cho, and W. Nam, Cyclometalated Iridium(III) Complexes for Phosphorescence Sensing of Biological Metal Ions, *Inorg. Chem.*, 2014, **53**, 1804–1815.
28. M. S. Lowry, and S. Bernhard, Synthetically Tailored Excited States: Phosphorescent, Cyclometalated Iridium(III) Complexes and Their Applications, *Chem. Eur. J.*, 2006, **12**, 7970 – 7977.
29. W. Cai, R. Zhang, Y. Yao, and S. Deemyad, Piezochromism, structural and electronic properties of benz[a]anthracene under pressure, *Phys. Chem. Chem. Phys.*, 2017, **19**, 6216–6223.
30. G. G. Shan, H. B. Li, H. T. Cao, D. X. Zhu, P. Li, Z. M. Su, and Y. Liao, Reversible piezochromic behavior of two new cationic iridium(III) complexes, *Chem. Comm.*, 2012, **48**, 2000–2002.
31. A. Marini, A. Muñoz-Losa, A. Biancardi, and B. Mennucci, What is Solvatochromism?, *J. Phys. Chem. B*, 2010, **114**, 17128–17135.
32. O. S. Wenger, Vapochromism in Organometallic and Coordination Complexes: Chemical Sensors for Volatile Organic Compounds, *Chem. Rev.*, 2013, **113**, 3686–3733.

33. A. Nakagawa, Y. Hisamatsu, S. Moromizato, M. Kohno, and S. Aoki, Synthesis and Photochemical Properties of pH Responsive TrisCyclometalated Iridium(III) Complexes That Contain a Pyridine Ring on the 2-Phenylpyridine Ligand, *Inorg. Chem.*, 2014, **53**, 1, 409–422.
34. E. H. Ghazvini-Zadeh, S. Tang, A. W. Woodward, T. Liu, M. V. Bondar, and K. D. Belfield, Chromophoric materials derived from a natural azulene: syntheses, halochromism and one-photon and two-photon microlithography, *J. Mater. Chem. C*, 2015, **3**, 8495-8503.
35. A. Juarranz, P. Jaén, F. Sanz-Rodríguez, J. Cuevas, and S. González, Photodynamic therapy of cancer. Basic principles and applications, *Clin. Transl. Oncol.*, 2008, **10**, 148-54.
36. G. M. Fioramonti Calixto, J. Bernegossi, L. M. De Freitas, C. R. Fontana, and M. Chorilli, Nanotechnology-Based Drug Delivery Systems for Photodynamic Therapy of Cancer: A Review, *Molecules*, 2016, **21**, 342.
37. M. Broekgaarden, R. Weijer, T. M. van Gulik, M. R. Hamblin, and M. Heger, Tumor cell survival pathways activated by photodynamic therapy: a molecular basis for pharmacological inhibition strategies, *Cancer Metastasis Rev.*, 2015, **34**, 643-690.
38. A. F. dos Santos, D. R. Queiroz de Almeida, L. F. Terra, M. S. Baptista, and L. Labriola, Photodynamic therapy in cancer treatment - an update review, *J Cancer Metastasis Treat.*, 2019, **5**, 25.
39. K. L. Haas, and K. J. Franz, Application of Metal Coordination Chemistry To Explore and Manipulate Cell Biology, *Chem. Rev.*, 2009, **109**, 4921–4960.
40. S. A. Sharma, P. Sudhindra, R. Nilmadhab, P. Priyankar, Advances in novel iridium (III) based complexes for anticancer applications: A review, *Inorganica Chim. Acta*, 2020, **513**, 119925.
41. X. Yin, X. Y. Lai, X. Wang, and Y. T. Liu, Theoretical insight into the photophysical properties of long-lifetime Ir(III) and Rh(III) complexes for two-photon photodynamic therapy, *Phys. Chem. Chem. Phys.*, 2019, **21**, 8394.
42. S. Monro, K. L. Colón, H. Yin, J. Roque III, P. Konda, et al., Transition Metal Complexes and Photodynamic Therapy from a Tumor-Centered Approach: Challenges, Opportunities, and Highlights from the Development of TLD1433, *Chem. Rev.*, 2019, **119**, 797–828.
43. J. Liu, C. Zhang, T. W. Rees, L. Ke, L. Ji, and H. Chao, Harnessing ruthenium(II) as photodynamic agents: Encouraging advances in cancer therapy, *Coord. Chem. Rev.*, 2018, **363**, 17–28.
44. C. K. Prier, D. A. Rankic, and D. W. C. MacMillan, Visible Light Photoredox Catalysis with Transition Metal Complexes: Applications in Organic Synthesis, *Chem. Rev.*, 2013, **113**, 5322–5363.
45. A. H. Bonardi, F. Dumur, G. Noirbent, J. Lalevée, and Didier Gigmes, Organometallic vs organic photoredox catalysts for photocuring reactions in the visible region, *Beilstein J. Org. Chem.*, 2018, **14**, 3025–3046.
46. V. Mdluli, S. Diluzio, J. Lewis, J. F. Kowalewski, T. U. Connell, D. Yaron, T. Kowalewski, and S. Bernhard, High-throughput Synthesis and Screening of Iridium(III) Photocatalysts for the Fast and Chemoselective Dehalogenation of Aryl Bromides, *ACS Catal.*, 2020, **10**, 6977–6987.
47. T. P. yoon, M. A. Ischay, and J. Du, Visible light photocatalysis as a greener approach to photochemical synthesis, *Nat. Chem.*, 2010, **2**, 527-532.
48. D. A. Nicewicz and D. W. C. MacMillan, Merging Photoredox Catalysis with Organocatalysis: The Direct Asymmetric Alkylation of Aldehydes, *Science*, 2008, **322**, 77-80.
49. A. Gualandi, D. Mazzarella, A. Ortega-Martínez, L. Mengozzi, et al., Photocatalytic Radical Alkylation of Electrophilic Olefins by Benzylic and Alkyllic Zinc-Sulfonates, *ACS Catal.*, 2017, **7**, 5357–5362.

50. D. A. Nagib, M. E. Scott, and D. W. C. MacMillan, Enantioselective  $\alpha$ -Trifluoromethylation of Aldehydes via Photoredox, *J. Am. Chem. Soc.*, 2009, **131**, 10875–10877.
51. H. W. Shih, M. N. Vander Wal, R. L. Grange, and D. W. C. MacMillan, Enantioselective  $\alpha$ -Benzylation of Aldehydes via Photoredox Organocatalysis, *J. Am. Chem. Soc.*, 2010, **132**, 13600–13603.
52. D. Petzold, M. Giedyk, A. Chatterjee, and B. König, A Retrosynthetic Approach for Photocatalysis, *Eur. J. Org. Chem.*, 2019, 1193–1244.
53. M. A. Ischay, Z. Lu, and T. P. Yoon, [2+2] Cycloadditions by Oxidative Visible Light Photocatalysis, *J. Am. Chem. Soc.*, 2010, **132**, 8572–8574.
54. J. Du, and Tehshik P. Yoon, Crossed Intermolecular [2+2] Cycloadditions of Acyclic Enones via Visible Light Photocatalysis, *J. Am. Chem. Soc.*, 2009, **131**, 14604–14605.
55. J. Lalevéé, N. Blanchard, M. A. Tehfe, M. Peter, F. Morlet-Savary, and J. P. Fouassier, A Novel Photopolymerization Initiating System Based on an Iridium Complex Photocatalyst, *Macromol. Rapid Commun.*, 2011, **32**, 917–920.
56. Y. Kuramochi, and O. Ishitani, An Ir(III) Complex Photosensitizer With Strong Visible Light Absorption for Photocatalytic CO<sub>2</sub> Reduction, *Front. Chem.*, 2019, **7**, 259.
57. K. Sekizawa, K. Maeda, K. Domen, K. Koike, and O. Ishitani, Artificial Z-Scheme Constructed with a Supramolecular Metal Complex and Semiconductor for the Photocatalytic Reduction of CO<sub>2</sub>, *J. Am. Chem. Soc.*, 2013, **135**, 4596–4599.
58. V. K. Khanna, *Fundamentals of solid-state lighting: LEDs, OLEDs, and their applications in illumination and displays*, 2014, CRC press.
59. K. P. S. Zanoni, R. L. Coppo, R. C. Amaral, and N. Y. M. Iha, Ir(III) complexes designed for light-emitting devices: beyond the luminescence color array, *Dalton Trans.*, 2015, **44**, 14559–14573.
60. K. P.S. Zanoni, A. Ito, and N. Y. M. Iha, Molecular-Engineered [Ir(Fppy)<sub>2</sub>(Mepic)] Towards Efficient Blue-Emission, *New J. Chem.*, 2015, **39**, 6367–6376.
61. P. T. Chou, and Y. Chi, Osmium- and Ruthenium-Based Phosphorescent Materials: Design, Photophysics, and Utilization in OLED Fabrication, *Eur. J. Inorg. Chem.*, 2006, 3319–3332.
62. S. B. Meier, D. Tordera, A. Pertegás, C. Roldán-Carmona, E. Ortí, and H. J. Bolink, Light-emitting electrochemical cells: recent progress and future prospects, *Mater. Today*, 2014, **17**, 217–223.
63. H. Rudmann, S. Shimada, and M. F. Rubner, Solid-State Light-Emitting Devices Based on the Tris-Chelated Ruthenium(II) Complex. 4. High-Efficiency Light-Emitting Devices Based on Derivatives of the Tris(2,2'-bipyridyl) Ruthenium(II) Complex, *J. Am. Chem. Soc.*, 2002, **124**, 4918–4921.
64. H. Xia, C. Zhang, X. Liu, S. Qiu, P. Lu, F. Shen, J. Zhang, and Y. Ma, Ruthenium(II) Complex as Phosphorescent Dopant for Highly Efficient Red Polymers Light-Emitting Diodes, *J. Phys. Chem. B*, 2004, **108**, 3185–3190.
65. F. S. M. Canisaresa, A. G. Bispo-Jr, A. M. Piresa, S. A. M. Lima, Syntheses and characterization of Schiff base ligands and their Ir(III) complexes as coating for phosphor-converted LEDs, *Optik*, 2020, **219**, 164995.
66. B. Wang a, W. Li, T. Miao, J. Liu, S. Hou, G. Fu, and X. Lü, Efficient all-solution-processed near-infrared (NIR) polymer light-emitting diode (PLED) based on the [Ir(C<sup>N</sup>1)<sub>2</sub>(C<sup>N</sup>2)]-heteroleptic Ir(III)-complex [Ir(iqbt)<sub>2</sub>(Br-ppy)], *J. Lumin.*, 2021, **231**, 117770.

67. Y. He, G. Fu, W. Li, B. Wang, T. Miao, M. Tan, W. Feng, and X. Lü, Efficient near-infrared (NIR) polymer light-emitting diode (PLED) based on the binuclear  $[(C^{\wedge}N)_2Ir-(bis-N^{\wedge}O)-Ir(C^{\wedge}N)_2]$  complex with aggregation-induced phosphorescent enhancement (AIPE) character, *J. Lumin.*, 2020, **218**, 116847.
68. F. Wei, Z. Qian, S. L. Lai, S. Zhao, M. Y. Chan, and K. M. C. Wong, Organic Light-Emitting Devices with High External Quantum Efficiency and Operational Stability Based on Highly Phosphorescent Cyclometalating Rhodium(III) Complexes, *Energy Fuels*, 2021, **35**, 19123–19131.
69. K. K. W. Lo, S. P. Y. Li, and K. Y. Zhang, Development of luminescent iridium(III) polypyridine complexes as chemical and biological probes, *New J. Chem.*, 2011, **35**, 265–287.
70. Y. Clarke, W. Xu, J. N. Demas, and B. A. DeGraff, Lifetime-Based pH Sensor System Based on a Polymer-Supported Ruthenium(II) Complex, *Anal. Chem.*, 2000, **72**, 3468-3475.
71. P. Kumar, and S. Kumar, Detection of Bio-Relevant Metal Ions by Luminescent Ru(II)-Polypyridyl Based Sensors, 2021.
72. J. Xu, Y. Liu, and M. J. Li, The functionalized ruthenium(II) polypyridine complexes for the highly selective sensing of mercury ions, *Spectrochim. Acta A Mol. Biomol. Spectrosc.*, 2019, **219**, 141–146.
73. S. Das, S. Karmakar, S. Mardanya, and S. Baitalik, Synthesis, structural characterization, and multichannel anion and cation sensing studies of a bifunctional Ru(II) polypyridyl–imidazole based receptor, *Dalton Trans.*, 2014, **43**, 3767.
74. Tang, S. M., Phosphorescent Ruthenium (II) and Iridium (III) Complexes as Bioimaging Reagents and Bioorthogonal Probes (Doctoral dissertation, City University of Hong Kong), 2017.
75. S. Abbas, I. ud Din Din, A. Raheel, A. T. ud Din, Cyclometalated Iridium (III) complexes: Recent advances in phosphorescence bioimaging and sensing applications, *Appl. Organometal. Chem.*, 2020, **34**, e5413.
76. J. Shum, P. K. K. Leung, and K. K. W. Lo, Luminescent Ruthenium(II) Polypyridine Complexes for a Wide Variety of Biomolecular and Cellular Applications, *Inorg. Chem.*, 2019, **58**, 2231–2247.
77. X. Zhen, R. Qu, W. Chen, W. Wu, and Xiqun Jiang, The development of phosphorescent probes for in vitro and in vivo bioimaging, *Biomater. Sci.*, 2021, **9**, 285.
78. K. K. W. Lo, and K. Y. Zhang, Iridium(III) complexes as therapeutic and bioimaging reagents for cellular applications, *RSC Advances*, 2012, **2**, 12069–12083.
79. Y. You, Phosphorescence bioimaging using cyclometalated Ir(III) complexes, *Curr. Opin. Chem. Biol.*, 2013, **17**, 699–707.
80. P. Y. Ho, C. L. Ho, W. Y. Wong, Recent advances of iridium(III) metallophosphors for health-related applications, *Coord. Chem. Rev.*, 2020, **413**, 213267.
81. D. Ma, T. Tsuboi, Y. Qiu, and L. Duan, Recent Progress in Ionic Iridium(III) Complexes for Organic Electronic Devices, *Adv. Mater.*, 2017, **29**, 1603253.
82. W. Lin, Q. Zhao, H. Sun, K. Y. Zhang, H. Yang, Q. Yu, X. Zhou, S. Guo, S. Liu, and Wei Huang, An Electrochromic Phosphorescent Iridium(III) Complex for Information Recording, Encryption, and Decryption, *Adv. Optical Mater.*, 2015, **3**, 368–375.
83. S. N. F. Mohd-Nasir, M. Y. Sulaiman, N. Ahmad-Ludin, M. A. Ibrahim, K. Sopian, and M. A. Mat-Teridi, Review of Polymer, Dye-Sensitized, and Hybrid Solar Cells, *Int. J. Photoenergy*, 2014, **2014**.
84. A. H. Chander, M. Krishna, and Y. Srikanth, Comparison of Different types of Solar Cells – a Review, *IOSR j. electr. electron. eng.*, 2015, **10**, 151-154.

85. R. Vidal, J. A. Alberola-Borràs, N. Sánchez-Pantoja, and I. Mora-Seró, Comparison of Perovskite Solar Cells with other Photovoltaics Technologies from the Point of View of Life Cycle Assessment, *Adv. Energy Sustainability Res.*, 2021, **2**, 2000088.
86. T. Yang, Y. He, Y. Cheng, X. Gao, Y. Wu, W. Yuan, and Y. Tao, Cyclometalated Ir(III) complexes as potential electron acceptors for organic solar cells, *Dalton Trans.*, 2021, **50**, 9871-9880.
87. W. Lee, T. H. Kwon, J. Kwon, J. Y. Kim, C. Lee, and J. I. Hong, Effect of main ligands on organic photovoltaic performance of Ir(III) complexes, *New J. Chem.*, 2011, **35**, 2557–2563.
88. A. Sinopoli, C. J. Wood, E.A. Gibson, P. I. P. Elliott, New cyclometalated iridium(III) dye chromophore complexes for p-type dye-sensitized solar cells, *Dyes Pigm.*, 2017, **140**, 269e277.
89. O. Dayan, N. Özdemir, F. Yakuphanoğlu, Z. Şerbetci, A. Bilici, Bekir Çetinkaya, and Melek Tercan, Synthesis and photovoltaic properties of new Ru(II) complexes for dyesensitized solar cells, *J. Mater. Sci.: Mater. Electron.*, 2018, **29**, 11045–11058.
90. Y. G. Kim, R. Mosurkal, L. Li, J. Walker, J. He, L. A. Samuelson, and J. Kumar, Synthesis and Characterization of a Ruthenium(II) Complex for Photovoltaic Cells, *J. Macromol. Sci. - Pure Appl. Chem.*, 2007, **44**, 1255–1260.
91. Y. Qin, and Q. Peng, Ruthenium Sensitizers and Their Applications in Dye-Sensitized Solar Cells, *Int. J. Photoenergy*, 2012, **2012**, 291579.





---

***Part 1. Ir(III) and Rh(III) tris-  
chelate complexes for  
photodynamic therapy (PDT)***

---

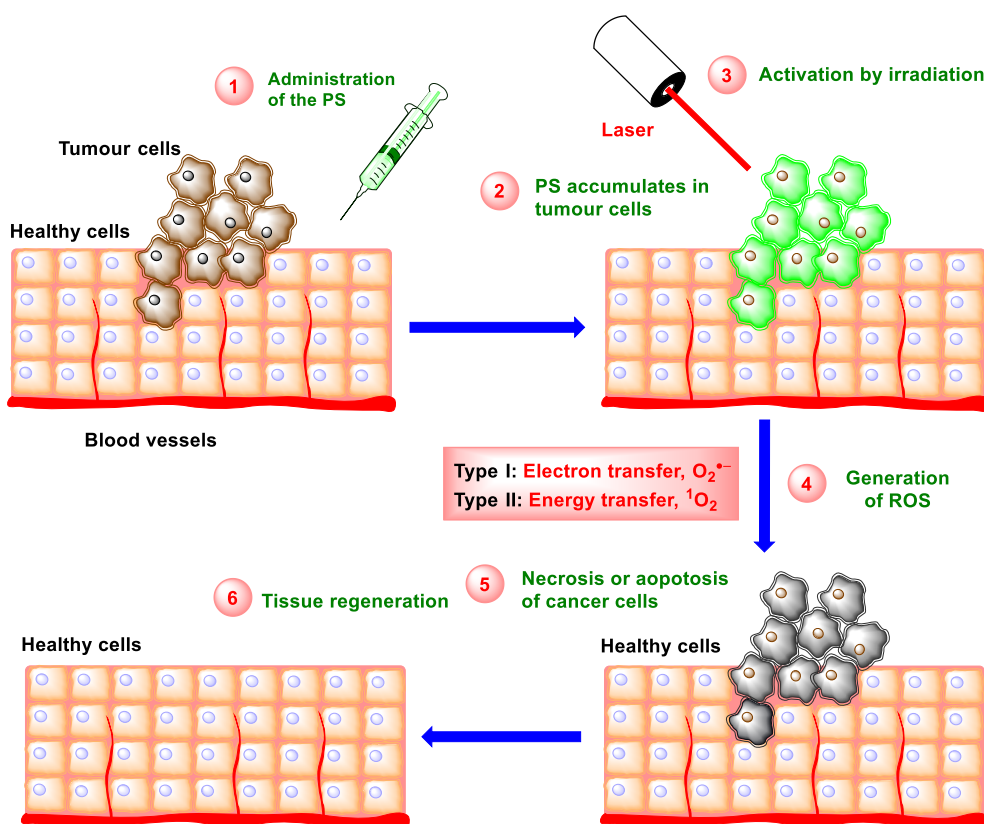




## Objectives

Main Objective: To design and develop new metal-based complexes as potential photosensitizers (PSs) for photodynamic therapy (PDT). This objective can be divided in various secondary objectives:

- To study the effect of the structure in the performance of the PS for PDT.
- To Study the relationship between the structure and the photophysical properties.
- To shed light on the biological mechanism of action, that is, to elucidate the uptake pathway, the intracellular localization, and cytotoxicity mechanism (ROS generation, DNA damage) and the cell death mechanism of the different PSs.
- To identify the possible molecular targets of the PSs by testing their activity in the photooxidation of relevant biomolecules.







---

***Cancer through the history,  
metals in medicine and  
photodynamic therapy (PDT)***

---





## 0. Introduction to cancer

Cancer represents a major public health problem worldwide and is one of the main causes of death, accounting for almost 10 million deaths in 2020 and an estimate of 20 million new cases.<sup>1</sup> Cancer in the broader sense, refers to more than 277 different types of cancer diseases. The most common cancer types in Europe are: lung, female breast, colorectal and prostate. Moreover, lung cancer is one of the most prevalent around the world and the one with the higher mortality.<sup>1,2</sup> The most common cancer types vary by gender and also by age: men are predominantly affected by prostate, lung and bronchus, colon and rectum, and urinary bladder cancers; while in women the most common are breast, lung and bronchus, colon and rectum, uterine corpus and thyroid cancers;<sup>3</sup> and in the case of children, the most common types are blood cancer, and cancers related to the brain and lymph nodes.<sup>4,5</sup>

But, what is cancer? In a simple way, cancer can be understood like a disease associated to an uncontrolled cell growth that can cause tumours, which are able to spread to other parts of the body (metastasis). The adult human is composed of approximately  $10^{15}$  cells, and it is calculated that there are around  $10^{12}$  divisions per day in the stem cells (the cells with the capacity for division and replenishment), so it is obvious that the body has an extremely precise control over cell multiplication, which is accomplished by a network of overlapping molecular mechanisms that govern cell proliferation and cell death (apoptosis). It is clear that genes, more precisely, the random mutations in the genes which control the replication and the death rate of individual cells are the cause of the carcinogenic process.<sup>6</sup> Most mutations that cause cancer are not inherited; they appear spontaneously as a result of some kind of DNA damage that alters the function of crucial genes.<sup>7</sup> This DNA damage may have several sources, for instance, chemical compounds have an obvious role in gene mutation, specially, exposure to tobacco, which leads to lung cancer.<sup>8</sup> Overall, around 70% of all cancer in western populations can be attributed to diet and lifestyle issues; 30% of this is related to tobacco and the other 40% is mainly due to an unbalanced diet, particularly, a deficient intake of fruits and vegetables, which play a protective role against cancer induction.<sup>9,10</sup> Viruses, bacteria and electromagnetic radiation also play a role, comprising about 7% of all cancers.<sup>11</sup>

It is important to note that DNA damage itself is not a mutagenic event; DNA replication and cell division are necessary to convert damage into an inheritable variation in the DNA, which is what we really call mutation.<sup>12</sup> Also, it is worth mentioning that spontaneous DNA mutations can occur directly as a consequence of errors in replication. However, because of the proofreading capabilities and the fact that 97% of DNA is non-coding and the redundancy of codon recognition, the error rate

during DNA replication is extremely low. Hence, the main causes that trigger the cascade of events leading to cancer are those above mentioned.<sup>13,14</sup>

## 1. Cancer and treatment: a brief story

### 1.1. From surgical treatments to radiotherapy

Cancer has existed on Earth before human: in some fossils of dinosaurs and prehistoric animals, traces of bone tumours (osteosarcomas and bone metastases) have been found.<sup>15,16</sup> The first historical records of tumours in humans appeared in a papyrus from the Egyptian period (around 3000 BC) where a case of breast cancer is described,<sup>17</sup> but it was only in 400 BC when cancer was recognized as a disease and not some kind of curse related to esoteric forces.<sup>18</sup> In fact, Hippocrates (460-370 BC) was the first to describe it with his theory of human humors,<sup>19,20</sup> which was later refined and improved by Galenus (129–216 AD).<sup>21</sup> These theories remained the most accepted until the Modern Era. Until the end of the XIX century, a healthy diet, cautery and radical surgical approaches were used for treating superficial tumours, whereas palliative pain therapies were used for the deeper types.<sup>18</sup> These inefficient treatments usually led to death of the patient, either by the advance of the tumour or by the sequelae of the surgery, like infections caused by the surgery itself or by the poor hygienic conditions.<sup>22</sup>

By the end of the XIX century radiotherapy started to be developed and used for the treatment of cancer. Claudius Regaud (1870-1940) is considered the father of modern radiotherapy when around 1920 discovered that it was possible to treat some types of cancers reducing the side effects of the treatment by fractioning the radiation doses.<sup>23,24</sup>

### 1.2. Chemotherapy

The serendipitous discover of nitrogen mustard as a DNA alkylating agent during the Second World War is considered the dawn of chemotherapy and the beginning in the use of cytotoxic compounds for the treatment of cancer.<sup>18,25</sup> An overview of different chemotherapeutic agents is provided below.

The first generation nitrogen mustards had important drawbacks, such as high toxicity or acquired resistance, and only cyclophosphamide, which is able to interfere with cycle of active and quiescent cells, remains in clinical use nowadays.<sup>18,26</sup>

Some other alkylating agents that are worth mentioning include nitrosourea compounds (streptozocin, nimustine, carmustine, lomustine), alkyl sulfates (mannosulfan, busulfan, treosulfan) and triazene compounds (dacarbazine, temozolomide).<sup>25</sup>



Antimetabolites are molecules that mimic the structure of physiological metabolites, so they block enzymatic chains, which are essential in the purines synthesis, a fact that results in the induction of apoptosis, inhibiting the cell proliferation. The main antimetabolites are folate analogs (pemetrexed, aminopterin, methotrexate), purine analogs (mercaptopurine) and pyrimidine analogs (fluorouracil).<sup>18,27,28</sup>

In the late 50s antimitotics of natural origin were discovered. These compounds and extracts are able to interfere with the formation of microtubules, thus, blocking cell proliferation.<sup>18,29</sup> There are several families including the Vinca alkaloids (vinblastine, vincristine, vinorelbine and vindesine), which are already broadly used in first and second line therapy for treating a wide variety of cancer types, and epipodophyllotoxins (teniposide (VM-26) and etoposide (VP-16)) being used for treating acute monoblastic leukemia and non-seminomatous testis carcinomas because of their higher selectivity and their fewer side effects.<sup>18,30</sup>

Then, Paclitaxel, a natural product extracted from the tree *Taxus brevifolia*, was discovered.<sup>18,31</sup> This first led to its clinical use (under the brand name Taxol, first generation) and later to the synthesis of derived drugs like docetaxel (second generation) and cabazitaxel (third generation), which was ground-breaking in the treatment of solid tumours such as head cancer, neck cancer, NSCLC, prostatic cancer, gastric cancer, metastatic pancreatic cancer and metastatic breast cancer.<sup>18,32,33</sup>

There are also antibiotics and derivatives that possess an important cytotoxic activity used as chemotherapeutics. These drugs, which are mainly of natural origin, act forming covalent bonds with nucleic acids or intercalating between DNA base pairs, interfering in this way with the synthesis of DNA.<sup>18,34</sup> The most successful, which were obtained from *Streptomyces*, are doxorubicin (initially named as adriamycin) and actinomycin D (both are intercalating agents) and bleomycin.<sup>35</sup>

The chemotherapeutic agents seen above can be used individually or in combined therapeutic protocols. It should be noted that the use of combinations of several anticancer agents for treating a tumour has significant advantages. Its efficacy is far higher than that of individual drugs, and combined therapeutic protocols prevent, or at least, slow down the development of drug resistance. In general, combined protocols are more effective options for cancer treatment than individual drugs and the development of a wide variety of combined protocols routinely used in different types of cancer has significantly improved the prognosis of the patients.<sup>36</sup>

### 1.3. Targeted therapies

In the 1980s, occurred the second revolution in pharmacology for cancer treatment with the development of targeted therapies. The advances in immunology and molecular and cell biology allowed researchers to study the mechanisms involved in

the neoplastic transformations of cells thus identifying druggable molecular targets that could be selectively blocked/inhibited by small molecules or monoclonal antibodies. Thus, opposite to classic chemotherapy, where the drugs can affect both healthy and cancer cells, in targeted therapies only cancer cells are affected, ideally causing only minor side effects to the healthy cells.<sup>18,37</sup>

### 1.3.1. Monoclonal antibodies

The production of monoclonal antibodies developed by Köhler and Milstein in 1975 using the hybridoma technology opened up the possibility of using these proteins for the treatment of cancer.<sup>18,38</sup> Studies of the human genome and the technologies for DNA sequencing also boosted this strategy by the end of the last century.<sup>18,39</sup> A wide variety of monoclonal antibodies was developed, since then, with 30 different monoclonal antibodies approved for cancer treatment and 6 for cancer diagnosis in 2017. Initially, the produced antibodies were mouse antibodies, but now, there are 4 types available, which are: chimeric, murine, humanized and human monoclonal antibodies; the difference between them lies in the percentage of murine protein portion in the immunoglobulin.<sup>18,40</sup> Trastuzumab (Herceptin) a human epidermal growth factor receptor 2 (HER2)/neu inhibitor<sup>41</sup> and Rituximab (IDEC-C2B8), a chimeric antibody directed against the CD-20 antigen,<sup>42</sup> were among the first monoclonal antibodies approved as anticancer agents, starting a new era for cancer treatments.

There are several monoclonal antibodies that target surface receptors. Cetuximab is a chimeric (mouse/human) monoclonal antibody that targets the epidermal growth factor receptor (EGFR), which is usually altered in NSCLC, colorectal carcinomas and head and neck cancers.<sup>18,43</sup> Another human monoclonal antibody used for treating metastatic colorectal cancer that acts over EGFR is Panitumumab.<sup>44</sup>

It is worth mentioning that the monoclonal antibody Bevacizumab was the first anti-angiogenic factor developed. Bevacizumab inhibits the vascular endothelial growth factor A (VEGF-A), blocking angiogenesis.<sup>45</sup> and it is used for treating several types of cancer.<sup>18,46</sup>

### 1.3.2. Selective kinase inhibitors

The knowledge of molecular pathways that suffer alterations due to cancer has made feasible the development of small molecules which are able to bind selectively to molecular targets of cancerous cells, causing in that way their inhibition and apoptosis.<sup>47</sup> The inhibitors have a wide variety of targets, including cell-cycle proteins, growth factors, signalling molecules, modulators of apoptosis and molecules promoters of angiogenesis.<sup>18,48</sup>

Examples of Tyrosine kinase inhibitor include Imatinib, a competitive ATP inhibitor of the BCR-ABL protein (fusion protein typical of patients with chronic myelogenous leukemia (CML) and acute lymphocytic leukemia (ALL)). A second and a third generation BCR-ABL inhibitors were later prepared: Bosutinib, Dasatinib, Nilotinib, Ponatinib...<sup>18,49</sup>

Another group of tyrosine kinase inhibitors was designed to target the EGFR ATP-binding site, being capable in that way to inhibit the abnormal activation of MAPK and PI3K/AKT pathways, which are commonly overexpressed in cancerous cells.<sup>50</sup> Gefitinib and Erlotinib are two examples.<sup>18,51</sup>

Another type of tyrosine kinase inhibitors are those known as VEGF (Vascular Endothelial Growth Factor) inhibitors (directed to the ATP binding pocket of VEGF).<sup>18,52</sup> examples of this class of drugs are Sorafenib, Sunitinib, Aflibercept and Pegaptanib sodium. VEGF inhibitors are useful for the treatment of several types of cancers.<sup>53</sup>

Other group of selective inhibitors are the mTOR inhibitors. mTOR is an intracellular serine/threonine kinase that takes part in both the regulation of gene expression and the progression of the cell cycle from G1 to S phase.<sup>18,54</sup> The first developed mTOR inhibitor was rapamycin, from which Temsirolimus and Everolimus, two inhibitors already in use, were derived.<sup>55</sup>

Other group of serine/threonine kinase inhibitors are BRAF and MEK inhibitors. The BRAF inhibitors Vemurafenib and Dabrafenib, both approved in 2010, are used for treating melanomas with mutated BRAF<sup>V600E</sup>. Both drugs act by the same mechanism; they interfere with the B-Raf/MEK/ERK pathway triggering cancerous cell apoptosis. If we consider that a high percentage (40–60%) of melanoma patients are positive to the V600E mutation, the development of these inhibitors is a clear milestone in melanoma treatment.<sup>18,56</sup>

### 1.3.3. Proteasome inhibitors

Another interesting type of selective inhibitors are the proteasome inhibitors. Their action mechanism consists in inhibiting the proteasome, thus preventing the degradation of pro-apoptotic factors, which favors the apoptosis of cancerous cells. Of this type of inhibitors, Bortezomib and Carfilzomib are approved for their use in the treatment of haematological malignancies, such as multiple myeloma and mantle cell lymphoma.<sup>18,57</sup>

All of these target therapeutic agents mentioned above, are frequently used in combined therapies with other chemotherapeutic agents or monoclonal antibodies and/or selective inhibitors.<sup>18,58</sup> This has made clinical treatments more effective and has made possible to overcome drug resistances in several cases.<sup>59</sup>

#### 1.3.4. Molecular radiotherapy

Molecular radiotherapy (MRT) is a therapeutic approach which uses radioactive compounds, known as radiopharmaceuticals, for treating several diseases. The first MRT agent that was developed was Iodine-131, which is essentially sodium iodide in the form of the radioactive isotope 131 of iodine.<sup>18,60</sup> This compound is mainly used for treating thyroid cancer because of the great affinity of iodide for the thyroid gland, but it can also be used for treating benign diseases where the beta radiation of the radioiodine can have a beneficial effect.<sup>18,61</sup>

Other MRT agents such as Strontium-89 chloride, Radium-223 chloride, and Samarium-153 EDTMP are used as palliative treatments for secondary bone metastatic disseminations of various cancer types.<sup>18,62</sup> Strontium and Radium mimic calcium, and they can be incorporated by the bone whereas in the case of samarium, it is thanks to its covalent bond to tetraphosphate EDTMP that is taken by the osteoblasts.<sup>18,63</sup>

Other MRT agents are Phosphorus-32 and Yttrium-90, which are used for treating the colorectal liver metastasis,<sup>18,64,65</sup> <sup>131</sup>I-MIBG metaiodo-benzylguanidine, which is used for the treatment of pheochromocytoma and neuroblastoma,<sup>18,66</sup> and Yttrium-90 and Lutetium-177, both used for treating neuroendocrine tumours.<sup>18,67</sup>

#### 1.4. Immune checkpoint inhibitors

After 2010, new treatments known as immune checkpoint inhibitors were introduced, representing a new milestone in modern cancer therapies.<sup>18,68</sup> These inhibitors are anti-cytotoxic T-lymphocyte-associated antigen 4 (anti-CTLA4; located in the membrane surface of T-cell) and anti-programmed cell death protein 1 antibody (anti-PD1; located in the membrane surface of cancer cells). These drugs facilitate the activation of T cells, which attack and destroy cancer cells. Examples of approved immune checkpoint inhibitors are Ipilimumab, Nivolumab, Nivolumab and Pembrolizumab.<sup>18,69</sup>

Immune checkpoint inhibitors, like other types of drugs seen before, are usually used in combined therapies with each other or with other chemotherapeutic drugs. In this way a higher efficacy with less side effects can be achieved. Particularly, the combination of anti-PD1 and anti-CTLA-4 inhibitors has demonstrated a high efficacy. It is worth mentioning that the immune checkpoint inhibitors caused an epochal turning in the treatment of incurable tumours like NSCLC and metastatic melanoma.<sup>70</sup>

### 1.5. New directions in cancer therapy

Oncology is constantly evolving, and new approaches to cancer treatment appear regularly. CAR-T (Chimeric-Antigen Receptor) cell therapy is one of them. CAR-T cell therapy is based in inserting designed receptors, specific for antigens of the cancer cells, to the T cells, which acquire in this way a high specificity against cancer cells. The designed receptors are known as chimeric receptors, because they are formed with protein structures derived from DNA of different organisms and sources.<sup>18,71</sup> To accomplish the CAR-T cell therapy, it is necessary to take T cells from patients to make their genetic modification *in vitro*, which allows to add the receptor of interest to them. Then, the modified T cells are reinfused to the patient, inducing in this way a selective cell death of the cancerous cells mediated by the immune system. Technically, it is possible to treat any type of cancer with this technique.<sup>72</sup> Despite the high cost of these treatments they are very effective for treating relapsed/refractory cancers. Approved CAR-T cell therapies for treating non-solid tumors related to malignant B cells include axicabtagene ciloleucel (Axi-cel) therapy and tisagenlecleucel. Currently, there are ongoing studies which try to apply CAR-T therapy in the treatment of solid tumours by the use of heterogeneous cells produced in cell factories.<sup>18,73</sup>

In the last years, another approach against cancer has been developed, the anticancer vaccines. These vaccines are designed based on the specific characteristics of the tumour with the aim of activating the immune system against cancer cells and improving their eradication. The first anticancer vaccine, the Oncophage vaccine, was approved in 2008. It consists of the heat shock protein 96, which is extracted from the tumour tissue itself, being able to stimulate immune response against cancerous cells of the same tumour. This vaccine, is used for treating renal cancer, glioma and metastatic melanoma.<sup>18,74</sup> In 2010, another vaccine, known as sipuleucel-T, was approved. Sipuleucel-T, which is used for treating metastatic, hormone-refractory, prostate cancer, consists of pulsed patient's dendritic cells with recombinant prostatic acid phosphatase, which appears in the 95% of prostate cancer cells. In this way, there is an increase in the immune response selectively directed against cancer cells, causing their death. There are other vaccines under study, but the production system has to be improved, being this the mayor drawback, which makes it a particularly expensive therapy.<sup>18,75</sup>

It is worth mentioning other new approaches to cancer treatment under development. For example, some of these are based on genomic editing using CRISPR/Cas9 technology, with the aim of correcting the genetics aberrations responsible for cancer development itself.<sup>18,76</sup>

## 2. Metals in medicine

Metals in medicine is an interesting topic that is usually underrated because of the widespread general opinion against metals in health, being considered as toxic and pollutants that should be avoided in our daily life.

Although ancient civilizations like Mesopotamian, Egyptian, Indian and Chinese, have known that metal ions possess a key role in the processes of the organism, being used for therapy in the treatment of several diseases,<sup>77,78</sup> medicinal inorganic chemistry or the more mature and precise version we know today, biomedical inorganic chemistry, is a recent area of the knowledge. This area is based in a deep and accurate knowledge of the nature of formulated metallodrugs and in the understanding of their biological mechanisms of action.<sup>79,80,81,82</sup>

Nowadays, we know that there are 24 essential elements (H, C, N, O, F, Na, Mg, Si, P, S, Cl, K, Ca, V, Mn, Fe, Co, Ni, Cu, Zn, Se, Mo, Sn, and I). We also know that nonessential and even radioactive elements can be useful in medicine for treating a wide variety of diseases (arthritis, inflammation, depression, ulcers, gastrointestinal disorders, microbe and bacteria related disease, cancer...) and in diagnosis as detailed below.<sup>83,84</sup>

### 2.1. Properties of metal complexes

Metal complexes have properties that makes them an interesting option for several applications in medicine:

-Charge Variation: In aqueous solution, the metal ions exist as cationic species, but depending on the coordination environment of the metal, the charge can be modified. This allows to generate cationic, anionic or neutral species, which can be very useful for binding different types of charged biomolecules.<sup>85</sup>

-Structural diversity: metal complexes have a vast range of coordination geometries. Moreover, the bond lengths and angles at the coordination site are different for each metal and oxidation state. If we compare metal complexes with organic compounds, we can see that whilst a carbon atom with four different substituents only can have two enantiomers, an octahedral transition metal complex with six substituents has thirty possible structural isomers.<sup>85,86,87</sup>

-Metal-ligand Interactions: there are different forms of interactions between the metal and the ligands, and the thermodynamics and kinetics of these interactions influence the ligand exchange reactions. This type of reactions eases the interaction and coordination between the metals and biological molecules, which is of great importance.<sup>85</sup>

-Lewis acid properties: metals are characterized by high electron affinity, which causes that their ions can easily polarize groups coordinated to them. This behaviour eases the hydrolysis of these groups, facilitating the interaction with several biomolecules of interest.<sup>85,88</sup>

-Redox activity: transition metals tend to undergo reduction and oxidation reactions. The oxidation state of the metal in a coordination compound is a key fact, because in biochemical redox catalysis metal ions usually are the centers responsible of the activation of the coordinated substrates and participate in redox active sites for charge accumulation.<sup>88</sup>

-Partially filled D shell: the number of electrons in the D shell, for transition metals, or the F shell, for lanthanides, influences the electronic and magnetic properties of the complexes, providing them with a wider range of possibilities compared to organic compounds.<sup>88</sup>

## 2.2. Imaging and Diagnosis

Imaging techniques are based on the use of fluorescent compounds, radionuclides and contrast-enhancing agents, which can be combined with antibodies and proteins to enhance their target specificity. These agents should have some properties for their clinical use: they have to preferentially accumulate in target tissues, be cleared by non-target organs, possess low toxicity to normal cells and be cost-effective.<sup>80,89</sup>

Small molecules that possess intrinsic fluorescence can be used as probes for dual mode optical and positron emission tomography (PET). For instance, Zn(II) complexes have found their place in these techniques, for example, {Bis(4-allyl-3-thiosemicarbazonato) acenaphthenequinone} fluorescent complexes of Zn (II) (Fig. 1) have been used to image MCF-7 breast cancer cells.<sup>80,90</sup>

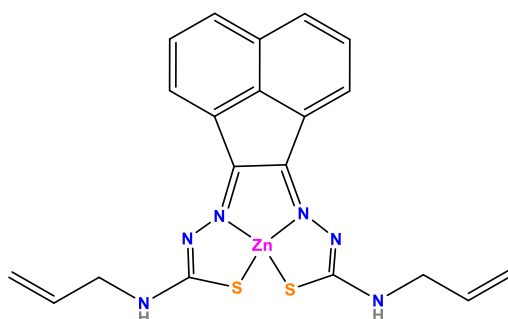


Fig. 1. Fluorescent Zn(II) complex.

Diagnostic radiopharmaceuticals are used to assess the state of organs and tissues previous to or during the treatment.<sup>80,91</sup> For diagnostic radio-imaging, the radionuclide

mean lifetime has to be long enough to allow the synthesis of the radiopharmaceutical complex, the accumulation in the target tissue and the removal through the non-target organs. However, the half-life also has to be short enough to minimize the patient's exposure time to radiation.<sup>79,80,92</sup> There are two different types of clinical radio-imaging:

-Single-photon emission computed tomography (SPECT): generally used for tumour imaging, thyroid imaging, infection imaging and bone scintigraphy. This technique requires a pharmaceutical labelled with a  $\gamma$ -emitting radionuclide. Some of the  $\gamma$ -emitting nuclides used clinically are:  $^{67}\text{Ga}$ ,  $^{111}\text{In}$ ,  $^{99\text{m}}\text{Tc}$  and  $^{201}\text{Tl}$ , being  $^{99\text{m}}\text{Tc}$  the most used.<sup>93,94</sup>

-Positron emission tomography (PET): PET allows to visualize and measure metabolic processes, blood flow and local chemical composition. It is frequently used in the imaging of tumours and to make the diagnosis of metastases, but it can also be used for the diagnosis of diffuse brain diseases. PET requires a pharmaceutical labelled with a positron,  $\beta^+$  emitting radionuclide. Some of these positron emitting nuclides used in medicine are:  $^{55}\text{Co}$ ,  $^{64}\text{Cu}$ ,  $^{66}\text{Ga}$ ,  $^{68}\text{Ga}$ ,  $^{82}\text{Rb}$  and  $^{86}\text{Y}$ .<sup>93,95</sup>

It is also worth mentioning the possibility to use radiopharmaceuticals as therapeutic agents. This application of radiopharmaceuticals is based on the selective delivery of cytotoxic doses of ionizing radiation, which comes from  $\alpha$  particles (helium-4 nuclei,  $^4_2\text{He}^{2+}$ ) or  $\beta^-$  particles (electrons), to the target tissues. Some well-known examples of clinically used  $\beta^-$  emitters radiopharmaceuticals are:  $^{131}\text{I}$ ,  $^{32}\text{P}$ ,  $^{89}\text{Sr}$ ,  $^{153}\text{Sm}$  and  $^{186}\text{Re}$ . Indeed,  $^{131}\text{I}$  is really effective in the treatment of both thyroid cancer and hyperthyroidism.<sup>96</sup>

Another relevant imaging technique is the magnetic resonance imaging (MRI), which is a non-invasive technique used in clinical diagnosis. It uses a harmless magnetic field (1–1.5 T) and radio frequency (40–70 MHz) to provide information related to several diseases like cancer, musculoskeletal disorders, stroke, heart and vascular diseases.<sup>97,98</sup> The MRI is able to detect the spatial distribution of the protons in the body; hence, diseases are detected from the differences in the  $^1\text{H}$  NMR (nuclear magnetic radiation) resonances between healthy and unhealthy tissues. Most of the detected NMR signals come from water and fat, which are the components that contain most of the hydrogen in the human body.<sup>98</sup>

The most used metal ion in MRI contrast agents is Gd (III). Some approved Gd(III) contrast agents are:  $[\text{Gd}(\text{DOTA})(\text{H}_2\text{O})]^-$  (Dotarem),  $[\text{Gd}(\text{DTPA-BMA})(\text{H}_2\text{O})]$  (Omniscan),  $[\text{Gd}(\text{HP-DO3A})(\text{H}_2\text{O})]$  (ProHance),  $[\text{Gd}(\text{BOPTA})(\text{H}_2\text{O})]^{2-}$  (MultiHance) and  $[\text{Gd}(\text{DO3A-butrol})(\text{H}_2\text{O})]$  (Gadovist) (Fig. 2). These complexes are kinetically inert (the release of  $\text{Gd}^{\text{III}}$  is very slow) and thermodynamically very stable. In fact, both features are important to prevent adverse effects in humans.<sup>99,100</sup>



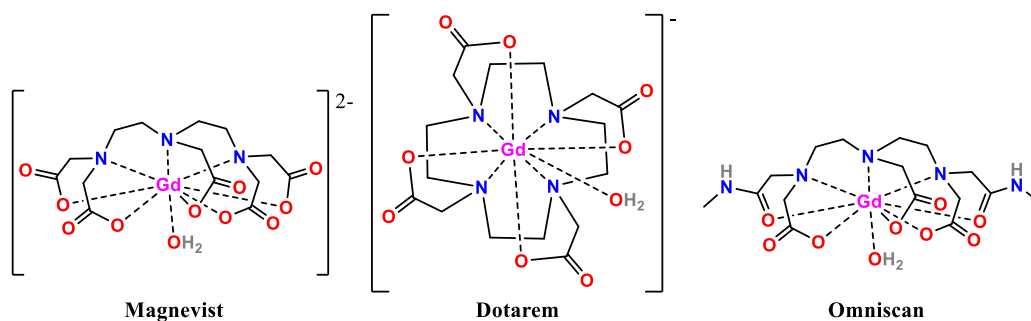


Fig. 2. Gadolinium MRI contrast agents.

## 2.3. Metal complexes as therapeutic agents

### 2.3.1. Gold antiarthritic drugs

Gold complexes act over the immune system, although the mechanism of action is not totally understood.<sup>80,101,102</sup>

Au(I) complexes are currently in use for treating rheumatoid arthritis. These Gold complexes include the water-soluble sodium aurothiomalate (Myocrisin), aurothioglucose (Solganol) and sodium aurothiopropion sulfonate (Allochrysin) (Fig. 3).<sup>103</sup> These Au(I) thiolate derivatives have complex structures in solution, forming chains and rings, with sulphur atoms bridging metal centers.<sup>104,105</sup>

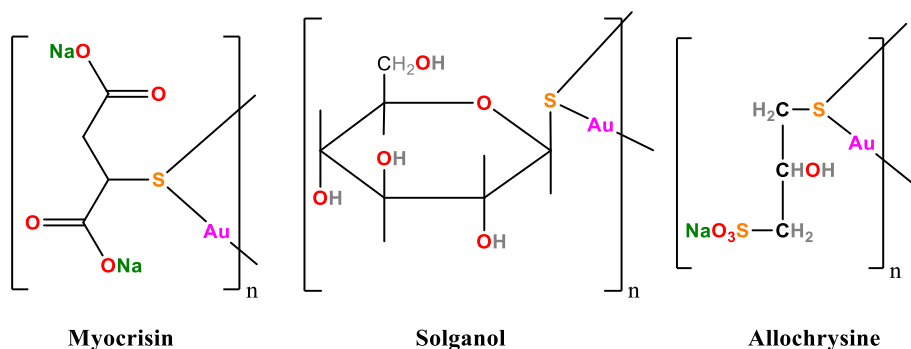


Fig. 3. Injectable antiarthritic gold drugs.

Gold antiarthritic complex in clinical use auranofin (Ridaura) (Fig. 4) is the first example of a drug that contains a phosphine. Auranofin has some interesting properties: it is able to inhibit cathepsins K and S (proteases that are able to destroy joint tissue), it is highly cytotoxic to cancer cells in culture and it is active against psoriasis.<sup>106,107,108</sup>

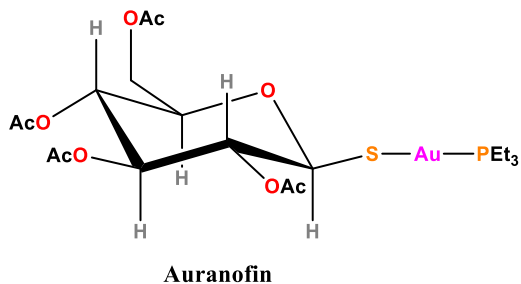


Fig. 4. Oral antiarthritic gold drug auranofin.

$[\text{Au}(\text{CN})_2]^-$  is a common metabolite that is present in urine and plasma of patients treated with gold complexes. This metabolite, easily enters the cells and it is able to inhibit the oxidative burst of white blood cells. Hence, it is thought to be an active metabolite of the gold drugs.<sup>109</sup>

### 2.3.2. Antimicrobial and antiviral agents

Bismuth compounds have been used in medicine for over 200 years, for a wide variety of clinical applications mainly because of their low toxicity. However, recent interest is focused in the antimicrobial activity of Bi(III).<sup>110,111,112</sup>

The best known examples are the citrate complexes, whose structure is based in dimeric units like  $[(\text{cit})\text{BiBi}(\text{cit})]^{2-}$  (cit is tetradeprotonated citric acid) (Fig. 5), These oligomers have an important antiulcer activity in the treatment of *Helicobacter pylori*, as they are deposited on the surface of the ulcers, covering them.<sup>113,114</sup>

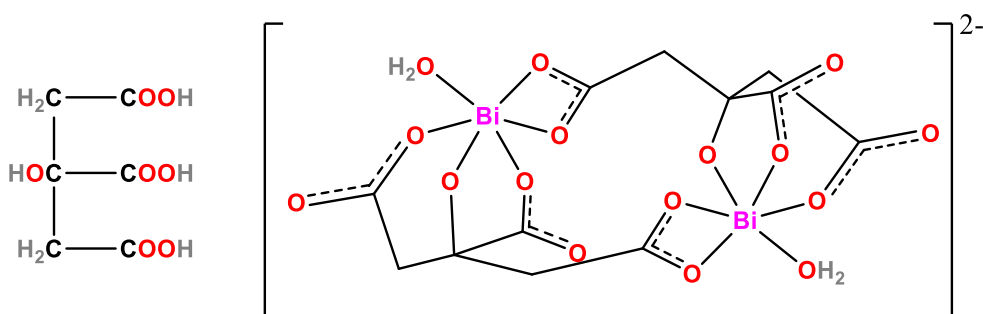


Fig. 5. Citric acid and dimeric Bi(III) citrate complex.

Antimicrobial activity of Ag(I) ions is well known although the mechanism of action is not completely understood. It seems that is related to targeting some enzymes which are involved in the biosynthesis of the cell wall. The silver sulfadiazine (Ag(I)) (Fig. 6) is a polymeric insoluble complex used clinically as antibacterial agent (also has antifungal properties) for treating severe burn wounds, that are easy to become infected.<sup>115</sup>

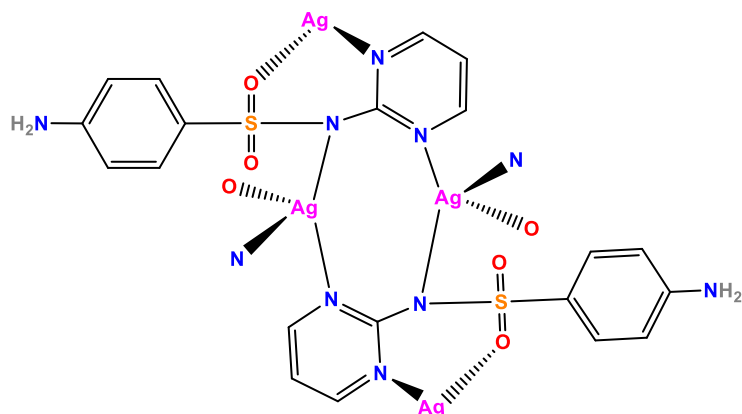


Fig. 6. Antibacterial silver sulfadiazine.

It is worth noting, that metal complexation can increase the efficacy of organic antiparasitic drugs. Following this feature, ferroquine (Fig. 7), the ferrocene conjugate of chloroquine, has been developed for treating malaria, showing really interesting results.<sup>116,117</sup>

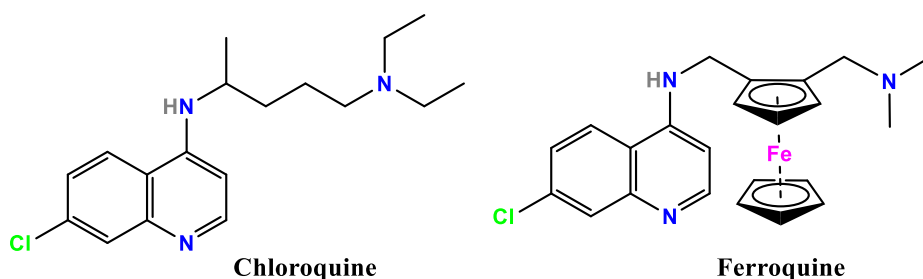


Fig. 7. Antimalarial agents chloroquine and ferroquine.

There are several metal complexes displaying antiviral activity. Thus, bismacrocyclic xylyl-bicyclam AMD3100, as well as the Zn(II) bicyclam complex (Fig. 8), are able to block the early stages of the replication of the human immunodeficiency virus (HIV) and block its entry into the cells by interacting with the co-receptor protein CXCR4. However, AMD3100 has important side-effects, so its use for treating AIDS has been stopped.<sup>118,119</sup> But the interest in this drug is still alive because of its ability to mobilize stem cells, being approved for this purpose in 2008.<sup>120</sup>

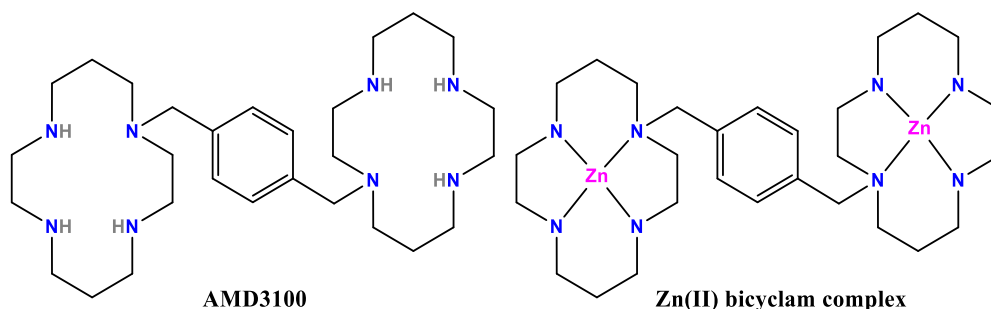


Fig. 8. HIV inhibitors AMD3100 and Zn(II) bicyclam complex.

Aurocyanide,  $[\text{Au}(\text{CN})_2]^-$ , a natural metabolite of gold antiarthritic drugs, is able to inhibit proliferation of HIV in white blood cells even at low concentrations (20 nM), so it might be useful in combined therapies against AIDS.<sup>121</sup>

Another interesting complex with anti HIV-1 activity is the  $\text{V}^{\text{IV}}$ -porphyrin complex functionalized with an aminosulfonyl group (Fig. 9). This compound is able to inhibit the HIV-1 replication in Hut/CCR5 cells even at low concentrations ( $5\mu\text{M}$ ).<sup>122,123</sup>

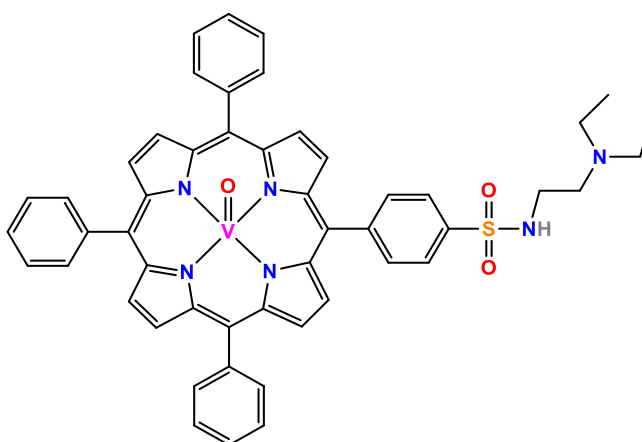


Fig. 9. HIV-1 inhibitor  $\text{V}^{\text{IV}}$ -porphyrin complex.

### 2.3.3. Insulin mimetics

Drugs with low toxicity that can mimic the effects of insulin (insulin mimetics) can be an interesting option for treating diabetes. Some vanadium<sup>124</sup> and chromium<sup>125</sup> complexes are under study for this purpose.

Oxo vanadium complexes of both oxidation states, 4 (vanadate) and 5 (vanadyl), are able to stimulate the synthesis, uptake and oxidation of glucose. They are sometimes described as insulin-enhancing agents. The complex Bis(maltolato)oxovanadium (IV) (BMOV) (Fig. 10), acts lowering the plasma glucose levels. Its analogue

bis(ethylmaltolato)oxovanadium (IV) (BEOV) (Fig. 10) has completed Phase I of clinical trials,<sup>80,124,126</sup> and another maltol analogue, bis(isopropylmaltolato)oxovanadium (IV) (BIOV) (Fig. 10), is more active than BMOV without significant toxicity in trials.<sup>127</sup> It is important to mention that the mechanism of action of these compounds is not totally clear and it is also not clear whether V(IV) or V(V) is the active species in insulin mimetics.<sup>128</sup>

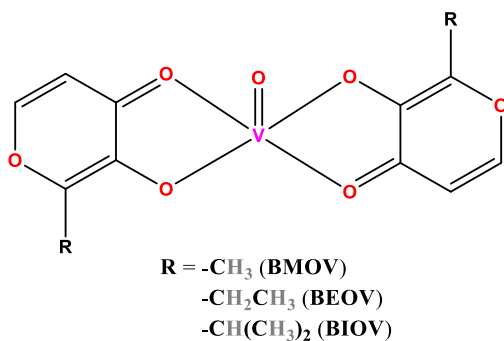


*Fig. 10. Maltolate oxovanadium insulin mimetics.*

Chromium, which is an essential element, improves the action of insulin and it has been found that patients with type 2 diabetes have lower levels of chromium in blood. Moreover, it affects the metabolism of lipids, proteins and carbohydrates. The widely used weight-loss supplement chromium picolinate ( $[\text{Cr}^{\text{III}}(\text{picolinate})_3]$ ) (Fig. 11) is able to reduce fructosamine and glucose levels in patients affected by diabetes of type 2. and to lower the insulin resistance and hyperglycemia.<sup>125,129</sup>

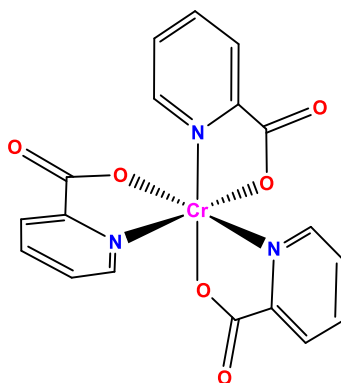


*Fig. 11. Chromium picolinate complex.*

### 2.3.4. Cardiovascular system

The Fe(II) complex sodium nitroprusside (Fig. 12), which is the only metal-nitrosyl complex used medically, is used to reduce blood pressure. Its hypotensive effect is very effective and fast, allowing to achieve the desired blood pressure in one or two minutes.<sup>130</sup> Moreover, it is useful for emergency hypertension, heart attacks, and surgery.<sup>131,132</sup> Its mechanism of action is based on the release of nitric oxide (NO) which is able to cause the relaxation of vascular smooth muscle; it is thought that the mechanism *in vivo* involves the reduction to  $[\text{Fe}(\text{CN})_5(\text{NO})]^{3-}$ , then the release of a cyanide anion to produce  $([\text{Fe}(\text{CN})_4(\text{NO})]^{2-})$  and finally the release of nitric oxide.<sup>133,134</sup>

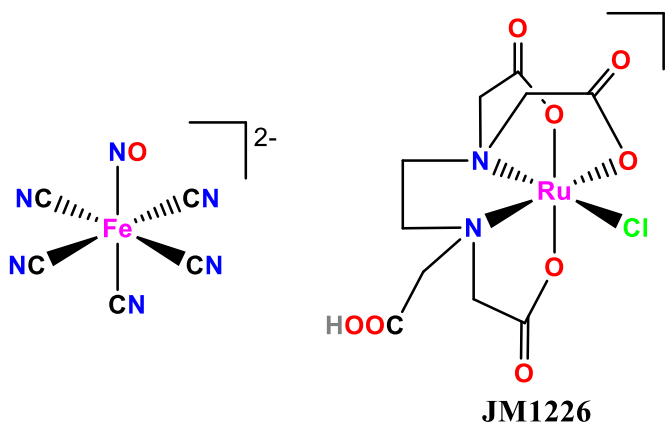


Fig. 12. Sodium nitroprusside Fe(II) complex and JM1226.

Ruthenium complexes like  $\text{K}[\text{Ru}(\text{Hedta})\text{Cl}]$  (JM1226) (Fig. 12) have been suggested as nitric oxide scavengers with the aim of controlling its levels in medical applications. For instance, to improve the poor response of artery vasoconstrictor drugs, an important fact when treating septic shock, which is related with a dangerous low arterial pressure.<sup>135</sup>

### 2.3.5. Anticancer agents

#### 2.3.5.1. Platinum anticancer agents

Platinum drugs are the most successful metal anticancer drugs, with several complex being used in the clinic.<sup>136</sup> Cisplatin (cis-diamminedichloroplatinum(II)) (Fig. 13) is the most employed.<sup>137</sup> Cisplatin was first synthesized in 1844, but its anticancer properties were not discovered until 1965 (Rosenberg).<sup>138</sup> Cisplatin is very effective for treating ovarian carcinoma and testicular cancer, and is also used for treating head and neck, lung, bladder and cervical cancer among others.<sup>137</sup>

Cisplatin is administered intravenously in saline media, because it readily suffers aquation (hydrolysis) in aqueous and low chloride media.<sup>139</sup> In plasma, the dominant

species of cisplatin are the dichloro and the chloro-hydroxo species. Whereas in cell nucleus and cytoplasm, where chloride concentration is lower, there is a higher concentration of the aqua species. Thus, the aquation occurs easily inside cells and this is very important, because the aqua species are more reactive than cisplatin and can bind the DNA.<sup>140</sup> However, these species are also more damaging to kidney.<sup>141</sup>

The major target site of cisplatin in DNA is N7 of guanine, because it is the electron richest site on the DNA molecule. This is the easiest position to oxidize, and it is also easily accessible (located in the major groove of B-DNA) for cisplatin.<sup>139,140,142</sup> Other important binding site is N7 of adenine.<sup>136,139</sup> These binding sites are located in the dinucleotide sequences GG and AG, so the main intrastrand adducts formed are 1,2-d(GG), 1,2-d(AG)<sup>143</sup> and 1,3-d(GG),<sup>144</sup> respectively. The formation of these adducts causes major structural changes in DNA (it causes DNA to kink) which leads to the arrest of the replication, the inhibition of the transcription, the arrest of the cell cycle, and finally, the cell death by apoptosis.<sup>137,144</sup> Interstrand adducts (1,3-d(GG)) are rarer, but are also important for cytotoxicity.<sup>145</sup>

Cisplatin toxicity and side effects (peripheral neuropathy, nephrotoxicity, ototoxicity...) spurred the interest in developing new platinum based drugs active against more cancer types (breast, lung, colon...), and which are not cross-resistant to cisplatin in treatments extended in time.<sup>146,147</sup>

In this regard, it is important to consider the 3 main structural features related to the activity of platinum drugs: they are neutral in charge, they have square-planar Pt(II) or octahedral Pt(IV) geometries bearing two monodentate N ligands or one bidentate diamine (the amines have to be primary or secondary), and they have two monodentate leaving groups or one bidentate leaving group, like Cl<sup>-</sup> or carboxylate, which are reactive enough without being excessively reactive.<sup>146,147,148</sup>

The second clinically approved drug was carboplatin (*cis*-diamine[1,1-cyclobutanedicarboxylato]platinum(II)) (Fig. 13). Carboplatin differs from cisplatin in the fact that it has a bidentate dicarboxylate ligand (CycloButane DiCarboxylic Acid, CBDCA) instead of the two chloride ligands. It is used for treating a wide variety of cancers which include lung, head and neck, ovarian and brain cancer, and neuroblastoma. It can also be used for treating testicular cancer, but is less effective than cisplatin for this purpose. The main benefits of carboplatin, compared with cisplatin, are that it is less toxic and less reactive, so the side effects are reduced. Nephrotoxic (kidney poisoning) effects are not present in the treatment with carboplatin and nausea and vomiting are weaker.<sup>147,148,149</sup>

Nedaplatin (Cis-Diammine(Glycolato)platinum(II)) (Fig. 13), also has a chelated ligand (a glycolate) instead of the chlorides that possess cisplatin. It was approved for clinical

use in Japan in 1995 (the only country where it has been approved so far) for treating oesophageal, ovarian, cervical, head and neck, testicular and NSCLC. Nedaplatin causes less nephrotoxicity than cisplatin, but other adverse effects like nausea and vomiting, and mild peripheral neuropathy can appear during the treatment. Also, the ototoxicity (loss of high frequency hearing) is similar to the one caused by cisplatin. Like cisplatin and carboplatin, nedaplatin is administered with intravenous injections.<sup>147,148,150</sup>

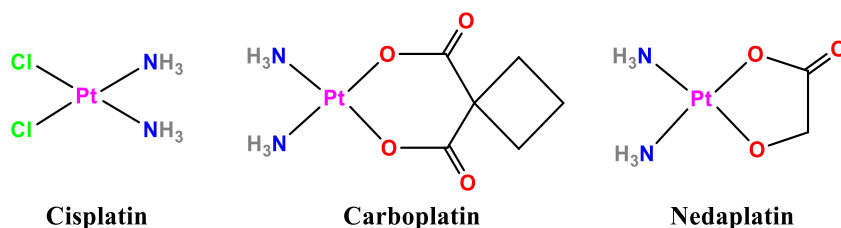


Fig. 13. Cisplatin, carboplatin and nedaplatin.

The complexes with the bidentate ligand 1,2-diaminocyclohexane (dach) are usually active against cancer cells with cisplatin resistance. Based on this, the third generation platinum anticancer drug oxaliplatin ((*trans*-R,R-1,2-diaminocyclohexaneoxalato)platinum(II)) (Fig. 14) was designed. Structurally, oxaliplatin has a bidentate 1,2-diaminocyclohexane instead of the two monodentate ammine ligands seen in the platinum compounds above. Its clinical use was approved in 2002 for treating colorectal cancer in combination with 5-fluorouracil. It has several advantages compared with cisplatin and carboplatin: (a) it has a higher cytotoxicity and DNA synthesis inhibition, (b) it is active against cisplatin resistant cancer cells and it is less nephrotoxic.<sup>147,148,151</sup>

Picoplatin (cis-(2-methylpyridine)(ammine)dichloroplatinum(II)) (Fig. 14) has very similar structure to cisplatin; the only difference is the substitution of one of the ammine ligands for 2-methylpyridine (2-picoline). It reacts slower than cisplatin due to the slower aquation of the chloride ligand cis to 2-picoline (2-5 times slower). This occurs because the steric effect of the methyl group, which difficult the attack on platinum. Picoplatin is in phase III clinical trials for SCLC, colorectal and prostate cancer; it has proved to be active against platinum-sensitive, -resistant, and -refractory cancer cells without significant nephrotoxicity and neurotoxicity.<sup>148,152</sup>



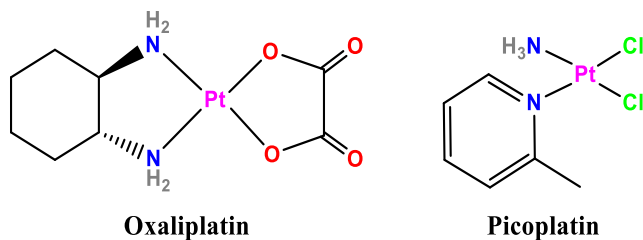


Fig. 14. Oxaliplatin and picoplatin.

Other examples of third generation anticancer platinum compounds include lobaplatin (1,2-diamino-methyl-cyclobutaneplatinum(II)-lactate) and heptaplatin (*cis*-malonato[(4*R*,5*R*)-4,5-bis(aminomethyl)-1,3-dioxolane] platinum(II)) (Fig. 15). These complexes are approved for its clinical use in China, Japan and South Korea. The structure of these compounds differs from that of cisplatin in the fact that they have a bidentate diamine derivative instead of the two monodentate amine ligands and a bidentate lactate group (lobaplatin) or a dicarboxylate group (heptaplatin) instead of the two chlorides; the substitution of de chlorides for the carboxylates makes the complexes less reactive and so less toxic.<sup>147,148</sup> Lobaplatin is a mixture in an approximately 1:1 proportion of the two diastereoisomers SSS (LP-D1) and RRS (LP-D2), and it is approved for the treatment of chronic myeloid leukemia and NSCLC.<sup>147,148,153</sup> Heptaplatin is effective against cisplatin resistant gastric cancer cells, showing a low nephrotoxicity compared to cisplatin, so it is used for this purpose. Also, it seems to be active against colorectal and NSCLC.<sup>147,148,154</sup>

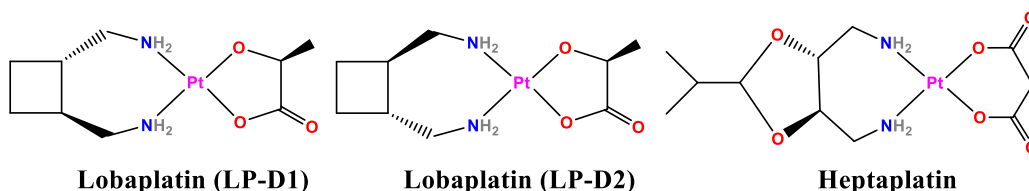


Fig. 15. Lobaplatin and heptaplatin.

Platinum(IV) octahedral complexes are more inert than their analogues of platinum(II) and offer more design options, due to the two additional coordination sites. These Pt(IV) compounds are reduced to Pt(II) *in vivo* by the action of reductants like thiols or ascorbate.<sup>155,156</sup>

Satraplatin (bis(acetato)amminedichlorocyclohexylamine platinum(IV)) (Fig. 16) is a fourth generation platinum complex. It presents an octahedral structure with two chlorides, two monodentate acetates, one ammonia ligand and one cyclohexylamine ligand. Its mechanism of action is similar to that of cisplatin, it binds to the DNA molecule of cancer cells, making them unable to divide. It has activity against cisplatin resistant cancers like ovarian, prostate and SCLC, being preregistered in Europe for the

treatment of prostate cancer and in phase II/III in Europe and USA for other cancers. It is worth to mention that Satraplatin is an oral drug.<sup>147,148,157</sup>

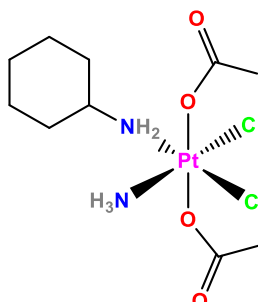


Fig. 16. Satraplatin.

A new type of potential platinum anticancer drugs are the multinuclear platinum complexes. These compounds act by an interstrand DNA cross-linking mechanism. Being positively charged, these compounds have an important increased uptake compared with cisplatin and suitable drug delivery methods are being explored. Examples of this type of drugs include BBR3464 (trinuclear) and BBR3571 (dinuclear) (Fig. 17). Both compounds can induce cell cycle arrest in the G2/M phase without causing cell death (cisplatin causes apoptosis).<sup>158</sup>

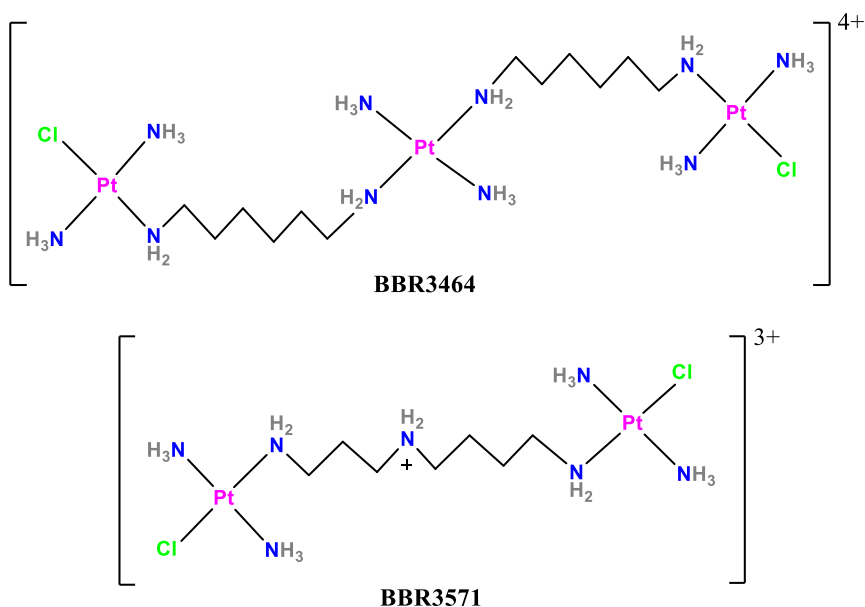
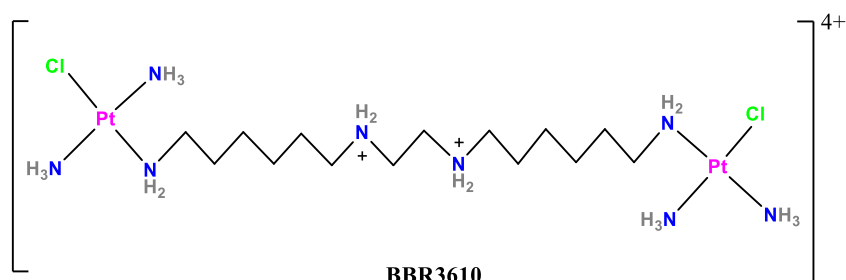


Fig. 17. BBR3464 and BBR3571.

Another BBR dinuclear compound, BBR3610 (CT-3610) (Fig. 18 induces apoptosis via a caspase 8-dependent mechanism, being more cytotoxic than cisplatin, oxaliplatin and BBR3464 on several colon and rectal cancer cell lines.<sup>159,160</sup>



*Fig. 18. BBR3610.*

### 2.3.5.2. Other metal-based anticancer agents

The tetrahedral titanium(IV) complex titanocene dichloride, [TiCp<sub>2</sub>Cl<sub>2</sub>] (Fig. 19), has shown good activity against breast, lung, and gastrointestinal cancers in mice, even though this has not been confirmed in humans yet.<sup>161,162</sup>

Variations in the ligands lead to Titanocene Y (bis-[(p-methoxybenzyl)cyclopentadienyl] titanium dichloride) and Titanocene Z ([1,2-di(cyclopentadienyl)-1,2-bis(3',5'-dimethoxyphenyl)-ethanediyl] (Fig. 19). Titanocene Y shows specific activity against renal cancer cells,<sup>163,164</sup> whereas Titanocene Z is used for treating advanced prostate cancer.<sup>165</sup> The mechanism of action of titanocenes is not clear. It is known that they lose both chloride ligands in two steps (the first one faster than the second),<sup>166</sup> but it is not clear which is the primary target of the titanocenes: they can bind to the phosphate groups of the DNA or to some proteins like transferrin (Fe(III) transport protein), interfering with iron biochemistry. However, they could also bind to other biomolecules.<sup>167,168</sup>

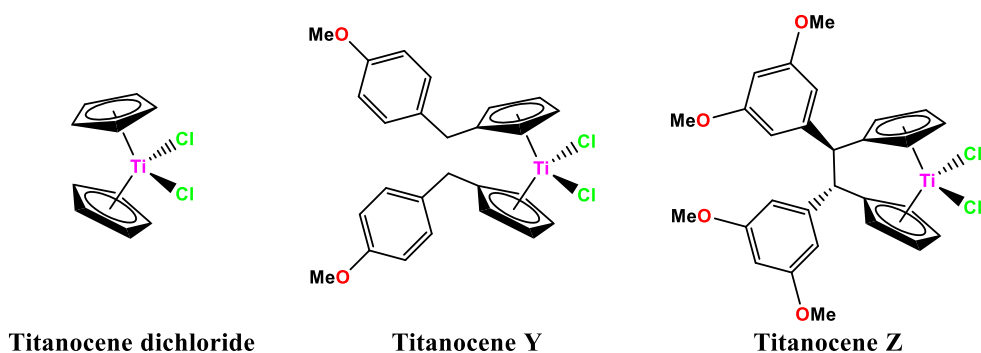


*Fig. 19. Titanium anticancer agents.*

Ruthenium complexes are gaining interest in medicinal chemistry, for example, the octahedral Ru(III) complexes *cis*-[RuCl<sub>2</sub>(NH<sub>3</sub>)<sub>4</sub>]Cl and *fac*-[RuCl<sub>3</sub>(NH<sub>3</sub>)<sub>3</sub>] (Fig. 20) have an important anticancer activity, although their low solubility has prevented their clinical use.<sup>169</sup> Ru(III) complexes with imidazole or indazole are also interesting for cancer treatment.<sup>170,171</sup> An example is NAMI-A, ((ImH)[trans-Ru<sup>III</sup>Cl<sub>4</sub>(Me<sub>2</sub>SO)(Im)]) (Fig. 20), which entered clinical trials in 2000, being the first ruthenium complex to achieve it. This complex is not very toxic to cancer cells, but prevents metastasis.<sup>172,173</sup> The second ruthenium compound to reach clinical trials (2003), is KP1019 ((IndH)[trans-Ru<sup>III</sup>Cl<sub>4</sub>(Ind)<sub>2</sub>]) (Fig. 21), which has shown interesting results against colon carcinomas with low toxicities.<sup>174</sup> Its mechanism of action is based on mitochondrial mediated apoptosis, being effective against primary and secondary tumours.<sup>175</sup>

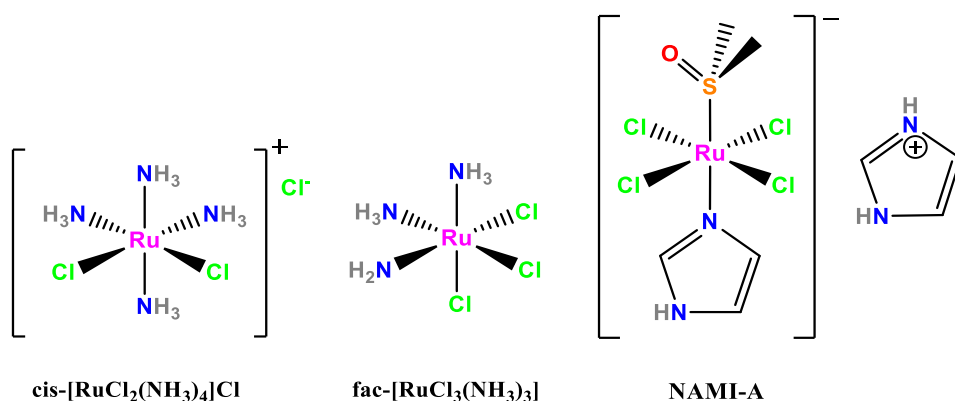


Fig. 20. *cis*-[RuCl<sub>2</sub>(NH<sub>3</sub>)<sub>4</sub>]Cl, *fac*-[RuCl<sub>3</sub>(NH<sub>3</sub>)<sub>3</sub>] and Nami-A.

The mechanism of action of these Ru(III) compounds is complex and involves several steps and possibilities, which are not totally clear up to date. In a first step, the complexes suffer aquation and in the second, the Ru(III) is reduced to Ru(II) (tumours are hypoxic and contain reductants like thiols). The formation of Ru(II) weakens the bonds between the metal and the  $\sigma$ -donor ligands, which promotes ligand substitution reactions. Ruthenium, both (II) and (III), binds to DNA (preferently to G-N7). Ru(III) also binds to proteins like transferrin (a Fe(III) transport protein), so maybe, part of the activity of these compounds can be related to interfering with the biochemistry of iron in cancer cells, which is needed for cell division. Also, it is important to note that Ru–transferrin complexes show anticancer activity by themselves.<sup>176,177,178</sup>

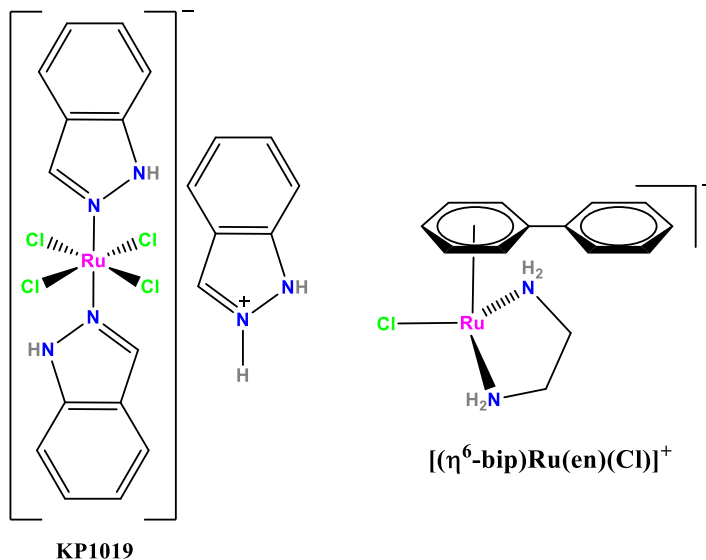


Fig. 21. KP1019 and  $[(\eta^6\text{-bip})\text{Ru}(\text{en})\text{Cl}]^+$ .

Another type of structure of ruthenium anticancer complexes is the one known as “piano-stool” or “half-sandwich”. A paradigmatic example of this type of Ru(II) compounds is  $[(\eta^6\text{-arene})\text{Ru}(\text{en})\text{Cl}]^+$  (en=ethylenediamine), which is shown in Fig. 21 with a biphenyl as the arene. The chloride bonded to the ruthenium atom in these compounds suffers aquation easily.<sup>179</sup> The mechanism of these complexes is based on their capacity to bind to DNA through N7 of Guanine, and also, by hydrogen bonding from NH of ethylenediamine to OC6 of G. Moreover, if the arene is big enough, like a biphenyl or a tetrahydroanthracene, arene-purine base stacking is also possible, and therefore a dual interaction mode can take place, namely, covalent binding plus intercalation into DNA.<sup>180,181</sup>

The Au(III) compounds are isostructural (square planar) and isoelectronic ( $5d^8$ ) with Pt(II) compounds. Nevertheless, they suffer a faster ligand substitution and their reduction potentials are higher; this can be seen with the gold analogue of cisplatin, which is excessively reactive and is quickly reduced. However, there are also more stable Au(III) complexes with anticancer activity, which are achieved with a design that includes strong  $\sigma$ -donors and rigid ligand scaffolds.<sup>182</sup> An example is the Au(III) porphyrin complex  $[\text{Au}(\text{TPP})\text{Cl}]$  (Fig. 22), which has shown a high efficacy against several cancer cell lines, even versus those resistant to cisplatin and multidrug treatments. Also, it is important to consider its selectivity toward cancer cells, causing a very low toxicity to normal cell compared to cancer cells. It is thought that the complex acts by a mechanism based on the release of cytochrome c, which causes the activation of caspases, which subsequently, triggers an apoptotic cell death.<sup>183,184</sup>

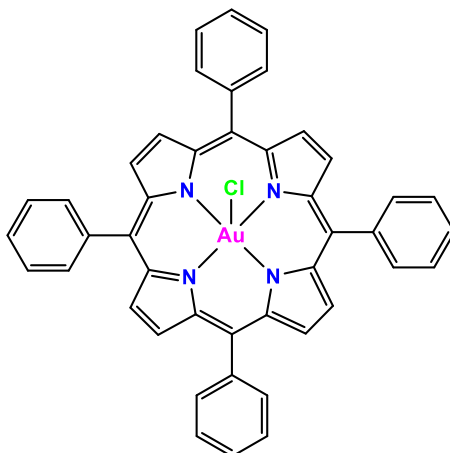


Fig. 22. Au(III) porphyrin complex [Au (TPP)Cl].

Square planar Rh(I) complexes, as for instance, the rhodium cyclooctadiene derivative (Fig. 23) and Rh(III) analogues of the Ru compounds discussed before, had shown anticancer activity.<sup>185,186,187</sup> Moreover, rhodium(II) propionate, [Rh<sub>2</sub>(prop)<sub>4</sub>], and its analogues with nicotinate (nic) and isonicotinate (isonic), [Rh<sub>2</sub>(prop)<sub>4</sub>(nic)<sub>2</sub>]<sup>2-</sup> and [Rh<sub>2</sub>(prop)<sub>4</sub>(isonic)<sub>2</sub>]<sup>2-</sup> show good antitumour activity against the Ehrlich ascites tumours.<sup>188</sup>

There are iridium compounds with anticancer activity such as the “half-sandwich” Ir(III) analogues of the above-mentioned Ru(II) arene-complexes. The iridium derivatives typically exhibit three different ligands: the Cp\* (1,2,3,4,5-pentamethylcyclopentadiene), a bidentate diamine and a chloride.<sup>189,190</sup> Another type of biologically active Ir(III) complexes are the polypyridyl iridium complexes of the general formula *fac*-[IrCl<sub>3</sub>(DMSO)(L<sup>Λ</sup>L)] (L<sup>Λ</sup>L can be a 2,2'-bipyridine, 1,10-phenanthroline, 1,8-Bis(diphenylphosphino)naphthalene, etc). These compounds have shown to be active against breast cancer and colon carcinoma cells; a representation of this type of compounds with a phenanthroline as the polypyridyl ligand can be seen in Fig. 23.<sup>191</sup>

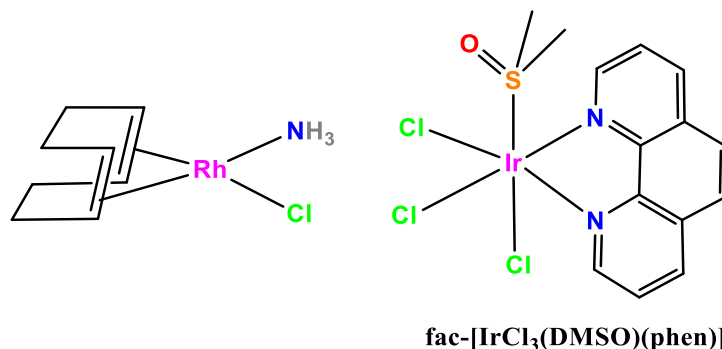


Fig. 23. Rhodium cyclooctadiene derivative and fac-[IrCl<sub>3</sub>(DMSO)(phen)].

Some Cu(I) and Cu(II) compounds have also anticancer properties against various types of cancers like colon, breast, prostate and lung cancer. Examples of these are the phenanthroline and thiosemicarbazone derivatives (A and B in Fig. 24).<sup>192,193</sup> Cobalt(III) compounds of the type alkylcobalt, like the one showed in Fig. 24, can be used like precursors for generating alkyl radicals, which are able to damage DNA. This opens the door to a new type of strategy for the design of anticancer drugs.<sup>194</sup>

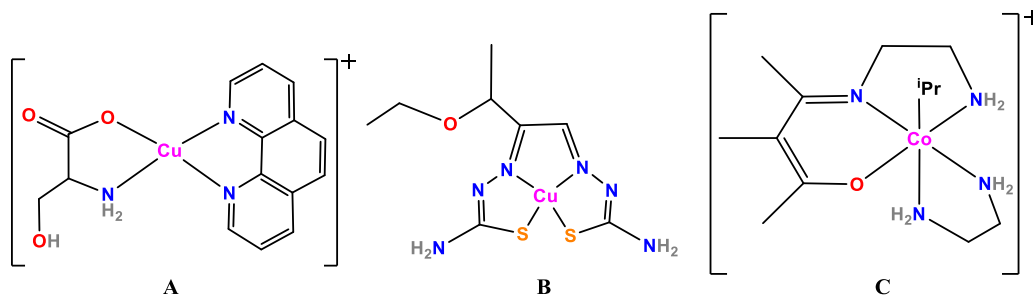


Fig. 24. Cu-phenanthroline (A) and -thiosemicarbazone (B) derivatives, and alkylcobalt type compound (C).

Fe(II) complexes are also a promising class of anticancer drugs. For instance, ferrocene derivatives with tamoxifen based ligands such as hydroxyferrocifens are very active against hormone-dependent and hormone-independent breast cancers. Coordinating the organic ligand to a metal has an important enhancing effect in the biological activity, and the iron complex is active even against breast cancer cell lines (MDA-MB321) for which tamoxifen or its derivatives like hydroxytamoxifen are inactive.<sup>195,196</sup> Finally, it is also worth mentioning that Ni(II) compounds with Schiff bases as ligands feature high capacity to inhibit telomerase, which finally leads to the inhibition of the cell division of cancerous cells itself.<sup>197</sup> An example of this type of drugs is shown in Fig. 25.

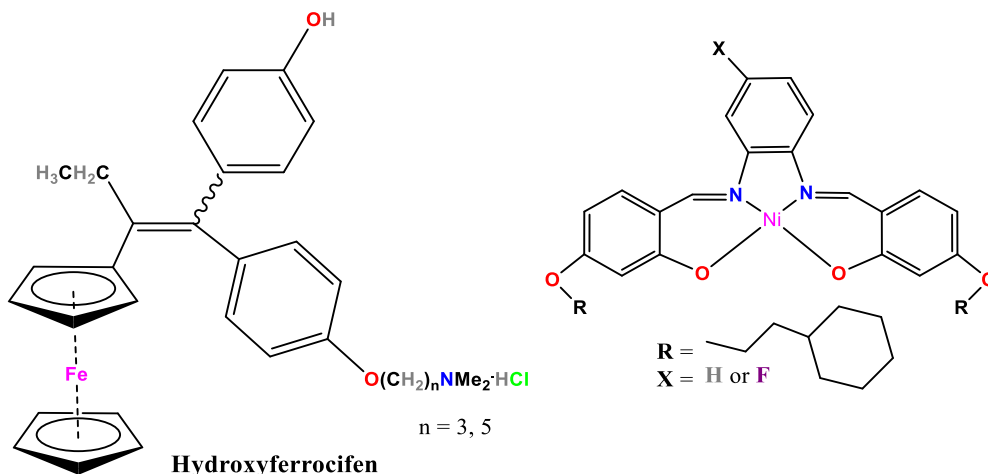


Fig. 25. Hydroxyferrocifen and telomerase inhibiting Ni(II) complex.

### 3. Photodynamic therapy (PDT)

#### 3.1. Historical development of photodynamic therapy

The therapeutic effect of light has been known since 3000 years ago. Ancient civilizations like the Egyptian, Indian and Chinese used it, combined with reactive chemicals (mainly some plant extracts) in most cases, for treating several diseases like psoriasis, vitiligo and skin cancer.<sup>198,199</sup>

In the second half of the 19<sup>th</sup> century, the interest in heliotherapy (therapy based in the patient exposure to sunlight for treating skin conditions) grew.<sup>200</sup> In 1877 Downes and Blunt discovered that sunlight was able to kill anthrax bacilli,<sup>201</sup> and in 1890, Palm suggested that sun light could help treating rachitis, but he was ignored (it was only in 1919 when phototherapy started to be used for treating rickets).<sup>202</sup> Also in 1890, König presented the results he obtained in the treatment of peritoneal tuberculosis with sun exposure.<sup>203</sup> By the end of the 19<sup>th</sup> century, people started to perceive that UV rays from the sun were the most important wavelengths for therapeutic purposes. This prompted the use of artificial light sources and filtered solar radiation.<sup>201</sup>

In 1893, Niels Finsen used filtered sunlight for treating lupus vulgaris, opening a new avenue for medicine, and in 1894 Lahmann constructed and used a carbon arc lamp, combined with a parabolic mirror, to heal patients suffering from lupus vulgaris in the nose. With these advances, heliotherapy started to be surpassed by phototherapy.<sup>201</sup>

The first book devoted to phototherapy (*Die Heilkraft des Lichtes*) was published in 1898 by Willibald Gebhardt. This book gathers the methods and equipment for treating



through phototherapy a variety of diseases such as lupus vulgaris, prurigo, psoriasis, leprosy, acne, syphilis and pellagra.<sup>204</sup>

In 1901, Niels Finsen published the results obtained from treating lupus vulgaris with UV radiation from a carbon arc lamp, which made/allowed him to be rewarded with the Nobel prize in 1903.<sup>205</sup> At the same period of time, in 1900, Raab, a student of the group of Von Tappeiner, found by accident that acridine killed paramecia in the presence of day light when he was looking for new antimalarials; observing for the first time the so-called photodynamic effect.<sup>206</sup> Von Tappeiner thought that fluorescent substances could be used along with light for therapeutic purposes, so in 1903, he started, along with Jesionek, the first experiments in humans using an eosin dye; the study was centred in treating skin diseases (syphilitic, cancerous and tuberculous skin conditions) because their easy accessibility.<sup>207</sup> In 1904 Von Tappeiner and Jodlbauer demonstrated that oxygen was essential in this therapeutic action and coined the term photodynamic.<sup>208</sup>

In 1908, Hausmann studied the photodynamic effect of hematoporphyrin (Hp)<sup>209,210</sup> and in 1912, Meyer-Betz made a self-experiment: he injected himself Hp and then irradiated his forearm with a Finsen lamp; ulceration appeared in the area of irradiation, and even days later, casual exposure to daylight caused a phototoxic reaction.<sup>211</sup>

There were several studies using Hp for treating psoriasis (in combination with UV light)<sup>212</sup> and for tumour localization (red fluorescence appears in the tumours due to the accumulation of Hp),<sup>213,214</sup> with the final aim of using Hp as a photosensitizer for treating cancer thanks to its tumour localization.<sup>215</sup> But there were several problems such as the impurities and the fact that Hp was obtained as a mixture of distinct porphyrins, which caused undesired phototoxic reactions and subsequently the use of Hp for these purposes was abandoned.<sup>216</sup>

In 1955 there was a key discovery in the photodynamic field. Samuel Schwartz achieved the isolation of the hematoporphyrin derivative (HpD, later known as Photofrin) by acetylation and reduction of hematoporphyrin.<sup>217</sup> Then, Lipson used HpD for tumour localization in animals and humans,<sup>218,219</sup> and, in 1966, he reported for the first time the use of HpD combined with light irradiation for breast cancer treatment.<sup>220</sup> The term photodynamic therapy (PDT) appeared for the first time in 1972.<sup>221</sup> In 1978, Dougherty reported the first controlled human clinical study in cancer treatment with PDT. In this study, dihematoporphyrin-ether (DHE) or HpD in combination with filtered light from a xenon arc lamp (600-700 nm) were used on 25 patients for treating cutaneous or subcutaneous tumours with good results (111 of the 113 tumours showed complete or partial remission). Since this first study, more than 283 clinical trials based on PDT have been launched (44 are active nowadays).<sup>222</sup>

In 1993, the first PDT agent, photofrin, was approved. Then, several PDT agents such as visudyne, levulan, foscan, etc., were approved.<sup>223</sup> All of these agents and the state-of-the-art of the photodynamic therapy will be discussed later in this section. It is worth mentioning, as evidence of the current interest in this area, that in the last two decades more than 300 reviews treating the PDT topic have appeared in the literature.<sup>224</sup>

### 3.2. Cellular Mechanisms of PDT

There are 3 main elements, whose individual effects are non-toxic for cells, to be considered in photodynamic therapy. These elements are: the photosensitizer (PS), light of an adequate wavelength ( $\lambda$ ) and the molecular oxygen of the cells ( $O_2$ ). The typical PDT process starts with the administration of the PS either topically or by injection and its subsequent transport to tissues. Then, the PS is uptaken by cells, ideally is in its innocuous form. Once the PS reaches a maximum concentration in the vasculature and in the tumour,<sup>225,226,227</sup> the cancerous tissue is irradiated with a suitable light source. The PS absorbs a photon of this light and is promoted to a singlet excited state ( $^1PS^*$ ). Then, it suffers a partial relaxation to a triplet excited state ( $^3PS^*$ ) by a process known as intersystem crossing (ISC).<sup>228</sup>  $^3PS^*$  can reduce cellular  $O_2$  generating the superoxide radical anion  $O_2^{\cdot-}$  (hydrogen peroxide  $H_2O_2$  and hydroxyl radicals  $\cdot OH$  are also generated) through an electron transfer mechanism or type I mechanism. Alternatively, the  $^3PS^*$  can interact with the ground state of oxygen to generate singlet oxygen  $^1O_2$  by energy transfer (ET) (type II mechanism). Singlet oxygen is an electronically excited state form of molecular oxygen and is very reactive.<sup>229,230</sup> In general, all these oxygen species are very reactive, being called as ROS (reactive oxygen species), and can damage essential biomolecules like DNA and proteins through oxidation reactions, which ultimately can trigger cancer cells death in an efficient and selective manner (the mechanism of action in PDT is depicted in Fig. 26).<sup>231,232</sup>

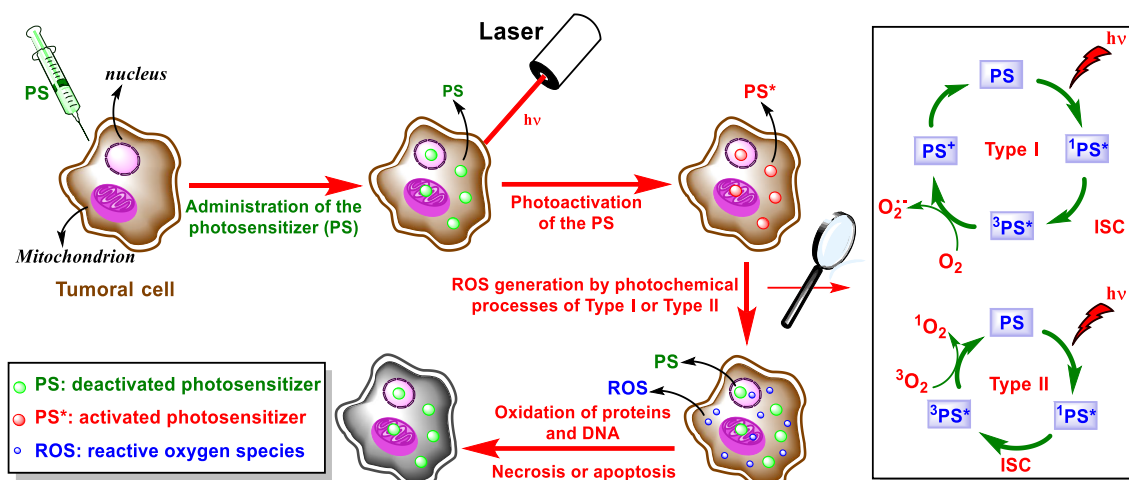


Fig. 26. Mechanism of action in PDT.

Potential advantages of PDT over other treatments are: (a) it is a localized therapy, only affecting the area of interest thanks to the application of directed light and the selective accumulation of the PS in the tumour, (b) the cytotoxic mechanism of action does not damage connective tissues, (c) the possibility of repeating the treatment multiple times, (d) the fact that PDT inhibits the drug resistance mechanisms and (e) the activation of immunological responses caused by PDT, which makes it an interesting option for its use in combined therapies along with immunotherapy.<sup>225,233</sup>

### 3.3. Requirements for the photosensitizers (PS)

The following requirements are critical for PSs used in PDT:

- Non-toxic soluble counterion: this requirement is mainly for metallic complexes used in PDT, which are positively charged. The counterion has an effect over the solubility of the complex, and a poor water solubility can cause the formation of colloids and nanoaggregates and decrease the cellular uptake.<sup>234,235</sup> Hexafluorophosphate ( $\text{PF}_6^-$ ) is a widely spread counterion for this type of compounds, because it facilitates the isolation of the products and it is non-toxic, but it has the important drawback of its low solubility in water, which can affect negatively the biological activity of the complex. To overcome this, chloride ion ( $\text{Cl}^-$ ) is an interesting alternative as counterion for biological studies.<sup>236,237</sup>

- High absorption in the visible range: the absorption is a key parameter for PDT because it determines the excitation window for the PS. The wavelength of the irradiation source affects the penetration depth of the light across the tissues. So, while for topical applications visible light of short wavelengths is used, for treatments where the target tissues are deeper, longer wavelengths, in the so-called therapeutic window

(600-900 nm), are needed. Red light is the most common light used for PDT, because it possesses the longest wavelength (618-780 nm) in the visible spectrum. Also, it is important to note that PSs must possess large molar extinction coefficients ( $\epsilon$ ) for the wavelengths of interest. The best and most used light sources for PDT in clinical applications are diode lasers and LED array lasers.<sup>238,239</sup>

- Long excited state lifetime: as seen before, when  $^1\text{PS}^*$  undergoes a relaxation by an ISC pathway,  $^3\text{PS}^*$  is formed. This triplet excited state is able to interact with oxygen to form ROS, generating in this way the photodynamic effect of interest.<sup>228,229,230</sup> So, to enable this interaction with oxygen,  $^3\text{PS}^*$  needs to be long lived. In this regard, the metal core of the complex plays a key role. Alternatively, an easy way to extend the lifetime of the excited state of a complex, is to introduce iodide atoms in the ligand to take advantage of the heavy atom effect.<sup>240</sup>

- Ability to generate reactive oxygen Species: the photocatalytic generation of ROS is compulsory for a PS, because these species are responsible for the therapeutic phototoxic effect. PSs are distinguished by their mechanism of ROS generation: as explained above, type I mechanism, mediated by electron transfer (eT), generates the superoxide radical anion  $\text{O}_2^{\cdot-}$ , and also hydrogen peroxide  $\text{H}_2\text{O}_2$  and hydroxyl radicals  $\cdot\text{OH}$ , and type II mechanism, mediated by energy transfer (ET), generates singlet oxygen  $^1\text{O}_2$ . Most of the PSs used clinically generate ROS by the type II mechanism,<sup>241</sup> but considering that cancerous tissue usually has a low oxygen concentration (hypoxia), PSs that act through  $\text{O}_2$ -independent mechanisms are also desirable for PDT. As it can be seen, tumours possess challenging conditions for PSs,<sup>242,243</sup> so complexes with high singlet oxygen quantum yields ( $\Phi_\Delta$ ; 20-50 % under normoxia) or high yields for other ROS generation are needed to overcome them.<sup>241,244</sup>

- High stability and photostability: both stability and photostability are very important for PSs.<sup>245</sup> The PS has to be stable and avoid degradation in the biological media. The metal core of the complex is stable, but the organic moiety can suffer transformations, compromising the stability of the whole complex. Moreover, a PS has to be stable upon irradiation, which is the moment when ROS are generated. This is more challenging, because some complexes that are stable in the dark, decompose easily under light irradiation. It is difficult to predict the photostability of the complexes, because small changes in the structure can have important effects on their stability.<sup>246,247</sup>

- Low dark toxicity: PDT agents are ideally non-toxic in the dark and should not affect the functions of the cell, even its metabolic breakdown by-products should be innocuous. PDT agents have to be cytotoxic only under light irradiation, through the generation of ROS.<sup>248</sup>

- High penetration through three-dimensional cellular architectures: cellular studies are good initial models to determine the biological activity of a complex, but they do not represent the reality inside the tissue. Many complexes that have an interesting activity in a monolayer cell model (2D model) lose their activity when tested in an *in vivo* model (3D model), mainly due to the failure of the drug delivery process.<sup>249,250</sup> Multicellular spheroids (MCTS) are an interesting model to assay the drug delivery of the compounds, being a more accurate approximation to real conditions in the tissues. Moreover, MCTS have a hypoxic centre, making them a close approximation to the tumours. Using z-stack confocal microscopy it is possible to study the penetration of the PSs inside this 3D model. It is worth mentioning that the use of these models does not substitute the use of animal models, which present tumours in real conditions.<sup>251,252</sup>

- High selectivity for cancer cells/tissue: PDT has intrinsically a first level of selectivity, because light activation of the PS allows an spatio-temporal control of its cytotoxic activity. But it is interesting to obtain also a second level of selectivity by selective accumulation of the PSs in cancer cells. This can be usually obtained through drug delivery systems, which are classified into two types: active or passive depending on the pathway. In active transport, tumour cells are targeted thanks to specific interactions, which are achieved by conjugating to the complex a signalling moiety such as a peptide,<sup>253,254,255</sup> an oligonucleotide,<sup>256,257</sup> a protein,<sup>258,259</sup> an antibody<sup>260</sup> or others. On the other hand, the passive transport takes advantage of the enhanced permeability and retention (EPR) effect present in cancer cells.<sup>261,262,263</sup>

- Fast clearance from the body: upon selective accumulation into the targeted tissue and after the accomplishment of the treatment, a fast clearance of the PS out of the body is preferred to prevent patients from suffering photosensitivity.<sup>264,265</sup> The PSs currently in clinical use are based on a tetrapyrrolic scaffold and exhibit very long excretion times, for example photofrin has a half-life time of 452 hours.<sup>266</sup>

### 3.4. PDT targets

#### 3.4.1. Targets at the molecular level

Cells contain a variety of biomolecules that can be potentially oxidized by the ROS generated in the photodynamic process. There are some important factors that determine the probability that the generated ROS react with these potential substrates: the distance between the PS and the target, the abundance of both PS and target and the reaction rate constants for that specific oxidation process. The main molecular targets for PDT are: proteins, lipids and nucleic acids.<sup>267,268</sup>

-Proteins: They are the main target for PDT, due to their abundance and their high reaction rate constants with singlet oxygen (and other ROS). The rate constants are very different for each amino acid, depending on the side chains. The most easily

oxidized are methionine, cysteine, histidine, tyrosine and tryptophan, so these residues are the primary oxidation sites in proteins.<sup>269</sup> Regarding the specific transformations that they undergo, methionine and cysteine are oxidized to sulfoxides, histidine evolves to an endoperoxide which is thermally unstable, tyrosine suffers a phenolic oxidative coupling, and tryptophan yields N-formylkynurenine.<sup>270</sup>

In the case of the hydroxyl radical ( $\cdot\text{OH}$ ), it reacts with most amino acids at rates controlled by diffusion,<sup>271</sup> so the damage on proteins depends on the concentration of the target amino acid and the reactivity of the products that are formed initially.<sup>272</sup> The oxidation with  $\cdot\text{OH}$  causes the formation of the corresponding radical form of the amino acid, which then reacts with  $\text{O}_2^{\cdot-}$  being possible either the regeneration of the initial amino acid or the formation of the hydroperoxide derivative of the amino acid by the addition of  $\text{O}_2^{\cdot-}$ .<sup>273,274,275</sup> The formation of these hydroperoxides causes protein damage by several pathways: it causes the release of Fe from 4Fe-4S clusters, it participates in reactions with free radical intermediates, and it generates peroxynitrite ( $\text{ONOO}^-$ ), which is able to react directly with sulphur containing amino acids or to generate the carbonate radical ( $\text{CO}_3^{\cdot-}$ ) which is a strong oxidant itself.<sup>276,277</sup>

Apart from the photooxidation of amino acids, other modifications can occur in the proteins,<sup>278</sup> such as the photo-binding between photosensitizer and protein, as well as protein crosslinking, which causes the formation of molecular aggregates.<sup>279</sup> Moreover, it is important to note that the damage extent over a protein depends not only on the amino acids content, but also on the position of vulnerable amino acids, and, therefore, the distance (the proximity) between the PS and these sites is a crucial factor.<sup>278</sup>

-Lipids: There is a high concentration of unsaturated fatty acids in biomembranes. This makes organelles and plasma membranes important targets for singlet oxygen and other ROS.<sup>280</sup> Moreover, oxygen is very soluble in lipids, which favors the photodynamic activity. Radicals can induce lipid peroxidation by hydrogen abstraction, but singlet oxygen is far more effective causing oxidative damage. The mechanism of action of singlet oxygen is based on its capacity to add directly to the unsaturated fatty acids and generate lipid peroxides,<sup>281</sup> which in presence of metallic traces decompose into peroxy and alkoxy radicals.<sup>282</sup> These radicals initiate free-radical chain reactions which cause the destruction of the biomembranes bilayer.<sup>283</sup> So, lipid peroxidation not only causes direct damages to the lipids, which affects membrane functions,<sup>284</sup> it also causes secondary modifications in proteins and nucleotides.<sup>285</sup> This can lead to the malfunctioning of the cell metabolism and signalling,<sup>286,287</sup> which finally causes cell death.<sup>288</sup>

-Nucleic acids: DNA damage induced by oxidation is one of the main causes of cell death triggered by PDT. This can be mediated by one-electron oxidants,  $\text{O}_2^{\cdot-}$  /  $\cdot\text{OH}$  or  $^1\text{O}_2$ .<sup>285,289</sup> Direct one-electron oxidation happens when a photosensitizer in a triplet excited state

abstracts an electron from a nucleobase.<sup>290</sup> Guanine is the base that undergoes this process more easily, because of its low ionization energy,<sup>291</sup> yielding the guanine cation radical ( $G^{\bullet+}$ ). This radical cation can evolve to 2,6-diamino-4-hydroxy-5-formamidopyrimidine and 8-oxo-7,8-dihydro-2'-deoxyguanosine by one-electron oxidation and reduction reactions or to the deprotonated guanine radical,  $Gua(-H)^{\bullet}$ , which is very reactive and can lead to 2,2,4-triamino-5(2H)-oxazolone by an addition reaction with  $O_2^{\bullet-}$ .<sup>291,292</sup> Moreover,  $G^{\bullet+}$  can react with serine, arginine and lysine in proteins by a nucleophilic addition, causing DNA-protein cross-links.<sup>289</sup>

The hydroxyl radical  $\bullet OH$  is the most damaging species generated through the PDT type I mechanism, since it can react indiscriminately with all DNA constituents. The hydroxyl radical causes base modifications by addition to double bonds, a reaction which competes with hydrogen abstraction from the 2-amino group of guanine and methyl group of thymine by the hydroxyl radical itself.<sup>293</sup> The hydrogen abstraction from the DNA backbone causes strand breaks.<sup>289,294</sup>

With respect to singlet oxygen, which is very selective regarding DNA modifications.<sup>295</sup> The main target is guanine,<sup>293</sup> which is converted into 8-oxo-7,8-dihydro-2'-deoxyguanosine by a series of reactions.<sup>296</sup>  $^1O_2$  is also able to cause the formation of nicks in the DNA by secondary oxidation of 8-oxo-7,8-dihydro-2'-deoxyguanosine, but it is not able to cut the DNA backbone, because it cannot react with 2-deoxyribose. Finally, singlet oxygen causes an important oxidative stress in the cells, which ultimately leads to cell death.<sup>295,297</sup>

#### 3.4.2. Targets at the cellular level

The sensitivity of the different cellular compartments to the photo-generated ROS differs importantly, so the subcellular distribution of the PSs helps to predict their efficacy. The distribution of the PSs in the cells also affects the regulatory pathways of the cells and the cell death mechanism.<sup>298</sup>

- Lysosomes: Initially, it was thought that lysosomes were the main target for PDT. The proposed mechanism for cell death was the disruption of the lysosomal membrane by the photo-generated ROS. However, posterior studies demonstrated that even if PSs located in the lysosomes can cause cell death, their efficacy is lower than that of PSs localized in either mitochondria or other organelles. This could happen because of the inactivation of the lysosomal enzymes by the photo-activity of the PSs itself or by the inhibition of the enzymes by the cytosolic inhibitors or the cytosolic pH.<sup>299</sup>

- Mitochondria: Targeting mitochondria is of special interest in anticancer therapies because damaging them and/or inhibiting their function is critical for cell survival leading quickly to cell death by apoptosis.<sup>300</sup> The photodynamic damage done to the mitochondria is a primary event in the chain of events that causes the disruption of the

electron transport chain, the collapse of the mitochondrial membrane potential and the mitochondrial swelling.<sup>301</sup>

- Biomembranes: The efficacy of the activity of a PS is directly related with its capacity to interact favourably with the membranes.<sup>302</sup> If a PS is able to anchor inside a membrane, the triplet excited state of the PS generated after irradiation will be able to interact with higher amounts of oxygen to generate more  $^1\text{O}_2$ . Moreover, the  $^1\text{O}_2$  generated inside the membrane has more chances to interact with sensitive membrane components like polyunsaturated fatty acids. In contrast, a PS located outside the membrane (in the cell boundary or in the water environment) will be in contact with lower oxygen concentrations, so it will generate less  $^1\text{O}_2$ , and also, more of this singlet oxygen will be deactivated before being able to interact with (and oxidize) sensitive cellular components.<sup>303</sup> Biomembranes have a high complexity and a crucial role in cell survival, so it is not a surprise that even a mild oxidation originated in the membrane by a PS can cause the loss of the membrane barrier function, the interruption of cell signalling cascades and the modification of cell receptors, which finally can cause cell death.<sup>278,284,304</sup>

- Cytoskeleton: Even if it receives less attention than other cellular targets, cytoskeleton is also a very interesting target for PDT. The PSs that are able to interact with non-polymerized tubulin can cause an important cytotoxic effect. This occurs because these PSs, even at low doses, after irradiation, can prevent the polymerization of tubulin, causing an effect similar to that of the microtubule function inhibitors.<sup>305,306</sup> This leads to the formation of micronuclei and giant cells. And also, the accumulation of cells in mitosis.<sup>299</sup>

### 3.5. Cell death pathways in PDT

The cell death type caused by PDT varies depending on the PS localization, the quantity and the type of ROS produced during the process, because this establishes the extend of the oxidative damage.<sup>307</sup> It has been observed that the same PS can cause cell death by necrosis in normoxic conditions and apoptosis in hypoxic conditions.<sup>308</sup> The proposal to explain this consists in the fact that under high PDT intensity, enzymes and other components of the apoptotic cascade that are essential, are photo-inactivated.<sup>309</sup> So, sub-lethal damage signals the cell to die by an apoptotic pathway, but lethal damage blocks the ATP production, preventing the cell death by apoptosis and obligating the cell to die by a necrotic pathway.<sup>310,311</sup>

Of special interest is the localization of the PS. If we consider this factor alone, we can see that the PSs that target mitochondria usually induce cell death by apoptosis. Indeed, apoptosis can be caused not only by the primary ROS generated by the PS, but also by the superoxide anion generated as a secondary product because of the photo-



damage caused on the constituents of the electron transport chain.<sup>312</sup> In the case of PSs localized in lysosomes, they block, or at least delay, the apoptotic pathway, causing cell death by necrosis. For PSs that target the plasma membrane, the cell death mechanism depends on the intensity of the oxidative damage: mild damage causes cell death by apoptosis, while extensive damage that causes the loss of the integrity of the plasma membrane leads to cell death mediated by necrosis. In the case of PSs located in the endoplasmic reticulum/Golgi membranes the cell death follows a necrotic pathway.<sup>298,313,314</sup>

Recent studies have suggested that the cell death pathway caused by PDT is a crucial factor in the results of the clinical treatment. Inducing cell death by an apoptotic mechanism is usually desirable,<sup>315,316</sup> since it lowers side effects, enhances tumour control and lessens the morbidity associated to the treatment, without affecting the efficacy of the treatment.<sup>317,318</sup>

## 3.6. Photosensitizers for PDT

### 3.6.1. First generation

As seen in the historical development (section 3.1.), hematoporphyrin and its derivatives were the first studied PSs.<sup>209,210,217</sup> After them, by further purification of hematoporphyrin, photofrin was obtained, which was the first approved PDT agent (1993).<sup>318</sup> Nevertheless, they have several drawbacks such as poor chemical purity and tissue selectivity, short excitation wavelengths, long clearance times from the body and the resulting photosensitivity after treatment.<sup>319,320</sup>

#### **Photofrin**

Photofrin (Porfimer sodium) (Fig. 27) is still in use for treating bladder, lung and cervical cancers, as well as NSCLC.<sup>321,322,323</sup> Photofrin is administered intravenously and irradiated with laser light of 630 nm for its activation.<sup>324</sup>

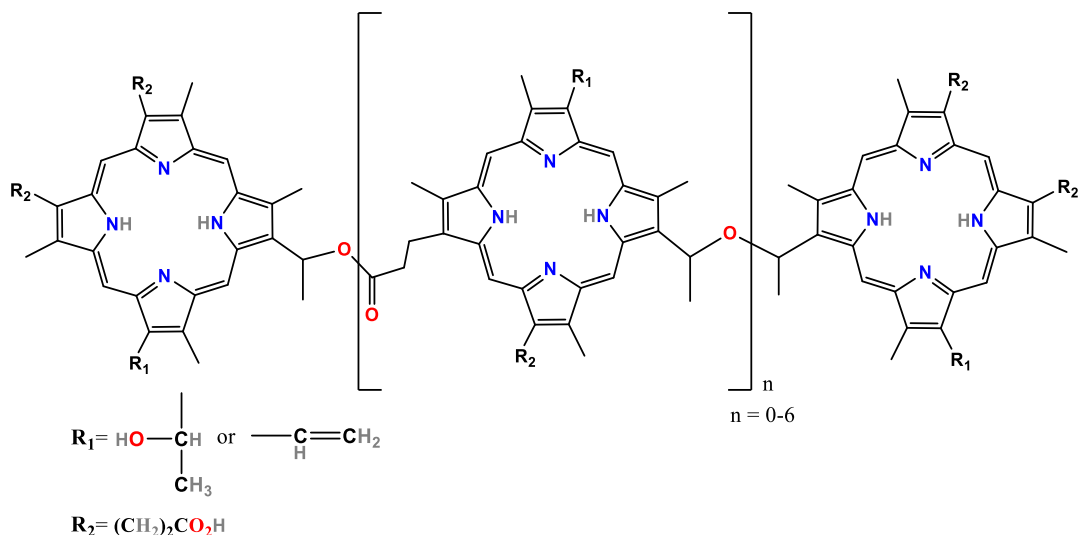


Fig. 27. Photofrin.

### 3.6.2. Second generation

The second-generation PSs possess a higher purity, they absorb light of longer wavelengths (the use of a more penetrating light improves the efficacy of the treatment and allows to access deeper tissues), they are cleared from the body faster and cause less photosensitivity and they are more selective towards cancer cells. Most of the PSs of second generation are based on the structures of Porphyrin and Chlorin (Fig. 28) and were designed to target mitochondria. This generation of PSs has been developed for several decades and includes compounds as Temoporfin (Foscan or Biolitec), Motexafin lutetium (Lutrin or Lutex), Palladium bacteriopheophorbide (Tookad), purpurins (Purlytin) and Verteporfin (Visudyne).<sup>325,326,327</sup>

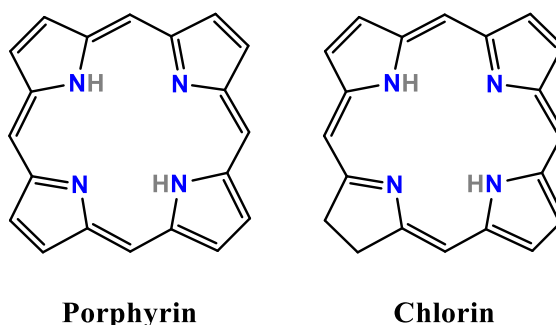


Fig. 28. Porphyrin and Chlorin.

Related with this aim of improving the properties of the PSs, it is worth mentioning the use of metals. Compared with organic drugs, metals can offer important advantages like more structural diversity, a broader variety of oxidation states, more stability (both

chemical and photophysical), better photophysical properties (absorbance at longer wavelengths, longer lifetimes for the excited state and higher quantum yields), greater solubility and a higher production of ROS among others. So, it is not a surprise that an important amount of PSs developed after the first generation are metal-based.<sup>328,329</sup>

### **Lutex and Xcytrin**

Lutex (Motexafin lutetium) (Fig. 29) is a second-generation porphyrin-based PS used for the treatment of prostate cancer. Thanks to the macrocyclic modification it can absorb at longer wavelengths than the PSs seen before. It is irradiated with light of 730-770 nm for its activation. It is usually administered by an intramuscular injection or by a suppository. Recent studies have proved that higher doses of Lutex are more efficient than lower doses, which can be related to the PDT-induced photobleaching observed for LUTEX in prostate cancer treatment.<sup>330,331</sup>

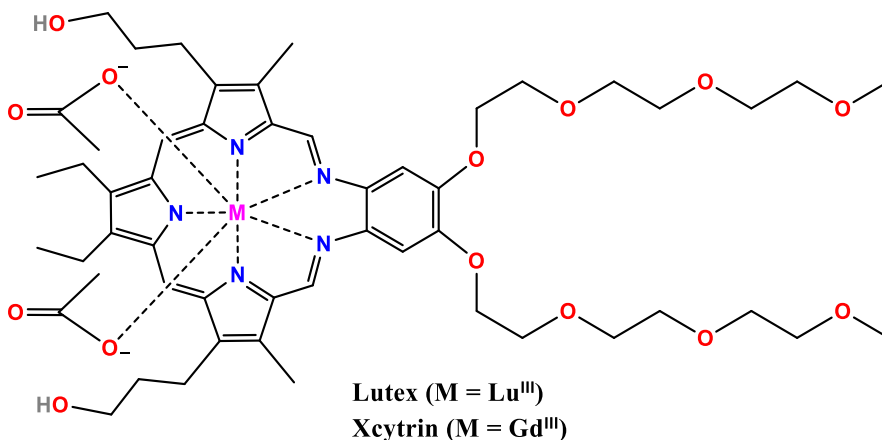


*Fig. 29. Lutex and Xcytrin.*

An analogue of Lutex, which has a gadolinium(III) ion instead of the lutetium(III) cation, known as Motexafin gadolinium or Xcytrin (Fig. 29), is also used as a PS. This PS, which is administered intravenously, is used for treating brain metastasis and lung cancer.<sup>332,333,334</sup>

### **Tookad soluble**

Tookad soluble (Palladium bacteriopheophorbide) (Fig. 30) is a second-generation PS used for vascular targeted PDT.<sup>335,336</sup> This PS is accumulated selectively in the blood vessels of the tumours, where it stays until it causes the phototoxic damage and destroys the tumour, then being quickly cleared from the body.<sup>328</sup> For its activation, it is irradiated with light of 753 nm, allowing deep tissue penetration. After activation, Tookad soluble experiments a systemic circulation, causing an intravascular generation of O<sub>2</sub><sup>•-</sup> and <sup>•</sup>OH which kills cancer cells; it has been observed that there are no serious

negative effects due to the treatment.<sup>337,338</sup> Tookad soluble has been used for prostate cancer in phase II and III, being approved for use in 31 European countries, Israel, and Mexico.<sup>324</sup>

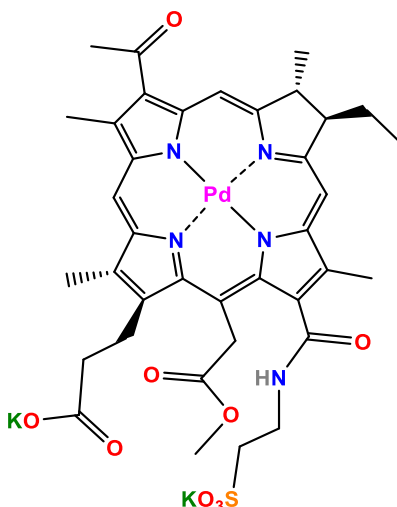


Fig. 30. Tookad soluble.

### Levulan

Levulan (5-Aminolaevulinic acid or ALA) (Fig. 31) is a prodrug used for imaging and treating superficial cancers, being approved for treating actinic keratosis in Europe and United States, and in clinical trials for head and neck tumours, basal-cell carcinoma and gynaecological tumours. Levulan is not a PS by itself, but is a crucial precursor in the biosynthesis of heme or haem (Fig. 31), which is a naturally occurring porphyrin that is a structural component of some haemoproteins like haemoglobin and myoglobin.

Naturally occurring ALA is produced from succinyl-CoA and glycine in the mitochondria and yields to protoporphyrin IX (PPIX) (Fig. 31) by several enzymatic steps, which then leads to the formation of haem by coordination of an iron ion to the PPIX. It is important to notice, that haem is not a good PS, because the coordination of the paramagnetic iron ion causes an important decrease in its excited state lifetime. However, PPIX itself is a good PS, so the key for using it for a clinical treatment is administering Levulan to the patients, due to the fact that when there is a high concentration of PPIX in the organism a significant fraction is not converted into haem.<sup>339,340,341</sup>

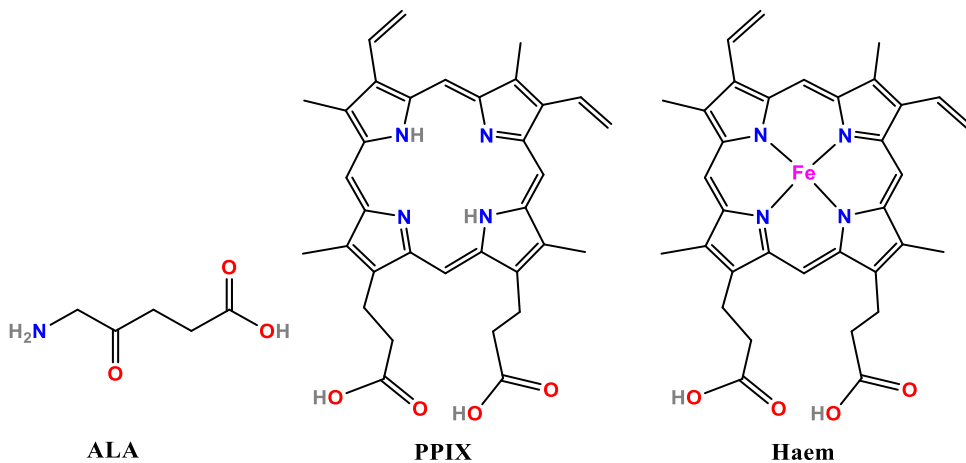


Fig. 31. ALA, PPIX and Haem.

Some other second-generation PSs are collected in Fig. 32:<sup>328,342</sup>

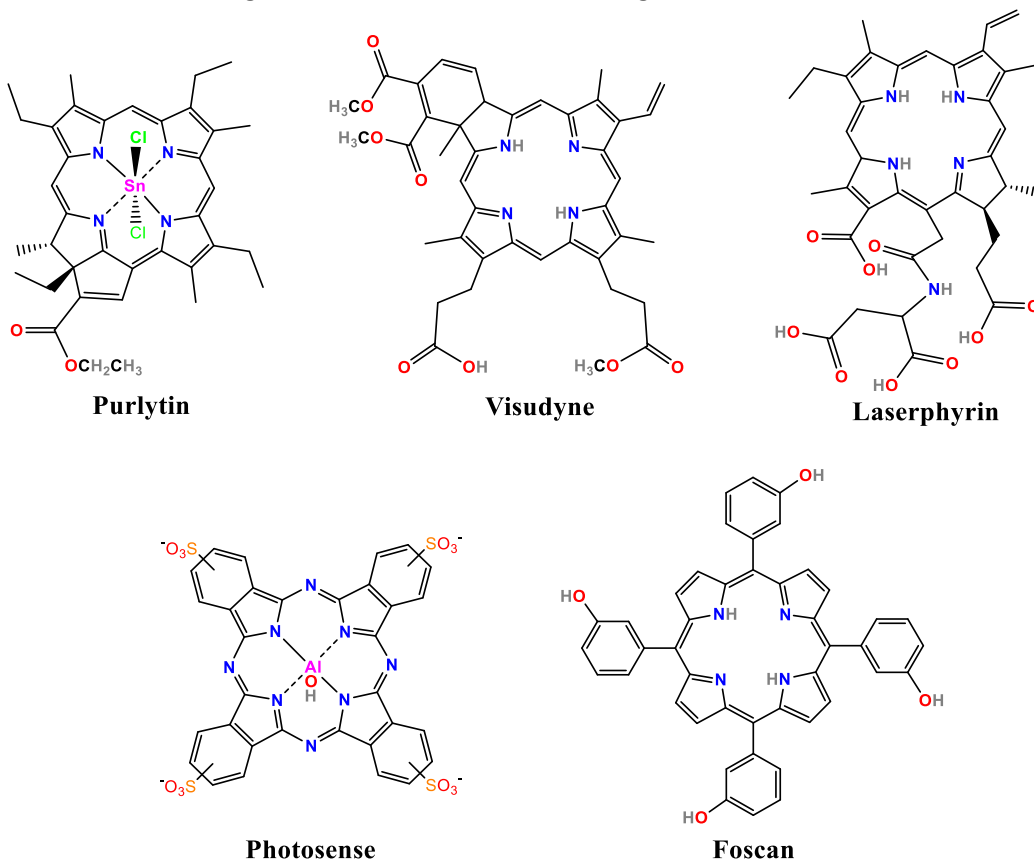


Fig. 32. Second generation PSs.

### 3.6.3. Third generation photosensitizers

In this section, some new PSs that improve the results of the past PSs will be discussed.<sup>223,343,344</sup> Regarding these PSs, it is important to note, that I will focus on Ir(III) and Ru(II) trischelate complexes, because this type of compounds are closely related to those described in our work.

Redaporfin (LUZ111) (Fig. 33), is a third generation PS based in the bacteriochlorin scaffold currently in phase II trials for advanced head and neck cancer. This PS allows a better tissue penetration and has a higher efficacy than second generation PSs. It also has a very efficient ROS generation. It is worth mentioning that Redaporfin, which is administered intravenously and activated with NIR light of 749 nm, causes phototoxicity by both type I and type II mechanisms, overcoming through this way the drawbacks associated with the hypoxic conditions of certain tumours.<sup>345,346</sup> Other interesting facts are that Redaporfin targets both the Golgi apparatus and the endoplasmic reticulum, and more interestingly, that Redaporfin is able to cause cancer cells death by two mechanisms: the typical antineoplastic effect and the immune system dependent cancer cell destruction. This occurs because Redaporfin is able to induce T cells activation against the cancer cells, which makes it a potential drug to use in combined therapies along with immune checkpoint inhibitors.<sup>347</sup>

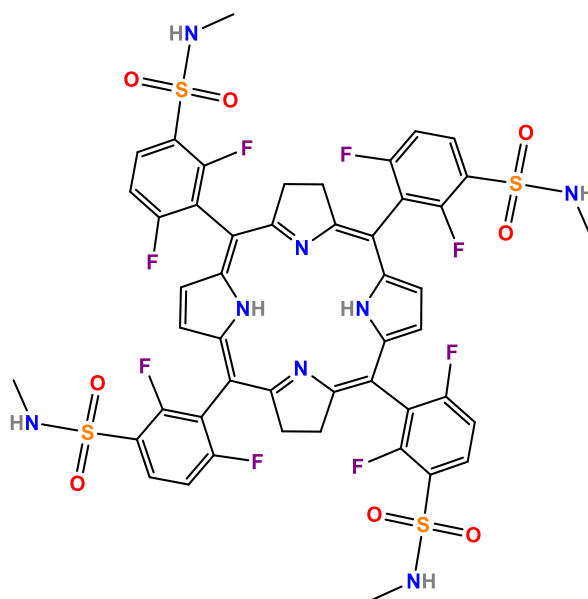


Fig. 33. Redaporfin.

In 2015, Redaporfin received the orphan drug designation (a drug that is not developed by the pharmaceutical industry by itself because it treats an uncommon illness, being not profitable, but which is developed with government grants due to its interest for

the public health) by EMA (European Medicines Agency) for the treatment of biliary tract cancer.<sup>348</sup>

### **PS based on iridium(III) complexes**

The tris-chelate Ir(III) complex bearing two 2-phenylpyridinates as bis-cyclometalated ligands and one 1,10-Methylenebis(3-butyl-1H-imidazol-3-ium) as the ancillary ligand (Fig. 34) showed an outstanding photocytotoxicity index (3488) obtained for A549R cells after irradiation with a 365 nm light source. This complex was tested in several cancer cell lines like HeLa (human cervical cancer), A549 (human pulmonary carcinoma), A549R (cisplatin-resistant A549), showing better results in the dark than cisplatin even in cisplatin-resistant cells, being also more selective against cancer cells. Moreover, it is interesting to comment that this complex targets mitochondria specifically and activates the apoptotic cell death mechanism without causing cell cycle arrest.<sup>349</sup>

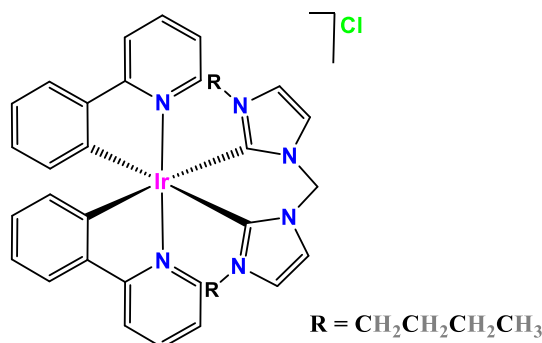


*Fig. 34. Iridium(III) bis-N-heterocyclic carbene complex.*

The tris-chelate Ir(III) complex with two N,N-diphenyl-4-(quinolin-2-yl)aniline as the bis-cyclometalated ligands and one 2-(pyridin-2-yl)pyrimidine derivative with a hexyltriphenylphosphine pendant as the ancillary ligand (Fig. 35) was shown to selectively accumulate in the mitochondria. This complex showed no toxicity in the dark in HeLa cells (human cervical cancer), but caused an important cytotoxic response after irradiation at 475 nm even under hypoxic conditions. This result is of special interest, because the hypoxic conditions of the tumours are one of the main drawbacks found in PDT, and it is difficult to overcome.<sup>350</sup>

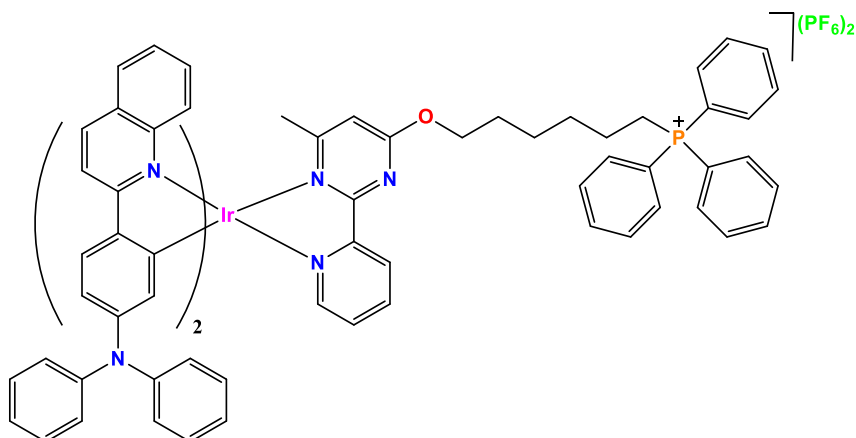


Fig. 35. Iridium(III) hexyltriphenylphosphine complex.

The iridium(III) quinolin-naphtoimidazole complex shown in Fig. 36 was designed to target specifically lysosomes. This derivative is more efficient in the singlet oxygen production in acidic media, like the one found in the lysosomes (pH 4.5-5.5), than in neutral media. Moreover, this PS shows no dark toxicity in the cell lines in which it has been tested (HeLa, A549, A549R), but it shows an important photocytotoxicity in all of them after activation with a 425 nm light, providing the best results in HeLa cells (PI 476). This PS causes cell death by a caspase-dependent apoptosis mechanism. Moreover, it is worth mentioning that this complex shows anti-metastatic activity.<sup>351</sup>

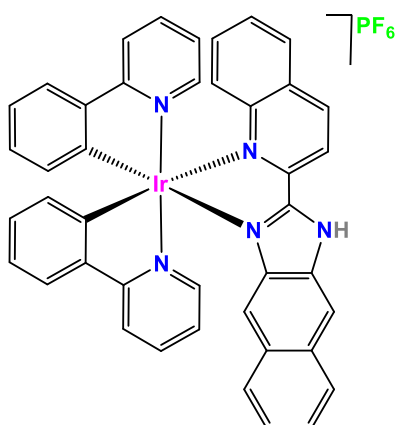
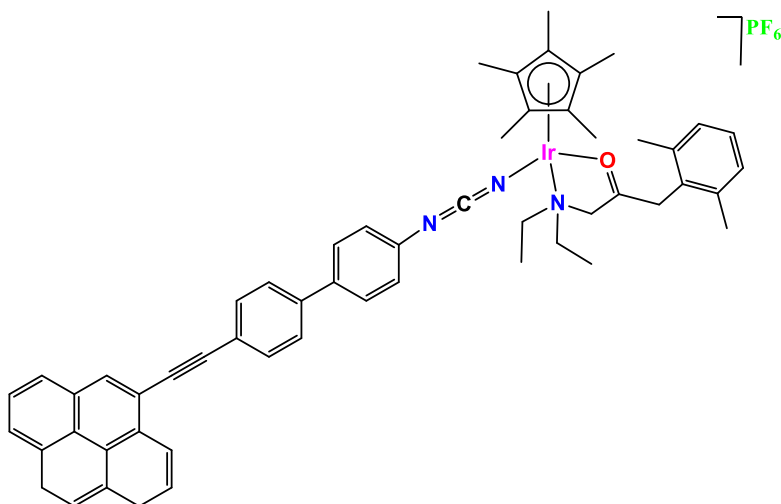


Fig. 36. Iridium(III) quinolin-naphtolimidazole complex.

Ir(III) half-sandwich complexes are scarce as PS because most of them are non-emissive. Nevertheless, The Ir(III) complex with Cp\* (1,2,3,4,5-pentamethylcyclopentadienyl), lidocaine and 4'-(pyren-10-yl)ethynyl-4-cyanamidobiphenyl as ligands (Fig. 37). has some interesting properties to be used as a PDT agent. This PS exhibits a high water solubility, is photo-stable, has a good cellular uptake, possesses a high singlet oxygen



generation capacity and has a low dark toxicity in HeLa cells, but on the contrary is very cytotoxic upon irradiation at 450 nm (PI 417). Moreover, this complex causes DNA cleavage after irradiation.<sup>352</sup>



*Fig. 37. Iridium(III) half-sandwich with lidocaine and phenylcyanamide derivative complex.*

### **PS based on ruthenium(II) complexes**

A Ru(II) homoleptic tris-chelate complex with three bathophenanthroline (4,7-diphenyl-1,10-phenanthroline) derivatives with one sulfonate in each of the six phenyl rings has been studied as a PS for PDT (Fig. 38). Even though this complex has four negative charges, it shows a sufficient cellular uptake and is accumulated in the cytoplasm. It has been tested in several cell lines showing no dark toxicity, but demonstrating an important photocytotoxicity (with a good singlet oxygen generation ability) in all of them after activation with a light source with a longer wavelength than 400 nm, triggering cell death by an apoptotic pathway. Moreover, it damages DNA after activation. This is an interesting example of a well-known complex used for biological staining and in solar cells repurposed as PS.<sup>353</sup>

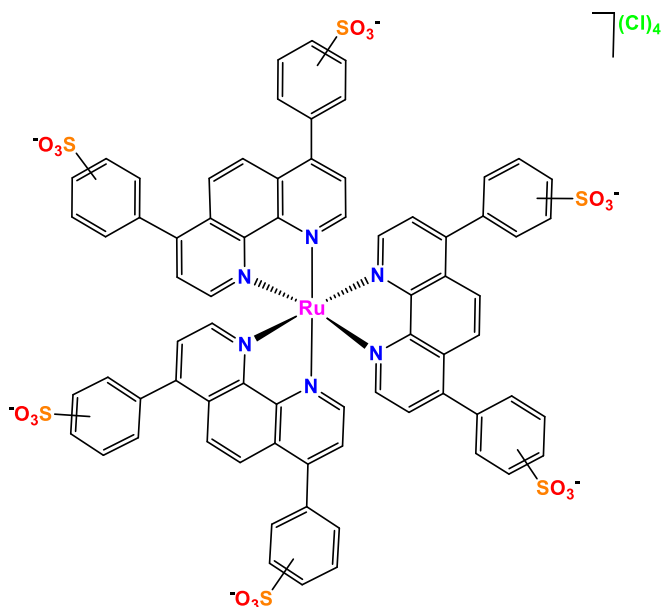


Fig. 38. Ruthenium(II) complex  $[Ru(Ph_2phen-SO_3)_3]Cl_4$ .

A trinuclear mixed Ru(II) and Rh(III) complex, with two ruthenium and one rhodium cations is presented in Fig. 39. The Ru(II) moieties have a tris-chelate type structure with two 2,2'-bipyridine and one 2,3-bis(2-pyridyl)pyrazine ligands, and the Rh(III), which has two chloride ligands, acts as a bridge between the two ruthenium moieties, being coordinated to both 2,3-bis(2-pyridyl)pyrazine ligands. This complex is water soluble and presents no dark toxicity against Vero cells (green monkey kidney epithelial cells), but shows an important photocytotoxicity after activation with light of a longer wavelength than 460 nm. It also shows photo-cleavage of DNA with the same light source thanks to the rhodium atom.<sup>354,355</sup>

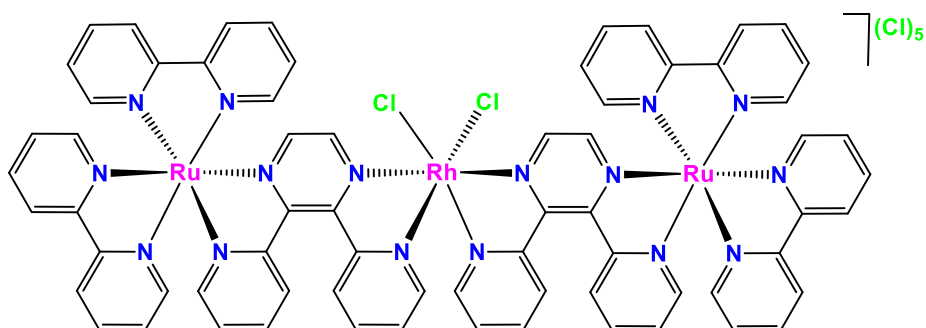


Fig. 39. Mixed ruthenium(II) and rhodium(III) trinuclear complex  $[(bpy)_2Ru(dpp)_2RhCl_2]Cl_5$ .

The Ru(II) tris-chelate complex, with two 2,2'-bipyridine ligands and one 5-pyren-1-ylethynyl-1,10-phenanthroline (5-PEP) ligand (Fig. 40) shows interesting features like

water solubility and a high singlet oxygen generation capacity. This complex was assayed against HL60 cells (human leukemia cells) demonstrating no dark toxicity and a very high photocytotoxicity after activation with white light, providing a phototoxicity index of 1747. It is worth mentioning, that this PS can also act by an oxygen-independent type I mechanism apart from the oxygen-dependent type II mechanism, which is very interesting as mentioned above because of the hypoxic conditions of the tumours. To verify this point, this PS was tested in a metastatic melanoma model, giving good results.<sup>356</sup>

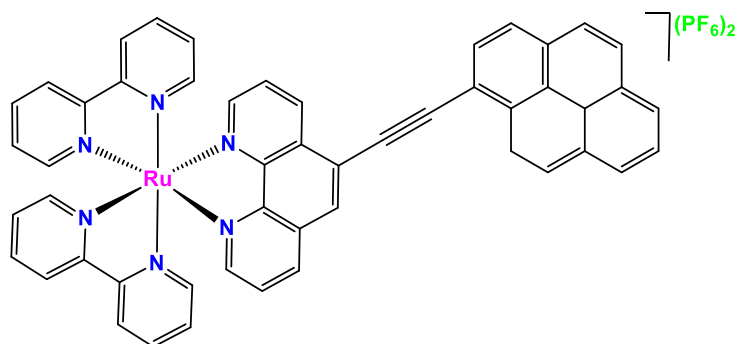


Fig. 40. Ruthenium(II) complex of formula  $[Ru(bpy)_2(5\text{-PEP})](PF_6)_2$ .

TLD-1433 is a Ru(II) tris-chelate complex, bearing two 4,4'-dimethyl-2,2'-bipyridine ligands and one 2-(2',2'':5'',2'''-terthiophene)-imidazo[4,5-f][1,10]phenanthroline ligand (Fig. 41). This complex is the first ruthenium PS to enter clinical trials, being studied for the treatment of non-muscle-invasive bladder cancer. TLD-1433 is water soluble, it has a high singlet oxygen quantum yield and does not present dark toxicity. This PS presents an important photocytotoxicity after activation, which is usually performed with light of wavelengths around 520 nm, but also, it is possible to activate it with light of 850 nm, permitting deeper tissue penetration when needed.<sup>357,358</sup> It is worth mentioning that TLD-1433 shows a great activity in several cell lines and it is also active against bacteria like *Staphylococcus aureus* and methicillin-resistant *Staphylococcus aureus*.<sup>358,359</sup> This important activity is related to the dual mechanism of photosensitization, since it is able to act by both type I and type II PDT mechanisms, which allows it to work even in hypoxic conditions, maintaining its efficacy against bacteria and with different degrees of efficacy in cancer cells, depending on their nature. It is assumed that TLD1433, which is administered by injection, is located predominantly in either the endoplasmic reticulum, the lysosomes or the cytoplasm.<sup>223,357,358</sup>

Moreover, the derivative drug called Rutherrin has been studied. Rutherrin consists in a formulation of TLD1433 bonded to transferrin (iron transporter protein). It has been demonstrated that this formulation improves the properties of TLD1433

(photobleaching is lowered and dark toxicity is decreased compared to the PS alone) and provides an interesting way of transport for the PS to easily reach the tumour, because of the upregulation of the transferrin receptor existing in many types of cancer (especially in the bladder cancer).<sup>360,361</sup>

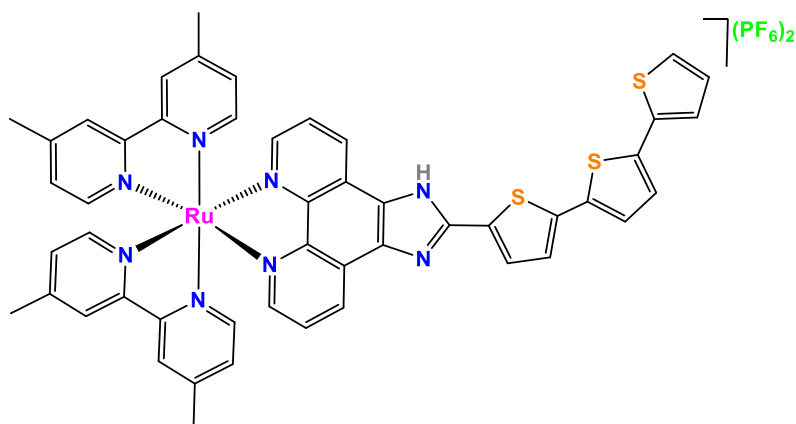


Fig. 41. TLD-1433 ( $[Ru(dmb)_2(IP-TT)](PF_6)_2$ ).

### 3.7 Recent advances in PDT

#### 3.7.1. Two-photon PDT

As afore-mentioned, metal complexes possess interesting properties to be used as PSs for PDT. On the other hand, the short wavelength of the light sources used in their activation (which are usually in the range between 380 and 600 nm approximately) represents an important drawback. This type of visible light has a poor tissue penetration. Thus, disables the use of PDT for non-superficial cancers. In order to solve this important issue, the interest in using 2-photon (2P) irradiation instead of 1-photon irradiation has grown.<sup>362,363</sup>

In 2P-PDT, the PS simultaneously absorbs two photons of long wavelength (600-900 nm). This reduces the photodamage of the treatment compared with 1P-PDT, because these photons are of low energy. Furthermore, 2P-PDT processes allow a deeper tissue penetration and take place in a dependent way to the square of the luminescence intensity, while 1P-PDT processes occur with a linear dependency to this intensity.<sup>364</sup> To carry out 2P-PDT process, focused lasers, which have a very high photon density are needed. This again is an important drawback, because these lasers have a high cost and are not present in the clinic yet, which has prevented the practical application of this technique up to date. Moreover, this type of lasers possesses a small irradiation volume, which makes vast areas difficult to treat.<sup>365,366</sup>

The first 2P-PDT experiments in biological tissues started in the 1980s,<sup>367</sup> but there were not remarkable advances until 2006, when Wilson and co-workers started using

femtosecond NIR Ti:sapphire lasers for this technique.<sup>368</sup> Nowadays, there is a continuous advance in this technique. Indeed, recently some groups have described metal complexes as candidates for 3P absorption.<sup>369,370</sup> Some examples of iridium<sup>371,372</sup> and ruthenium<sup>373,374</sup> tris-chelate complexes tested for 2P-PDT are summarized in Fig. 42. These complexes can be excited with light of wavelengths between 700 and 900 nm (Near-IR), which as mentioned above overcomes one of the main drawbacks of PDT.

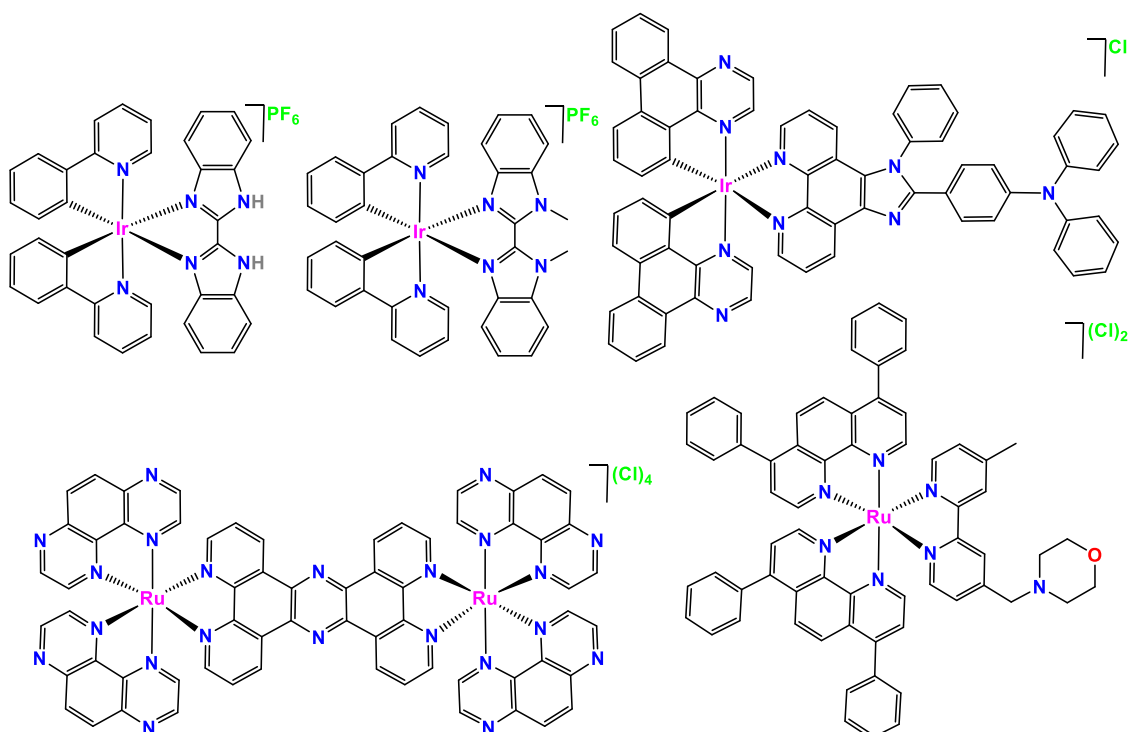


Fig. 42. Iridium and ruthenium tris-chelate complexes tested for 2P-PDT.

### 3.7.2. Upconverting nanoparticles (UCNPs) for PDT

Another new approach in PDT, based again in a strategy centred in overcoming the poor tissue penetration related to the short wavelengths usually involved in the activation of the PSs, is the application of NIR-excitable upconverting nanoparticles (UCNPs) in PDT, using them as energy donors to activate the PSs.<sup>375,376</sup> UCNPs are nanoparticles of 1-100 nm diameter, being frequently lanthanide-doped nanocrystals, which are able to convert two or more absorbed photons of low energy (NIR light photons) into one emitted photon of high energy (visible or ultraviolet photon). The up-conversion luminescence shows some interesting advantages compared with the down-conversion fluorescence such as a deeper tissue penetration, an improved photochemical stability and a background that is free from auto-fluorescence.<sup>377,378,379</sup>

The most common UCNPs are based on a crystalline host matrix of  $\text{NaYF}_4$ , which contains a combination of an up-conversion sensitizer, being the  $\text{Yb}^{3+}$  the most common option, and an activator, which is a lanthanide ion, being the most frequent choices  $\text{Er}^{3+}$  and  $\text{Tm}^{3+}$ . Three habitual methods are employed to load the photosensitizers into the nanoparticles: silica encapsulation, non-covalently physical adsorption and covalent conjugation via chemical linkages.<sup>380,381</sup>

Several PSs have been tried along with this strategy, with various coatings and with different cancer types as their target. Some of the most used PSs are: Merocyanine 540,<sup>382,383</sup> zinc phthalocyanine,<sup>384,385</sup>  $\text{TiO}_2$ ,<sup>386,387,388</sup> Chlorin e6,<sup>389,390</sup> and Rose Bengal (Fig. 43).<sup>391,392</sup> Even though iridium<sup>393</sup> and ruthenium<sup>394</sup> tris-chelate complexes have not been so widely tested in this approach, there are also examples of this type of complexes used in combination with UCNPs (see Fig. 44).

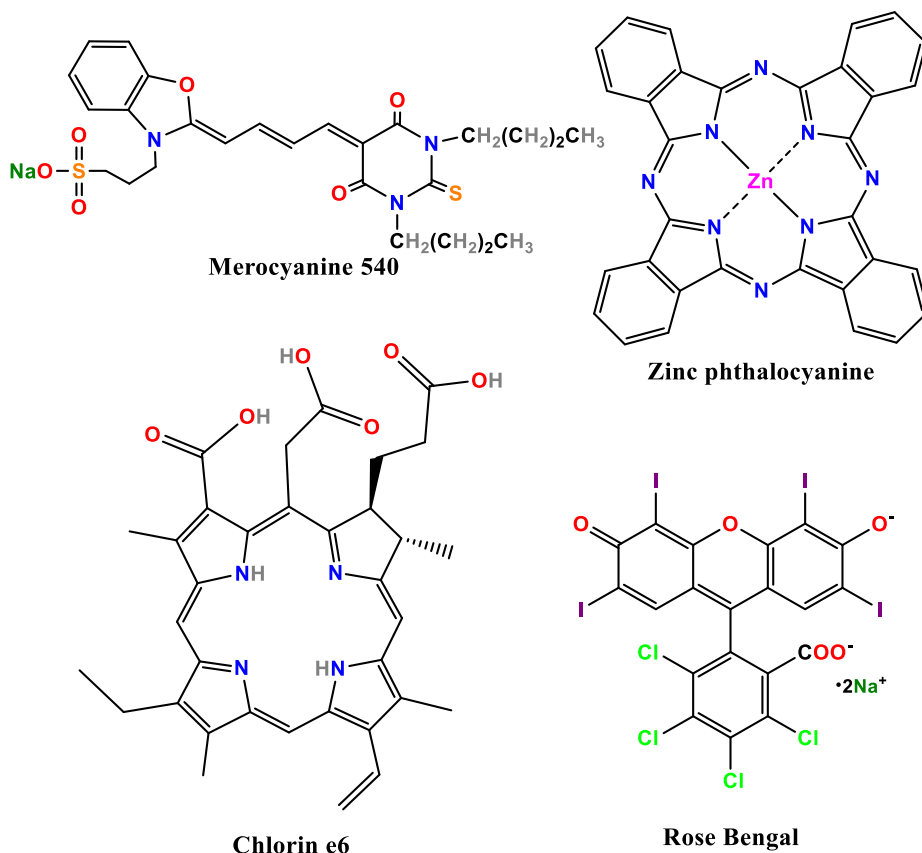


Fig. 43. Some of the most used PSs with UCNPs.

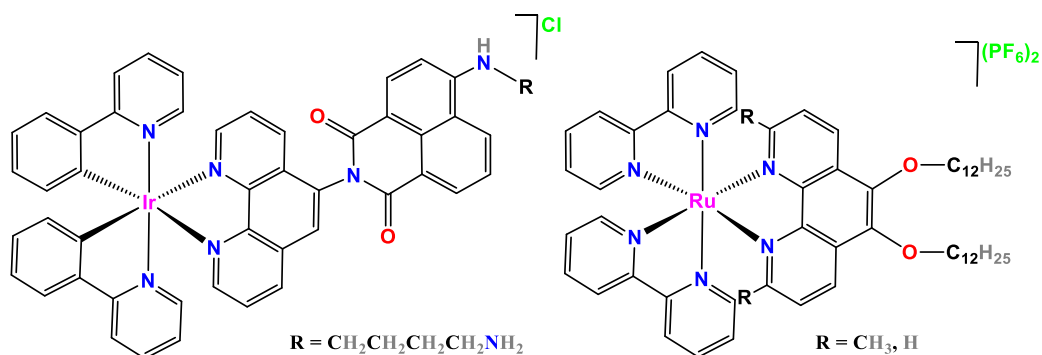


Fig. 44. Iridium and ruthenium PSs used with UCNPs.

### 3.7.3. Dual function PSs (theragnosis)

Theragnosis results from the combination of the words therapy and diagnosis. The possibility of using PSs as theragnosis agents has been scarcely exploited until recent years.<sup>495,496</sup> Cancer imaging is an excellent tool to assess the pre-treatment state of the cancer, the uptake, the localization and distribution of the anticancer drugs and the state of the cancer after the treatment in patients.<sup>395</sup> The luminescent properties of the PSs allow them to be used for fluorescence-guided imaging (optical imaging), which offers, compared with conventional imaging methods, better spatial and temporal imaging, being also much safer for the patient. Other imaging techniques that can also be used along with a regular PDT treatment are, for instance, ultrasound imaging, magnetic resonance imaging (MRI) and nuclear imaging (PET and SPECT).<sup>396,397</sup>

Some iridium<sup>398,399</sup> and ruthenium<sup>400</sup> complexes that have been studied for their use as theragnosis agents can be seen in Fig. 45.

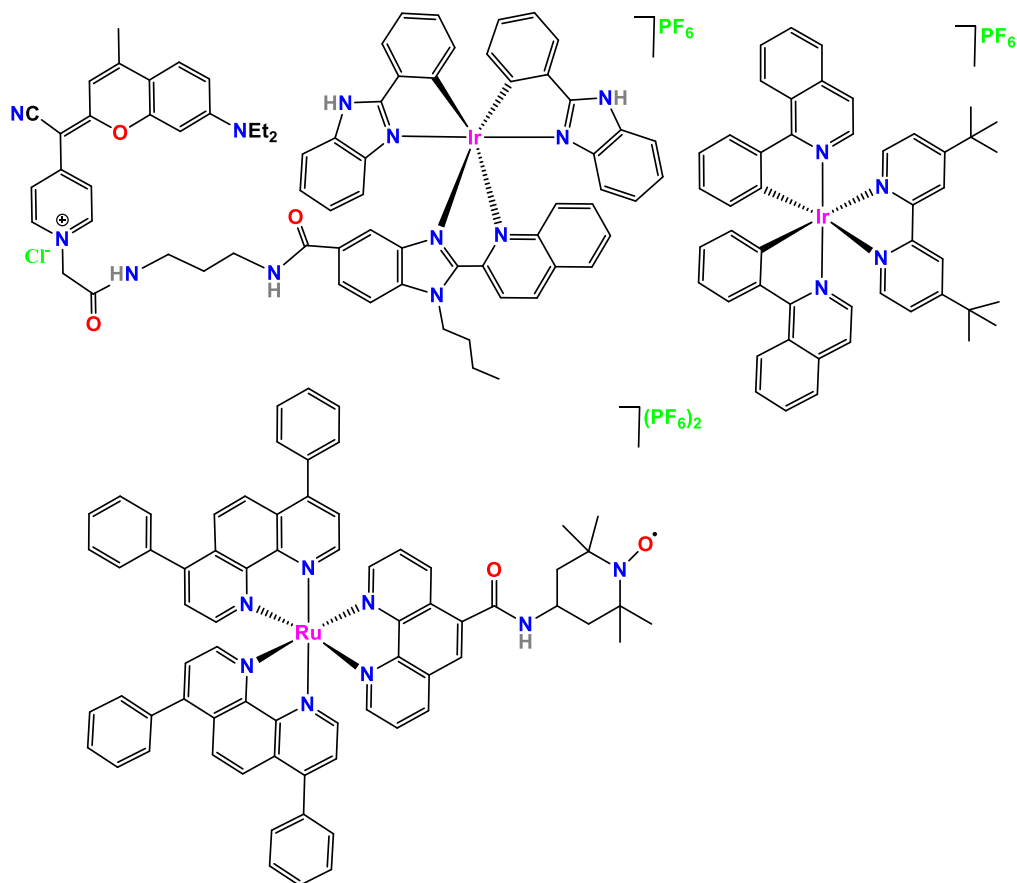


Fig. 45. Some iridium and ruthenium complexes studied for their use as theragnosis agents.

Another interesting option for the development of theragnosis agents in PDT, apart from the regular PSs, is the use of double functionalized nanoparticles, commonly known as theragnosis nanoparticles, that are functionalized with both an imaging and a therapeutic moiety.<sup>401,402,403</sup>

#### 3.7.4. Complexation of a BODIPY-based ligand

Organic dyes possess interesting photophysical properties, and among them, BODIPY (4,4-difluoro-4-bora-3a,4a-diaza-s-indacene) type chromophores are of particular interest due to their good absorption in the visible region and their photostability. Moreover, it is easy to modify the BODIPY core, which allows to tune diverse properties, such as the photophysical parameters or lipophilicity. However, they are not good PSs due to the fact that they are very inefficient in populating the triplet state ( $T_1$ ) because they possess very high fluorescence quantum yields, so they scarcely generate ROS.<sup>404,405</sup>



Nevertheless, there are several ways to improve the performance of the BODIPYs as PSs. One of them, which is of special interest, is to coordinate it to a metal centre. The connection between both units is usually achieved by  $\pi$ -conjugated linkers or through acetylide or even acetylacetonate (acac) units. This strategy is of particular interest because it solves at the same time several drawbacks of both the BODIPY and the metal complex, giving a new complex with improved features: the inefficiency of the BODIPY in populating the triplet state disappears thanks to the metal ion, which favours the ISC; the metal complex gains absorbance at higher wavelengths (visible region) thanks to the BODIPY, making it a more interesting PS for PDT; and also, the complex increases its emission, which favours its use as a theragnosis agent.<sup>406,407,408</sup> Some iridium<sup>409,410</sup> and ruthenium<sup>411</sup> compounds obtained following this strategy can be seen in Fig. 46.

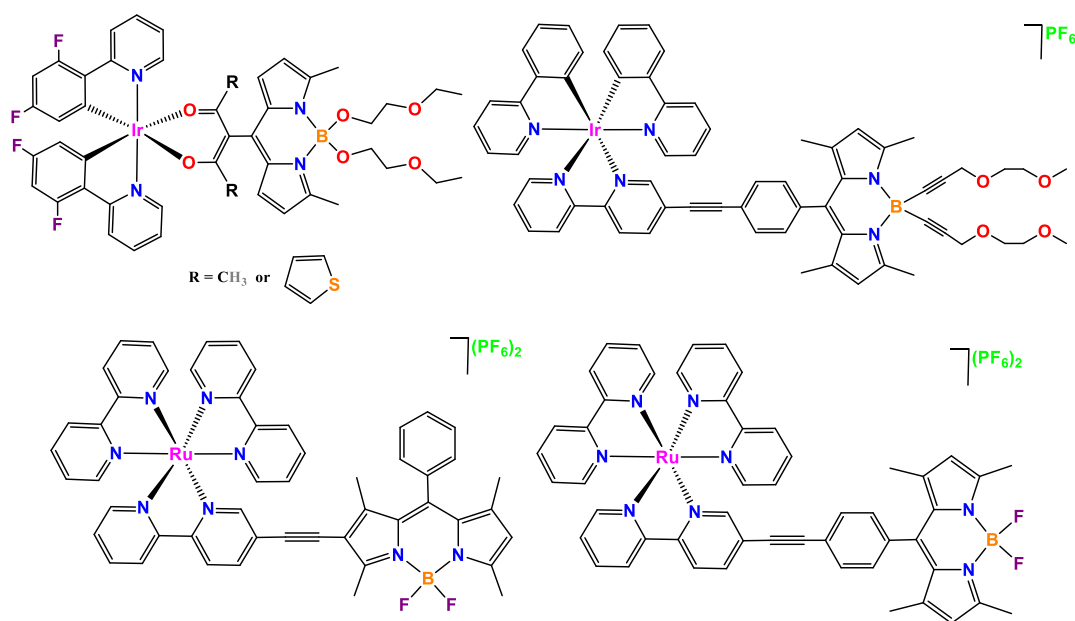


Fig. 46. Some iridium and ruthenium compounds with BODIPYs.

### 3.7.5. Use of nanocarriers

As stated before, a frequent drawback typical of many PSs, is the poor water solubility, which causes their aggregation under physiological conditions, causing an important decrease in their photophysical properties, and thereby in their ROS generation ability.<sup>412,413</sup> Moreover, even when the PSs have been modified to increase their water solubility, another important drawback persists: their selective accumulation in the target cells or tissues, which usually is still insufficient for an effective clinical use. To overcome these limitations, carriers, specially nanocarriers, have become an interesting option.<sup>414,415</sup>

The encapsulation or immobilization process of the PS into the carrier, depending on the method used, can be achieved by both physical (electrostatic or hydrophobic interactions) and chemical (conjugation reactions) methods.<sup>415,416</sup> It is important to note, that apart from the increase in the solubility and the selective accumulation of the PS mentioned above, nanocarriers also guarantee the stability of the PS in physiological conditions and the controlled release of the drug into the site of action.<sup>415,417</sup>

Nanocarriers can be divided into two big groups: organic nanocarriers and inorganic nanocarriers. The main types of organic nanocarriers are liposomes and polymeric nanoparticles (they can exhibit natural origin as albumin, chitosan and hyaluronic acid, or synthetic, which are organized in five main groups: homopolymers, block copolymers, graft copolymers, dendrimers and hyperbranched polymers, and hydrogels). The main types of inorganic nanocarriers are quantum dots (QDs), ceramic-based nanoparticles (SiO<sub>2</sub> and TiO<sub>2</sub> are among the most popular), metallic nanoparticles (gold nanoparticles are the preferred options), carbon materials (fullerene, carbon nanotube, and graphene and its derivatives, as for instance graphene oxide). It is worth mentioning, that thanks to the great variety of nanocarriers that are available this strategy is applicable to almost any PS.<sup>415,417,418</sup>

### 3.7.6. Use of targeting biomolecules

Another way of improving the selectivity of many PSs is the use of targeting biomolecules in the ligands or to bind them to the PSs. These biomolecules have a special affinity for receptors that are over-expressed in cancer cells, but not in normal/healthy cells, so in this way, the PSs containing these functions can accumulate selectively in the cancer cells. This would increase the effectivity of the PDT treatment, avoiding at the same time undesired collateral damages to healthy tissues and side effects. The most common types of biomolecules used for selective targeting are proteins, peptides, antibodies, nanobodies, non-protein (biomolecules non-derived from proteins) and aptamers.<sup>419,420</sup>

In the group of the proteins, the most used is transferrin, which is an iron transporter protein. Transferrin receptors (TfR1) are over-expressed in cancer cells and transferrin has a high affinity for them.<sup>421,422</sup> An interesting example of the use of transferrin as a targeting agent, is Rutherrin (see section 3.6.3.), which is a drug made by binding TLD1433 to transferrin. In this case, the binding of transferrin to the PS not only enhances the selectivity of the PS, it also improves its properties (photobleaching and dark toxicity are lowered compared to the PS alone).<sup>361</sup>

RGD, Lyp-1, GE11, F3 are among the most popular low molecular weight biocompatible peptides used for this purpose. These peptides are easy to prepare and to conjugate.

Moreover, they show a high affinity for surface receptors present in cancer cells and an enhanced diffusion in the tumours.<sup>423,424,425,426</sup> A pair of examples of PS conjugated to peptides are shown in Fig. 47. The first one is a Ru(II) tris-chelate complex bearing the RGD peptide for  $\alpha_v\beta_3$  integrin targeting,<sup>427</sup> and the second one, is a Zn(II) phthalocyanine bound to the GE11 peptide for EGFR (epidermal growth factor receptor) targeting.<sup>428</sup>

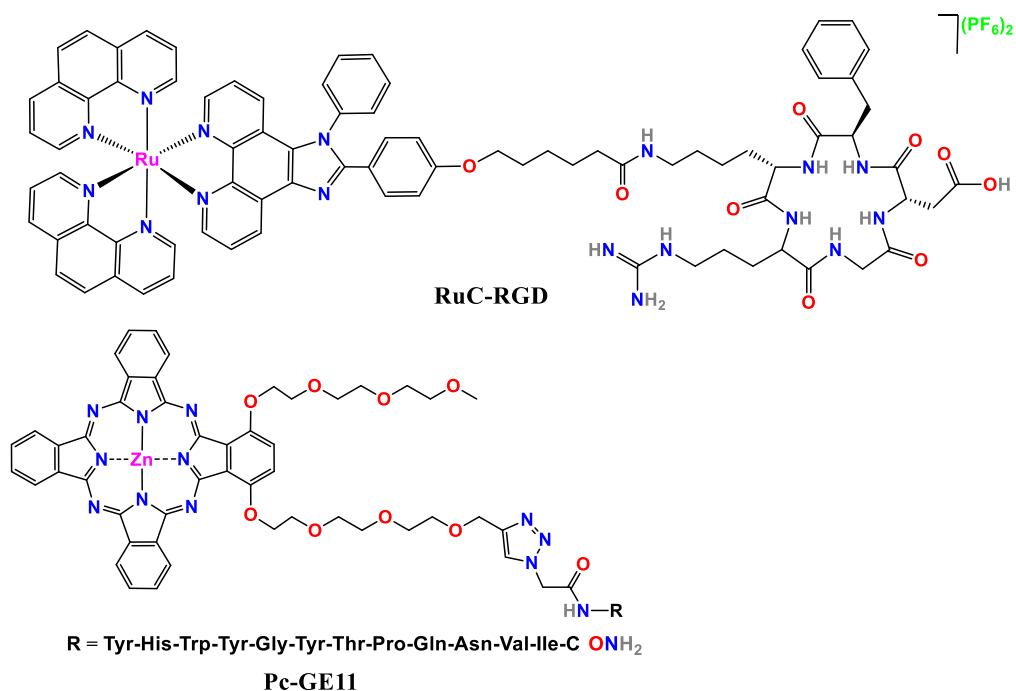
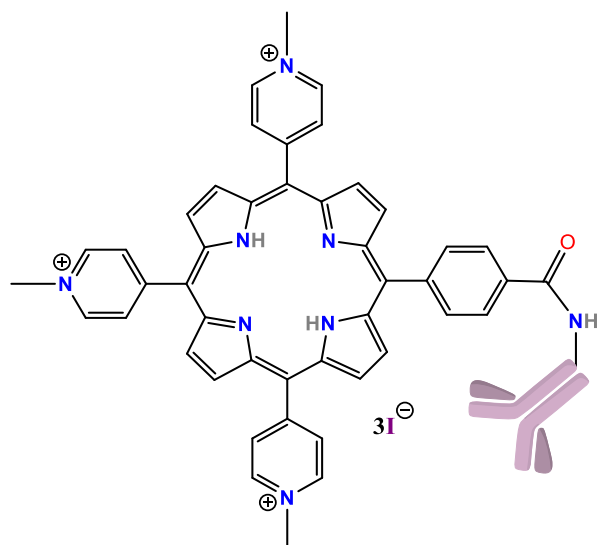


Fig. 47. Ru(II) tris-chelate complex with a RGD peptide and Zn(II) phthalocyanine with a GE11 peptide.

Trastuzumab, Rituximab, Bevacizumab and Cetuximab are good examples of monoclonal antibodies (mAb) used for targeting. Antibodies are the preferred option for enhancing PSs selectivity thanks to their high affinity to receptors overexpressed in the cancer cells surface and their high stability *in vivo*. However, they also have several drawbacks: they can cause immunogenicity, their production is expensive and their large size reduces their tumour penetration.<sup>429,430,431</sup> An example of this strategy can be seen in Fig. 48, where a porphyrin-trastuzumab conjugate is represented.<sup>432</sup>



**Porphyrin-trastuzumab**

*Fig. 48. Porphyrin conjugate with the monoclonal antibody trastuzumab.*

Nanobodies or single-domain antibodies (sdAb), which consist in only one variable domain from the heavy chain of an antibody, are also used to improve the selectivity of the PSs. Examples of these biomolecules are 7D12, 7D12-9G8 and R2 nanobodies. They possess some interesting features like an important targeting capacity, high stability and tissue penetration, and a reduced potential for causing immunogenicity compared to mAbs.<sup>431,433,434</sup> Following this strategy, 7D12, 7D12-9G8 and R2 nanobodies have been conjugated to the PS IRDye700DX (Fig. 49), which is a silicon phthalocyanine derivative, improving in this way its PDT potency.<sup>435</sup>

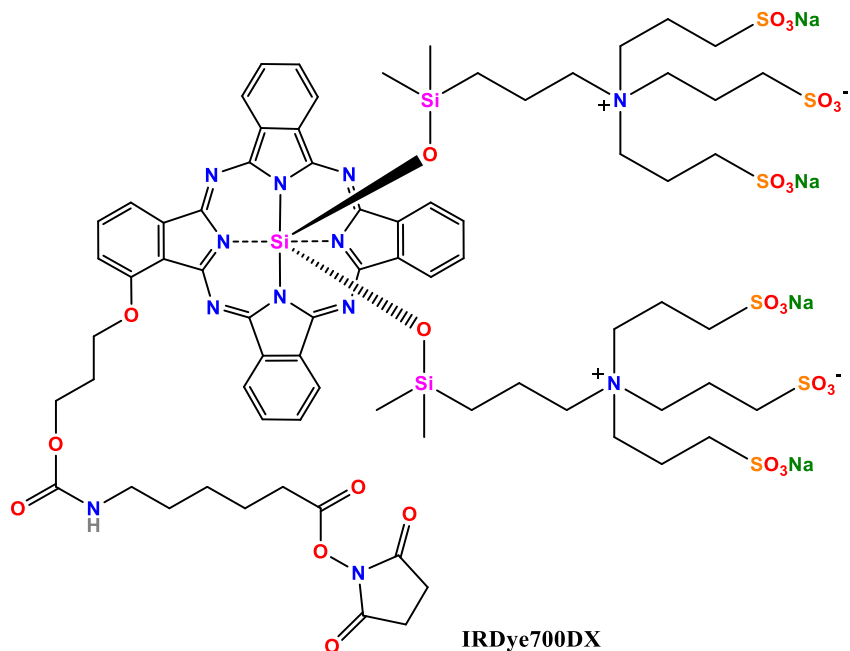


Fig. 49. IRDye700DX, a PS to which some nanobodies have been conjugated.

The group of non-proteins includes different types of biomolecules like Folic acid (FA; is a type Vitamin B (B9)), Hyaluronic acid (HA; is a polysaccharide) and Bile acids (BAs; are steroid acids). Their main features are their high affinity for receptors in the cancer cells surface and their minimal immunogenicity. Foscan-bile acid<sup>436</sup> and platinum porphyrin-folate<sup>437</sup> conjugates (Fig. 50) are examples of targeting PSs obtained following this strategy.

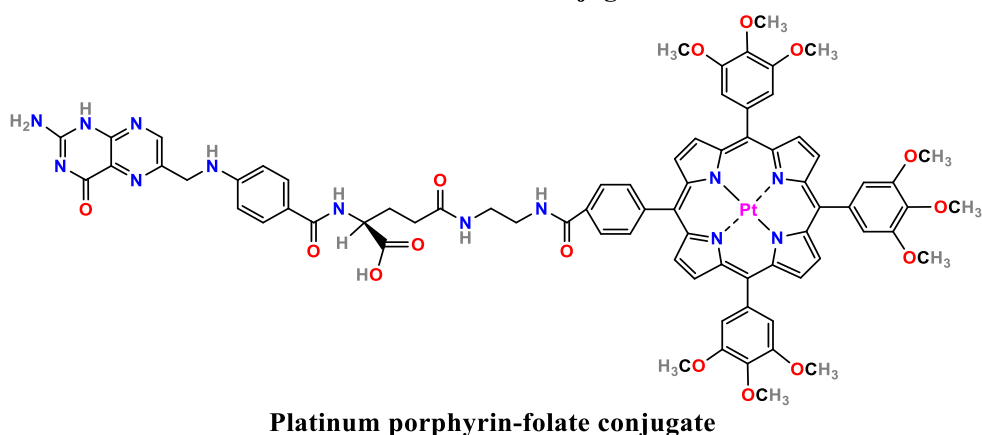
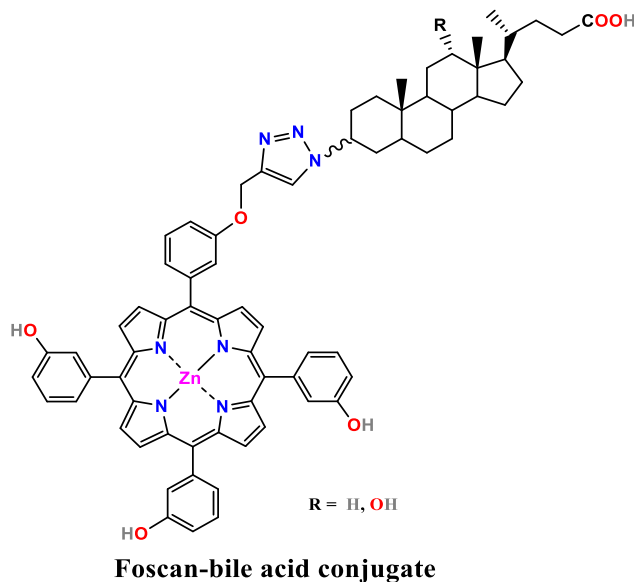


Fig. 50. Foscan-bile acid and platinum porphyrin-folate conjugates.

The last group of targeting biomolecules are aptamers. Aptamers are nucleic acids of single chain (ssDNA and RNA) which can recognize several target molecules by folding into several secondary and tertiary structures. Common examples of aptamers are A10 PSMA and AS1411. This group of biomolecules present several advantages like high targeting affinity and minimal immunogenicity, high stability and low costs of production, being even possible to produce them on a large scale.<sup>438,439,440</sup> In Fig. 51, a pair of examples of PS-aptamer conjugates are depicted. One is a Chlorin e6 (Ce6) linked to AS1411 using PEG (polyethylene glycol) as a linker,<sup>441</sup> and the other is a Ru(II) polypyridyl complex linked to AS1411 by a thymine chain.<sup>442</sup>

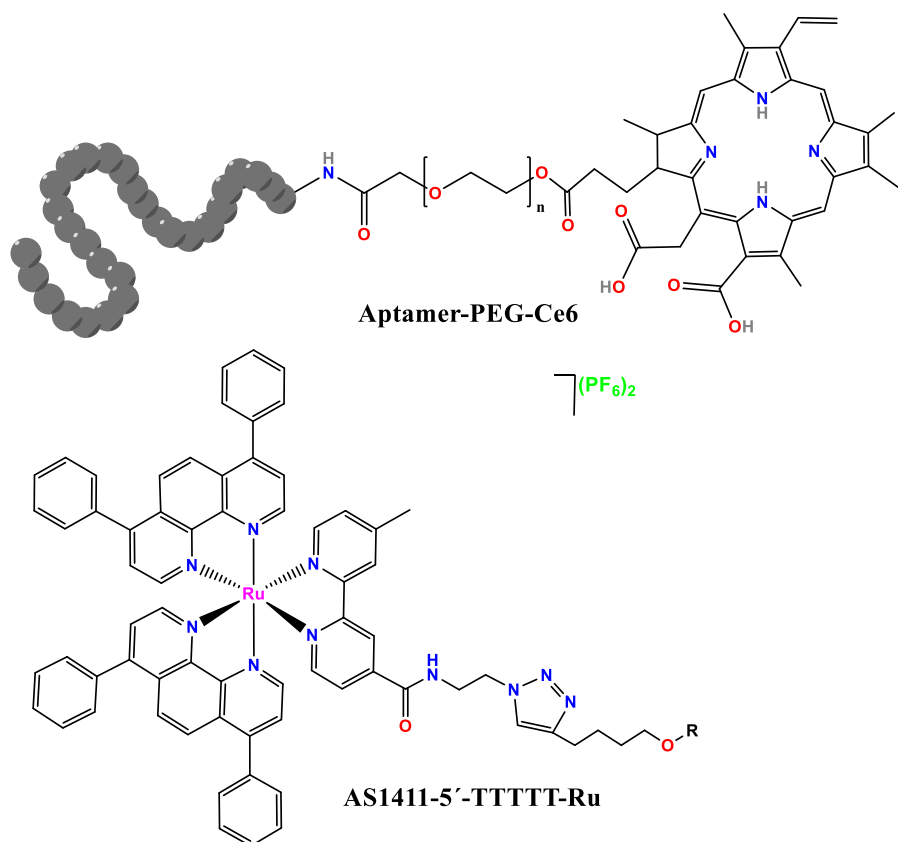


Fig. 51. Aptamer-PEG-Ce6 and AS1411-5'-TTTTT-Ru.

Importantly, this strategy of preparing PSs with targeting biomolecules can be combined with nanocarriers. For this purpose, the targeting biomolecules are attached to the surface of the nanocarriers instead of being linked directly to the PSs. This combined strategy is sometimes preferred, because it is easier to modify the surface of the nanocarriers than that of the PSs and this permits more alternatives.<sup>443,444,445</sup>

### 3.7.7. X-ray PDT

Thanks to its high tissue penetration, due to its high energy photons (from keV to MeV), X-rays has been extensively used in radiotherapy for cancer treatment. However, in order to achieve an efficient treatment, high radiation doses are needed, which also damages the healthy tissues surrounding the target. This problem that can be overcome with X-ray PDT, because the X-ray doses needed for the treatment are much lower.<sup>446,447,448</sup>

For the efficient activation of the PSs, a physical transducer, known as a scintillator, is needed. A scintillator is a material which is able to absorb X-ray radiation and re-emit

it like visible photons that can be absorbed by the PS. This process is known as XEOL (X-ray excited optical luminescence). Of course, the choice of the scintillator depends directly on the PS to be used, because the output radiation varies among them. There is a wide range of scintillators available; some of the most used for X-ray PDT are:  $\text{LaF}_3:\text{Tb}$ ,  $\text{Gd}_2\text{O}_2\text{S}:\text{Tb}$ ,  $[\text{Hf}_6\text{O}_4(\text{OH})_4(\text{HCO}_2)_6]$  SBUs (Secondary building units),  $\text{SrAl}_2\text{O}_4:\text{Eu}$ .<sup>449,450</sup>

This strategy offers advantages due to the dual mechanism of X-ray PDT: X-ray radiation damages DNA, and ROS generated by the PS damage several cellular compartments depending on the PS. This multitarget mechanism of action allows to overcome the repairing mechanisms of the cancer cells and causes both apoptosis and necrosis simultaneously.<sup>451,452</sup>

Several PSs have been studied for their use in X-ray PDT, like porphyrins (see section 3.6.2.)<sup>453</sup> and Photofrin (see section 3.6.1.),<sup>454</sup> or even  $[\text{Ir}(\text{bpy})(\text{ppy})_2]^+$  and  $[\text{Ru}(\text{bpy})_3]^{2+}$  (Fig. 52), although these two complexes have been integrated in MOLs (metal organic layers) for their use.<sup>455</sup>

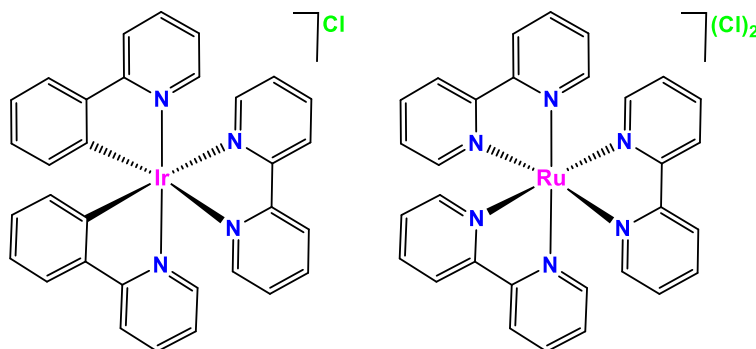


Fig. 52.  $[\text{Ir}(\text{bpy})(\text{ppy})_2]^+$  and  $[\text{Ru}(\text{bpy})_3]^{2+}$ .

### 3.7.8. AIE (aggregation induced emission)

Some PSs display aggregation induced emission (AIE). AIE consists in an increase in the emission intensity of a compound upon aggregation or in the solid state relative to its emission when is solvated.<sup>456,457</sup> The mechanism beyond the AIE involves the restriction of intramolecular motions/rotations (RIM/RIR). It is common for compounds presenting AIE to possess molecular rotors (rotatable aromatic rings are the most frequent chemical motifs), which rotate freely when the compound is solvated, consuming in this way the energy of the excited state, leading to a non-radiative decay. However, when these compounds undergo aggregation, the interactions between their molecules restrict the rotations of the rotatory groups, favoring the radiative decay pathway.<sup>457,458</sup>



Some examples of iridium<sup>459,460</sup> and ruthenium<sup>461,462</sup> complexes presenting AIE are depicted in Fig. 53.

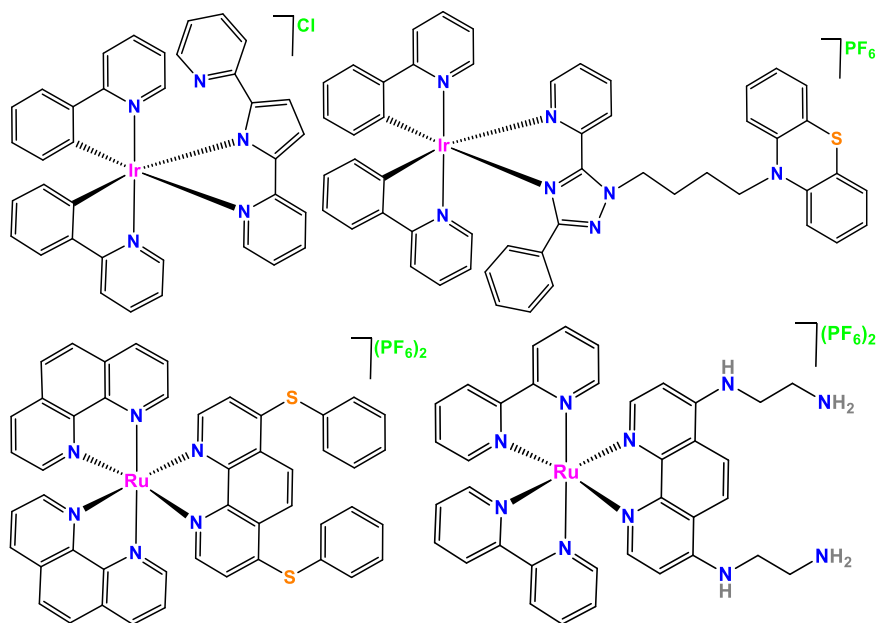


Fig. 53. Some iridium and ruthenium complexes that present AIE.

## Bibliography

1. a) J. Ferlay, I. Soerjomataram, R. Dikshit, et al., Cancer incidence and mortality worldwide: sources, methods and major patterns in GLOBOCAN 2012, *In. J. Cancer*, 2015, **136**, E359–E386. b) globocan 2020, recovered from: <https://gco.iarc.fr/today/data/factsheets/cancers/39-All-cancers-fact-sheet.pdf>
2. J. Ferlay, E. Steliarova-Foucher, J. Lortet-Tieulent, et al., Cancer incidence and mortality patterns in Europe: estimates for 40 countries in 2012, *Eur. J. Cancer*, 2013, **49**, 1374–1403.
3. R.L Siegel, K. D. Miller, and A. Jemal, Cancer statistics 2016, *CA Cancer J. Clin.*, 2016, **66**, 7-30.
4. D. Schottenfeld, and J. F. Fraumeni Jr., *Cancer Epidemiology and Prevention*. Oxford University Press, 2006.
5. K. Y. Yoo, and H. R. Shin, Cancer epidemiology and prevention, *Korean J. Epidemiol.*, 2003, **25**, 1-15.
6. J. S. Bertram, The molecular biology of cancer, *Molecular Aspects of Medicine*, 2001, **21**, 167-223.
7. S. L. Poon, J. R. McPherson, P. Tan, B. T. Teh, and S. G. Rozen, Mutation signatures of carcinogen exposure: genome-wide detection and new opportunities for cancer prevention, *Genome Med.*, 2014, **6**, 24.
8. K. Aizawa, C. Liu, S. Tang, et al., Tobacco carcinogen induces both lung cancer and non-alcoholic steatohepatitis and hepatocellular carcinomas in ferrets which can be attenuated by lycopene supplementation, *Int. J. Cancer.*, 2016, **139**, 1171-1181.
9. R. Doll, and R. Peto, The causes of cancer: quantitative estimates of avoidable risks of cancer in the United States today, *J. Natl. Cancer Inst.*, 1981, **66**, 1191-1308.
10. J. Trafialek, and W. Kolanowski, Dietary exposure to meat-related carcinogenic substances: is there a way to estimate the risk?, *Int. J. Food Sci. Nutr.*, 2014, **65**, 774-780.
11. D. M. Parkin, The global health burden of infection-associated cancers in the year 2002, *Int. J. Cancer*, 2006, **118**, 3030-3044.
12. B. N. Ames, M. K. Shigenaga, and L. S. Gold, DNA lesions, inducible DNA repair, and cell division: three key factors in mutagenesis and carcinogenesis, *Environ. Health Perspect.*, 1993, **101**, 35-44.
13. A. L. Jackson, and L. A. Loeb, The mutation rate and cancer, *Genetics*, 1998, **148**, 1483-1490.
14. L. A. Loeb, Mutator phenotype may be required for multistage carcinogenesis, *Cancer Res.*, 1991, **51**, 3075-3079.
15. B. M. Rothschild, D. H. Tanke, M. Helbling, and L. D. Martin, Epidemiologic study of tumours in dinosaurs, *Naturwissenschaften*, 2003, **90**, 495–500.
16. M. D. Dumbravbrevea, B. M. Rothschild, D. B. Weishampel, Z. Csiki-Sava, et al., A dinosaurian facial deformity and the first occurrence of ameloblastoma in the fossil record, *Sci. Rep.*, 2016, **6**, 29271.
17. G. M. Sanchez, and E. S. Meltzer, *The Edwin Smith Papyrus: Updated Translation of the Trauma Treatise and Modern Medical Commentaries*, Atlanta, GA, Lockwood Press, 2012.
18. L. Falzone, S. Salomone, and M. Libra, Evolution of cancer pharmacological treatments at the turn of the third millennium, *Front. Pharmacol.*, 2018, **9**, 1300.

19. A. Karpozilos, and N. Pavlidis, The treatment of cancer in Greek antiquity, *Eur. J. Cancer*, 2004, **40**, 2033–2040.
20. G. Tsoucalas, and M. Sgantzos, Hippocrates (ca 460-370 BC) on nasal cancer, *J. B.U.O.N.*, 2016, **21**, 1031–1034.
21. N. Papavramidou, T. Papavramidis, and T. Demetriou, Ancient Greek and Greco-Roman methods in modern surgical treatment of cancer, *Ann. Surg. Oncol.*, 2010, **17**, 665–667.
22. G. B. Faguet, A brief history of cancer: age-old milestones underlying our current knowledge database, *Int. J. Cancer*, 2015, **136**, 2022–2036.
23. L. Deloch, A. Derer, J. Hartmann, B. Frey, R. Fietkau, and U. S. Gaipl, Modern radiotherapy concepts and the impact of radiation on immune activation, *Front. Oncol.*, 2016, **6**, 141.
24. J. E. Moulder, and C. Seymour, Radiation fractionation: the search for isoeffect relationships and mechanisms, *Int. J. Radiat. Biol.*, 2017, **2**, 1–9.
25. P. Brookes, The early history of the biological alkylating agents, 1918–1968. *Mutat. Res.*, 1990, **233**, 3–14.
26. M. Lane, Some effects of cyclophosphamide (cytoxan) on normal mice and mice with L1210 leukemia, *J. Natl. Cancer Inst.*, 1959, **23**, 1347–1359.
27. S. B. Kaye, New antimetabolites in cancer chemotherapy and their clinical impact., *Br. J. Cancer*, 1998, **3**, 1–7.
28. M. Tiwari, Antimetabolites: established cancer therapy, *J. Cancer Res. Ther.*, 2012, **8**, 510–519.
29. R. J. van Vuuren, M. H. Visagie, A. E. Theron, and A. M. Joubert, Antimitotic drugs in the treatment of cancer, *Cancer Chemother. Pharmacol.*, 2015, **76**, 1101–1112.
30. A. Minocha, and B. H. Long, Inhibition of the DNA catenation activity of type II topoisomerase by VP16-213 and VM26, *Biochem. Biophys. Res. Commun.*, 1984, **122**, 165–170.
31. M. C. Wani, H. L. Taylor, M. E. Wall, P. Coggon, and A. T. McPhail, Plant antitumor agents. VI. The isolation and structure of taxol, a novel antileukemic and antitumor agent from *Taxus brevifolia*, *J. Am. Chem. Soc.*, 1971, **93**, 2325–2327.
32. M. C. Bissery, D. Guénard, F. Guéritte-Voegelein, and F. Lavelle, Experimental antitumor activity of taxotere (RP 56976, NSC 628503), a taxol analogue, *Cancer Res.*, 1991, **51**, 4845–4852.
33. A. C. Mita, L. J. Denis, E. K. Rowinsky, J. S. Debono, A. D. Goetz, L. Ochoa, et al., Phase I and pharmacokinetic study of XRP6258 (RPR116258A), a novel taxane, administered as a 1-hour infusion every 3 weeks in patients with advanced solid tumors, *Clin. Cancer Res.*, 2009, **15**, 723–730.
34. R. B. Weiss, The anthracyclines: will we ever find a better doxorubicin?, *Semin. Oncol.*, 1992, **19**, 670–686.
35. J. Chen, and J. Stubbe, Bleomycins: towards better therapeutics, *Nat. Rev. Cancer*, 2005, **5**, 102–112.
36. R. C. Lilenbaum, J. E. Herndon, M. A. List, C. Desch, D. M. Watson, A. A. Miller, et al., Single-agent versus combination chemotherapy in advanced non-small-cell lung cancer: the cancer and leukemia group B (study 9730), *J. Clin. Oncol.*, 2005, **23**, 190–196.

37. J. T. Hartmann, M. Haap, H. G. Kopp, and H. P. Lipp, Tyrosine kinase inhibitors—a review on pharmacology, metabolism and side effects, *Curr. Drug Metab.*, 2009, **10**, 470–481.
38. G. Köhler, and C. Milstein, Continuous cultures of fused cells secreting antibody of predefined specificity, *Nature*, 1975, **256**, 495–497.
39. A. M. Tsimberidou, Targeted therapy in cancer, *Cancer Chemother. Pharmacol.*, 2015, **76**, 1113–1132.
40. J. T. Pento, Monoclonal antibodies for the treatment of cancer, *Anticancer Res.*, 2017, **37**, 5935–5939.
41. G. Hudes, M. Carducci, P. Tomczak, J. Dutcher, R. Figlin, A. Kapoor, et al., Temsirolimus, interferon alfa, or both for advanced renal-cell carcinoma, *N. Engl. J. Med.*, 2007, **356**, 2271–2281.
42. B. Coiffier, C. Haioun, N. Ketterer, A. Engert, H. Tilly, D. Ma, et al., Rituximab (anti-CD20 monoclonal antibody) for the treatment of patients with relapsing or refractory aggressive lymphoma: a multicenter phase II study, *Blood*, 1998, **92**, 1927–1932.
43. E. E. Vokes, and E. Chu, Anti-EGFR therapies: clinical experience in colorectal, lung, and head and neck cancers, *Oncology (Williston Park)*, 2006, **20**, 15–25.
44. M. Poulin-Costello, L. Azoulay, E. Van Cutsem, M. Peeters, S. Siena, and M. Wolf, An analysis of the treatment effect of panitumumab on overall survival from a phase 3, randomized, controlled, multicenter trial (20020408) in patients with chemotherapy refractory metastatic colorectal cancer, *Target Oncol.*, 2013, **8**, 127–136.
45. H. X. Chen, R. E. Gore-Langton, and B. D. Cheson, Clinical trials referral resource: current clinical trials of the anti-VEGF monoclonal antibody bevacizumab, *Oncology (Williston Park)*, 2001, **15**, 1017, 1020, 1023–6.
46. G. M. Keating, Bevacizumab: a review of its use in advanced cancer, *Drugs*, 2014, **74**, 1891–1925.
47. J. A. McCubrey, S. L. Abrams, K. Stadelman, W. H. Chappell, M. Lahair, R. A. Ferland, et al., Targeting signal transduction pathways to eliminate chemotherapeutic drug resistance and cancer stemcells, *Adv. Enzyme Regul.*, 2010, **50**, 285–307.
48. P. Wu, M. H. Clausen, and T. E. Nielsen, Allosteric small-molecule kinase inhibitors, *Pharmacol. Ther.*, 2015, **156**, 59–68.
49. F. Rossari, F. Minutolo, and E. Orciuolo, Past, present, and future of Bcr-Abl inhibitors: from chemical development to clinical efficacy, *J. Hematol. Oncol.*, 2018, **11**, 84.
50. R. I. Nicholson, J.M. Gee, and M. E. Harper, EGFR and cancer prognosis, *Eur. J. Cancer*, 2001, **37**, S9–S15.
51. M. Steins, M. Thomas, and M. Geißler, Erlotinib. Recent Results, *Cancer Res.*, 2018, **211**, 1–17.
52. S. P. Ivy, J. Y. Wick., and B. M. Kaufman, An overview of small molecule inhibitors of VEGFR signaling, *Nat. Rev. Clin. Oncol.*, 2009, **6**, 569–579.
53. L. Lytvynchuk, A. Sergienko, G. Lavrenchuk, and G. Petrovski, Antiproliferative, apoptotic, and autophagic activity of ranibizumab, bevacizumab, pegaptanib, and aflibercept on fibroblasts: implication for choroidal neovascularization, *J. Ophthalmol.*, 2015, **2015**, 934963.

54. A. Fasolo, and C. Sessa, Targeting mTOR pathways in human malignancies, *Curr. Pharm. Des.*, 2012, **18**, 2766–2777.
55. J. Hasskarl, Everolimus, *Recent Results Cancer Res.*, 2018, **211**, 101–123.
56. C. Robert, B. Karaszewska, J. Schachter, P. Rutkowski, A. Mackiewicz, D. Stroiakovski, et al., Improved overall survival in melanoma with combined dabrafenib and trametinib, *N. Engl. J. Med.*, 2015, **372**, 30–39.
57. E. E. Manasanch, and R. Z. Orlowski, Proteasome inhibitors in cancer therapy, *Nat. Rev. Clin. Oncol.*, 2017, **14**, 417–433.
58. M. Vanneman, and G. Dranoff, Combining immunotherapy and targeted therapies in cancer treatment, *Nat. Rev. Cancer*, 2012, **12**, 237–251.
59. R. B. Mokhtari, T. S. Homayouni, N. Baluch, E. Morgatskaya, S. Kumar, B. Das, et al., Combination therapy in combating cancer, *Oncotarget*, 2017, **8**, 38022–38043.
60. J. K. Chung, H. W. Youn, J. H. Kang, H. Y. Lee, and K. W. Kang, Sodium iodide symporter and the radioiodine treatment of thyroid carcinoma, *Nucl. Med. Mol. Imaging*, 2010, **44**, 4–14.
61. E. B. Silberstein, A. Alavi, H. R. Balon, S. E. Clarke, C. Divgi, M. J. Gelfand, et al., The SNMMI practice guideline for therapy of thyroid disease with <sup>131</sup>I 3.0, *J. Nucl. Med.*, 2012, **53**, 1633–1651.
62. J. Y. Choi, Treatment of bone metastasis with bone-targeting radiopharmaceuticals, *Nucl. Med. Mol. Imaging*, 2018, **52**, 200–207.
63. P. M. Anderson, V. Subbiah, and E. Rohren, Bone-seeking radiopharmaceuticals as targeted agents of osteosarcoma: samarium- 153-EDTMP and radium-223, *Adv. Exp. Med. Biol.*, 2014, **804**, 291–304.
64. Y. Cheng, A. P. Kiess, J. M. Herman, M. G. Pomper, S. J. Meltzer, J. M. and Abraham, Phosphorus-32, a clinically available drug, inhibits cancer growth by inducing DNA double-strand breakage, *PLoS ONE*, 2015, **10**, e0128152.
65. M. Hadaki, R. Praseedom, R. Brais, T. C. See, K. Balan, and C. B. Wilson, Selective internal radiation therapy with <sup>90</sup>Y-SIR-Spheres microspheres for non-resectable colorectal metastases in the liver, *BMJ Case Rep.*, 2011, bcr0120113793.
66. F. Sudbrock, M. Schmidt, T. Simon, W. Eschner, F. Berthold, and H. Schicha, Dosimetry for <sup>131</sup>I-MIBG therapies in metastatic neuroblastoma, pheochromocytoma and paraganglioma, *Eur. J. Nucl. Med. Mol. Imaging*, 2010, **37**, 1279–1290.
67. F. Forrer, H. Uusijärvi, D. Storch, H. R. Maecke, and J. Mueller-Brand, Treatment with <sup>177</sup>Lu-DOTATOC of patients with relapse of neuroendocrine tumors after treatment with <sup>90</sup>Y-DOTATOC, *J. Nucl. Med.*, 2005, **46**, 1310–1316.
68. J. B. Haanen, and C. Robert, Immune checkpoint inhibitors, *Prog. Tumor Res.*, 2015, **42**, 55–66.
69. J. A. Seidel, A. Otsuka, and K. Kabashima, Anti-PD-1 and Anti-CTLA-4 therapies in cancer: mechanisms of action, efficacy, and limitations, *Front. Oncol.*, 2018, **8**, 86.
70. K. M. Mahoney, P. D. Rennert, and G. J. Freeman, Combination cancer immunotherapy and new immunomodulatory targets, *Nat. Rev. Drug Discov.*, 2015, **14**, 561–584.

71. D. Xu, G. Jin, D. Chai, X. Zhou, W. Gu, Y. Chong, J. Song, et al., The development of CAR design for tumor CAR-T cell therapy, *Oncotarget*, 2018, **9**, 13991–14004.
72. S. Srivastava, and S. R. Riddell, Engineering CAR-T cells: design concepts, *Trends Immunol.*, 2015, **36**, 494–502.
73. D. L. Porter, B. L. Levine, M. Kalos, A. Bagg, and C. H. June, Chimeric antigen receptor-modified T cells in chronic lymphoid leukemia, *N. Engl. J. Med.*, 2011, **365**, 725–733.
74. A. di Pietro, G. Tosti, P. F. Ferrucci, and A. Testori, Oncophage: step to the future for vaccine therapy in melanoma, *Expert Opin. Biol. Ther.*, 2008, **8**, 1973–1984.
75. R. So-Rosillo, and E. J. Small, Sipuleucel-T (APC8015) for prostate cancer, *Expert Rev. Anticancer Ther.*, 2006, **6**, 1163–1167.
76. T. Zhan, N. Rindtorff, J. Betge, M. P. Ebert, and M. Boutros, CRISPR/Cas9 for cancer research and therapy, *Semin. Cancer Biol.*, 2019, **55**, 106–119.
77. C. Orvig and M. J. Abrams, Medicinal Inorganic Chemistry: Introduction, *Chem. Rev.*, 1999, **99**, 2201–2204.
78. A. W. Jones, Early drug discovery and the rise of pharmaceutical chemistry, *Drug Test Anal.*, 2011, **3**, 337–44.
79. P. J. Sadler, Inorganic Chemistry and Drug Design, *Adv. Inorg. Chem.* 1991, **36**, 1 – 48.
80. A. Mukherjee, and P. J. Sadler, Metals in Medicine: Therapeutic Agents, *Wiley Encyclopedia of Chemical Biology*, 2007, 1-47.
81. Z. Guo, P. J. Sadler, Medicinal inorganic chemistry, *Adv. Inorg.Chem.*, 2000, **49**, 183–306.
82. Z. Guo, P. J. Sadler, Metals in medicine, *Angew. Chem. Int. Ed.*, 1999, **38**, 1512–1531.
83. R. Kour Sodhi and S. Paul, Metal Complexes in Medicine: An Overview and Update from Drug Design Perspective, *Canc. Therapy & Oncol. Int. J.*, 2019, **14**, 25-32.
84. G. Gasser, Metal Complexes and Medicine: A Successful Combination, *CHIMIA International Journal for Chemistry*, 2015, **7**, 442-446.
85. M. Frezza, S. Hindo, D. Chen, et al., Novel metals and metal complexes as platforms for cancer therapy, *Curr. Pharm. Des.*, 2010, **16**, 1813–1825.
86. Y. K. Yan, M. Melchart, A. Habtemariam, P. J. Sadler, Organometallic chemistry, biology and medicine: ruthenium arene anticancer complexes, *Chem. Commun.*, 2005, **38**, 4764–4776.
87. M. S. Salga, H. M. Ali, M. A. Abdulla, S. I. Abdelwahab, Acute oral toxicity evaluations of some zinc (II) complexes derived from 1-(2-Salicylaldiminoethyl) piperazine schiff bases in rats, *Int. J. Mol. Sci.*, 2012, **13**, 1393–1404.
88. K. L. Haas, K. J. Franz KJ, Application of metal coordination chemistry to explore and manipulate cell biology, *Chem. Rev.*, 2010, **109**, 4921–4960.
89. D. E. Reichert, J. S. Lewis and C. J. Anderson, Metal complexes as diagnostic tools, *Coord. Chem. Rev.*, 1999, **184**, 3 – 66.

90. S. I. Pascu, P. A. Waghorn, T. D. Conry, H. M. Betts, J. R. Dilworth, G. C. Churchill, T. Pokrovska, M. Christlieb, F. I. Aigbirhio, and J. E. Warren, Designing Zn(II) and Cu(II) derivatives as probes for invitro fluorescence imaging, *Dalton Trans.*, 2007, **43**, 4988–4997.
91. M. W. Bourassa and L. M. Miller, Metal imaging in neurodegenerative diseases, *Metallomics*, 2012, **4**, 721-738.
92. F. B. Payolla<sup>1</sup>, A. C. Massabni and C. Orvig, Radiopharmaceuticals for diagnosis in nuclear medicine: a short review, *Eclética Química Journal*, 2019, **44**, 11-19.
93. G. B. Saha, W. J. MacIntyre and R. T. Go, Radiopharmaceuticals for Brain Imaging, *Seminars in Nuclear Medicine*, 1994, **24**, 324-349.
94. L. K. Anzola, F. Galli, R. A. Dierckx, SPECT radiopharmaceuticals for imaging chronic inflammatory diseases in the last decade, *The Quarterly Journal of Nuclear Medicine and Molecular Imaging*, 2015, **59**,197-213.
95. S. Schwarz, J. Norenberg, M. Berridge, et al., The future of USP monographs for PET drugs, *Journal of Nuclear Medicine*, 2013, **54**, 472-475.
96. G. Sgouros, L. Bodei, M.R. McDevitt, et al., Radiopharmaceutical therapy in cancer: clinical advances and challenges, *Nat. Rev. Drug Discov.*, 2020, **19**, 589–608.
97. T. W. Redpath, MRI developments in perspective, *Br. J. Radiol.*, 1997, **70**, 70-80.
98. J. Wahsner, E. M. Gale, A. Rodríguez-Rodríguez, and Peter Caravan, Chemistry of MRI Contrast Agents: Current Challenges and New Frontiers, *Chem. Rev.*, 2019, **119**, 2, 957–1057.
99. T. J. Clough, L. Jiang, K. L. Wong, et al., Ligand design strategies to increase stability of gadolinium-based magnetic resonance imaging contrast agents, *Nat. Commun.*, 2019, **10**, 1-14.
100. Z. Sahraei, M. Mirabzadeh, D. F. Fouladi, N. Eslami, and A. Eshraghi, Magnetic Resonance Imaging Contrast Agents: A Review of Literature, *J. Pharm. Care*, 2014, **2**, 177-182.
101. S. L. Best, P. J. Sadler, Gold drugs: mechanism of action and toxicity, *Gold Bull.*, 1996, **29**, 87–93.
102. G. G. Graham, G. D. Champion, and, J.B. Ziegler, The antirheumatic gold complexes: Considerations of chemical form in studies on their mechanism of action, *Inflammopharmacology*, 1991, **1**, 99-102.
103. G. Jones, and P. M. Brooks, Injectable gold compounds: an overview, *British Journal of Rheumatology*, 1996, **35**, 1154-1158.
104. R. C. Elder, K. Ludwig, J. N. Cooper, and M. K. Eidsness, EXAFS and WAXS structure determination for an antiarthritic drug, sodium gold (I) thiomalate, *J. Am. Chem. Soc.*, 1985, **107**, 5024-5025.
105. M. A. Mazid, M. T. Razi, P. J. Sadler, G. N. Greaves, S. J. Gurman, M. H. J. Koch, and J. C. Phillips, An EXAFS study of gold co-ordination in the anti-arthritis drugs Myocrisin and Solganol, *J. Chem. Soc. Chem. Commun.*, 1980, **24**, 1261-1263.
106. A. Chircorian, and A. M. Barrios, Inhibition of lysosomal cysteine proteases by chrysotherapeutic compounds: a possible mechanism for the antiarthritic activity of Au(I), *Bioorganic Med. Chem. Lett.*, 2004, **14**, 5113-5116.
107. D. T. Walz, M. J. DiMartino, D. E. Griswold, A. P. Intoccia, T. L. Flanagan, Biologic actions and pharmacokinetic studies of auranofin, *The American Journal of Medicine*, 1983, **75**, 90-108.

108. K. Helm, J. Marks, J. J. Leyden, C. Guzzo, G. G. Krueger, T. W. Griffiths, and C. E. M. Griffiths, Topical auranofin ointment for the treatment of plaque psoriasis, *J. Am. Acad. Dermatol.*, 1995, **33**, 517-519.
109. G. G. Graham, G. D. Champion, and J. B. Ziegler, The antirheumatic gold complexes: Considerations of chemical form in studies on their mechanism of action, *Inflammopharmacology*, 1991, **1**, 99-102.
110. P. Domenico, R. J. Salo, S. G. Novick, P. E. Schoch, K. Van Horn, B. A. Cunha, Enhancement of bismuth antibacterial activity with lipophilic thiol chelators, *Antimicrob Agents Chemother*, 1997, **41**, 1697-1703.
111. N. Burford, M. D. Eelman, D. E. Mahony, M. Morash, Definitive identification of cysteine and glutathione complexes of bismuth by mass spectrometry: assessing the biochemical fate of bismuth pharmaceutical agents, *Chem. Commun.*, 2003, **1**, 146-147.
112. H. Sun, H. Li, I. Harvey, P. J. Sadler, Interactions of bismuth complexes with metallothionein(II), *J. Biol. Chem.*, 1999, **274**, 29094-29101.
113. W. Li, L. Jin, N. Zhu, X. Hou, F. Deng, H. Sun, Structure of colloidal bismuth subcitrate (CBS) in dilute HCl: unique assembly of bismuth citrate dinuclear units ([Bi(cit)2Bi]2-), *J. Am. Chem. Soc.*, 2003, **125**, 12408-12409.
114. N. Yang, Y. An, Y., J. Cai, et al., Polymeric architectures of bismuth citrate based on dimeric building blocks, *Sci. China Chem.*, 2010, **53**, 2152-2158.
115. A. Mastrolorenzo, A. Scozzafava, and C. T. Supuran, Antifungal Activity of Ag(I) and Zn(II) Complexes of Aminobenzolamide (5-Sulfanylamido-1,3,4-Thiadiazole-2-Sulfonamide) Derivatives, *J. Enzyme Inhibition*, 2000, **15**, 517-531.
116. C. Biot, D. Taramelli, I. Forfar-Bares, L. A. Maciejewski, M. Boyce, G. Nowogrocki, J. S. Brocard, N. Basilico, P. Olliaro, T. J. Egan, Insights into the mechanism of action of ferroquine. Relationship between physicochemical properties and antiplasmodial activity, *Mol. Pharm.*, 2005, **2**, 185-193.
117. D. Dive, and C. Biot, Ferrocene conjugates of chloroquine and other antimalarials: the development of ferroquine, a new antimalarial, *Chem. Med. Chem.*, 2008, **3**, 383-391.
118. G. Bertini, H. B. Gray, H. Gray, J. S. Valentine, E. I. Stiefel, and E. Stiefel, Biological inorganic chemistry: structure and reactivity, *University Science Books*, 2007.
119. J. Wang, B. A. Tannous, M. C. Poznansky, H. Chen, CXCR4 antagonist AMD3100 (plerixafor): From an impurity to a therapeutic agent, *Pharmacol. Res.*, 2020, **159**, 105010.
120. E. De Clercq, MozobilVR (Plerixafor, AMD3100), 10 years after its approval by the US Food and Drug Administration, *Antiviral Chemistry and Chemotherapy*, 2019, **27**, 1-8.
121. C. F. Shaw III, Gold Progress in Chemistry, Biochemistry and Technology (Ed.: H. Schmidbaur), *Wiley*, New York, 1999.
122. S.-Y. Wong, R. W.-Y. Sun, N. P.-Y. Chung, C.-L. Linb and C.-M. Che, Physiologically stable vanadium(IV) porphyrins as a new class of anti-HIV agents, *Chem. Commun.*, 2005, **28**, 3544-3546.
123. F. Nareetsilea, S. Ndlovua, J. T.P. Matshwelea, and M. Ngaskia, Transition Metal Complexes with HIV/AIDS Inhibitory Properties, *Chem. Rev. Lett.*, 2020, **3**, 140-160.
124. K. H. Thompson, and C. Orvig, Vanadium in diabetes: 100 years from Phase 0 to Phase I, *J. Inorg. Biochem.*, 2006, **100**, 1925-1935.



125. C. L. Broadhurst, and P. Domenico, Clinical studies on chromium picolinate supplementation in diabetes mellitus—a review, *Diabetes. Technol. Ther.*, 2006, **8**, 677–687.
126. B. D. Liboiron, K. H. Thompson, G. R. Hanson, E. Lam, N. Aebischer, and C. Orvig, New insights into the interactions of serum proteins with bis(maltolato)oxovanadium(IV): transport and biotransformation of insulin-enhancing vanadium pharmaceuticals, *J. Am. Chem. Soc.*, 2005, **127**, 5104–5115.
127. K.H. Thompson, B. D. Liboiron, Y. Sun, K. D. Bellman, I. A. Setyawati, B. O. Patrick, V. Karunaratne, G. Rawji, J. Wheeler, K. Sutton, S. Bhanot, C. Cassidy, J. H. McNeill, V. G. Yuen, C. Orvig, Preparation and characterization of vanadyl complexes with bidentate maltol-type ligands; in vivo comparisons of anti-diabetic therapeutic potential, *J. Biol. Inorg. Chem.*, 2003, **8**, 66–74.
128. M. C. Cam, R. W. Brownsey, J. H. McNeill, Mechanisms of vanadium action: insulin-mimetic or insulin-enhancing agent?, *Can. J. Physiol. Pharmacol.*, 2000, **78**, 829-47.
129. K. R. Manygoats, M. Yazzie, and D. M. Stearns, Ultrastructural damage in chromium picolinate-treated cells: a TEM study. Transmission electron microscopy, *J. Biol. Inorg. Chem.*, 2002, **7**, 791–798.
130. I. H. Tuzel, Sodium Nitroprusside: A Review of Its Clinical Effectiveness as a Hypotensive Agent, *J. Clin. Pharmacol.*, 1974, **14**, 494 - 503.
131. D. S. Thompson, S. M. Juul, P. Wilmschurst, N. Naqvi, D. J. Coltart, B. S. Jenkins, M. M. Webb-Peploe, Effects of sodium nitroprusside upon cardiac work, efficiency, and substrate extraction in severe left ventricular failure, *Br. Heart J.*, 1981, **46**, 394-400.
132. D. Drover, H. Gregory, B. Jeffrey, C. Carol, R. Tammy, Z. Anne, S. Scott, Evaluation of sodium nitroprusside for controlled hypotension in children during surgery, *Front. Pharmacol.*, 2015, **6**, 136.
133. C. Glidewell, and I. L. Johnson, Definitive identification of the primary reduction product of the nitroprusside ion, pentacyanonitrosylferrate(2-), in aqueous solution, *Inorg. Chim. Acta*, 1987, **132**, 145 - 147.
134. A. R. Butler, A. M. Calsey-Harrison, C. Glidewell, I. L. Johnson, J. Reglinski, W. E. Smith, The interaction of sodium nitroprusside with peripheral white blood cells in vitro: a rationale for cyanide release in vivo, *Inorg. Chim. Acta*, 1988, **151**, 281 - 286.
135. B. A. Fricker, E. Slade, N. A. Powell, O. J. Vaughan, G. R. Henderson, B. A. Murrer, I. L. Megson, S. K. Bisland, F. W. Flitney, Ruthenium complexes as nitric oxide scavengers: a potential therapeutic approach to nitric oxide-mediated diseases, *Br. J. Pharmacol.*, 1997, **122**, 1441 - 1449.
136. S. Dilruba, and G.V. Kalayda, Platinum-based drugs: past, present and future, *Cancer Chemother. Pharmacol.*, 2016, **77**, 1103–1124.
137. S. A. Aldossary, Review on pharmacology of cisplatin: clinical use, toxicity and mechanism of resistance of cisplatin, *Biomed. and Pharmacol. J.*, 2019, **12**, 7-15.
138. B. A. Chabner, Barnett Rosenberg: In Memoriam (1924–2009), *Cancer Res.*, 2010, **70**, 428-429.
139. S. Dasari, and P. B. Tchounwou, Cisplatin in cancer therapy: molecular mechanisms of action, *Eur. J. Pharmacol.*, 2014, **740**, 364-378.
140. R. B. Martin, Platinum complexes: hydrolysis and binding to N (7) and N (1) of purines, *Cisplatin: Chemistry and biochemistry of a leading anticancer drug*, 1999, 183-205.

141-214. T. Karasawa, and P. S. Steyger, An integrated view of cisplatin-induced nephrotoxicity and ototoxicity, *Toxicol. Lett.*, 2015, **237**, 219-227.

142. A. M. Galea, and V. Murray, The anti-tumour agent, cisplatin, and its clinically ineffective isomer, transplatin, produce unique gene expression profiles in human cells, *Cancer Inform.*, 2008, **6**, 315-355.

143. J. N. Burstyn, W. J. Heiger-Bernays, S. M. Cohen, S. J. Lippard, Formation of cis-diamminedichloroplatinum(II) 1,2-intrastrand cross-links on DNA is flanking-sequence independent, *Nucleic Acids Res.*, 2000, **28**, 4237-4243.

144. B. W. Johnson, V. Murray, and M. D. Temple, Characterisation of the DNA sequence specificity, cellular toxicity and cross-linking properties of novel bispyridine-based dinuclear platinum complexes, *BMC Cancer*, 2016, **16**, 333.

145. A. Amin, and M. A. Buratovich, New Platinum and Ruthenium Complexes - the Latest Class of Potential Chemotherapeutic Drugs - a Review of Recent Developments in the Field, *Mini-Reviews in Medicinal Chemistry*, 2009, **9**, 1489-1503.

146. N. Farrell, Current status of structure-activity relationships of platinum anticancer drugs: activation of the trans geometry, *Met. ions biol. syst.*, 1996, **32**, 603-639.

147. T. C. Johnstone, K. Suntharalingam, S. J. Lippard, The Next Generation of Platinum Drugs: Targeted Pt(II) Agents, Nanoparticle Delivery, and Pt(IV) Prodrugs, *Chem Rev.*, 2016, **116**, 3436-3486.

148. A. M. Montana, and C. Batalla, The rational design of anticancer platinum complexes: the importance of the structure-activity relationship, *Curr. Med. Chem.*, 2009, **16**, 2235-2260.

149. C. H. Yarbrow, Carboplatin: A clinical review, *Semin. Oncol. Nurs.*, 1989, **5**, 63-69.

150. N. Uchida, H. Kasai, Y. Takeda, et al., Synergy of the combination of nedaplatin with etoposide in murine and human lung carcinoma, *Anticancer Res.*, 1998, **18**, 247-252.

151. J. L. Misset, Oxaliplatin in practice, *Br. J. Cancer*, 1998, **77**, 4-7.

152. S. D. Brown, K. D. Trotter, O. B. Sutcliffe, J. A. Plumb, B. Waddell, N. E. B. Briggsa, and N. J. Wheate, Combining aspects of the platinum anticancer drugs picoplatin and BBR3464 to synthesize a new family of sterically hindered dinuclear complexes; their synthesis, binding kinetics and cytotoxicity, *Dalton Trans.*, 2012, **41**, 11330-11339.

153. M. J. McKeage, Lobaplatin: a new antitumour platinum drug, *Exp. Opin. Invest. Drugs*, 2001, **10**, 119-128.

154. N. K. Kim, T. Y. Kim, S. G. Shin, Y. I. Park, J. A. Lee, Y. B. Cho, K. H. Kim, D. K. Kim, D. S. Heo, Y. J. Bang, A phase I study of cis-malonato[(4R,5R)-4,5-bis(aminomethyl)-1,3-dioxolane] platinum(II) in patients with advanced malignancies, *Cancer*, 2001, **91**, 1549-1556.

155. M. D. Hall, H. R. Mellor, R. Callaghan, and T. W. Hambley, Basis for Design and Development of Platinum(IV) Anticancer Complexes, *J. Med. Chem.*, 2007, **50**, 3403-3411.

156. R. C. Todd, S. J. Lippard, Inhibition of transcription by platinum antitumor compounds, *Metallomics*, 2009, **1**, 280-91.

157. A. Bhargava, and U. N. Vaishampayan, Satraplatin: leading the new generation of oral platinum agents, *Expert Opin. Investig. Drugs*, 2009, **18**, 1787-1797.

158. a) Harris AL, Ryan JJ, Farrell NP. Biological consequences of trinuclear platinum complexes: comparison of  $[[\text{trans-PtCl}(\text{NH}_3)_2]_2\mu\text{-(trans-Pt}(\text{NH}_3)_2(\text{H}_2\text{N}(\text{CH}_2)_6\text{-NH}_2)_2)]_4^+$  (BBR 3464) with its noncovalent congeners, *Mol. Pharmacol.*, 2006, **69**, 666–672. b) J D Roberts, J Peroutka, G Beggiolin, C Manzotti, L Piazzoni, and N Farrell, Comparison of cytotoxicity and cellular accumulation of polynuclear platinum complexes in L1210 murine leukemia cell lines, *J. Inorg. Biochem.*, 1999,**77**, 47-50.
159. C. Billecke, S. Finniss, L. Tahash, et al., Polynuclear platinum anticancer drugs are more potent than cisplatin and induce cell cycle arrest in glioma, *Neuro Oncol.*, 2006, **8**, 215-226.
160. C. Mitchell, P. Kabolizadeh, J. Ryan, J. D. Roberts, A. Yacoub, D. T. Curiel, P. B. Fisher, M. P. Hagan, N. P. Farrell, S. Grant and P. Dent, Low-Dose BBR3610 Toxicity in Colon Cancer Cells Is p53-Independent and Enhanced by Inhibition of Epidermal Growth Factor Receptor (ERBB1)-Phosphatidylinositol 3 Kinase Signaling, *Mol. Pharmacol.*, 2007, **72**, 704-714.
161. B. Desoize, Metals and Metal Compounds in Cancer Treatment, *Anticancer Res.*, 2004, **24**, 1529-1544.
162. Köpf-Maier, P. Complexes of metals other than platinum as antitumour agents, *Eur. J. Clin. Pharmacol.*, 1994, **47**, 1-16.
163. O. Oberschmidt, A. R. Hanauske, C. Pampillon, N. J. Sweeney, K. Strohfeltdt, and M. Tacke, Antiproliferative activity of Titanocene Y against tumor colony-forming units, *Anticancer Drugs*, 2007, **18**, 317–321.
164. K. O'Connor, C. Gill, M. Tacke, F. J. Rehmann, K. Strohfeltdt, N. Sweeney, J. M. Fitzpatrick, and R. W. Watson, Novel titanocene anti-cancer drugs and their effect on apoptosis and the apoptotic pathway in prostate cancer cells, *Apoptosis*, 2006, **11**, 1205–1214.
165. G. Kelter, N. J. Sweeney, K. Strohfeltdt, H. H. Fiebig, and M. Tacke, In-vitro anti-tumor activity studies of bridged and unbridged benzyl-substituted titanocenes, *Anticancer Drugs*, 2005, **16**, 1091–1098.
166. H. Wittrisch, H. P. Schröer, J. Vogt, and C. Vogt, Determination of titanocene, a new drug with anticancer potential, and its metabolism in solution by capillary electrophoresis, *Electrophoresis*, 1998, **19**, 3012–3017.
167. Murray J, Harding MM. Organometallic anticancer agents: the effect of the central metal and halide ligands on the interaction of metallocene dihalides  $\text{Cp}_2\text{MX}_2$  with nucleic acid constituents, *J. Med. Chem.*, 1994, **37**, 1936–1941.
168. H. Sun, H. Li, R. A. Weir, and P. J. Sadler, The first specific  $\text{TiIV}$ -protein complex: potential relevance to anticancer activity of titanocenes, *Angew. Chem. Int. Ed.*, 1998, **37**, 1577-1579.
169. I. Bratsosa, S. Jednera, T. Gianferrara, and E. Alessio, Ruthenium Anticancer Compounds: Challenges and Expectations, *Chimia*, 2007, **61**, 692–697.
170. I. Kostova, Ruthenium complexes as anticancer agents, *Curr. Med. Chem.*, 2006, **13**, 1085–1107.
171. Y. K. Yan, M. Melchart, A. Habtemariam, and P. J. Sadler, Organometallic chemistry, biology and medicine: ruthenium arene anticancer complexes, *Chem. Commun.*, 2005, **38**, 4764–4776.
172. G. Zhao, and H. A. Lin, review on NAMI-A: Metal complexes with aromatic N-containing ligands as potential agents in cancer treatment, *Anti-Cancer Agents Med. Chem.*, 2005, **5**, 137–147.

173. J. M. Rademaker-Lakhai, D. van den Bongard, D. Pluim, J. H. Beijnen, and J. H. Schellens., A phase I and pharmacological study with imidazolium-trans-DMSO-imidazole-tetrachlororuthenate, a novel ruthenium anticancer agent, *Clin. Cancer Res.*, 2004, **10**, 3717–3727.
174. C. G. Hartinger, S. Zorbas-Seifried, M. A. Jakupec, B. Kynast, H. Zorbas, and B. K. Keppler, From bench to bedside—preclinical and early clinical development of the anticancer agent indazolium trans-[tetrachlorobis(1H-indazole)ruthenate(III)] (KP1019 or FFC14A), *J. Inorg. Biochem.*, 2006, **100**, 891–904.
175. M. A. Jakupec, V. B. Arion, S. Kapitza, E. Reisner, A. Eichinger, M. Pongratz, B. Marian, N. Graf von Keyserlingk, B. K. Keppler, KP1019 (FFC14A) from bench to bedside: preclinical and early clinical development—an overview, *Int. J. Clin. Pharmacol. Ther.*, 2005, **43**, 595–596.
176. M. Groessl, E. Reisner, C. G. Hartinger, R. Eichinger, O. Semenova, A. R. Timerbaev, M. A. Jakupec, V. B. Arion, and B. K. Keppler, Structure-activity relationships for NAMI-A-type complexes (HL)[trans-RuCl<sub>4</sub>L(S-dmso)ruthenate(III)] (L=imidazole, indazole,1,2,4-triazole, 4-amino-1,2,4-triazole, and 1-methyl-1,2,4-triazole): aquation, redox properties, protein binding, and antiproliferative activity, *J. Med. Chem.*, 2007, **50**, 2185–2193.
177. P. M. van Vliet, J. G. Haasnoot, and J. Reedijk, Binding of 9-Methylhypoxanthine and 9-Ethylguanine to [cis-Ru(2,2'-bipyridine)<sub>2</sub>]<sup>2+</sup>, NMR and X-ray Structure of cis-Chlorobis(2,2'-bipyridine)(9-ethylguanine-κ<sub>N7</sub>)ruthenium(II) Chloride, *Inorg. Chem.*, 1994, **33**, 9, 1934–1939.
178. M. J. Clarke, and M. Stubbs, Interactions of metallopharmaceuticals with DNA, *Met. Ions Biol. Syst.*, 1996, **32**, 727-80.
179. F. Wang, A. Habtemariam, E. P. van der Geer, R. Fernández, M. Melchart, R. J. Deeth, R. Aird, S. Guichard, F. P. Fabbiani, P. Lozano-Casal, I. D. Oswald, D. I. Jodrell, S. Parsons, P. J. Sadler, Controlling ligand substitution reactions of organometallic complexes: tuning cancer cell cytotoxicity, *Proc. Natl. Acad. Sci. U. S. A.*, 2005, **102**, 18269–18274.
180. A. Habtemariam, M. Melchart, R. Fernández, S. Parsons, I. D. H. Oswald, A. Parkin, F. P. A. Fabbiani, J. E. Davidson, A. Dawson, R. E. Aird, D. I. Jodrell, P. J. Sadler, Structure-activity relationships for cytotoxic ruthenium(II) arene complexes containing N,N-, N,O and O,O-chelating ligands, *J. Med. Chem.*, 2006, **49**, 6858–6868.
181. S. K. Singha, and D. S. Pandey, Multifaceted half-sandwich arene–ruthenium complexes: interactions with biomolecules, photoactivation, and multinuclearity approach, *RSC Adv.*, 2014, **4**, 1819-1840.
182. I. Kostova, Gold coordination complexes as anticancer agents, *Anticancer Agents, Med. Chem.*, 2006, **6**, 19–32.
183. Y. Wang, Q.Y. He, R. W. Sun, C. M. Che, J.F. Chiu, Cellular pharmacological properties of gold(III) porphyrin, a potential anticancer drug lead, *Eur. J. Pharmacol.*, 2007, **554**, 113–122.
184. T. Ka-Chung, H. Di, W. Pui-Ki, L. Chun-Nam, C. Chi-Ming, Anticancer Gold(III) Compounds With Porphyrin or N-heterocyclic Carbene Ligands, *Front. Chem.*, 2020, **8**, 919-930.
185. N. Katsaros, and A. Anagnostopoulou, Rhodium and its compounds as potential agents in cancer treatment, *Crit. Rev. Oncol./Hematol.*, 2002, **42**, 297–308.
186. J. Gao, L. Guo, Y. Wu, Y. Cheng, X. Hu, J. Liu, and Zhe Liu, 16-Electron Half-Sandwich Rhodium(III), Iridium(III), and Ruthenium(II) Complexes as Lysosome-Targeted Anticancer Agents, *Organometallics*, 2021, **40**, 3999–4010.

187. J. M. Cross, Dr. T. R. Blower, N. Gallagher, Dr. J. H. Gill, K. L. Rockley, Dr. and J. W. Walton, Anticancer Rull and RhIII Piano-Stool Complexes that are Histone Deacetylase Inhibitors, *ChemPlusChem*, 2016, **81**,1276–1280.
188. A. R. de Souza, E. P. Coelho, and S. B. Zyngier, Comparison of the anti-neoplastic effects of dirhodium(II) tetrapropionate and its adducts with nicotinate and isonicotinate anions in mice bearing Ehrlich tumors, *Eur. J. Med. Chem.*, 2006, **41**, 1214–1216.
189. Z. Ziu, A. Habtemariam, A. M. Pizarro, S. A. Fletcher, A. Kisova, O. Vrana, L. Salassa, P. C. A. Bruijninx, G. J. Clarkson, V. Brabec, and P. J. Sadler, Organometallic half-sandwich iridium anticancer complexes, 2011, *J. Med. Chem.*, **54**, 3011-3026.
190. P. Zhang, and P. J. Sadler, Advances in the design of organometallic anticancer complexes, *J. Organomet. Chem.*, 2017, **839**, 5-14.
191. Y. Geldmacher, M. Oleszak, and W. S. Sheldrick, Rhodium(III) and iridium(III) complexes as anticancer agents, *Inorg. Chim. Acta*, 2012, **393**, 84.
192. P. J. Blower, J. R. Dilworth, R. I. Maurer, G. D. Mullen, C. A. Reynolds, and Y. Zheng, Toward new transition metal-based hypoxic selective agents for therapy and imaging, *J. Inorg. Biochem.*, 2001, **85**, 15–22.
193. I. Gracia-Mora, L. Ruiz-Ramirez, C. Gómez-Ruiz, M. Tinoco-Méndez, A. Márquez-Quifinones, L. Romero-DelLira, Á. Márin-Hernandez, L. Macías-Rosales, M.E. Bravo-Gómez, Knight's move in the periodic table, from copper to platinum, novel antitumor mixed chelate copper compounds, casiopeinas, evaluated by an in vitro human and murine cancer cell line panel, *Metal Based Drugs*, 2001, **8**, 19–28.
194. M. Jung, D. E. Kerr, P. D. Senter, Bioorganometallic chemistry synthesis and antitumor activity of cobalt carbonyl complexes, *Arch. Pharm.*, 1997, **330**, 173–176.
195. S. Top, J. Tang, A. Vessieres, D. Carrez, C. Provot, and G. Jaouen, Ferrocenyl hydroxytamoxifen: a prototype for a new range of oestradiol receptor site-directed cytotoxics, *Chem. Commun.*, 1996, **8**, 955–956.
196. A. Vessières, S. Top, W. Beck, E. Hillard, and J. Gérard, Metal complex SERMs (selective oestrogen receptor modulators). The influence of different metal units on breast cancer cell antiproliferative effects, *Dalton Trans.*, 2006, **4**, 529–541.
197. J. E. Reed, A. A. Arnal, S. Neidle, and R. Vilar, Stabilization of G-quadruplex DNA and inhibition of telomerase activity by square planar nickel(II) complexes, *J. Am. Chem. Soc.*, 2006, **128**, 5992–5993.
198. M. D. Daniell, and J. S. Hill, A history of photodynamic therapy, *Aust. N. Z. J. Surg.*, 1991, **61**, 340-8.
199. R. Ackroyd, C. Kelty, N. Brown, and M. Reed, The history of photodetection and photodynamic therapy, *Photochem. Photobiol.*, 2001, **74**, 656-69.
200. P. Gusain, R. Paliwal, R. Joga, N. Gupta, and V. Singh, Ancient light therapies: a boon to medical science, *Sci. Cult.*, 2016, **82**, 231-236.
201. R. Roelandts, History of human photobiology, *Photodermatology*, CRC Press, 2007, 1-14.
202. T. A. Palm, The geographical distribution and aetiology of rickets, *Practitioner*, 1890, **45**, 270-342.

203. P. S. Ziegelroth, Die elektrische Belichtung bei Lupus, *Blätter für klinische Hydrotherapie und verwandte Heilmethoden*, 1895, **5**, 138-140.
204. H. Meffert, and B. T. W. Gebhardt, Sein Leben und seine Verdienste um die Photomedizin, *Dermatol. Monatsschr.*, 1989, **175**, 699-705.
205. F. H. Montgomery, The present status of phototherapy, *J. Cutan. Dis.*, 1903, **21**, 529-48.
206. O. Raab, On the effect of fluorescent substances on infusoria, *Z. Biol.*, 1900, **39**, 524-546.
207. H. Tappeiner, and A. Jesionek, Therapeutische Versuche Mit Fluoreszierenden Stoffen, *Muench. Med. Wochenschr.*, 1903, **1**, 2042-2044.
208. A. Jodlbauer, and H. von Tappeiner, On the participation of oxygen in the photodynamic effect of fluorescent substances, *Muench. Med. Wochenschr.*, 1904, **52**, 1139-1141.
209. W. Hausmann, Die sensibilisierende Wirkung tierischer Farbstoffe und ihre physiologische Bedeutung, *Wien. Klin. Wochenschr.*, 1908, **21**, 1527-1528.
210. W. Hausmann, Die sensibilisierende Wirkung des Hamatoporphyrins. *Biochem. Z.*, 1911, **30**, 276-316.
211. E. Meyer-Betz, Untersuchungen über die biologische (photodynamische) Wirkung des Hämatoporphyrins und andere Derivate des Blut- und Gallenfarbstoffes, *Dtsch. Arch. Klin. Med.*, 1913, **112**, 476-503.
212. H. Silver, Psoriasis vulgaris treated with hematoporphyrin, *Arch. Dermatol. Syph.*, 1937, **36**, 1118-1119.
213. A. Policard, Etude sur les aspects offerts par des tumeurs expérimentales examinées à la lumière de Wood, *C.R. Soc. Biol.*, 1924, **91**, 1423-1424.
214. H. Auler, and G. Banzer, Untersuchungen über die Rolle der Porphyrine bei geschwulstkranken Menschen und Tieren, *Z. Krebsforsch.*, 1942, **53**, 65-68.
215. E. H. J. Figge, G. S. Weiland, and L. J. Manganiello, Cancer detection and therapy, affinity of neoplastic, embryonic, and traumatized tissues for porphyrins and metalloporphyrins, *Proc. Soc. Exp. Biol. Med.*, 1948, **68**, 640-641.
216. D. S. Rassmussen-Taxdal, G. E. Ward, and E. H. J. Figge, Fluorescence of human lymphatic and cancer tissues following high doses of intravenous hematoporphyrin, *Cancer*, 1955, **8**, 78-81.
217. S. Schwartz, K. Absolon, and H. Vermund, Some relationships of porphyrins, x-rays and tumors, *Med. Bull.*, 1955, **27**, 7-13.
218. R. L. Lipson, E. J. Baldes, and A. M. Olsen, Hematoporphyrin derivative: a new aid of endoscopic detection of malignant disease, *J. Thorac. Cardiovasc. Surg.*, 1961, **42**, 623-629.
219. R. L. Lipson, E. J. Baldes, and A. M. Olsen, A further evaluation of the use of hematoporphyrin derivative as a new aid for the endoscopic detection of malignant disease, *Dis. Chest.*, 1964, **46**, 676-679.
220. R. L. Lipson, E. J. Baldes, and M. J. Gray, Hematoporphyrin derivative for the detection and management of cancer, *Cancer*, 1967, **20**, 2255-2257.
221. I. Diamond, A. F. McDonagh, C. B. Wilson, S. G. Granelli, S. Nielsen, and R. Jaenicke, Photodynamic Therapy of Malignant Tumours, *Lancet*, 1972, **300**, 1175-1177.

222. T. J. Dougherty, J. E. Kaufman, A. Goldfarb, K. R. Weishaupt, D. Boyle, and A. Mittleman, Photoradiation therapy for the treatment of malignant tumors. *Cancer Res.*, 1978, **38**, 2628-2635.
223. S. Monro, K. L. Colon, H. Yin, J. Roque, P. Konda, S. Gujar, R. P. Thummel, L. Lilje, C. G. Cameron, and Sherri A. McFarland, Transition Metal Complexes and Photodynamic Therapy from a Tumor-Centered Approach: Challenges, Opportunities, and Highlights from the Development of TLD1433, *Chem. Rev.*, 2018, **119**, 797-828.
224. J. F. Algorri, M. Ochoa, P. Roldán-Varona, L. Rodríguez-Cobo, J. M. López-Higuera, Photodynamic Therapy: A Compendium of Latest Reviews, *Cancers*, 2021, **13**, 4447.
225. A. Juarranz, P. Jaén, F. Sanz-Rodríguez, J. Cuevas, and S. González, Photodynamic therapy of cancer. Basic principles and applications, *Clin. Transl. Oncol.*, 2008, **10**, 148-54.
226. A. Kawczyk-Krupka, B. Pucelik, A. Międzybrodzka, A. Sieron, and J. M. Dąbrowski, Photodynamic therapy as an alternative to antibiotic therapy for the treatment of infected leg ulcers, *Photodiagn. Photodyn. Ther.*, 2018, **23**, 132–143.
227. M. Oszejca, M. Brindell, Ł. Orzeł, J.M. Dąbrowski, K. Spiewak, P. Łabuz, M. Pacia, A. Stochel-Gaudyn, W. Macyk, R. van Eldik, and G. Stochel, Mechanistic studies on versatile metal-assisted hydrogen peroxide activation processes for biomedical and environmental incentives, *Coord. Chem. Rev.*, 2016, **327**, 143–165.
228. A. Gorman, J. Killoran, C. O’Shea, T. Kenna, W. M. Gallagher and D. F. O’Shea, In Vitro Demonstration of the Heavy-Atom Effect for Photodynamic Therapy, *J. Am. Chem. Soc.*, 2004, **126**, 10619–10631.
229. X. Hu, Y.-Y. Huang, Y. Wang, X. Wang and M. R. Hamblin, Antimicrobial Photodynamic Therapy to Control Clinically Relevant Biofilm Infections, *Front. Microbiol.*, 2018, **9**, 1299.
230. A. P. Castano, T. N. Demidova and M. R. Hamblin, Mechanisms in photodynamic therapy: part one--- photosensitizers, photochemistry and cellular localization, *Photodiagn. Photodyn. Ther.*, 2004, **1**, 279–293.
231. M. Broekgaarden, R. Weijer, T. M. van Gulik, M. R. Hamblin, and M. Heger, Tumor cell survival pathways activated by photodynamic therapy: a molecular basis for pharmacological inhibition strategies, *Cancer Metastasis Rev.*, 2015, **34**, 643-690.
232. A. F. dos Santos, D. R. Queiroz de Almeida, L. F. Terra , M. S. Baptista , and L. Labriola, Photodynamic therapy in cancer treatment - an update review, *J Cancer Metastasis Treat.*, 2019, **5**, 25.
233. G. M. Fioramonti Calixto, J. Bernegossi, L. M. De Freitas, C. R. Fontana, and M. Chorilli, Nanotechnology-Based Drug Delivery Systems for Photodynamic Therapy of Cancer: A Review, *Molecules*, 2016, **21**, 342.
234. E. A. Thackaberry, Non-clinical toxicological considerations for pharmaceutical salt selection, *Expert. Opin. Drug Metab. Toxicol.*, 2012, **8**, 1419–1433.
235. B.-Z. Zhu, X.-J. Chao, and C.-H. Huang, Y. Li Delivering the cell-impermeable DNA ‘light-switching’ Ru(II) complexes preferentially into live-cell nucleus via an unprecedented ion-pairing method, *Chem. Sci.*, 2016, **7**, 4016–4023.
236. D. Zhao, Y. Liao, and Z. Zhang, Toxicity of ionic liquids, *Clean: Soil, Air, Water*, 2007, **35**, 42–48.
237. R. Biczak, B. Pawlowska, C. Podsiadlo, and A. Telesinski, Toxicity of ammonium hexafluorophosphate to selected terrestrial plants, *Fresenius Environ. Bull.*, 2019, **28**, 7101–7107.

238. K. Ogawa, and Y. Kobuke, Recent advances in two-photon photodynamic therapy, *Anti-Cancer Agents Med. Chem.*, 2008, **8**, 269–279.
239. B. C. Wilson, W. P. Jeeves, and D. M. Lowe, In vivo and post mortem measurements of the attenuation spectra of light in mammalian tissues, *Photochem. Photobiol.*, 1985, **42**, 153–162.
240. J. Karges, U. Basu, O. Blacque, H. Chao, and G. Gasser, Polymeric encapsulation of novel homoleptic Bis(dipyrrinato) Zinc(II) complexes with long lifetimes for applications as photodynamic therapy photosensitisers, *Angew. Chem. Int. Ed.*, 2019, **58**, 14334–14340.
241. K. Plaetzer, B. Krammer, J. Berlanda, F. Berr, and T. Kiesslich, Photophysics and photochemistry of photodynamic therapy: fundamental aspects, *Laser Med. Sci.*, 2009, **24**, 259–268.
242. P. Vaupel, O. Thews, and M. Hoekel, Treatment resistance of solid tumors: Role of hypoxia and anemia, *Med. Oncol.*, 2001, **18**, 243–259.
243. A. Casas, G. Di Venosa, T. Hasan, and B. Al, Mechanisms of resistance to photodynamic therapy, *Curr. Med. Chem.*, 2011, **18**, 2486–2515.
244. A. Juzeniene, K. P. Nielsen, and J. Moan, Biophysical Aspects of Photodynamic Therapy, *J. Environ. Pathol. Toxicol. Oncol.*, 2006, **25**, 7–28.
245. S. Keller, Y. C. Ong, Y. Lin, K. Cariou, and G. Gasser, A tutorial for the assessment of the stability of organometallic complexes in biological media, *J. Organomet. Chem.*, 2020, **906**, 121059.
246. J. Karges, O. Blacque, P. Goldner, H. Chao, and G. Gasser, Towards long wavelength absorbing photodynamic therapy photosensitizers via the extension of a [Ru(bipy)<sub>3</sub>]<sup>2+</sup> Core, *Eur. J. Inorg. Chem.*, 2019, **32**, 3704–3712.
247. J. Karges, F. Heinemann, M. Jakubaszek, F. Maschietto, C. Subecz, M. Dotou, R. Vinck, O. Blacque, M. Tharaud, B. Goud, E. V. Zahinos, B. Spingler, I. Ciofini, and G. Gasser, Rationally designed long-wavelength absorbing Ru(II) polypyridyl complexes as photosensitizers for photodynamic Therapy, *J. Am. Chem. Soc.*, 2020, **142**, 6578–6587.
248. S. Al-Omari, Toward a molecular understanding of the photosensitizer-copper interaction for tumor destruction, *Biophys. Rev.*, 2013, **5**, 305–311.
249. A. Pluen, Y. Boucher, S. Ramanujan, T. D. McKee, T. Gohongi, E. di Tomaso, E. B. Brown, Y. Izumi, R. B. Campbell, D. A. Berk, and R. K. Jain, 2001, Role of tumor–host interactions in interstitial diffusion of macromolecules: Cranial vs. subcutaneous tumors, *Proc. Natl. Acad. Sci.*, 2001, **98**, 4628–4633.
250. P. A. Netti, D. A. Berk, M. A. Swartz, A. J. Grodzinsky, and R. K. Jain, Role of extracellular matrix assembly in interstitial transport in solid tumors. *Cancer Res.*, 2000, **60**, 2497–2503.
251. P. J. Dyson, The rise of 3D cellular spheroids: efficient culture via upward growth from a superamphiphobic surface, *National Sci. Rev.*, 2019, **6**, 1068–1069.
252. J. M. Lee, D. Y. Park, L. Yang, E.-J. Kim, C. D. Ahrberg, K.-B. Lee, B. G. Chung, Generation of uniform-sized multicellular tumor spheroids using hydrogel microwells for advanced drug screening, *Sci. Rep.*, 2018, **8**, 17145.
253. Z. Zhao, X. Zhang, C.-E. Li, and T. Chen Designing luminescent ruthenium prodrug for precise cancer therapy and rapid clinical diagnosis, *Biomaterials*, 2019, **192**, 579–589.



254. F. Barragán, P. López-Senín, L. Salassa, S. Betanzos-Lara, A. Habtemariam, V. Moreno, P. J. Sadler, and V. Marchán, Photocontrolled DNA binding of a receptor-targeted organometallic ruthenium(II) complex, *J. Am. Chem. Soc.*, 2011, **133**, 14098–14108.
255. M. Jakubaszek, J. Rossier, J. Karges, J. Delasoie, B. Goud, G. Gasser, and F. Zobi, Evaluation of the potential of cobalamin derivatives bearing Ru(II) polypyridyl complexes as photosensitizers for photodynamic therapy, *Helv. Chim. Acta*, 2019, **102**, e1900104.
256. Y. Huang, W. Huang, L. Chan, B. Zhou, and T. Chen, A multifunctional DNA origami as carrier of metal complexes to achieve enhanced tumoral delivery and nullified systemic toxicity, *Biomaterials*, 2016, **103**, 183–196.
257. X. Zhu, H. Zhou, Y. Liu, Y. Wen, C. Wei, Q. Yu, and J. Liu, Transferrin/aptamer conjugated mesoporous ruthenium nanosystem for redox-controlled and targeted chemo-photodynamic therapy of glioma, *Acta. Biomater.*, 2018, **82**, 143–157.
258. S. Chakraborty, B. K. Agrawalla, A. Stumper, N. M. Vegi, S. Fischer, C. Reichardt, M. Kögler, B. Dietzek, M. Feuring-Buske, C. Buske, S. Rau, T. Weil, Mitochondria targeted protein-ruthenium photosensitizer for efficient photodynamic applications, *J. Am. Chem. Soc.*, 2017, **139**, 2512–2519.
259. K. Arora, M. Herroon, M. H. Al-Afyouni, N. P. Toupin, T. N. Rohrabough, L. M. Loftus, I. Podgorski, C. Turro, and J. J. Kodanko, Catch and release photosensitizers: combining dual-action ruthenium complexes with protease inactivation for targeting invasive cancers, *J. Am. Chem. Soc.*, 2018, **140**, 14367–14380.
260. J. Karges, M. Jakubaszek, C. Mari, K. Zarschler, B. Goud, H. Stephan, and G. Gasser, Synthesis and characterization of an epidermal growth factor receptor-selective ruii polypyridyl-nanobody conjugate as a photosensitizer for photodynamic therapy, *Chem-BioChem*, 2020, **21**, 531–542.
261. H. Maeda, J. Wu, T. Sawa, Y. Matsumura, and K. Hori, Tumor vascular permeability and the EPR effect in macromolecular therapeutics: a review, *J. Control Release*, 2000, **65**, 271–284.
262. E. Villemin, Y. C. Ong, C. M. Thomas, and G. Gasser, Polymer encapsulation of ruthenium complexes for biological and medicinal applications, *Nat. Rev. Chem.*, 2019, **3**, 261–282.
263. N. Soliman, G. Gasser, and C. M. Thomas, Incorporation of Ru(II) polypyridyl complexes into nanomaterials for cancer therapy and diagnosis, *Adv. Mat.*, 2020, **32**, e2003294.
264. R. R. Allison, and C. H. Sibata, Oncologic photodynamic therapy photosensitizers: a clinical review, *Photodiagnosis Photodyn. Ther.*, 2010, **7**, 61–75.
265. H. Abrahamse, and M. R. Hamblin, New photosensitizers for photodynamic therapy, *Biochem. J.*, 2016, **473**, 347–364.
266. H. J. Jones, D. I. Vernon, and S. B. Brown, Photodynamic therapy effect of m-THPC (Foscan®) in vivo: correlation with pharmacokinetics, *Br. J. Cancer*, 2003, **89**, 398–404.
267. I. Ashur, R. Goldschmidt, I. Pinkas, et al., Photocatalytic generation of oxygen radicals by the water-soluble bacteriochlorophyll derivative WST11, noncovalently bound to serum albumin, *J. Phys. Chem. A.*, 2009, **113**, 8027–8037.
268. F. Collin, Chemical Basis of Reactive Oxygen Species Reactivity and Involvement in Neurodegenerative Diseases, *Int. J. Mol. Sci.*, 2019, **20**, 2407.

269. M. J. Davies, Reactive species formed on proteins exposed to singlet oxygen, *Photochem. Photobiol. Sci.*, 2004, **3**, 17–25.
270. M. J. Davies, The oxidative environment and protein damage, *Biochim. Biophys. Acta.*, 2005, **1703**, 93–109.
271. W. M. Garrison, Reaction mechanisms in the radiolysis of peptides, polypeptides, and proteins, *Chem. Rev.*, 1987, **87**, 381–398.
272. P. Nagy, A. J. Kettle, and C. C. Winterbourn, Superoxide-mediated formation of tyrosine hydroperoxides and methionine sulfoxide in peptides through radical addition and intramolecular oxygen transfer, *J. Biol. Chem.*, 2009, **284**, 14723–14733.
273. C. C. Winterbourn, H. N. Parsons-Mair, S. Gebicki, et al., Requirements for superoxide-dependent tyrosine hydroperoxide formation in peptides, *Biochem. J.*, 2004, **381**, 241–248.
274. A. B. Das, P. Nagy, H. F. Abbott, et al., Reactions of superoxide with the myoglobin tyrosyl radical, *Free Radic. Biol. Med.*, 2010, **48**, 1540–1547.
275. N. d'Alessandro, G. Bianchi, X. Fang, et al., Reaction of superoxide with phenoxyl-type radicals, *J. Chem. Soc. Perkin Trans. II*, 2000, **9**, 1862–1867.
276. S. V. Lymar, and J. K. Hurst, Rapid reaction between peroxonitrite ion and carbon dioxide: implications for biological activity, *J. Am. Chem. Soc.*, 1995, **117**, 8867–8868.
277. B. Alvarez, and R. Radi, Peroxynitrite reactivity with amino acids and proteins, *Amino Acids*, 2003, **25**, 295–311.
278. L. Benov, J. Craik, I. Batinic-Haberle, Protein damage by photo-activated Zn(II) N-alkylpyridylporphyrins, *Amino Acids*, 2012, **42**, 117–128.
279. S. C. Afonso, R. Enríquez De Salamanca, and A. M. Del C. Batlle, The photodynamic and non-photodynamic actions of porphyrins, *Brazil J. Med. Biol. Res.*, 1999, **32**, 255–266.
280. A. W. Girotti, Photosensitized oxidation of membrane lipids: reaction pathways, cytotoxic effects, and cytoprotective mechanisms, *J. Photochem. Photobiol.*, 2001, **63**, 103–113.
281. A. W. Girotti, and Kriska T, Role of lipid hydroperoxides in photo-oxidative stress signalling, *Antioxid. Redox Signal.*, 2004, **6**, 301–310.
282. Y. Yoshida, and E. Niki, Oxidation of methyl linoleate in aqueous dispersions induced by copper and iron, *Arch. Biochem. Biophys.*, 1992, **295**, 107–114.
283. F. Guéraud, M. Atalay, N. Bresgen, et al., Chemistry and biochemistry of lipid peroxidation products, *Free Radic. Res.*, 2010, **44**, 1098–1124.
284. D. A. Al-Mutairi, J. D. Craik, I. Batinic-Haberle, et al., Photosensitizing action of isomeric zinc N-methylpyridyl porphyrins in human carcinoma Cells, *Free Radic. Res.*, 2006, **40**, 477–483.
285. B. Epe, DNA damage spectra induced by photosensitization, *Photochem. Photobiol. Sci.*, 2012, **11**, 98–106.
286. G. Barrera, S. Pizzimenti, and M. U. Dianzani, Lipid peroxidation: control of cell proliferation, cell differentiation and cell death, *Mol. Aspects Med.*, 2008, **29**, 1–8.

287. A. Negre-Salvayre, N. Auge, V. Ayala, et al., Pathological aspects of lipid peroxidation, *Free Radic. Res.*, 2010, **44**, 1125–1171.
288. A. W. Girotti, T. Kriska, Role of lipid hydroperoxides in photo-oxidative stress signalling, *Antioxid. Redox Signal.*, 2004, **6**, 301–310.
289. J. Cadet, J. L. Ravanat, M. TavernaPorro, et al., Oxidatively generated complex DNA damage: tandem and clustered lesions, *Cancer Lett.*, 2012, **327**, 5–15.
290. J. Cadet, T. Douki, J. L. Ravanat, One-electron oxidation of DNA and inflammation processes, *Nat. Chem. Biol.*, 2006, **2**, 348–349.
291. J. Cadet, T. Douki, J. L. Ravanat, Oxidatively generated damage to the guanine moiety of DNA: mechanistic aspects and formation in cells, *Acc. Chem. Res.*, 2008, **41**, 1075–1083.
292. J. Cadet, S. Mouret, J. L. Ravanat, et al., Photoinduced damage to cellular DNA: direct and photosensitized reactions, *Photochem. Photobiol.*, 2012, **88**, 1048–1065.
293. J. Cadet, T. Douki, J. L. Ravanat, Oxidatively generated base damage to cellular DNA, *Free Radic. Biol. Med.*, 2010, **49**, 9–21.
294. J. P. Pouget, T. Douki, M. J. Richard, et al., DNA damage induced in cells by  $\gamma$  and UVA radiation as measured by HPLC/GC-MS and HPLC-EC and comet assay, *Chem. Res. Toxicol.*, 2000, **13**, 541–549.
295. B. Epe, Genotoxicity of singlet oxygen, *Chem. Biol. Interact.*, 1991, **80**, 239–260.
296. M. S. Cooke, S. Loft, R. Olinski, et al., Recommendations for standardized description of and nomenclature concerning oxidatively damaged nucleobases in DNA, *Chem. Res. Toxicol.*, 2010, **23**, 705–707.
297. M. Riethmüller, N. Burger, and G. Bauer, Singlet oxygen treatment of tumor cells triggers extracellular singlet oxygen generation, catalase inactivation and reactivation of intercellular apoptosis-inducing signalling, *Redox Biol.*, 2015, **6**, 157–168.
298. P. Agostinis, E. Buytaert, H. Breysens, et al., Regulatory pathways in photodynamic therapy induced apoptosis, *Photochem. Photobiol. Sci.*, 2004, **3**, 721–729.
299. N. L. Oleinick, and H. H. Evans, The photobiology of photodynamic therapy: cellular targets and mechanisms, *Radiat. Res.*, 1998, **150**, S146–S156.
300. F. Ricchelli, L. Franchi, G. Miotto, et al., Mesosubstituted tetra-cationic porphyrins photosensitize the death of human fibrosarcoma cells via lysosomal targeting, *Int. J. Biochem. Cell Biol.*, 2005, **37**, 306–319.
301. B.H. Nadia, K. Wided, B. Kheira, R. Hassiba, B. Lamia, S. Rhouati, M. Alyane, A. Zellagui, and M. Lahouel, Disruption of mitochondrial membrane potential by ferulenol and restoration by propolis extract: antiapoptotic role of propolis, *Acta Biol. Hung.*, 2009, **60**, 385–98.
302. C. Pavani, A. F. Uchoa, C. S. Oliveira, et al., Effect of zinc insertion and hydrophobicity on the membrane interactions and PDT activity of porphyrin photosensitizers, *Photochem. Photobiol. Sci.*, 2009, **8**, 233–240.
303. F. M. Engelmann, S. V. O. Rocha, H. E. Toma, et al., Determination of n -octanol/water partition and membrane binding of cationic porphyrins, *Int. J. Pharm.*, 2007, **329**, 12–18.

304. A. B. Uzdensky, Signal transduction and photodynamic therapy, *Curr. Signal Transduct. Ther.*, 2008, **3**, 55–74.
305. T. Liu, L. Y. Wu, and C. E. Berkman, Prostate-specific membrane antigen-targeted photodynamic therapy induces rapid cytoskeletal disruption, *Cancer Lett.*, 2010, **296**, 106–112.
306. J. C. Stockert, A. Juarranz, A. Villanueva, et al., Photodynamic damage to HeLa cell microtubules induced by thiazine dyes, *Cancer Chemother. Pharmacol.*, 1996, **39**, 167–169.
307. L. Benov, J. Craik, and I. Batinic-Haberle, The potential of Zn(II) N-alkylpyridylporphyrins for anticancer therapy, *Curr. Med. Chem. Anticancer Agents*, 2011, **11**, 233–241.
308. D. A. Al-Mutairi, J. D. Craik, I. Batinic-Haberle, et al., Induction of oxidative cell damage by photo-treatment with zinc N-methylpyridylporphyrin. *Free Radic. Res.*, 2007, **41**, 89–96.
309. A. P. Castano, T. N. Demidova and M. R. Hamblin, Mechanisms in photodynamic therapy. Part 2. Cellular signaling, cell metabolism and modes of cell death. *Photodiagnosis Photodyn. Ther.*, 2005, **2**, 1–23.
310. R. D. Almeida, B. J. Manadas, A. P. Carvalho, et al., Intracellular signaling mechanisms in photodynamic therapy, *Biochim. Biophys. Acta*, 2004, **1704**, 59–86.
311. I. J. MacDonald, and T. J. Dougherty, Basic principles of photodynamic therapy, *J. Porphyr. Phthalocyanines*, 2001, **5**, 105–129.
312. S. Wu, F. Zhou, Y. Wei, et al., Cancer phototherapy via selective photoinactivation of respiratory chain oxidase to trigger a fatal superoxide anion burst, *Antioxid. Redox Signal.*, 2014, **20**, 733–746.
313. E. Buytaert, M. Dewaele, and P. Agostinis, Molecular effectors of multiple cell death pathways initiated by photodynamic therapy, *Biochim. Biophys. Acta*, 2007, **1776**, 86–107.
314. N. L. Oleinick, R. L. Morris, and I. Belichenko, The role of apoptosis in response to photodynamic therapy: what, where, why, and how, *Photochem. Photobiol. Sci.*, 2002, **1**, 1–21.
315. A. François, A. Salvadori, A. Bressenot, et al., How to avoid local side effects of bladder photodynamic therapy: impact of the fluence rate, *J. Urol.*, 2013, **190**, 731–736.
316. B. W. Henderson, S. O. Gollnick, J. W. Snyder, et al., Choice of oxygen-conserving treatment regimen determines the inflammatory response and outcome of photodynamic therapy of tumors, *Cancer Res.*, 2004, **64**, 2120–2126.
317. S. H. Ibbotson, and J. Ferguson, Ambulatory photodynamic therapy using low irradiance inorganic light-emitting diodes for the treatment of non-melanoma skin cancer: an open study, *Photodermatol. Photoimmunol. Photomed.*, 2012, **28**, 235–239.
318. G. S. Rogers, Continuous low-irradiance photodynamic therapy: a new therapeutic paradigm, *J. Natl. Compr. Canc. Netw.*, 2012, **10**, S-14–S-17.
319. R. R. Allison, V. S. Bagnato, R. Cuenca, G. H. Downie, and C. H. Sibata, The future of photodynamic therapy in oncology, *Future Oncol.*, 2006, **2**, 53–71.
320. D. A. Bellnier, W. R. Greco, G. M. Loewen, H. Nava, A. R. Oseroff, and T. J. Dougherty, Clinical pharmacokinetics of the PDT photosensitizers porfimer sodium (Photofrin), 2-[1-hexyloxyethyl]-2-devinyl

- pyropheophorbide-a (Photochlor) and 5-ALA-induced protoporphyrin IX, *Lasers Surg. Med.*, 2006, **38**, 439–44.
321. J. Usuda, H. Kato, T. Okunaka, K. Furukawa, H. Tsutsui; Yamada K, Y. Suga, H. Honda, Y. Nagatsuka, T. Ohira, M. Tsuboi, and T. Hirano, Photodynamic Therapy (PDT) for Lung Cancers, *J. Thorac. Oncol. Off. Publ. Int. Assoc. Study Lung Cancer*, 2006, **1**, 489–493.
322. R. R. Allison, and C. H. Sibata, Oncologic photodynamic therapy photosensitizers: a clinical review, *Photodiagn. Photodyn. Ther.*, 2010, **7**, 61–75.
323. J. D. Breskey, S. E. Lacey, B. J. Vesper, W. A. Paradise, J. A. Radosevich, and M.D. Colvard, Photodynamic therapy: occupational hazards and preventative recommendations for clinical administration by healthcare providers, *Photomed. Laser Surg.*, 2013, **31**, 398–407.
324. V. G. Schweitzer, Photofrin-mediated photodynamic therapy for treatment of early stage oral cavity and laryngeal malignancies, *Lasers Surg. Med.*, 2001, **29**, 305–13.
325. D. Wöhrle, A. Hirth, T. Bogdahn-Rai, G. Schnurpfeil, and M. Shopova, Photodynamic therapy of cancer: second and third generations of photosensitizers, *Russ. Chem. Bull.*, 1998, **47**, 807-816.
326. C. J. Gomer, Preclinical examination of first and second generation photosensitizers used in photodynamic therapy, *Photochem. Photobiol.*, 1991, **54**, 1093-1107.
327. J. Kou, D. Dou, and L. Yang, Porphyrin photosensitizers in photodynamic therapy and its applications, *Oncotarget*, 2017, **8**, 81591-81603.
328. S. A. McFarland, A. Mandel, R. Dumoulin-White, G. Gasser, Metal-based photosensitizers for photodynamic therapy: the future of multimodal oncology?, *Curr. Opin. Chem. Biol.*, 2020, **56**, 23-27.
329. A. C. Jung, F. Moinard-Butot, C. Thibaudeau, G. Gasser, and C. Gaiddon, Antitumor Immune Response Triggered by Metal-Based Photosensitizers for Photodynamic Therapy: Where Are We?, *Pharmaceutics*, 2021, **13**, 1788.
330. H. Patel, R. Mick, J. Finlay, T. C. Zhu, et al., Motexafin lutetium-photodynamic therapy of prostate cancer: short- and long-term effects on prostate-specific antigen, *Clin. Cancer Res.*, 2008, **14**, 4869–76.
331. J. C. Finlay, T. C. Zhu, A. Dimofte, D. Stripp, et al., In vivo determination of the absorption and scattering spectra of the human prostate during photodynamic therapy, *Proc. SPIE Int. Soc. Opt. Eng.*, 2014, **5315**, 132–42.
332. S. R. Thomas, and D. Khuntia, Motexafin gadolinium: a promising radiation sensitizer in brain metastasis, *Expert Opin. Drug Discov.*, 2011, **6**, 195–203.
333. S. R. Thomas, D. Khuntia, Motexafin gadolinium injection for the treatment of brain metastases in patients with non-small cell lung cancer, *Int. J. Nanomedicine*, 2007, **2**, 79-87.
334. K. A. Bradley, T. Zhou, R. Y. McNall-Knapp, R. I. Jakacki, et al., Motexafin-gadolinium and involved field radiation therapy for intrinsic pontine glioma of childhood: a children's oncology group phase 2 study, *Int. J. Radiat. Oncol. Biol. Phys.*, 2013, **85**, e55–60.
335. A. R. Azzouzi, S. Lebdaï, F. Benzaghrou, and C. Stief, Vascular-targeted photodynamic therapy with TOOKAD(R) soluble in localized prostate cancer: standardization of the procedure, *World J. Urol.*, 2015, **33**, 937–44.

336. N. Betrouni, S. Boukris, and F. Benzaghoul, Vascular targeted photodynamic therapy with TOOKAD(R) soluble (WST11) in localized prostate cancer: efficiency of automatic pre-treatment planning, *Lasers Med. Sci.*, 2017, **32**, 1301–1307.
337. J. Trachtenberg, A. Bogaards, R. A. Weersink, M. A. Haider, et al., Vascular targeted photodynamic therapy with palladiumbacteriopheophorbide photosensitizer for recurrent prostate cancer following definitive radiation therapy: assessment of safety and treatment response, *J. Urol.*, 2007, **178**, 1974–1979.
338. S. S. Taneja, J. Bennett, J. Coleman, R. Grubb, et al., Final results of a phase I/II multicenter trial of WST11 vascular targeted photodynamic therapy for hemi-ablation of the prostate in men with unilateral low risk prostate Cancer performed in the United States, *J. Urol.*, 2016, **196**, 1096–1104.
339. R. Bonnett, Photosensitizers of the porphyrin and phthalocyanine series for photodynamic therapy, *Chem. Soc. Rev.*, 1995, **24**, 19–33.
340. M. R. Detty, S. L. Gibson, and S. J. Wagner, Current clinical and preclinical photosensitizers for use in photodynamic therapy, *J. M. Chem.*, 2004, **47**, 3897–3915.
341. B. Krammer, and K. Plaetzer, ALA and its clinical impact, from bench to bedside, *Photochem. Photobiol. Sci.*, 2008, **7**, 283–289.
342. J. Karges, Clinical Development of Metal Complexes as Photosensitizers for Photodynamic Therapy of Cancer, *Angew. Chem. Int. Ed.*, 2022, **61**, e202112236.
343. L. B. Josefsen, and R. W. Boyle, Photodynamic Therapy and the Development of Metal-Based Photosensitisers, *Metal-Based Drugs*, 2008, **276109**, 1-24.
344. W. Parka, S. Choa, J. Hanb, H. Shinb, et al., Advanced Smart-photosensitizers for More Effective Cancer Treatment, *Biomater Sci.*, 2017, **19**, 6, 79–90.
345. H. Shi, and P. J. Sadler, How promising is phototherapy for cancer?, *Br. J. Cancer*, 2020, **123**, 871-873.
346. M. Karwicka, B. Pucelik, M. Gonet, M. Elas, and J. M. Dąbrowski, Effects of Photodynamic Therapy with Redaporfn on Tumor Oxygenation and Blood Flow in a Lung Cancer Mouse Model, *Sci. Rep.*, 2019, **9**, 12655.
347. L. C. Gomes-da-Silva, L. Zhao, L. Bezu, H. Zhou, et al., Photodynamic therapy with redaporfin targets the endoplasmic reticulum and Golgi apparatus, *The EMBO J.*, 2018, **37**, e98354.
348. L. B. Rocha, F. Schaberle, J. M. Dąbrowski, S. Simões, and L. G. Arnaut, Intravenous single-dose toxicity of redaporfin-based photodynamic therapy in rodents, *Int. J. Mol. Sci.*, 2015, **16**, 29236-29249.
349. Y. Li, C.P. Tan, W. Zhang, L. He, L.N. Ji, and Z.W. Mao, Phosphorescent iridium(III)-bis-N-heterocyclic carbene complexes as mitochondria-targeted theranostic and photodynamic anticancer agents, *Biomaterials*, 2015, **39**, 95-104.
350. W. Lv, Z. Zhang, K. Y. Zhang, H. Yang, et al., A Mitochondria-Targeted Photosensitizer Showing Improved Photodynamic Therapy Effects Under Hypoxia, *Angew. Chem. Int. Ed.*, 2016, **55**, 9947–9951.
351. F. X. Wang, M. H. Chen, Y. N. Lin, H. Zhang, C. P. Tan, L. N. Ji, and Z. W. Mao, Dual Functions of Cyclometalated Iridium(III) Complexes: AntiMetastasis and Lysosome-Damaged Photodynamic Therapy, *ACS Appl. Mater. Interfaces*, 2017, **9**, 42471–42481.

352. L. Tabrizi, The discovery of half-sandwich iridium complexes containing lidocaine and (pyren-1-yl)ethynyl derivatives of phenylcyanamide ligands for photodynamic therapy, *Dalton Trans.*, 2017, **46**, 7242.
353. M. Dickerson, Y. Sun, B. Howerton, and E. C. Glazer, Modifying Charge and Hydrophilicity of Simple Ru(II) Polypyridyl Complexes Radically Alters Biological Activities: Old Complexes, Surprising New Tricks, *Inorg. Chem.*, 2014, **53**, 10370–10377.
354. S. Swavey, and K. J. Brewer, Visible Light Induced Photocleavage of DNA by a Mixed-Metal Supramolecular Complex:  $[(bpy)_2Ru(dpp)]_2RhCl_2]^{5+}$ , *Inorg. Chem.*, 2002, **41**, 6196–6198.
355. A. A. Holder, D. F. Zigler, M. T. Tarrago-Trani, B. Storrie, and K. J. Brewer, Photobiological Impact of  $[(bpy)_2Ru(dpp)]_2RhCl_2]Cl_5$  and  $[(bpy)_2Os(dpp)]_2RhCl_2]Cl_5$  [bpy ) 2,2'-Bipyridine; dpp ) 2,3-Bis(2-pyridyl)pyrazine] on Vero Cells, *Inorg. Chem.*, 2007, **46**, 4760–4762.
356. R. Lincoln, L. Kohler, S. Monro, H. Yin, M. Stephenson, R. Zong, A. Chouai, C. Dorsey, R. Hennigar, R. P. Thummel, and S. A. McFarland, Exploitation of Long-Lived  $^3IL$  Excited States for Metal–Organic Photodynamic Therapy: Verification in a Metastatic Melanoma Model, *J. Am. Chem. Soc.*, 2013, **135**, 17161–17175.
357. G. Shi, S. Monro, R. Hennigar, J. Colpitts, J. Fong, K. Kasimova, H. Yin, R. DeCoste, C. Spencer, L. Chamberlain, A. Mandel, L. Lilge, S. A. McFarland, Ru(II) dyads derived from  $\alpha$ -oligothiophenes, A new class of potent and versatile photosensitizers for PDT, *Coord. Chem. Rev.*, 2015, **282–283**, 127–138.
358. J. Mo, N. P. M. Le, and R. Priefer, Evaluating the mechanisms of action and subcellular localization of ruthenium(II)-based photosensitizers, *Eur. J. Med. Chem.*, 2021, **225**, 113770.
359. Q. Chen, V. Ramu, Y. Aydar, A. Groenewoud, X. Q. Zhou, M. J. Jager, H. Cole, C. G. Cameron, S. A. McFarland, S. Bonnet, and B. E. Snaar-Jagalska, TLD1433 Photosensitizer Inhibits Conjunctival Melanoma Cells in Zebrafish Ectopic and Orthotopic Tumour Models, *Cancers*, 2020, **12**, 587.
360. S. Tortorella, and T. C. Karagiannis, Transferrin Receptor-Mediated Endocytosis: A Useful Target for Cancer Therapy, *J. Membr. Biol.*, 2014, **247**, 291–307.
361. P. Kaspler, S. Lasic, S. Forward, Y. Arenas, A. Mandel, and L. Lilge, L. A ruthenium(II) based photosensitizer and transferrin complexes enhance photo-physical properties, cell uptake, and photodynamic therapy safety and efficacy, *Photochem. Photobiol. Sci.*, 2016, **15**, 481–495.
362. K. Ogawa, and Y. Kobuke, Recent advances in two-photon photodynamic therapy, *Anti-Cancer Agents, Med. Chem.*, 2008, **8**, 269–279
363. B. C. Wilson, W. P. Jeeves, and D. M. Lowe, In vivo and post mortem measurements of the attenuation spectra of light in mammalian tissues, *Photochem. Photobiol.*, 1985, **42**, 153–162.
364. B. G. Wang, K. König, and K. J. Halhuber, Two-photon microscopy of deep intravital tissues and its merits in clinical research, *J. Microsc.*, 2010, **238**, 1–20.
365. R. K. P. Benninger, and D. W. Piston, Two-photon excitation microscopy for the study of living cells and tissues, *Curr. Protoc. Cell Biol.*, 2013, **59**, 4.11.11–14.11.24.
366. U. Tauer, Advantages and risks of multiphoton microscopy in physiology, *Exp. Physiol.*, 2002, **87**, 709–714.

367. R. Marchesini, E. Melloni, G. Fava, G. Pezzoni, G. Savi, F. Zunino, and Docchio F, A study on the possible involvement of nonlinear mechanism of light absorption by HpD with Nd: YAG laser, *Lasers Surg. Med.*, 1986, **6**, 323–327.
368. A. Karotki, M. Khurana, J. R. Lepock, and B. C. Wilson, Simultaneous two-photon excitation of photofrin in relation to photodynamic therapy, *Photochem. Photobiol.*, 2006, **82**, 443–452.
369. C. Jin, F. Liang, J. Wang, L. Wang, J. Liu, et al., Rational design of cyclometalated iridium(III) complexes for three-photon phosphorescence bioimaging, *Angew. Chem. Int. Ed.*, 2020, **59**, 15987–15991.
370. Y. Fan, D. Ding, and D. Zhao D, Two- and three-photon absorption and excitation phosphorescence of oligofluorene-substituted Ir(ppy)<sub>3</sub>, *Chem. Comm.*, 2015, **51**, 3446–3449.
371. L. K. McKenzie, I. V. Sazanovich, E. Baggaley, M. Bonneau, V. Guerchais, J. A. G. Williams, J. A. Weinstein, and H. E. Bryant, Metal Complexes for Two-Photon Photodynamic Therapy: A Cyclometalated Iridium Complex Induces Two-Photon Photosensitization of Cancer Cells under Near-IR Light, *Chem. Eur. J.*, 2017, **23**, 234–238.
372. J. P. Liu, C. Z. Jin, B. Yuan, X. G. Liu, Y. Chen, L. N. Ji, and H. Chao, Selectively lighting up two-photon photodynamic activity in mitochondria with AIE-active iridium(III) complexes, *Chem. Commun.*, 2017, **53**, 2052–2055.
373. A. Raza, S. A. Archer, S. D. Fairbanks, K. L. Smitten, S. W. Botchway, J. A. Thomas, S. MacNeil, and J. W. Haycock, A dinuclear ruthenium(II) complex excited by near-infrared light through two-photon absorption induces phototoxicity deep within hypoxic regions of melanoma cancer spheroids, *J. Am. Chem. Soc.*, 2020, **142**, 4639–4647.
374. K. Qiu, Y. Wen, C. Ouyang, X. Liao, C. Liu, T. W. Rees, Q. Zhang, L. Ji, and H. Chao H, The stepwise photodamage of organelles by two-photon luminescent ruthenium(ii) photosensitizers, *Chem. Comm.*, 2019, **55**, 11235–11238.
375. G. Chen, J. Shen, T. Y. Ohulchanskyy, N. J. Patel, et al., (alpha-NaYbF(4):Tm(3+))/CaF(2) Core/Shell Nanoparticles with Efficient Near-Infrared to Near-Infrared Upconversion for High-Contrast Deep Tissue Bioimaging, *Acs. Nano.*, 2012, **6**, 8280–8287.
376. J. Wang, F. Wang, C. Wang, Z. Liu, and X. G. Liu, Single-Band Upconversion Emission in Lanthanide-Doped KMnF<sub>3</sub> Nanocrystals, *Angew. Chem. Int. Edit.*, 2011, **50**, 10369–10372.
377. J. F. C. Loo, Y. H. Chien, F. Yin, S. K. Kong, H. P. Ho, and K.-T. Yong, Upconversion and downconversion nanoparticles for biophotonics and nanomedicine, *Coord. Chem. Rev.*, 2019, **400**, 213042.
378. F. Wang, D. Banerjee, Y. S. Liu, X. Y. Chen, and X. G., Upconversion nanoparticles in biological labeling, imaging, and therapy, *Analyst.*, 2010, **135**, 1839–1854.
379. M. Haase, and H. Schafer, Upconverting Nanoparticles, *Angew. Chem. Int. Edit.*, 2011, **50**, 5808–5829.
380. G. Liang, H. Wang, H. Shi, H. Wang, M. Zhu, A. Jing, J. Li, and G. Li, Recent progress in the development of upconversion nanomaterials in bioimaging and disease treatment, *J. Nanobiotechnol.*, 2020, **18**, 154.
381. S. Wilhelm, Perspectives for Upconverting Nanoparticles, *ACS Nano*, 2017, **11**, 10644–10653.
382. P. Zhang, W. Steelant, M. Kumar, and M. Scholfield, Versatile Photosensitizers for Photodynamic Therapy at Infrared Excitation, *J. Am. Chem. Soc.*, 2007, **129**, 4526–4527.



383. H. S. Qian, H. C. Guo, P. C. L. Ho, R. Mahendran, and Y. Zhang, Mesoporous-Silica-Coated Up-Conversion Fluorescent Nanoparticles for Photodynamic Therapy, *Small*, 2009, **5**, 2285–2290.
384. H. C. Guo, H. S. Qian, N. M. Idris, and Y. Zhang, Singlet oxygen-induced apoptosis of cancer cells using upconversion fluorescent nanoparticles as a carrier of photosensitizer, *NanoMed.-Nanotechnol. Biol. Med.*, 2010, **6**, 486–495.
385. S. S. Cui, H. Y. Chen, H. Y. Zhu, H. Y., J. M. Tian, X. M. Chi, Z. Y. Qian, S. Achilefu, and Y. Q. Gu, Amphiphilic chitosan modified upconversion nanoparticles for in vivo photodynamic therapy induced by near-infrared light, *J. Mater. Chem.*, 2012, **22**, 4861–4873.
386. L. Y. Zeng, Y. W. Pan, Y. Tian, X. Wang, W. Z. Ren, S. J. Wang, G. M. Lu, and A. G. Wu, Doxorubicin-loaded NaYF<sub>4</sub>:Yb/Tm-TiO<sub>2</sub> inorganic photosensitizers for NIR-triggered photodynamic therapy and enhanced chemotherapy in drug-resistant breast cancers, *Biomaterials*, 2015, **57**, 93–106.
387. L. E. Zhang, L. Y. Zeng, Y. W. Pan, S. Luo, W. Z. Ren, A. Gong, X. H. Ma, H. Z. Liang, G. M. Lu, and A. G. Wu, Inorganic photosensitizer coupled Gd-based upconversion luminescent nanocomposites for in vivo magnetic resonance imaging and near-infrared-responsive photodynamic therapy in cancers, *Biomaterials*, 2015, **44**, 82–90.
388. S. S. Lucky, N. M. Idris, Z. Q. Li, K. Huang, K. C. Soo, and Y. Zhang, Titania Coated Upconversion Nanoparticles for Near-Infrared Light Triggered Photodynamic Therapy, *ACS Nano*, 2015, **9**, 191–205.
389. C. Wang, H. Q. Tao, L. Cheng, and Z. Liu, Near-Infrared Light Induced In Vivo Photodynamic Therapy of Cancer Based on Upconversion Nanoparticles, *Biomaterials*, 2011, **32**, 6145–6154.
390. Y. Park, H. M. Kim, J. H. Kim, K. C. Moon, et al., Theranostic Probe Based on Lanthanide-Doped Nanoparticles for Simultaneous In Vivo Dual-Modal Imaging and Photodynamic Therapy, *Adv. Mater.*, 2012, **24**, 5755–5761.
391. K. Liu, X. M. Liu, Q. H. Zeng, Y. L. Zhang, et al., Covalently Assembled NIR Nanoplatform for Simultaneous Fluorescence Imaging and Photodynamic Therapy of Cancer Cells, *ACS Nano*, 2012, **6**, 4054–4062.
392. H. Y. Wang, L. Hou, H. L. Li, X. Wang, et al., A nanosystem loaded with perfluorohexane and rose bengal coupled upconversion nanoparticles for multimodal imaging and synergetic chemo-photodynamic therapy of cancer, *Biomater. Sci.*, 2020, **8**, 2488-2506.
393. J. Z. Zhao, S. Sun, X. Li, W. Zhang, and S. Gou, Enhancing Photodynamic Therapy Efficacy of Upconversion-Based Nanoparticles Conjugated with a Long-Lived Triplet Excited State Iridium(III)-Naphthalimide Complex: Toward Highly Enhanced Hypoxia-Inducible Factor-1, *ACS Appl. Bio Mater.*, 2020, **3**, 1, 252–262.
394. M. S. Meijer, V. S. Talens, M. F. Hilbers, R. E. Kieltyka, A. M. Brouwer, M. M. Natile, and S. Bonnet, NIR-Light-Driven Generation of Reactive Oxygen Species Using Ru(II)-Decorated Lipid-Encapsulated Upconverting Nanoparticles, *Langmuir*, 2019, **35**, 12079–12090.
395. J. P. Celli, B. Q. Spring, I. Rizvi, et al., Imaging and photodynamic therapy: mechanisms, monitoring, and optimization, *Chem Rev.*, 2010, **110**, 2795-2838.
396. J. C. Simões, S. Sarpaki, P. Papadimitroulas, B. Therrien, and G. Loudos, Conjugated photosensitizers for imaging and PDT in cancer research, *J. Med. Chem.*, 2020, **63**, 14119-14150.

397. P. Sarbadhikary, B. P. George, and H. Abrahamse, Recent advances in photosensitizers as multifunctional theranostic agents for imaging-guided photodynamic therapy of cancer, *Theranostics*, 2021, **11**, 9054.
398. V. Novohradsky, A. Rovira, C. Hally, A. Galindo, et al., Towards Novel Photodynamic Anticancer Agents Generating Superoxide Anion Radicals: A Cyclometalated Ir<sup>III</sup> Complex Conjugated to a Far-Red Emitting Coumarin, *Angew. Chem. Int. Ed.*, 2019, **58**, 6311–6315.
399. K. J. Wu, S. H. Ho, J. Y. Dong, L. Fu, et al., Aliphatic Group-Tethered Iridium Complex as a Theranostic Agent against Malignant Melanoma Metastasis, *ACS Appl. Bio. Mater.*, 2020, **3**, 2017–2027.
400. J. Yang, Q. Cao, W. L. Hu, R. R. Ye, et al., Theranostic TEMPO-functionalized Ru(II) complexes as photosensitizers and oxidative stress indicators, *Dalton Trans.*, 2017, **46**, 445–454.
401. S. M. Janib, A. S. Moses, and J. A. MacKay, Imaging and Drug Delivery Using Theranostic Nanoparticles, *Adv. Drug Deliv. Rev.*, 2010, **62**, 1052–1063.
402. X. Yang, X. Shi, J. Ji, and G. Zhai, Development of redox-responsive theranostic nanoparticles for near-infrared fluorescence imaging-guided photodynamic/chemotherapy of tumor. *Drug Deliv.*, 2018, **25**, 780–96.
403. P. Liu, C. Yue, Z. Sheng, G. Gao, et al., Photosensitizer-conjugated redox-responsive dextran theranostic nanoparticles for near-infrared cancer imaging and photodynamic therapy, *Polym. Chem.*, 2014, **5**, 874–81.
404. N. Boens, B. Verbelen and W. Dehaen, Postfunctionalization of the BODIPY core: Synthesis and spectroscopy, *Eur. J. Org. Chem.*, 2015, **30**, 6577–6595.
405. N. Epelde-Elezcano, V. Martínez-Martínez, E. Peña-Cabrera, C. F. A. Gómez-Durán, I. López Arbeloa, and S. Lacombe, Modulation of singlet oxygen generation in halogenated BODIPY dyes by substitution at their meso position: towards a solvent-independent standard in the vis region, *RSC Adv.*, 2016, **6**, 41991–41998.
406. B. Bertrand, K. Passador, C. Goze, F. Denat, E. Bodio, and M. Salmain, Metal-based BODIPY derivatives as multimodal tools for life sciences, *Coord. Chem. Rev.*, 2018, **358**, 108–124.
407. J. Zhao, K. Xu, W. Yang, Z. Wang, and F. Zhong, The triplet excited state of Bodipy: formation, modulation and application, *Chem. Soc. Rev.*, 2015, **44**, 8904.
408. R. Prieto-Montero, A. Prieto-Castañeda, R. Sola-Llano, A. R. Agarrabeitia, et al., Exploring BODIPY Derivatives as Singlet Oxygen Photosensitizers for PDT, *Photochem. Photobiol.*, 2020, **96**, 458–477.
409. E. Palao, R. Sola-Llano, A. Tabero, H. Manzano, A. R. Agarrabeitia, A. Villanueva, I. Lopez-Arbeloa, V. Martínez-Martínez, and M. J. Ortiz, AcetylacetonateBODIPY-biscyclometalated Iridium (III) complexes: Effective strategy towards smarter fluorescent photosensitizer agents, *Chem. Eur. J.*, 2017, **23**, 10139–10147.
410. A. A. Rachford, R. Ziessel, T. Bura, P. Retailleau, and F. N. Castellano, Boron Dipyrromethene (Bodipy) Phosphorescence Revealed in [Ir(ppy)<sub>2</sub>(bpy-C≡C-Bodipy)]<sup>+</sup>, *Inorg. Chem.*, 2010, **49**, 3730–3736.
411. W. Wu, J. Sun, X. Cui, and J. Zhao, Observation of the room temperature phosphorescence of Bodipy in visible light-harvesting Ru(II) polyimine complexes and application as triplet photosensitizers for triplet-triplet-annihilation upconversion and photocatalytic oxidation, *J. Mater. Chem. C*, 2013, **1**, 4577–4589.

412. D. Bechet, P. Couleaud, C. Frochot, M. L. Viriot, F. Guillemin, and M. Barberi-Heyob, Nanoparticles as vehicles for delivery of photodynamic therapy agents, *Trends Biotechnol.*, 2008, **26**, 612–21.
413. J. P. Keene, I. D. Kesse, E. J. Land, R. W. Redmond, and T. G. Truscott, Direct detection of singlet oxygen sensitized by haematoporphyrin and related compounds, *Photochem. Photobiol.*, 1986, **43**, 117–20.
414. E. J. Hong, D. G. Choi, and M. S. Shim, Targeted and effective photodynamic therapy for cancer using functionalized nanomaterials, *Acta Pharm. Sin. B*, 2016, **6**, 297-307.
415. D. Peer, J. M. Karp, S. Hong, O. C. Farokhzad, R. Margalit, and R. Langer, Nanocarriers as an emerging platform for cancer therapy, *Nat. Nanotechnol.*, 2007, **2**, 751-760.
416. N. Lammari, M. Tarhini, K. Miladi, O. Louaer, A. H. Meniai, S. Sfar, H. Fessia, and Abdelhamid Elaissari, Chapter 14 - Encapsulation methods of active molecules for drug delivery, in *Developments in Biomedical Engineering and Bioelectronics, Drug Delivery Devices and Therapeutic Systems*, Academic Press, 2021, 289-306.
417. T. A. Debele, S. Peng, and H. C. Tsai, Drug Carrier for Photodynamic Cancer Therapy, *Int. J. Mol. Sci.*, 2015, **16**, 22094-22136.
418. F. ud Din, W. Aman, I. Ullah, O. S. Qureshi, O. Mustapha, S. Shafique, and A. Zeb, Effective use of nanocarriers as drug delivery systems for the treatment of selected tumors, *Int. J. Nanomedicine*, 2017, **12**, 7291.
419. M. Olivo, R. Bhuvaneshwari, S. S. Lucky, N. Dendukuri, and P. S. Thong, Targeted Therapy of Cancer Using Photodynamic Therapy in Combination with Multi-faceted Anti-Tumor Modalities, *Pharmaceuticals (Basel)*, 2010, **3**, 1507–1529.
420. J. Zhang, C. Jiang, J.P.F. Longo, R. B. Azevedo, H. Zhang, and L. A. Muehlmann, An updated overview on the development of new photosensitizers for anticancer photodynamic therapy, *Acta Pharm. Sin. B*, 2018, **8**, 137–146.
421. T.R. Daniels, E. Bernabeu, J. A. Rodríguez, S. Patel, M. Kozman, D. A. Chiappetta, E. Holler, J. Y. Ljubimova, G. Helguera, and M. L. Penichet, The transferrin receptor and the targeted delivery of therapeutic agents against cancer, *Biochim. Biophys. Acta*, 2012, **1820**, 291–317.
422. A. A. Alexander-Bryant, W. S. Vanden Berg-Foels, and X. Wen, Chapter One—Bioengineering Strategies for Designing Targeted Cancer Therapies. In *Advances in Cancer Research*, K.D. Tew, P.B. Fisher, Eds.; Academic Press: Cambridge, MA, USA, 2013, 118, 1–59.
423. U. Chitgupi, Y. Qin, and J. F. Lovell, Targeted Nanomaterials for Phototherapy, *Nanotheranostics*, 2017, **1**, 38–58.
424. Z. J. Li, and C. H. Cho, Peptides as targeting probes against tumor vasculature for diagnosis and drug delivery, *J. Transl. Med.*, 2012, **10**, S1.
425. Y. Zhong, F. Meng, C. Deng, and Z. Zhong, Ligand-directed active tumor-targeting polymeric nanoparticles for cancer chemotherapy, *Biomacromolecules*, 2014, **15**, 1955-69.
426. Brown, K.C. Peptidic tumor targeting agents: The road from phage display peptide selections to clinical applications, *Curr. Pharm. Des.*, 2010, **16**, 1040–1054.
427. Z. Zhao, K. Qiu, J. Liu, X. Hao, and J. Wang, Two-photon photodynamic ablation of tumour cells using an RGD peptide-conjugated ruthenium(II) photosensitiser, *Chem. Commun.*, 2020, **56**, 12542–12545.

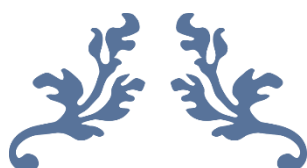
428. L. Yu, Q. Wang, R. C. H. Wong, S. Zhao, D. K.P. Ng, and P. C. Lo, Synthesis and biological evaluation of phthalocyanine-peptide conjugate for EGFR-targeted photodynamic therapy and bioimaging, *Dyes Pigm.*, 2019, **163**, 197–203.
429. D. Schrama, R. A. Reisfeld, and J. C. Becker, Antibody targeted drugs as cancer therapeutics, *Nat. Rev. Drug Discov.*, 2006, **5**, 147–159.
430. J. Sandland, and R. W. Boyle, Photosensitizer Antibody–Drug Conjugates: Past, Present, and Future, *Bioconjug. Chem.*, 2019, **30**, 975–993.
431. M. Kijanka, B. Dorresteyn, S. Oliveira, and P. M. van Bergen en Henegouwen, Nanobody-based cancer therapy of solid tumors, *Nanomedicine*, 2015, **10**, 161–174.
432. B. Korsak, G. M. Almeida, S. Rocha, C. Pereira, et al., Porphyrin modified trastuzumab improves efficacy of HER2 targeted photodynamic therapy of gastric cancer, *Int. J. Cancer*, 2017, **141**, 1478–1489.
433. M. M. Deken, M. M. Kijanka, I. Beltrán Hernández, M. D. Slooter, et al., Nanobody-targeted photodynamic therapy induces significant tumor regression of trastuzumab-resistant HER2-positive breast cancer, after a single treatment session, *J. Control. Release*, 2020, **323**, 269–281.
434. P. B. A. A. van Driel, M. C. Boonstra, M. D. Slooter, R. Heukers, et al., EGFR targeted nanobody–photosensitizer conjugates for photodynamic therapy in a pre-clinical model of head and neck cancer, *J. Control. Release*, 2016, **229**, 93–105.
435. R. Heukers, P. M. V. B. en Henegouwen, and S. Oliveira, Nanobody–photosensitizer conjugates for targeted photodynamic therapy, *Nanomed.: Nanotechnol. Biol. Med.*, 2014, **10**, 1441-1451.
436. L. Rogers, F. Majer, N. N. Sergeeva, E. Paszko, J. F. Gilmer, and M. O. Senge, Synthesis and biological evaluation of Foscan®bile acid conjugates to target esophageal cancer cells, *Bioorg. Med. Chem. Lett.*, 2013, **23**, 2495–2499.
437. M. Yang, J. Deng, D. Guo, J. Zhang, L. Yang, and F. A. Wu, folate-conjugated platinum porphyrin complex as a new cancer-targeting photosensitizer for photodynamic therapy, *Org. Biomol. Chem.*, 2019, **17**, 5367–5374.
438. Y. Morita, M. Leslie, H. Kameyama, D. E. Volk, and T. Tanaka, Aptamer Therapeutics in Cancer: Current and Future, *Cancers*, 2018, **10**, 80.
439. J. Yan, T. Gao, Z. Lu, J. Yin, Y. Zhang, and R. Pei, Aptamer-Targeted Photodynamic Platforms for Tumor Therapy, *ACS Appl. Mater. Interfaces*, 2021, **13**, 27749–27773.
440. O. C. Farokhzad, S. Jon, A. Khademhosseini, T. N. T. Tran, D. A. LaVan, and R. Langer, Nanoparticle-Aptamer Bioconjugates, *Cancer Res.*, 2004, **64**, 7668.
441. J. Kim, W. Park, D. Kim, E. S. Lee, D. H. Lee, S. Jeong, J. M. Park, and K. Na, Tumor-Specific Aptamer-Conjugated Polymeric Photosensitizer for Effective Endo-Laparoscopic Photodynamic Therapy, *Adv. Funct. Mater.*, 2019, **29**, 1900084.
442. L. K. McKenzie, M. Flamme, P. S. Felder, J. Karges, F. Bonhomme, A. Gandioso, A., C. Malosse, G. Gasser, and M. Hollenstein, A ruthenium–oligonucleotide bioconjugated photosensitizing aptamer for cancer cell specific photodynamic therapy, *RSC Chem. Biol.*, 2022, **3**, 85-95.
443. R. Bazak, M. Houri, S. El Achy, S. Kamel, and T. Refaat, Cancer active targeting by nanoparticles: A comprehensive review of literature, *J. Cancer Res. Clin. Oncol.*, 2015, **141**, 769–784.

444. M. Das, C. Mohanty, and S. K. Sahoo, Ligand-based targeted therapy for cancer tissue, *Expert Opin. Drug Deliv.*, 2009, **6**, 285–304.
445. C. A. Kruger, and H. Abrahamse, Utilisation of Targeted Nanoparticle Photosensitiser Drug Delivery Systems for the Enhancement of Photodynamic Therapy, *Molecules*, 2018, **23**, 2628.
446. E. Mladenov, S. Magin, A. Soni, and G. Iliakis, DNA Double-Strand Break Repair as Determinant of Cellular Radiosensitivity to Killing and Target in Radiation Therapy, *Front. Oncol.*, 2013, **3**, 113.
447. H. Chen, G. D. Wang, Y. J. Chuang, Z. Zhen, et al., Nanoscintillator-mediated X-ray inducible photodynamic therapy for in vivo cancer treatment, *Nano Lett.*, 2015, **15**, 2249-2256.
448. F. Bistolfi, Red Radioluminescence and Radiochemiluminescence: Premises for a Photodynamic Tumour Therapy with X-Rays and Haematoporphyrin Derivatives: A Working Hypothesis, *Panminerva Med.*, 2000, **42**, 69-75.
449. X. D. Ren, X. Y. Hao, H. C. Li, M. R. Ke, B. Y. Zheng, and J. D. Huang JD, Progress in the Development of Nanosensitizers for X-Ray-Induced Photodynamic Therapy, *Drug Discov. Today*, 2018, **23**, 1791-800.
450. W. Sun, Z. Zhou, G. Pratz, X. Chen, and H. Chen, Nanoscintillator-Mediated X-Ray Induced Photodynamic Therapy for Deep-Seated Tumors: From Concept to Biomedical Applications, *Theranostics*, 2020, **10**, 1296-1318.
451. G. D. Wang, H. T. Nguyen, H. Chen, P. B. Cox, et al., X-Ray Induced Photodynamic Therapy: A Combination of Radiotherapy and Photodynamic Therapy, *Theranostics*, 2016, **6**, 2295-305.
452. B. Halliwell, and J. M. C. Gutteridge, Oxygen Free Radicals and Iron in Relation to Biology and Medicine: Some Problems and Concepts, *Arch. Biochem. Biophys.*, 1986, **246**, 501-514.
453. A. L. Bulin, C. Truillet, R. Chouikrat, F. Lux, et al., X-Ray-Induced Singlet Oxygen Activation with Nanoscintillator-Coupled Porphyrins, *J. Phys. Chem. C*, 2013, **117**, 21583-21589.
454. N. Y. Morgan, G. Kramer-Marek, P. D. Smith, K. Camphausen, and J. Capala, Nanoscintillator Conjugates as Photodynamic Therapy-based Radiosensitizers: Calculation of Required Physical Parameters, *Radiat. Res.*, 2009, **171**, 236-244.
455. G. Lan, K. Ni, R. Xu, K. Lu, et al., Nanoscale Metal–Organic Layers for Deeply Penetrating X-ray-Induced Photodynamic Therapy, *Angew. Chem. Int. Ed.*, 2017, **56**, 12102-12106.
456. J. Luo, Z. Xie, J. W. Lam, L. Cheng, et al., Aggregation-Induced Emission of 1-Methyl-1,2,3,4,5-Pentaphenylsilole, *Chem. Commun.*, 2001, **18**, 1740–1741.
457. J. Mei, Y. Hong, J. W. Lam, A. Qin, Y. Tang and B. Z. Tang, Aggregation-induced emission: the whole is more brilliant than the parts, *Adv. Mater.*, 2014, **26**, 5429–5479.
458. Y. N. Hong, J. W. Y. Lam, B. Z. Tang, Aggregation-induced emission: phenomenon, mechanism and applications, *Chem. Commun.*, 2009, **29**, 4332 –4353.
459. K. Yang, Y. Zhou, Y. Wang, S. Zhao, X. Wu, X. Peng, L. Huang, L. Jiang, M. Lan, X. Y. Yi, An Iridium Complex as an AIE-active Photosensitizer for Image-guided Photodynamic Therapy, *Chem. Asian J.*, 2021, **16**, 1780-1785.

460. X. G. Hou, Y. Wu, H. T. Cao, H. Z. Sun, H. B. Li, G. G. Shan, and Z. M. Su, A cationic iridium(III) complex with aggregation induced emission (AIE) properties for highly selective detection of explosives, *Chem. Commun.*, 2014, **50**, 6031-6034.

461. S. K. Patra, B. Sen, M. Rabha and S. Khatua, An aggregation-induced emission-active bis-heteroleptic ruthenium(II) complex of thiophenyl substituted phenanthroline for the selective "turn-off" detection of picric acid, *New J. Chem.*, 2022, **46**, 169.

462. B. Sen, S. K. Patra, and S. Khatua, Ruthenium(II) Polypyridine Complex-Based Aggregation-Induced Emission Luminogen for Rapid and Selective Detection of Phosgene in Solution and in the Gas Phase, *Inorg. Chem.*, 2021, **60**, 19175–19188.



---

***Chapter 1. Thiabendazole-based  
Rh(III) and Ir(III) Biscyclometalated  
Complexes with Mitochondria-  
Targeted Anticancer Activity and  
Metal-Sensitive Photodynamic  
Activity***

---







## Authorship Statement

This chapter is the result of a collaboration with Cristina Pérez Arnaiz, Natalia Busto and Begoña García from the University of Burgos (UBU), and María Isabel Acuña and Fernando Domínguez from the University of Santiago de Compostela (USC), so the biological experiments were made by them. I have accomplished the following sections: Synthesis of ligands and complexes, characterization of complexes, crystal structures, photophysical properties (in acetonitrile), Ir(III)-promoted singlet oxygen photo-generation and photooxidation of sulphides (photo-stability of complexes **[Ir-a]Cl** and **[Ir-b]Cl**), photo-oxidation of thioanisole and photo-oxidation of L-cysteine and L-methionine).

This work can be found published as: C. Pérez-Arnaiz, M. I. Acuña, N. Busto, I. Echevarría, M. Martínez-Alonso, G. Espino, B. García, and F. Domínguez, Thiabendazole-based Rh(III) and Ir(III) Biscyclometalated Complexes with Mitochondria-Targeted Anticancer Activity and Metal-Sensitive Photodynamic Activity, *Eur. J. Med. Chem.*, 2018, **157**, 279-293.

## 0. Abstract

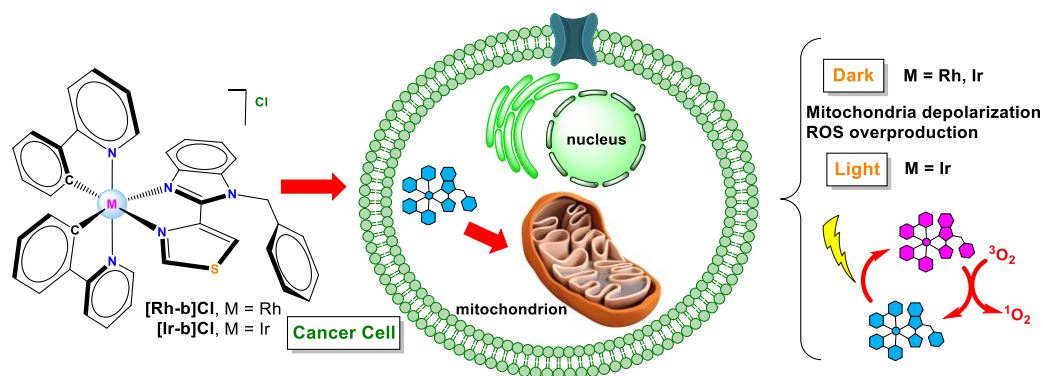


Fig.1. Schematic representation of the biological mechanism of action of the complexes.

Two pairs of Rh(III) and Ir(III) bis-cyclometalated complexes bearing the ligands thiabendazole (L<sup>1</sup>), and N-benzyl-thiabendazole (L<sup>2</sup>), named **[Ir-a]Cl** - **[Rh-a]Cl**, and **[Ir-b]Cl** - **[Rh-b]Cl**, respectively, have been designed and synthesized to explore the photophysical and biological effects that arise from changing both the metal centre and the N,N ancillary ligand. In the dark, the four metal complexes exhibit greater cytotoxicity than cisplatin against human colon (SW480) and human lung (A549) adenocarcinoma cell lines. Moreover, the pair of complexes bearing the ligand L<sup>2</sup> is markedly more cytotoxic and present higher uptake values than complexes with L<sup>1</sup>,

thereby their biological properties were studied further to determine their mechanism of action. Interestingly, in spite of the different metal centre both **[Ir-b]Cl** and **[Rh-b]Cl** are responsible for the loss of mitochondrial functionality and the activation of apoptotic cell death pathways. Moreover, the photodynamic activity of the four complexes, **[Ir-a]Cl**, **[Ir-b]Cl**, **[Rh-a]Cl** and **[Rh-b]Cl**, was tested using visible blue light (460 nm) under soft irradiation conditions (20 min, 5.5 mW×cm<sup>-2</sup>). While the Rh complexes are not photopotiated, the phototoxicity index (IC<sub>50</sub> non-irradiated/IC<sub>50</sub> irradiated) of **[Ir-a]Cl** and **[Ir-b]Cl** was 15.8 and 3.6, respectively. We also demonstrate that only the Ir derivatives are capable of photocatalyzing the oxidation of sulfur-containing L-amino acids under blue light irradiation. Indeed, **[Ir-a]Cl** is more active than **[Ir-b]Cl**, which provides a reasonable mechanism for their biological action, meaning that oxidative stress could be selectively promoted through their photocatalytic activity upon irradiation. This different PDT behaviour depending on the metal centre and the ancillary substituent may be useful for the future rational design of metal-based photosensitizers.

## 1. Introduction

A great deal of effort has been invested over the past few decades to develop non-platinum metal complexes with anticancer activity by mechanisms different from those of cisplatin to circumvent the platinum resistance and its undesired side effects. In line with this, cyclometalated complexes of various metal centres such as palladium(II), gold(III), ruthenium(II), platinum(II), rhodium(III) and iridium(III) constitute an interesting field of research due to their variety of cellular targets and mechanisms of action.<sup>1</sup> Among the formers, mitochondria stands out, as it plays a key role in the cell metabolism. It is well known that central metabolic pathways operating in malignant cells are different from those in normal cells.<sup>2,3</sup> Cancer cells exhibit various degrees of alterations in the mitochondria function, such as higher mitochondrial membrane potential (MMP) and increased oxidative stress.<sup>4</sup> Because of this, recent studies point to the potential benefits of targeting mitochondria metabolism for anticancer therapy<sup>5</sup> and several mitochondria-targeted drugs are currently in clinical trials.<sup>6</sup> These drugs often act by directly disturbing mitochondrial function, which triggers the activation of mitochondrial cell death pathways via apoptosis.

Biscyclometalated complexes of the type  $[\text{Ir}(\text{C}^{\wedge}\text{N})_2(\text{N}^{\wedge}\text{N})]^+$  accumulate within a wide variety of cellular targets depending on the ancillary ligands. Indeed, mitochondria,<sup>7,8,9,10,11,12</sup> lysosomes,<sup>13,14,15</sup> endoplasmic reticulum,<sup>16,17</sup> endosomes<sup>18</sup> or nucleus<sup>19,20</sup> have all been recognized as target organelles for different Ir(III) biscyclometalated derivatives. Nonetheless, cyclometalated Rh(III) complexes have not received much attention so far, probably due to the lack of the exceptional

photophysical properties typical of analogous Ir(III) complexes. However, Rh complexes could also be a potential alternative to platinum metallodrugs,<sup>21</sup> and their biological properties deserve further study.

In addition, Photodynamic Therapy (PDT) has emerged as a prominent chemotherapeutic anti-cancer treatment, as it renders feasible local and transitory activation of drugs to achieve spatio-temporal control over its biological action and therapeutic effects.<sup>22</sup> The resulting selective activity over target (tumour) tissues eventually contributes to reducing systemic toxicity. PDT requires the combined action of three individually non-toxic elements: light, oxygen and a photosensitizer (PS), in such a way that the excited PS agent (PS\*) can generate reactive oxygen species (ROS) and specifically singlet oxygen ( $^1\text{O}_2$ ) from triplet oxygen ( $^3\text{O}_2$ ) through energy transfer (ET) upon excitation with UV, visible or even near-infrared (NIR) light of specific wavelengths.<sup>23</sup>  $^1\text{O}_2$  is a very reactive species and can damage biomolecules such as DNA and proteins through redox reactions, which ultimately triggers cancer cells death. Alternatively,  $^1\text{O}_2$  can evolve to other cytotoxic ROS. Cyclometalated Ir(III) complexes are currently being studied as potential PDT agents due to their outstanding photophysical properties.<sup>23,24</sup> The crucial advantage over organic fluorescent molecules is the high spin-orbit coupling constant of the iridium metal core ( $\xi = 3909 \text{ cm}^{-1}$ ) that favours the singlet-to-triplet intersystem crossing (ISC).<sup>25</sup> This peculiarity is responsible for other features of these Ir(III) compounds such as their long triplet excited state lifetimes, their appropriate energy gap that exceeds the excitation energy of  $^3\text{O}_2$  and, overall, their high capability as  $\text{O}_2$  photosensitizers.<sup>26</sup>

In this context, arylazoles are attractive ancillary  $\text{N}^{\wedge}\text{N}$  ligands, as they can be prepared and modified readily and can offer a remarkable structural and chemical diversity. Therefore, they can be used to fine-tune the photophysical and chemical properties of this type of organometallic compounds.<sup>27</sup> Specifically, the imidazole ring can be easily functionalized through the reactive N-H bond.<sup>28</sup> In this work, we have replaced the N-H function of thiabendazole ( $\text{L}^1$ ) with a benzyl group N- $\text{CH}_2\text{Ph}$  ( $\text{L}^2$ ) in an attempt to increase their lipophilicity, which could improve their cellular internalization properties,<sup>29</sup> and to improve their chemo-stability, since the N-H group can exhibit both acid-base and redox reactivity. As a result, we have prepared two pairs of Rh(III) and Ir(III) biscyclometalated complexes of general formula  $[\text{M}(\text{ppy})_2(\text{N}^{\wedge}\text{N})]\text{Cl}$  ( $\text{M} = \text{Rh}, \text{Ir}$ ;  $\text{ppy} = 2\text{-phenylpyridinate}$ ) bearing  $\text{N}^{\wedge}\text{N}$  ligands based on the thiabendazole scaffold ( $\text{L}^1$  and  $\text{L}^2$ ), and we have studied their potential use as anticancer drugs and PDT agents. First, we have demonstrated that actually the rational benzyl modification in  $\text{L}^2$  yields an appreciable improvement in the cytotoxic activity of their complexes in the dark. A deeper biological study has demonstrated that both complexes bearing the  $\text{L}^2$  ligand induce apoptosis via mitochondrial perturbation. Secondly, considering the increasing interest in finding sensitizers capable of potentiating their cytotoxic activity upon

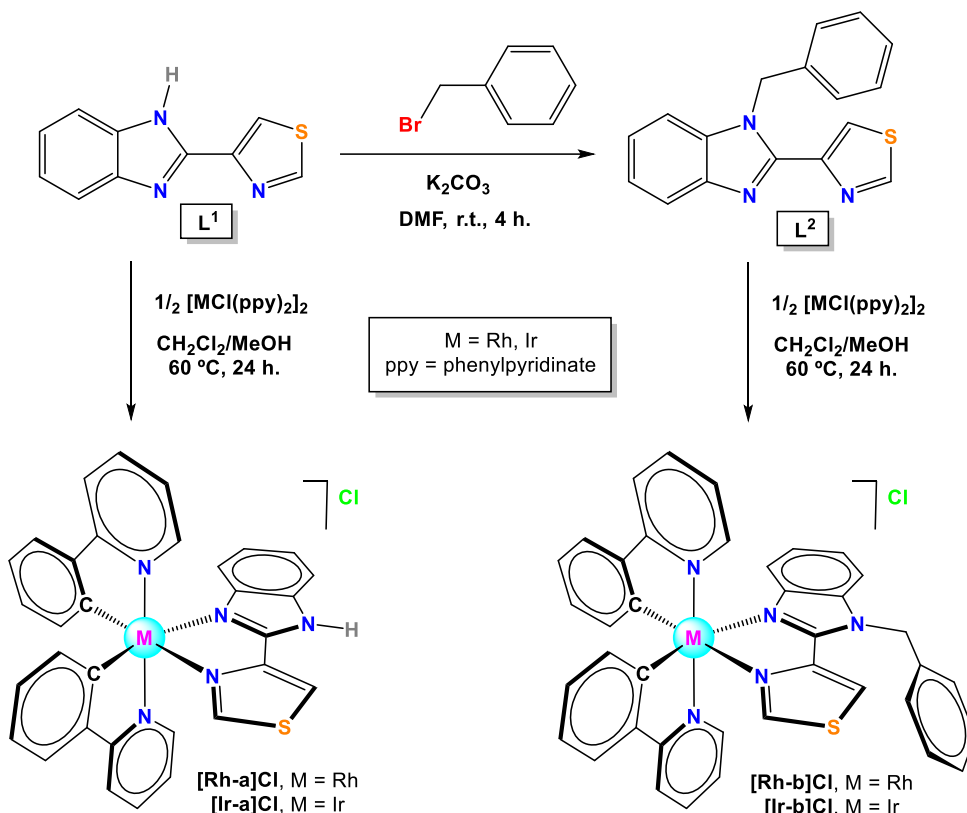
irradiation,<sup>27</sup> we have also tested the PDT behaviour of the four complexes under soft irradiation conditions, using blue visible light ( $\lambda_{\text{max}} = 460 \text{ nm}$ ) and minimizing the exposure time of cells to light. Interestingly, only the Ir complexes, bearing either the ligand **L**<sup>1</sup> or **L**<sup>2</sup>, present a remarkable photopotential of their cytotoxic activity and are capable of photocatalyzing the oxidation of sulfur-containing L-amino acids.

## 2. Results and discussion

### 2.1. Synthesis of ligands and complexes

The ancillary ligand **L**<sup>2</sup> (see Scheme 1) was prepared by reacting 2-(4-thiazolyl)benzimidazole (thiabenzazole, TBZ, **L**<sup>1</sup>) with benzyl bromide in the presence of  $\text{K}_2\text{CO}_3$  as the base and using DMF as the solvent, according to a method adapted from the literature.<sup>30,31</sup>

The complexes [**Rh-a,b**]Cl and [**Ir-a,b**]Cl depicted in Scheme 1 were synthesized following the classical two-steps procedure reported by Nonoyama et al.<sup>32</sup> and the experimental details are given in the SI. These complexes were isolated as white (Rh) or yellow (Ir) solids, consisting of racemic mixtures of  $\Delta$  and  $\Lambda$  enantiomers with good yields and purities according to analytical and spectroscopic data. Moreover, they are soluble in common organic solvents such as DMSO, acetone, acetonitrile, methanol and dichloromethane and only slightly soluble in water. The structure and composition of all the new derivatives were determined by multinuclear NMR, IR, and mass spectroscopy, as well as by elemental analysis. 2D NMR experiments were conducted to partially assign the signals in the  $^1\text{H}$  and  $^{13}\text{C}\{^1\text{H}\}$  NMR spectra (SI Fig. 1-6).



Scheme 1. Synthesis of ligand  $\text{L}^2$  and the new Rh(III) and Ir(III) complexes. Complexes were isolated as racemic mixtures, but the structures only show the  $\Delta$  enantiomer.

## 2.2. Characterization of complexes

The  $^1\text{H}$  and  $^{13}\text{C}\{^1\text{H}\}$  NMR spectra of complexes  $[\text{Rh-a,b}]\text{Cl}$  and  $[\text{Ir-a,b}]\text{Cl}$  showed resonances for the coordinated ancillary ( $\text{N}^{\wedge}\text{N}$ ) and cyclometalated ( $\text{C}^{\wedge}\text{N}$ ) ligands with the following relevant features: (1) Two different sets of peaks were observed for the two inequivalent 2-phenylpyridinate ( $\text{ppy}^-$ ) ligands of every complex due to their  $\text{C}_1$ -asymmetric nature; (2) Broad singlets around 15 ppm were recorded for the N-H protons of  $[\text{Rh-a}]\text{Cl}$  and  $[\text{Ir-a}]\text{Cl}$  in their  $^1\text{H}$  NMR spectra; (3) Two mutually coupled doublets ( $^2J_{\text{HH}} = 17.5$  Hz) were detected at 6.2 and 6.1 ppm for the diastereotopic protons of the  $-\text{CH}_2$  groups in the  $^1\text{H}$  NMR spectra of  $[\text{Rh-b}]\text{Cl}$  and  $[\text{Ir-b}]\text{Cl}$  owing to the helical chirality implicit in trischelate octahedral complexes, while free  $\text{L}^2$  (achiral) gave a singlet for the  $-\text{CH}_2$ ; (4) The  $^{13}\text{C}\{^1\text{H}\}$  NMR spectra of complexes  $[\text{Rh-b}]\text{Cl}$  and  $[\text{Ir-b}]\text{Cl}$  exhibited a singlet at around 48 ppm for the  $-\text{CH}_2$  group, whereas the spectra of both Rh derivatives showed two doublets ( $^1J(^{103}\text{Rh}-^{13}\text{C}) \approx 33$  Hz) above 165 ppm, for the metalated C atoms of  $\text{ppy}^-$  (see SI Fig. 1–6 for the NMR spectra).

The ESI + MS spectra display peaks whose  $m/z$  values and isotopic distribution are congruent with those calculated for the cationic metal complexes with formula  $[M(\text{ppy})_2(\text{L}^n)]^+$  ( $M = \text{Rh}, \text{Ir}; \text{L}^n = \text{L}^1, \text{L}^2$ ) (see Section 4.2.). Molar conductivity measurements carried out on solutions of complexes **[Rh-b]Cl** and **[Ir-b]Cl** in acetonitrile ( $10^{-3}$  M) are consistent with a 1:1 electrolyte nature. However, complexes **[Rh-a]Cl** and **[Ir-a]Cl** provided very low values of  $\Lambda_M$  likely due to ion pairing through N-H...Cl hydrogen bonding interactions (see Section 4.2.).

### 2.3. Crystal structures

Attempts to crystalize the chloride salts **[Rh-b]Cl** and **[Ir-b]Cl** were unsuccessful. However, single crystals of the respective  $\text{PF}_6^-$  salts, **[Rh-b]PF<sub>6</sub>** and **[Ir-b]PF<sub>6</sub>·CH<sub>3</sub>COCH<sub>3</sub>** suitable for X-ray diffraction analysis were obtained by slow diffusion of a saturated solution of  $\text{NH}_4\text{PF}_6$  in water into a solution of either **[Rh-b]Cl** in methanol or **[Ir-b]Cl** in methanol/acetone. The ORTEP diagrams for  $(\Delta)$ -**[Rh-b]PF<sub>6</sub>** and  $(\Delta)$ -**[Ir-b]PF<sub>6</sub>** are depicted in Fig. 2. Selected bond lengths and angles are given in Table 1, and crystallographic refinement parameters in SI Table 1. The corresponding unit cells show two pairs of the enantiomers ( $\Delta$ ) and ( $\Lambda$ ) stemming from helical chirality. Furthermore, the unit cell contains four  $\text{PF}_6^-$  counterions and four  $\text{CH}_3\text{COCH}_3$  molecules in the case of **[Ir-b]PF<sub>6</sub>**. The metal centres display a slightly distorted octahedral coordination geometry with the expected *cis*-C,C and *trans*-N,N mutual disposition for the C^N ligands.

The M-C<sub>ppy</sub> and M-N<sub>ppy</sub> ( $M = \text{Rh}, \text{Ir}$ ) bond distances lie within the expected ranges for the 2-phenylpyridanate ligands, that is, very close to 2 Å.<sup>33,34,35,36,37,38</sup> The M–N bond lengths for the ancillary ligand are significantly longer due to the strong *trans* influence attributed to the C atoms of the C^N ligands,<sup>24,39</sup> and the effect is even more pronounced in the Rh complex (Table 1).<sup>40</sup> The bond angles are comparable to those previously reported for similar derivatives.<sup>15,41</sup> Furthermore, the three chelate rings are essentially planar.

The 3D crystal networks of **[Rh-b]PF<sub>6</sub>** and **[Ir-b]PF<sub>6</sub>·CH<sub>3</sub>COCH<sub>3</sub>** are mainly held down by intermolecular hydrogen bonding contacts with involvement of  $\text{PF}_6^-$  anions as acceptors (SI Tables 2 and 3 and SI Fig. 7a and 7b). Remarkably, the crystal structure of **[Ir-a]PF<sub>6</sub>**, previously reported by some of us,<sup>42</sup> features dimeric entities as a result of  $\pi$ - $\pi$  interactions between the benzimidazole units of two neighbour complexes. However, similar contacts have not been found either in **[Rh-b]PF<sub>6</sub>** nor in **[Ir-b]PF<sub>6</sub>**. Consequently, we surmise that the bulkiness of the benzyl group works against these intermolecular interactions, preventing the aggregation of complex cations in highly concentrated solutions of **[Ir-b]PF<sub>6</sub>** or in cellular environments.<sup>43</sup> The crystal structure of free  $\text{L}^2$  has also been

determined by X-diffraction (see SI Fig. 8).

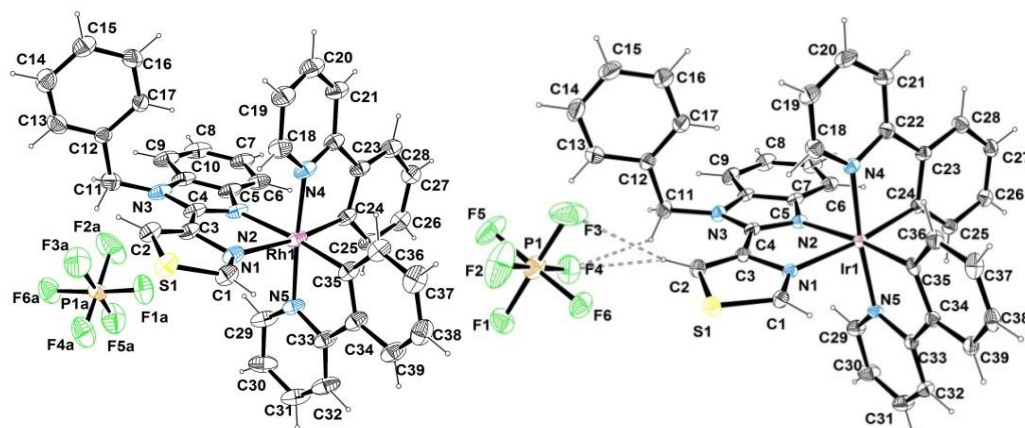


Fig. 2. ORTEP diagrams for  $(\Delta)$ - $[\text{Rh-b}]\text{PF}_6$  and  $(\Delta)$ - $[\text{Ir-b}]\text{PF}_6$  forming part of the asymmetric unit of racemic  $[\text{Rh-b}]\text{PF}_6$  and  $[\text{Ir-b}]\text{PF}_6 \cdot \text{CH}_3\text{COCH}_3$ . Thermal ellipsoids are shown at the 30% probability level. The molecule of  $\text{CH}_3\text{COCH}_3$  has been omitted in the diagram of  $[\text{Ir-b}]\text{PF}_6 \cdot \text{CH}_3\text{COCH}_3$  for the sake of clarity.

Table 1. Selected bond lengths (Å) and angles ( $^\circ$ ) for compounds  $[\text{Rh-b}]\text{PF}_6$  and  $[\text{Ir-b}]\text{PF}_6 \cdot \text{CH}_3\text{COCH}_3$ .

Distances/angles	$[\text{Rh-b}]\text{PF}_6$	Distances/angles	$[\text{Ir-b}]\text{PF}_6$
Rh(1)-N(1)	2.162(6)	Ir(1)-N(1)	2.144(4)
Rh(1)-N(2)	2.163(6)	Ir(1)-N(2)	2.146(4)
Rh(1)-N(4)	2.032(5)	Ir(1)-N(4)	2.040(4)
Rh(1)-N(5)	2.038(5)	Ir(1)-N(5)	2.031(4)
Rh(1)-C(24)	1.964(7)	Ir(1)-C(24)	2.000(5)
Rh(1)-C(35)	1.990(7)	Ir(1)-C(35)	2.002(5)
C(24)-Rh(1)-N(4)	81.5(3)	C(24)-Ir(1)-N(4)	80.88(18)
C(35)-Rh(1)-N(5)	81.2(3)	C(35)-Ir(1)-N(5)	80.90(18)
N(2)-Rh(1)-N(1)	76.0(2)	N(2)-Ir(1)-N(1)	75.72(15)
N(5)-Rh(1)-N(4)	176.1(2)	N(5)-Ir(1)-N(4)	174.25(16)
C(24)-Rh(1)-N(1)	171.8(2)	C(24)-Ir(1)-N(1)	173.00(16)
C(35)-Rh(1)-N(2)	173.2(3)	C(35)-Ir(1)-N(2)	172.09(17)

## 2.4. pH stability

The pH effect in aqueous media was evaluated for the four metal-complexes. As expected,  $[\text{Rh-a}]\text{Cl}$  and  $[\text{Ir-a}]\text{Cl}$  undergo deprotonation of the reactive N-H group in  $\text{L}^1$  upon increasing the pH, and display  $\text{pK}_a$  values of  $7.30 \pm 0.01$  and  $6.76 \pm 0.03$  (see SI Fig. 9), respectively, which implies that they would be partially deprotonated at physiological pH. On the other hand,  $[\text{Rh-b}]\text{Cl}$  and  $[\text{Ir-b}]\text{Cl}$  do not undergo acid-base processes over the whole pH range tested (pH = 3–12).

## 2.5. Photophysical properties

The UV–Vis absorption spectra of complexes **[Rh-a,b]Cl** and **[Ir-a,b]Cl** were recorded in air-saturated aqueous buffer (SI Fig. 10) and also in deoxygenated acetonitrile (Fig. 3-A). All the complexes exhibit intense ( $\epsilon > 30000 \text{ M}^{-1} \text{ cm}^{-1}$ ), broad absorption bands in the UV region below 340 nm, attributed to spin-allowed intra-ligand transitions ( ${}^1\text{IL}$ ) ( ${}^1\pi \rightarrow \pi^*$ ) within the cyclometalated (C^N) and ancillary (N^N) ligands. In the case of the Rh(III) complexes, the band at about 370 nm is attributed to a MLCT transition. On the other hand, the absorption of the Ir(III) complexes (MLCT) spreads slightly into the visible region of the spectrum.

The emission spectra of the four complexes were also recorded in air-saturated aqueous buffer (SI Fig. 10) and deoxygenated acetonitrile (Fig. 3-B) and the photophysical parameters are collected in Table 2. The Ir complexes present excitation bands at  $\lambda_{\text{exc}} = 305 \text{ nm}$  and  $\lambda_{\text{exc}} = 385 \text{ nm}$  and exhibit broad emission bands with one maximum for **[Ir-a]Cl** at 500 nm and two maxima for **[Ir-b]Cl** at 480 nm and 506 nm. Both Ir complexes display large Stokes shifts, moderate quantum yields ( $\phi_{\text{PL}}$ ) and long emission lifetimes ( $\tau$ ) compatible with a phosphorescence emission mechanism. On the contrary, the Rh complexes displayed no emission bands at any of the tested excitation wavelengths ( $\lambda_{\text{exc}} = 290\text{-}500 \text{ nm}$ ). The emission spectra of iridium complexes are collected in Fig. 3, revealing the noticeable dependence of the photophysical properties on the nature of the metal centre.

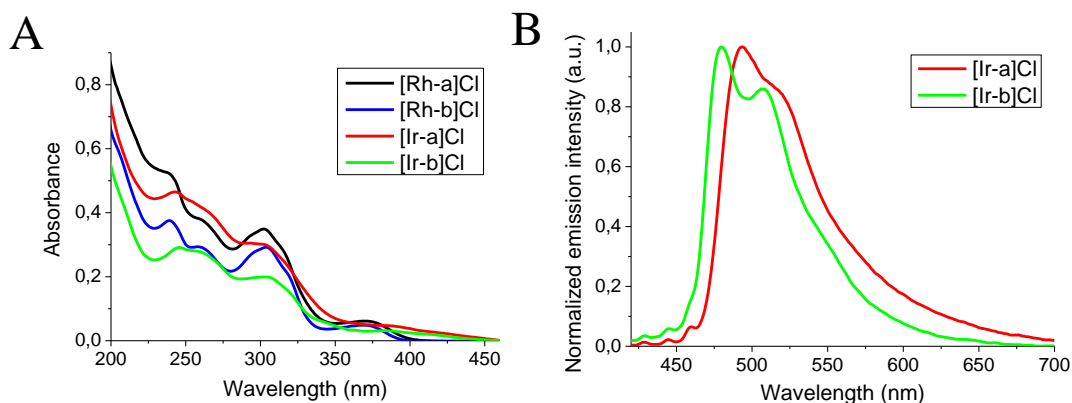


Fig. 3. (A) Overlaid UV–vis absorption spectra of the four metal complexes ( $10^{-5} \text{ M}$ ) in  $\text{CH}_3\text{CN}$  at  $25^\circ \text{C}$  (left). (B) Overlaid emission spectra of **[Ir-a]Cl** and **[Ir-b]Cl** ( $10^{-5} \text{ M}$ ) in deoxygenated  $\text{CH}_3\text{CN}$  at  $25^\circ \text{C}$  upon excitation with  $\lambda_{\text{exc}} = 405 \text{ nm}$  (right).



Table 2. Photophysical parameters for complexes **[Ir-a,b]Cl** and the corresponding ligands **L<sup>1</sup>** and **L<sup>2</sup>** in either deoxygenated acetonitrile or aqueous buffered solution at pH = 7.0 at 25 °C.

Compound	$\lambda_{exc}$ (nm)	$\lambda_{em}$ (nm)	$\phi_{PL}$ (%)	$\tau$ (ns)
<b>L<sup>1</sup></b>	295	346	5.1	8.3
<b>L<sup>2</sup></b>	295	350	5.0	7.7
<b>[Ir-a]Cl</b>	405	494, 509 (sh)	2.3	48.4
<b>[Ir-b]Cl</b>	405	480, 506	1.8, 6.1 <sup>a</sup>	53.2, 228 <sup>a</sup>

<sup>a</sup>Values corresponding to air-saturated aqueous buffer solutions (pH = 7.4).

## 2.6. Biological properties

### 2.6.1. In vitro cytotoxicity

The *in vitro* antiproliferative activity of **[Ir-a,b]Cl** and **[Rh-a,b]Cl** was evaluated against human lung carcinoma (A549) and human colon adenocarcinoma (SW480) cell lines to compare the cytotoxic activity of the four metal complexes. The IC<sub>50</sub> (half maximal inhibitory concentration) values are summarized in Table 3. The four metal complexes exhibit lower IC<sub>50</sub> values than cisplatin against both cell lines. Moreover, the Ir and Rh complexes bearing the ligand **L<sup>2</sup>**, **[Ir-b]Cl** and **[Rh-b]Cl**, exhibit greater cytotoxic activity than their analogues bearing ligand **L<sup>1</sup>**.

Table 3. IC<sub>50</sub> ( $\mu$ M) of **[Ir-a,b]Cl**, **[Rh-a,b]Cl** and cisplatin against A549 (human lung) and SW480 (human colon) cancer cell lines after 24 h of treatment. Data were obtained from quadruplicates of three independent experiments and expressed as mean values  $\pm$  standard deviation (SD).

Complex	IC <sub>50</sub> ( $\mu$ M)	
	A549	SW480
<b>[Ir-a]Cl</b>	18.9 $\pm$ 0.2	10.0 $\pm$ 0.1
<b>[Rh-a]Cl</b>	10.3 $\pm$ 0.1	7.7 $\pm$ 0.4
<b>[Ir-b]Cl</b>	4.0 $\pm$ 0.4	2.9 $\pm$ 0.1
<b>[Rh-b]Cl</b>	4.1 $\pm$ 0.2	3.3 $\pm$ 0.1
<b>Cisplatin</b>	50 $\pm$ 3	37 $\pm$ 6

### 2.6.2. Cellular uptake

The cellular uptake of the two pairs of complexes was evaluated to assess if the benzyl introduction in **L<sup>2</sup>**, which provides the complexes with stability against acid-base reactions at physiological pH, succeeded in increasing the cellular internalization of their complexes. A549 cells were treated with each complex at a concentration of 5 mM for 4 h and then harvested and analyzed by ICP-MS. Indeed, the uptake of **[Ir-a]Cl** was a 50.9% ( $\pm$ 5) lower than that of **[Ir-b]Cl**, and the uptake of **[Rh-a]Cl** was a 23.3% ( $\pm$ 2) lower than that of **[Rh-b]Cl** (SI Fig. 11). Considering this result, the pair of complexes formed by **[Ir-b]Cl** and **[Rh-b]Cl**, which are also the most cytotoxic (see Table 3), were selected to carry out a

deeper biological study and determine their mechanism of action.

### 2.6.3. Cell cycle arrest

The cytotoxicity of many anticancer drugs often is associated with DNA damage and cell cycle perturbation.<sup>44</sup> For instance, although cisplatin interacts with several cell components, its primary biological target is DNA.<sup>45</sup> As a result, this antitumour complex causes arrest at the G2-phase.<sup>46</sup> The effect of **[Ir-b]Cl** and **[Rh-b]Cl** on cell cycle distribution was investigated by flow cytometry and propidium iodide (PI) staining (Fig. 4). Treatment of A549 cells with the complexes at a concentration close to their IC<sub>50</sub> values (5 μM) caused a marked accumulation of cells in the G0/G1 phase. Compared with the vehicle-treated (DMSO) control cells, the percentage of cells in the G0/G1 phase increased by 32.8% and 33.3% at 24 h and 35.9% and 36.9% at 48 h for **[Ir-b]Cl** and **[Rh-b]Cl**, respectively. Accordingly, the number of cells in the S-phase strongly decreased (Table 4). These results point out that both complexes can act through mechanisms of action different from cisplatin.<sup>46</sup> Although some previously reported mitochondria targeted compounds display no effects on the cell cycle distribution,<sup>47,48</sup> our results concur with recent studies on other Ir(III) complexes that also can induce dose-dependent G0/G1 cell cycle arrest.<sup>7</sup>

Table 4. Percentage (%) of cells in the G0/G1, S and G2-M phases of the cell cycle upon treatment with **[Ir-b]Cl** and **[Rh-b]Cl** at 5 μM for 24 h and 48 h. Differences between % of cells in G0/G1 phase for vehicle-treated cells and cells treated with **[Ir-b]Cl** or **[Rh-b]Cl** are significant at  $p = 0.0009$  after 24 h and at  $p = 0.002$  at 48 h. Differences between % of cells in S phase for vehicle-treated cells and cells treated with **[Ir-b]Cl** or **[Rh-b]Cl** are significant at  $p = 0.0004$  after 24 h and at  $p = 0.0008$  at 48 h. Data were obtained from duplicates of two independent experiments and expressed as mean values ± standard deviation (SD).

	24 h			48 h		
	G0/G1	S	G2/M	G0/G1	S	G2/M
Vehicle	49.7 ± 0.9	27.6 ± 0.1	22.7 ± 0.1	52.8 ± 0.8	25.5 ± 0.7	21.7 ± 0.5
<b>[Ir-b]Cl</b>	82 ± 1	7.4 ± 0.6	10.6 ± 0.5	89 ± 1	4.7 ± 0.3	6.3 ± 0.1
<b>[Rh-b]Cl</b>	83.0 ± 0.3	7.9 ± 0.6	9.1 ± 0.9	89.7 ± 0.7	1.8 ± 0.2	8.5 ± 0.5

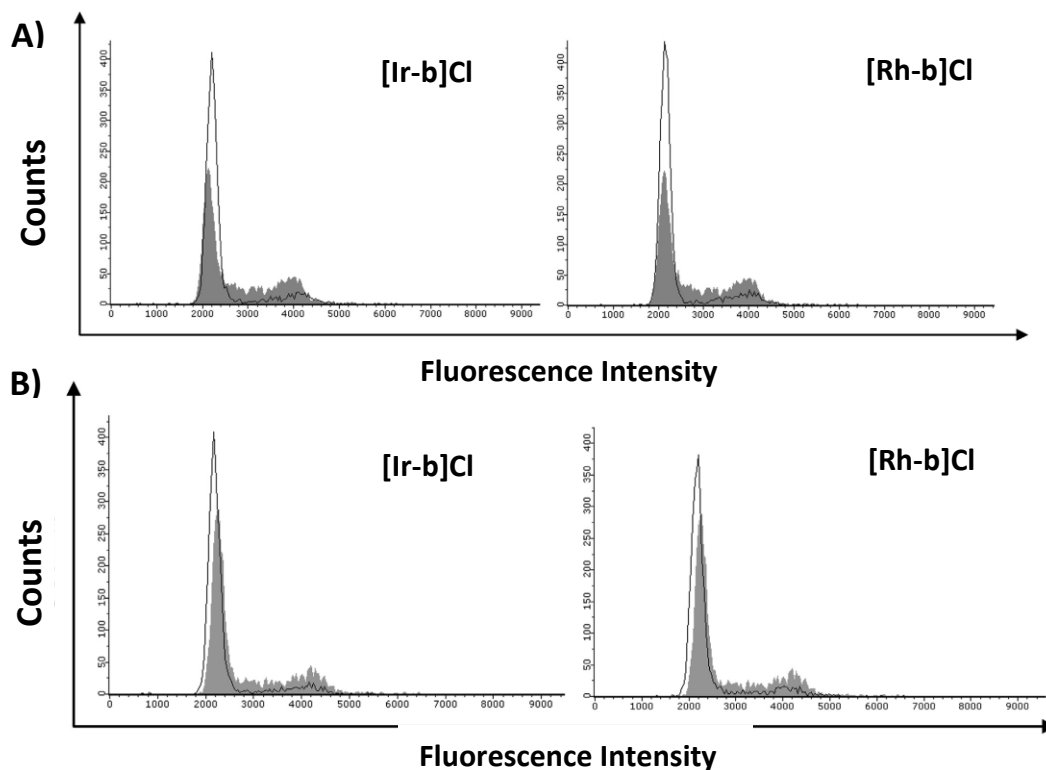


Fig. 4. Effect of **[Ir-b]Cl** and **[Rh-b]Cl** on A549 cell cycle distribution analysed by PI staining with flow cytometry after treatment at  $C_{\text{complex}} = 5 \mu\text{M}$  for 24 h (A) and for 48 h (B). Vehicle-treated cells are represented by the grey area and **[Ir-b]Cl** and **[Rh-b]Cl**-treated cells by the black line.

#### 2.6.4. Induction of apoptosis

The evolution of cell morphology was followed by microscopy and fluorescence microscopy for 48 h upon treatment with  $5 \mu\text{M}$  of **[Ir-b]Cl** or **[Rh-b]Cl** to seek for morphological hallmarks of apoptosis. After 48 h, a net fall in the number of cells was observed compared to the vehicle-treated cells. Morphological changes compatible with apoptosis: cell shrinkage, rounded forms, membrane blabbing and formation of apoptotic bodies were seen and the number of cells affected increased with time (SI Fig. 12). Staining with Hoechst and propidium iodide (PI) can help to differentiate between apoptotic and necrotic cells. After 24 h of treatment with each complex few PI positive cells were found, and they were associated with secondary necrosis with a balloon-like morphology (Fig. 5). Thus, necrosis can be excluded as the principal cause of dead.

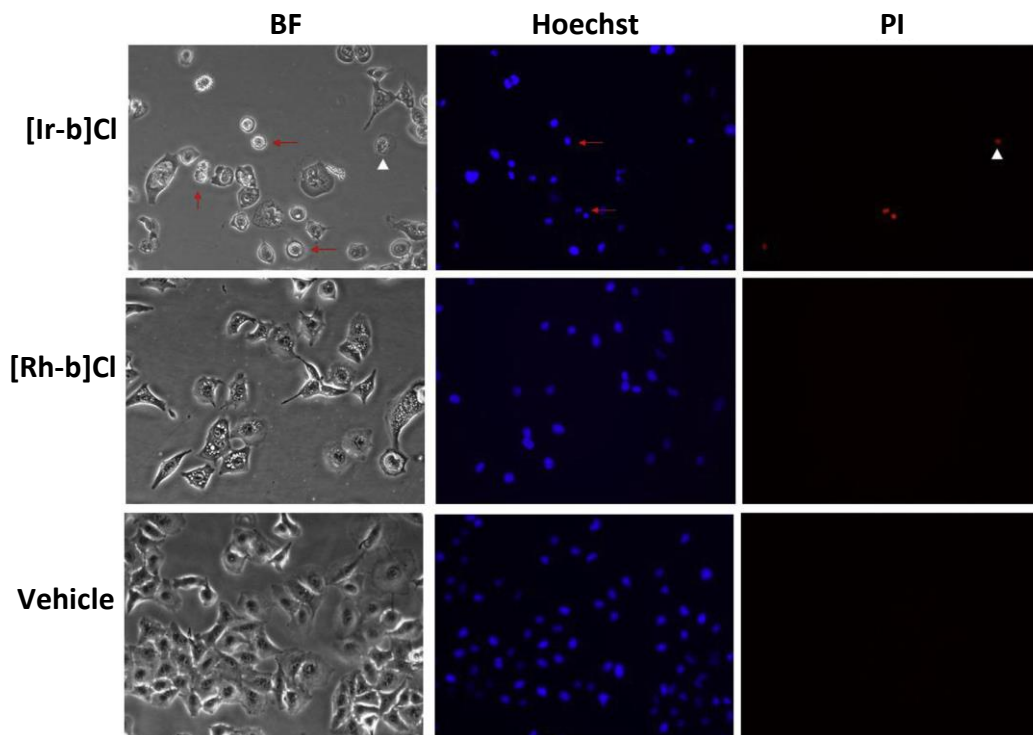


Fig. 5. Morphological changes induced by **[Ir-b]Cl**, **[Rh-b]Cl** and DMSO (vehicle) in A459 cells after treatment at  $C_{\text{complex}} = 5 \mu\text{M}$  for 24 h. Bright field (BF), Hoechst 33342 nuclear staining (Hoechst) and Propidium Iodide necrotic cells staining (PI) (Magnification 20X). **[Ir-b]Cl** treated cells show an apoptotic morphology (red arrows): rounding, membrane babbling, retraction of cytoplasm, nuclear fragmentation, formation of apoptotic bodies. Some cells presented secondary necrosis (white arrows). **[Rh-b]Cl** treatment induced cytoplasmic vacuole, rounding cells and emission of cytoplasmic prolongations. No necrotic cells were seen

To further confirm that the cell death occurred via apoptosis, time-lapse fluorescence microscopy was used to detect activation of caspase-3/7. A549 cells were treated with **[Ir-b]Cl** or **[Rh-b]Cl** ( $5 \mu\text{M}$ ) and images were recorded every 30 min for 24 h to monitor the process. During this procedure, the cells remained continuously under culture conditions at  $37 \text{ }^\circ\text{C}$  and  $5\% \text{ CO}_2$ . In the case of **[Ir-b]Cl**, its intrinsic green emission interfered with the fluorogenic probe used to detect the activation of caspase-3/7. However, this activation was clearly observed for **[Rh-b]Cl**, with the bulk amount of activation events starting after 12 h of the treatment.

Additionally, A549 cells were treated with **[Ir-b]Cl** or **[Rh-b]Cl** for 24 h in the presence or absence of  $20 \mu\text{M}$  of the Z-VAD-FMK caspase inhibitor. Fig. 6 shows that caspase inhibition increases the survival rate after treatment with both **[Ir-b]Cl** and **[Rh-b]Cl** in a significant manner ( $p < 0.03$ ) by 17.4 % and 18.1 %, respectively. This confirms the role of apoptosis in the cell death induced by these complexes.<sup>4</sup>

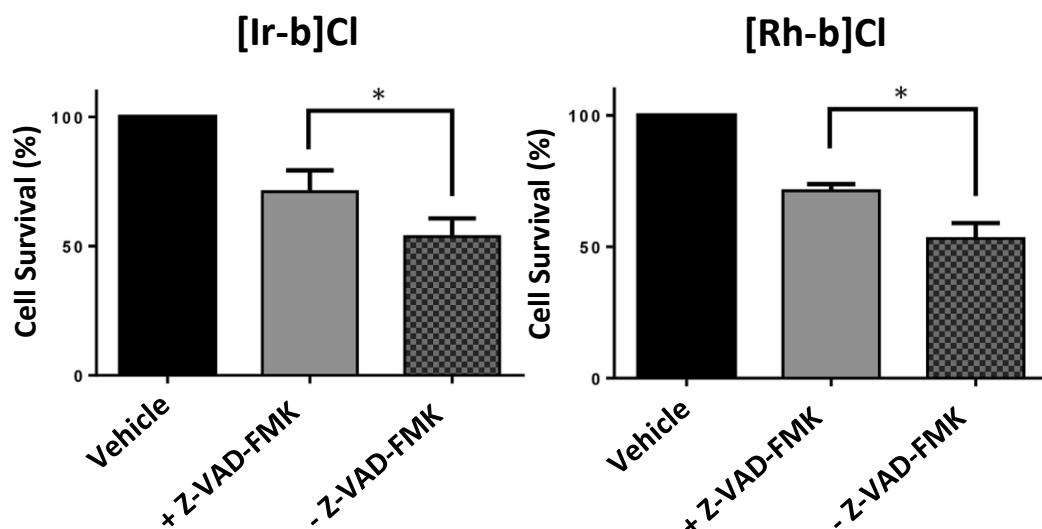


Fig. 6. A549 cells were treated with 5  $\mu$ M of [Ir-b]Cl or [Rh-b]Cl and co-treated (+ Z-VAD-FMK) or not (- Z-VAD-FMK) with the caspase inhibitor Z-VAD-FMK for 24 h. Cell survival was assessed by flow cytometry through the Guava ViaCount Assay (Millipore). Difference significant at \* $p < 0.03$  compared to cells not treated with the caspase inhibitor.

#### 2.6.5. Cellular localization

The subcellular localization of [Ir-b]Cl can be determined by confocal microscopy thanks to its intrinsic emission properties. The colocalization experiments were performed after treatment with a low dose of [Ir-b]Cl (1.5  $\mu$ M), in which cell survival was nearly 100%. As shown in Fig. 7, [Ir-b]Cl displays an intense and punctate staining pattern as a result of its compartmentalization. Colocalization experiments of [Ir-b]Cl with the sensitive probe for mitochondrial membrane potential, TMRM (Fig. 7A) and with the lysosome dye LysoTracker (Fig. 7B) demonstrates that [Ir-b]Cl selectively accumulates in mitochondria. In fact, Pearson's colocalization coefficient with TMRM is 0.80, whereas with LysoTracker the value is 0.09.

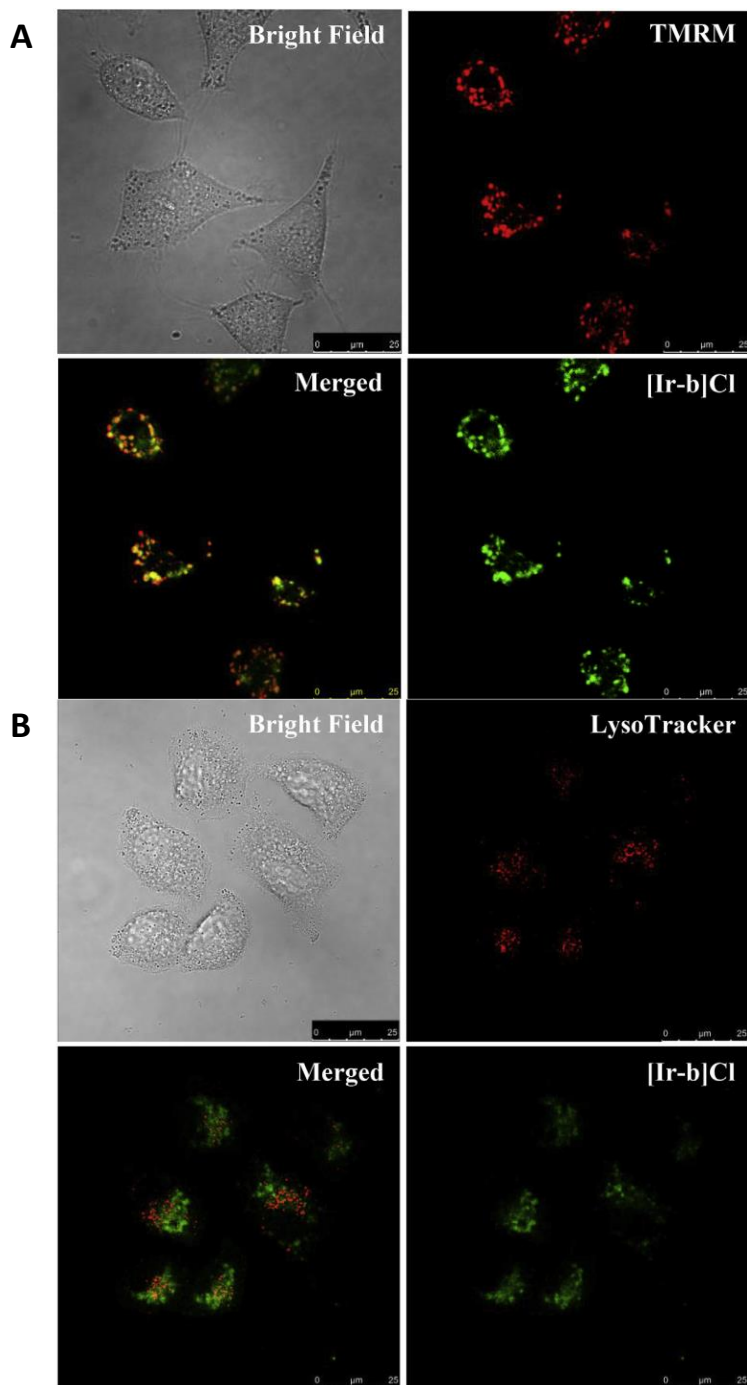


Fig. 7. **A)** Representative confocal images of A549 cells exposed to [Ir-b]Cl (1.5  $\mu$ M, 1h) and to TMRM (100 nM, 30 min). **B)** Representative confocal images of A549 cells exposed to [Ir-b]Cl (1.5  $\mu$ M, 1h) and to LysoTracker (75 nM, 30 min).

### 2.6.6. Effect on the Mitochondrial Membrane Potential

To assess if the accumulation of complex **[Ir-b]Cl** in mitochondria leads to an actual mitochondrial dysfunction, the state of mitochondrial membrane potential (MMP,  $\Delta\Psi_m$ ) was analysed by staining living cells with the fluorescent cationic red dye TMRM, which accumulates only in active, polarized mitochondria due to their relatively negative charge. Depolarized or inactive mitochondria displays decreased membrane potential and fail to sequester TMRM. A treatment with 5  $\mu$ M of **[Ir-b]Cl** or **[Rh-b]Cl** leads to the quick loss of TMRM fluorescence in less than 2 h (Fig. 8). These results indicate that **[Ir-b]Cl** and **[Rh-b]Cl** cause mitochondrial depolarization.

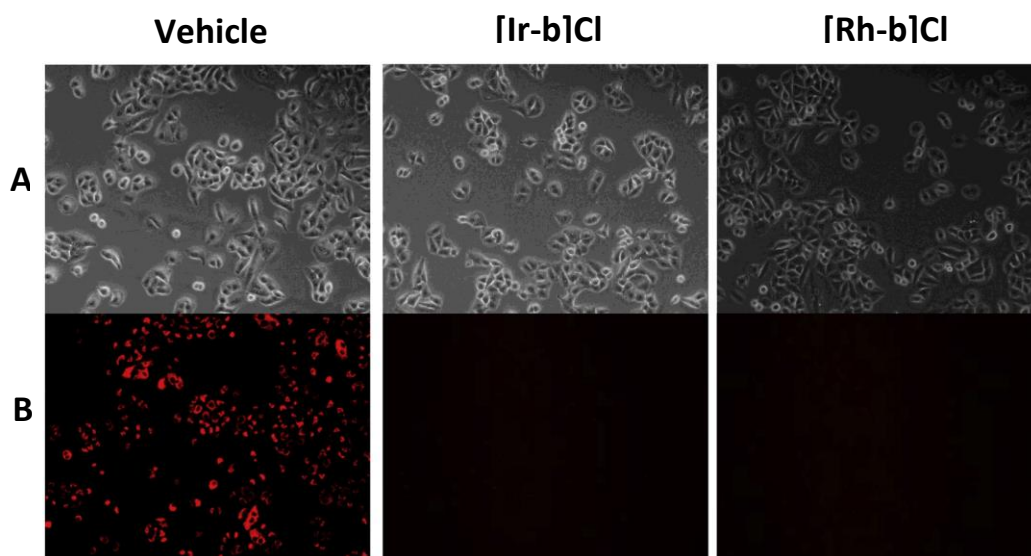


Fig. 8. Effect of **[Ir-b]Cl** and **[Rh-b]Cl** treatment on the mitochondrial membrane potential observed by TMRM fluorescence (red). Representative images of A549 cells treated with DMSO (vehicle), **[Ir-b]Cl** (5  $\mu$ M) and **[Rh-b]Cl** (5  $\mu$ M) for 2 h under the same experimental conditions. A) Phase contrast image. B) Red fluorescence emission.

### 2.6.7. Intracellular ROS detection

It is well known that mitochondrial depolarization is followed by other mitochondrial and non-mitochondrial perturbations. Mitochondria are the major source of intracellular reactive oxygen species (ROS), and mitochondrial dysfunction is closely related to ROS accumulation in the process of apoptosis.<sup>50</sup> To elucidate whether the observed depolarization of mitochondria (Fig. 8) leads to ROS accumulation in the cell, the intracellular ROS levels were examined by using DHE (dihydroethidium) and H<sub>2</sub>DCFDA (2',7'-dichlorodihydrofluorescein diacetate). DHE allows to measure cytosolic superoxide ( $O_2^{\cdot-}$ ) and H<sub>2</sub>DCFDA other radical species including hydrogen peroxide ( $H_2O_2$ ), in intact adherent cells.<sup>51</sup> These probes are oxidized by the afore-mentioned reactive oxygen species to generate the corresponding fluorescent products, which

then can be measured by flow cytometry. **[Ir-b]Cl** could not be included in this assay due to its green emission that partially overlapped with that of the fluorescent probes. A549 cells were treated with **[Rh-b]Cl** (5  $\mu$ M) for 2 or 4 h. A treatment with H<sub>2</sub>O<sub>2</sub> (0.25 mM) was used as a positive control, as it causes oxidative stress that generates ROS overproduction in the cell. Fig. 9A shows that the population of cells with enhanced levels of superoxide after treatment with **[Rh-b]Cl** is even higher than that corresponding to the treatment with H<sub>2</sub>O<sub>2</sub>. For each experiment, the fluorescence of non-treated cells (negative control) is shown in grey. The generation of other radical species was also detected (Fig. 9B), but this time the treatment with H<sub>2</sub>O<sub>2</sub> induced a greater effect than the treatment with **[Rh-b]Cl**. These results entail that superoxide is probably the main radical species generated in the cell by **[Rh-b]Cl**.

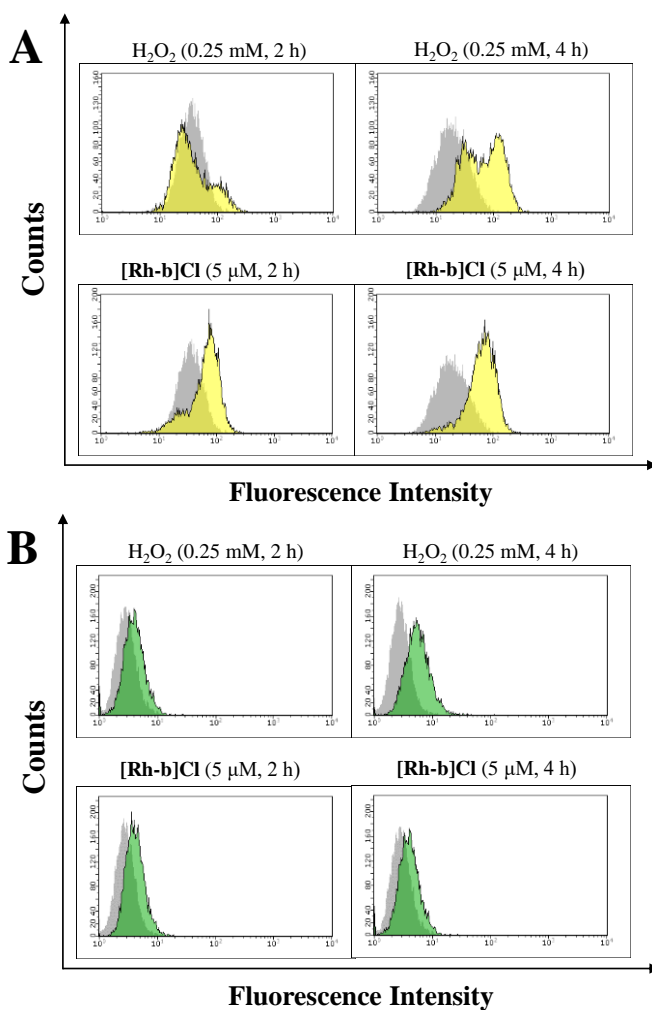


Fig. 9. The level of intracellular ROS was detected by DHE (A, yellow) and H<sub>2</sub>DCFDA (B, green) assays using flow cytometric analysis in A549 cells treated with **[Rh-b]Cl** (5  $\mu$ M) or H<sub>2</sub>O<sub>2</sub> (0.25 mM) for 2 or 4 h. Grey: control cells; coloured: treated cells.



### 2.6.8. Study of Cardiolipin oxidation

Because of depolarization, mitochondria overproduce ROS which, in turn, oxidize mitochondrial cardiolipins. The damage in mitochondria produced by ROS can be determined indirectly by assessing the oxidation state of cardiolipin, a lipid restricted to the inner mitochondrial membrane that plays a key role in the apoptotic cell death pathway.<sup>52</sup> The fluorescent dye 10-N-nonyl acridine orange (NAO) is extensively used for location and quantitative determination of cardiolipin in living cells. NAO interacts with intact, non-oxidized cardiolipin forming NAO dimers, which can be detected based on their red emission.<sup>53</sup> Therefore, a reduction in NAO fluorescence indicates a decrease in cardiolipin content.<sup>54</sup> A549 cells were pre-incubated with NAO and then treated for 4 h with **[Rh-b]Cl** at different concentrations. The fluorescence of NAO in the cells was then measured by flow cytometry (Fig. 10). **[Rh-b]Cl** featured a great dose-dependent impact on NAO fluorescence intensity in agreement with cardiolipin oxidation. Again, **[Ir-b]Cl** could not be included in this study due to its emission features.

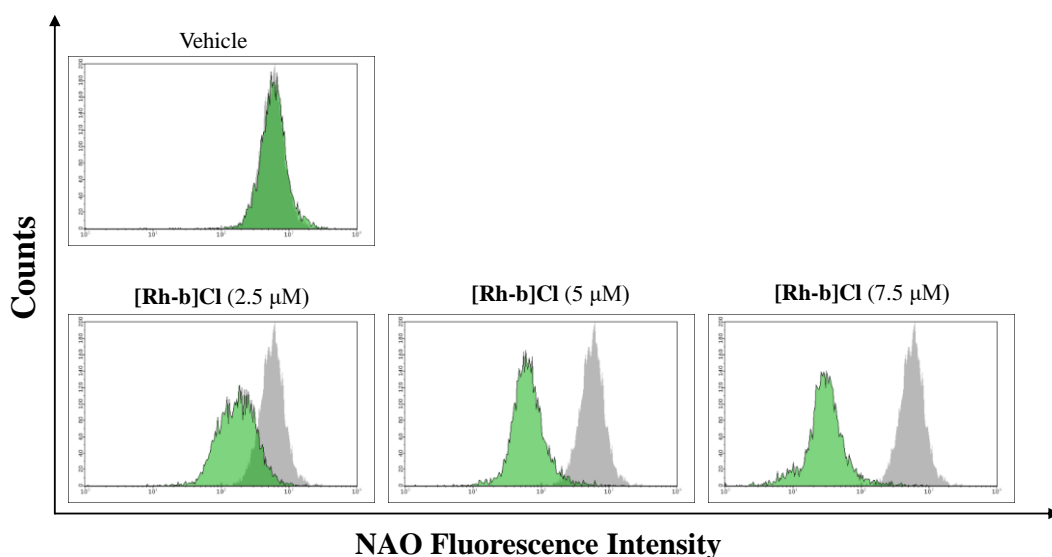


Fig. 10. The decrease of NAO fluorescence upon treatment for 4 h with **[Rh-b]Cl** at different concentrations (2.5, 5 and 7.5  $\mu\text{M}$ ) was analysed by flow cytometry. Grey: control cells; coloured: treated cells.

### 2.6.9. Photodynamic activity

The PDT effect of the **[Ir-b]Cl** and **[Rh-b]Cl** was first examined on A549 cells irradiated in the UV region at 365 nm (where all the complexes present strong absorption) for a short period of 5 min at  $20 \text{ mW}\cdot\text{cm}^{-2}$ . Interestingly, the cytotoxicity of **[Ir-b]Cl** increased significantly, displaying a phototoxicity index ( $\text{IC}_{50} \text{ non-irradiated}/\text{IC}_{50} \text{ irradiated}$ ) of  $18 \pm 2$ , whereas no significant changes were observed for the **[Rh-b]Cl** complex that displayed a phototoxicity index of  $1.1 \pm 0.1$  (SI Fig. 13). Although the phototoxicity index quoted

for **[Ir-b]Cl** is a promising result, the use of visible light and non-toxic photosensitizers is preferable in PDT therapy. Hence, irradiation of cells treated with the four metal complexes included in this work with blue light ( $\lambda_{\max} = 460$  nm) was tested. Fig. 11 summarizes the cytotoxic activity of complexes **[Ir-a,b]Cl** and **[Rh-a,b]Cl** with and without irradiation for 20 min with blue LED light at  $5.5 \text{ mW}\cdot\text{cm}^{-2}$ . Control experiments were carried out to check whether irradiation itself under these experimental conditions can affect cell survival. After 20 min of irradiation with blue LED light at  $5.5 \text{ mW}\cdot\text{cm}^{-2}$  the survival rate obtained for non-treated A549 cells (control) was 97.7 % ( $\pm 0.8$  %). The phototoxicity index values obtained for complexes **[Ir-a]Cl** and **[Ir-b]Cl** were  $15.8 \pm 0.7$  and  $3.6 \pm 0.3$ , respectively, whereas **[Rh-a]Cl** and **[Rh-b]Cl** did not display significant difference in their  $\text{IC}_{50}$  values with and without irradiation. It is worth noting that the  $\text{IC}_{50}$  for **[Ir-a]Cl** and **[Ir-b]Cl** after blue light irradiation is nearly the same for both complexes ( $1.2 \pm 0.1 \mu\text{M}$  and  $1.1 \pm 0.1 \mu\text{M}$ , respectively). However, the phototoxicity index of **[Ir-a]Cl** is considerably higher due to its lower cytotoxicity in the dark.

Thus, despite the similar biological properties of the Ir and the Rh complexes in the dark, the different photophysical features give rise to very distinct photodynamic activity. The explanation could lie on the heavy atom effect provided by the Ir(III) core within complexes **[Ir-a,b]Cl**, which favours an intersystem crossing process and long-lived triplet excited states, which in turn promotes the excitation of the triplet molecular oxygen molecule to generate singlet oxygen. This circumstance is absent for the **[Rh-a,b]Cl** complexes.

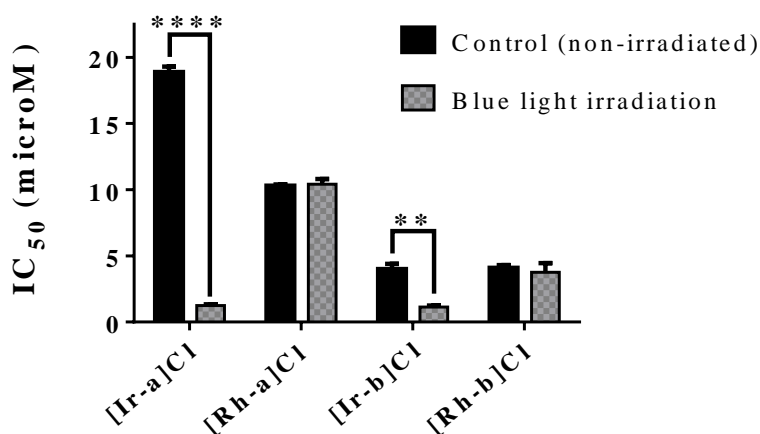


Fig. 11.  $\text{IC}_{50}$  ( $\mu\text{M}$ ) values obtained for A549 cells treated with **[Ir-a,b]Cl** and **[Rh-a,b]Cl** for 24 h with (grey columns) and without (black columns) irradiation for 20 min with blue LED light at  $5.5 \text{ mW}\cdot\text{cm}^{-2}$ . Difference significant at  $**p = 0.0019$  and  $****p = 0.00001$ .

## 2.7. Ir(III)-promoted singlet oxygen photo-generation and photooxidation of sulphides

The results obtained for complexes **[Ir-a,b]Cl** on A549 cells irradiated with blue light prompted us to assess the potential ability of the Ir complexes to photo-catalyze the generation of ROS and the photooxidation of different substrates under irradiation with blue light. The results could provide a reasonable mechanism for the biological action of these Ir(III) complexes under irradiation. For comparison purposes, the Rh(III) complexes were also included in this study.

### 2.7.1. Photo-stability of complexes **[Ir-a]Cl** and **[Ir-b]Cl**

The photo-stability of complexes **[Ir-a]Cl** and **[Ir-b]Cl** was studied by  $^1\text{H}$  NMR over a period of 24 h under irradiation (blue LED light,  $\lambda_{\text{max}} = 460$  nm) in an NMR tube open to air atmosphere (SI Fig. 14 and 15). Both complexes undergo slight photo-decomposition to give the same degradation product which we attribute to  $[\text{IrCl}(\text{ppy})_2(\text{CD}_3\text{SOCD}_3)]$ . The photo-degradation percentages were calculated from the corresponding integration values as 1.6 and 1.3% after 6 h and 6.0 and 4.7% after 24 h for **[Ir-a]Cl** and **[Ir-b]Cl**, respectively, suggesting that the photolysis process is slightly slower for **[Ir-b]Cl**. Conversely, equivalent solutions of **[Ir-a]Cl** and **[Ir-b]Cl** are stable in the dark after 5 days.

### 2.7.2. Photo-oxidation of thioanisole

To properly analyze the ability of the new complexes to photo-catalyze the potential generation of  $^1\text{O}_2$  or other ROS, we evaluated the oxidation of thioanisole by  $^1\text{H}$  NMR in the presence of **[Rh-a,b]Cl** and **[Ir-a,b]Cl** under irradiation at room temperature with a blue LED strip (blue LED light,  $\lambda_{\text{max}} = 460$  nm, 24 W). This model reaction (eq (1)) was reported previously as an illustrative  $^1\text{O}_2$ -mediated photo-oxidation process.<sup>55</sup> The respective sulfoxide (methyl phenyl sulfoxide, MPS) was obtained in a chemo-selective manner in the presence of both Ir(III) PS, although the conversion values determined experimentally demonstrate certain degree of dependence on the coordinated ancillary ligand. Thus, complex **[Ir-a]Cl** bearing **L<sup>1</sup>** gave full conversion after 12 h, whereas **[Ir-b]Cl** with **L<sup>2</sup>** gave 82 % conversion under the same conditions (entries 1 and 2, **¡Error! No se encuentra el origen de la referencia.5** and SI Fig. 16). On the other hand, negligible conversions were obtained in the presence of either the free ligands or their Rh(III) derivatives (entries 3 to 6 in **¡Error! No se encuentra el origen de la referencia.5**).

To gain some insight into the reaction mechanism, several control experiments were performed. Thus, the oxidation of thioanisole was inhibited in the absence of light (entry 7 in **¡Error! No se encuentra el origen de la referencia.5**) or in the absence of the Ir(III) PS (entry 8, **¡Error! No se encuentra el origen de la referencia.5**), which

proved the Ir(III)-induced photocatalytic nature of the transformation. On the other hand, the low conversion obtained under nitrogen atmosphere (N<sub>2</sub> bubbling) supported the role of O<sub>2</sub> as the oxidant source (compare entries 2 and 9 in Table 5). Nonetheless, two mechanisms have been described in the literature for the photocatalytic oxidation of sulfides with O<sub>2</sub> under visible light.<sup>56</sup> The first one put forward the formation of <sup>1</sup>O<sub>2</sub>, by means of an ET process and its involvement as the actual oxidant, whereas the second involves the formation of superoxide via electron-transfer processes. In particular, in our photocatalytic oxidation system the participation of <sup>1</sup>O<sub>2</sub> was established by using NaN<sub>3</sub> (11 mM), a specific <sup>1</sup>O<sub>2</sub> scavenger, which dramatically inhibited the formation of the sulfoxide (entry 10, **iError! No se encuentra el origen de la referencia.**5). Moreover, the presence of a scavenger of the superoxide radical anion O<sub>2</sub><sup>•-</sup>, such as 1,4-benzoquinone, also led to a relative decrease in the conversion (entry 11, Table 5), suggesting that O<sub>2</sub><sup>•-</sup> could also contribute to some degree to the oxidation of organo-sulfides. Hence, both the energy transfer and electron transfer pathways seem to play a role in this reaction.<sup>57</sup>

Table 5. Catalyst screening and control experiments in the photo-oxidation of thioanisole under an O<sub>2</sub> atmosphere and blue-LED irradiation.

eq (1)

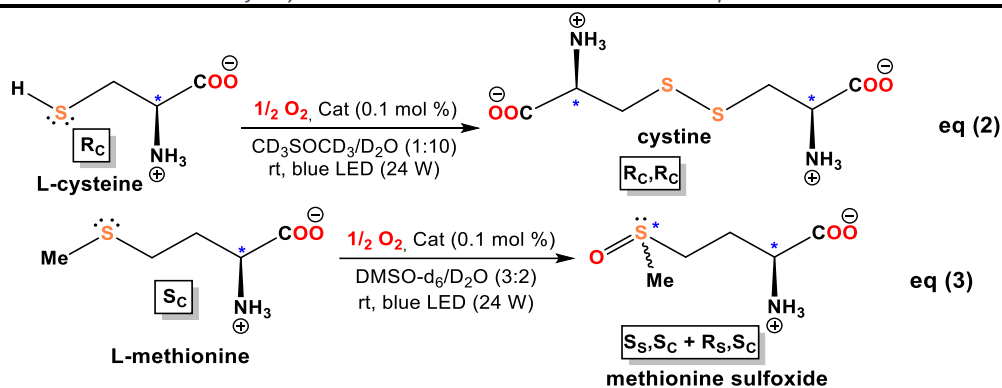
Entry	Conditions (Cat / Light / Gas) <sup>a</sup>	Conv (% , 12 h) <sup>b</sup>
1	[Ir-a]Cl / Yes / O <sub>2</sub>	100
2	[Ir-b]Cl / Yes / O <sub>2</sub>	82
3	[Rh-a]Cl / Yes / O <sub>2</sub>	1.1
4	[Rh-b]Cl / Yes / O <sub>2</sub>	1.3
5	L <sup>1</sup> / Yes / O <sub>2</sub>	6.7
6	L <sup>2</sup> / Yes / O <sub>2</sub>	3.3
7	[Ir-b]Cl / No / O <sub>2</sub>	0
8	No / Yes / O <sub>2</sub>	1.7
9	[Ir-b]Cl / Yes / N <sub>2</sub>	8.3
10	[Ir-b]Cl / Yes / O <sub>2</sub> / NaN <sub>3</sub> <sup>c</sup>	0.2
11	[Ir-b]Cl / Yes / O <sub>2</sub> / bzq <sup>d</sup>	23.6

<sup>a</sup>Thioanisole (10 mM), PS (10<sup>-2</sup> mM), see experimental part. <sup>b</sup>Conversion yields were determined by integration from <sup>1</sup>H NMR spectra of the crude mixtures as average values of two independent experiments. <sup>c</sup>NaN<sub>3</sub> (11 mM). <sup>d</sup>*p*-benzoquinone (bzq, 11 mM).

## 2.7.3. Photo-oxidation of L-cysteine and L-methionine

In addition, the photo-oxidation of L-cysteine (eq (2)) and L-methionine (eq (3)) in Table 6 were proved under similar conditions in the presence of **[Ir-a]Cl** and **[Ir-b]Cl**. Both PSs produced the disulfide derivative of L-cysteine (cystine) in a quantitative manner, whereas the control experiments in the absence of light or PS gave only partial conversions (Table 6, entries 1 to 4 and SI Fig. 17). The oxidation of L-methionine afforded methionine sulfoxide very efficiently with both PS, while the control experiments without PS or in the dark did not produce the sulfoxide (Table 6, entries 5 to 8 and SI Fig. 18). The irreversible oxidation of exposed L-cysteine and L-methionine residues in tissue enzymes can alter the weak interactions responsible for their secondary and tertiary structure leading to misfolding and consequently rendering these enzymes dysfunctional.<sup>26</sup> Hence, the aforementioned results suggest a possible mechanism for the potential photo-cytotoxic activity of the Ir(III) complexes **[Ir-a]Cl** and **[Ir-b]Cl**.

Table 6. Photo-oxidation of L-cysteine and L-methionine under an O<sub>2</sub> atmosphere and blue-LED irradiation.



Entry	Substrate	Conditions <sup>a</sup>	%Conv, 12 h (18 h) <sup>b</sup>
1	Cys	<b>[Ir-a]Cl</b> / Blue light / O <sub>2</sub>	> 99
2	Cys	<b>[Ir-b]Cl</b> / Blue light / O <sub>2</sub>	> 99
3	Cys	<b>[Ir-b]Cl</b> / No light / O <sub>2</sub>	45
4	Cys	No Cat / Blue light / O <sub>2</sub>	44
5	Met	<b>[Ir-a]Cl</b> / Blue light / O <sub>2</sub>	100
6	Met	<b>[Ir-b]Cl</b> / Blue light / O <sub>2</sub>	79 (100)
7	Met	<b>[Ir-b]Cl</b> / No light / O <sub>2</sub>	0
8	Met	No Cat / Blue light / O <sub>2</sub>	0

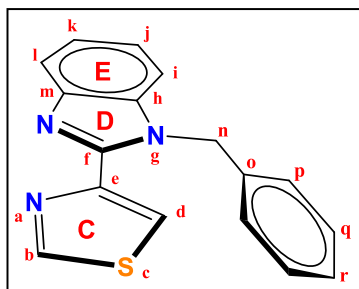
<sup>a</sup>L-cysteine/L-methionine (10 mM), PS (10<sup>-2</sup> mM, 0.1 mol %), see experimental part. <sup>b</sup>Conversion yields were determined by integration from <sup>1</sup>H NMR spectra of the crude mixtures as average values of two independent experiments.

### 3. Conclusions

Two pairs of Rh(III) and Ir(III) biscyclometalated complexes of general formula  $[M(ppy)_2(N^{\wedge}N)]Cl$  ( $M = Rh, Ir$ ) bearing  $N^{\wedge}N$  ligands based on the thiabendazole scaffold ( $L^1$  and  $L^2$ ) have been designed, synthesized and their potential as anticancer and PDT agents has been evaluated. In the dark, the Rh and Ir benzyl-derivatives are one order more cytotoxic against human lung carcinoma (A549) and human colon carcinoma (SW480) cell lines than cisplatin. Additional biological studies with the Rh and Ir benzyl-derivatives show that both complexes interfere with mitochondria functionality, causing the activation of apoptotic cell death pathways. Moreover, the **[Ir-a]Cl** and **[Ir-b]Cl** complexes exhibit enhanced cytotoxic activity after irradiation with visible blue light and photo-oxidation of sulphur-containing aminoacids was successfully demonstrated, suggesting that under irradiation conditions oxidative stress could be selectively promoted through a photocatalytic activity. On the contrary, the non-photoluminescent Rh complexes, which are unable to induce this photo-oxidation, do not exhibit enhanced cytotoxicity upon irradiation with neither UV nor visible light.

## 4. Synthesis and characterization

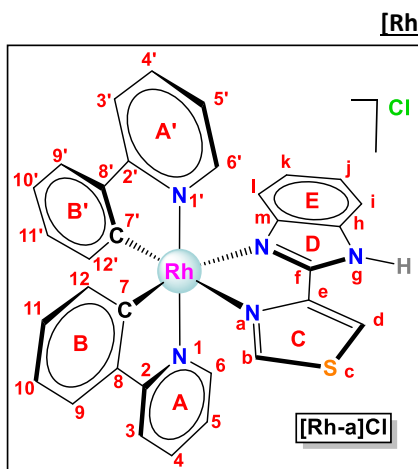
### 4.1. $L^2$



#### Ligand $L^2$

In a 100 mL Schlenk flask,  $K_2CO_3$  (0.500 g, 3.62 mmol) was added to a solution of 2-(4-Thiazolyl)benzimidazole (thiabendazole, TBZ) (0.450 g, 2.24 mmol) in DMF (7 mL). The mixture/suspension was stirred at room temperature for 30 minutes. Benzyl bromide (0.500 g, 3.62 mmol) was then added. The stirring was extended for 4 hours at room temperature. The solvent was removed under vacuum and the residue was redissolved in DMSO (5 mL). Water (10 mL) was added to precipitate a white solid that was filtrated and dried under vacuum. Yield: 0.425 g (1.46 mmol, 65%).  $M_r$  ( $C_{17}H_{13}N_3S$ ) = 291,37 g/mol.  $^1H$  NMR (400 MHz,  $CDCl_3$ , 25 °C)  $\delta$  8.89 (dd,  $J = 7.9, 2.0$  Hz, 1H,  $H^d$ ), 8.33 (dd,  $J = 15.2, 2.0$  Hz, 1H,  $H^b$ ), 7.86 (d,  $J = 7.8$  Hz, 1H,  $H^f$ ), 7.38 – 7.24 (m, 7H), 7.18 (d,  $J = 6.6$  Hz, 3H), 6.11 (s, 2H,  $H^n, H^o$ ) ppm. FT-IR (ATR,  $cm^{-1}$ ) selected bands: 3028 (w,  $\nu_{C-H}$ ), 1603 (s,  $\nu_{C=C + C-N}$ ), 1450 (s,  $\nu_{C=N}$ ), 1155 (m,  $\nu_{C-C}$ ), 1067-1027 (m,  $\delta_{C-Hip}$ ), 782 (m,  $\delta_{C-C}$ ), 749-737-724 (vs,  $\delta_{C-Hoop}$ ). Solubility: soluble in dimethyl sulfoxide, dichloromethane, methanol, acetone.

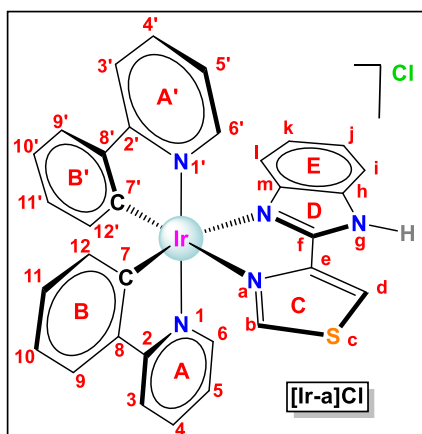
## 4.2. Rh(III) and Ir(III)-complexes



In a 100 mL Schlenk flask, previously purged with nitrogen, the ancillary ligand L<sup>1</sup> (0.0553 g, 0.273 mmol) was added to a solution of [Rh( $\mu$ -Cl)(ppy)<sub>2</sub>]<sub>2</sub> (0.1001 g, 0.093 mmol) in a mixture of dichloromethane (14 mL) / methanol (14 mL), and the mixture was stirred at 55 °C for 24 hours under a N<sub>2</sub> atmosphere. The resulting solution was concentrated to half the volume under vacuum and diethyl ether (15 mL) was added to precipitate a crude solid that was isolated by filtration and washed with diethyl ether (2×5 mL). Ethanol (3 mL) was added to the crude solid to remove soluble impurities and the resulting suspension was kept in the cooler for 16 hours, then the solid was recovered

by filtration. Finally, the product was washed with diethyl ether (2×5 mL) again and was dried under vacuum to produce a white powder. Yield: 0.0755 g (0.117 mmol, 52%). **M<sub>r</sub> (C<sub>32</sub>H<sub>23</sub>ClN<sub>5</sub>RhS)** = 647,98 g/mol. **Anal. Calcd for C<sub>32</sub>H<sub>23</sub>ClN<sub>5</sub>RhS(H<sub>2</sub>O)(CH<sub>3</sub>OH):** C 56.78; H 4.19; N 10.03; S 4.02; **Found:** C 56.82; H 4.28; N 9.69. **<sup>1</sup>H NMR (400 MHz, DMSO-d<sub>6</sub>, 25 °C)**  $\delta$  14.86 (s, 1H, H<sup>N-H</sup>), 8.96 (s, 1H, H<sup>d</sup>), 8.57 (d, J = 1.8 Hz, 1H, H<sup>b</sup>), 8.27 (d, J = 8.2 Hz, 1H, H<sup>3</sup>), 8.21 (d, J = 8.1 Hz, 1H, H<sup>3</sup>), 8.03 – 7.92 (m, 4H, H<sup>4</sup>, H<sup>4'</sup>, H<sup>9</sup>, H<sup>9'</sup>), 7.70 (d, J = 5.7 Hz, 2H, H<sup>6</sup>, H<sup>i</sup>), 7.66 (d, J = 8.2 Hz, 1H, H<sup>6</sup>), 7.28 – 7.17 (m, 3H, H<sup>5</sup>, H<sup>5'</sup>, H<sup>i</sup>), 7.14 (t, J = 7.5 Hz, 1H, H<sup>10</sup>), 7.08 (t, J = 7.4 Hz, 1H, H<sup>10</sup>), 7.02 – 6.91 (m, 3H, H<sup>11</sup>, H<sup>11'</sup>, H<sup>k</sup>), 6.33 (d, J = 7.7 Hz, 1H, H<sup>12</sup>), 6.29 (d, J = 7.6 Hz, 1H, H<sup>12</sup>), 6.11 (d, J = 8.3 Hz, 1H, H<sup>l</sup>) ppm. **<sup>13</sup>C{<sup>1</sup>H} NMR (101 MHz, DMSO-d<sub>6</sub>, 25 °C)**  $\delta$  164.16, 159.09, 149.18, 148.93, 144.28, 144.14, 138.68, 138.54, 132.58, 132.34, 129.54, 129.25, 124.57, 124.49, 123.77, 123.37, 122.97, 119.97, 119.73, 116.38, 113.47 ppm. **FT-IR (KBr, cm<sup>-1</sup>) selected bands:** 3374 (w,  $\nu_{\text{N-H associated}}$ ), 3060 (w,  $\nu_{\text{C-H}}$ ), 1605- 1577-1566 (m,  $\nu_{\text{C=C + C-N}}$ ), 1420 (w,  $\nu_{\text{C=N}}$ ), 1227 (m) 1152 (m,  $\nu_{\text{C-C}}$ ), 1061-1026 (m,  $\delta_{\text{C-Hip}}$ ), 795 (w,  $\delta_{\text{C-C}}$ ), 754-738 (vs,  $\delta_{\text{C-Hoop}}$ ). **HR ESI+ MS (DCM/DMSO, 4:1):** m/z<sub>exp</sub> (%) = 612.0730 (100) (m/z<sub>calcd</sub> [C<sub>32</sub>H<sub>23</sub>N<sub>5</sub>RhS]<sup>+</sup> = 612.0729). **Molar Conductivity (CH<sub>3</sub>CN):** 24 S·cm<sup>2</sup>·mol<sup>-1</sup>. **Solubility:** soluble in dichloromethane, methanol, dimethyl sulfoxide and acetone.

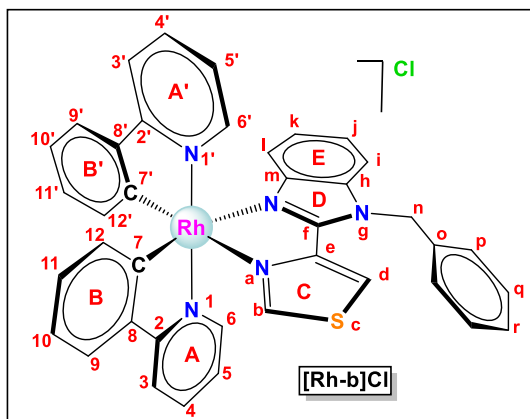
**[Ir(ppy)<sub>2</sub>(L<sup>1</sup>)]Cl: [Ir-a]Cl**



In a 100 mL Schlenk flask, previously purged with nitrogen, the ancillary ligand L<sup>1</sup> (0.0375 g, 0.186 mmol) was added to a solution of [Ir(μ-Cl)(ppy)<sub>2</sub>]<sub>2</sub> (0.100 g, 0.093 mmol) in a mixture of dichloromethane (8 mL) / methanol (10 mL), and the mixture was stirred at 60 °C for 24 hours under a N<sub>2</sub> atmosphere. The resulting solution was concentrated to half the volume under vacuum and diethyl ether (15 mL) was added to precipitate a crude solid that was isolated by filtration and washed with diethyl ether (2×5 mL). The product was dried under vacuum to produce a yellow powder. Yield: 0.110 g (0.153 mmol, 82%). **M<sub>r</sub>** (C<sub>32</sub>H<sub>23</sub>ClIrN<sub>5</sub>S) = 737.3069 g/mol.

**Anal. Calcd for C<sub>32</sub>H<sub>23</sub>N<sub>4</sub>SClIr·(CH<sub>2</sub>Cl<sub>2</sub>)<sub>0.7</sub>(H<sub>2</sub>O)<sub>0.8</sub>:** C 49.27; H 3.29; N 7.03; S 4.02; **Found:** C 49.32; H 3.33; N 7.11; S 4.19. **<sup>1</sup>H NMR (400 MHz, CDCl<sub>3</sub>, 25 °C)** δ 15.73 (s, 1H, H<sup>N-H</sup>), 10.09 (d, J = 1.3 Hz, 1H, H<sup>d</sup>), 8.13 (d, J = 2.1 Hz, 1H, H<sup>b</sup>), 7.89 (d, J = 8.7 Hz, 1H, H<sup>3</sup>), 7.85 (d, J = 7.8 Hz, 1H, H<sup>3</sup>), 7.78 (d, J = 8.2 Hz, 1H, H<sup>1</sup>), 7.76 – 7.70 (m, 2H, H<sup>4</sup>, H<sup>6</sup>), 7.70 – 7.62 (m, 3H, H<sup>4</sup>, H<sup>9</sup>, H<sup>9</sup>), 7.52 (d, J = 5.8 Hz, 1H, H<sup>6</sup>), 7.25 (t, J = 8.2 Hz, 1H, H<sup>l</sup>), 7.07 (t, J = 7.5 Hz, 1H, H<sup>10</sup>), 7.00 (t, J = 7.5 Hz, 1H, H<sup>10</sup>), 6.98 – 6.85 (m, 5H, H<sup>k</sup>, H<sup>5</sup>, H<sup>5</sup>, H<sup>11</sup>, H<sup>11</sup>), 6.45 (d, J = 7.9 Hz, 1H, H<sup>12</sup>), 6.40 (d, J = 7.3 Hz, 1H, H<sup>12</sup>), 6.16 (d, J = 8.3 Hz, 1H, H<sup>l</sup>) ppm. **<sup>13</sup>C{<sup>1</sup>H} NMR (101 MHz, CDCl<sub>3</sub>, 25 °C)** δ 168.4 (s, 1C, C<sup>2</sup>), 168.1 (s, 1C, C<sup>2</sup>), 155.1 (s, 1C, C<sup>b</sup>), 149.8 (s, 1C, C<sup>6</sup>), 148.6 (s, 1C, C<sup>7</sup>), 148.29 (s, 1C, C<sup>6</sup>), 148.25 (s, 1C, C<sup>6</sup>), 146.73 (s, 1C, C<sup>7</sup>), 146.65 (s, 1C, C<sup>f</sup>), 144.5 (s, 1C, C<sup>8</sup>), 144.3 (s, 1C, C<sup>8</sup>), 139.8 (s, 1C, C<sup>m</sup>), 137.9 (s, 1C, C<sup>4</sup>), 137.7 (s, 1C, C<sup>4</sup>), 134.9 (s, 1C, C<sup>h</sup>), 132.5 (s, 1C, C<sup>12</sup>), 132.3 (s, 1C, C<sup>12</sup>), 130.5 (s, 1C, C<sup>11</sup>), 130.1 (s, 1C, C<sup>11</sup>), 125.6 (s, 1C, C<sup>d</sup>), 125.1 (s, 1C, C<sup>j</sup>), 124.59 (s, 1C, C<sup>9</sup>), 124.56 (s, 1C, C<sup>9</sup>), 124.2 (s, 1C, C<sup>k</sup>), 123.2 (s, 1C, C<sup>5</sup>), 122.9 (s, 1C, C<sup>5</sup>), 122.5 (s, 1C, C<sup>10</sup>), 122.4 (s, 1C, C<sup>10</sup>), 119.3 (s, 2C, C<sup>3</sup>, C<sup>3</sup>), 117.1 (s, 1C, C<sup>l</sup>), 114.4 (s, 1C, C<sup>i</sup>) ppm. **FT-IR (KBr, cm<sup>-1</sup>) selected bands:** 3372 (w, ν<sub>N-H</sub>), 3034 (w, ν<sub>C=CH</sub>), 2618 (w, ν<sub>C-H</sub>), 1606-1579 (m, ν<sub>C=C+C-N</sub>), 1476 (s), 1455 (w, ν<sub>C=N</sub>), 1416 (s), 1267 (m), 1227 (m), 1161 (m, ν<sub>C-C</sub>), 1060-1030-1011-994 (m, δ<sub>C-Hip</sub>), 830 (m), 795 (w, δ<sub>C-C</sub>), 751 (vs, δ<sub>C-Hoop</sub>), 630 (m), 560 (m), 436-421 (m). **FAB+ MS (DCM/DMSO, 4:1):** m/z<sub>exp</sub> (%) = 703 (100) (m/z<sub>calcd</sub> [C<sub>32</sub>H<sub>23</sub>IrN<sub>5</sub>S]<sup>+</sup> = 703); m/z<sub>exp</sub> (%) = 502 (58) (m/z<sub>calcd</sub> [C<sub>22</sub>H<sub>16</sub>IrN<sub>2</sub>]<sup>+</sup> = 502). **Molar Conductivity (CH<sub>3</sub>CN):** 21 S·cm<sup>2</sup>·mol<sup>-1</sup>. **Solubility:** soluble in dichloromethane, chloroform and acetone. Partially soluble in methanol and insoluble in water.

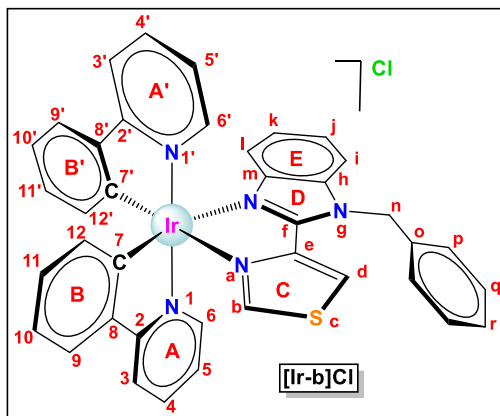


**[Rh(ppy)<sub>2</sub>(L<sup>2</sup>)]Cl: [Rh-b]Cl**

**[Rh-b]Cl** was synthesized from  $[\text{Rh}(\mu\text{-Cl})(\text{ppy})_2]_2$  (0.1002 g, 0.093 mmol) in a similar manner to that of **[Rh-a]Cl** except that the ancillary ligand was replaced with  $\text{L}^2$  (0.0817 g, 0.280 mmol). Yield: 0.131 g (0.178 mmol, 79%).  $M_r$  ( $\text{C}_{39}\text{H}_{29}\text{N}_5\text{RhSCl}$ ) = 738.121 g/mol. **Anal. Calcd for  $\text{C}_{39}\text{H}_{29}\text{RhN}_5\text{SCl} \cdot (\text{H}_2\text{O})_2$ :** C 60.51; H 4.30; N 9.05; **Found:** C 60.60; H 4.64; N 9.14.  $^1\text{H}$  NMR (400 MHz,  $\text{DMSO-d}_6$ , 25 °C)  $\delta$  8.91 (s, 1H, H<sup>d</sup>), 8.57 (s, 1H, H<sup>b</sup>), 8.30 (d,  $J = 7.9$  Hz, 1H, H<sup>3</sup>), 8.23 (d,  $J = 8.0$  Hz, 1H, H<sup>3'</sup>), 7.99 (dd,  $J = 15.6, 8.4$  Hz, 4H, H<sup>4</sup>, H<sup>4'</sup>, H<sup>9</sup>, H<sup>9'</sup>), 7.83 (dd,

$J = 12.4, 6.9$  Hz, 2H, H<sup>6</sup>, H<sup>6'</sup>), 7.66 (d,  $J = 5.4$  Hz, 1H, H<sup>6'</sup>), 7.37 – 7.21 (m, 6H, H<sup>q</sup>, H<sup>q'</sup>, H<sup>r</sup>, H<sup>r'</sup>, H<sup>5</sup>, H<sup>5'</sup>), 7.16 (t,  $J = 7.5$  Hz, 1H, H<sup>p</sup>), 7.12 – 6.93 (m, 6H, H<sup>p</sup>, H<sup>10</sup>, H<sup>10'</sup>, H<sup>k</sup>, H<sup>11</sup>, H<sup>11'</sup>), 6.35 (d,  $J = 7.7$  Hz, 1H, H<sup>12</sup>), 6.28 (d,  $J = 7.6$  Hz, 1H, H<sup>12'</sup>), 6.25 – 6.18 (m, 1H, H<sup>l</sup>), 6.15 (s, 1H, H<sup>n</sup>), 6.07 (d,  $J = 17.6$  Hz, 1H, H<sup>n</sup>) ppm.  $^{13}\text{C}\{^1\text{H}\}$  NMR (101 MHz,  $\text{DMSO-d}_6$ , 25 °C)  $\delta$  166.19 (d, 1C,  $^1J(^{103}\text{Rh}-^{13}\text{C}) = 33.0$  Hz, Rh-C), 165.58 (d, 1C  $^1J(^{103}\text{Rh}-^{13}\text{C}) = 33.8$  Hz, Rh-C), 164.17 (d,  $J = 1.7$  Hz), 164.13 (d,  $J = 1.7$  Hz), 158.72, 149.24, 148.80, 147.01, 144.32, 144.03, 142.16, 139.08, 138.83, 138.72, 136.25, 135.16, 132.64, 132.33, 129.65, 129.37, 129.04 (s, 2C, C<sup>o</sup> N-Bn), 127.89, 126.04 (s, 2C, C<sup>m</sup> N-Bn), 125.54, 125.12, 124.70, 124.63, 124.47, 123.83, 123.68, 123.15, 123.08, 120.11, 119.87, 116.98, 112.28, 47.64 (s, 1C, N-CH<sub>2</sub>-Ph) ppm. **FT-IR (ATR, cm<sup>-1</sup>) selected bands:** 3031 (w,  $\nu_{\text{C-H}}$ ), 2969 (w,  $\nu_{\text{C-H}}$ ), 1605 (s,  $\nu_{\text{C=C+C-N}}$ ), 1580 (s,  $\nu_{\text{C=C+C-N}}$ ), 1559 (s,  $\nu_{\text{C=C+C-N}}$ ), 1428 (s,  $\nu_{\text{C=N}}$ ), 1159 (m,  $\nu_{\text{C-C}}$ ), 1062 (m,  $\delta_{\text{C-Hip}}$ ), 1030 (m,  $\delta_{\text{C-Hip}}$ ), 792 (m,  $\delta_{\text{C-C}}$ ), 755 (vs,  $\delta_{\text{C-Hoop}}$ ), 728 (vs,  $\delta_{\text{C-Hoop}}$ ). **HR ESI+ MS (DCM/DMSO, 4:1):**  $m/z_{\text{exp}}$  (%) = 702.1185 (100) ( $m/z_{\text{calcd}}$  [ $\text{C}_{39}\text{H}_{29}\text{N}_5\text{RhS}$ ]<sup>+</sup> = 702.1199). **Molar Conductivity (CH<sub>3</sub>CN):** 133.6 S·cm<sup>2</sup>·mol<sup>-1</sup>. **Solubility:** soluble in dimethyl sulfoxide, dichloromethane, methanol, acetone.

**[Ir(ppy)<sub>2</sub>(L<sup>2</sup>)]Cl: [Ir-b]Cl**



**[Ir-b]Cl** was synthesized from [Ir( $\mu$ -Cl)(ppy)<sub>2</sub>]<sub>2</sub> (0.100 g, 0.093 mmol) in a similar manner to that of **[Ir-a]Cl** except that the ancillary ligand was replaced with L<sup>2</sup> (0.068 g, 0.233 mmol). Yield: 0.123 g (0.149 mmol, 80%). **M<sub>r</sub>** (C<sub>39</sub>H<sub>29</sub>IrN<sub>5</sub>SCl) = 827.416 g/mol. **Anal.** **Calcd for C<sub>39</sub>H<sub>29</sub>IrN<sub>5</sub>SCl·(H<sub>2</sub>O)<sub>2</sub>:** C 54.25; H 3.85; N 8.11; **Found:** C 53.93; H 3.82; N 8.10. **<sup>1</sup>H NMR (400 MHz, DMSO-d<sub>6</sub>, 25 °C)**  $\delta$  8.93 (d, J = 1.7 Hz, 1H, H<sup>d</sup>), 8.48 (d, J = 1.7 Hz, 1H, H<sup>b</sup>), 8.28 (d, J = 8.4 Hz, 1H, H<sup>3</sup>), 8.20 (d, J = 8.4 Hz, 1H, H<sup>3'</sup>), 8.04 – 7.79 (m, 6H, H<sup>4</sup>, H<sup>4'</sup>, H<sup>9</sup>, H<sup>9'</sup>, H<sup>6</sup>, H<sup>1</sup>), 7.70 (d, J = 5.9 Hz, 1H, H<sup>6'</sup>), 7.42 – 7.26 (m,

4H, H<sup>q</sup>, H<sup>q'</sup>, H<sup>r</sup>, H<sup>l</sup>), 7.19 (t, J = 6.6 Hz, 2H, H<sup>5</sup>, H<sup>5'</sup>), 7.14 – 6.98 (m, 5H, H<sup>p</sup>, H<sup>p'</sup>, H<sup>10</sup>, H<sup>10'</sup>, H<sup>k</sup>), 6.98 – 6.82 (m, 2H, H<sup>11</sup>, H<sup>11'</sup>), 6.36 (d, J = 7.6 Hz, 1H, H<sup>12</sup>), 6.27 (d, J = 7.6 Hz, 1H, H<sup>12'</sup>), 6.24 – 6.15 (m, 2H, H<sup>n</sup>, H<sup>l</sup>), 6.10 (d, J = 17.5 Hz, 1H, H<sup>n</sup>) ppm. **<sup>13</sup>C{<sup>1</sup>H} NMR (101 MHz, CD<sub>3</sub>SOCD<sub>3</sub>, 25 °C)**  $\delta$  167.11, 166.99, 158.83, 149.44, 148.83, 148.44, 148.35, 147.29, 144.61, 144.43, 142.83, 138.83, 138.69, 138.55, 135.95, 135.10, 131.80, 131.44, 129.91, 129.59, 129.13 (s, 2C, C<sup>o</sup> N-Bn), 128.03, 126.68, 126.14 (s, 2C, C<sup>m</sup> N-Bn), 125.44, 124.91, 124.83, 124.77, 123.86, 123.64, 122.13, 122.08, 119.93, 119.59, 116.84, 112.51, 47.75 (s, 1C, N-CH<sub>2</sub>-Ph) ppm. **FT-IR (ATR, cm<sup>-1</sup>) selected bands:** 3031 (w,  $\nu_{C-H}$ ), 2969 (w,  $\nu_{C-H}$ ), 1605 (s,  $\nu_{C=C+C-N}$ ), 1580 (s,  $\nu_{C=C+C-N}$ ), 1559 (s,  $\nu_{C=C+C-N}$ ), 1428 (s,  $\nu_{C=N}$ ), 1159 (m,  $\nu_{C-C}$ ), 1062-1030 (m,  $\delta_{C-Hip}$ ), 792 (m,  $\delta_{C-C}$ ), 755-728 (vs,  $\delta_{C-Hoop}$ ). **HR ESI+ MS (DCM/DMSO, 4:1):** m/z<sub>exp</sub> (%) = 792.1777 (100) (m/z<sub>calcd</sub> [C<sub>39</sub>H<sub>29</sub>IrN<sub>5</sub>S]<sup>+</sup> = 792.1773). **Molar Conductivity (CH<sub>3</sub>CN):** 132.5 S·cm<sup>2</sup>·mol<sup>-1</sup>. **Solubility:** soluble in dimethyl sulfoxide, dichloromethane, methanol, acetone.

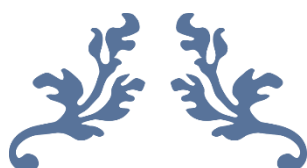
## Bibliography

1. N. Cutillas, G.S. Yellol, C. de Haro, C. Vicente, V. Rodriguez, and J. Ruiz, Anticancer cyclometalated complexes of platinum group metals and gold., *Coord. Chem. Rev.*, 2013, **257**, 2784–2797.
2. R.A. Cairns, I.S. Harris, and T.W. Mak, Regulation of cancer cell metabolism., *Nat. Rev. Cancer*, 2011, **11**, 85–95.
3. R.J. De Berardinis, and N.S. Chandel, Fundamentals of cancer metabolism., *Sci. Adv.*, 2016, **2**, 1–18.
4. S. Fulda, L. Galluzzi, and G. Kroemer, Targeting mitochondria for cancer therapy., *Nat. Rev. Drug Discov.*, 2010, **9**, 447–464.
5. S.E. Weinberg, and N.S. Chandel, Targeting mitochondria metabolism for cancer therapy., *Nat. Chem., Biol.*, 2015, **11**, 9–15.
6. S.D. van, V. Mashayekhi, S. Oliveira, B.H.S. de, D.J. Robinson, and S. Oliveira, Oncologic Photodynamic Therapy: Basic Principles, Current Clinical Status and Future Directions, *Cancers (Basel)*, 2017, **9**.
7. J.-J. Cao, C.-P. Tan, M.-H. Chen, N. Wu, D.-Y. Yao, X.-G. Liu, L.-N. Ji, and Z.-W. Mao, Targeting cancer cell metabolism with mitochondria-immobilized phosphorescent cyclometalated iridium(III) complexes., *Chem. Sci.*, 2017, **8**, 631–640.
8. L.K. McKenzie, I. V Sazanovich, E. Baggaley, M. Bonneau, V. Guerchais, J.A.G. Williams, J.A. Weinstein, and H.E. Bryant, Metal Complexes for Two-Photon Photodynamic Therapy: A Cyclometallated Iridium Complex Induces Two-Photon Photosensitization of Cancer Cells under Near-IR Light, *Chem. - A Eur. J.*, 2017, **23**, 234–238.
9. W. Lv, Z. Zhang, K.Y. Zhang, H. Yang, S. Liu, A. Xu, S. Guo, Q. Zhao, and W. Huang, A Mitochondria-Targeted Photosensitizer Showing Improved Photodynamic Therapy Effects Under Hypoxia., *Angew. Chemie, Int. Ed.*, 2016, **55**, 9947–9951.
10. M.-H. Chen, F.-X. Wang, J.-J. Cao, C.-P. Tan, L.-N. Ji, Z.-W. and Mao, Light-Up Mitophagy in Live Cells with Dual-Functional Theranostic Phosphorescent Iridium(III) Complexes., *ACS Appl. Mater. Interfaces.*, 2017, **9**, 13304–13314.
11. J. Liu, C. Jin, B. Yuan, X. Liu, Y. Chen, L. Ji, and H. Chao, Selectively lighting up two-photon photodynamic activity in mitochondria with AIE-active iridium(III) complexes., *Chem. Commun.*, 2017, **53**, 2052–2055.
12. C. Jin, J. Liu, Y. Chen, R. Guan, C. Ouyang, Y. Zhu, L. Ji, and H. Chao, Cyclometalated Iridium(III) Complexes as AIE Phosphorescent Probes for Real-Time Monitoring of Mitophagy in Living Cells., *Sci. Rep.*, 2016, **6**, 22039.
13. L. He, C.-P. Tan, R.-R. Ye, Y.-Z. Zhao, Y.-H. Liu, Q. Zhao, L.-N. Ji, and Z.-W. Mao, Theranostic Iridium(III) Complexes as One- and Two-Photon Phosphorescent Trackers to Monitor Autophagic Lysosomes., *Angew. Chemie, Int. Ed.*, 2014, **53**, 12137–12141.
14. L. He, Y. Li, C.-P. Tan, R.-R. Ye, M.-H. Chen, J.-J. Cao, L.-N. Ji, and Z.-W. Mao, Cyclometalated iridium(III) complexes as lysosome-targeted photodynamic anticancer and real-time tracking agents., *Chem. Sci.*, 2015, **6**, 5409–5418.
15. F.-X. Wang, M.-H. Chen, Y.-N. Lin, H. Zhang, C.-P. Tan, L.-N. Ji, and Z.-W. Mao, Dual Functions of Cyclometalated Iridium(III) Complexes: Anti-Metastasis and Lysosome-Damaged Photodynamic Therapy., *ACS Appl. Mater. Interfaces*, 2017, **9**, 42471–42481.

16. R. Cao, J. Jia, X. Ma, M. Zhou, and H. Fei, Membrane Localized Iridium(III) Complex Induces Endoplasmic Reticulum Stress and Mitochondria-Mediated Apoptosis in Human Cancer Cells., *J. Med. Chem.*, 2013, **56**, 3636–3644.
17. S. Mandal, D.K. Poria, R. Ghosh, P.S. Ray, and P. Gupta, Development of a cyclometalated iridium complex with specific intramolecular hydrogen-bonding that acts as a fluorescent marker for the endoplasmic reticulum and causes photoinduced cell death., *Dalt. Trans.*, 2014, **43**, 17463–17474.
18. V. Novohradsky, A. Zamora, A. Gandioso, V. Brabec, J. Ruiz, and V. Marchan, Somatostatin receptor-targeted organometallic iridium(III) complexes as novel theranostic agents., *Chem. Commun.*, 2017, **53**, 5523–5526.
19. X. Tian, Y. Zhu, M. Zhang, L. Luo, J. Wu, H. Zhou, L. Guan, G. Battaglia, and Y. Tian, Localization matters: a nuclear targeting two-photon absorption iridium complex in photodynamic therapy., *Chem. Commun.*, 2017, **53**, 3303–3306.
20. C. Li, M. Yu, Y. Sun, Y. Wu, C. Huang, and F. Li, A Nonemissive Iridium(III) Complex That Specifically Lights-Up the Nuclei of Living Cells., *J. Am. Chem. Soc.*, 2011, **133**, 11231–11239.
21. C.-H. Leung, H.-J. Zhong, D.S.-H. Chan, and D.-L. Ma, Bioactive iridium and rhodium complexes as therapeutic agents., *Coord. Chem. Rev.*, 2013, **257**, 1764–1776.
22. Z. Huang, H. Xu, A.D. Meyers, A.I. Musani, L. Wang, R. Tagg, A.B. Barqawi, and Y.K. Chen, Photodynamic therapy for treatment of solid tumors-potential and technical challenges., *Technol. Cancer Res. Treat.*, 2008, **7**, 309–320.
23. A. Zamora, G. Viguera, V. Rodriguez, M.D. Santana, and J. Ruiz, Cyclometalated iridium(III) luminescent complexes in therapy and phototherapy., *Coord. Chem. Rev.*, 2018, **360**, 34–76.
24. W. Lin, Q. Zhao, H. Sun, K.Y. Zhang, H. Yang, Q. Yu, X. Zhou, S. Guo, S. Liu, and W. Huang, An Electrochromic Phosphorescent Iridium(III) Complex for Information Recording, Encryption, and Decryption., *Adv. Opt. Mater.*, 2015, **3**, 368–375.
25. R.D. Costa, E. Orti, H.J. Bolink, F. Monti, G. Accorsi, and N. Armaroli, Luminescent Ionic Transition-Metal Complexes for Light-Emitting Electrochemical Cells., *Angew. Chemie, Int. Ed.*, 2012, **51**, 8178–8211.
26. J.S. Nam, M.-G. Kang, J. Kang, S.-Y. Park, S.J.C. Lee, H.-T. Kim, J.K. Seo, O.-H. Kwon, M.H. Lim, H.-W. Rhee, and T.-H. Kwon, Endoplasmic Reticulum-Localized Iridium(III) Complexes as Efficient Photodynamic Therapy Agents via Protein Modifications., *J. Am. Chem. Soc.*, 2016, **138**, 10968–10977.
27. J. Pracharova, G. Viguera, V. Novohradsky, N. Cutillas, C. Janiak, H. Kosthunova, J. Kasparkova, J. Ruiz, and V. Brabec, Exploring the Effect of Polypyridyl Ligands on the Anticancer Activity of Phosphorescent Iridium(III) Complexes: From Proteosynthesis Inhibitors to Photodynamic Therapy Agents., *Chem. - A Eur. J.*, 2018, **24**, 1–14.
28. L. He, J. Qiao, L. Duan, G. Dong, D. Zhang, L. Wang, and Y. Qiu, Toward Highly Efficient Solid-State White Light-Emitting Electrochemical Cells: Blue-Green to Red Emitting Cationic Iridium Complexes with Imidazole-Type Ancillary Ligands., *Adv. Funct. Mater.*, 2009, **19**, 2950–2960.
29. K.K.-W. Lo, A.W.-T. Choi, and W.H.-T. Law, Applications of luminescent inorganic and organometallic transition metal complexes as biomolecular and cellular probes., *Dalt. Trans.*, 2012, **41**, 6021–6047.

30. Q. Cao, D.S. Bailie, R. Fu, and M.J. Muldoon, Cationic palladium(II) complexes as catalysts for the oxidation of terminal olefins to methyl ketones using hydrogen peroxide., *Green Chem.*, 2015, **17**, 2750–2757.
31. W.-K. Huang, C.-W. Cheng, S.-M. Chang, Y.-P. Lee, and E.W.-G. Diau, Synthesis and electron-transfer properties of benzimidazole-functionalized ruthenium complexes for highly efficient dye-sensitized solar cells., *Chem. Commun.*, 2010, **46**, 8992–8994.
32. M. Nonoyama, [Benzo[h]quinolin-10-yl-N]iridium(III) complexes., *Bull. Chem. Soc. Jpn.*, 1974, **47**, 767–768.
33. E. Baranoff, B.F.E. Curchod, J. Frey, R. Scopelliti, F. Kessler, I. Tavernelli, U. Rothlisberger, M. Gratzel, and M.K. Nazeeruddin, Acid-induced degradation of phosphorescent dopants for OLEDs and its application to the synthesis of tris-heteroleptic iridium(III) bis-cyclometalated complexes., *Inorg. Chem.*, 2012, **51**, 215–224.
34. K.S. Bejoymohandas, T.M. George, S. Bhattacharya, S. Natarajan, and M.L.P. Reddy, AIPE-active green phosphorescent iridium(III) complex impregnated test strips for the vapor-phase detection of 2,4,6-trinitrotoluene (TNT)., *J. Mater. Chem. C Mater. Opt. Electron. Devices.*, 2014, **2**, 515–523.
35. H. Sun, S. Liu, W. Lin, K.Y. Zhang, W. Lv, X. Huang, F. Huo, H. Yang, G. Jenkins, Q. Zhao, and W. Huang, Smart responsive phosphorescent materials for data recording and security protection., *Nat. Commun.*, 2014, **5**, 4601/1-4601/9.
36. G.E. Schneider, H.J. Bolink, E.C. Constable, C.D. Ertl, C.E. Housecroft, A. Pertegas, J.A. Zampese, A. Kanitz, F. Kessler, and S.B. Meier, Chloride ion impact on materials for light-emitting electrochemical cells., *Dalt. Trans.*, 2014, **43**, 1961–1964.
37. A. Maity, L.Q. Le, Z. Zhu, J. Bao, and T.S. Teets, Steric and Electronic Influence of Aryl Isocyanides on the Properties of Iridium(III) Cyclometalates., *Inorg. Chem.*, 2016, **55**, 2299–2308.
38. E. Baranoff, and B.F.E. Curchod, Flrpic: archetypal blue phosphorescent emitter for electroluminescence., *Dalt. Trans.*, 2015, **44**, 8318–8329.
39. H. Cao, H. Sun, Y. Yin, X. Wen, G. Shan, Z. Su, R. Zhong, W. Xie, P. Li, and D. Zhu, Iridium(III) complexes adopting 1,2-diphenyl-1H-benzimidazole ligands for highly efficient organic light-emitting diodes with low efficiency roll-off and non-doped feature., *J. Mater. Chem. C Mater. Opt. Electron. Devices*, 2014, **2**, 2150–2159.
40. R.D. Costa, E. Orti, H.J. Bolink, S. Graber, S. Schaffner, M. Neuburger, C.E. Housecroft, and E.C. Constable, Archetype Cationic Iridium Complexes and Their Use in Solid-State Light-Emitting Electrochemical Cells., *Adv. Funct. Mater.*, 2009, **19**, 3456–3463.
41. A.F. Henwood, A.K. Bansal, D.B. Cordes, A.M.Z. Slawin, I.D.W. Samuel, and E. Zysman-Colman, Solubilised bright blue-emitting iridium complexes for solution processed OLEDs., *J. Mater. Chem. C Mater. Opt. Electron. Devices*, 2016, **4**, 3726–3737.
42. M. Martinez-Alonso, J. Cerda, C. Momblona, A. Pertegas, J.M. Junquera-Hernandez, A. Heras, A.M. Rodriguez, G. Espino, H. Bolink, and E. Orti, Highly Stable and Efficient Light-Emitting Electrochemical Cells Based on Cationic Iridium Complexes Bearing Arylazole Ancillary Ligands., *Inorg. Chem.*, 2017, **56**, 10298–10310.

43. X. Li, X. Tong, Y. Yin, H. Yan, C. Lu, W. Huang, and Q. Zhao, Using highly emissive and environmentally sensitive o-carborane-functionalized metallophosphors to monitor mitochondrial polarity., *Chem. Sci.*, 2017, **8**, 5930–5940.
44. G.I. Shapiro, and J.W. Harper, Anticancer drug targets: cell cycle and checkpoint control., *J. Clin. Invest.*, 1999, **104**, 1645–1653.
45. E.R. Jamieson, and S.J. Lippard, Structure, recognition, and processing of cisplatin-DNA adducts., *Chem. Rev.*, 1999, **99**, 2467–2498.
46. S. Dasari, and P. Bernard Tchounwou, Cisplatin in cancer therapy: Molecular mechanisms of action., *Eur. J. Pharmacol.*, 2014, **740**, 364–378.
47. S.P. Wisnovsky, J.J. Wilson, R.J. Radford, M.P. Pereira, M.R. Chan, R.R. Laposa, S.J. Lippard, and S.O. Kelley, Targeting Mitochondrial DNA with a Platinum-Based Anticancer Agent., *Chem. Biol.*, 2013, **20**, 1323–1328.
48. Y. Li, C.-P. Tan, W. Zhang, L. He, L.-N. Ji, and Z.-W. Mao, Phosphorescent iridium(III)-bis-N-heterocyclic carbene complexes as mitochondria-targeted theranostic and photodynamic anticancer agents, *Biomaterials*, 2015, **39**, 95–104.
49. S.A. Susin, H.K. Lorenzo, N. Zamzami, I. Marzo, B.E. Snow, G.M. Brothers, J. Mangion, E. Jacotot, P. Costantini, M. Loeffler, N. Larochette, D.R. Goodlett, R. Aebersold, D.P. Siderovski, J.M. Penninger, and G. Kroemer, Molecular characterization of mitochondrial apoptosis-inducing factor., *Nature*, 1999, **397**, 441–446.
50. D. Trachootham, J. Alexandre, and P. Huang, Targeting cancer cells by ROS-mediated mechanisms: a radical therapeutic approach?., *Nat. Rev. Drug Discov.*, 2009, **8**, 579–591.
51. A. Wojtala, M. Bonora, D. Malinska, P. Pinton, J. Duszynski, and M.R. Wieckowski, Methods to monitor ROS production by fluorescence microscopy and fluorometry., *Methods Enzymol.*, 2014, **542**, 243–262.
52. M. Ott, B. Zhivotovsky, and S. Orrenius, Role of cardiolipin in cytochrome c release from mitochondria., *Cell Death Differ.*, 2007, **14**, 1243–1247.
53. P. Kaewsuya, N.D. Danielson, and D. Ekhterae, Fluorescent determination of cardiolipin using 10-N-nonyl acridine orange., *Anal. Bioanal. Chem.*, 2007, **387**, 2775–2782.
54. N. Zamzami, C. Maise, D. Metivier, and G. Kroemer, Measurement of membrane permeability and the permeability transition of mitochondria., *Methods Cell Biol.*, 2007, **80**, 327–340.
55. A. Nakagawa, Y. Hisamatsu, S. Moromizato, M. Kohno, and S. Aoki, Synthesis and Photochemical Properties of pH Responsive Tris-Cyclometalated Iridium(III) Complexes That Contain a Pyridine Ring on the 2-Phenylpyridine Ligand., *Inorg. Chem.*, 2014, **53**, 409–422.
56. A. Casado-Sanchez, R. Gomez-Ballesteros, F. Tato, F.J. Soriano, G. Pascual-Coca, S. Cabrera, and J. Aleman, Pt(II) coordination complexes as visible light photocatalysts for the oxidation of sulfides using batch and flow processes., *Chem. Commun. (Cambridge, United Kingdom)*, 2016, **52**, 9137–9140.
57. J. Dad'ova, E. Svobodova, M. Sikorski, B. Koenig, and R. Cibulka, Photooxidation of Sulfides to Sulfoxides Mediated by Tetra-O-Acetylriboflavin and Visible Light., *ChemCatChem.*, 2012, **4**, 620–623.



---

***Chapter 2. Photodynamic Therapy  
with Mitochondria-targeted  
Biscyclometalated Ir(III) Complexes.  
Multi-action Mechanism and Strong  
influence of the Cyclometalating  
Ligand***

---







## Authorship Statement

This chapter is the result of a collaboration with Elisenda Zafon, Sílvia Barrabés, and Anna Massaguer from the University of Girona (UdG), so the biological experiments were made by them. I have accomplished the following sections: Synthesis and general characterization, X-ray diffraction, electrochemical measurements, photophysical properties,  $^1\text{O}_2$  generation, and photocatalytic oxidation of NADH.

This work can be found published as: E. Zafon, I. Echevarría, S. Barrabés, B. R. Manzano, F. A. Jalón, A. M. Rodríguez, A. Massaguer, and G. Espino, Photodynamic therapy with mitochondria-targeted biscyclometalated Ir (III) complexes. Multi-action mechanism and strong influence of the cyclometalating ligand, *Dalton Trans.*, 2022, **51**, 111-128.

## 0. Abstract

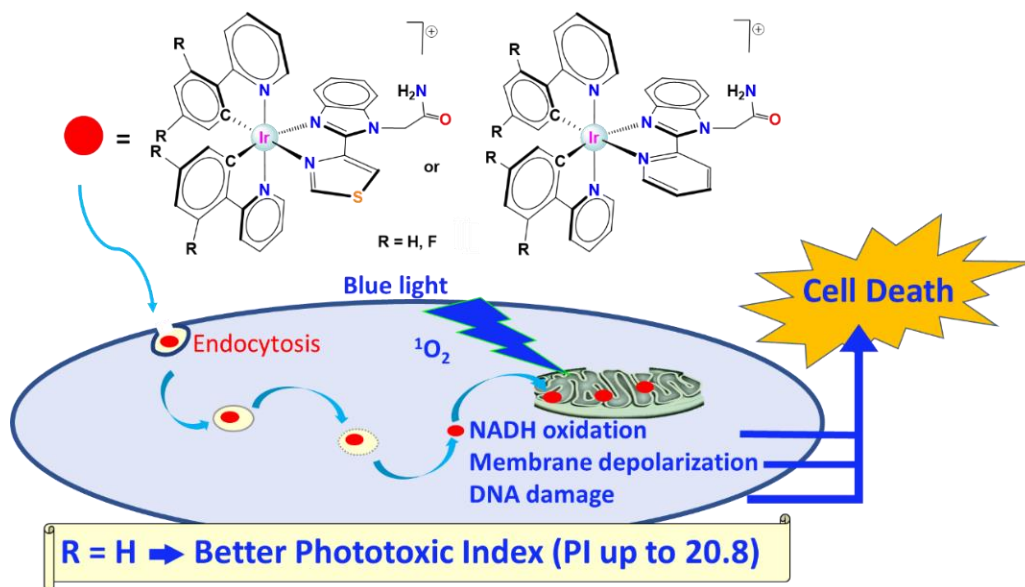


Fig.1. Schematic representation of the photo-biological pathway of action of the complexes.

Photodynamic therapy is an alternative to classical chemotherapy due to its potential to reduce side effects by a controlled activation of a photosensitizer through local irradiation with light. The photosensitizer then interacts with oxygen and generates reactive oxygen species. In this context, iridium biscyclometalated complexes are very promising photosensitizers due to their exceptional photophysical properties and their ability to target mitochondria. Four Ir(III) biscyclometalated complexes of formula  $[\text{Ir}(\text{C}^{\wedge}\text{N})_2(\text{N}^{\wedge}\text{N}')]\text{Cl}$ , where  $\text{N}^{\wedge}\text{N}'$  is a ligand containing a benzimidazolyl fragment, have been synthesized and characterized.

The C<sup>N</sup> ligands were 2-phenylpyridinate (ppy) and 2-(2,4-difluorophenyl)pyridinate (dfppy). The complexes exhibited high photostability. The electrochemical and photophysical properties were modulated by both the cyclometalating and the ancillary ligands. The dfppy derivatives yielded the highest emission energy values, quantum yields of phosphorescence and excited state lifetimes. All these complexes generated <sup>1</sup>O<sub>2</sub> in aerated solutions upon irradiation. Biological studies revealed that these PSs have a moderate cytotoxicity in the dark against different human cancer cell lines: prostate (PC-3), colon (CACO-2) and melanoma (SK-MEL-28), and against non-malignant fibroblasts (CCD-18Co). However, derivatives with ppy ligands (**[1a]Cl**, **[2a]Cl**) yielded a relevant photodynamic activity upon light irradiation (450 nm, 24.1 J·cm<sup>-2</sup>), with phototoxicity indexes (IC<sub>50,dark</sub>/IC<sub>50,light</sub>) of 20.8 and 17.3, respectively, achieved in PC-3 cells. Mechanistic studies showed that these complexes are taken up by the cells through endocytosis and preferentially accumulate in mitochondria. Upon photoactivation, the complexes induced mitochondrial membrane depolarization and presumably mt-DNA damage, thus triggering cell death, mainly by apoptosis. Complex **[1a]Cl** is also able to oxidize NADH. This mitochondria-targeted photodynamic mechanism greatly inhibited the reproductive capacity of cancer cells and provides a valuable alternative to traditional chemotherapy for the controlled treatment of cancer.

## 1. Introduction

Cancer has a great incidence in modern societies. One of the most successful strategies in the battle against cancer is chemotherapy. Metal complexes with antiproliferative activity constitute a proven alternative to conventional organic drugs. Although platinum compounds are widely used in this context, they generally exhibit a number of side effects, a limited range of activity and a certain degree of tumour resistance.<sup>1,2</sup> Consequently, numerous research groups have devoted a great deal of effort to the development of new complexes of metal cations other than Pt.<sup>3,4</sup> Furthermore, different strategies are being developed with the aim of reducing side effects and these include the use of targeted drug delivery to cancer cells<sup>5,6</sup> or the use of prodrugs that are activated in the tumour environment. In the context of the latter approach, photodynamic therapy<sup>7,8,9,10,11</sup> (PDT) is a very promising alternative that provides spatial and temporal control over the activation of a prodrug. PDT refers to the “damage or destruction of living tissue by the combined action of visible light, a photosensitizer and oxygen”.<sup>12</sup> Irradiation of the photosensitizer (PS) leads to the promotion of the latter from its ground state (S<sub>0</sub>) to its singlet excited state (S<sub>1</sub>). From this unstable and typically short-lived state, the PS can either return to its ground state by emitting light (fluorescence) or heat, or either can populate the triplet excited state T<sub>1</sub> by a process

called intersystem crossing (ISC is favoured by second or third row transition metals). The activated PS in the  $T_1$  state can produce chemical changes in nearby molecules by two competing pathways: (i) Type-I, where the transfer of electrons to oxygen or other molecules leads to the formation of a radical anion. These radicals will react with molecular oxygen to produce ROS (reactive oxygen species); (ii) Type-II, which involves an energy transfer process from the PS  $T_1$  excited state to the oxygen ground state ( $^3O_2$ ), which is transformed into the very reactive  $^1O_2$ . Both type-I and type-II photochemical reactions usually occur in parallel, and the ratio between them depends on parameters such as the photosensitizer features and the oxygen concentration.<sup>13</sup>

PDT has been used for cancer treatment since the 1990s using Photofrin® and a significant number of porphyrinoid and non-porphyrinoid PSs have been reported as potential PDT agents. Indeed, some of these compounds have been approved by the FDA.<sup>14</sup> However, their clinical use is limited by the short lifetime of their excited-state.<sup>15</sup> An interesting alternative to these organic PSs for PDT are complexes based on transition metals.<sup>16,17</sup> As stated above, systems that contain heavy atoms exhibit enhanced ISC and a favourably long lifetime of their triplet MLCT (metal to ligand charge transfer) excited state, both of which may enhance  $^1O_2$  production. In addition, these materials offer a bathochromic shift in the absorption spectra with respect to organic molecules and this favours a deeper tissue penetration ability of the corresponding light stimulus. More specifically, transition metal complexes with  $d^3$  and  $d^6$  electronic configurations are particularly promising due to the advantageous photophysical properties and their relative low lability.<sup>18</sup> A large number of metal complexes screened as PSs are octahedral polypyridine Ru(II) complexes<sup>19,20</sup> and, in fact, a Ru(II) polypyridyl complex reported by McFarland (TLD-1433) has entered clinical trials.<sup>21</sup> Octahedral cyclometalated iridium(III) complexes are especially attractive in this context due to their exceptional photophysical properties and photostability.<sup>15</sup> Such complexes have been tested in cellular imaging as biomolecular probes,<sup>22,23,24,25</sup> as anticancer agents and as PDT photosensitizers.<sup>26,27,28</sup> The cellular targets of Ir(III) PSs<sup>28</sup> include lysosomes,<sup>29,30,31</sup> the endoplasmic reticulum (ER),<sup>32</sup> the nucleus, some cellular proteins<sup>33</sup> and very frequently, mitochondria.<sup>34,35,36,37</sup> The localization in mitochondria arises from the negative potential of mitochondrial membranes and the cationic nature of these PSs and it is also favoured by a lipophilic nature of the complex.<sup>38,39</sup>

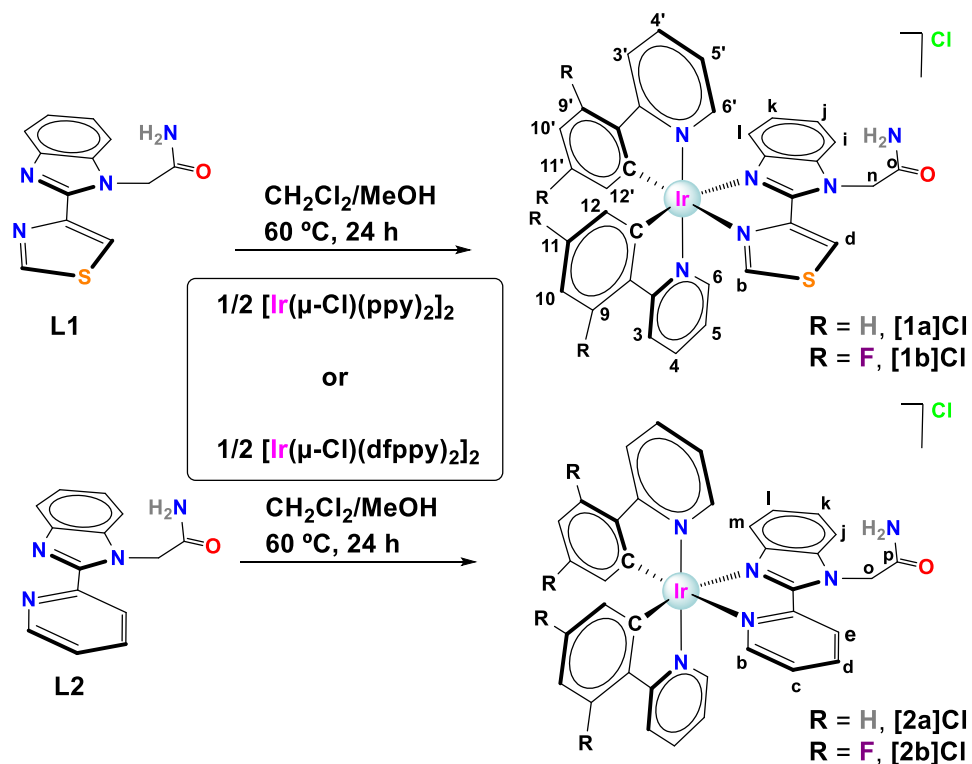
Mitochondria play numerous basic functions in cells and these include energy production, regulation of cell death and redox balance.<sup>34,40,41</sup> Thus, mitochondria have gradually become more attractive as target organelles for developing selective anticancer drugs,<sup>42,43</sup> especially for PDT treatment.<sup>11,41</sup> It has been reported that even low levels of  $^1O_2$  generated either inside or close to the mitochondria are more effective than a large amount produced in the cell nucleus.<sup>44</sup>

In a previous paper<sup>45</sup> we reported on the biological and photocatalytic properties of two sets of neutral Ir(III) bis-cyclometalated complexes of general formula  $[\text{Ir}(\text{C}^{\wedge}\text{N})_2(\text{N}^{\wedge}\text{O})]$  with a phenolate ring. It was found that complexes containing the scaffold benzimidazolyl as the N donor fragment in the  $\text{N}^{\wedge}\text{O}$  ligand presented enhanced cytotoxic activity after irradiation. In addition, the  $\text{C}^{\wedge}\text{N}$  ligand had an influence on the biological properties, since a complex with 2-(2,4-difluorophenyl)pyridinate gave a better Phototoxicity Index (PI). Thus, in this work we decided to synthesize, characterize and analyse the biological properties of a set of complexes of the type  $[\text{Ir}(\text{C}^{\wedge}\text{N})_2(\text{N}^{\wedge}\text{N}')]\text{Cl}$  with  $\text{N}^{\wedge}\text{N}'$  ligands that contained a benzimidazolyl unit bonded to either a pyridinyl or a thiazolyl ring (see Scheme 1). Two different  $\text{C}^{\wedge}\text{N}$  ligands were chosen, namely 2-phenylpyridinate (ppy) and 2-(2,4-difluorophenyl)pyridinate (dfppy), with the aim of evaluating the effect of both the cyclometalating ( $\text{C}^{\wedge}\text{N}$ ) and the ancillary ( $\text{N}^{\wedge}\text{N}'$ ) ligands on the biological properties of the complexes and, more specifically, on the ability to behave as photosensitizers in PDT processes. According to several studies, higher quantum yields and longer triplet excited state lifetimes are expected for the biscyclometalating complexes with dfppy versus those with ppy ligands<sup>45,46,47,48,49,50,51,52</sup> and one aim was to ascertain whether a high value of these parameters could favour PDT activity. Considering the positive results in anticancer activity of some complexes that contain an amide group,<sup>53,54</sup> including selectivity for cancer cells,<sup>55</sup> we decided to include an amide group in the benzimidazolyl ring. Moreover, this functional group could facilitate further derivatization or conjugation in the future development of the leading compounds.

## 2. Results and discussion

### 2.1. Synthesis and general characterization

The ligands were prepared by reaction of 2-bromoacetamide with the corresponding benzimidazole precursors, *i.e.*, 2-(4-thiazolyl)benzimidazole for **L1** or 2-(2-pyridyl)benzimidazole in the case of **L2**. **L1** and **L2** were then reacted with the chloro-bridged dimeric iridium(III) complexes<sup>56</sup>  $\text{rac}[\text{Ir}(\mu\text{-Cl})(\text{ppy})_2]_2$  (ppy = 2-phenylpyridinate- $\text{C}^2, \text{N}$ )<sup>57</sup> or  $\text{rac}[\text{Ir}(\mu\text{-Cl})(\text{dfppy})_2]_2$  (dfppy = 2-(2,4-difluorophenyl)pyridinate- $\text{C}^2, \text{N}$ )<sup>45,58,59</sup> (see Scheme 1) to give the ionic complexes **[1a]Cl**, **[1b]Cl**, **[2a]Cl** and **[2b]Cl** of formula  $[\text{Ir}(\text{C}^{\wedge}\text{N})_2(\text{N}^{\wedge}\text{N}')]\text{Cl}$  in moderate to good yields as yellow or orange solids. The compounds are soluble in common organic solvents and partially soluble in water.



Scheme 1. Synthesis and molecular structures of the iridium complexes, including atom labelling for NMR discussion.

The new compounds have  $C_1$  molecular symmetry and helicoidal chirality due to the presence of three bis(chelate) ligands. The complexes were isolated as racemic mixtures and characterized by multinuclear NMR, IR, mass spectrometry, and elemental analysis. X-ray diffraction studies were also carried out to determine the molecular and crystalline structures of **[1a]PF<sub>6</sub>** and **[2a]PF<sub>6</sub>**. The  $^1\text{H}$ ,  $^{13}\text{C}\{^1\text{H}\}$ , and  $^{19}\text{F}$  NMR spectra of the new complexes contain one set of peaks for each of the two inequivalent C<sup>^N</sup> ligands due to the asymmetric nature of the N<sup>^N'</sup> ligands, but it was possible to assign all the  $^1\text{H}$  and  $^{19}\text{F}$  NMR resonances by using 2-D NMR experiments. It is worth noting that some protons undergo strong shielding due to the effect of the ring current anisotropy of nearby rings. For example, the protons *ortho* to the metalated C atom ( $\text{H}^{12}$ ,  $\text{H}^{12'}$ ) appear in the range 6.12–6.32 ppm or 5.72–5.76 ppm for the ppy or dfppy complexes, respectively. This effect has previously been reported for the dimeric precursors.<sup>57</sup> Besides, the  $\text{H}^6$ ,  $\text{H}^{6'}$  protons appear much more shielded (7.63–7.80 ppm) than in the chloro-bridged complexes (>9 ppm)<sup>57</sup> and this is due to the effect of the rings of the N<sup>^N'</sup> ligands. A marked shift to higher field is also observed for the  $\text{H}^l$  (**L1**) or  $\text{H}^m$  (**L2**) protons belonging to the N<sup>^N'</sup>

ligands (shift of around 1.3–1.5 ppm with respect to the free ligands). It is also worth noting that in the four complexes, one of the two broad singlets of the NH<sub>2</sub> group is shifted to lower field with respect to the free ligands (about 1 ppm), a change that is likely due to the formation of a hydrogen bond with the chloride counteranion.<sup>60,61,62</sup> The fluoro-substituents give rise to two quartets (F<sup>11</sup>, F<sup>11'</sup>) and two triplets (F<sup>9</sup>, F<sup>9'</sup>) (partially overlapped in the case of **[1b]Cl**), with similar values for the <sup>4</sup>J<sub>F-F</sub> and <sup>3</sup>J<sub>F-H</sub> coupling constants. The HR ESI mass spectra show envelope peaks whose *m/z* ratio and isotopic distribution are consistent with those of the [M]<sup>+</sup> cations. In addition, peaks due to [Ir(C<sup>^</sup>N)<sub>2</sub>]<sup>+</sup> fragments are observed in all the spectra, which suggests that the N<sup>^</sup>N' ligands are more labile than the corresponding cyclometalated ligands (see SI Fig. 1–26 for the NMR and mass spectra).

## 2.2. X-ray diffraction

The molecular and crystalline structures of complexes *rac*-**[1a]PF<sub>6</sub>** and *rac*-**[2a]PF<sub>6</sub>** were determined by X-ray diffraction. Suitable single crystals were obtained by slow diffusion of a saturated aqueous solution of NH<sub>4</sub>PF<sub>6</sub> into solutions of **[1a]Cl** and **[2a]Cl** in methanol/dichloromethane. Both complexes crystallize in the monoclinic system and in the space groups *C2/c* (**[1a]PF<sub>6</sub>**) and *P2<sub>1</sub>/c* (**[2a]PF<sub>6</sub>**), respectively. Selected bond distances and angles are gathered in Table 1 and the corresponding crystallographic data are compiled in SI Table 1. The ORTEP representations for one optical isomer are provided in Fig. 2, although both enantiomers are present in the crystals. As one would expect, the complexes exhibit a distorted octahedral geometry with the typical *trans*-N,N and *cis*-C,C relative disposition for the C<sup>^</sup>N ligands. The bite angles of the C<sup>^</sup>N ligands are in the range 80.0(4)–80.4(3)°, whereas for the two N<sup>^</sup>N' ligands the values are very similar (75.8(3)° for **[1a]PF<sub>6</sub>** and 75.3(5)° for **[2a]PF<sub>6</sub>**). The Ir–N distances of the N<sup>^</sup>N' ligands (2.121(13) to 2.186(14) Å) are longer than those of the cyclometalating ligands (2.032(6) to 2.052(5) Å), thus demonstrating the high *trans* influence of the carbon atoms in the phenyl rings.<sup>36,63,64,65</sup> The Ir–N<sub>bzlm</sub> distance is shorter than the other Ir–N distances of the ancillary ligands. The Ir–C distances are within the expected range (2.000(6)– 2.032(7) Å).<sup>36,64,65</sup> The torsion angles of the cyclometalated ligands (0.6–8.3°) and the N<sup>^</sup>N' ligands (4.1–57.9°) are low, which imparts a high degree of planarity on all the ligands in both complexes. The 3D-structure is built up through the formation of hydrogen bonds involving the PF<sub>6</sub><sup>-</sup> anions, the C=O group and the S atom (for **L1**) as H-bond acceptors and the NH<sub>2</sub> fragment and different CH groups of the rings as H-bond donors.

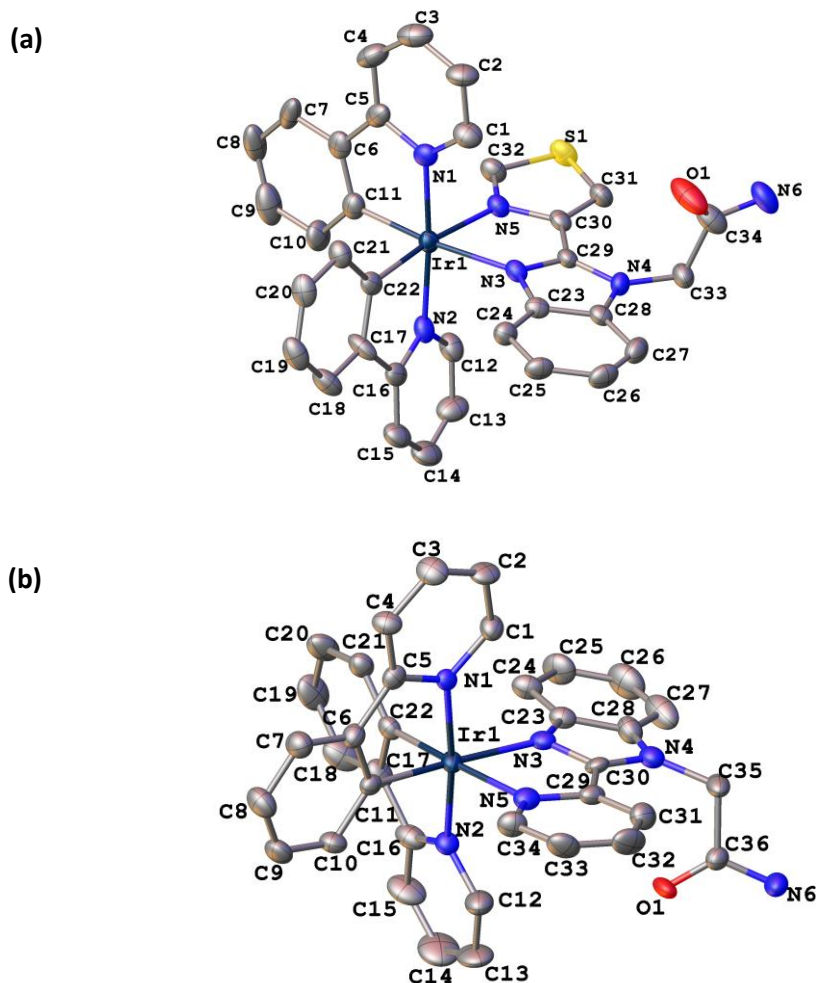


Fig. 2. ORTEP representations of: (a) cation  $\Delta$ -[1a]<sup>+</sup> and (b) cation  $\Delta$ -[2a]<sup>+</sup>. Ellipsoids are represented at the 30% level. Hydrogen atoms and counteranions have been omitted for the sake of clarity.

Table 1. Bond Lengths (Å) and Angles (°) for [1a]PF<sub>6</sub> and [2a]PF<sub>6</sub>.

[1a]PF <sub>6</sub>				[2a]PF <sub>6</sub>			
Bond Lengths		Angles (°)		Bond Lengths		Angles (°)	
Ir1- N3	2.148(9)	N1- Ir1- N2	175.0(3)	Ir1- N3	2.121(13)	N2- Ir1- N1	174.4(4)
Ir1- N5	2.163(8)	C22- Ir1- N5	172.9(4)	Ir1- N1	2.032(6)	C11- Ir1- N3	173.2(5)
Ir1- N1	2.053(5)	C11- Ir1- N3	172.7(3)	Ir1- N5	2.186(14)	C22- Ir1- N5	173.7(5)
Ir1- C22	2.001(11)	C31- S1- C32	90.0(6)	Ir1- N2	2.031(8)	O1- C35- N6	125.1(16)
Ir1- N2	2.052(9)	O1- C34- C33	122.7(13)	Ir1- C11	2.035(8)	O1- C35- C34	120.5(16)
Ir1- C11	2.002(6)	O1- C34- N6	121.6(13)	Ir1- C22	2.021(8)	N6- C35- C34	114.4(14)
S1- C32	1.700(12)	N6- C34- C33	115.6(13)	O1- C35	1.22(2)	C11-Ir1-N1	80.0(4)
S1- C31	1.668(13)	C11-Ir1-N1	80.4(3)	N4- C34	1.46(2)	C22-Ir1-N2	80.3(4)
O1- C34	1.207(17)	C22-Ir1-N2	80.3(4)	N6- C35	1.31(2)	N3-Ir1-N5	75.3(5)
N4- C33	1.445(13)	N3-Ir1-N5	75.7(3)				
N6- C34	1.333(17)						



### 2.3. Electrochemical measurements

The redox potentials of complexes **[1a]Cl**, **[1b]Cl**, **[2a]Cl** and **[2b]Cl** were experimentally determined by cyclic voltammetry (CV) in acetonitrile solutions ( $5 \times 10^{-4}$  M) using  $[n\text{Bu}_4\text{N}][\text{PF}_6]$  (0.1 M) as the supporting electrolyte with a three-electrode setup that included a glassy carbon working electrode. Oxygen was removed from the solutions by bubbling argon through them. Potentials are referenced to the ferrocenium/ferrocene ( $\text{Fc}^+/\text{Fc}$ ) couple. The cyclic voltammograms are shown in SI Fig. 31 (see also data in Table 2). Two peaks can be observed in the anodic region: (i) an irreversible peak between +0.54 and +0.61 V (see SI Fig. 31), which is assigned to the oxidation of the  $\text{Cl}^-$  counteranion ( $\text{Cl}^-/\text{Cl}_2$  redox couple),<sup>65</sup> and (ii) a reversible peak that differs depending on the cyclometalating ligand (0.83–0.86 V for the ppy complexes and 1.18–1.19 V for those containing the dfppy ligand). According to DFT studies, the HOMO orbital in this kind of complexes is composed of a mixture of Ir(III)  $d_\pi$  orbitals ( $t_{2g}$ ) and phenyl  $\pi$  orbitals of the C^N ligands<sup>66,67,68</sup> and thus the resulting oxidized species can be described by the combination of three canonical structures that involve the oxidation of either the iridium centre ( $[\text{Ir}^{\text{IV}}(\text{C}^{\wedge}\text{N}^-)_2(\text{N}^{\wedge}\text{N}')^{2+}]$ ) or one of the C^N ligands ( $[\text{Ir}^{\text{III}}(\text{C}^{\wedge}\text{N}^-)(\text{C}^{\wedge}\text{N}^*)(\text{N}^{\wedge}\text{N}')^{2+}]$ ). This HOMO is more stabilized for the dfppy complexes due to the electron-withdrawing effect of the fluoro-substituents,<sup>46</sup> a fact that explains the higher values for the oxidation peaks of **[1b]Cl** and **[2b]Cl**. The values for **[1a]Cl** and **[2a]Cl** compare well with those reported for other ppy complexes with N^N ligands<sup>65,69</sup> including  $[\text{Ir}(\text{ppy})(\text{bpy})]\text{PF}_6$  (0.87 V vs.  $\text{Fc}^+/\text{Fc}$ ).<sup>70</sup> On considering the features of the HOMOs for this class of complexes, the ancillary ligand has usually a minor effect on these oxidation values. Two reduction potentials are observed in the cathodic region. With the exception of the two first reduction peaks of complexes with ligand **L2**, which are quasi reversible, the other peaks are irreversible and this indicates the instability of the reduced species. Considering that the main contribution to the LUMO comes from the ancillary ligand,<sup>66,67,68</sup> the peaks should correspond to stepwise reduction processes on **L1** or **L2** and should be affected by the electronic properties of these ligands. In fact, in the first reduction peaks, values in the range –2.11 to –2.04 V or –1.78 to –1.71 V are observed for complexes with **L1** or **L2**, respectively, and the nature of the cyclometalating ligands has only a minor effect. The less negative values found for complexes with **L1** are in accordance with the destabilizing effect of replacing a pyridine for a thiazolyl fragment found for the LUMO in ppy iridium complexes that contain N^N' ligands.<sup>71</sup> Moreover, a very low intensity irreversible peak is observed for **[2a]Cl** and **[2b]Cl** at –1.88 and –1.82 V, respectively. This peak is only observed in the return scan and is assigned to the oxidation of a species formed by chemical decomposition during the respective CV experiments.



Table 2 Redox potentials recorded by cyclic voltammetry referenced to Fc<sup>+</sup>/Fc in acetonitrile solution and excited-state redox properties of [1a]Cl, [1b]Cl, [2a]Cl and [2b]Cl.<sup>a</sup>

Complex	E <sup>ox1</sup> <sub>1/2</sub> (V)	E <sup>ox2</sup> <sub>1/2</sub> (V)	E <sup>red1</sup> <sub>1/2</sub> (V)	E <sup>red2</sup> <sub>1/2</sub> (V) <sup>b</sup>	ΔE <sub>1/2</sub> (V) <sup>c</sup>	E <sub>em</sub> (eV)	E (PS <sup>+</sup> /PS <sup>*</sup> ) (V) <sup>d</sup>	E (PS <sup>*</sup> /PS <sup>-</sup> ) (V) <sup>e</sup>
[1a]Cl	+0.61 (irr)	+0.83 (rev)	-2.11 (irr)	-2.26 (qr)	2.94	2.505	-1.675	0.395
[1b]Cl	+0.55 (irr)	+1.18 (rev)	-2.04 (irr)	-2.20 (qr)	3.22	2.649	-1.469	0.609
[2a]Cl	+0.59 (irr)	+0.86 (rev)	-1.78 (qr)	-2.32 (qr)	2.64	2.043	-1.183	0.263
[2b]Cl	+0.54 (irr)	+1.19 (rev)	-1.71 (qr)	-2.26 (qr)	2.90	2.262	-1.072	0.552

<sup>a</sup> Voltammograms recorded in acetonitrile solution ( $5 \times 10^{-4}$  M) using 0.1 M [*n*Bu<sub>4</sub>N][PF<sub>6</sub>] as supporting electrolyte and recorded with scan rate of 0.10 V·s<sup>-1</sup> and referenced to Fc<sup>+</sup>/Fc. <sup>b</sup> Two minor irreversible peaks are also observed for [2a]Cl and [2b]Cl at -1.88 and -1.82 V, respectively. <sup>c</sup> ΔE<sub>1/2</sub> = E<sup>ox2</sup><sub>1/2</sub> - E<sup>red1</sup><sub>1/2</sub>. <sup>d</sup> E (PS<sup>+</sup>/PS<sup>\*</sup>) = E<sup>ox2</sup><sub>1/2</sub> - E<sub>em</sub>. <sup>e</sup> E (PS<sup>\*</sup>/PS<sup>-</sup>) = E<sub>em</sub> - E<sup>red1</sup><sub>1/2</sub>.

The redox potentials for the excited states were calculated using the redox potentials of the ground state and the emission energy (see below),<sup>72</sup> as the reducing and oxidizing ability of the T<sub>1</sub> excited states can be crucial in the biological properties of our PSs under light excitation (see below) and may be critical to induce cell death. The values are provided in Table 1. The complexes, with the exception of [2a]Cl, exhibit higher oxidation power (E (PS<sup>+</sup>/PS<sup>\*</sup>)) in the excited state than the archetypal complex [Ir(ppy)<sub>2</sub>(bpy)]PF<sub>6</sub> (complex A, bpy = 2,2'-bipyridine), for which the value is +0.28 V. The complexes with ligand L1 also showed stronger excited state reducing ability (E (PS<sup>\*</sup>/PS<sup>-</sup>)) than complex A (-1.19 V).

#### 2.4. Photophysical properties

The UV-vis spectra of complexes [1a]Cl, [1b]Cl, [2a]Cl and [2b]Cl show strong absorption bands in the UV region 250–315 nm (Fig. 3 and Table 3) and these are assigned to singlet spin-allowed ligand-centred transitions (<sup>1</sup>LC, π-π<sup>\*</sup>) in both the cyclometalated (C<sup>^</sup>N) and the ancillary (N<sup>^</sup>N') ligands. Medium intensity bands are observed in the lower energy region (350–400 nm) and these are assigned to <sup>1</sup>MLCT and <sup>1</sup>LLCT transitions. The weak absorptions with tails that extend into the visible region should correspond to <sup>3</sup>MLCT transitions.<sup>29,65,71,73,74</sup> We are aware that the poor absorption of our complexes in the phototherapeutic window (650–850 nm) limits its practical application. However, this drawback could be overcome in future developments of these photosensitizers by mean of two different strategies recently reported in the literature: (a) two-photon activation<sup>75</sup> and (b)

conjugation of the complex to suitable organic chromophores<sup>76,77</sup> through the amide group of the N,N'ligand.

The emission spectra of the four complexes in deoxygenated DMSO/water (6:94) at room temperature are gathered in Fig. 3 and the corresponding data are provided in Table 3. Complexes with ligand **L1** exhibit a structured band while derivatives with ligand **L2** give rise to broad and structureless emission spectra. The presence of a structured band is indicative of a pronounced LC  $\pi-\pi^*$  character for the emitting state and a weaker MLCT contribution, while the absence of this structure suggests a substantial MLCT character for the emitting state.<sup>78,79</sup> On comparing complexes with the same ancillary ligand, blue shifted emissions were observed for the dfppy derivatives, as one would expect for the afore-mentioned stabilization of the HOMO orbitals typical of this C<sup>N</sup> ligand. However, a more marked effect on the emission energy is attributed to the N<sup>N'</sup> ligands, with blue shifted emissions for complexes with ligand **L1**. This is consistent with the higher energy values expected for the LUMO orbital in **[1a]Cl** and **[1b]Cl** containing the thiazolyl fragment<sup>71</sup> and fits well with the higher values found for the reduction potential for these derivatives relative to complexes with **L2**. As far as the quantum yields ( $\Phi_{PL}$ ) and the excited-state lifetimes are concerned, clearly higher values are found for the dfppy derivatives (Table 3,  $\Phi_{PL} = 75-76\%$ ,  $\tau = 1320-1357$  ns) with only a small influence of the N<sup>N'</sup> ancillary ligands. In the case of the ppy complexes, a certain influence of the N<sup>N'</sup> ligand was observed and higher values for both parameters were determined for derivatives containing ligand **L1**. The radiative and the overall non-radiative rate constants ( $k_r$  and  $k_{nr}$ , respectively) were calculated from the  $\Phi_{PL}$  and the  $\tau$  values<sup>80</sup> on assuming an intersystem crossing efficiency of 1 ( $k_r = \Phi_{PL}/\tau$  and  $k_{nr} = (1 - \Phi_{PL})/\tau$ ). The data are gathered in Table 3. On comparing complexes with the same N<sup>N'</sup> ligand (similar excited states expected), the energy gap law is observed, as  $\ln(K_{nr})$  increases with decreasing energy of the emission maxima.<sup>81</sup> Thus, the complexes that contain ppy as a cyclometalating ligand have higher  $K_{nr}$  values.

Table 3. Photophysical properties for complexes **[1a]Cl**, **[1b]Cl**, **[2a]Cl** and **[2b]Cl** ( $10^{-5}$  M) in DMSO/water (6:94) at 25 °C.

Complex	$\lambda_{\text{abs}}$ (nm)	$\epsilon$ [ $\text{M}^{-1} \text{cm}^{-1}$ ]	$\epsilon$ (at 450 nm) [ $\text{M}^{-1} \text{cm}^{-1}$ ]	$\lambda_{\text{em}}$ (nm) <sup>a</sup>	$\phi_{\text{PL}}$ (%)	$\tau$ (ns)	$k_r$ ( $\text{s}^{-1}$ )	$k_{\text{nr}}$ ( $\text{s}^{-1}$ )
<b>[1a]Cl</b>	246	39100	400	479	27	262	$10.30 \times 10^6$	$2.79 \times 10^6$
	304	28500		507				
	351	6200						
<b>[1b]Cl</b>	245	34100	0	453	76	1320	$5.75 \times 10^5$	$1.82 \times 10^5$
	305	23000		482				
	364	3600						
<b>[2a]Cl</b>	249	62100	2000	607	6	82	$7.32 \times 10^5$	$1.15 \times 10^7$
	315	41300						
<b>[2b]Cl</b>	243	39300	500	548	75	1357	$5.53 \times 10^5$	$1.84 \times 10^5$
	315	22000						

<sup>a</sup> $\lambda_{\text{ex}} = 405$  nm

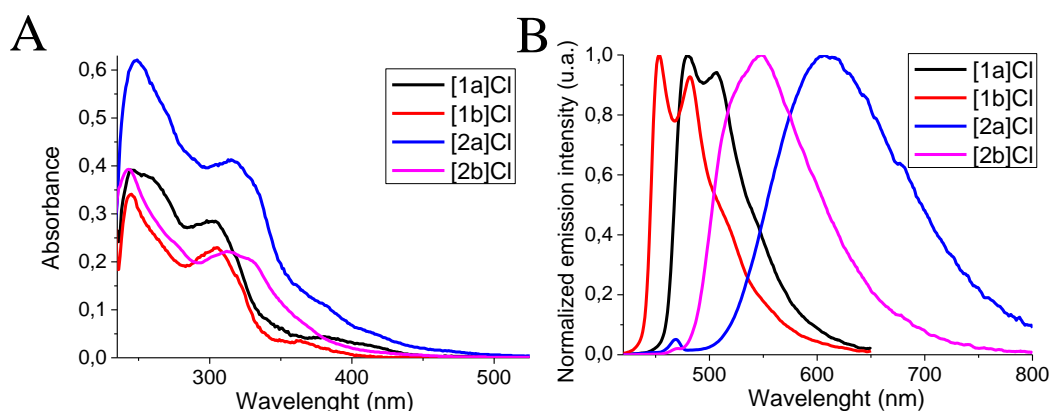


Fig. 3. (A) Overlaid UV-Vis spectra of complexes **[1a]Cl**, **[1b]Cl**, **[2a]Cl** and **[2b]Cl** ( $10^{-5}$  M) in DMSO/Water (6:94) at 25 °C. (B) Emission spectra for complexes **[1a]Cl**, **[1b]Cl**, **[2a]Cl** and **[2b]Cl** ( $10^{-5}$  M) in deoxygenated DMSO/water (6:94) at 25 °C under a nitrogen atmosphere ( $\lambda_{\text{ex}} = 405$  nm).

The photostability of the four complexes was evaluated in DMSO- $d_6$ :D<sub>2</sub>O (3:2) at 25 °C after irradiation with blue LED light ( $\lambda_{\text{ir}} = 460$  nm). The complexes were very photostable and the values found for decomposition were in between 0% (**[2a]Cl**) and 7% (**[1b]Cl**) after 24 hours of irradiation (SI Fig. 27–30).

### 2.5. $^1\text{O}_2$ generation

Singlet oxygen is considered to be the main cytotoxic species in PDT. Therefore, the ability to generate singlet oxygen ( $^1\text{O}_2$ ) was evaluated for **[1a]Cl** and **[2a]Cl** in acetonitrile by monitoring, through UV-Vis spectroscopy, the oxidation of 1,3-diphenylisobenzofuran (DPBF, yellow) to 1,2-dibenzoylbenzene (colorless) in the presence of our PSs under blue light irradiation (see Material and Methods

section for details). DPBF was selected as the  $^1\text{O}_2$  scavenger due to its fast reaction with  $^1\text{O}_2$ . A decrease in the intensity of the DPBF bands was observed with time, thus demonstrating the formation of  $^1\text{O}_2$  in the presence of both complexes (see SI Fig. 32 for **[1a]Cl** and 33 for **[2a]Cl**).

## 2.6. Phototoxicity studies and internalization kinetics

The efficacy of this family of compounds for cancer PDT was initially explored in PC-3 prostate cancer cells (Table 4). Based on the absorption spectra of the complexes (Fig. 3), blue light (450 nm) was used to photoactivate the complexes. The light dose applied was  $24.1 \text{ J}\cdot\text{cm}^{-2}$ , which is in the typical range used to activate other Ir(III) PSs.<sup>82</sup> All the complexes were moderately cytotoxic in the dark and they showed a similar behaviour ( $\text{IC}_{50}$  values between  $24.3 \pm 5.9 \mu\text{M}$  and  $31.1 \pm 4.3 \mu\text{M}$ ), although a slightly higher cytotoxicity was found for the complexes with ligand **L1**. However, upon irradiation the activities of complexes **[1a]Cl** and **[2a]Cl** increased markedly, with  $\text{IC}_{50,\text{light}}$  values of  $2.7 \pm 1.2 \mu\text{M}$  and  $2.4 \pm 1.4 \mu\text{M}$ , respectively. These values are similar to the  $\text{IC}_{50}$  of cisplatin in this cell line. The resulting photocytotoxic indexes ( $\text{PI} = \text{IC}_{50,\text{dark}}/\text{IC}_{50,\text{light}}$ ) calculated for **[1a]Cl** and **[2a]Cl** were 11.7 and 10.7. In contrast, the activity of the fluorinated complexes was only slightly enhanced after photoactivation for **[2b]Cl** (PI: 2.2), whereas **[1b]Cl** did not display photoinduced cytotoxic activity (PI: 1.1). The result for **[1b]Cl** can be easily explained due to the lack of absorption at  $\lambda_{\text{ex}} = 450 \text{ nm}$  observed for this complex (see Table 3). Moreover, the difference in the antitumour activity upon light exposure is mainly determined by the cyclometalating ligand. As stated previously, the  $\Phi_{\text{PL}}$  and lifetime of the excited state were clearly higher for complexes with dfppy ligands. However, an increase in these parameters did not improve the PDT ability, at least for our complexes. Furthermore, the most active compounds had higher  $K_{\text{nr}}$  constant values (Table 3). In any case, we consider that there are insufficient data to draw clear conclusions about the effect of this parameter.

Considering the photocytotoxic activity of the new complexes, we focused our attention on complexes **[1a]Cl** and **[2a]Cl** for further studies on their mechanism of action.

Table 4. Cytotoxic activity against PC-3 cells.

Complex	IC <sub>50, dark</sub> (μM)	IC <sub>50, light</sub> (μM) <sup>a</sup>	PI <sup>b</sup>
[1a]Cl	31.1 ± 4.3	2.7 ± 1.2	11.7
[1b]Cl	29.8 ± 5.0	28 ± 6.0	1.1
[2a]Cl	25.8 ± 0.9	2.4 ± 1.4	10.7
[2b]Cl	24.3 ± 5.9	11.2 ± 1.2	2.2
Cisplatin	2.53 ± 0.73	--	--

<sup>a</sup> PC-3 cells were pre-incubated with the compounds for 1 h and then activated with a blue LED light (1 h, 6.7 mW/cm<sup>2</sup>, λ: 450 nm) or kept in the dark. 48 h later, IC<sub>50</sub> values were determined by an MTT assay. Data represent the mean ± SD of three independent experiments, each performed in quadruplicate. <sup>b</sup> PI: phototoxicity index = IC<sub>50, dark</sub>/IC<sub>50, light</sub>.

The cellular internalization kinetics of these compounds were analysed first in order to determine the time required for their optimal accumulation inside the cells before photoactivation. To this end, the intracellular luminescence properties of [2a]Cl were evaluated after excitation with the blue laser (488 nm) used in flow cytometry. As shown in Fig. 4, the intracellular fluorescence levels, which correspond to the uptake of the complex, increased in a linear manner during the first six hours. The internalization rate then dropped markedly. Based on these results, it was considered that an incubation period of six hours would allow the accumulation of most of the compound within the cells before irradiation, thus optimizing its photocytotoxic potential.

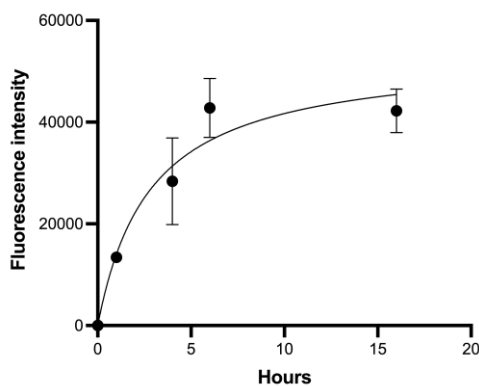


Fig. 4. Internalization kinetics of [2a]Cl. PC-3 cells were incubated for 1, 4, 6, and 16 h at 37 °C with the compound at 5 μM, and the median fluorescence intensity of 10000 cells was determined by flow cytometry (λ<sub>ex</sub> = 488 nm). Data represent the mean ± SD of three independent experiments.

Based on the above result, further photocytotoxicity experiments were performed with [1a]Cl and [2a]Cl while extending the pre-incubation time to six hours. In addition, the study was expanded to other cancer cell lines (CACO-2: colon cancer and SK-MEL-28: melanoma) as well as to CCD-18Co non-cancerous fibroblasts in order to assess the

degree of selectivity exhibited by these complexes. In all cell lines, **[1a]Cl** and **[2a]Cl** exerted a dark cytotoxic activity that increased sharply after irradiation (Table 5). In particular, photoactivated **[1a]Cl** and **[2a]Cl** were very active against SK-MEL-28 cells, with  $IC_{50,light}$  values in the nanomolar range ( $0.77 \pm 0.19 \mu\text{M}$  and  $0.62 \pm 0.08 \mu\text{M}$ ) and PI values of 9.9 and 11.4, respectively. Furthermore, it should be noted that in PC-3 cells, a longer incubation time resulted in enhanced photocytotoxicity, with PI values almost doubling those obtained with one hour of pre-incubation (PI of 20.8 for **[1a]Cl** and PI of 17.3 for **[2a]Cl**), thus confirming that the optimal intracellular accumulation of the compounds enhanced their photocytotoxic capacity. In contrast, upon irradiation both **[1a]Cl** and **[2a]Cl** displayed a moderate cytotoxicity against CACO-2 cells ( $IC_{50,light}$  values of  $3.48 \pm 1.38 \mu\text{M}$  and  $2.31 \pm 0.54 \mu\text{M}$ , respectively) and CCD-18Co fibroblasts ( $IC_{50,light}$  values of  $4.49 \pm 0.35 \mu\text{M}$  and  $2.41 \pm 0.10 \mu\text{M}$ ). It should be noted that the  $IC_{50,light}$  values of **[1a]Cl** and **[2a]Cl** in the SK-MEL-28 cell line were, respectively, 30.6 and more than 80.6 times lower than the corresponding  $IC_{50,dark}$  values in non-cancerous fibroblasts. Therefore, the dose required for PDT-based treatment of a melanoma would not be toxic to healthy cells that are not exposed to light irradiation. In addition, haemolytic assays revealed that neither of the two compounds display toxicity against red blood cells at the corresponding  $IC_{50,dark}$  (Table 5).

Table 5. Cytotoxic activities of **[1a]Cl** and **[2a]Cl** against different cell lines.

Cell line	<b>[1a]Cl</b>			<b>[2a]Cl</b>		
	$IC_{50,dark}$ ( $\mu\text{M}$ )	$IC_{50,light}^a$ ( $\mu\text{M}$ )	PI <sup>b</sup>	$IC_{50,dark}$ ( $\mu\text{M}$ )	$IC_{50,light}^a$ ( $\mu\text{M}$ )	PI <sup>b</sup>
PC-3	$31.05 \pm 4.29$	$1.49 \pm 0.48$	20.8	$25.78 \pm 0.69$	$1.49 \pm 0.57$	17.3
CACO-2	$16.65 \pm 4.65$	$3.48 \pm 1.38$	4.8	$26.49 \pm 4.20$	$2.31 \pm 0.54$	11.5
SK-MEL-28	$7.66 \pm 1.36$	$0.77 \pm 0.19$	9.9	$7.04 \pm 0.79$	$0.62 \pm 0.08$	11.4
CCD-18Co	$23.83 \pm 4.48$	$4.49 \pm 0.35$	5.3	>50	$2.41 \pm 0.10$	--
Haemolytic activity <sup>c</sup>	< 5 %			< 5 %		

<sup>a</sup> Cells were pre-incubated with the compounds for 6 h and then irradiated with a blue LED light (1 h, 6.7 mW/cm<sup>2</sup>,  $\lambda$ : 450 nm) or kept in the dark. 48 h later,  $IC_{50}$  values were determined by an MTT assay. Data represent the mean  $\pm$  SD of at least two independent experiments, each performed in quadruplicate. Complexes with  $IC_{50}$  values greater than 50  $\mu\text{M}$  were considered to be inactive. <sup>b</sup> PI: phototoxicity index =  $IC_{50,dark}/IC_{50,light}$ . <sup>c</sup> Percentage of haemolysis at the  $IC_{50, dark}$ .

## 2.7. Internalization mechanism and intracellular distribution

The internalization mechanism of a compound has implications on its cell-type specificity, uptake rate and intracellular distribution.<sup>83</sup> Different cell entry pathways have been proposed for Ir(III) complexes and these include passive

diffusion through the membrane, protein-mediated transport and endocytosis.<sup>84,85,86</sup> These pathways can be energy-independent, as is the case of passive diffusion and transport across channels or protein carriers, or energy-dependent as for endocytosis and active protein-mediated transport. In an effort to gain an insight into the uptake mechanism of our complexes, flow cytometry experiments were carried out after blocking different internalization pathways. Based on its luminescence properties, **[2a]Cl** was selected for the experiments. PC-3 cells were incubated with **[2a]Cl** at 5  $\mu\text{M}$  for one hour at 37  $^{\circ}\text{C}$  to allow any possible cellular uptake mechanism to occur and the median fluorescence of the cells was set as 100 % of compound internalization (Fig. 5). The incubation of the cells at a lower temperature (4  $^{\circ}\text{C}$ ) caused a decrease in the intracellular fluorescence levels by 90.4%, which shows that the uptake of the compound requires metabolic energy. In addition, treatment at 37  $^{\circ}\text{C}$  in the presence of dynasore, an endocytosis inhibitor that blocks the formation of endocytic vesicles from the plasma membrane, reduced the internalization of the complex by 81.7%. Overall, these results indicate that the complex internalizes into the cells primarily by an energy-dependent endocytic mechanism, as previously described for other Ir(III) biscyclometalated complexes.<sup>87</sup> The experiments were performed in serum-free culture medium and therefore the endocytosis of the compounds does not involve serum lipids or proteins.

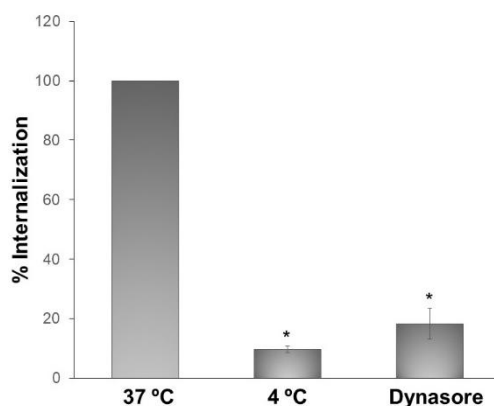


Fig. 5. Cellular uptake mechanism for **[2a]Cl**. PC-3 cells were incubated with the compound at 5  $\mu\text{M}$  for 1 h under different conditions: at 37  $^{\circ}\text{C}$ , at 4  $^{\circ}\text{C}$  (metabolic inhibition) or at 37  $^{\circ}\text{C}$  in the presence of dynasore (endocytosis inhibition). The median fluorescence intensity of the cells, corresponding to the internalization of **[2a]Cl**, was determined by flow cytometry. The % of internalization under different conditions was calculated in comparison to cells incubated at 37  $^{\circ}\text{C}$  (100 % internalization). Each bar represents the median fluorescence intensity of at least two independent experiments  $\pm$  SD. \* $p < 0.05$  vs cells treated at 37  $^{\circ}\text{C}$ .

To be effective, the compound must reach the target location inside the cells.<sup>83</sup> In particular, the intracellular localization plays a key role in the photodamage displayed by a PS, since ROS act close to their site of generation.<sup>7</sup> The subcellular distribution of **[1a]Cl** and **[2a]Cl** was examined by confocal microscopy after exposure of the cells to the compounds for one hour. For co-localization studies, cells were co-stained with the red-fluorescent dye MitoTracker™ Red CMXRos. As shown in Fig. 6, a dotted green fluorescent staining with a cytosolic distribution was detected in cells exposed to both **[1a]Cl** and **[2a]Cl**, while fluorescence emission was not observed from inside the nucleus. Merged images of **[1a]Cl** or **[2a]Cl** and MitoTracker™ Red CMXRos staining showed that the green dots are mainly located in the mitochondria, as indicated by the yellow fluorescence. These results reveal that, once internalized, **[1a]Cl** and **[2a]Cl** mainly accumulate in the mitochondria. This distribution is chemically favoured by the cationic nature of **[1a]Cl** and **[2a]Cl** and the negative potential across the mitochondrial membrane, as described for other positively charged cyclometalated Ir(III) complexes with lipophilic character stemming from their ligands.<sup>38,39</sup>

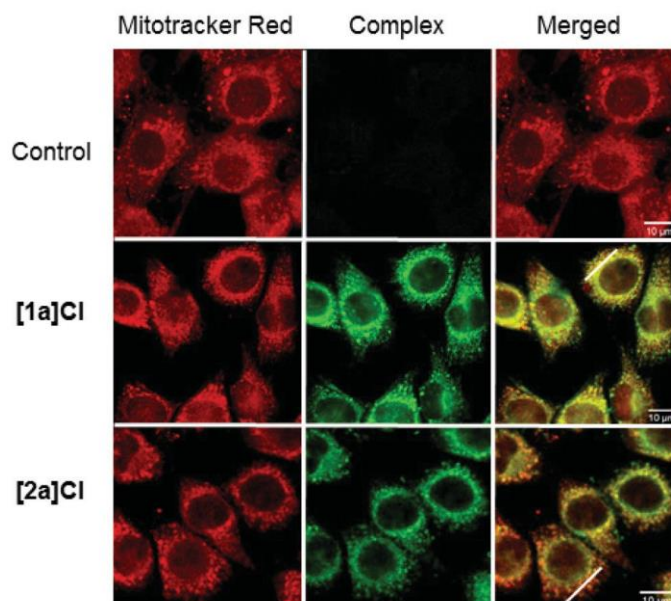


Fig. 6. Subcellular localization of **[1a]Cl** and **[2a]Cl**. SK-MEL-28 cells were incubated with the compounds at 25  $\mu$ M or with medium alone (control) for 1 h at 37  $^{\circ}$ C. Mitochondria were stained in red with MitoTracker™Red CMXRos. The localization of the compounds is indicated by the green fluorescence. Colocalization is observed in yellow in the merged images.

Additional studies on mitochondrial functional damage were performed in order to understand better the mechanism of action of **[1a]Cl** and **[2a]Cl**.



## 2.8. Mitochondrial membrane damage

Mitochondria use the energy released by the metabolic oxidation of substrates to establish a proton gradient across their inner membrane through the electron transport chain, thus generating a mitochondrial membrane potential (MMP) that is essential in the process of energy storage in the form of adenosine triphosphate (ATP). ATP drives fundamental biochemical reactions in the cell.<sup>40</sup> Therefore, disruption of the MMP can effectively compromise the cell viability. The effect induced by **[1a]Cl** and **[2a]Cl** on the MMP was analyzed by observing the fluorescence of the JC-1 dye by flow cytometry. JC-1 is a cationic dye that aggregates inside mitochondria in healthy cells and emits red fluorescence; however, upon mitochondrial membrane depolarization, JC-1 is disaggregated and remains in the cytosol in the form of monomeric molecules that emit green fluorescence. PC-3 cells were incubated with the compounds at the corresponding  $IC_{50,light}$  in the dark or under light irradiation. In control untreated cells, red emission from JC-1 aggregates was detected in 74.19 % of the cells while 24.96 % of the cells only emitted green fluorescence corresponding to JC-1 monomers (Fig. 7). A very similar fluorescence pattern was observed in PC-3 cells exposed to **[1a]Cl** and **[2a]Cl** in the dark, indicating that the MMP was not altered. However, under light irradiation, the fluorescence of JC-1 was green-shifted and only 20.82% and 24.21% of the cells exposed to photoirradiated **[1a]Cl** and **[2a]Cl**, respectively, were positive in the red channel (FL2), thus revealing a loss of MMP. Similar results were obtained in cells treated with carbonyl cyanide *m*-chlorophenyl hydrazone (CCCP), a mitochondrial uncoupler that increases the proton permeability across the mitochondrial inner membrane and dissipates the MMP. These results confirmed that the photodynamic activity of **[1a]Cl** and **[2a]Cl** generates an important mitochondrial membrane depolarization that may affect important functions of mitochondria and activate apoptotic cell death.

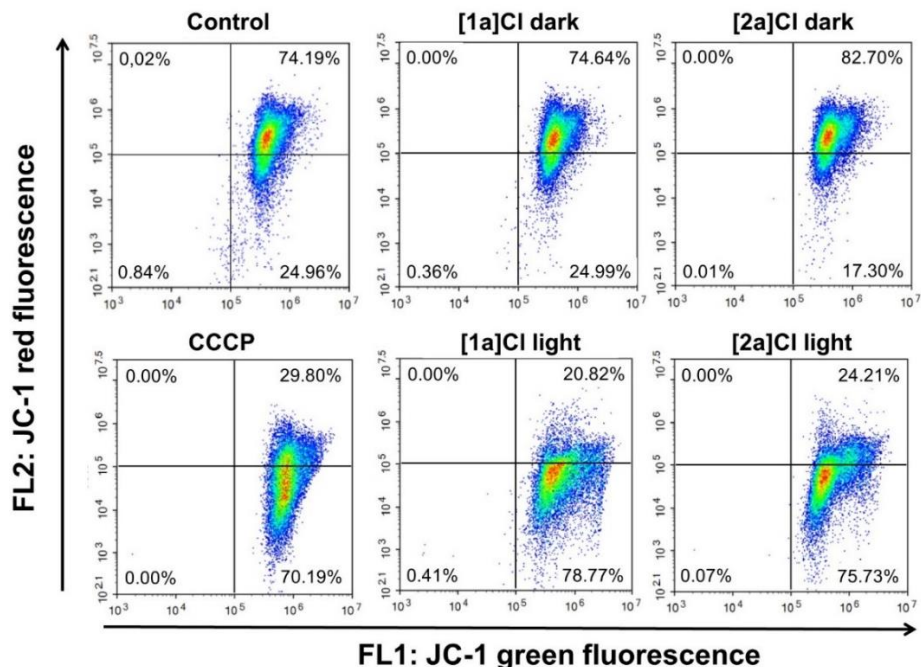


Fig. 7. Flow cytometry analysis of the mitochondrial membrane potential (MMP) after treatment with **[1a]Cl** and **[2a]Cl** using the JC-1 dye. PC-3 cells were incubated with medium alone as a control or with the compounds at the corresponding  $IC_{50,light}$  and then kept in the dark or irradiated with light. CCCP, a mitochondrial uncoupler, was used as a control to induce membrane depolarization. Plots represent fluorescence intensities of Green JC-1 monomers (FL1) and red JC-1 aggregates (FL2) in the cells. The percentage of positive cells is given in the respective quadrants. Decrease of red fluorescence indicates the loss of MMP.

## 2.9. Photocatalytic oxidation of NADH

NADH (1,4-dihyronicotinamide adenine dinucleotide) plays a very important role in numerous biological processes<sup>88,89,90</sup> and is a coenzyme in more than 400 oxidoreductases.<sup>91</sup> It is the main electron source in the mitochondrial electron transport chain (ETC) and participates in the maintenance of the intracellular redox balance.<sup>92</sup> The potential of iridium complexes as photocatalysts for the oxidation of NADH has recently been explored in several works.<sup>88,90,93</sup>

With these premises in mind, we decided to verify the ability of **[1a]Cl** to oxidize NADH to NAD<sup>+</sup>. The study was performed by monitoring through UV-vis spectroscopy the evolution of a solution of NADH in MeOH/H<sub>2</sub>O (1:1) in the presence of **[1a]Cl** under air and with exposure to blue light at room temperature for 24 hours (see Fig. 8). Although there were no clear changes after 30 minutes, the intensity of the band centred at  $\lambda = 339$  nm (maximum of NADH) decreased notably after 24 hours, whereas the band at 259 nm (maximum of NAD<sup>+</sup>) increased, thus revealing the oxidation process of NADH. The

measured TON and TOF values were 1193.86 and 49.74 h<sup>-1</sup>, respectively. Control experiments without catalyst (SI Fig. 34) or in the presence of **[1a]Cl** without light exposure (SI Fig. 35) showed the absence of oxidation, thus disclosing the photocatalytic nature of the process. Thus, it is concluded that NADH could be a mitochondrial target for our complexes, which could induce an imbalance of the redox homeostasis and the loss of the mitochondrial membrane potential and hence it might lead to apoptosis.

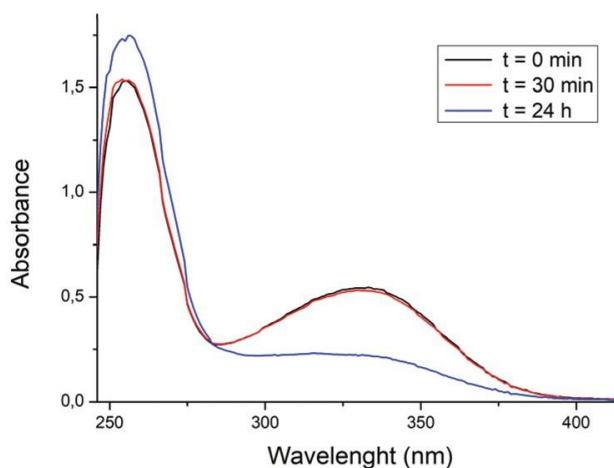


Fig. 8. Evolution of the UV-Vis spectrum of NADH (100  $\mu\text{M}$ ) in MeOH/ H<sub>2</sub>O (1:1, v/v, 2.5 mL) in the presence of **[1a]Cl** (5  $\mu\text{M}$ ) at room temperature during 24 h under air and blue light exposure ( $\lambda_{ir}$  = 460 nm).

### 2.10. DNA interaction

Since mitochondria have their own genome, we were interested in validating mitochondrial DNA (mtDNA) as a possible molecular target of the photodynamic activity of **[1a]Cl** and **[2a]Cl**. Oxidative damage to mtDNA can lead to lethal injury through the subsequent loss of electron transport, mitochondrial membrane potential and ATP generation.<sup>94</sup> The potential effect on mtDNA was assayed as the ability of **[1a]Cl** and **[2a]Cl** to modify the conformation of the pUC18 plasmid. This plasmid has a natural supercoiled conformation (SC) that can be relaxed by a single strand break upon external damage, which leads to an open circular conformation (OC) with a reduced electrophoretic mobility. When the damage is severe, the plasmid is highly fractionated by double strand breaks, which generate fragments that elute from the gel without being detected. Electrophoretic mobility experiments were carried out after exposing the plasmid in the dark or upon irradiation in the presence of the compounds at concentrations ranging from 0 to 100  $\mu\text{M}$ , based on previous experiments.<sup>95</sup> As shown in Fig. 9, in response to hydrogen

peroxide-induced oxidative DNA damage (control experiment), an intense band corresponding to the OC form of the plasmid was generated (lane 2). Treatment with **[1a]Cl** or **[2a]Cl** at 25  $\mu\text{M}$  and 50  $\mu\text{M}$  in the dark barely altered the electrophoretic mobility of the plasmid. However, the OC band became more intense for the corresponding irradiated samples, thus revealing a photoinduced nuclease activity. At 50  $\mu\text{M}$ , a general reduction of the intensity of the bands revealed more extensive damage to the plasmid DNA, especially in the case of **[2a]Cl**. At 75  $\mu\text{M}$  the bands were almost undetectable both in the dark or upon irradiation, which indicates massive cleavage of the DNA. These results indicate that the photodynamic activity of these compounds may induce mtDNA damage that would contribute to mitochondrial dysfunction.

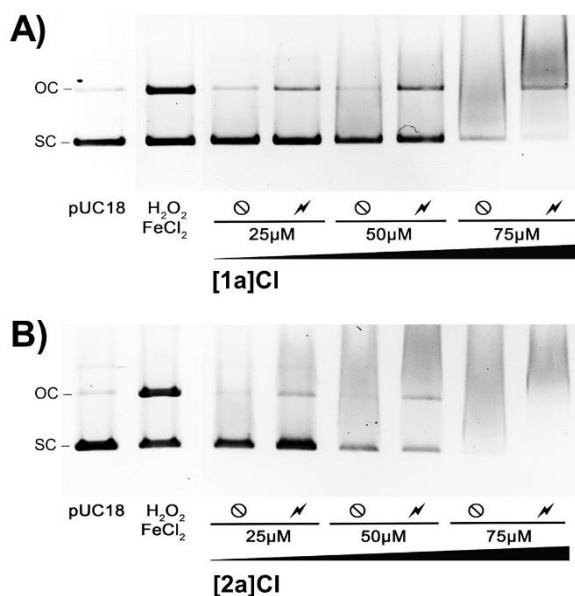


Fig. 9. Electrophoretic mobility of the pUC18 plasmid exposed to the complexes **[1a]Cl** (A) and **[2a]Cl** (B). Treatments are indicated under each lane of the gel. Bands corresponding to untreated pUC18 can be observed in the first lane as a control. SC: supercoiled conformation of the plasmid, OC: open circular conformation of the plasmid.  $\odot$ : incubation in dark conditions,  $\diagup$ : incubation under irradiation.

### 2.11. Effect on cell cycle

The therapeutic action of metal-based anticancer drugs such as cisplatin is mostly related to genomic DNA damage and cell cycle perturbation. However, **[1a]Cl** and **[2a]Cl** do not reach the cell nucleus and their nuclease activity is most likely restricted to mtDNA. In order to explore whether their photodynamic activity has an effect on cell cycle progression, PC-3 cells were exposed for 24 hours to photoactivated **[1a]Cl** and **[2a]Cl** at their respective  $\text{IC}_{50,\text{light}}$  or cisplatin as control, and the cell cycle distribution was analyzed by propidium iodide (PI)

staining. Treatment with cisplatin led to a significant decrease in the proportion of cells in G1 and to an increase in the percentage of cells in S and in G2/M phases ( $41.8 \pm 7.6\%$  in G1,  $25.0 \pm 7.1\%$  in S and  $31.3 \pm 13.8\%$  in G2/M) in comparison to control untreated cells ( $63.2 \pm 8.4$  in G1,  $10.3 \pm 2.3$  in S and  $25.0 \pm 5.55\%$  in G2/M) (Fig. 10), which is in agreement with previous reports.<sup>96</sup> In contrast, complexes **[1a]Cl** and **[2a]Cl** exerted a modest effect on the cell cycle. Only an increase in the percentage of subdiploid population (subG1), corresponding to apoptotic cells, was observed ( $14.4 \pm 6.3\%$  and  $8.2 \pm 4.2\%$  respectively *versus*  $1.5 \pm 0.6$  in control cells). These results indicate that **[1a]Cl** and **[2a]Cl** induce cell death through a mechanism that activates apoptosis without interfering with the cell cycle progression, as previously reported for other mitochondrial targeted compounds.<sup>35</sup>

### 2.12. Cell death mechanism

PSs that target mitochondria are the most likely to induce apoptotic cell death.<sup>97</sup> In order to gain further insights into the cell death mechanism induced by **[1a]Cl** and **[2a]Cl**, flow cytometry experiments were carried out to detect the phosphatidylserine externalization in apoptotic cells and the membrane permeabilization in late apoptotic and necrotic cells by annexin V/PI staining. After 24 hours of treatment, 9.63 % of cells exposed to cisplatin showed a positive staining for annexin V and PI (Fig. 11). Similarly, 9.56 % of the cells treated with **[1a]Cl** and 26.37 % of the cells treated with **[2a]Cl** at their respective  $IC_{50,light}$  under photoactivation conditions were positive for annexin V and PI. This percentage increased markedly to 53.71 % when the concentration of **[1a]Cl** was increased to 5  $\mu$ M. Double stained cells are considered to be in a late apoptosis although they can also be necrotic cells. In fact, after treatment with **[1a]Cl** at 5  $\mu$ M, 9.71 % of the cells were in early apoptosis (annexin V positive) and 7.91 % were necrotic cells (PI positive), thus revealing that both cell death mechanisms were activated in response to the treatment. Since **[1a]Cl** and **[2a]Cl** have been shown to damage the mitochondrial membrane, they are most likely to trigger an apoptotic response by leakage of cytochrome c into the cytosol and activation of the caspase pathway.<sup>7</sup> However, increasing photodamage can provoke a shift from apoptotic to necrotic cell death due to enhanced ROS production or intense depletion of ATP levels.<sup>98</sup>

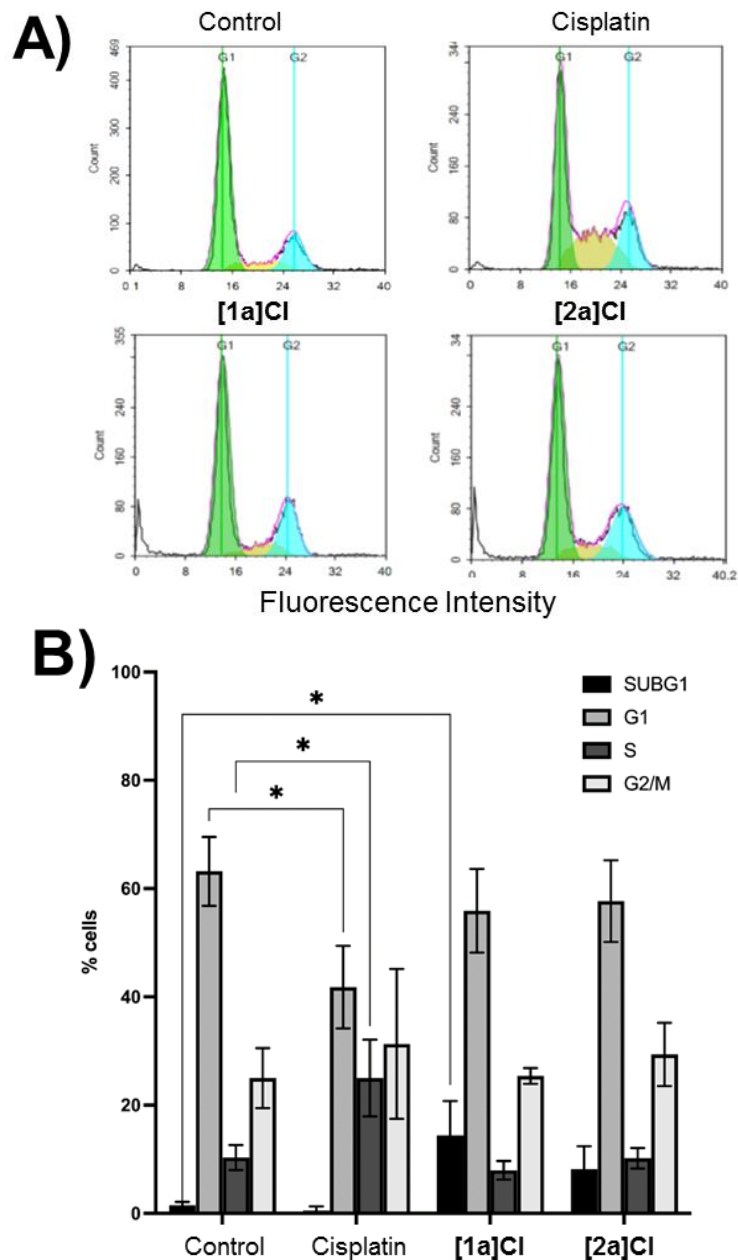


Fig. 10. Effect of [1a]Cl and [2a]Cl on cell cycle distribution. PC-3 cells were treated for 24 h with medium alone as a control, cisplatin (5  $\mu$ M) or with [1a]Cl and [3a]Cl at the  $IC_{50,light}$  under photoactivation conditions. (A) Representative cell cycle profiles of propidium iodide-stained cells obtained by flow cytometry. (B) Bar graph of the mean cell cycle distributions obtained in three independent experiments is shown. \* $p < 0.05$  versus control cells.

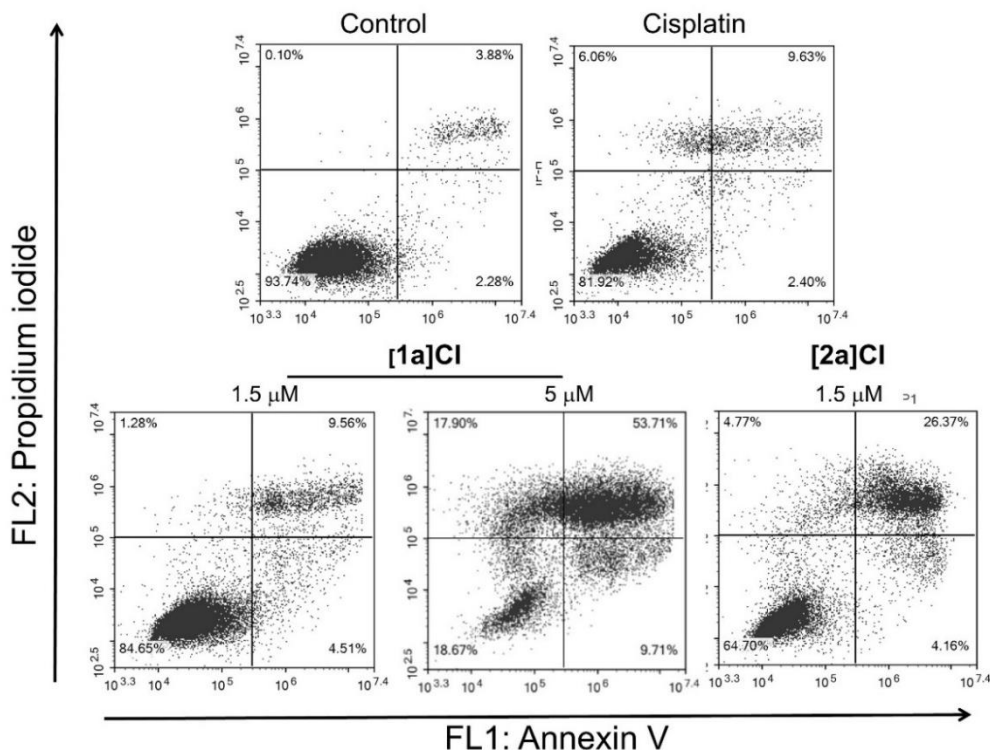


Fig. 11. Cell death mechanism induced by **[1a]Cl** and **[2a]Cl**. PC-3 cells were treated with medium alone as a control, cisplatin (25 μM) or with **[1a]Cl** (1.5 μM and 5 μM) and **[2a]Cl** (1.5 μM) under photoactivation conditions. After 24 h, cells were double stained with propidium iodide and Annexin V-FITC and analysed by flow cytometry. The x-axis shows annexin V-FITC staining and the y-axis shows propidium iodide staining. The percentages of cells in each quadrant are indicated.

### 2.13. Clonogenic assays

Finally, the effect of the compounds on the reproductive viability of the cells was examined by measuring the capacity of **[1a]Cl** and **[2a]Cl** to inhibit the ability of single cells to divide and form colonies after survival. PC-3 cells were incubated with **[1a]Cl** and **[2a]Cl** at the corresponding  $IC_{50,light}$  for six hours and then photoactivated for one hour. Cisplatin was used as positive control. Cells were immediately plated at low density, allowed to reproduce for 10 days and the number of colonies in each plate was determined. As shown in Fig. 12, following the treatments, clonogenicity was almost abolished in cells exposed to **[1a]Cl**, while the number of colonies was inhibited by 91.5% in cells exposed to **[2a]Cl**, which revealed a greater inhibitory activity than cisplatin (89.9%). These results indicate that the phototoxic activity of our compounds markedly inhibits the capacity of the cells to reproduce.



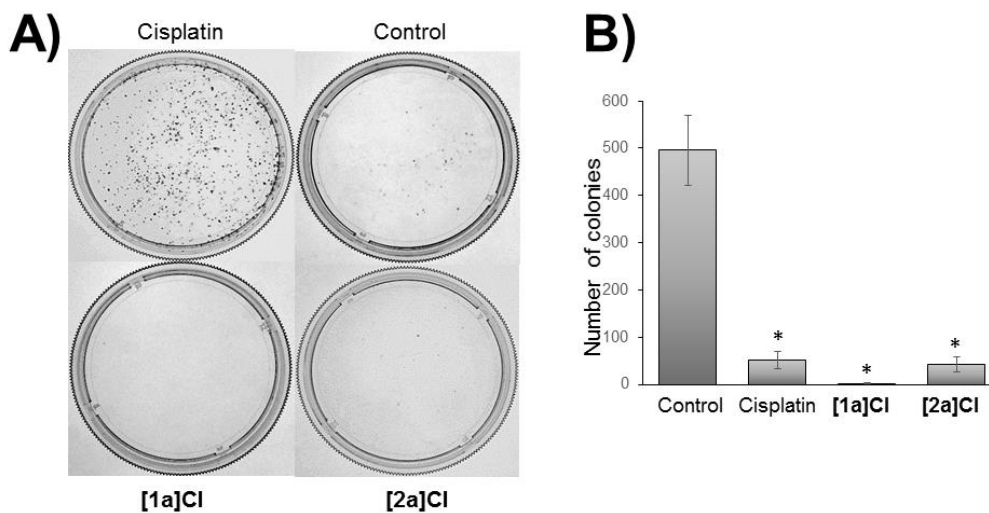


Fig. 12. Clonogenic assay. (A) Colony formation of PC-3 cells after exposure to [1a]Cl and [2a]Cl for 6 h at the  $IC_{50, light}$  followed by 1 h irradiation. Control cells were treated with medium alone. Cisplatin at 5  $\mu$ M was used as a positive control. (B) Bar charts represent the number of colonies after each treatment (mean  $\pm$  SD of 3 experiments. \* $p < 0.05$  versus control cells).

### 3. Conclusions

Four new Ir(III) biscyclometallated complexes of general formula  $[Ir(C^{\wedge}N)_2(N^{\wedge}N')Cl]$  ( $C^{\wedge}N = 2\text{-phenyl-pyridinate, ppy, and } 2\text{-}(2,4\text{-difluorophenyl})\text{pyridinate, dfppy}$ ) with  $N^{\wedge}N'$  ancillary ligands have been prepared and characterized as photosensitizers for PDT studies. The  $N^{\wedge}N'$  ligands contain an amide-substituted benzimidazole fragment and thiazolyl (**L1**) or pyridine (**L2**) rings. The variation of the electrochemical and photophysical properties of these complexes is determined by two factors: (a) the stabilizing effect on the HOMO attributed to the fluoro-substituents of dfppy relative to ppy, regarding the  $C^{\wedge}N$  ligands and (b) the destabilizing effect on the LUMO ascribed to the thiazolyl ring of **L1** relative to the py ring in **L2**. In general, a strong reducing and oxidizing power of the excited states was found. The complexes are photostable. Blue shifted emission was observed for the dfppy derivatives compared to the ppy analogues, although a stronger effect was produced by the ancillary  $N^{\wedge}N'$  ligand, with blue-shifted emissions for complexes with ligand **L1** relative to derivatives with **L2**. The  $\Phi_{PL}$  and the excited-state lifetime were clearly higher for the dfppy derivatives ( $\Phi_{PL} = 75\text{--}76\%$ ,  $\tau = 1320\text{--}1357$  ns) with negligible influence of the  $N^{\wedge}N'$  ancillary ligands. The generation of  $^1O_2$  was demonstrated, but the formation of  $O_2^{\cdot-}$  cannot be ruled out. Biological studies showed that these complexes are moderately toxic to cells in the dark.

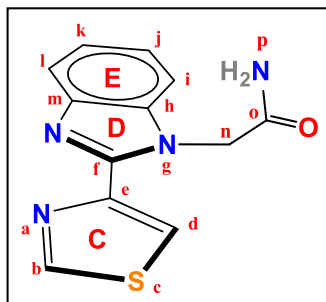


Moreover, in the case of complexes bearing ppy ligands (**[1a]Cl** and **[2a]Cl**), the cytotoxic activity can be enhanced by up to 20 times upon blue light irradiation. However, **[1b]Cl** did not display photo-activation of its cytotoxicity under blue light exposure because of its lack of absorption in the visible region and **[2b]Cl** showed a PI of only 2.2. It is concluded that, at least for our complexes, high values of both  $\Phi_{PL}$  and excited state lifetimes are not enough for a suitable PDT behavior, since their absorption profiles do not allow excitation with visible light. The photoactivatable complexes (**[1a]Cl** and **[2a]Cl**) are particularly active against prostate cancer cells (PC-3) and melanoma cells (SK-MEL-28) upon irradiation and  $IC_{50}$  values in the nanomolar range were found. Moreover, a high degree of selectivity for melanoma cells was observed with respect to CCD-18Co non-malignant cells that had not been exposed to light irradiation. Regarding the mechanism of action, it was demonstrated that the complexes are efficiently taken up by cells through endocytosis, with a maximum cellular internalization achieved after six hours of incubation. Indeed, longer pre-incubation times before irradiation resulted in better uptake into cells and this led to an enhanced photocytotoxic response. Hence, we speculate that **[1a]Cl** and **[2a]Cl** are accumulated primarily in mitochondria, where their photodynamic activity alters membrane potential, disrupts the electron transport chain *via* the photocatalytic oxidation of NADH and presumably induces mtDNA damage, effectively compromising mitochondrial function and activating cell death by apoptosis. This multi-action mechanism strongly inhibits the capacity of cancer cells to survive and reproduce. It should be noted that **[1a]Cl** and **[2a]Cl** do not alter the cell cycle progression, which indicates that they do not target nuclear DNA and exert their anticancer activity through mechanisms that are different from that of cisplatin. Therefore, in addition to their promising activity in PDT, these mitochondria-targeted complexes have great potential to overcome resistance developed towards current chemotherapeutic drugs in many cancer treatments. However, future developments of these photosensitizers should involve conjugation to organic chromophores aiming to operate in the phototherapeutic window.

## 4. Synthesis and characterization

### 4.1. Ligands

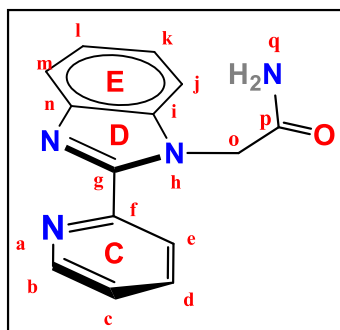
#### L1



In a 100 mL Schlenk flask,  $K_2CO_3$  (0.3288 g, 1.990 mmol) was added to a solution of 2-(4-Thiazolyl)benzimidazole (thiabenzazole, TBZ) (0.4008 g, 1.992 mmol) in DMF (11 mL). The mixture/suspension was stirred at room temperature for 30 minutes. 2-bromoacetamide (0.2748 g, 1.992 mmol) was then added. The stirring was extended for 22 hours at room temperature. The solvent was removed under vacuum and the residue was redissolved in DMSO (5 mL). Water (10 mL) was added to precipitate a white solid that was filtrated, redissolved in ethanol (15 ml) and took to dryness (2 times)

and then redissolved in toluene (15 ml) and took to dryness. The white solid was dried under vacuum. Yield: 0.3848 g (1.490 mmol, 75%). **Mr** ( $C_{12}H_{10}N_4OS$ ) = 258.30 g/mol. **Anal. Calcd for  $C_{12}H_{10}N_4OS((CH_3)_2SO)_{0.15}$** : C 54.71; H 4.07; N 20.75; **Found**: C 54.45; H 3.87; N 21.10.  **$^1H$  NMR (400 MHz, DMSO- $d_6$ , 25 °C)**  $\delta$  9.30 (dd,  $J = 2.1, 0.6$  Hz, 1H,  $H^d$ ), 8.51 (dd,  $J = 2.1, 0.6$  Hz, 1H,  $H^b$ ), 7.69–7.66(m, 2H,  $H^p, H^i$ ), 7.55 – 7.48 (m, 1H,  $H^l$ ), 7.29 – 7.22 (m, 2H,  $H^j, H^k$ ), 7.20 (s, 1H,  $H^p$ ), 5.46 (s, 2H,  $H^n, H^n$ ) ppm.  **$^{13}C\{^1H\}$  NMR (101 MHz, DMSO- $d_6$ , 25 °C)**  $\delta$  168.76, 155.14, 147.17, 146.93, 142.33, 136.39, 122.66, 122.21, 122.13, 118.89, 110.54, 47.07 ppm. **FT-IR (KBr,  $cm^{-1}$ ) selected bands**: 3305 (w,  $\nu_{N-H}$ ), 3099 (w,  $\nu_{Car-H}$ ), 1603–1573 (m,  $\nu_{C=C + C-N}$ ), 1421 (w,  $\nu_{C=N}$ ), 1164 (m,  $\nu_{C-C}$ ), 1072 (m,  $\delta_{C-Hip}$ ), 735 (vs,  $\delta_{C-Hoop}$ ). **HR ESI+ MS (DCM/DMSO, 4:1)**:  $m/z_{exp} = 259.0651$  ( $m/z_{calcd} [M+H^+] = m/z_{calcd} [C_{12}H_{11}N_4OS]^+ = 259.0654$ ). **Solubility**: soluble in dichloromethane, methanol, chloroform, dimethylformamide, dimethyl sulfoxide and acetone. Partially soluble in water.

#### L2



In a 100 mL Schlenk flask,  $K_2CO_3$  (0.4236 g, 2.564 mmol) was added to a solution of 2-(2-Pyridyl)benzimidazole (pybzim) (0.5001 g, 2.562 mmol) in DMF (7 mL). The mixture/suspension was stirred at room temperature for 30 minutes. 2-bromoacetamide (0.4241 g, 3.074 mmol) was then added. The stirring was extended for 22 hours at room temperature. The solvent was removed under vacuum and the residue was tried to redissolve with ethanol (15 mL), dichloromethane (15 mL) and methanol (10 mL), which is not possible, but while there is a white-yellow solid, the solution is brown-orange coloured so it is filtered and the solid is

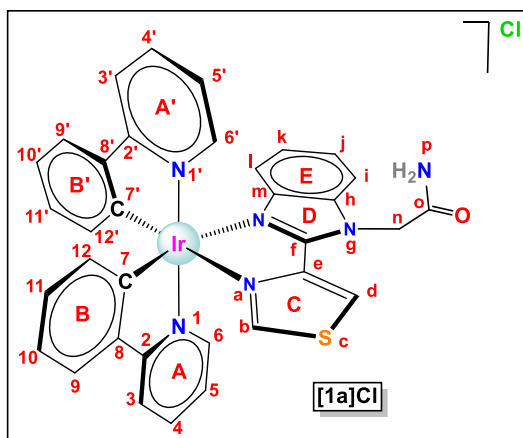
washed with water (3 mL). The pale brown solid is dried under vacuum. Yield: 0.5007 g (1.985 mmol, 77%). **Mr** ( $C_{14}H_{12}N_4O$ ) = 252.27 g/mol. **Anal. Calcd for  $C_{14}H_{12}N_4O((CH_3)_2SO)_{0.15}$** : C 65.06; H 4.93; N 21.22; **Found**: C 65.05; H 4.77; N 21.50.  **$^1H$  NMR (400 MHz, DMSO- $d_6$ , 25 °C)**  $\delta$  8.70 – 8.65 (m, 1H,  $H^e$ ), 8.38 – 8.32 (m, 1H,  $H^b$ ), 7.99 (td,  $J = 7.9, 1.8$  Hz, 1H,  $H^c$ ), 7.73 (dd,  $J = 7.0, 1.5$  Hz, 1H,  $H^m$ ), 7.65 (s, 1H,  $H^q$ ), 7.59 – 7.54 (m, 1H,  $H^l$ ), 7.49 (ddd,  $J = 7.6, 4.9, 1.3$  Hz, 1H,  $H^d$ ), 7.33 – 7.25 (m, 2H,  $H^k, H^l$ ), 7.15 (s, 1H,  $H^q$ ), 5.54 (s, 2H,  $H^o$ ) ppm.  **$^{13}C\{^1H\}$  NMR (101 MHz, DMSO- $d_6$ , 25 °C)**  $\delta$  169.04, 150.13, 149.60, 148.56, 141.97, 137.36, 137.29, 124.16, 123.93, 123.18, 122.34, 119.42, 110.73, 47.71 ppm. **FT-IR (KBr,  $cm^{-1}$ ) selected bands**: 3317 (w,  $\nu_{N-H}$ ), 3147 (w,  $\nu_{Car-H}$ ), 1593–1584 (m,  $\nu_{C=C + C-N}$ ), 1415 (w,  $\nu_{C=N}$ ), 1171 (m,  $\nu_{C-C}$ ), 1045 (m,  $\delta_{C-Hip}$ ), 748 (vs,  $\delta_{C-Hoop}$ ). **HR ESI+**

**MS (DCM/DMSO, 4:1):**  $m/z_{\text{exp}} = 253.1087$  ( $m/z_{\text{calcd}} [\text{M}+\text{H}^+] = m/z_{\text{calcd}} [\text{C}_{14}\text{H}_{13}\text{N}_4\text{O}]^+ = 253.1089$ ).

**Solubility:** soluble in dichloromethane, methanol, chloroform, dimethylformamide, dimethyl sulfoxide and acetone. Partially soluble in water.

## 4.2. Ir(III)-complexes

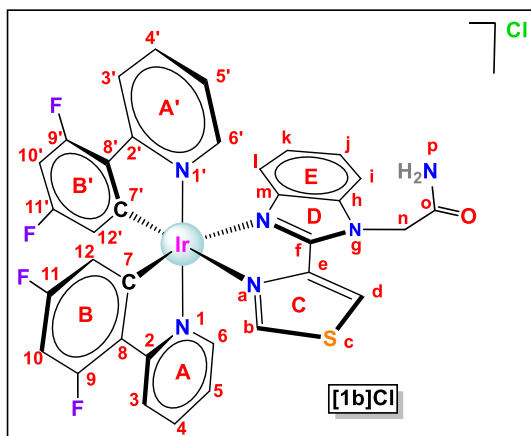
### **[Ir(ppy)<sub>2</sub>(L1)]Cl: [1a]Cl**



In a 100 mL Schlenk flask, previously purged with nitrogen, the ancillary ligand L<sup>x</sup> (0.0542 g, 0.210 mmol) was added to a solution of [Ir(μ-Cl)(ppy)<sub>2</sub>]<sub>2</sub> (0.1003 g, 0.094 mmol) in a mixture of dichloromethane (8 mL) / methanol (10 mL), and the mixture was stirred at 60 °C for 24 hours under a N<sub>2</sub> atmosphere. The resulting solution was concentrated to half the volume under vacuum and diethyl ether (15 mL) was added to precipitate a crude solid that was isolated by filtration and washed with diethyl ether (2×5 mL). The product was

dried under vacuum to produce a yellow powder. Yield: 0.1182 g (0.149 mmol, 80%). **M<sub>r</sub>** (C<sub>34</sub>H<sub>26</sub>ClIrN<sub>6</sub>OS) = 794.34 g/mol. **Anal. Calcd for C<sub>34</sub>H<sub>26</sub>ClIrN<sub>6</sub>OS·(CH<sub>2</sub>Cl)<sub>2</sub>·1.04:** C 47.68; H 3.21; N 9.52; **Found:** C 47.70; H 3.30; N 9.32. **<sup>1</sup>H NMR (400 MHz, DMSO-d<sub>6</sub>, 25 °C)** δ 8.97 (s, 1H, H<sup>d</sup>), 8.51 (s, 1H, H<sup>b</sup>), 8.31 (s, 1H, H<sup>NH</sup>), 8.26 (d, J = 8.1 Hz, 1H, H<sup>3</sup>), 8.21 (d, J = 8.0 Hz, 1H, H<sup>3'</sup>), 7.96 – 7.86 (m, 5H, H<sup>i</sup>, H<sup>4</sup>, H<sup>4'</sup>, H<sup>9</sup>, H<sup>9'</sup>), 7.73 (d, J = 5.8 Hz, 1H, H<sup>6'</sup>), 7.70 (d, J = 5.8 Hz, 1H, H<sup>6</sup>), 7.64 (s, 1H, H<sup>NH</sup>), 7.36 (t, J = 7.8 Hz, 1H, H<sup>j</sup>), 7.19 (t, J = 6.8 Hz, 1H, H<sup>5</sup>), 7.13 (t, J = 6.1 Hz, 1H, H<sup>5'</sup>), 7.06 (t, J = 7.2 Hz, 1H, H<sup>10</sup>), 7.01 (t, J = 7.5 Hz, 2H, H<sup>10'</sup>, H<sup>k</sup>), 6.92 (t, J = 7.6 Hz, 1H, H<sup>11</sup>), 6.89 (t, J = 7.5 Hz, 1H, H<sup>11'</sup>), 6.32 (d, J = 7.5 Hz, 1H, H<sup>12</sup>), 6.25 (d, J = 7.5 Hz, 1H, H<sup>12'</sup>), 6.15 (d, J = 8.2 Hz, 1H, H<sup>l</sup>), 5.64 – 5.52 (AB system, 2H, H<sup>n</sup>) ppm. **<sup>13</sup>C{<sup>1</sup>H} NMR (101 MHz, DMSO-d<sub>6</sub>, 25 °C)** δ 167.12, 167.00, 158.58, 149.23, 148.86, 148.46, 147.30, 144.55, 144.42, 143.31, 138.63, 138.57, 138.43, 136.27, 131.73, 131.27, 129.85, 129.53, 126.07, 125.06, 124.86, 124.75, 124.40, 123.65, 122.06, 121.98, 119.86, 119.50, 116.61, 112.20, 47.30 ppm. **FT-IR (KBr, cm<sup>-1</sup>) selected bands:** 3319 (w, ν<sub>N-H</sub>), 3038 (w, ν<sub>Car-H</sub>), 1604-1581 (m, ν<sub>C=C + C-N</sub>), 1426 (w, ν<sub>C=N</sub>), 1161 (m, ν<sub>C-C</sub>), 1062 (m, δ<sub>C-Hip</sub>), 754-739 (vs, δ<sub>C-Hoop</sub>). **HR ESI+ MS (DCM/DMSO, 4:1):**  $m/z_{\text{exp}} = 759.1513$  ( $m/z_{\text{calcd}} [\text{M}^+] = m/z_{\text{calcd}} [\text{C}_{34}\text{H}_{26}\text{IrN}_6\text{OS}]^+ = 759.1518$ ); 501.0935 ( $m/z_{\text{calcd}} [\text{M}^+-\text{L1}] = m/z_{\text{calcd}} [\text{C}_{22}\text{H}_{16}\text{IrN}_2]^+ = 501.0943$ ). **Solubility:** soluble in dimethyl sulfoxide, dichloromethane, methanol, acetonitrile, acetone, dimethylformamide, tetrahydrofuran. Partially soluble in water.

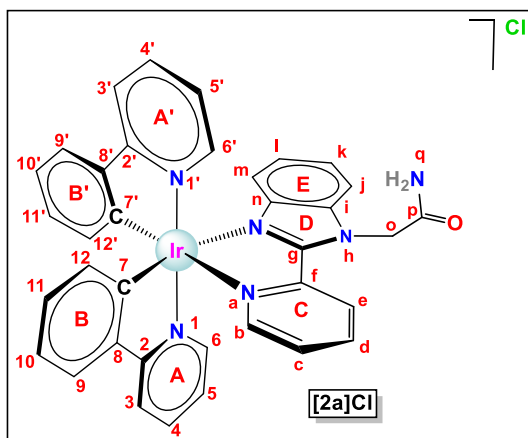
**[Ir(dfppy)<sub>2</sub>(L1)]Cl: [1b]Cl**



In a 100 mL Schlenk flask, previously purged with nitrogen, the ancillary ligand L<sup>x</sup> (0.0473 g, 0.183 mmol) was added to a solution of [Ir(μ-Cl)(dfppy)<sub>2</sub>]<sub>2</sub> (0.1001 g, 0.082 mmol) in a mixture of dichloromethane (8 mL) / methanol (10 mL), and the mixture was stirred at 60 °C for 24 hours under a N<sub>2</sub> atmosphere. The resulting solution was concentrated to half the volume under vacuum and diethyl ether (15 mL) was added to precipitate a crude solid that was isolated by filtration and washed with

diethyl ether (2×5 mL). The product was dried under vacuum to produce a yellow powder. Yield: 0.0848 g (0.098 mmol, 60%). **M<sub>r</sub>** (C<sub>34</sub>H<sub>22</sub>ClF<sub>4</sub>IrN<sub>6</sub>OS) = 866.31 g/mol. **Anal. Calcd for C<sub>34</sub>H<sub>22</sub>ClF<sub>4</sub>IrN<sub>6</sub>OS (CH<sub>2</sub>Cl<sub>2</sub>)<sub>0.90</sub>**: C 44.46; H 2.54; N 8.91; **Found**: C 44.54.49; H 2.60; N 9.20. **<sup>1</sup>H NMR (400 MHz, DMSO-d<sub>6</sub>, 25 °C)** δ 9.01 (s, 1H, H<sup>d</sup>), 8.73 (s, 1H, H<sup>b</sup>), 8.30 (d, J = 7.6 Hz, 1H, H<sup>3</sup>), 8.29 (s, 1H, H<sup>NH</sup>), 8.24 (d, J = 8.7 Hz, H<sup>3'</sup>), 8.03 (t, J = 8.1 Hz, 1H, H<sup>4</sup>), 7.99 (t, J = 8.1 Hz, 1H, H<sup>4'</sup>), 7.91 (d, J = 8.3 Hz, 1H, H<sup>i</sup>), 7.79 (d, J = 5.8 Hz, 1H, H<sup>6</sup>), 7.75 (d, J = 5.7 Hz, 1H, H<sup>6'</sup>), 7.65 (s, 1H, H<sup>NH</sup>), 7.42 (t, J = 7.9 Hz, 1H, H<sup>l</sup>), 7.28 (t, J = 6.8 Hz, 1H, H<sup>5</sup>), 7.24 (t, J = 6.8 Hz, 1H, H<sup>5'</sup>), 7.18 (t, J = 7.7 Hz, 1H, H<sup>k</sup>), 7.09 – 6.91 (m, 2H, H<sup>10</sup>, H<sup>10'</sup>), 6.21 (d, J = 8.2 Hz, 1H, H<sup>l</sup>), 5.76 (d, J<sub>H-F</sub> = 6.6 Hz, 1H, H<sup>12</sup> or H<sup>12'</sup>), 5.66 (d, J<sub>H-F</sub> = 8.5 Hz, 1H, H<sup>12</sup> or H<sup>12'</sup>), 5.58 (AB system 2H, H<sup>n</sup>) ppm. **<sup>19</sup>F NMR (376 MHz, DMSO-d<sub>6</sub>, 25 °C)** δ -107.01 (c, J = 9.8 Hz, 1F, F<sup>11</sup> or F<sup>11'</sup>), -107.04 (c, J = 9.5 Hz, 1F, F<sup>11</sup> or F<sup>11'</sup>), -109.12 (t, J = 11.0 Hz, 1F, F<sup>9</sup> or F<sup>9'</sup>), -109.19 (t, J = 11.6 Hz, 1F, F<sup>9</sup> or F<sup>9'</sup>) ppm. **<sup>13</sup>C{<sup>1</sup>H} NMR (101 MHz, DMSO-d<sub>6</sub>, 25 °C)** δ 166.99, 162.93, 162.86, 161.65, 161.08, 159.50, 152.50, 151.58, 149.79, 149.24, 142.78, 139.91, 139.79, 138.26, 136.22, 128.39, 128.15, 127.57, 126.39, 125.35, 124.96, 124.34, 123.57, 123.14, 115.91, 115.82, 113.84, 112.56, 109.55, 99.19, 47.39 ppm. **FT-IR (KBr, cm<sup>-1</sup>) selected bands**: 3069 (w, ν<sub>Car-H</sub>), 1601-1574 (m, ν<sub>C=C + C-N</sub>), 1429 (w, ν<sub>C=N</sub>), 1163 (m, ν<sub>C-C</sub>), 1070 (m, δ<sub>C-Hip</sub>), 745 (vs, δ<sub>C-Hoop</sub>). **HR ESI+ MS (DCM/DMSO, 4:1)**: m/z<sub>exp</sub> = 831.1136 (m/z<sub>calcd</sub> [M<sup>+</sup>] = m/z<sub>calcd</sub> [C<sub>34</sub>H<sub>22</sub>F<sub>4</sub>IrN<sub>6</sub>OS]<sup>+</sup> = 831.1141); 573.0556 (m/z<sub>calcd</sub> [M<sup>+</sup>-L1] = m/z<sub>calcd</sub> [C<sub>22</sub>H<sub>12</sub>F<sub>4</sub>IrN<sub>2</sub>]<sup>+</sup> = 573.0566). **Solubility**: soluble in dimethyl sulfoxide, dichloromethane, methanol, acetonitrile, acetone, dimethylformamide, tetrahydrofuran. Partially soluble in water.

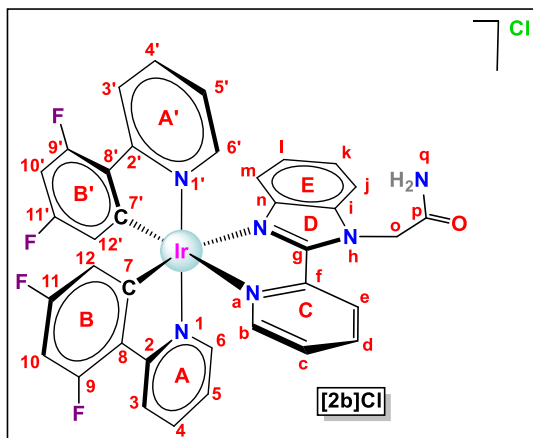
### Synthesis of $[\text{Ir}(\text{ppy})_2(\text{L}2)]\text{Cl}$ : $[\text{2a}]\text{Cl}$



In a 100 mL Schlenk flask, previously purged with nitrogen, the ancillary ligand  $\text{L}^x$  (0.0537 g, 0.213 mmol) was added to a solution of  $[\text{Ir}(\mu\text{-Cl})(\text{ppy})_2]_2$  (0.1004 g, 0.094 mmol) in a mixture of dichloromethane (8 mL) / methanol (10 mL), and the mixture was stirred at 60 °C for 24 hours under a  $\text{N}_2$  atmosphere. The resulting solution was concentrated to half the volume under vacuum and diethyl ether (15 mL) was added to precipitate a crude solid that was isolated by filtration and washed with diethyl ether (2x5 mL). The product was

dried under vacuum to produce an orange powder. Yield: 0.1036 g (0.131 mmol, 70%). **Mr** ( $\text{C}_{36}\text{H}_{28}\text{ClIrN}_6\text{O}$ ) = 788.32 g/mol. **Anal. Calcd for  $\text{C}_{36}\text{H}_{28}\text{ClIrN}_6\text{O} \cdot (\text{CH}_2\text{Cl}_2)_{0.80}$** : C 51.62; H 3.48; N 9.81; **Found**: C 51.64; H 3.56; N 9.78.  **$^1\text{H}$  NMR (400 MHz, DMSO- $d_6$ , 25 °C)**  $\delta$  8.47 (d,  $J = 8.2$  Hz, 1H,  $\text{H}^e$ ), 8.32 – 8.19 (m, 4H,  $\text{H}^d$ ,  $\text{H}^3$ ,  $\text{H}^{3'}$ ,  $\text{H}^{\text{NH}}$ ), 7.97-7.86 (m, 6H,  $\text{H}^b$ ,  $\text{H}^j$ ,  $\text{H}^9$ ,  $\text{H}^9$ ,  $\text{H}^4$ ,  $\text{H}^4$ ), 7.71-7.66 (m, 3H,  $\text{H}^c$ ,  $\text{H}^{\text{NH}}$ ,  $\text{H}^6$ ), 7.60 (d,  $J = 5.5$  Hz, 1H,  $\text{H}^6$ ), 7.43 (t,  $J = 7.8$  Hz, 1H,  $\text{H}^k$ ), 7.16-7.01 (m, 5H,  $\text{H}^5$ ,  $\text{H}^{5'}$ ,  $\text{H}^{10}$ ,  $\text{H}^{10'}$ ,  $\text{H}^l$ ), 6.93 (t,  $J = 6.7$  Hz, 1H,  $\text{H}^{11}$ ), 6.91 (t,  $J = 6.8$  Hz, 1H,  $\text{H}^{11'}$ ), 6.29 (d,  $J = 7.3$  Hz, 1H,  $\text{H}^{12}$ ), 6.22 (d,  $J = 7.7$  Hz, 1H,  $\text{H}^m$ ), 6.20 (d,  $J = 7.0$  Hz, 1H,  $\text{H}^{12'}$ )  $\text{H}^m$ ), 5.69 (s, 2H,  $\text{H}^o$ ,  $\text{H}^o$ ) ppm.  **$^{13}\text{C}\{^1\text{H}\}$  NMR (101 MHz, DMSO- $d_6$ , 25 °C)**  $\delta$  167.41, 167.09, 166.94, 153.51, 151.46, 150.99, 149.28, 149.02, 147.53, 146.90, 144.43, 144.13, 139.59, 138.67, 138.64, 138.48, 136.85, 131.76, 130.89, 130.31, 129.65, 128.67, 125.86, 125.40, 125.16, 124.89, 124.84, 123.76, 123.68, 122.26, 122.13, 119.98, 119.65, 116.99, 112.40, 48.10 ppm. **FT-IR (KBr,  $\text{cm}^{-1}$ ) selected bands**: 3310 (w,  $\nu_{\text{N-H}}$ ), 3029 (w,  $\nu_{\text{C-H}}$ ), 1606-1581 (m,  $\nu_{\text{C=C} + \text{C-N}}$ ), 1436 (w,  $\nu_{\text{C=N}}$ ), 1143 (m,  $\nu_{\text{C-C}}$ ), 1064 (m,  $\delta_{\text{C-Hip}}$ ), 761-742 (vs,  $\delta_{\text{C-Hoop}}$ ). **HR ESI+ MS (DCM/DMSO, 4:1)**:  $m/z_{\text{exp}} = 753.1949$  ( $m/z_{\text{calcd}} [\text{M}^+] = m/z_{\text{calcd}} [\text{C}_{36}\text{H}_{28}\text{IrN}_6\text{O}]^+ = 753.1954$ ); 501.0934 ( $m/z_{\text{calcd}} [\text{M}^+ - \text{L}2] = m/z_{\text{calcd}} [\text{C}_{22}\text{H}_{16}\text{IrN}_2]^+ = 501.0943$ ). **Solubility**: soluble in dimethyl sulfoxide, dichloromethane, methanol, acetonitrile, acetone, dimethylformamide, tetrahydrofuran.

### Synthesis of $[\text{Ir}(\text{dfppy})_2(\text{L}2)]\text{Cl}$ : $[\mathbf{2b}]\text{Cl}$



In a 100 mL Schlenk flask, previously purged with nitrogen, the ancillary ligand  $\text{L}^*$  (0.0417 g, 0.165 mmol) was added to a solution of  $[\text{Ir}(\mu\text{-Cl})(\text{dfppy})_2]_2$  (0.1002 g, 0.082 mmol) in a mixture of dichloromethane (8 mL) / methanol (10 mL), and the mixture was stirred at 60 °C for 24 hours under a  $\text{N}_2$  atmosphere. The resulting solution was concentrated to half the volume under vacuum and diethyl ether (15 mL) was added to precipitate a crude solid that was isolated by filtration and washed with diethyl ether (2x5 mL).

The product was dried under vacuum to produce a yellow powder. Yield: 0.0720 g (0.084 mmol, 51%).  **$M_r$**  ( $\text{C}_{36}\text{H}_{24}\text{ClF}_4\text{IrN}_6\text{O}$ ) = 860.28 g/mol. **Anal. Calcd for  $\text{C}_{36}\text{H}_{24}\text{ClF}_4\text{IrN}_6\text{O} \cdot (\text{CH}_2\text{Cl}_2)_{1.6}$** : C 45.34; H 2.75; N 8.44; **Found**: C 45.37; H 2.80; N 8.60.  **$^1\text{H NMR}$  (400 MHz,  $\text{DMSO-d}_6$ , 25 °C)**  $\delta$  8.55 (d,  $J$  = 6.9 Hz, 1H,  $\text{H}^e$ ), 8.36-8.29 (m, 3H,  $\text{H}^d$ ,  $\text{H}^{\text{NH}}$ ,  $\text{H}^3$  or  $\text{H}^{3'}$ ), 8.24 (d,  $J$  = 7.9 Hz, 1H,  $\text{H}^3$  or  $\text{H}^{3'}$ ), 7.99 (m, 4H,  $\text{H}^b$ ,  $\text{H}^4$ ,  $\text{H}^{4'}$ ,  $\text{H}^j$ ), 7.80 – 7.63 (m, 4H,  $\text{H}^c$ ,  $\text{H}^6$ ,  $\text{H}^{6'}$ ,  $\text{H}^{\text{NH}}$ ), 7.48 (t,  $J$  = 8.7 Hz, 1H,  $\text{H}^k$ ), 7.26-7.18 (m, 3H,  $\text{H}^5$ ,  $\text{H}^l$ ,  $\text{H}^{5'}$ ), 7.04 (t,  $J_{\text{H-F}}$  = 8.7 Hz, 1H,  $\text{H}^{10}$  or  $\text{H}^{10'}$ ), 6.98 (t,  $J_{\text{H-F}}$  = 8.7 Hz, 1H,  $\text{H}^{10}$  or  $\text{H}^{10'}$ ), 6.27 (d,  $J$  = 8.3 Hz, 1H,  $\text{H}^m$ ), 5.74 (m, 3H,  $\text{H}^o$ ,  $\text{H}^{12}$ ), 5.62 (d,  $J_{\text{H-F}}$  = 7.7 Hz, 1H,  $\text{H}^{12'}$ ) ppm.  **$^{19}\text{F NMR}$  (376 MHz,  $\text{DMSO-d}_6$ , 25 °C)**  $\delta$  -106.49 (q,  $J$  = 9.3 Hz, 1F,  $\text{F}^{11}$  or  $\text{F}^{11'}$ ), -106.92 (q,  $J$  = 9.6 Hz, 1F,  $\text{F}^{11}$  or  $\text{F}^{11'}$ ), -108.62 (t,  $J$  = 11.9 Hz, 1F,  $\text{F}^9$  or  $\text{F}^{9'}$ ), -109.11 (t,  $J$  = 11.2 Hz, 1F,  $\text{F}^9$  or  $\text{F}^{9'}$ ) ppm.  **$^{13}\text{C}\{^1\text{H}\}$  NMR (101 MHz,  $\text{DMSO-d}_6$ , 25 °C)**  $\delta$  167.28, 164.23, 163.65, 162.87, 162.11, 161.69, 161.11, 159.53, 159.40, 159.23, 158.48, 155.46, 155.39, 153.53, 151.86, 151.80, 151.54, 149.76, 146.48, 140.19, 139.96, 138.27, 136.78, 129.18, 128.26, 126.08, 125.68, 124.37, 123.26, 123.09, 116.25, 113.83, 112.96, 112.77, 99.07, 48.17 ppm. **FT-IR (KBr,  $\text{cm}^{-1}$ ) selected bands**: 3065 (w,  $\nu_{\text{C-H}}$ ), 1601-1575 (m,  $\nu_{\text{C=C}} + \text{C-N}$ ), 1429 (w,  $\nu_{\text{C=N}}$ ), 1163 (m,  $\nu_{\text{C-C}}$ ), 1069 (m,  $\delta_{\text{C-Hip}}$ ), 745 (vs,  $\delta_{\text{C-Hoop}}$ ). **HR ESI+ MS (DCM/DMSO, 4:1)**:  $m/z_{\text{exp}} = 825.1575$  ( $m/z_{\text{calcd}} [\text{M}^+] = m/z_{\text{calcd}} [\text{C}_{36}\text{H}_{24}\text{F}_4\text{IrN}_6\text{O}]^+ = 825.1577$ ); 573.0556 ( $m/z_{\text{calcd}} [\text{M}^+ - \text{L}2] = m/z_{\text{calcd}} [\text{C}_{22}\text{H}_{12}\text{F}_4\text{IrN}_2]^+ = 573.0566$ ). **Solubility**: soluble in dimethyl sulfoxide, dichloromethane, methanol, acetonitrile, acetone, dimethylformamide, tetrahydrofuran.

## Bibliography

1. S. Ghosh, Cisplatin: The first metal based anticancer drug, *Bioorg. Chem.*, 2019, **88**, 102925.
2. D. Wang and S. J. Lippard, Cellular processing of platinum anticancer drugs, *Nat. Rev. Drug Discov.*, 2005, **4**, 307–320.
3. S. Medici, M. Peana, V. M. Nurchi, J. I. Lachowicz, G. Crisponi and M. A. Zoroddu, Noble metals in medicine: Latest advances, *Coord. Chem. Rev.*, 2015, **284**, 329–350.
4. S. H. van Rijt and P. J. Sadler, Current applications and future potential for bioinorganic chemistry in the development of anticancer drugs, *Drug Discov. Today*, 2009, **14**, 1089–1097.
5. S. Jaracz, J. Chen, L. V. Kuznetsova and I. Ojima, Recent advances in tumor-targeting anticancer drug conjugates, *Bioorganic Med. Chem.*, 2005, **13**, 5043–5054.
6. C. Sanchez-Cano and M. J. Hannon, Novel and emerging approaches for the delivery of metallo-drugs, *Dalt. Trans.*, 2009, 10702–10711.
7. D. van Straten, V. Mashayekhi, H. de Bruijn, S. Oliveira and D. Robinson, Oncologic photodynamic therapy: basic principles, current clinical status and future directions, *Cancers (Basel)*, 2017, **9**, 19.
8. W. Fan, P. Huang and X. Chen, Overcoming the Achilles' heel of photodynamic therapy, *Chem. Soc. Rev.*, 2016, **45**, 6488–6519.
9. K. Plaetzer, B. Krammer, J. Berlanda, F. Berr and T. Kiesslich, Photophysics and photochemistry of photodynamic therapy: fundamental aspects. Lasers in medical science, *Lasers Med. Sci.*, 2009, **24**, 259–268.
10. N. Mehraban and H. S. Freeman, Developments in PDT sensitizers for increased selectivity and singlet oxygen production, *Materials (Basel)*, 2015, **8**, 4421–4456.
11. A. P. Castano, T. N. Demidova and M. R. Hamblin, Mechanisms in photodynamic therapy: part one—photosensitizers, photochemistry and cellular localization, *Photodiagnosis Photodyn. Ther.*, 2004, **1**, 279–293.
12. R. Bonnett, *Chemical Aspects of Photodynamic Therapy*, Gordon and Breach Science Publishers, London and Newark, 2000.
13. M. Ochsner, Photophysical and photobiological processes in the photodynamic therapy of tumours, *J. Photochem. Photobiol. B Biol.*, 1997, **39**, 1–18.
14. A. B. Ormond and H. S. Freeman, Dye sensitizers for photodynamic therapy, *Materials (Basel)*, 2013, **6**, 817–840.
15. A. Zamora, G. Viguera, V. Rodríguez, M. D. Santana and J. Ruiz, Cyclometalated iridium (III) luminescent complexes in therapy and phototherapy, *Coord. Chem. Rev.*, 2018, **360**, 34–76.
16. J. Li and T. Chen, Transition metal complexes as photosensitizers for integrated cancer theranostic applications, *Coord. Chem. Rev.*, 2020, **418**, 213355.
17. S. A. McFarland, A. Mandel, R. Dumoulin-White and G. Gasser, Metal-based photosensitizers for photodynamic therapy: the future of multimodal oncology?, *Curr. Opin. Chem. Biol.*, 2020, **56**, 23–27.
18. N. J. Farrer, L. Salassa and P. J. Sadler, Photoactivated chemotherapy (PACT): the potential of excited-

state d-block metals in medicine, *Dalt. Trans.*, 2009, 10690–10701.

19. C. Mari, V. Pierroz and G. Gasser, Combination of Ru (II) complexes and light: new frontiers in cancer therapy, *Chem. Sci.*, 2015, **6**, 2660–2686.

20. F. Heinemann, J. Karges and G. Gasser, Critical overview of the use of Ru (II) polypyridyl complexes as photosensitizers in one-photon and two-photon photodynamic therapy, *Acc. Chem. Res.*, 2017, **50**, 2727–2736.

21. S. Monro, K. L. Colón, H. Yin, J. Roque, P. Konda, S. Gujar, R. P. Thummel, L. Lilge, C. G. Cameron and S. A. McFarland, Transition metal complexes and photodynamic therapy from a tumor-centered approach: challenges, opportunities, and highlights from the development of TLD1433, *Chem. Rev.*, 2019, **119**, 797–828.

22. K. K. W. Lo, M. W. Louie and K. Y. Zhang, Design of luminescent iridium (III) and rhenium (I) polypyridine complexes as in vitro and in vivo ion, molecular and biological probes, *Coord. Chem. Rev.*, 2010, **254**, 2603–2622.

23. D. L. Ma, S. Lin, K. H. Leung, H. J. Zhong, L. J. Liu, D. S. H. Chan, A. Bourdoncle, J. L. Mergny, H. M. D. Wang and C. H. Leung, An oligonucleotide-based label-free luminescent switch-on probe for RNA detection utilizing a G-quadruplex-selective iridium (III) complex, *Nanoscale*, 2014, **6**, 8489–8494.

24. K. H. Leung, H. Z. He, V. P. Y. Ma, H. Yang, D. S. H. Chan, C. H. Leung and D. L. Ma, A G-quadruplex-selective luminescent switch-on probe for the detection of sub-nanomolar human neutrophil elastase, *RSC Adv.*, 2013, **3**, 1656–1659.

25. H. Huang, P. Zhang, K. Qiu, J. Huang, Y. Chen, L. Ji and H. Chao, Mitochondrial dynamics tracking with two-photon phosphorescent terpyridyl iridium (III) complexes, *Sci. Rep.*, 2016, **6**, 20887.

26. K. K.-W. Tso, K.K.-S., Lo, *Strategic applications of luminescent iridium(III) complexes as biomolecular probes, cellular imaging reagents, and photodynamic therapeutics*, John Wiley & Sons Ltd, Chichester, UK, 2017.

27. L. Zhang and D. Ding, Recent advances of transition Ir (III) complexes as photosensitizers for improved photodynamic therapy, *View*, 2021, 20200179.

28. H. Huang, S. Banerjee and P. J. Sadler, Recent advances in the design of targeted iridium (III) photosensitizers for photodynamic therapy, *ChemBioChem*, 2018, 1–17.

29. L. He, Y. Li, C. P. Tan, R. R. Ye, M. H. Chen, J. J. Cao, L. N. Ji and Z. W. Mao, Cyclometalated iridium (III) complexes as lysosome-targeted photodynamic anticancer and real-time tracking agents, *Chem. Sci.*, 2015, **6**, 5409–5418.

30. S. Moromizato, Y. Hisamatsu, T. Suzuki, Y. Matsuo, R. Abe and S. Aoki, Design and synthesis of a luminescent cyclometalated iridium (III) complex having N, N-diethylamino group that stains acidic intracellular organelles and induces cell death by photoirradiation, *Inorg. Chem.*, 2012, **51**, 12697–12706.

31. F. X. Wang, M. H. Chen, Y. N. Lin, H. Zhang, C. P. Tan, L. N. Ji and Z. W. Mao, Dual functions of cyclometalated iridium (III) complexes: anti-metastasis and lysosome-damaged photodynamic therapy, *ACS Appl. Mater. Interfaces*, 2017, **9**, 42471–42481.

32. J. Pracharova, G. Viguera, V. Novohradsky, N. Cutillas, C. Janiak, H. Kostrhunova, J. Kasparkova, J. Ruiz and V. Brabec, Exploring the effect of polypyridyl ligands on the anticancer activity of phosphorescent



iridium (III) complexes: From proteosynthesis inhibitors to photodynamic therapy agents, *Chem. - A Eur. J.*, 2018, **24**, 4607–4619.

33. C. H. Leung, H. J. Zhong, H. Yang, Z. Cheng, D. S. H. Chan, V. P. Y. Ma, R. Abagyan, C. Y. Wong and D. L. Ma, A Metal-Based Inhibitor of Tumor Necrosis Factor- $\alpha$ , *Angew. Chemie - Int. Ed.*, 2012, **51**, 9010–9014.

34. B. B. Chen, N. L. Pan, J. X. Liao, M. Y. Huang, D. C. Jiang, J. J. Wang, H. J. Qiu, J. X. Chen, L. Li and J. Sun, Cyclometalated iridium (III) complexes as mitochondria-targeted anticancer and antibacterial agents to induce both autophagy and apoptosis, *J. Inorg. Biochem.*, 2021, **219**, 111450.

35. Y. Li, C. P. Tan, W. Zhang, L. He, L. N. Ji and Z. W. Mao, Phosphorescent iridium (III)-bis-N-heterocyclic carbene complexes as mitochondria-targeted theranostic and photodynamic anticancer agents, *Biomaterials*, 2015, **39**, 95–104.

36. C. Pérez-Arnaiz, M. I. Acuña, N. Busto, I. Echevarría, M. Martínez-Alonso, G. Espino, B. García and F. Domínguez, Thiabendazole-based Rh (III) and Ir (III) biscyclometallated complexes with mitochondria-targeted anticancer activity and metal-sensitive photodynamic activity, *Eur. J. Med. Chem.*, 2018, **157**, 279–293.

37. J. J. Cao, C. P. Tan, M. H. Chen, N. Wu, D. Y. Yao, X. G. Liu, L. N. Ji and Z. W. Mao, Targeting cancer cell metabolism with mitochondria-immobilized phosphorescent cyclometalated iridium (III) complexes, *Chem. Sci.*, 2016, **8**, 631–640.

38. R. W. Horobin, F. Rashid-Doubell, J. D. Pediani and G. Milligan, Predicting small molecule fluorescent probe localization in living cells using QSAR modeling. 1. Overview and models for probes of structure, properties and function in single cells, *Biotech. Histochem.*, 2013, **88**, 440–460.

39. K. Qiu, Y. Liu, H. Huang, C. Liu, H. Zhu, Y. Chen, L. Ji and H. Chao, Biscyclometalated iridium (iii) complexes target mitochondria or lysosomes by regulating the lipophilicity of the main ligands, *Dalt. Trans.*, 2016, **45**, 16144–16147.

40. L. D. Zorova, V. A. Popkov, E. Y. Plotnikov, D. N. Silachev, I. B. Pevzner, S. S. Jankauskas, V. A. Babenko, S. D. Zorov, A. V. Balakireva, M. Juhaszova, S. J. Sollott and D. B. Zorov, Mitochondrial membrane potential, *Anal. Biochem.*, 2018, **552**, 50–59.

41. K. Han, Q. Lei, S. B. Wang, J. J. Hu, W. X. Qiu, J. Y. Zhu, W. N. Yin, X. Luo and X. Z. Zhang, Dual-stage-light-guided tumor inhibition by mitochondria-targeted photodynamic therapy, *Adv. Funct. Mater.*, 2015, **25**, 2961–2971.

42. A. Erxleben, Mitochondria-targeting anticancer metal complexes, *Curr. Med. Chem.*, 2018, **26**, 694–728.

43. R. A. J. Smith, R. C. Hartley and M. P. Murphy, Mitochondria-targeted small molecule therapeutics and probes, *Antioxidants Redox Signal.*, 2011, **15**, 3021–3038.

44. N. Rubio, S. P. Fleury and R. W. Redmond, Spatial and temporal dynamics of in vitro photodynamic cell killing: extracellular hydrogen peroxide mediates neighbouring cell death, *Photochem. Photobiol. Sci.*, 2009, **8**, 457–464.

45. M. Martínez-Alonso, N. Busto, L. D. Aguirre, L. Berlanga, M. C. Carrión, J. V. Cuevas, A. M. Rodríguez, A. Carbayo, B. R. Manzano, E. Ortí, F. A. Jalón, B. García and G. Espino, Strong influence of the ancillary ligand over the photodynamic anticancer properties of neutral biscyclometalated Ir(III) complexes bearing 2-benzazole-phenolates, *Chem. - A Eur. J.*, 2018, **24**, 17523–17537.

46. J. Torres, M. C. Carrión, J. Leal, F. A. Jalón, J. V. Cuevas, A. M. Rodríguez, G. Castañeda and B. R. Manzano, Cationic Bis (Cyclometalated) Ir (III) Complexes with Pyridine–Carbene Ligands. Photophysical Properties and Photocatalytic Hydrogen Production from Water, *Inorg. Chem.*, 2018, **57**, 970–984.
47. Y. Chen, L. Qiao, L. Ji and H. Chao, Phosphorescent iridium (III) complexes as multicolor probes for specific mitochondrial imaging and tracking, *Biomaterials*, 2014, **35**, 2–13.
48. F. Zhang, L. Duan, J. Qiao, G. Dong, L. Wang and Y. Qiu, Solution-processed blue–green organic light-emitting diodes based on cationic iridium complexes with 1-pyridyl-3-methylimidazolin-2-ylidene-C, C2' as the ancillary ligand, *Org. Electron.*, 2012, **13**, 1277–1288.
49. Y. E. Begantsova, L. N. Bochkarev, E. V. Baranov and V. A. Ilichev, Cyclometalated Iridium(III) Complexes with a Norbornene-Substituted Picolinate Ligand and Electroluminescent Polymers Based on them, *Russ. J. Coord. Chem. Khimiya*, 2019, **45**, 856–866.
50. L. P. Li, S. Y. Yao, Y. L. Ou, L. Q. Wei and B. H. Ye, Diastereoselective synthesis and photophysical properties of bis-cyclometalated Ir (III) stereoisomers with dual stereocenters, *Organometallics*, 2017, **36**, 3257–3265.
51. W. Jiang, Y. Gao, Y. Sun, F. Ding, Y. Xu, Z. Bian, F. Li, J. Bian and C. Huango, Zwitterionic iridium complexes: synthesis, luminescent properties, and their application in cell imaging, *Inorg. Chem.*, 2010, **49**, 3252–3260.
52. S. Yi, J. H. Kim, Y. J. Cho, J. Lee, T. S. Choi, D. W. Cho, C. Pac, W. S. Han, H. J. Son and S. O. Kang, Stable blue phosphorescence iridium (III) cyclometalated complexes prompted by intramolecular hydrogen bond in ancillary ligand, *Inorg. Chem.*, 2016, **55**, 3324–3331.
53. A. Mishra, H. Jung, J. W. Park, H. K. Kim, H. Kim, P. J. Stang and K. W. Chi, Anticancer activity of self-assembled molecular rectangles via arene–ruthenium acceptors and a new unsymmetrical amide ligand, *Organometallics*, 2012, **31**, 3519–3526.
54. H. Goitia, Y. Nieto, M. D. Villacampa, C. Kasper, A. Laguna and M. C. Gimeno, Antitumoral gold and silver complexes with ferrocenyl-amide phosphines, *Organometallics*, 2013, **32**, 6069–6078.
55. M. Pellei, V. Gandin, M. Marinelli, C. Marzano, M. Yousufuddin, H. V. R. Dias and C. Santini, Synthesis and biological activity of ester- and amide-functionalized imidazolium salts and related water-soluble coinage metal N-heterocyclic carbene complexes, *Inorg. Chem.*, 2012, **51**, 9873–9882.
56. M. Nonoyama, Benzo [h] quinolin-10-yl-N Iridium (III) Complexes, *Bull. Chem. Soc. Jpn.*, 1974, **47**, 767–768.
57. S. Sprouse, K. A. King, P. J. Spellane and R. J. Watts, Photophysical effects of metal-carbon. sigma. bonds in ortho-metalated complexes of iridium (III) and rhodium (III), *J. Am. Chem. Soc.*, 1984, **106**, 6647–6653.
58. Y. Shiba, A. Inagaki and M. Akita, C–C Bond Forming Reductive Elimination from Diarylplatinum Complexes Driven by Visible-Light-Mediated Photoredox Reactions, *Organometallics*, 2015, **34**, 4844–4853.
59. E. Baranoff, B. F. E. Curchod, J. Frey, R. Scopelliti, F. Kessler, I. Tavernelli, U. Rothlisberger, M. Grätzel and M. K. Nazeeruddin, Acid-induced degradation of phosphorescent dopants for OLEDs and its application to the synthesis of tris-heteroleptic iridium (III) bis-cyclometalated complexes, *Inorg. Chem.*, 2012, **51**, 215–224.

60. E. Arunan, G. R. Desiraju, R. A. Klein, J. Sadlej, S. Scheiner, I. Alkorta, D. C. Clary, R. H. Crabtree, J. J. Dannenber, P. Hobza, H. G. Kjaergaard, A. C. Legon, B. Mennucci and D. J. Nesbitt, Definition of the hydrogen bond (IUPAC Recommendations 2011), *Pure Appl. Chem.*, 2011, **83**, 1637–1641.
61. M. M. Mautner, The ionic hydrogen bond, *Chem. Rev.*, 2005, **105**, 213–284.
62. M. Martínez-Alonso, P. Sanz, P. Ortega, G. Espino, F. A. Jalón, M. Martín, A. M. Rodríguez, J. A. López, C. Tejel and B. R. Manzano, Analysis of Ion Pairing in Solid State and Solution in p-Cymene Ruthenium Complexes, *Inorg. Chem.*, 2020, **59**, 14171–14183.
63. T. G. Appleton, H. C. Clark and L. E. Manzer, The trans-influence: Its measurement and significance, *Coord. Chem. Rev.*, 1973, **10**, 335–422.
64. F. Gärtner, S. Denurra, S. Losse, A. Neubauer, A. Boddien, A. Gopinathan, A. Spannenberg, H. Junge, S. Lochbrunner, M. Blug, S. Hoch, J. Busse, S. Gladiali and M. Beller, Synthesis and characterization of new iridium photosensitizers for catalytic hydrogen generation from water, *Chem. - A Eur. J.*, 2012, **18**, 3220–3225.
65. J. Sanz-Villafuela, C. Martínez-Alonso, I. Echevarría, M. Vaquero, A. Carbayo, J. Fidalgo, A. M. Rodríguez, J. V. Cuevas-Vicario, J. C. Lima, A. J. Moro, B. R. Manzano, F. A. Jalón and G. Espino, One-pot photocatalytic transformation of indolines into 3-thiocyanate indoles with new Ir (iii) photosensitizers bearing  $\beta$ -carboline, *Inorg. Chem. Front.*, 2021, **8**, 1253–1270.
66. X. D. Bi, R. Yang, Y. C. Zhou, D. Chen, G. K. Li, Y. X. Guo, M. F. Wang, D. Liu and F. Gao, Cyclometalated iridium (III) complexes as high-sensitivity two-photon excited mitochondria dyes and near-infrared photodynamic therapy agents, *Inorg. Chem.*, 2020, **59**, 14920–14931.
67. R. D. Costa, F. Monti, G. Accorsi, A. Barbieri, H. J. Bolink, E. Ortí and N. Armaroli, Photophysical properties of charged cyclometalated Ir (III) complexes: A joint theoretical and experimental study, *Inorg. Chem.*, 2011, **50**, 7229–7238.
68. R. D. Costa, E. Ortí, H. J. Bolink, S. Graber, S. Schaffner, M. Neuburger, C. E. Housecroft and E. C. Constable, Archetype Cationic Iridium Complexes and Their Use in Solid-State Light-Emitting Electrochemical Cells, *Adv. Funct. Mater.*, 2009, **19**, 3456–3463.
69. M. Vaquero, A. Ruiz-Riaguas, M. Martínez-Alonso, F. A. Jalón, B. R. Manzano, A. M. Rodríguez, G. García-Herbosa, A. Carbayo, B. García and G. Espino, Selective Photooxidation of Sulfides Catalyzed by Bis-cyclometalated Ir(III) Photosensitizers Bearing 2, 2'-Dipyridylamine-Based Ligands, *Chem. - A Eur. J.*, 2018, **24**, 10662–10671.
70. S. Ladouceur, D. Fortin and E. Zysman-Colman, Enhanced luminescent iridium (III) complexes bearing aryltriazole cyclometalated ligands, *Inorg. Chem.*, 2011, **50**, 11514–11526.
71. M. Martínez-Alonso, J. Cerdá, C. Momblona, A. Pertegás, J. M. Junquera-Hernández, A. Heras, A. M. Rodríguez, G. Espino, H. Bolink and E. Ortí, Highly stable and efficient light-emitting electrochemical cells based on cationic iridium complexes bearing arylazole ancillary ligands, *Inorg. Chem.*, 2017, **56**, 10298–10310.
72. Kalyanasundaram, *Photochemistry of Polypyridine and Porphyrin Complexes*, Academic Press, San Diego, CA, 1992.
73. J. B. Waern, C. Desmarets, L. M. Chamoreau, H. Amouri, A. Barbieri, C. Sabatini, B. Ventura and F. Barigelletti, Luminescent Cyclometalated Rh(III), Ir(III), and (DIP) 2Ru(II) complexes with carboxylated bipyridyl

ligands: synthesis, X-ray molecular structure, and photophysical properties, *Inorg. Chem.*, 2008, **47**, 3340–3348.

74. R. Bevernaegie, S. A. M. Wehlin, B. Elias and L. Troian-Gautier, A Roadmap Towards Visible Light Mediated Electron Transfer Chemistry with Iridium (III) Complexes, *ChemPhotoChem*, 2021, **5**, 217–234.

75. S. Kuang, L. Sun, X. Zhang, X. Liao, T. W. Rees, L. Zeng, Y. Chen, X. Zhang, L. Ji and H. Chao, A Mitochondrion-Localized Two-Photon Photosensitizer Generating Carbon Radicals Against Hypoxic Tumors, *Angew. Chemie - Int. Ed.*, 2020, **400201**, 20697–20703.

76. V. Novohradsky, A. Rovira, C. Hally, A. Galindo, G. Viguera, A. Gandioso, M. Svitelova, R. Bresolí-Obach, H. Kostrhunova, L. Markova, J. Kasparkova, S. Nonell, J. Ruiz, V. Brabec and V. Marchán, Towards Novel Photodynamic Anticancer Agents Generating Superoxide Anion Radicals: A Cyclometalated Ir(III) Complex Conjugated to a Far-Red Emitting Coumarin, *Angew. Chemie Int. Ed.*, 2019, **58**, 6311–6315.

77. Y. Wu, J. Wu and W.-Y. Wong, A new near-infrared phosphorescent iridium (iii) complex conjugated to a xanthene dye for mitochondria-targeted photodynamic therapy, *Biomater. Sci.*, 2021, **9**, 4843–4853.

78. S. Lamansky, P. Djurovich, D. Murphy, F. Abdel-Razzaq, H. E. Lee, C. Adachi, P. E. Burrows, S. R. Forrest and M. E. Thompson, Highly phosphorescent bis-cyclometalated iridium complexes: synthesis, photophysical characterization, and use in organic light emitting diodes, *J. Am. Chem. Soc.*, 2001, **123**, 4304–4312.

79. J. Torres, M. C. Carrión, J. Leal, F. A. Jalón, J. V. Cuevas, A. M. Rodríguez, G. Castañeda and B. R. Manzano, Cationic Bis (Cyclometalated) Ir (III) Complexes with Pyridine–Carbene Ligands. Photophysical Properties and Photocatalytic Hydrogen Production from Water, *Inorg. Chem.*, 2018, **57**, 970–984.

80. D. Tordera, M. Delgado, E. Ortí, H. J. Bolink, J. Frey, M. K. Nazeeruddin and E. Baranoff, Stable green electroluminescence from an iridium tris-heteroleptic ionic complex, *Chem. Mater.*, 2012, **24**, 1896–1903.

81. J. V Caspar, E. M. Kober, B. P. Sullivan and T. J. Meyer, Application of the energy gap law to the decay of charge-transfer excited states, *J. Am. Chem. Soc.*, 1982, **104**, 630–632.

82. L. K. McKenzie, H. E. Bryant and J. A. Weinstein, Transition metal complexes as photosensitisers in one- and two-photon photodynamic therapy, *Coord. Chem. Rev.*, 2019, **379**, 2–29.

83. C. A. Puckett, R. J. Ernst and J. K. Barton, Exploring the cellular accumulation of metal complexes, *Dalt. Trans.*, 2010, **39**, 1159–1170.

84. C. Zhang, R. Guan, X. Liao, C. Ouyang, J. Liu, L. Ji and H. Chao, Mitochondrial DNA targeting and impairment by a dinuclear Ir–Pt complex that overcomes cisplatin resistance, *Inorg. Chem. Front.*, 2020, **7**, 1864–1871.

85. E. Baggaley, J. A. Weinstein and J. A. G. Williams, Lighting the way to see inside the live cell with luminescent transition metal complexes, *Coord. Chem. Rev.*, 2012, **256**, 1762–1785.

86. X. Tian, Y. Zhu, M. Zhang, L. Luo, J. Wu, H. Zhou, L. Guan, G. Battaglia and Y. Tian, Localization matters: a nuclear targeting two-photon absorption iridium complex in photodynamic therapy, *Chem. Commun.*, 2017, **53**, 3303–3306.

87. H. Yuan, Z. Han, Y. Chen, F. Qi, H. Fang, Z. Guo, S. Zhang and W. He, Ferroptosis photoinduced by new cyclometalated iridium (III) complexes and its synergism with apoptosis in tumor cell inhibition, *Angew. Chemie Int. Ed.*, 2021, **60**, 8174–8181.

88. Z. Liu, I. Romero-Canelón, B. Qamar, J. M. Hearn, A. Habtemariam, N. P. E. Barry, A. M. Pizarro, G. J. Clarkson and P. J. Sadler, The potent oxidant anticancer activity of organoiridium catalysts, *Angew. Chemie Int. Ed.*, 2014, **53**, 3941–3946.
89. Z. Liu, R. J. Deeth, J. S. Butler, A. Habtemariam, M. E. Newton and P. J. Sadler, Reduction of quinones by NADH catalyzed by organoiridium complexes, *Angew. Chemie Int. Ed.*, 2013, **52**, 4194–4197.
90. X. Liu, X. He, X. Zhang, Y. Wang, J. Liu and X. Hao, New Organometallic Tetraphenylethylene- Iridium (III) Complexes with Antineoplastic Activity, *ChemBioChem*, 2019, **2767**, 2767–2776.
91. A. Chiarugi, C. Dölle, R. Felici and M. Ziegler, The NAD metabolome—a key determinant of cancer cell biology, *Nat. Rev. Cancer*, 2012, **12**, 741–752.
92. H. Huang, S. Banerjee, K. Qiu, P. Zhang, O. Blacque, T. Malcomson, M. J. Paterson, G. J. Clarkson, M. Staniforth, V. G. Stavros, G. Gasser, H. Chao and P. J. Sadler, Targeted photoredox catalysis in cancer cells, *Nat. Chem.*, 2019, **11**, 1041–1048.
93. C. Huang, C. Liang, T. Sadhukhan, S. Banerjee, Z. Fan, T. Li, Z. Zhu, P. Zhang, K. Raghavachari and H. Huang, In-vitro and In-vivo Photocatalytic Cancer Therapy with Biocompatible Iridium (III) Photocatalysts, *Angew. Chemie - Int. Ed.*, 2021, **60**, 9474–9479.
94. B. Van Houten, V. Woshner and J. H. Santos, Role of mitochondrial DNA in toxic responses to oxidative stress, *DNA Repair (Amst)*, 2006, **5**, 145–152.
95. J. Leal, L. Santos, D. M. Fernández-Aroca, J. V. Cuevas, M. A. Martínez, A. Massaguer, F. A. Jalón, M. J. Ruiz Hidalgo, R. Sánchez-Prieto, A. M. Rodríguez, G. Castañeda, G. Durá, M. C. Carrión, S. Barrabés and B. R. Manzano, Effect of the aniline fragment in Pt (II) and Pt (IV) complexes as anti-proliferative agents. Standard reduction potential as a more reliable parameter for Pt (IV) compounds than peak reduction potential, *J. Inorg. Biochem.*, 2021, **218**, 111403.
96. Z. H. Siddik, Cisplatin: mode of cytotoxic action and molecular basis of resistance, *Oncogene*, 2003, **22**, 7265–7279.
97. D. Kessel and J. J. Reiners Jr, Apoptosis and autophagy after mitochondrial or endoplasmic reticulum photodamage, *Photochem. Photobiol.*, 2007, **83**, 1024-1028..
98. E. Buytaert, M. Dewaele and P. Agostinis, Molecular effectors of multiple cell death pathways initiated by photodynamic therapy, *Biochim. Biophys. Acta - Rev. Cancer*, 2007, **1776**, 86–107.





---

***Chapter 3. Rational Design of  
Mitochondria Targeted  
Thiabendazole-based Ir(III)  
Biscyclometalated Complexes for a  
Multimodal Photodynamic Therapy  
of Cancer***

---







## Authorship Statement

This chapter is the result of a collaboration with Elisenda Zafon, Sílvia Barrabés, María Ángeles Martínez and Anna Massaguer from the University of Girona (UdG), and Sonia Ramos-Gómez and Natividad Ortega from the University of Burgos (UBU), so the biological experiments were made by them. I have accomplished the following sections: Synthesis of ligands and iridium(III) complexes, characterization of the Ir(III)-compounds, discussion of crystal structures by X-ray diffraction, photostability experiments, theoretical calculations, electrochemical properties, photophysical properties, ability of  $^1\text{O}_2$  generation, photocatalytic oxidation of NADH and all the related parts of the supporting information.

This work can be found published as: I. Echevarría, E. Zafon, S. Barrabés, M. A. Martínez, S. Ramos-Gómez, N. Ortega, B. R. Manzano, F. A. Jalón, R. Quesada, G. Espino, and A. Massaguer, Rational design of mitochondria targeted thiabendazole-based Ir (III) biscyclometalated complexes for a multimodal photodynamic therapy of cancer, *J. Inorg. Biochem.*, 2022, **231**, 111790.

## 0. Abstract

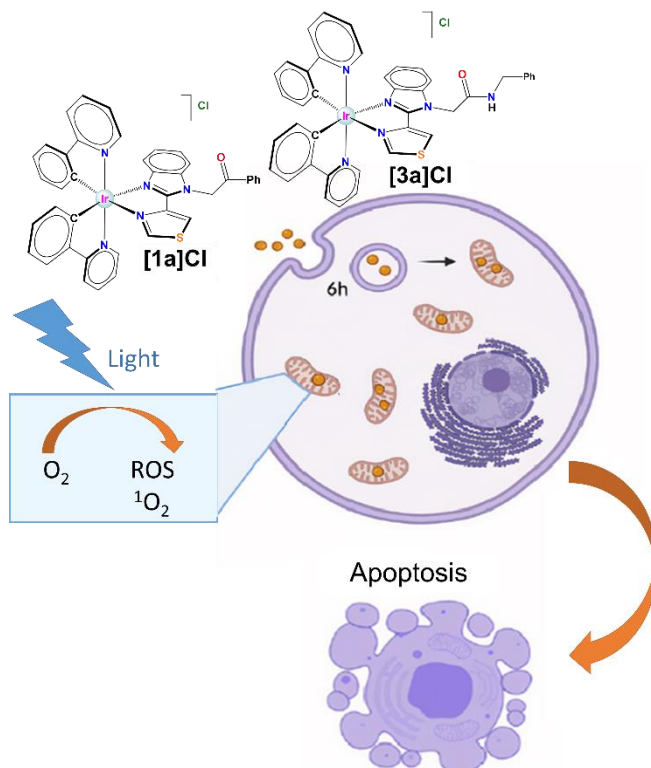


Fig.1. Schematic representation of the biological mechanism of action of the two leading complexes.

Despite their outstanding properties as potential photosensitizers for photodynamic therapy (PDT), Ir(III) bis-cyclometalated complexes need both further developments to overcome remaining limitations and in-depth investigations into their mechanisms of action to reach clinic application in the treatment of cancer. This work describes the synthesis of a family of Ir(III) complexes of general formula  $[\text{Ir}(\text{C}^{\wedge}\text{N})_2(\text{N}^{\wedge}\text{N}')]\text{Cl}$  ( $\text{N}^{\wedge}\text{N}' =$  thiabendazole-based ligands;  $\text{C}^{\wedge}\text{N} =$  ppy (2-phenylpyridinate) (**Series A**), or dfppy (2-(2,4-difluorophenyl)pyridinate) (**Series B**)) and their evaluation as potential PDT agents. These complexes are partially soluble in water and exhibit cytotoxic activity in the absence of light irradiation versus several cancer cell lines. Furthermore, the cytotoxic activity of derivatives of Series A is enhanced upon irradiation, particularly for complexes **[1a]Cl** and **[3a]Cl**, which show photocytotoxicity indexes (PI) above 20. Endocytosis was established as the uptake mechanism for **[1a]Cl** and **[3a]Cl** in prostate cancer cells by flow cytometry. These derivatives mainly accumulate in the mitochondria as shown by colocalization confocal microscopy experiments. Presumably, **[1a]Cl** and **[3a]Cl** induce death on cancer cells under irradiation through apoptosis triggered by a multimodal mechanism of action, which likely involves damage over mitochondrial DNA and mitochondrial membrane depolarization. Both processes seem to be the result of photocatalytic oxidation processes.

## 1. Introduction

Photodynamic therapy (PDT) is a non-invasive chemotherapeutic protocol indicated for the treatment of non-oncological diseases and some cancer types. It is based on the administration of a photosensitive compound called photosensitizer (PS), whose excitation by irradiation with light specifically directed towards the malignant tissue triggers the photochemical generation of reactive oxygen species (ROS) from cellular  $\text{O}_2$ , and subsequently causes death on cancer cells. It features some inherent advantages, such as reduced side-effects based on selective photoactivation of the drug on cancer tissues (i.e.: improved selectivity), diminished acquired resistance of cancer cells stemming from their multiple cellular targets and mechanisms of action (i.e.: enhanced efficiency), and a broad spectrum of treatable cancer types.<sup>1,2,3,4</sup>

Ir(III) biscyclometalated complexes are under investigation as promising PDT agents for the treatment of different cancer types due to their remarkable photophysical properties.<sup>5,6,7,8</sup> In particular, their strong spin-orbit coupling constant favours the access to a triplet excited state that can interact with molecular oxygen in the cells to produce ROS through either an electron transfer pathway (superoxide radical anion,  $\text{O}_2^{\cdot-}$ ) or an energy transfer mechanism (singlet oxygen,  $^1\text{O}_2$ ). More importantly, these processes are photocatalytic in nature, which potentially leads to a very efficient therapeutic activity and allows decreasing the PS dosage.<sup>5,9,10,11</sup> Several additional

features will condition the potential applicability of selected Ir-based PSs in specific clinical PDT protocols. Among these desired features it is worth mentioning the following: (1) reasonable aqueous solubility to facilitate administration, (2) straightforward synthetic procedures to reduce costs, (3) good photostability and photocytotoxicity indexes ( $PI = IC_{50,dark}/IC_{50,light}$ ) to ensure a selective photo-enhanced activity and (4) suitable absorption profiles in relation to the cancer type to be treated, that is, blue light-sensitive PSs can be used to treat superficial or cutaneous cancers but near infrared (NIR) or red light-sensitive PSs are needed to deal with tumours on internal tissues, due to the higher tissue penetration of this type of light stimulus.<sup>12,13,14</sup> Nonetheless, this determinant can be bypassed to some extent using two-photon excitation PDT<sup>15</sup> or employing endoscopic light delivery devices based on laser or light emitting diode (LED) optical fibers.<sup>16</sup>

Recently, several researching groups have reported encouraging advances in the field of Ir(III) PSs for PDT. For instance, the group of Huang has described a tricationic Ir(III) PS with high photocytotoxicity in both *in vitro* cancer cell lines and *in vivo* mouse cancer models and high photocatalytic activity on the oxidation of the reduced form of nicotinamide adenine dinucleotide (NADH), nicotinamide adenine dinucleotide phosphate (NADPH) and amino acids.<sup>17</sup> Gou et al. have reported an Ir(III) complex containing a Donor-Acceptor-Donor ligand that can be directly promoted to the excited state by NIR radiation to produce ROS and heat, so that it exhibits a dual phototherapeutic action, i.e. photodynamic therapy plus photothermal therapy. In addition, this complex has been conjugated to polyethylene glycol (PEG) to generate highly soluble nanoparticles and display a significant tumour inhibition *in vivo*.<sup>18</sup> The group of He has prepared an Ir(III) complex that features high PI values in different cancer cell lines and multicellular spheroids under hypoxia through a synergistic effect between ferroptosis and apoptosis, induced by the generation of the radicals superoxide ( $O_2^{\cdot-}$ ) and hydroxyl ( $\cdot OH$ ).<sup>19</sup> The group of Bryce has rationally designed two Ir-porphyrin conjugates that show synergistic PDT-photothermal activity under long-wavelength excitation (635 nm).<sup>20</sup>

Many of the PSs currently in clinical or pre-clinical studies localize in or have a major influence on mitochondria, promoting a PDT induced apoptotic cell death.<sup>21</sup> Mitochondria are considered as the powerhouses of cells, in as much as they produce energy in the form of adenosine triphosphate (ATP) through different biochemical processes such as oxidative phosphorylation.<sup>22</sup> ATP drives fundamental biochemical reactions and cell functions through hydrolysis into adenosine diphosphate (ADP) and phosphate anions at the sites where energy is required in cells. In fact, mitochondria have their own circular DNA (mtDNA), which encodes thirteen different protein subunits of enzyme complexes involved in the oxidative phosphorylation process. In addition to their role as energy suppliers, mitochondria are the principal regulators of

the apoptotic pathways. Mitochondria dysfunction as a result of damage on mtDNA or mitochondrial membrane depolarization induces an apoptotic response by releasing cytochrome c and other apoptosis-related proteins into the cytosol and activates the caspase pathway.<sup>23</sup> Therefore, a rational design of new Ir(III) biscyclometalated cationic complexes, based on a suitable combination of lipophilic and hydrophilic ligands and counteranions, can lead to mitochondria targeted anticancer agents<sup>24,25</sup> and in-depth mechanistic studies can contribute to elucidate their biological mechanism of action.

Previously, we reported on the PDT activity of two Ir(III) complexes of general formula  $[\text{Ir}(\text{C}^{\wedge}\text{N})_2(\text{N}^{\wedge}\text{N}')]\text{Cl}$  (**[Ir1]Cl**, N<sup>^</sup>N' thiabendazole (tbz); or **[Ir2]Cl**, N<sup>^</sup>N' N-benzyl-thiabendazole (Bn-tbz)) and found out that the replacement of the reactive N-H group in **[Ir1]Cl** with the N-Bn group in **[Ir2]Cl** prevents deprotonation and leads to higher cellular uptake.<sup>26</sup> Following with our investigations in the field, more recently we have found that a second generation complex of the same type, **[Ir3]Cl**, with a thiabendazole-based N,N'-ligand bearing an alkylacetamide substituent (N-CH<sub>2</sub>CONH<sub>2</sub>) provides a better excited state lifetime than the analogue complex with the 2-pyridyl-benzimidazole scaffold in the N,N'-ligand.<sup>27</sup> Moreover, it is well-known that the C<sup>^</sup>N ligands exert a great influence on the photophysical properties of these photosensitizers. In particular, electron-withdrawing groups on the C<sup>^</sup>N ligands stabilize the HOMO (Highest Occupied Molecular Orbital), provide higher HOMO-LUMO (Lowest Unoccupied Molecular Orbital) energy gaps and usually exhibit longer triplet excited state lifetimes,<sup>28,29</sup> which favours the interaction with O<sub>2</sub> to form either <sup>1</sup>O<sub>2</sub> or O<sub>2</sub><sup>•-</sup>. As a matter of fact, Mao has reported a family of Ir(III) PSs, where the derivative with 2-(2,4-difluorophenyl)pyridinate as the C<sup>^</sup>N ligand exhibits the highest photocytotoxicity index (PI = 18.9) upon exposure to blue light.<sup>30</sup>

With these premises in mind, we decided to synthesize two sets of new Ir(III) biscyclometalated complexes of formula  $[\text{Ir}(\text{C}^{\wedge}\text{N})_2(\text{N}^{\wedge}\text{N}')]\text{Cl}$ , combining two C<sup>^</sup>N ligands (2-phenylpyridinate (ppy) and 2-(2,4-difluorophenyl)pyridinate (dfppy)) and four different thiabendazole-based N<sup>^</sup>N' ligands with diverse alkyl substituents on the N atom (N-R). In particular, we have chosen several alkyl-ketone or alkyl-amide groups which could be used in future derivatizations of these metallodrugs. Hence, the rationale behind the design of these complexes is to achieve new photosensitizers as potential anticancer PDT agents endowed with pH stability, good cellular uptake and long triplet excited state lifetimes to produce ROS. Moreover, we intend to assess the influence of two different structural features on the electrochemical, photophysical and biological properties of these complexes and particularly on their PI: (1) the effect of the different alkyl substituents on the benzimidazole fragment (N-R) and (2) the effect of the two afore-mentioned C<sup>^</sup>N ligands. Besides, we have examined different aspects of their mechanism of biological action, including uptake pathway, organelle localization, cell death, ROS generation, mtDNA damage, etc. As a result, we have

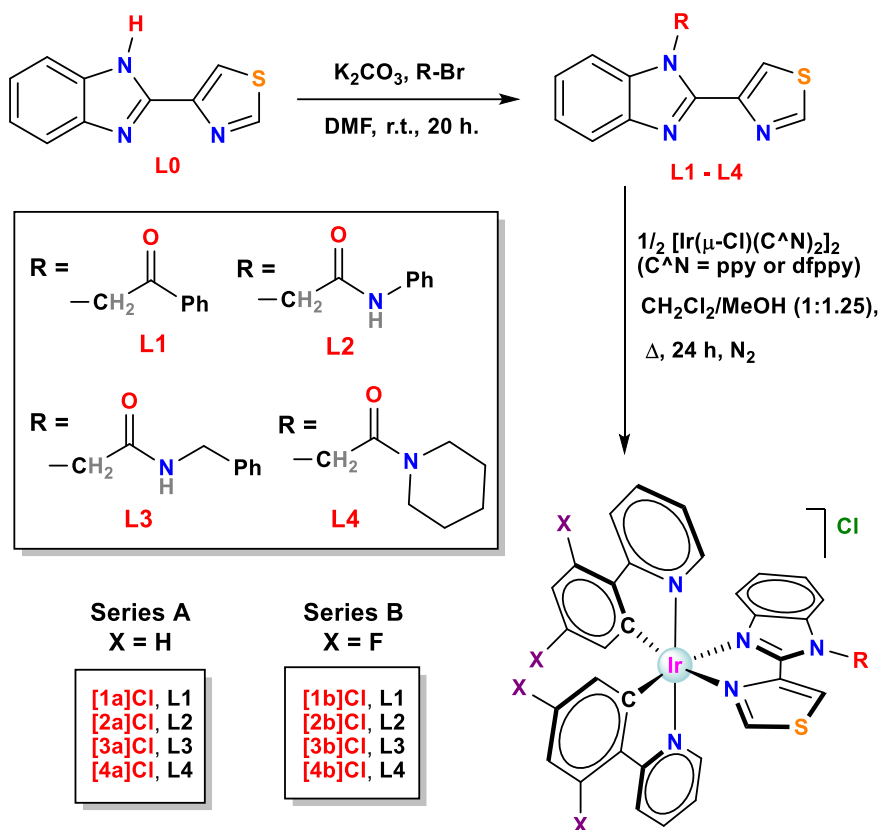
established some structure-activity relationships and we have identified two metallodrugs as the most efficient PSs in the potential treatment of cancer. Last but not least, we have outlined the mechanism of biological action upon light excitation for these chemo-therapeutics.

## 2. Results and discussion

### 2.1. Synthesis of ligands and iridium(III) complexes

A new library of Ir(III) biscyclometalated compounds of general formula  $rac-[Ir(C^{\wedge}N)_2(N^{\wedge}N')Cl]$  has been prepared aiming to study their anticancer properties as potential PDT agents. In particular, we have used two different  $C^{\wedge}N$  ligands and four different  $N^{\wedge}N'$  ligands based on the 2-(4-thiazolyl)benzimidazole (thiabendazole) scaffold. Thiabendazole (**L0**) is an antifungal and antiparasitic agent commercially available and can be easily functionalized by mean of alkylation reactions on the reactive N–H group. Thus, the ligands (**L1-L4**) with different amido-alkyl and keto-alkyl groups were obtained through a procedure adapted from the literature,<sup>31,32</sup> which involves the reaction of **L0** with the appropriate alkyl bromide at room temperature in the presence of  $K_2CO_3$  and using dimethylformamide (DMF) as solvent (Scheme 1). Ligands **L1-L4** were designed to possess protecting hydrophilic motifs instead of the slightly acidic N–H on the imidazole ring. More specifically, hydrogen bonding donor and acceptor groups were chosen to bestow a certain degree of hydrophilicity on the resulting complexes by contrast with the lipophilicity attributed to the  $[Ir(C^{\wedge}N)_2]^+$  fragment.

The corresponding Ir(III) derivatives [**1a**]Cl - [**4a**]Cl (**series A**) and [**1b**]Cl - [**4b**]Cl (**series B**) were synthesized by refluxing the appropriate iridium dimer  $[Ir(\mu-Cl)(C^{\wedge}N)_2]_2$  ( $C^{\wedge}N$  = ppy (2-phenylpyridinate), or dfppy (2-(2,4-difluorophenyl)pyridinate)) in the presence of ligands **L1-L4** in a mixture of dichloromethane-methanol (1:1.25; v/v) (Scheme 1). The desired products were isolated as solid chloride salts in the form of racemic mixtures with bright yellow colours and display moderate solubility in aqueous media because of the presence of hydrophilic groups and the chloride counterion.



Scheme 1. Synthesis and molecular structures of ligands **L1** – **L4** and complexes **[1a]Cl** – **[4a]Cl** and **[1b]Cl** – **[4b]Cl**.

## 2.2. Characterization of the Ir(III)-compounds

The composition and molecular structure of the new Ir complexes was established by multinuclear NMR, mass spectrometry, elemental analysis and IR spectroscopy. In addition, the molecular structure of complexes **[1b]<sup>+</sup>**, **[2a]<sup>+</sup>** and **[3a]<sup>+</sup>** was ascertained by X-ray diffraction.

The  $^1\text{H}$ ,  $^{13}\text{C}\{^1\text{H}\}$  and  $^{19}\text{F}$  NMR spectra of **[1a]Cl** – **[4a]Cl** and **[1b]Cl** – **[4b]Cl** were recorded in  $\text{DMSO-d}_6$  (SI Fig. 12-31) and show evident coordination-induced shifts relative to the free ligands as well as the following distinguishing attributes: (1) two sets of signals for the non-equivalent  $\text{C}^{\wedge}\text{N}$  ligands ( $\text{C}_1$ -symmetry); (2) two mutually coupled doublets, appearing as an AB quartet between 5.65 and 6.75 ppm for the diastereotopic protons of the  $-\text{CH}_2$  groups because of the helical chirality implicit in tris-chelate octahedral complexes.

The  $^{19}\text{F}$  NMR spectra of complexes **[1b]Cl** - **[4b]Cl** display two multiplets around 107 ppm ( $\text{F}^9$  and  $\text{F}^{9'}$ ) and two additional multiplets at about 109 ppm ( $\text{F}^{11}$  and  $\text{F}^{11'}$ ), for the two non-equivalent dfppy ligands (atom labelling shown in Section 4.3. and SI).

The HR ESI(+) mass spectra of **[1a]Cl** - **[4a]Cl** and **[1b]Cl** - **[4b]Cl** show an envelope of peaks with  $m/z$  values and isotopic distribution patterns fully compatible with those calculated for the monocationic species of formula  $[\text{Ir}(\text{C}^{\wedge}\text{N})_2(\text{N}^{\wedge}\text{N}')^+]$ , resulting from the loss of the chloride counterion in every case.

### 2.3. Crystal structures by X-ray diffraction

High quality single crystals were obtained for the  $\text{PF}_6^-$  salts of **[1b]<sup>+</sup>**, **[2a]<sup>+</sup>** and **[3a]<sup>+</sup>** by slow evaporation of solutions of either **[1b]Cl** and **[3a]Cl** in methanol or **[2a]Cl** in methanol/dichloromethane, upon addition of some drops of saturated aqueous  $\text{NH}_4\text{PF}_6$  in order to facilitate crystallization. The corresponding crystal structures of **[1b]PF<sub>6</sub>**, **[2a]PF<sub>6</sub>** and **[3a]PF<sub>6</sub>** were resolved by single crystal X-ray diffraction analysis. The complexes crystallize in the monoclinic  $\text{P}2_1/c$ ,  $\text{C}2/c$  and  $\text{C}2/c$  space groups, respectively. The unit cells of these complexes contain two pairs (**[1b]PF<sub>6</sub>**) or four pairs (**[2a]PF<sub>6</sub>** and **[3a]PF<sub>6</sub>**) of enantiomers ( $\Delta, \Lambda$ ) plus four or eight  $\text{PF}_6^-$  counteranions. The molecular structures for the  $\Lambda$  enantiomers of complex cations **[1b]<sup>+</sup>**, **[2a]<sup>+</sup>** and **[3a]<sup>+</sup>** are shown in Fig. 2. Selected bond distances and angles for the coordination environment are compiled in Table 1, and relevant crystallographic parameters are given in SI Table 3.

The molecular structures of these complexes exhibit the expected pseudo-octahedral geometry around the Ir centre with two cyclometalating  $\text{C}^{\wedge}\text{N}$  ligands adopting a mutual *trans*-N,N plus *cis*-C,C arrangement. Besides, each  $\text{N}^{\wedge}\text{N}'$  ligand assumes a *trans* disposition with regard to the C atoms of the  $\text{C}^{\wedge}\text{N}$  moieties (Fig. 2).<sup>33</sup> As an evidence of deviation from the ideal octahedral geometry, all the bite angles for the bidentate ligands are lower than  $90^\circ$ , i.e. around  $80^\circ$  for the  $\text{C}^{\wedge}\text{N}$  ligands, and about  $76^\circ$  for the  $\text{N}^{\wedge}\text{N}'$  ligands (Table 1). In all the complexes, the Ir–N bond distances for the  $\text{C}^{\wedge}\text{N}$  ligands (2.039(5) to 2.047(5) Å) are shorter than for the  $\text{N}^{\wedge}\text{N}'$  ligands (2.157(5) to 2.165(4) Å) due to the strong *trans* influence exerted by the coordinated phenyl rings.<sup>34</sup> The Ir–C bond distances are very close to 2 Å (2.003(6)–2.016(6) Å) and standard compared to those usually observed for similar complexes.<sup>35</sup>

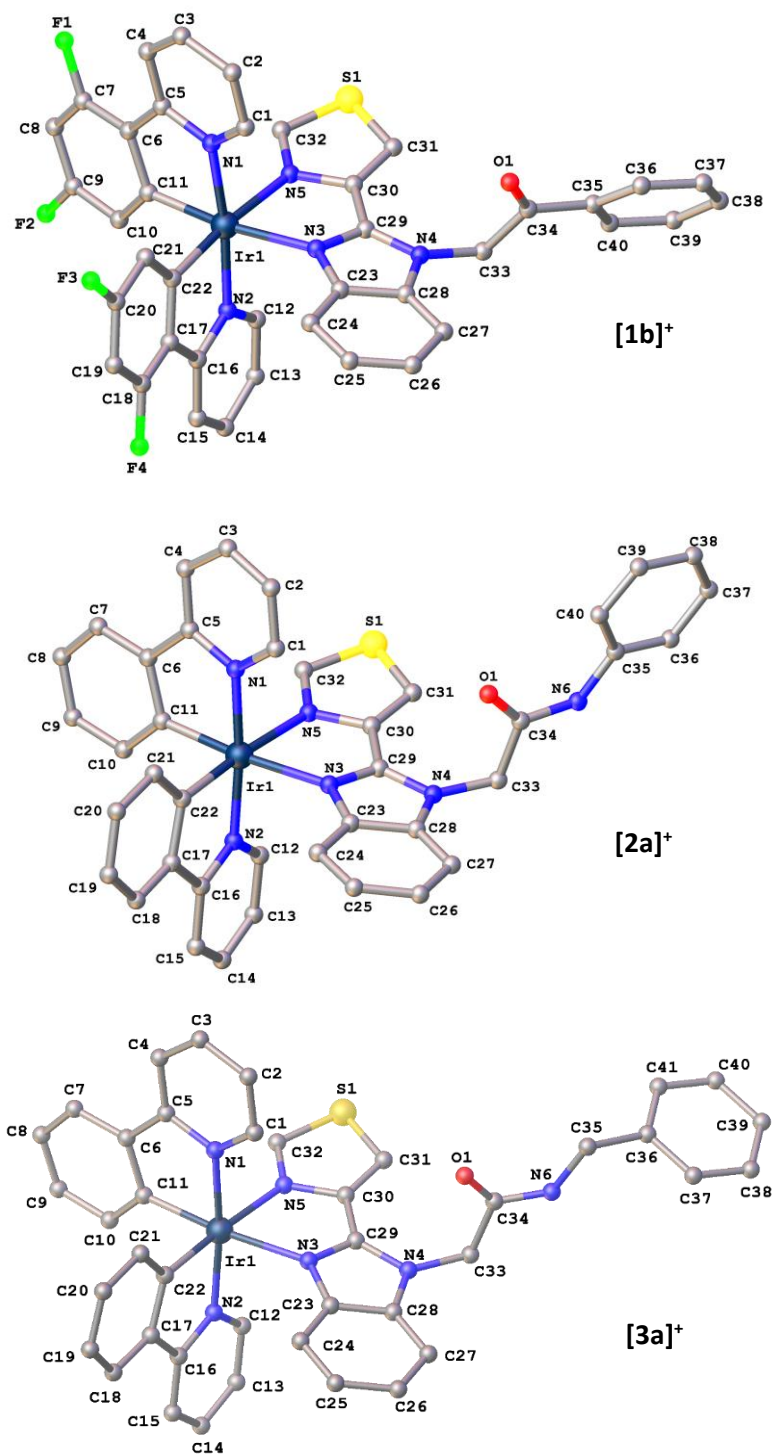


Fig. 2. Molecular structures of  $(\Lambda)$ -[1b]PF<sub>6</sub>,  $(\Lambda)$ -[2a]PF<sub>6</sub> and  $(\Lambda)$ -[3a]PF<sub>6</sub> obtained by X-ray diffraction analysis. The  $\Delta$  enantiomers, H atoms and PF<sub>6</sub><sup>-</sup> counterions have been omitted for the sake of clarity.



Table 1. Selected bond lengths (Å) and angles (°) for [1b]PF<sub>6</sub>, [2a]PF<sub>6</sub> and [3a]PF<sub>6</sub>.

[1b]PF <sub>6</sub>		[2a]PF <sub>6</sub>		[3a]PF <sub>6</sub>	
Ir(1)-N(1)	2.038(6)	Ir(1)-N(1)	2.047(5)	Ir(1)-N(1)	2.041(4)
Ir(1)-N(2)	2.050(6)	Ir(1)-N(2)	2.039(5)	Ir(1)-N(2)	2.049(4)
Ir(1)-N(3)	2.151(6)	Ir(1)-N(3)	2.165(4)	Ir(1)-N(3)	2.171(4)
Ir(1)-N(5)	2.155(5)	Ir(1)-N(5)	2.157(5)	Ir(1)-N(5)	2.159(4)
Ir(1)-C(11)	2.009(7)	Ir(1)-C(11)	2.016(6)	Ir(1)-C(11)	2.016(5)
Ir(1)-C(22)	2.013(7)	Ir(1)-C(22)	2.003(6)	Ir(1)-C(22)	2.004(5)
C(11)Ir(1)N(1)	81.3(3)	C(11)Ir(1)N(1)	81.4(2)	C(11)Ir(1)N(1)	81.12(19)
C(22)Ir(1)N(2)	79.5(3)	C(22)Ir(1)N(2)	81.3(2)	C(22)Ir(1)N(2)	80.72(18)
N(3)Ir(1)N(5)	76.1(2)	N(3)Ir(1)N(5)	75.6(2)	N(3)Ir(1)N(5)	75.31(14)

The 3-D crystal structures of these complexes are stabilized by hydrogen bonding interactions, involving C–H and N–H groups as donors and C=O groups as well as PF<sub>6</sub><sup>−</sup> anions as acceptors.

#### 2.4. Photostability experiments

Photostability under long irradiation is a key requirement for PDT photosensitizers, since it ensures more ROS-producing cycles for the PS and allows to reduce the PS dose.<sup>36</sup> In other words, a high photostability favours the PS efficiency. The photodegradation of the new Ir(III)-complexes was analysed by monitoring the changes in their <sup>1</sup>H NMR spectra (1.4·10<sup>−2</sup> M, CD<sub>3</sub>CN) over a period of 24 h under air exposure and illumination with blue light, (λ<sub>ir</sub> 460 nm, 24 W) at room temperature (SI Fig. 33-40). All the complexes are fully stable upon 6 h of irradiation, since no photo-degradation was observed during this period. However, after 24 h of irradiation we detected an emerging set of signals for degradation products that integrated between 1% and 5% (SI Table 4). These results confirm the sufficient photostability of our luminophores for PDT applications.

#### 2.5. Theoretical calculations

Density functional theory (DFT) and time-dependent DFT (TD-DFT) calculations were carried out on the molecular and electronic structures of the cation complexes [1a]<sup>+</sup>, [3a]<sup>+</sup>, [1b]<sup>+</sup> and [3b]<sup>+</sup> at their ground state for a deeper comprehension of their photophysical and electrochemical properties. Calculations were performed at the B3LYP/ (6-31GDP LANL2DZ) level including solvent effects (CH<sub>3</sub>CN) (see description in SI Section 9. and SI Tables 5, 6 and 7). The optimized molecular structures calculated for [1a]<sup>+</sup>, [3a]<sup>+</sup>, [1b]<sup>+</sup> and [3b]<sup>+</sup> at their electronic ground state (S<sub>0</sub>) exhibit a near-octahedral geometry for the metal coordination environment in agreement with the crystal structures previously discussed. SI Table 5 shows the isovalue contour plots and

the energies for the frontier molecular orbitals (MOs) of cations  $[1a]^+$ ,  $[3a]^+$ ,  $[1b]^+$  and  $[3b]^+$  at the  $S_0$  state. The HOMOs of these complexes are spread over the Ir and the phenyl or difluorophenyl rings of the C<sup>N</sup> ligands and are formed by an admixture of a  $t_{2g}$  orbital from Ir(III) and  $\pi$  orbitals of the two phenyl rings. Consequently, the energies computed for the HOMOs of  $[1a]^+$  and  $[3a]^+$  are virtually identical (5.61 and 5.62 eV), given that they have the same C<sup>N</sup> ligands (ppy<sup>-</sup>). Similarly, the energies obtained for the HOMOs of  $[1b]^+$  and  $[3b]^+$  are almost alike (5.94 and 5.95 eV), since they share the same C<sup>N</sup> ligands (dfppy<sup>-</sup>). The stabilization of the HOMOs for  $[1b]^+$  and  $[3b]^+$ , relative to the HOMOs of  $[1a]^+$  and  $[3a]^+$  is due to the electron-withdrawing nature of the -F atoms in dfppy<sup>-</sup>, as reported previously (Fig. 3).<sup>37,38</sup>

The LUMOs are distributed over the N<sup>N</sup>' ligands in all the cases, although their precise topology depends slightly on the ligand. Indeed, the participation of the alkyl group of  $[1a]^+$  and  $[1b]^+$  (-CH<sub>2</sub>COPh) in the electron density of their LUMO is relevant, while the participation of the alkyl group of  $[3a]^+$  and  $[3b]^+$  (-CH<sub>2</sub>CONHCH<sub>2</sub>Ph) in their LUMO is non-existent. The LUMO of  $[3a]^+$  exhibits a small destabilization relative to that of  $[1a]^+$  and a similar effect was observed for  $[3b]^+$  compared to  $[1b]^+$ . These predictions are in agreement with the electrochemical trends experimentally determined for the reduction potentials of these complexes (see below). Considering all the above, the resulting HOMO-LUMO gaps are higher for complexes of **series B** than for their congeners of **series A**.

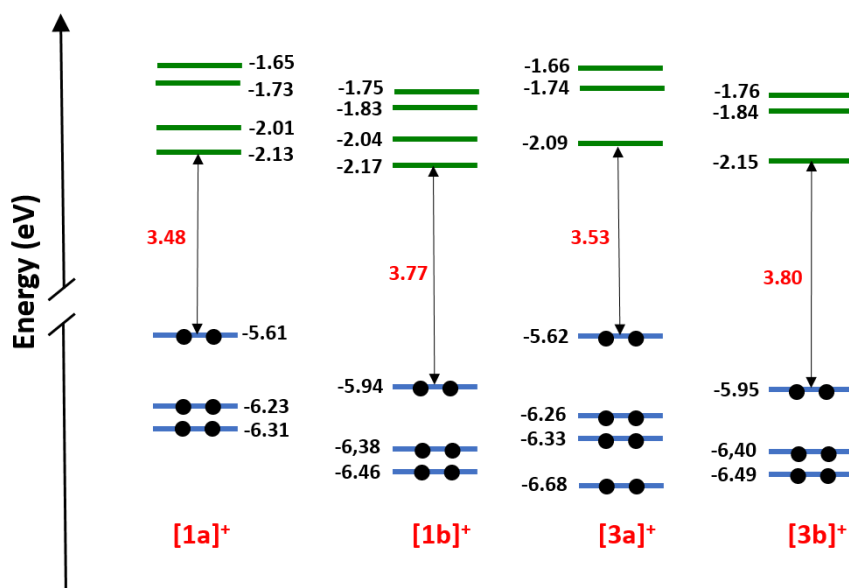


Fig. 3. Schematic representation displaying the energies computed for the frontier orbitals and the HOMO-LUMO energy gaps of  $[1a]^+$ ,  $[3a]^+$ ,  $[1b]^+$  and  $[3b]^+$ .

The nature of the lowest-energy singlet ( $S_n$ ) and triplet ( $T_n$ ) excited states and the respective energies were computed by mean of the TD-DFT method for the cations **[1a]<sup>+</sup>**, **[3a]<sup>+</sup>**, **[1b]<sup>+</sup>** and **[3b]<sup>+</sup>**. The results are compiled in SI Tables 6 and 7 and are sketched in SI Fig. 41(a). The lowest triplet excited states ( $T_1$ ) of **[1a]<sup>+</sup>** and **[3a]<sup>+</sup>** exhibit energies of 2.75 eV, while the corresponding states of **[1b]<sup>+</sup>** and **[3b]<sup>+</sup>** are destabilized to 2.85 eV. Hence, these estimations predict lower  $\lambda_{em}$  for **[1b]<sup>+</sup>** and **[3b]<sup>+</sup>** relative to **[1a]<sup>+</sup>** and **[3a]<sup>+</sup>** in agreement with the trends determined experimentally for the emission energies of these pairs (see below).

## 2.6. Electrochemical properties

The electrochemical behaviour of the ground and excited states of this type of complexes can play important roles in their biological activity both in the dark and upon photoactivation, respectively.<sup>39</sup> For that reason, the redox potentials of **[1a]Cl** - **[4a]Cl** and **[1b]Cl** - **[4b]Cl** were experimentally determined by cyclic voltammetry (CV) in deoxygenated acetonitrile solutions ( $5 \times 10^{-4}$  M) versus the ferrocenium/ferrocene ( $Fc^+/Fc$ ) couple. The cyclic voltammograms of **[1a]Cl** - **[1b]Cl** and **[3a]Cl** - **[3b]Cl** are shown in Fig. 4(A) as illustrative examples of their respective series. Voltammograms for the other derivatives are very similar to those of **[3a]Cl** and **[3b]Cl** and are presented in the SI (SI Fig. 42-44).

The anodic region of the voltammograms features one irreversible peak for all the complexes between +0.56 and +0.69 V ( $E^{ox1}_{1/2}$  in Table 2 and Fig. 4(A)) attributed to the oxidation of the  $Cl^-$  counter-anion ( $2 Cl^- \rightarrow Cl_2 + 2e^-$ ). This assignation was confirmed by recording the CV of **[3a]PF<sub>6</sub>**, where the afore-mentioned peak was missing (SI Fig. 44). The small variations noticed in the position of this oxidation peak depending on the complex are likely due to weak interactions between the chloride anion and the respective complex cation, which are responsible for the formation of ion pairs (see Molar conductivity measurements below). Moreover, a second reversible one-electron redox peak is observed at +0.85 V for **[1a]Cl** - **[4a]Cl** and at around +1.18 V for **[1b]Cl** - **[4b]Cl**. This wave is assigned to the reversible oxidation of the environment formed by the Ir(III) centre and both phenyl rings of the respective C<sup>N</sup> ligands, in agreement with the topology calculated for the HOMO of **[1a]<sup>+</sup>**, **[3a]<sup>+</sup>**, **[1b]<sup>+</sup>** and **[3b]<sup>+</sup>** (see SI Table 8 and canonical forms in Fig. 4(B)).<sup>40,41</sup> Thus, this peak is shifted to more anodic potentials (0.33 V, approximately) for complexes of **series B**, due to the presence of -F atoms on the phenyl rings. The electron-withdrawing effect of the -F atoms reduces the electron density at the Ir-Ph environment and stabilizes remarkably the HOMO (see calculations), hindering the extraction of the first electron from **[1b]Cl** - **[4b]Cl** relative to **[1a]Cl** - **[4a]Cl**.<sup>42,43</sup>

The cathodic region, on the other side, displays one irreversible wave peaking at around  $-2$  V for complexes of both series ( $E^{\text{red}1}_{1/2}$  in Table 2). The extra electron accepted by these complexes is accommodated in the N<sup>^</sup>N' ligand,<sup>45</sup> in agreement with the topology of their LUMO (see SI Table 5), giving place to a reduced radical form,  $[\text{Ir}^{\text{III}}(\text{C}^{\wedge}\text{N}^-)_2(\text{N}^{\wedge}\text{N}'^{\cdot-})]$  (Fig. 4(B)). All the complexes with alkyl-amide groups, except **[4b]Cl**, that is **[2a]Cl** - **[4a]Cl** and **[2b]Cl** - **[3b]Cl**, present more negative reduction potentials  $E^{\text{red}1}_{1/2}$  (in the range from  $-2.03$  to  $-2.11$  V) than the respective complexes with the alkyl-ketone group, namely, **[1a]Cl** and **[1b]Cl** ( $-1.96$  and  $-1.92$  V, respectively). This effect is likely due to the destabilization of the LUMO predicted theoretically for **[3a]**<sup>+</sup> and **[3b]**<sup>+</sup> relative to the LUMO of **[1a]**<sup>+</sup> and **[1b]**<sup>+</sup>, and it is attributed to both the positive mesomeric (electron donating) effect of the  $-\text{CH}_2\text{CONR}_2$  groups and the negative mesomeric (electron withdrawing) effect of the  $-\text{CH}_2\text{COPh}$  group. Moreover, calculations reported by us in a previous work for the reduced species of a similar complex,<sup>46</sup> predict a high spin density localized on one of the C atoms of the thiazole ring when the N<sup>^</sup>N' ligand is based on the thiabendazole scaffold. Thus, the irreversible nature of the reduction process observed for our complexes could be rationalized due to the limited delocalization of the afore-mentioned unpaired electron.

The electro-chemical band-gaps ( $\Delta E_{1/2}$ ) have been determined as the difference between  $E^{\text{ox}2}_{1/2}$  and  $E^{\text{red}1}_{1/2}$ . The so-calculated values are in the range between 2.81 and 2.96 eV for members of family A and in the range between 3.07 and 3.23 for their congeners of family B, which is in accordance with the higher HOMO-LUMO band-gap calculated theoretically for family B. Hence, the afore-mentioned stabilization of the HOMO in family B seems to be the main factor explaining the increase of  $\Delta E_{1/2}$  for **[1b]Cl** - **[4b]Cl** relative to **[1a]Cl** - **[4a]Cl**.

Interestingly, the excited states of this type of complexes usually exhibit an outstanding combination of reductive and oxidative character. In particular, our photosensitizers show higher excited state oxidation powers than the archetypal photosensitizer  $[\text{Ir}(\text{ppy})_2(\text{bpy})]\text{PF}_6$ , **[1]PF<sub>6</sub>**, that is,  $E_{1/2}(\text{Ir}^{\text{III}*}/\text{Ir}^{\text{II}})$  ranges from  $+0.47$  to  $+0.83$  V relative to  $+0.28$  V for **[1]PF<sub>6</sub>**. At the same time, these photosensitizers show better excited state reduction power than **[1]PF<sub>6</sub>**, since  $E_{1/2}(\text{Ir}^{\text{IV}}/\text{Ir}^{\text{III}*})$  ranges from  $-1.47$  to  $-1.75$  V relative to  $-1.19$  V for **[1]PF<sub>6</sub>** (Fig. 5 and SI Table 8). These redox properties *a priori* render our complexes excellent photoredox catalysts, which in turn could enhance their ability to generate ROS and improve their biological performance as PDT agents.

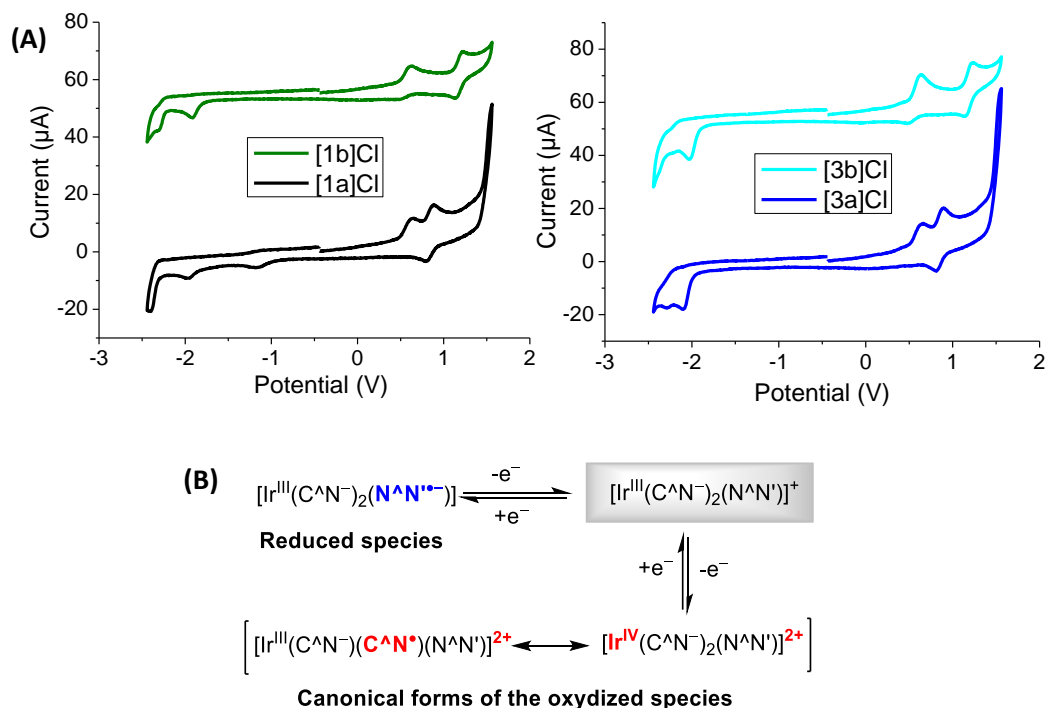


Fig. 4. (A) Cyclic voltammograms of complexes [1a]Cl - [1b]Cl and [3a]Cl - [3b]Cl in acetonitrile solution ( $5 \cdot 10^{-4}$  M), using 0.1 M  $[\text{nBu}_4\text{N}][\text{PF}_6]$  as supporting electrolyte and recorded with a scan rate of  $0.10 \text{ V} \cdot \text{s}^{-1}$ . (B) Reduced and oxidized species formed for complexes of formula  $[\text{Ir}^{\text{III}}(\text{C}^{\wedge}\text{N}^-)_2(\text{N}^{\wedge}\text{N}^{\bullet})]^+$ .

Table 2. Redox potentials recorded by cyclic voltammetry referenced to  $\text{Fc}^+/\text{Fc}$  in acetonitrile solution.<sup>[a]</sup>

Complex	$E^{\text{ox1}}_{1/2}$ (V)	$E^{\text{ox2}}_{1/2}$ (V)	$E^{\text{red1}}_{1/2}$ (V)	$E^{\text{red2}}_{1/2}$ (V)	$\Delta E_{1/2}$ (V)
[1](PF <sub>6</sub> )	-	+0.87 (rev)	-1.78 (qr)	-	2.65
[1a]Cl	+0.57 (ir)	+0.85 (rev)	-1.96 (ir)	-2.29 (ir)	2.81
[2a]Cl	+0.67 (ir)	+0.85 (rev)	-2.10 (ir)	-2.27 (ir)	2.95
[3a]Cl	+0.65 (ir)	+0.85 (rev)	-2.11 (ir)	-2.26 (ir)	2.96
[4a]Cl	+0.69 (ir)	+0.84 (rev)	-2.04 (ir)	-2.12 (ir)	2.88
[1b]Cl	+0.56 (ir)	+1.18 (rev)	-1.92 (ir)	-2.26 (ir)	3.10
[2b]Cl	+0.67 (ir)	+1.18 (rev)	-2.05 (ir)	-2.20 (ir)	3.23
[3b]Cl	+0.56 (ir)	+1.18 (rev)	-2.03 (ir)	-2.19 (ir)	3.21
[4b]Cl	+0.56 (ir)	+1.17 (rev)	-1.90 (ir)	-2.11 (ir)	3.07
[3a]PF <sub>6</sub>	-	+0.85 (rev)	-2.11 (ir)	-2.25 (ir)	2.96

<sup>[a]</sup>Voltammograms recorded in acetonitrile solution ( $5 \times 10^{-4}$  M), using 0.1 M  $[\text{nBu}_4\text{N}][\text{PF}_6]$  as supporting electrolyte and recorded with scan rate of  $0.10 \text{ V} \cdot \text{s}^{-1}$  and referenced to  $\text{Fc}^+/\text{Fc}$ . <sup>[b]</sup> Redox potentials for the reference complex have been obtained from the literature.<sup>44</sup>

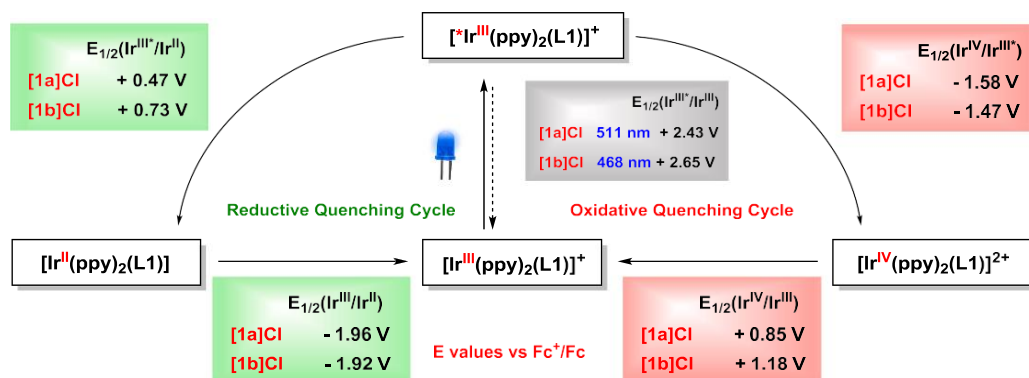


Fig. 5. Latimer diagrams for [1a]Cl and [1b]Cl with redox potentials determined by CV and the emission energy calculated from the photoluminescence spectrum. The redox potentials for [1a]<sup>+</sup>-[1b]<sup>+</sup> and its excited states [1a]<sup>+</sup>\*-[1b]<sup>+</sup>\* are given in V versus Fc<sup>+</sup>/Fc.  $E_{1/2}(\text{Ir}^{\text{IV}}/\text{Ir}^{\text{III}}^*) = E_{1/2}(\text{Ir}^{\text{IV}}/\text{Ir}^{\text{III}}) - E_{1/2}(\text{Ir}^{\text{III}}^*/\text{Ir}^{\text{III}})$  and  $E_{1/2}(\text{Ir}^{\text{III}}^*/\text{Ir}^{\text{II}}) = E_{1/2}(\text{Ir}^{\text{III}}/\text{Ir}^{\text{II}}) + E_{1/2}(\text{Ir}^{\text{III}}^*/\text{Ir}^{\text{III}})$ . All the potential values are given as reduction potentials regardless the sense of the arrows for the quenching cycles.

Molar conductivity measurements ( $\Lambda_{\text{M}}$ ) were performed for [3a]Cl and [3a]PF<sub>6</sub> in acetonitrile solutions (10<sup>-3</sup> M) at room temperature. Interestingly, the value obtained for [3a]PF<sub>6</sub> ( $\Lambda_{\text{M}} = 178 \text{ S}\cdot\text{cm}^2\cdot\text{mol}^{-1}$ ) is compatible with a 1:1 electrolyte, whereas the value determined for [3a]Cl ( $\Lambda_{\text{M}} = 81 \text{ S}\cdot\text{cm}^2\cdot\text{mol}^{-1}$ ) is remarkably lower revealing the formation of intimate ion pairs for [3a]Cl in this solvent. Thus, we hypothesize that the participation of the Cl<sup>-</sup> counteranion in ion pairing and the strength of the specific interactions involved in the formation of these entities could explain the small variations observed for  $E^{\text{ox}}_{1/2}$ .

## 2.7. Photophysical properties

The UV-Vis absorption and emission spectra of the new complexes were recorded in H<sub>2</sub>O-DMSO (94:6, v:v) (10<sup>-5</sup> M) at room temperature (Fig. 6(A) and SI Fig. 32(A) and Table 3). All the derivatives exhibit strong bands with maxima around 250 nm (<sup>1</sup>LC,  $\pi \rightarrow \pi^*$  for C<sup>^</sup>N and N<sup>^</sup>N' ligands) and 300 nm (<sup>1</sup>MLCT and <sup>1</sup>LLCT) and a weak but very broad tail above 350 nm (<sup>3</sup>MLCT and <sup>3</sup>LC).<sup>47,48,49</sup> This spin-forbidden band is enabled by the large spin-orbit coupling typical of the Ir(III) ion<sup>38</sup> and spreads well into the visible region for [1a]Cl - [4a]Cl, but faintly for [1b]Cl - [4b]Cl. The value of  $\epsilon$  [M<sup>-1</sup> cm<sup>-1</sup>] at the wavelength used in biological experiments (460 nm) is reflected in Table 3. Indeed, the absorption of derivatives of series A overlaps suitably with the emission band of our blue light source. However, *a priori* the analogues of series B with dfppy can hardly be excited with this light source, which could be a handicap for their use as PDT agents (see below). Blue and green lights display a low tissue penetration depth (1–1.4 mm), which precludes the use of PSs sensitive to short-wavelength visible lights for the treatment of deep-seated tumours. Nonetheless, this type of light stimulus combined with interstitial delivery of light is advantageous to avoid damage

on healthy, underlying tissue. Indeed, the Ru(II) PS TLD-1433, with a light excitation wavelength of 520 nm, is in clinical trials for the treatment of bladder cancer.<sup>13,50</sup> On the other hand, excitation at higher energy wavelengths (UV) is impractical, due to its limited tissue penetration along with its light-induced cytotoxicity.<sup>51,52</sup>

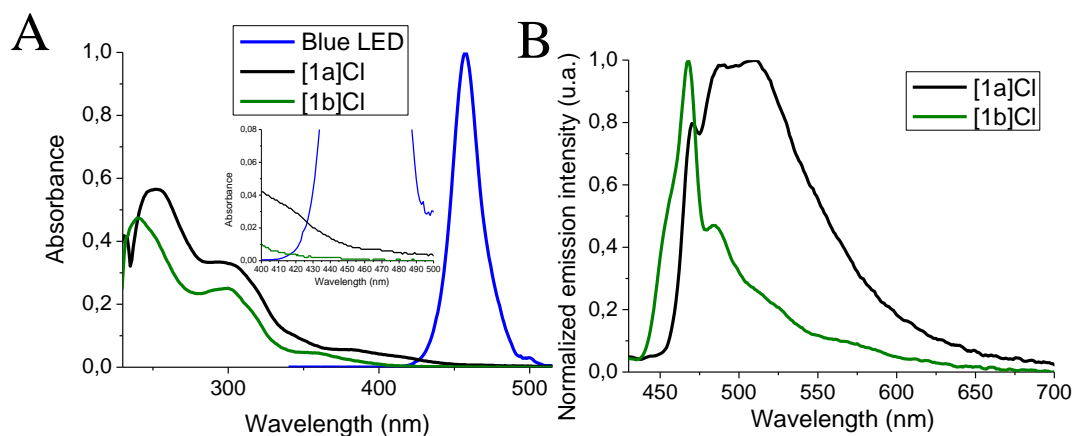


Fig. 6. (A) Overlaid UV-Vis absorption spectra of complexes [1a]Cl and [1b]Cl ( $10^{-5}$  M) in H<sub>2</sub>O-DMSO (94:6, v:v) at 25 °C, together with the emission band recorded for the blue light source used in biological experiments (overlapping region in the inset). (B) Overlaid emission spectra of complexes [1a]Cl and [1b]Cl in deoxygenated H<sub>2</sub>O-DMSO (94:6, v:v) ( $10^{-5}$  M) at 25 °C under a nitrogen atmosphere ( $\lambda_{ex} = 405$  nm).

In general, the emission of complexes with general formula  $[\text{Ir}(\text{C}^{\wedge}\text{N})_2(\text{N}^{\wedge}\text{N}')^+]$  takes place from the lowest lying triplet state ( $T_1$ ), which is formed by a combination of  ${}^3\text{MLCT}/{}^3\text{LLCT}$  and  ${}^3\text{LC}$  states. The emission spectra of our complexes exhibited a band with vibronic structure (two maxima), indicating a major  ${}^3\text{LC}$  ( ${}^3\pi\text{-}\pi^*$ ) character for the transition to the ground state as corroborated by theoretical calculations (Fig. 6 (B) and SI Fig. 32(B)).<sup>46,53,54,55</sup> The higher energy maximum appears between 479 and 511 nm for complexes of **series A** and between 454 and 468 nm for complexes of **series B**. Hence, the observed maximum wavelengths ( $\lambda_{max}$ ) for [1b]Cl - [4b]Cl are blue-shifted relative to those recorded for [1a]Cl - [4a]Cl, which reveals an increase of the  $S_0 \leftarrow T_1$  energy attributed to the presence of the -F atoms on the C<sup>∧</sup>N ligands as predicted by our calculations and reported in the literature.<sup>56,57,58</sup> Moreover, the presence of alkyl-amide groups on the N<sup>∧</sup>N' ligand results in a hypsochromic shift compared to the respective complex with an alkyl-ketone substituent in both series (32 nm in **series A** and 14 nm in **series B**). Triplet energy levels ( $E_T$ ) are directly calculated from the maximum emission peaks (Table 3) and are critical parameters for efficient energy transfer (ET) to  ${}^3\text{O}_2$  in the generation of  ${}^1\text{O}_2$ . Indeed, molecular oxygen ( $\text{O}_2$ ) has two singlet excited states ( ${}^1\Sigma_g$  and  ${}^1\Delta_g$ ) with absorption energies of 762 nm (1.63 eV) and 1268 nm (0.98 eV), respectively, so that the triplet energy level of an efficient  ${}^1\text{O}_2$  photosensitizer has to be higher than these values. Concurrently, PSs with

extremely high triplet energy values bring about inefficient ET owing to mismatch with the energy levels of  $^1\text{O}_2$ .<sup>59</sup> Therefore, we speculate that **[1a]Cl**, with the lowest triplet energy value (2.43 eV), could be the most appropriate  $^1\text{O}_2$  photosensitizer within this family of complexes.

The emission quantum yields (PLQY,  $\phi_{\text{PL}}$ ) were experimentally determined in deoxygenated  $\text{H}_2\text{O}$ -DMSO (94:6, v:v) and are low for **[1a]Cl** - **[4a]Cl** (3-9 %) and very low for **[1b]Cl** - **[4b]Cl** (< 1 %) (Table 3). On the other hand, the excited state lifetimes ( $\tau$ ) are only given for complexes of **series A** in deoxygenated  $\text{H}_2\text{O}$ -DMSO (94:6, v:v), due to the low  $\phi_{\text{PL}}$  values obtained for derivatives of **series B**. The replacement of the - $\text{CH}_2\text{COPh}$  group in **[1a]Cl** with different - $\text{CH}_2\text{CONR}_2$  groups in **[2a]Cl** - **[4a]Cl**, results in longer  $\tau$  values (Table 3), likely as a result of the energy-gap law.<sup>60,61,62</sup>

Table 3. Photophysical properties for complexes **[1a]Cl** - **[4a]Cl** to **[1b]Cl** - **[4b]Cl** determined in  $\text{H}_2\text{O}$ -DMSO (94:6, v:v) ( $10^{-5}$  M) at 25 °C under a nitrogen atmosphere with  $\lambda_{\text{ex}} = 405$  nm.

Complex	$\lambda_{\text{abs}}$ (nm)	$\epsilon$ [ $\text{M}^{-1} \text{cm}^{-1}$ ]	$\epsilon$ [ $\text{M}^{-1} \text{cm}^{-1}$ ] (at 460 nm)	$\lambda_{\text{em}}$ (nm) [ $E_{\text{T}}$ (eV)]	$\phi_{\text{PL}}$ (%)
<b>[1a]Cl</b>	252, 295, 382	56500, 33400, 5600	900	511 [2.43 eV]	9
<b>[2a]Cl</b>	242, 295, 373	56400, 31500, 5400	600	479 [2.59 eV], 506	8
<b>[3a]Cl</b>	242, 295, 381	42600, 29900, 4800	300	479 [2.59 eV], 505	7
<b>[4a]Cl</b>	241, 297, 373	38800, 26400, 4300	200	479 [2.59 eV], 505	3
<b>[1b]Cl</b>	240, 300, 357	47400, 25100, 4600	100	468 [2.65 eV]	0.03
<b>[2b]Cl</b>	240, 294, 355	41700, 22000, 5100	600	454 [2.73 eV], 482	0.13
<b>[3b]Cl</b>	240, 300, 357	50400, 31100, 5800	200	454 [2.73 eV], 482	0.52
<b>[4b]Cl</b>	240, 300, 365	42500, 25900, 4100	100	454 [2.73 eV], 482	0.08

## 2.8. Ability of $^1\text{O}_2$ generation

Singlet oxygen is considered as the main cytotoxic species in Type II PDT.<sup>63</sup> Moreover, 1,3-diphenylisobenzofuran (DPBF) is widely reckoned as a  $^1\text{O}_2$  capture agent.<sup>64</sup> Therefore, the ability to generate singlet oxygen ( $^1\text{O}_2$ ) was demonstrated for **[1a]Cl** and **[3a]Cl** in acetonitrile by recording the evolution of the respective UV-Vis spectra during the oxidation of DPBF (yellow) to 1,2-dibenzoylbenzene (colorless) in the presence of our photosensitizers under blue light irradiation ( $\lambda_{\text{ir}} = 460$  nm) at 1 second intervals for a total exposure period of 8 seconds (Fig. 7). Both kinetic experiments showed a decay in the intensity of DPBF consistent with the generation of  $^1\text{O}_2$ . A control experiment for the photooxidation of DPBF in acetonitrile under blue light irradiation in the absence of PS was also performed. In line with the results obtained by Li et al. in other solvents,<sup>65</sup> we observed that DPBF undergoes a certain degree of photooxidation under these conditions, although the rate is remarkably lower than those recorded in the presence of **[1a]Cl** and **[3a]Cl** (SI Table 9).



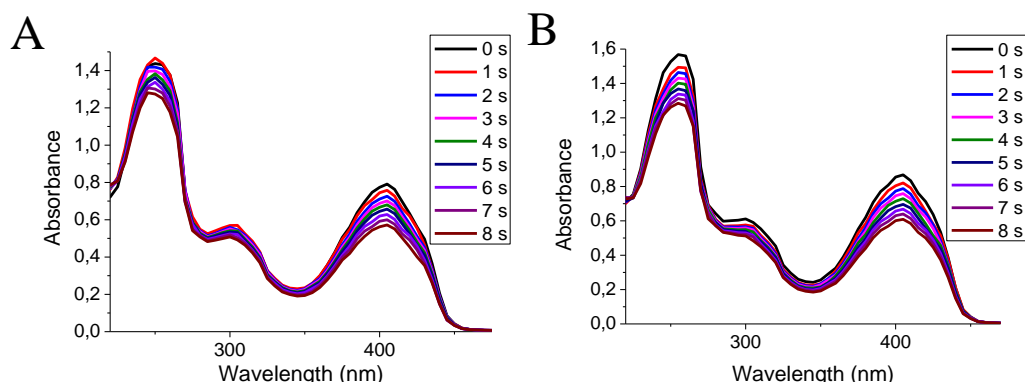


Fig. 7. Photocatalytic oxidation of DPBF in the presence of **[1a]Cl** (A) and **[3a]Cl** (B) in acetonitrile.

Considering the experimental results and the bibliographic background,<sup>40</sup> we postulate that our complexes can operate through a photochemical pathway consisting of several steps: (a) Photoexcitation of the Ir-PS from their ground state to the singlet excited state ( $[\text{Ir}^{\text{III}}] \rightarrow {}^1[\text{Ir}^{\text{III}}]^*$ ); (b) formation of the Ir long-lived triplet excited state *via* Intersystem crossing ( ${}^1[\text{Ir}^{\text{III}}]^* \rightarrow {}^3[\text{Ir}^{\text{III}}]^*$ ); (c) generation of  ${}^1\text{O}_2$  and other ROS by mean of an energy transfer step ( ${}^3[\text{Ir}^{\text{III}}]^* + {}^3\text{O}_2 \rightarrow [\text{Ir}^{\text{III}}] + {}^1\text{O}_2$ ). Alternatively,  ${}^3[\text{Ir}^{\text{III}}]^*$  could generate the radical anion superoxide ( $\text{O}_2^{\cdot -}$ ) through an electron transfer pathway, since we have proved that superoxide levels are increased upon treatment with photoactivated complexes (*vide infra*).

## 2.9. Phototoxic activity and cellular uptake

In order to assess the potential of these compounds for anticancer PDT, their cytotoxic activity against PC-3 prostate cancer cells was tested either in the dark or upon irradiation with a blue light ( $\lambda_{\text{ir}} = 450 \text{ nm}$ ) for 1 h. The light dose applied ( $24.1 \text{ J cm}^{-2}$ ) was similar to that used to photo-activate other Ir-based PSs.<sup>36</sup> Compounds were tested at concentrations up to  $50 \mu\text{M}$  and the concentration that inhibits the viability of cells by 50 % ( $\text{IC}_{50}$ ) was determined after 48 h of treatment using an MTT assay. All compounds exhibited a cytotoxic effect against PC-3 cells in the absence of irradiation, with  $\text{IC}_{50}$  values between  $12.76 \mu\text{M}$  and  $2.75 \mu\text{M}$  (Table 4). These values are in the range of cisplatin, a well-established anticancer agent, assayed under the same conditions (Table 4). Upon light irradiation, compounds **[1a]Cl** – **[4a]Cl** exhibited a marked increase in their cytotoxic activity, with  $\text{IC}_{50}$  values between  $0.32 \mu\text{M}$  and  $2.36 \mu\text{M}$ . In particular, the highest phototoxicity index values ( $\text{PI } \text{IC}_{50,\text{dark}}/\text{IC}_{50,\text{light}}$ ) were obtained for **[1a]Cl** (PI: 8.6) and **[3a]Cl** (PI: 7.5), while **[2a]Cl** and **[4a]Cl** displayed lower PI values of 4.5 and 4.2, respectively. In contrast, the activity of compounds **[1b]Cl** – **[4b]Cl** was essentially not enhanced by light irradiation. Only **[4b]Cl** showed higher activity upon irradiation, with a moderate PI of 2.3. As afore-

suggested, the negligible or weak photoactivation of complexes **[1b]Cl** – **[4b]Cl** is likely related to their weaker absorption in the visible region of the spectrum and in particular in the blue light region. In addition, the excited state lifetime seems not to be the determining factor in the PI value of our complexes, as **[1a]Cl** exhibits the lowest  $\tau$  of all these photosensitizers. We postulate that the higher photocytotoxicity of **[1a]Cl** compared to its congeners could be related to its good absorption profile in the blue light region, its appropriate  $E_T$  value and its ability to generate  $^1O_2$  (*vide supra*).

Based on these results, complexes **[1a]Cl** and **[3a]Cl**, which hold the highest potential for PDT, were chosen for further investigations on their biological mechanism of action.

Table 4. Cytotoxic activity against PC-3 cells.

Compound	IC <sub>50,dark</sub> (μM)	IC <sub>50,light</sub> (μM)	PI <sup>a</sup>
<b>[1a]Cl</b>	2.75 ± 0.37	0.32 ± 0.10	8.6
<b>[2a]Cl</b>	10.52 ± 1.17	2.36 ± 0.46	4.5
<b>[3a]Cl</b>	12.76 ± 0.44	1.71 ± 0.75	7.5
<b>[4a]Cl</b>	3.90 ± 1.13	0.92 ± 0.12	4.2
<b>[1b]Cl</b>	4.52 ± 0.02	1.94 ± 0.52	2.3
<b>[2b]Cl</b>	6.32 ± 0.73	6.01 ± 1.06	1.1
<b>[3b]Cl</b>	6.32 ± 0.48	5.57 ± 0.32	1.1
<b>[4b]Cl</b>	4.64 ± 1.21	4.75 ± 0.09	1.0
<b>Cisplatin</b>	2.53 ± 0.73	--	--

PC-3 cells were exposed to the compounds either in the dark or under light irradiation (1 h, 6.7 mW cm<sup>-2</sup>,  $\lambda_{ir}$  = 460 nm). IC<sub>50</sub> values were determined 48 h later by an MTT assay. Data represents the mean ± SD of at least two independent experiments, each performed in triplicate. <sup>a</sup> PI: phototoxicity index = IC<sub>50,dark</sub>/IC<sub>50,light</sub>.

An efficient accumulation of the PS into target cells is crucial to achieve an effective phototherapy. By contrast, low cellular uptake is widely regarded as one of the main causes of resistance to chemotherapy.<sup>6</sup> Taking advantage of the intrinsic fluorescence of **[1a]Cl** and **[3a]Cl**, their cellular internalization was studied by flow cytometry. First, the uptake kinetics of the complexes were analyzed to assess the optimal incubation time to ensure their accumulation into the cells prior to photoactivation. To this end, PC-3 cells were exposed to **[1a]Cl** and **[3a]Cl** at 5 μM for 1, 4, 6 and 16 h and the percentage of cells with green fluorescence emission, corresponding to the uptake of the complexes, was determined relative to non-treated cells. Uptake kinetic curves were obtained by fitting the measured data points to one-phase exponential association curves with GraphPad Software (Fig. 8). The plateau values of the kinetic curves were similar for both complexes, indicating that they have the same ability to internalize into cells. However, the estimated half-time to reach the plateau was lower for **[1a]Cl** (1.41 h) than for

**[3a]Cl** (4.28 h), revealing that **[1a]Cl** has a faster internalization rate.

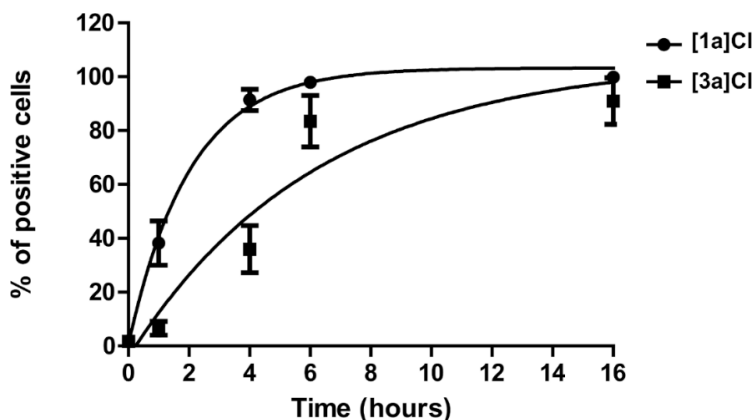


Fig. 8. Internalization kinetics of compounds **[1a]Cl** and **[3a]Cl**. PC-3 cells were incubated with the compounds at 5  $\mu\text{M}$  for 1, 4, 6, and 16 h at 37  $^{\circ}\text{C}$  and the % of cells with positive fluorescence relative to control untreated cells was determined by flow cytometry. Data represents the mean  $\pm$  SD of three independent experiments.

Based on the uptake kinetics, the cytotoxic effect of **[1a]Cl** and **[3a]Cl** was further evaluated, extending the incubation time before irradiation up to 6 h. In addition, SK-MEL-28 melanoma cells and non-malignant CCD-18Co fibroblasts, as healthy control cells, were included in the study (Table 5). The longer preincubation time resulted in a higher photocytotoxicity against PC-3 cells, with  $\text{IC}_{50,\text{light}}$  values of  $0.22 \pm 0.03$  for **[1a]Cl** and  $0.88 \pm 0.24$   $\mu\text{M}$  for **[3a]Cl**. These values are 1.4 and 1.9 fold lower than those obtained for **[1a]Cl** and **[3a]Cl** after 1 h of preincubation (Table 4). Notably, **[1a]Cl** and **[3a]Cl** exhibited high cytotoxicity against SK-MEL-28 cells in the dark and, more importantly, after irradiation (Table 5), resulting in a PI of 23.4 for **[1a]Cl** and 21.4 for **[3a]Cl**. The cytotoxic activity of the complexes in the dark or upon photoactivation against cancer cells is comparable to that of other families of Ir(III) complexes.<sup>11,19,48,66,67</sup> In contrast, their activity against non-tumoral CCD18-Co fibroblasts was moderate, with  $\text{IC}_{50,\text{dark}}$  values of  $5.87 \pm 0.66$   $\mu\text{M}$  and  $24.06 \pm 2.92$   $\mu\text{M}$  and  $\text{IC}_{50,\text{light}}$  values of  $0.54 \pm 0.10$   $\mu\text{M}$  and  $3.39 \pm 1.31$   $\mu\text{M}$ , for **[1a]Cl** and **[3a]Cl** respectively, revealing a lower toxic effect against healthy cells. The Selective Phototoxicity Indexes (SPI) of these complexes were calculated by comparing the  $\text{IC}_{50,\text{dark}}$  values in non-malignant cells to the  $\text{IC}_{50,\text{light}}$  values in cancer cells ( $\text{IC}_{50,\text{dark}}$  CCD-18Co/ $\text{IC}_{50,\text{light}}$  cancer cells). It should be noted that in the case of SK-MEL-28 cells, an SPI value of 117.4 was obtained for **[1a]Cl**, while an SPI value of 171.8 was determined for **[3a]Cl**. These results indicate that in the clinical setting, the dose required for a melanoma PDT-based treatment would not be toxic to healthy cells since they are not exposed to irradiation. Moreover, it is worth mentioning that neither of the two compounds displayed hemolytic activity against red blood cells at the  $\text{IC}_{50,\text{dark}}$  (Table 5) or even at concentrations up to 25  $\mu\text{M}$  (data not shown).

Table 5. Cytotoxic activity against PC-3 and SK-MEL-28 cancer cells and CCD-18Co fibroblasts.

Compound:	[1a]Cl				[3a]Cl			
	IC <sub>50</sub> (μM)		PI <sup>a</sup>	SPI <sup>b</sup>	IC <sub>50</sub> (μM)		PI <sup>a</sup>	SPI <sup>b</sup>
	Dark	Light			Dark	Light		
PC-3	2.75 ± 0.37	0.22 ± 0.03	12.5	26.7	12.76 ± 0.44	0.88 ± 0.24	14.5	27.3
SK-MEL-28	1.17 ± 0.28	0.05 ± 0.01	23.4	117.4	2,99 ± 0.23	0.14 ± 0.02	21.4	171.8
CCD-18Co	5.87 ± 0.66	0.54 ± 0.10	10.9		24.06 ± 2.92	3.39 ± 1.31	7.3	
Hemolysis <sup>c</sup>	< 5 %				< 5 %			

Cells were preincubated with the compounds for 6 h to allow the cellular uptake and then irradiated with a blue light (6.7 mW cm<sup>-2</sup>, λ<sub>ir</sub> = 450 nm) or incubated in the dark for 1 h. IC<sub>50</sub> values were determined 48 h later by an MTT assay. Data represents the mean ± SD of at least two independent experiments, each performed in triplicate. <sup>a</sup> PI: phototoxicity index = IC<sub>50,dark</sub>/IC<sub>50,light</sub>. <sup>b</sup> SPI: Selective Phototoxicity Index = IC<sub>50,dark</sub> CCD-18Co / IC<sub>50,light</sub> cancer cells. <sup>c</sup> Percentage of hemolysis at the IC<sub>50,dark</sub>.

## 2.10. Clonogenic assays

The long-term effectiveness of [1a]Cl and [3a]Cl was determined by measuring their capacity to inhibit the ability of single cells to survive and reproduce to form colonies. Cisplatin was used as positive control. PC-3 cells were incubated for 6 h with the complexes at their corresponding IC<sub>50,light</sub> and then kept in the dark or photoactivated for 1 h. Cells were immediately plated at low density and allowed to grow and form colonies for 10 days. Then, the colony number in each plate was determined. As shown in Fig. 9, a significant reduction of the number of colonies was observed in cells exposed to photoactivated [1a]Cl and [3a]Cl compared to control cells (90.0 ± 1.31 % and 98.8 ± 0.20 % of inhibition, respectively). These values are similar to those observed for cisplatin (89.8 ± 3.7 %). In contrast, the clonogenicity of the cells was only inhibited by 18.2 ± 3.8 % and by 21.4 ± 4.8 % when the treatments with [1a]Cl and [3a]Cl, respectively, were performed in the dark. These results point out that the photodynamic activity of these complexes can greatly reduce the number of cells with tumorigenic capacity.

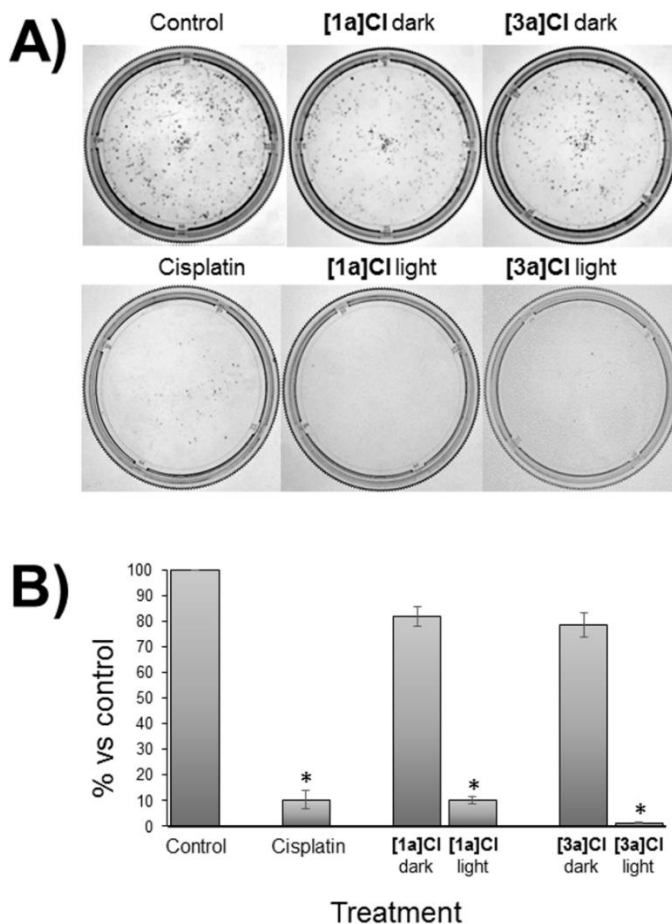


Fig. 9. Clonogenic assay. **(A)** Colony formation of PC-3 cells after exposure to [1a]Cl or [3a]Cl at the  $IC_{50,light}$  in the dark or under photoactivation. Control cells were treated with medium alone. Cisplatin was used as a positive control. **(B)** Bar charts represent the percentage of colonies relative to control untreated cells after each treatment (mean  $\pm$  SD of 3 experiments. \* $p < 0.05$  versus control cells).

### 2.11. Internalization Mechanism and Intracellular Localization

To know the cellular uptake mechanism of a potential drug is important for its potential therapeutic or diagnostic applications. It may require energy, as for endocytosis and active transport mediated by proteins, or be energy-independent, as happens in passive diffusion through the membrane or diffusion facilitated by channels and carriers. For instance, different reports have shown that Ir(III) complexes can be internalized into the cells by energy independent pathways,<sup>68</sup> non-endocytotic energy dependent pathways,<sup>69</sup> or endocytosis.<sup>70</sup>

To establish the internalization mechanism of [1a]Cl and [3a]Cl, PC-3 cells were incubated with the compounds at 5  $\mu$ M for 1 h: i) at 37 °C, to allow any possible cellular uptake mechanism; ii) at 4 °C, to inhibit processes that require metabolic energy, and

iii) at 37 °C after pre-incubation with dynasore, an specific inhibitor of endocytosis. After 1 h of incubation at 37 °C, Mean Fluorescence Intensity (MFI; the shift in fluorescence intensity of a population of cells) levels significantly increased (from  $8511 \pm 706$  in control cells to  $20425 \pm 2525$  in cells exposed to **[1a]Cl** and to  $13330 \pm 34$  in cells incubated with **[3a]Cl**), demonstrating an efficient cellular uptake of the compounds. However, these fluorescence levels were reduced by 87.3 % and 92.2 % respectively when cells were incubated at 4 °C (Fig. 10), indicating that the compounds are mainly internalized through an energy-dependent mechanism. In addition, pre-treatment with dynasore, almost completely abolished the internalization of both compounds. Dynasore is a cell-permeable molecule that inhibits activity of dynamin, a protein involved in vesicle scission from plasma membrane during endocytosis.<sup>71</sup> Thus, it can be concluded that **[1a]Cl** and **[3a]Cl** enter into the cells principally by endocytosis. Moreover, the experiments were performed in serum free culture medium and therefore, the endocytosis of the compounds is not assisted by serum lipids or proteins.

The intracellular localization of a PS is an important factor for the outcome of PDT since ROS have a short half-life and act close to their site of generation.<sup>72</sup> Therefore, the cellular damage induced by the compounds is highly dependent on their localization inside the cells. To obtain more insight into the subcellular localization of **[1a]Cl** and **[3a]Cl** confocal microscopy experiments were performed after exposing SK-MEL-28 cells to the compounds for 1 h. Colocalization studies with mitochondria were conducted by co-staining the cells with the red-fluorescent dye MitoTracker™ Red CMXRos.

As shown in Fig. 11(A), a punctuated green fluorescent staining was observed in cells exposed to **[1a]Cl** and **[3a]Cl**, indicating the accumulation of the compounds throughout the cytoplasm of the cells. In contrast, no fluorescence particles were detected inside the cell nucleus. Merged images of **[1a]Cl** or **[3a]Cl** and MitoTracker™ Red revealed a high degree of colocalization, which can be seen in yellow, with Pearson correlation coefficients of 0.908 and 0.809, respectively. The Mander's overlap coefficient between **[1a]Cl** and MitoTracker™ Red was 0.861 indicating that a high fraction of the complex colocalize with mitochondria. However, a lower Mander's coefficient was obtained for **[3a]Cl** (M: 0.55) revealing a lower degree of colocalization. In Fig. 11(B), a higher magnification image of **[3a]Cl** confirms that although the green particles are mainly located in the mitochondria, the complex is also detected in other subcellular locations, which point out that it can accumulate in other organelles, such as lysosomes or endoplasmic reticulum (ER) as described for other iridium complexes.<sup>7</sup>

Overall, these results showed that **[1a]Cl** and **[3a]Cl** mainly accumulate into the mitochondria in agreement with previous reports describing that positively charged cyclometalated Ir(III) complexes with moderate lipophilic character tend to accumulate

within these organelles, even in the absence of specific targeting groups. This fact seems to be favoured by the negative potential of mitochondrial membranes.<sup>26,73,74,75</sup> Thus, these PS show excellent properties for their potential application as probes in bioimaging of mitochondria, in particular **[1a]Cl**, provided that they are used at concentrations lower than its IC<sub>50</sub>.

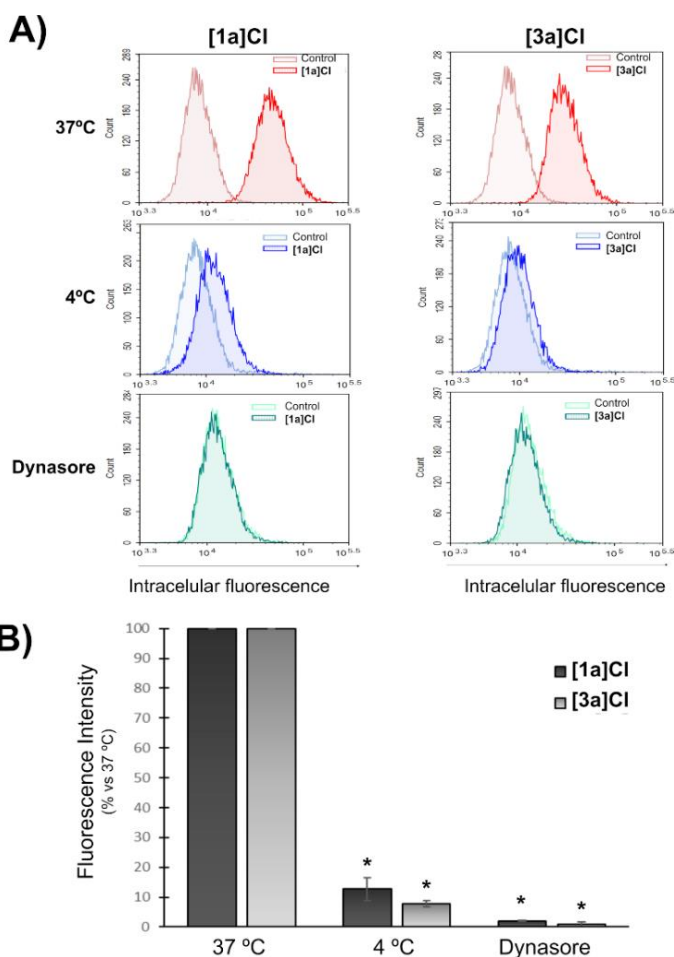


Fig. 10. Cellular uptake mechanism study for **[1a]Cl** and **[3a]Cl**. PC-3 cells were incubated with the compounds at 5  $\mu$ M or medium alone as a control for 1 h under different conditions: at 37 °C, at 4 °C (metabolic inhibition), and at 37 °C after dynasore pre-incubation (endocytosis inhibition). MFI of the cells, corresponding to the intracellular uptake of the complexes, was determined by flow cytometry. **(A)** Representative flow cytometry histograms obtained for control cells and for cells incubated with **[1a]Cl** and **[3a]Cl** **(B)** Percentage of intracellular fluorescence at the different conditions in comparison to cells incubated at 37 °C. Each bar represents the mean fluorescence intensity of at least two independent experiments  $\pm$  SD. \* $p$  < 0.05 vs cells treated at 37 °C.

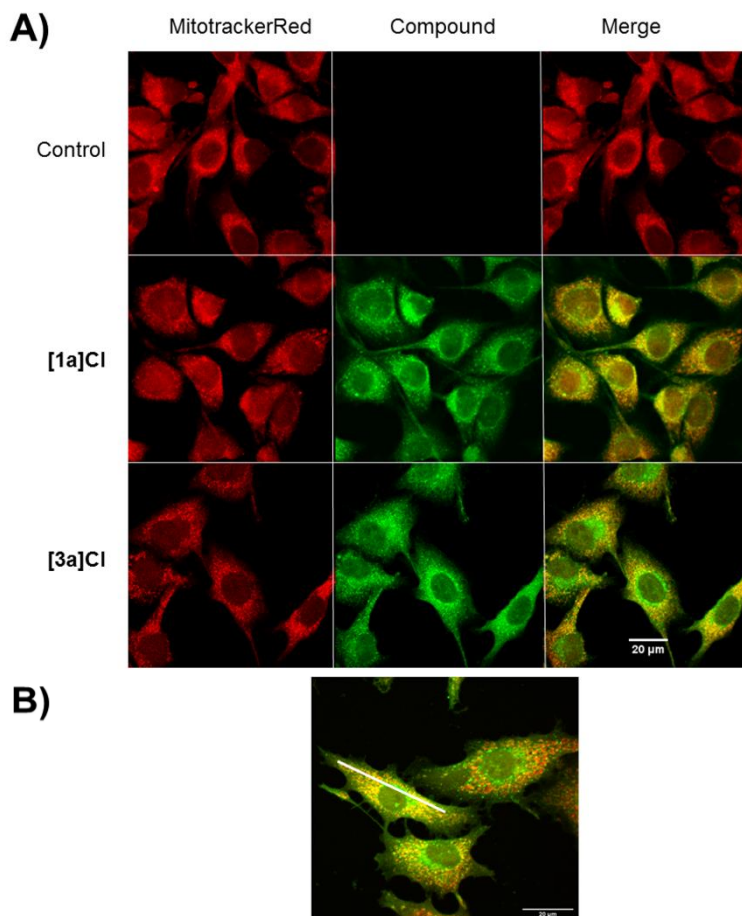


Fig. 11. Confocal microscopic imaging of the subcellular localization of **[1a]Cl** and **[3a]Cl**. SK-MEL-28 cells were incubated with the compounds at 25  $\mu\text{M}$  or with medium alone (control) for 1 h at 37  $^{\circ}\text{C}$ . Mitochondria were stained with MitoTrackerRed<sup>TM</sup>. **(A)** The localization of the compounds is indicated by the green fluorescence (excitation wavelength: 400 nm; emission wavelength: 525 nm). Mitochondria staining is shown by the red fluorescence (excitation wavelength: 543 nm; emission wavelength: 595 nm). Colocalization can be observed in yellow in the merged images. **(B)** High magnification image showing **[3a]Cl** and MitoTrackerRed co-staining.

## 2.12. Superoxide Production

The radical anion superoxide is considered the most important ROS in cells.<sup>76</sup> We analysed the ability of these complexes to generate this radical at the cellular level using a specific fluorescent probe. PC-3 cells were incubated with **[1a]Cl** and **[3a]Cl** for 6 h at the corresponding  $\text{IC}_{50,\text{light}}$  and then kept in the dark or photoactivated. The formation of superoxide radicals was immediately measured by flow cytometry (Fig. 12). The MFI of the cells increased by  $1.46 \pm 0.61$ -fold and by  $1.42 \pm 0.54$ -fold compared to control cells when exposed to photoactivated **[1a]Cl** and **[3a]Cl** respectively, revealing an increase of the intracellular superoxide levels. In contrast, the MFI of the



cells was not altered when treated with the complexes in the dark. Overall, these results confirm that the photodynamic activity of the complexes generates ROS at cellular level, which is in agreement with the photochemical mechanism proposed above.

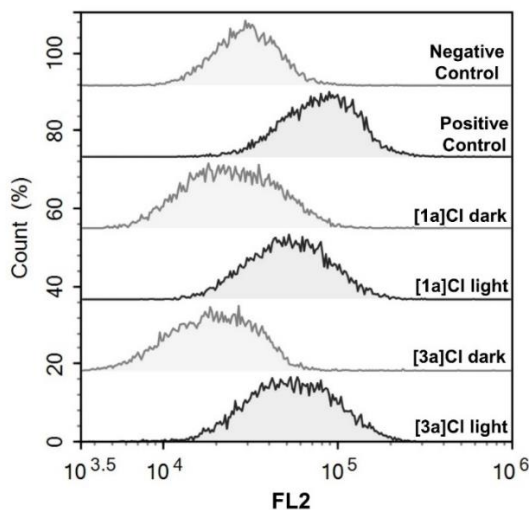


Fig. 12. Superoxide generation by **[1a]Cl** and **[3a]Cl** in PC-3 cells. Cells were incubated with the complexes at the  $IC_{50,light}$  for 6 h and then kept in the dark or photoactivated for 1 h. Pyocyanin was used as ROS inducer (positive control). Non-treated cells were used as negative control. Superoxide generation was monitored with a commercial fluorescent probe. Representative flow cytometry histograms show the MFI of 10000 cells in the FL2 channel.

### 2.13. Mitochondrial damage

Mitochondrial membrane potential (MMP) is an indicator of mitochondria activity and is essential for ATP production, cellular metabolism, cell signalling and redox balance.<sup>77</sup> In order to assess whether the photodynamic activity of **[1a]Cl** and **[3a]Cl** interferes with the MMP, as reported for other Ir complexes,<sup>78,79</sup> mitochondrial membrane depolarization was monitored by the JC-1 dye. In healthy cells, JC-1 exhibits an MMP-dependent accumulation in the mitochondria as aggregates that display a red fluorescence. However, when the mitochondrial membrane is depolarized, JC-1 remains in the cytosol as a monomer that emits green fluorescence. The ratio of this green/red fluorescence depends only on the MMP, as no fluorescence emission was detected in cells incubated with the complexes at the  $IC_{50,light}$  without the JC-1 (SI Fig. 47). In control cells, a red emission from JC-1 aggregates was detected together with a green fluorescence corresponding to JC-1 monomers (Fig. 13). A similar fluorescence pattern was observed in PC-3 cells exposed to **[1a]Cl** and **[3a]Cl** in the dark, indicating that the MMP was preserved. However, the emission of JC-1 shifted from red to green upon irradiation of **[1a]Cl** and **[3a]Cl** revealing the depolarization of the mitochondrial membrane in more than 90 % of the cells. Similar results were obtained after the

treatment of the cells with CCCP, a classical mitochondrial uncoupler that increases the proton permeability across the mitochondrial inner membrane, dissipating the transmembrane potential. These results reveal that the photodynamic activity of both [1a]Cl and [3a]Cl causes a mitochondrial dysfunction that can lead to cell death.

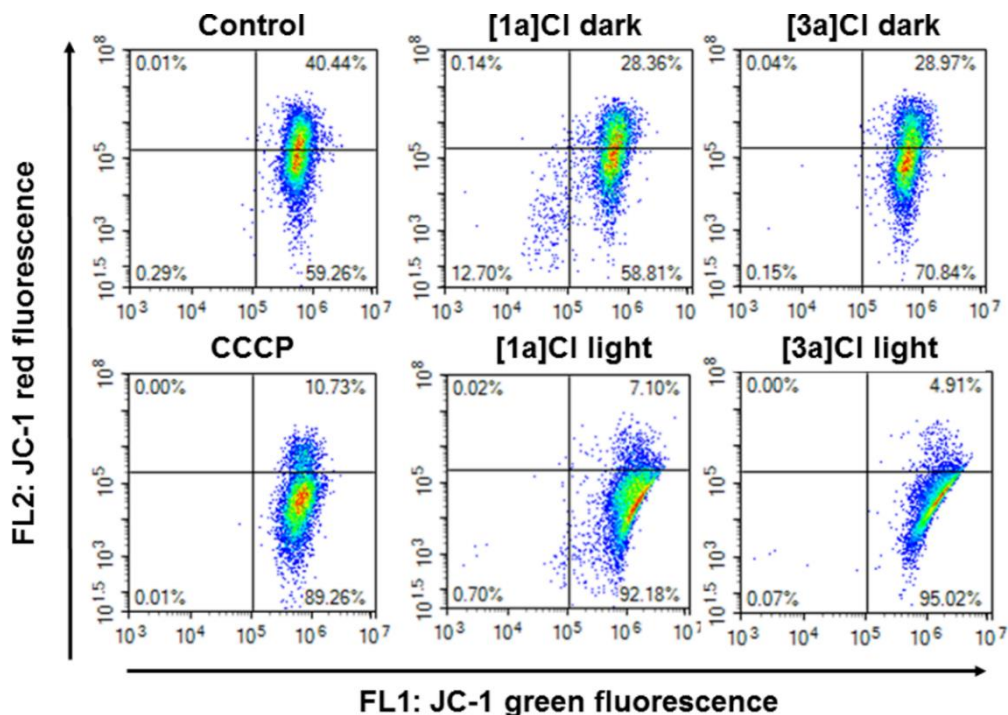


Fig. 13. Flow cytometry analysis of the mitochondrial membrane potential (MMP) after treatment with [1a]Cl and [3a]Cl using the JC-1 dye. PC-3 cells were incubated with medium alone as a control or with the compounds at the corresponding  $IC_{50,light}$  either in the dark or with light irradiation. CCCP, a mitochondrial uncoupler, was used as a positive control drug to induce a membrane depolarization. Plots represent fluorescence intensities of green JC-1 monomers (FL1) and red JC-1 aggregates (FL2) in the cells. The % population of positive cells is given in the respective quadrants. Reduced red fluorescence indicates decreased MMP.

#### 2.14. Photocatalytic Oxidation of NADH

NAD is a coenzyme that exists in both the oxidized ( $NAD^+$ ) and the reduced (NADH) forms and is involved in diverse biochemical redox processes. For instance, in the mitochondrial electron transport chain, complex I (NADH dehydrogenase) oxidizes NADH to  $NAD^+$  and the electrons are transported through a series of proteins and electron carriers to  $O_2$  in a process that concurrently pumps protons across the mitochondrial inner membrane. This process generates a proton gradient between the matrix and the intermembrane space, which is mainly responsible for the MMP and drives the ATP synthesis in eukaryotic cells (oxidative phosphorylation).<sup>80</sup> Thus, the alteration of the mitochondrial NADH/ $NAD^+$  ratio may disrupt the electron transport

chain and trigger cell death.<sup>81</sup> In two recent reports, the groups of Huang<sup>17</sup> and Sadler<sup>81</sup> have proved the activity of Ir(III) complexes on the photooxidation of NADH.

Thus, we studied the photocatalytic oxidation of NADH (100  $\mu\text{M}$ ) in MeOH/H<sub>2</sub>O (1:1, v/v, 2500  $\mu\text{L}$ ) in the presence of **[1a]Cl** (5  $\mu\text{M}$ ) under air and blue light exposure ( $\lambda_{\text{ir}} = 460 \text{ nm}$ ), by monitoring the evolution of the respective UV-Vis spectrum at room temperature during 24 h (Fig. 14). No symptoms of reaction were observed during the first 30 min. However, after 24 h the band centred at 339 nm (maximum of NADH) underwent a remarkable decrease, while the band at 259 nm (maximum of NAD<sup>+</sup>) experienced an increase, in agreement with the oxidation of NADH. The TON and TOF values were 6.23 and 0.26 h<sup>-1</sup>. The photocatalytic nature of this process was verified by mean of control experiments. Indeed, no oxidation was observed either in the absence of PS or in the dark after 24 h (SI Fig. 45 and 46). As a result, we concluded that the photocatalytic activity of **[1a]Cl** on the oxidation of NADH could contribute to the aforementioned mitochondrial membrane depolarization. Therefore, we postulate that NADH might be one of the molecular targets for **[1a]Cl** in mitochondria and that the impairment of the redox homeostasis stemming from the oxidation of NADH could trigger apoptosis.

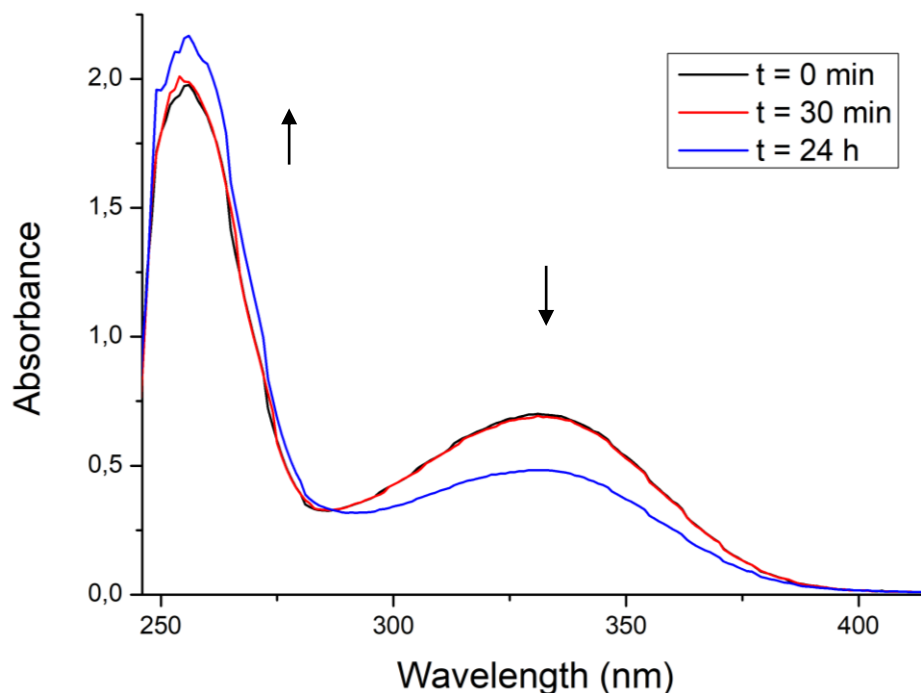


Fig. 14. Evolution of the UV-Vis spectrum of NADH (100  $\mu\text{M}$ ) in MeOH/H<sub>2</sub>O (1:1, v/v, 2.5 mL) in the presence of **[1a]Cl** (5  $\mu\text{M}$ ) under air and blue light exposure ( $\lambda_{\text{ir}} = 460 \text{ nm}$ ) at R.T. during 24 h.

### 2.15. Reaction with DNA

Cytotoxicity of traditional metal-based anticancer drugs is often associated with genomic DNA damage and cell cycle perturbation. However, mitochondria have been found to be the major target of **[1a]Cl** and **[3a]Cl**. Thus, we explored whether the photodynamic activity of the complexes can affect mtDNA. In fact, circular mtDNA has been shown to be more susceptible to ROS damage than nuclear DNA.<sup>82</sup>

The ability of **[1a]Cl** and **[3a]Cl** to interfere with DNA was first explored by electrophoretic mobility assays, which analyse the mobility shift of circular plasmid DNA due to an alteration of its conformation.<sup>83</sup> The plasmid used (pUC18) naturally has a supercoiled conformation (SC) with a high electrophoretic mobility. Under the action of damaging agents, such as ROS, the plasmid can suffer a single strand break that generates an open circular conformation (OC) with reduced electrophoretic mobility, or a double strand break that leads to a linear form with an intermediate mobility. When the damage is severe, the DNA can be greatly fractionated, and fractions are eluted from the gel undetected.

The activity of **[1a]Cl** and **[3a]Cl** on DNA cleavage was assayed in the dark and under irradiation at concentrations ranging from 0 to 100  $\mu\text{M}$ , based on a previous study.<sup>84</sup> A treatment with 1.75 %  $\text{H}_2\text{O}_2$  and 20  $\mu\text{M}$   $\text{FeCl}_2$  was used as positive control of ROS generation and nuclease activity. As shown in Fig. 15(A), neither of the compounds altered the electrophoretic mobility of the plasmid at 10  $\mu\text{M}$ . At 25  $\mu\text{M}$  and 50  $\mu\text{M}$  of either **[1a]Cl** or **[3a]Cl**, the ratio between the OC and SC forms of the plasmid was slightly higher in the irradiated samples than in samples incubated in the absence of light. Moreover, the total amount of DNA decreased at treatments from and above 50  $\mu\text{M}$ , being completely degraded at 75  $\mu\text{M}$  under irradiation and at 100  $\mu\text{M}$  in the dark, indicating a strong nuclease activity under these conditions.

In order to analyse whether ROS are involved in the nuclease activity of the complexes, treatments at 70  $\mu\text{M}$  were performed in the presence of ROS scavengers (sodium azide as a scavenger of singlet oxygen, DMSO as a scavenger of hydroxyl radical, and Tiron as a scavenger of the superoxide radical anion).<sup>85</sup> As shown in Fig. 15(B), DNA degradation caused by **[1a]Cl** was completely reverted by sodium azide and DMSO, and almost completely reverted by tiron both in the dark and under irradiation. The damage caused by **[3a]Cl** was completely reverted by the three ROS scavengers in both conditions, although DMSO was slightly less efficient in the dark. Overall, the oxidative activity of the compounds under irradiation appears to be modestly higher since some OC conformations are present, indicating that scavengers could not completely reverse the effect of the ROS. Overall, these results point out to an oxidative damage mechanism for Ir(III) complexes involving different ROS that could affect mtDNA among other target molecules in the mitochondria.

The interaction of the complexes with mtDNA was further evaluated at the cellular level. In particular, the impact of **[1a]Cl** and **[3a]Cl** on the transcription levels of genes *ND3* and *COX1*, which are located in the mitochondrial genome, was quantitatively assessed by RT-qPCR. *ND3* encodes the NADH dehydrogenase subunit 3 of the respiratory chain complex I and *COX1* (or *CO1*) encodes the cytochrome c oxidase subunit I of the complex IV. Changes in the expression of these genes were normalized using the housekeeping gene  $\beta$ -actin (*ACTB*) as a reference. The quantification cycle (Cq) values for *ACTB* in control cells ( $18.98 \pm 0.49$ ) and cells treated with **[1a]Cl** ( $18.64 \pm 0.81$ ) or **[3a]Cl** ( $18.80 \pm 0.33$ ) showed no statistical differences. As shown in Fig. 16, PC-3 cells exposed to **[1a]Cl** or **[3a]Cl** with photoactivation showed a significant reduction in the expression of both mitochondrial genes in comparison to control cells, which is a consequence of mtDNA damage. In particular, the expression of *ND3* was reduced by  $31 \pm 6\%$  and  $35 \pm 3\%$  after **[1a]Cl** and **[3a]Cl** treatments, respectively, while the expression of *COX1* was reduced by  $44 \pm 4\%$  in cells exposed to **[1a]Cl**, reaching a  $72 \pm 2\%$  reduction in cells exposed to **[3a]Cl**.

Thus, these results confirm that **[1a]Cl** and **[3a]Cl** can damage mtDNA at cellular level and hence affect mitochondrial functions.<sup>86</sup>

We also observed that photoactivated **[1a]Cl** and **[3a]Cl** induced a minimal effect on cell cycle progression, as assessed by propidium iodide staining and flow cytometry analysis after 24 h of treatment (SI Fig. 48). In contrast, cisplatin, whose mode of action is mediated by the interaction with nuclear DNA, generated a marked cell cycle arrest at the S and G2/M phases.<sup>87,88</sup> These results support that the nuclease activity of the complexes is most likely restricted to mtDNA, in agreement with their subcellular distribution.

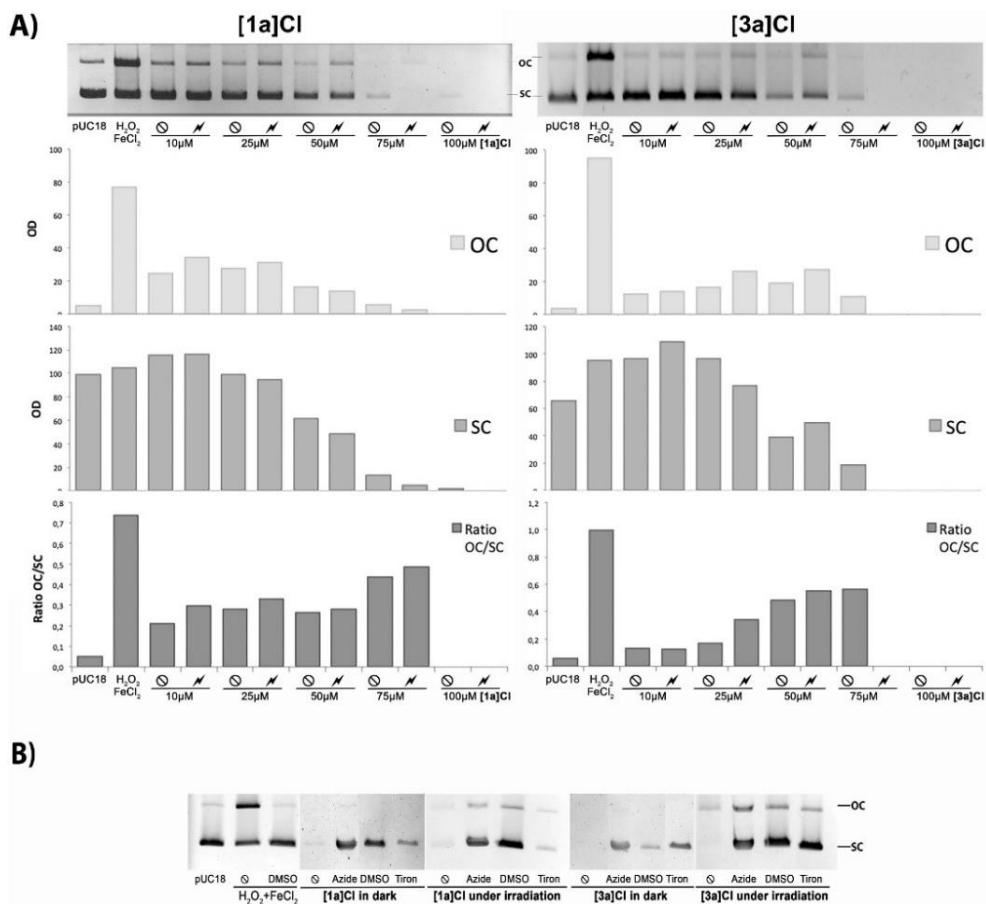


Fig. 15. Electrophoretic mobility assay. The specific treatments are indicated under each lane. pUC18 lane shows the electrophoretic pattern of the untreated plasmid. **(A)** Effect of irradiation on the activity on DNA of **[1a]Cl** and **[3a]Cl**. ⊙ states for the incubation in dark conditions and ☞ states for the incubation under irradiation. Graphs represent the densitometric analysis of the bands corresponding to the (open circular conformation (OC) and supercoiled conformation (SC) of the plasmid and the ratio between both conformations. **(B)** Analysis of ROS involved in the mechanism of action of compounds **[1a]Cl** and **[3a]Cl**, at 70 μM, incubated in the dark or after 1 h of irradiation. ⊙ indicates that no scavenger was used in that specific treatment. (SC): supercoiled plasmid conformation. (OC): open circular conformation.

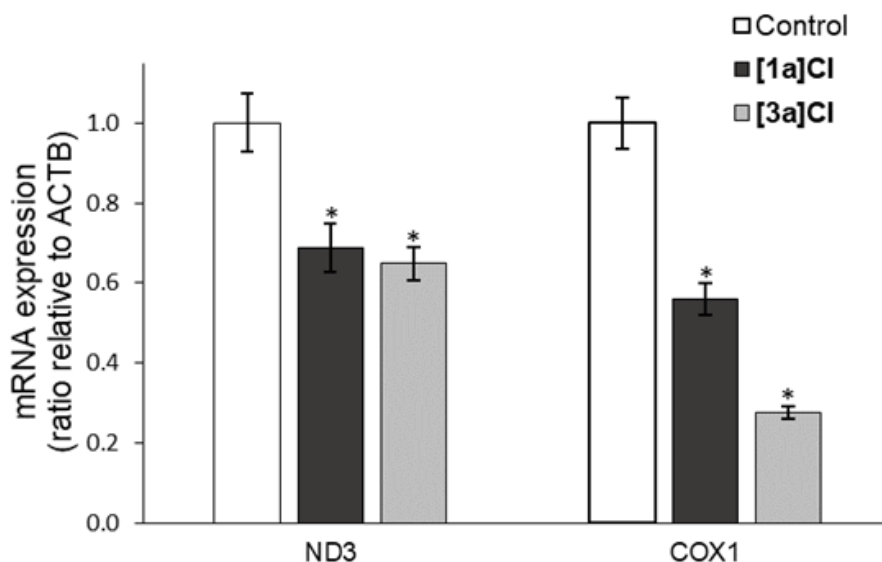


Fig. 16. Relative gene expression of the mitochondrial genes ND3 and COX1 in control untreated cells PC-3 and cells incubated with [1a]CI or [3a]CI at the corresponding  $IC_{50,light}$  under photoactivated conditions.  $\beta$ -actin (ACTB) was used as a reference gene. Four RT-qPCR analysis were conducted in two independent biological replicates. Error bars represent standard deviations for the eight assays. \* $p < 0.05$  vs control cells.

## 2.16. Cell Death Mechanism

Finally, we studied the cell death mechanism induced by photoactivated [1a]CI and [3a]CI by flow cytometry using the annexin V/propidium iodide dual staining protocol. Annexin V identifies apoptotic cells by its ability to bind to phosphatidylserine, a marker of apoptosis when it is on the outer side of the plasma membrane. Propidium iodide labels cellular DNA in necrotic cells or late apoptotic cells when the integrity of the membranes has been lost. After 24 h of treatment with photoactivated [1a]CI and [3a]CI at their respective  $IC_{50,light}$ , 26.9 % and 22.6 % of the cells were positive for both annexin V and propidium iodide staining, whereas only 3.96 % of control cells and 12.11 % of cells exposed to cisplatin showed a dual staining (Fig. 17). Double stained cells are frequently considered in late apoptosis, but necrosis is also possible. Since [1a]CI and [3a]CI generate mitochondrial membrane depolarization, they can induce an apoptotic response by leakage of cytochrome c into the cytosol in response to the depolarization, with the subsequent caspase activation.<sup>72</sup> However, increasing oxidative damage may finally lead to the plasma membrane permeabilization and a secondary necrosis.<sup>89</sup> Thus, the complexes could induce a dual cell apoptotic/necrotic death response upon light irradiation.

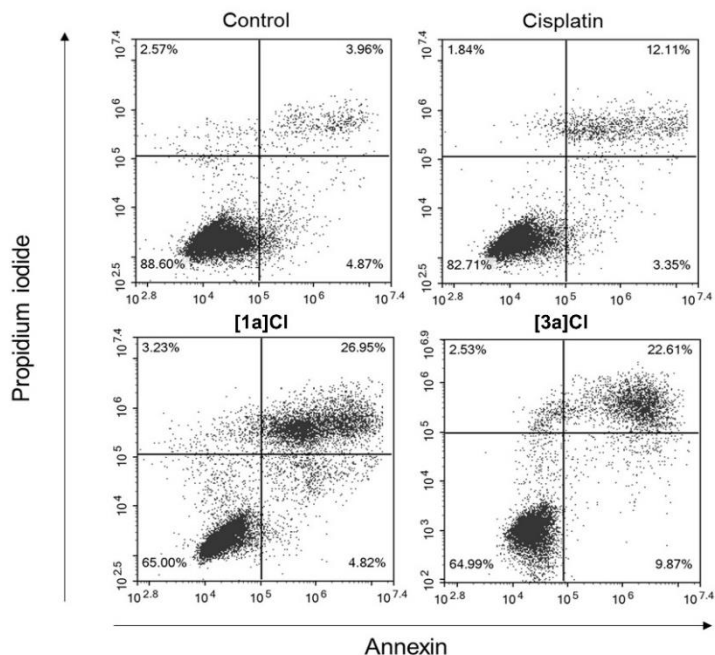


Fig. 17. Cell death mechanism. PC-3 cells were treated with medium alone as a control, cisplatin at 25  $\mu\text{M}$  or with **[1a]Cl** and **[3a]Cl** at the  $\text{IC}_{50,\text{light}}$  and photoactivated. After 24 h, cells were double stained with propidium iodide and Annexin V-FITC and analysed by flow cytometry. The x-axis shows annexin V-FITC staining and the y-axis shows propidium iodide staining. The percentages of cells in each quadrant are indicated.

### 3. Conclusions

In conclusion, with the objective of developing new potential PDT photosensitizers, we have prepared and fully characterized two series of new Ir(III) complexes of general formula  $[\text{Ir}(\text{C}^{\wedge}\text{N})_2(\text{N}^{\wedge}\text{N}')]\text{Cl}$ , using two different  $\text{C}^{\wedge}\text{N}$  ligands (ppy and dfppy) and four different  $\text{N}^{\wedge}\text{N}'$  ligands, which share the thiabendazole scaffold but show diverse N-alkyl groups. The complexes are partially soluble in aqueous media and keep their integrity under irradiation with blue light for 6 h. Moreover, we have analysed the electrochemical and photophysical properties of the Ir(III) dyes and interpreted the observed trends with the help of theoretical calculations. More specifically, the new PSs feature suitable  $\text{S}_0 \leftarrow \text{T}_1$  energy values to generate  $^1\text{O}_2$ , as well as appropriate excited state redox potentials to produce  $\text{O}_2^{\bullet-}$ . We have also evaluated the cytotoxic activity of the new derivatives in the dark and under blue light illumination. As a result, we have established a correlation between the lack of photocytotoxicity found for derivatives of **series B** and their absorption profile, which is strongly determined by the presence of -F atoms on the  $\text{C}^{\wedge}\text{N}$  ligands. By contrast, complexes of **series A** with more suited absorption profiles in the visible region, display high PI values, as for instance,  $\text{PI} = 23.4$



for **[1a]Cl** and PI = 21.4 for **[3a]Cl** in SK-MEL-28 melanoma cells, at concentrations in the nanomolar range. Furthermore, the activity of the lead complexes **[1a]Cl** and **[3a]Cl** against non-tumoral CCD18-Co fibroblasts was moderate, disclosing a high degree of selectivity, as expressed by the Selective Photocytotoxicity Index (SPI) ( $IC_{50, \text{dark}} \text{ CCD-18Co} / IC_{50, \text{light}} \text{ cancer cells}$ ) calculated for **[1a]Cl** (SPI = 117.4) and **[3a]Cl** (SPI = 171.8) in SK-MEL-28 with regard to CCD-18Co cells.

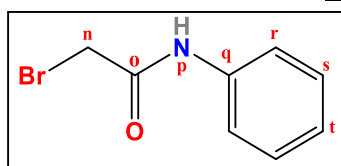
Regarding the biological mechanism of action, we have unveiled that **[1a]Cl** and **[3a]Cl** are internalized into cells by energy-dependent endocytosis and that after 6 hours of incubation they have been taken up by most of the cells. In addition, they are accumulated primarily within mitochondria. Indeed, we presume that specially **[1a]Cl** offers potential as a probe for bioimaging these organelles. More importantly, both PSs trigger a multi-target cytotoxic effect through a photocatalytic mechanism that induces the formation of ROS. We have proved that upon irradiation of both PS, the mitochondrial membrane undergoes depolarization, though the MMP is preserved in the dark. We believe that the ability of **[1a]Cl** to photo-catalyse the oxidation of NADH to  $\text{NAD}^+$  might contribute to the membrane depolarization. Moreover, **[1a]Cl** and **[3a]Cl** are able to cause severe cleavage on mtDNA, resulting in the inhibition of the expression of mitochondrial genes, so that we postulate that mtDNA is another of their cellular targets. We have revealed that **[1a]Cl** and **[3a]Cl** induce a minimal effect on cell cycle progression, in agreement with their inability to target nuclear DNA. As a result of the multimodal damage to mitochondria, we have found that **[1a]Cl** and **[3a]Cl** elicit a dual cell death response involving both apoptosis and necrosis. In addition, the long-term effect of our PSs was substantiated by performing clonogenic assays, which revealed the great capacity of the drugs to reduce the number of cells capable of reproducing and generate new colonies.

To sum up, we believe that the mitochondrial-targeted phototoxicity displayed by **[1a]Cl** and **[3a]Cl** represents a promising approach in the development of new metal-based PDT agents to treat cancers refractory to conventional chemotherapy.

## 4. Synthesis and characterization

### 4.1. Bromides

#### 2-bromo-N-phenylacetamide (Br1)

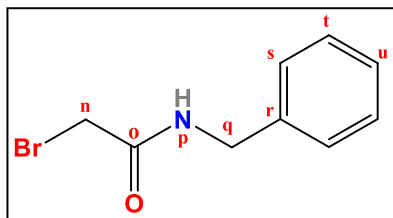


In a 100 mL Schlenk flask in an ice bath at 0 °C aniline (1.0000 g, 10.738 mmol) was added to a solution of bromoacetyl bromide (1.0836 g, 5.369 mmol) in DCM (31 mL). The mixture/suspension was stirred at room temperature for 30 minutes, and then, it is allowed to reach room temperature.

After 1 hour of stirring, a saturated solution of  $\text{NH}_4\text{Cl}$  (25 mL) is added. The mixture was

extracted with diethyl ether (2 x 20 mL). The extracted phase is dried with anhydrous Na<sub>2</sub>SO<sub>4</sub>, filtered and took to dryness. The resulting white solid was dried under vacuum. Yield: 83 % (0.9581 g, 4.476 mmol). **M<sub>r</sub>** (C<sub>8</sub>H<sub>8</sub>BrNO) = 214.06 g/mol. **Anal. Calcd for C<sub>8</sub>H<sub>8</sub>BrNO**: C 64.65; H 4.22; N 16.75 **Found**: C 64.98; H 4.47; N 16.94. **<sup>1</sup>H NMR (400 MHz, DMSO-d<sub>6</sub>, 25 °C)** δ 10.37 (s, 1H), 7.62 – 7.51 (m, 2H), 7.37 – 7.24 (m, 2H), 7.12 – 7.01 (m, 1H), 4.08 – 3.98 (m, 2H) ppm.

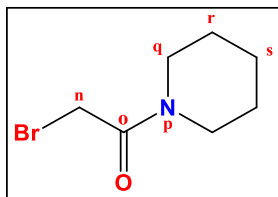
#### **N-benzyl-2-bromoacetamide (Br2)**



In a 100 mL Schlenk flask in an ice bath at 0 °C benzylamine (0.9996 g, 9.329 mmol) was added to a solution of bromoacetyl bromide (0.9430 g, 4.672 mmol) in DCM (31 mL), The mixture/suspension was stirred at room temperature for 30 minutes, and then, it is allowed to reach room temperature. After 1 hour of stirring, a saturated solution of NH<sub>4</sub>Cl (25 mL) is added. The

mixture was extracted with diethyl ether (2 x 20 mL). The extracted phase is dried with anhydrous Na<sub>2</sub>SO<sub>4</sub>, filtered and took to dryness. The resulting white solid was dried under vacuum. Yield: 87 % (0.9290 g, 4.073 mmol). **M<sub>r</sub>** (C<sub>9</sub>H<sub>10</sub>BrNO) = 228.09 g/mol. **<sup>1</sup>H NMR (400 MHz, DMSO-d<sub>6</sub>, 25 °C)** δ 8.78 (s, 1H), 7.43 – 7.20 (m, 5H), 4.30 (d, J = 5.9 Hz, 2H), 3.91 (s, 2H) ppm.

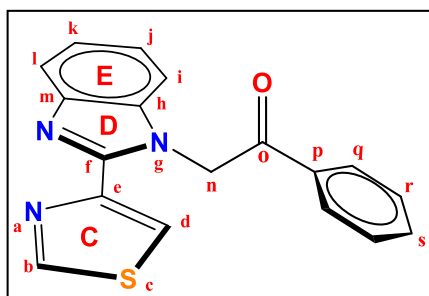
#### **2-bromo-1-(piperidin-1-yl)ethan-1-one (Br3)**



In a 100 mL Schlenk flask in an ice bath at 0 °C 1-(bromoacetyl)piperidine (1.0000 g, 11.744 mmol) was added to a solution of bromoacetyl bromide (1.1851 g, 5.871 mmol) in DCM (31 mL), The mixture/suspension was stirred at room temperature for 30 minutes, and then, it is allowed to reach room temperature.

After 1 hour of stirring, a saturated solution of NH<sub>4</sub>Cl (25 mL) is added. The mixture was extracted with diethyl ether (2 x 20 mL). The extracted phase is dried with anhydrous Na<sub>2</sub>SO<sub>4</sub>, filtered and took to dryness. The resulting white solid was dried under vacuum. Yield: 75 % (0.9089 g, 4.410 mmol). **M<sub>r</sub>** (C<sub>7</sub>H<sub>12</sub>BrNO) = 206.08 g/mol. **<sup>1</sup>H NMR (400 MHz, DMSO-d<sub>6</sub>, 25 °C)** δ 4.10 (s, 2H), 3.41 (m, 4H), 1.63 – 1.49 (m, 4H), 1.43 (p, J = 5.7 Hz, 2H) ppm.

## 4.2. Ligands

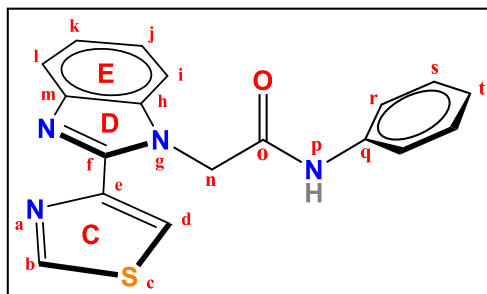


#### **L1**

In a 100 mL Schlenk flask, K<sub>2</sub>CO<sub>3</sub> (0.4107 g, 2.486 mmol) was added to a solution of 2-(4-Thiazolyl)benzimidazole (thiabenzazole, TBZ) (0.5000 g, 2.484 mmol) in DMF (12 mL). The mixture/suspension was stirred at room temperature for 30 minutes. N-benzyl-2-bromoacetophenone (0.4947 g, 2.485 mmol) was then added. The stirring was extended for 22 hours at room temperature. The solvent was removed

under vacuum and the residue was redissolved in DMSO (5 mL). Water (10 mL) was added to

precipitate a white solid that was filtrated, redissolved in ethanol (15 ml) and took to dryness (2 times) and then redissolved in toluene (15 ml) and took to dryness. The solid was redissolved in dichloromethane (15 mL) and then the solution is filtered and took to dryness. The resulting white solid was dried under vacuum. Yield: 54 % (0.4256 g, 1.333 mmol). **Mr** ( $C_{18}H_{13}N_3OS$ ) = 319.38 g/mol. **Anal. Calcd for  $C_{18}H_{13}N_3OS((CH_3)_2SO)_{0.1}$** : C 66.81; H 4.19; N 12.84; **Found**: C 66.89; H 4.30; N 13.07.  **$^1H$  NMR (400 MHz, DMSO- $d_6$ , 25 °C)**  $\delta$  9.09 (dd,  $J = 2.1, 0.6$  Hz, 1H,  $H^d$ ), 8.56 (dd,  $J = 2.1, 0.5$  Hz, 1H,  $H^b$ ), 8.14 – 8.09 (dd,  $J = 7.2, 1.2$  Hz, 2H,  $H^q, H^r$ ), 7.78 – 7.70 (m, 2H,  $H^i, H^l$ ), 7.67 – 7.60 (m, 3H,  $H^s, H^r, H^t$ ), 7.30 – 7.23 (m, 2H,  $H^k, H^j$ ), 6.43 (s, 2H,  $H^n, H^n$ ) ppm.  **$^{13}C\{^1H\}$  NMR (101 MHz, DMSO- $d_6$ , 25 °C)**  $\delta$  193.60, 155.17, 147.00, 146.76, 142.37, 136.49, 134.71, 133.86, 128.95, 128.14, 128.10, 122.72, 122.31, 121.98, 121.96, 118.93, 110.63, 51.85 ppm. **FT-IR (KBr,  $cm^{-1}$ ) selected bands**: 3039 (w,  $\nu_{Car-H}$ ), 1593-1578 (m,  $\nu_{C=C + C-N}$ ), 1424 (w,  $\nu_{C=N}$ ), 1162 (m,  $\nu_{C-C}$ ), 1078 (m,  $\delta_{C-Hip}$ ), 755-735 (vs,  $\delta_{C-Hoop}$ ). **HR ESI+ MS (DCM/DMSO, 4:1)**:  $m/z_{exp} = 320.0858$  ( $m/z_{calcd} [M+H^+] = m/z_{calcd} [C_{18}H_{14}N_3OS]^+ = 320.0858$ ). **Solubility**: soluble in dichloromethane, methanol, chloroform, dimethylformamide, dimethyl sulfoxide and acetone.

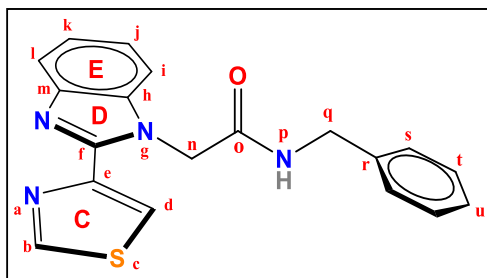


## L2

In a 100 mL Schlenk flask,  $K_2CO_3$  (0.2876 g, 1.741 mmol) was added to a solution of 2-(4-Thiazolyl)benzimidazole (thiabendazole, TBZ) (0.3502 g, 1.740 mmol) in DMF (9 mL). The mixture/suspension was stirred at room temperature for 30 minutes. 2-bromo-N-phenylacetamide (Br1) (0.4095 g, 1.913 mmol) was then added. The stirring was extended for 21 hours at room temperature. The solvent was

removed under vacuum and the residue was redissolved in dichloromethane (25 mL) and methanol (15 mL) heating at 46 °C. Then the solution is filtered and took to dryness. The resulting cream white solid was dried under vacuum. Yield: 96 % (0.5574 g, 1.667 mmol). **Mr** ( $C_{18}H_{14}N_4OS$ ) = 334.39 g/mol. **Anal. Calcd for  $C_{18}H_{14}N_4OS$** : C 64.65; H 4.22; N 16.75 **Found**: C 64.98; H 4.47; N 16.94.  **$^1H$  NMR (400 MHz, DMSO- $d_6$ , 25 °C)**  $\delta$  10.43 (s, 1H,  $H^{NH}$ ), 9.32 – 9.20 (dd,  $J = 2.1, 1.1$  Hz, 1H,  $H^d$ ), 8.55 (dd,  $J = 2.1, 1.3$  Hz, 1H,  $H^b$ ), 7.76 – 7.67 (m, 1H,  $H^i$ ), 7.66 – 7.59 (m, 1H,  $H^l$ ), 7.55 (d,  $J = 8.5$  Hz, 2H,  $H^r, H^t$ ), 7.35 – 7.16 (m, 4H,  $H^k, H^j, H^s, H^s$ ), 7.04 (t,  $J = 6.9$  Hz, 1H,  $H^l$ ), 5.70 (s, 2H,  $H^n, H^n$ ) ppm.  **$^{13}C\{^1H\}$  NMR (101 MHz, DMSO- $d_6$ , 25 °C)**  $\delta$  165.59, 155.05, 146.89, 146.69, 142.10, 138.60, 136.30, 128.59, 123.14, 122.56, 122.10, 121.97, 118.82, 118.72, 110.46, 47.72 ppm. **FT-IR (KBr,  $cm^{-1}$ ) selected bands**: 3258 (w,  $\nu_{N-H}$ ), 3070 (w,  $\nu_{Car-H}$ ), 1602-1573 (m,  $\nu_{C=C + C-N}$ ), 1421 (w,  $\nu_{C=N}$ ), 1164 (m,  $\nu_{C-C}$ ), 1073 (m,  $\delta_{C-Hip}$ ), 752-743 (vs,  $\delta_{C-Hoop}$ ). **HR ESI+ MS (DCM/DMSO, 4:1)**:  $m/z_{exp} = 335.0974$  ( $m/z_{calcd} [M+H^+] = m/z_{calcd} [C_{18}H_{15}N_4OS]^+ = 335.0961$ ). **Solubility**: soluble in dichloromethane, methanol, chloroform, dimethylformamide, dimethyl sulfoxide and acetone.

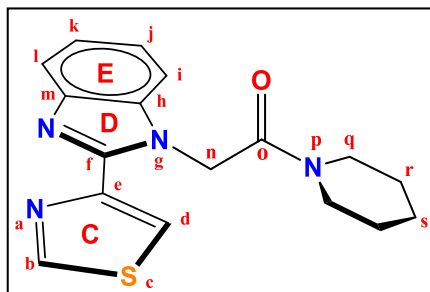
**L3**



In a 100 mL Schlenk flask,  $K_2CO_3$  (0.2879 g, 1.742 mmol) was added to a solution of 2-(4-Thiazolyl)benzimidazole (thiabenzazole, TBZ) (0.3501 g, 1.740 mmol) in DMF (5 mL). The mixture/suspension was stirred at room temperature for 30 minutes. N-benzyl-2-bromoacetamide (Br2) (0.4365 g, 1.914 mmol) was then added. The stirring was extended for 21 hours at room temperature. The solvent was

removed under vacuum and the residue was redissolved in dichloromethane (30 mL) and ethanol (10 mL) heating at 45 °C. Then the solution is filtered and took to dryness. The resulting off-white solid was dried under vacuum. Yield: 97 % (0.5851 g, 1.679 mmol). **M<sub>r</sub>** (**C<sub>19</sub>H<sub>16</sub>N<sub>4</sub>OS**) = 348.42 g/mol. **Anal. Calcd for C<sub>19</sub>H<sub>16</sub>N<sub>4</sub>OS**: C 65.50; H 4.63; N 16.08 **Found**: C 65.56; H 4.94; N 16.20. **<sup>1</sup>H NMR (400 MHz, DMSO-d<sub>6</sub>, 25 °C)** δ 9.29 (dd, J = 2.1, 0.6 Hz, 1H, H<sup>d</sup>), 8.72 (t, J = 5.9 Hz, 1H, H<sup>NH</sup>), 8.54 – 8.51 (dd, J = 2.1, 0.9 Hz, 1H, H<sup>b</sup>), 7.72 – 7.67 (m, 1H, H<sup>i</sup>), 7.59 – 7.55 (m, 1H, H<sup>l</sup>), 7.34 – 7.19 (m, 7H, H<sup>t</sup>, H<sup>s</sup>, H<sup>5</sup>, H<sup>5</sup>, H<sup>k</sup>, H<sup>j</sup>, H<sup>u</sup>), 5.55 (s, 2H, H<sup>n</sup>, H<sup>n</sup>), 4.28 (d, J = 6.0 Hz, 2H, H<sup>q</sup>, H<sup>q</sup>) ppm. **<sup>13</sup>C{<sup>1</sup>H} NMR (101 MHz, DMSO-d<sub>6</sub>, 25 °C)** δ 167.10, 155.16, 147.11, 146.94, 142.36, 139.16, 136.44, 128.21, 126.97, 126.72, 122.70, 122.27, 122.21, 118.93, 110.59, 47.40, 42.12 ppm. **FT-IR (KBr, cm<sup>-1</sup>) selected bands**: 3234 (w, ν<sub>N-H</sub>), 3065 (w, ν<sub>Car-H</sub>), 1620-1573 (m, ν<sub>C=C + C-N</sub>), 1421 (w, ν<sub>C=N</sub>), 1160 (m, ν<sub>C-C</sub>), 1092 (m, δ<sub>C-Hip</sub>), 743 (vs, δ<sub>C-Hoop</sub>). **HR ESI+ MS (DCM/DMSO, 4:1)**: m/z<sub>exp</sub> = 349.1132 (m/z<sub>calcd</sub> [M+H<sup>+</sup>] = m/z<sub>calcd</sub> [C<sub>19</sub>H<sub>17</sub>N<sub>4</sub>OS]<sup>+</sup> = 349.1117). **Solubility**: soluble in dichloromethane, methanol, chloroform, dimethylformamide, dimethyl sulfoxide and acetone.

**L4**



In a 100 mL Schlenk flask,  $K_2CO_3$  (0.2878 g, 1.742 mmol) was added to a solution of 2-(4-Thiazolyl)benzimidazole (thiabenzazole, TBZ) (0.3502 g, 1.740 mmol) in DMF (10 mL). The mixture/suspension was stirred at room temperature for 30 minutes. 2-bromo-1-(piperidin-1-yl)ethan-1-one (Br3) (0.3960 g, 1.922 mmol) was then added. The stirring was extended for 22 hours at room temperature. The solvent was removed

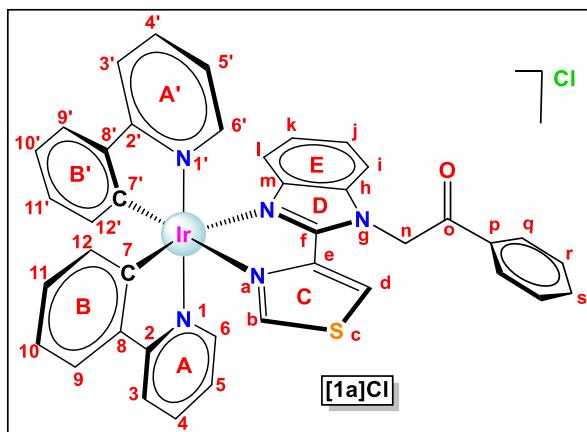
under vacuum and the residue was redissolved in dichloromethane (15 mL) and ethanol (5 mL). Then the solution is filtered and took to dryness. The resulting off-white solid was dried under vacuum. Yield: 97 % (0.5498 g, 1.684 mmol). **M<sub>r</sub>** (**C<sub>17</sub>H<sub>18</sub>N<sub>4</sub>OS**) = 326.42 g/mol. **Anal. Calcd for C<sub>17</sub>H<sub>18</sub>N<sub>4</sub>OS**: C 62.55; H 5.56; N 17.16; **Found**: C 62.55; H 5.74; N 17.20. **<sup>1</sup>H NMR (400 MHz, DMSO-d<sub>6</sub>, 25 °C)** δ 9.28 (d, J = 2.1 Hz, 1H, H<sup>d</sup>), 8.51 (d, J = 2.1 Hz, 1H, H<sup>b</sup>), 7.68 (m, 1H, H<sup>i</sup>), 7.59 – 7.50 (m, 1H, H<sup>l</sup>), 7.31 – 7.19 (m, 2H, H<sup>k</sup>, H<sup>l</sup>), 5.72 (s, 2H, H<sup>n</sup>, H<sup>n</sup>), 3.58 (s, 2H, H<sup>q</sup>, H<sup>q</sup>), 3.38 (s, 2H, H<sup>q</sup>, H<sup>q</sup>), 1.68 (s, 4H, H<sup>s</sup>, H<sup>s</sup>, H<sup>r</sup>, H<sup>r</sup>), 1.41 (s, 2H, H<sup>r</sup>, H<sup>r</sup>) ppm. **<sup>13</sup>C{<sup>1</sup>H} NMR (101 MHz, DMSO-d<sub>6</sub>, 25 °C)** δ 164.97, 154.93, 147.31, 147.00, 142.28, 136.61, 122.48, 122.05, 121.82, 118.81, 110.59, 46.35, 45.46, 42.73, 25.92, 25.32, 24.08 ppm. **FT-IR (KBr, cm<sup>-1</sup>) selected bands**: 3049 (w, ν<sub>Car-H</sub>), 1613-1573 (m, ν<sub>C=C + C-N</sub>), 1422 (w, ν<sub>C=N</sub>), 1166 (m, ν<sub>C-C</sub>), 1072 (m, δ<sub>C-Hip</sub>), 759 (vs, δ<sub>C-Hoop</sub>). **HR ESI+**

**MS (DCM/DMSO, 4:1):**  $m/z_{\text{exp}} = 327.1286$  ( $m/z_{\text{calcd}} [M+H^+] = m/z_{\text{calcd}} [C_{17}H_{19}N_4OS]^+ = 327.1274$ ).

**Solubility:** soluble in dichloromethane, methanol, chloroform, dimethylformamide, dimethyl sulfoxide and acetone.

### 4.3. Ir(III)-complexes

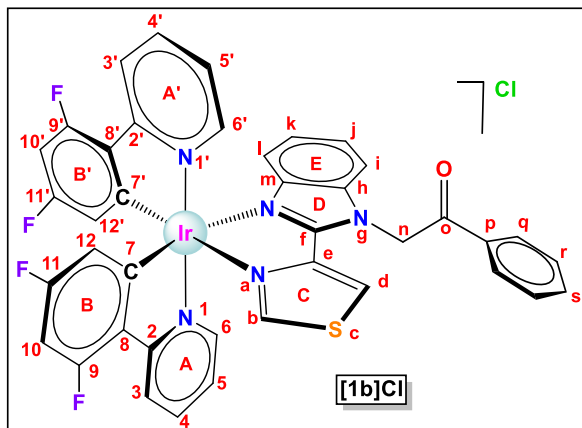
#### **[Ir(ppy)<sub>2</sub>(L1)]Cl: [1a]Cl**



In a 100 mL Schlenk flask, previously purged with nitrogen, the ancillary ligand L<sup>1</sup> (0.0627 g, 0.196 mmol) was added to a solution of [Ir(μ-Cl)(ppy)<sub>2</sub>]<sub>2</sub> (0.1002 g, 0.094 mmol) in a mixture of dichloromethane (8 mL) / methanol (10 mL), and the mixture was stirred at 60 °C for 24 hours under a N<sub>2</sub> atmosphere. The resulting solution was concentrated to half the volume under vacuum and diethyl ether (15 mL) was added to precipitate a crude solid that was isolated by filtration

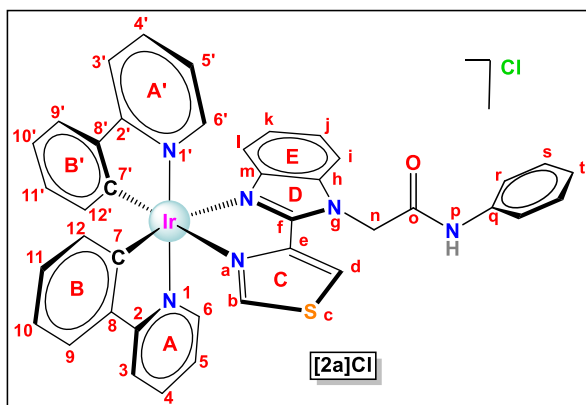
and washed with diethyl ether (2×5 mL). The solid is redissolved in dichloromethane (3 mL) and the solution is filtered, took to dryness under vacuum, washed with diethyl ether (5 mL). The product was dried under vacuum to produce a yellow powder. Yield: 35 % (0.0553 g, 0.065 mmol). **M<sub>r</sub>** (C<sub>40</sub>H<sub>29</sub>ClIrN<sub>5</sub>OS) = 855.43 g/mol. **Anal. Calcd for C<sub>40</sub>H<sub>29</sub>ClIrN<sub>5</sub>OS(CH<sub>2</sub>Cl<sub>2</sub>)<sub>0.75</sub>:** C 53.25; H 3.34; N 7.62; **Found:** C 53.28; H 3.36; N 7.80. **<sup>1</sup>H NMR (400 MHz, DMSO-d<sub>6</sub>, 25 °C)** δ 8.83 (s, 1H, H<sup>d</sup>), 8.51 (s, 1H, H<sup>b</sup>), 8.29 (d, J = 8.3 Hz, 1H, H<sup>3</sup>), 8.26 – 8.18 (m, 3H, H<sup>3'</sup>, H<sup>q</sup>, H<sup>q</sup>), 7.98 – 7.89 (m, 5H, H<sup>4</sup>, H<sup>4'</sup>, H<sup>9</sup>, H<sup>i</sup>, H<sup>9</sup>), 7.84 – 7.78 (m, 2H, H<sup>5</sup>, H<sup>6</sup>), 7.74 (d, J = 5.5 Hz, 1H, H<sup>6</sup>), 7.68 (t, J = 7.6 Hz, 2H, H<sup>r</sup>, H<sup>r</sup>), 7.34 (t, J = 7.8 Hz, 1H, H<sup>j</sup>), 7.25 (t, J = 6.6 Hz, 1H, H<sup>5</sup>), 7.23 (t, J = 6.6 Hz, 1H, H<sup>5'</sup>), 7.08 (t, J = 7.4 Hz, 1H, H<sup>10</sup>), 7.03 (t, J = 7.4 Hz, 1H, H<sup>k</sup>), 7.01 (t, J = 7.7 Hz, 1H, H<sup>10'</sup>), 6.94 (t, J = 7.4 Hz, 1H, H<sup>11</sup>), 6.90 (t, J = 7.4 Hz, 1H, H<sup>11</sup>), 6.81 – 6.67 (AB system, J = 19.3 Hz, 2H, H<sup>n</sup>, H<sup>n</sup>), 6.36 (d, J = 7.4 Hz, 1H, H<sup>12</sup>), 6.28 (d, J = 7.4 Hz, 1H, H<sup>12</sup>), 6.19 (d, J = 8.3 Hz, 1H, H<sup>l</sup>) ppm. **<sup>13</sup>C{<sup>1</sup>H} NMR (101 MHz, DMSO-d<sub>6</sub>, 25 °C)** δ 192.09, 167.13, 158.72, 149.69, 149.02, 148.88, 148.38, 147.28, 144.57, 144.39, 143.02, 138.72, 138.52, 136.14, 134.70, 133.86, 131.82, 131.71, 131.38, 131.27, 129.87, 129.56, 128.85, 126.19, 125.13, 124.92, 124.82, 124.61, 123.79, 123.71, 123.64, 122.07, 122.02, 119.94, 119.56, 116.71, 116.60, 112.41, 112.34, 54.91 ppm. **FT-IR (KBr, cm<sup>-1</sup>) selected bands:** 3032 (w, ν<sub>C-H</sub>), 1605-1581 (m, ν<sub>C=C</sub> + ν<sub>C-N</sub>), 1417 (w, ν<sub>C=N</sub>), 1161 (m, ν<sub>C-C</sub>), 1063 (m, δ<sub>C-Hip</sub>), 753-737 (vs, δ<sub>C-Hoop</sub>). **HR ESI+ MS (DCM/DMSO, 4:1):**  $m/z_{\text{exp}} = 820.1720$  ( $m/z_{\text{calcd}} [M^+] = m/z_{\text{calcd}} [C_{40}H_{29}IrN_5OS]^+ = 820.1722$ ); 501.0934 ( $m/z_{\text{calcd}} [M^+L1] = m/z_{\text{calcd}} [C_{22}H_{16}IrN_2]^+ = 501.0943$ ). **Solubility:** soluble in dimethyl sulfoxide, dichloromethane, methanol, acetonitrile, acetone, dimethylformamide, tetrahydrofuran.

**[Ir(dfppy)<sub>2</sub>(L<sup>1</sup>)]Cl: [1b]Cl**



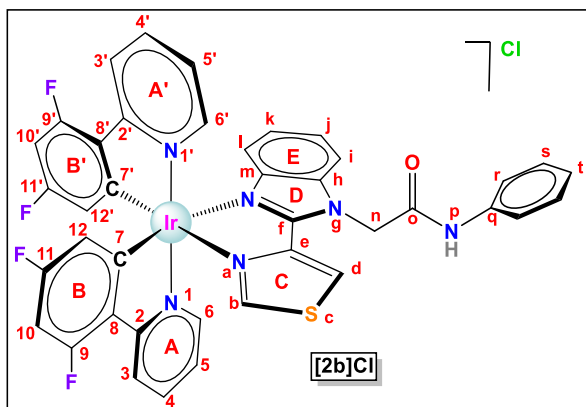
In a 100 mL Schlenk flask, previously purged with nitrogen, the ancillary ligand L<sup>1</sup> (0.0527 g, 0.165 mmol) was added to a solution of [Ir(μ-Cl)(dfppy)<sub>2</sub>]<sub>2</sub> (0.1003 g, 0.082 mmol) in a mixture of dichloromethane (8 mL) / methanol (10 mL), and the mixture was stirred at 60 °C for 24 hours under a N<sub>2</sub> atmosphere. The resulting solution was concentrated to half the volume under vacuum and diethyl ether (15 mL) was added to precipitate a crude solid that was isolated by

filtration and washed with diethyl ether (2×5 mL). The product was dried under vacuum to produce a yellow powder. Yield: 62 % (0.0953 g, 0.103 mmol). **M<sub>r</sub>** (C<sub>40</sub>H<sub>25</sub>ClF<sub>4</sub>IrN<sub>5</sub>OS) = 927.39 g/mol. **Anal. Calcd for C<sub>40</sub>H<sub>25</sub>ClF<sub>4</sub>IrN<sub>5</sub>OS·(CH<sub>2</sub>Cl<sub>2</sub>)<sub>0.5</sub>**: C 50.16; H 2.70; N 7.22; **Found**: C 50.07; H 2.38; N 7.53. **<sup>1</sup>H NMR (400 MHz, DMSO-d<sub>6</sub>, 25 °C)** δ 8.93 (s, 1H, H<sup>d</sup>), 8.73 (s, 1H, H<sup>b</sup>), 8.32 (d, J = 8.6 Hz, 1H, H<sup>3</sup>), 8.27 (d, J = 8.5 Hz, 1H, H<sup>3</sup>), 8.22 (d, J = 7.6 Hz, 2H, H<sup>q</sup>, H<sup>q</sup>), 8.04 (m, 3H, H<sup>4</sup>, H<sup>4</sup>, H<sup>i</sup>), 7.89 (d, J = 5.3 Hz, 1H, H<sup>6</sup>), 7.81 (m, 2H, H<sup>6</sup>, H<sup>5</sup>), 7.68 (t, J = 7.5 Hz, 2H, H<sup>r</sup>, H<sup>r</sup>), 7.36 (m, 3H, H<sup>j</sup>, H<sup>5</sup>, H<sup>5</sup>), 7.19 (t, J = 7.7 Hz, 1H, H<sup>k</sup>), 7.05 (t, J<sub>H-F</sub> = 11.0 Hz, 1H, H<sup>10</sup> or H<sup>10'</sup>), 6.98 (t, J<sub>H-F</sub> = 11.0 Hz, 1H, H<sup>10</sup> or H<sup>10'</sup>), 6.86 – 6.70 (AB system, J = 19.4 Hz, 2H, H<sup>n</sup>, H<sup>n</sup>), 6.26 (d, J = 8.2 Hz, 1H, H<sup>l</sup>), 5.80 (d, J<sub>H-F</sub> = 7.5 Hz, 1H, H<sup>12</sup>), 5.70 (d, J<sub>H-F</sub> = 8.0 Hz, 1H, H<sup>12</sup>) ppm. **<sup>13</sup>C{<sup>1</sup>H} NMR (101 MHz, DMSO-d<sub>6</sub>, 25 °C)** δ 192.04, 163.82, 163.67, 162.99, 162.91, 161.78, 161.29, 161.13, 159.68, 159.26, 159.20, 152.51, 151.68, 149.77, 149.74, 149.70, 142.55, 140.01, 138.39, 136.15, 134.76, 133.84, 128.98, 128.95, 128.45, 128.1, 126.66, 125.44, 124.48, 123.44, 123.04, 115.94, 113.91, 113.74, 113.63, 113.46, 112.80, 98.97, 98.82, 52.23 ppm. **<sup>19</sup>F NMR (376 MHz, DMSO-d<sub>6</sub>, 25 °C)** δ -106.92 (t, J = 9.5 Hz, 2F, F<sup>9</sup>, F<sup>9</sup>), -109.06 (q, J = 10.4 Hz, 2F, F<sup>11</sup>, F<sup>11</sup>). **FT-IR (KBr, cm<sup>-1</sup>) selected bands**: 3040 (w, ν<sub>Car-H</sub>), 1606-1582 (m, ν<sub>C=C + C-N</sub>), 1428 (w, ν<sub>C=N</sub>), 1159 (m, ν<sub>C-C</sub>), 1062 (m, δ<sub>C-Hip</sub>), 730 (vs, δ<sub>C-Hoop</sub>). **HR ESI+ MS (DCM/DMSO, 4:1)**: m/z<sub>exp</sub> = 892.1342 (m/z<sub>calcd</sub> [M<sup>+</sup>] = m/z<sub>calcd</sub> [C<sub>40</sub>H<sub>25</sub>F<sub>4</sub>IrN<sub>5</sub>OS]<sup>+</sup> = 892.1345). **Solubility**: soluble in dimethyl sulfoxide, dichloromethane, methanol, acetonitrile, acetone, dimethylformamide, tetrahydrofuran.

**[Ir(ppy)<sub>2</sub>(L<sub>2</sub>)]Cl: [2a]Cl**

In a 100 mL Schlenk flask, previously purged with nitrogen, the ancillary ligand L<sup>2</sup> (0.0625 g, 0.187 mmol) was added to a solution of [Ir(μ-Cl)(ppy)<sub>2</sub>]<sub>2</sub> (0.1002 g, 0.094 mmol) in a mixture of dichloromethane (8 mL) / methanol (10 mL), and the mixture was stirred at 60 °C for 24 hours under a N<sub>2</sub> atmosphere. The resulting solution was concentrated to half the volume under vacuum and diethyl ether (15 mL) was added to precipitate a crude

solid that was isolated by filtration and washed with diethyl ether (2×5 mL). The product was dried under vacuum to produce a yellow powder. Yield: 72 % (0.1167 g, 0.134 mmol). **M<sub>r</sub>** (C<sub>40</sub>H<sub>30</sub>ClIrN<sub>6</sub>OS) = 870.44 g/mol. **Anal. Calcd for C<sub>40</sub>H<sub>30</sub>ClIrN<sub>6</sub>OS·(CH<sub>2</sub>Cl<sub>2</sub>)<sub>0.15</sub>**: C 54.60; H 3.46; N 9.52; **Found**: C 54.61; H 3.59; N 9.65. **<sup>1</sup>H NMR (400 MHz, DMSO-d<sub>6</sub>, 25 °C)** δ 11.46 (s, 1H, H<sup>p(NH)</sup>), 9.21 (s, 1H, H<sup>d</sup>), 8.52 (s, 1H, H<sup>b</sup>), 8.27 (d, J = 8.1 Hz, 1H, H<sup>3</sup>), 8.21 (d, J = 8.2 Hz, 1H, H<sup>3'</sup>), 7.92 (m, 5H, H<sup>4</sup>, H<sup>4'</sup>, H<sup>i</sup>, H<sup>9</sup>, H<sup>9'</sup>), 7.73 (d, J = 5.7 Hz, 2H, H<sup>6</sup>, H<sup>6'</sup>), 7.66 (d, J = 8.0 Hz, 2H, H<sup>r</sup>, H<sup>r'</sup>), 7.38 (t, J = 7.7 Hz, 1H, H<sup>j</sup>), 7.32 (t, J = 7.6 Hz, 2H, H<sup>5</sup>, H<sup>5'</sup>), 7.21 (t, J = 6.5 Hz, 1H, H<sup>5</sup>), 7.17 (t, J = 6.5 Hz, 1H, H<sup>5'</sup>), 7.13 – 6.97 (m, 4H, H<sup>t</sup>, H<sup>k</sup>, H<sup>10</sup>, H<sup>10'</sup>), 6.92 (t, J = 7.6 Hz, 1H, H<sup>11</sup>), 6.89 (t, J = 7.6 Hz, 1H, H<sup>11'</sup>), 6.33 (d, J = 7.6 Hz, 1H, H<sup>12</sup>), 6.26 (d, J = 7.5 Hz, 1H, H<sup>12'</sup>), 6.17 (d, J = 8.2 Hz, 1H, H<sup>i</sup>), 5.92 (AB system, 2H, H<sup>n</sup>, H<sup>n'</sup>) ppm. **<sup>13</sup>C{<sup>1</sup>H} NMR (101 MHz, DMSO-d<sub>6</sub>, 25 °C)** δ 167.57, 167.47, 164.61, 158.97, 149.72, 149.62, 149.35, 148.90, 147.75, 145.03, 144.88, 143.73, 139.06, 138.89, 136.67, 132.19, 131.75, 130.32, 130.00, 129.25, 126.77, 125.66, 125.32, 125.22, 124.99, 124.34, 124.15, 122.51, 120.33, 119.96, 119.82, 117.11, 112.72, 109.99, 48.39 ppm. **FT-IR (KBr, cm<sup>-1</sup>) selected bands**: 3177 (w, ν<sub>N-H</sub>), 3031 (w, ν<sub>Car-H</sub>), 1605-1582 (m, ν<sub>C=C + C-N</sub>), 1418 (w, ν<sub>C=N</sub>), 1162 (m, ν<sub>C-C</sub>), 1064 (m, δ<sub>C-Hip</sub>), 754-738 (vs, δ<sub>C-Hoop</sub>). **HR ESI+ MS (DCM/DMSO, 4:1)**: m/z<sub>exp</sub> = 835.1840 (m/z<sub>calcd</sub> [M<sup>+</sup>] = m/z<sub>calcd</sub> [C<sub>40</sub>H<sub>30</sub>IrN<sub>6</sub>OS]<sup>+</sup> = 835.1831). **Solubility**: soluble in dimethyl sulfoxide, dichloromethane, methanol, acetonitrile, acetone, dimethylformamide, tetrahydrofuran.

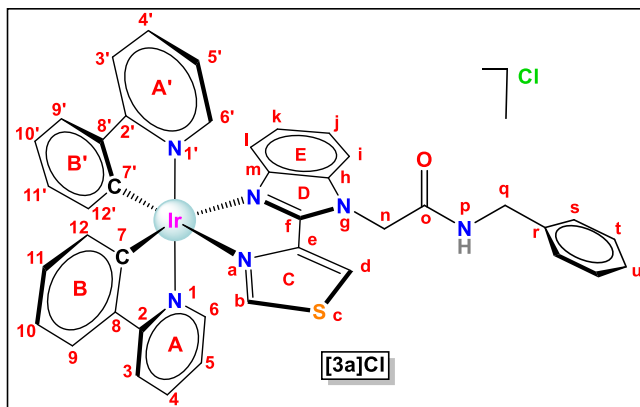
**[Ir(dfppy)<sub>2</sub>(L<sub>2</sub>)]Cl: [2b]Cl**

In a 100 mL Schlenk flask, previously purged with nitrogen, the ancillary ligand L<sup>2</sup> (0.0551 g, 0.165 mmol) was added to a solution of [Ir(μ-Cl)(dfppy)<sub>2</sub>]<sub>2</sub> (0.1002 g, 0.082 mmol) in a mixture of dichloromethane (8 mL) / methanol (10 mL), and the mixture was stirred at 60 °C for 24 hours under a N<sub>2</sub> atmosphere. The resulting solution was concentrated to half the volume under vacuum and diethyl ether (15 mL) was added to



precipitate a crude solid that was isolated by filtration and washed with diethyl ether (2×5 mL). The product was dried under vacuum to produce a yellow powder. Yield: 75 % (0.1162 g, 0.123 mmol). **M<sub>r</sub>** (C<sub>40</sub>H<sub>26</sub>ClF<sub>4</sub>IrN<sub>6</sub>OS) = 942.40 g/mol. **Anal. Calcd for C<sub>40</sub>H<sub>26</sub>ClF<sub>4</sub>IrN<sub>6</sub>OS**: C 50.98; H 2.78; N 8.92; **Found**: C 51.07.49; H 2.69; N 8.94. **<sup>1</sup>H NMR (400 MHz, DMSO-d<sub>6</sub>, 25 °C)** δ 11.44 (s, 1H, H<sup>P(NH)</sup>), 9.25 (s, 1H, H<sup>d</sup>), 8.74 (s, 1H, H<sup>b</sup>), 8.30 (d, J = 8.6 Hz, 1H, H<sup>3</sup>), 8.25 (d, J = 8.7 Hz, 1H, H<sup>3'</sup>), 8.02 (m, 3H, H<sup>4</sup>, H<sup>4'</sup>, H<sup>i</sup>), 7.80 (d, J = 5.4 Hz, 2H, H<sup>6</sup>, H<sup>6'</sup>), 7.65 (d, J = 8.0 Hz, 2H, H<sup>r</sup>, H<sup>r'</sup>), 7.44 (t, J = 7.9 Hz, 1H, H<sup>l</sup>), 7.30 (m, 4H, H<sup>5</sup>, H<sup>5'</sup>, H<sup>s</sup>, H<sup>s'</sup>), 7.19 (t, J = 7.8 Hz, 1H, H<sup>k</sup>), 7.03 (m, 3H, H<sup>t</sup>, H<sup>10</sup>, H<sup>10'</sup>), 6.23 (d, J = 8.4 Hz, 1H, H<sup>l</sup>), 5.93 (AB system, 2H, H<sup>n</sup>, H<sup>n'</sup>), 5.77 (d, J<sub>H-F</sub> = 8.2 Hz, 1H, H<sup>12</sup>), 5.67 (d, J<sub>H-F</sub> = 8.1 Hz, 1H, H<sup>12'</sup>) ppm. **<sup>13</sup>C{<sup>1</sup>H} NMR (101 MHz, DMSO-d<sub>6</sub>, 25 °C)** δ 163.99, 162.95, 162.89, 161.75, 161.10, 159.46, 152.55, 152.48, 151.64, 151.58, 149.73, 149.26, 142.76, 139.94, 139.84, 138.37, 138.22, 136.15, 128.82, 128.40, 128.17, 126.62, 125.50, 125.10, 124.44, 124.38, 123.94, 123.38, 123.19, 122.99, 122.80, 119.37, 115.92, 113.84, 113.56, 113.39, 112.58, 98.94, 98.79, 48.01 ppm. **<sup>19</sup>F NMR (376 MHz, DMSO-d<sub>6</sub>, 25 °C)** δ -106.94 (t, J = 10.5 Hz, 2F, F<sup>9</sup>, F<sup>9'</sup>), -109.09 (q, J = 10.5 Hz, 2F, F<sup>11</sup>, F<sup>11'</sup>) ppm. **FT-IR (KBr, cm<sup>-1</sup>) selected bands**: 3188 (w, ν<sub>N-H</sub>), 3026 (w, ν<sub>Car-H</sub>), 1601-1575 (m, ν<sub>C=C + C-N</sub>), 1433 (w, ν<sub>C=N</sub>), 1165 (m, ν<sub>C-C</sub>), 1070 (m, δ<sub>C-Hip</sub>), 751 (vs, δ<sub>C-Hoop</sub>). **HR ESI+ MS (DCM/DMSO, 4:1)**: m/z<sub>exp</sub> = 907.1456 (m/z<sub>calcd</sub> [M<sup>+</sup>] = m/z<sub>calcd</sub> [C<sub>40</sub>H<sub>26</sub>F<sub>4</sub>IrN<sub>6</sub>OS]<sup>+</sup> = 907.1454). **Solubility**: soluble in dimethyl sulfoxide, dichloromethane, methanol, acetonitrile, acetone, dimethylformamide, tetrahydrofuran.

**[Ir(ppy)<sub>2</sub>(L<sup>3</sup>)]Cl: [3a]Cl**



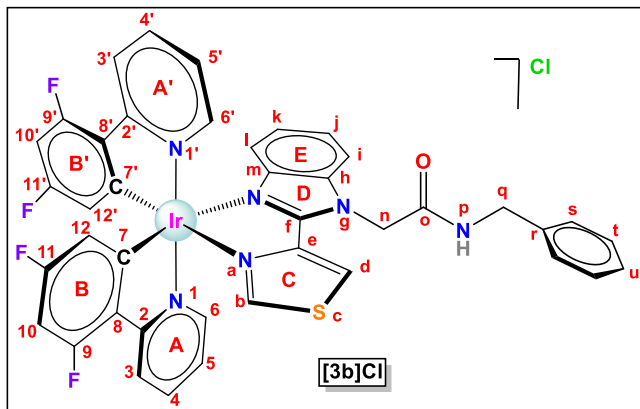
In a 100 mL Schlenk flask, previously purged with nitrogen, the ancillary ligand L<sup>3</sup> (0.0653 g, 0.187 mmol) was added to a solution of [Ir(μ-Cl)(ppy)<sub>2</sub>]<sub>2</sub> (0.1001 g, 0.093 mmol) in a mixture of dichloromethane (8 mL) / methanol (10 mL), and the mixture was stirred at 60 °C for 24 hours under a N<sub>2</sub> atmosphere. The resulting solution was concentrated to half the volume

under vacuum and diethyl ether (15 mL) was added to precipitate a crude solid that was isolated by filtration and washed with diethyl ether (2×5 mL). The product was dried under vacuum to produce a yellow powder. Yield: 73 % (0.1198 g, 0.135 mmol). **M<sub>r</sub>** (C<sub>41</sub>H<sub>32</sub>ClIrN<sub>6</sub>OS) = 884.47 g/mol. **Anal. Calcd for C<sub>41</sub>H<sub>32</sub>ClIrN<sub>6</sub>OS·(CH<sub>2</sub>Cl<sub>2</sub>)<sub>0.25</sub>**: C 54.70; H 3.62; N 9.28; **Found**: C 54.73; H 3.81; N 9.31. **<sup>1</sup>H NMR (400 MHz, DMSO-d<sub>6</sub>, 25 °C)** δ 9.39 (t, J = 5.8 Hz, 1H, H<sup>P(NH)</sup>), 8.92 (s, 1H, H<sup>d</sup>), 8.50 (s, 1H, H<sup>b</sup>), 8.27 (d, J = 8.1 Hz, 1H, H<sup>3</sup>), 8.20 (d, J = 8.1 Hz, 1H, H<sup>3'</sup>), 7.90 (m, 5H, H<sup>4</sup>, H<sup>4'</sup>, H<sup>9</sup>, H<sup>9'</sup>, H<sup>i</sup>), 7.75 (d, J = 5.8 Hz, 1H, H<sup>6</sup>), 7.67 (d, J = 5.7 Hz, 1H, H<sup>6'</sup>), 7.38 (t, J = 7.8 Hz, 1H, H<sup>l</sup>), 7.29 – 7.20 (m, 5H, H<sup>5</sup>, H<sup>5'</sup>, H<sup>t</sup>, H<sup>t'</sup>, H<sup>u</sup>), 7.17 (t, J = 7.2 Hz, 1H, H<sup>5</sup>), 7.11 (t, J = 7.2 Hz, 1H, H<sup>5'</sup>), 7.09 – 6.98 (m, 3H, H<sup>10</sup>, H<sup>10'</sup>, H<sup>k</sup>), 6.92 (t, J = 7.4 Hz, 1H, H<sup>11</sup>), 6.89 (t, J = 7.4 Hz, 1H, H<sup>11'</sup>), 6.33 (d, J = 7.7 Hz, 1H, H<sup>12</sup>), 6.24 (d, J = 7.5 Hz, 1H, H<sup>12'</sup>), 6.15 (d, J = 8.5 Hz, 1H, H<sup>l</sup>), 5.76 – 5.59 (AB system, J = 17.5 Hz, 2H, H<sup>n</sup>, H<sup>n'</sup>), 4.33 (d, J = 5.6 Hz, 2H, H<sup>q</sup>, H<sup>q'</sup>) ppm. **<sup>13</sup>C{<sup>1</sup>H} NMR (101 MHz, DMSO-d<sub>6</sub>, 25 °C)** δ 167.12, 166.97, 165.55, 158.47, 149.30, 149.21, 148.82, 148.41, 147.29, 144.57, 144.43, 143.21,



138.70, 138.61, 138.58, 138.45, 136.23, 131.75, 131.28, 129.87, 129.55, 128.23, 127.38, 126.98, 126.20, 125.14, 124.86, 124.77, 124.48, 123.72, 123.63, 122.08, 122.00, 119.83, 119.52, 116.68, 112.17, 64.93, 47.54, 42.54 ppm. **FT-IR (KBr,  $\text{cm}^{-1}$ ) selected bands:** 3180 (w,  $\nu_{\text{N-H}}$ ), 3028 (w,  $\nu_{\text{C-H}}$ ), 1601-1582 (m,  $\nu_{\text{C=C+C-N}}$ ), 1418 (w,  $\nu_{\text{C=N}}$ ), 1162 (m,  $\nu_{\text{C-C}}$ ), 1064 (m,  $\delta_{\text{C-Hip}}$ ), 748-738 (vs,  $\delta_{\text{C-Hoop}}$ ). **HR ESI+ MS (DCM/DMSO, 4:1):**  $m/z_{\text{exp}} = 849.1998$  ( $m/z_{\text{calcd}} [\text{M}^+] = m/z_{\text{calcd}} [\text{C}_{41}\text{H}_{32}\text{IrN}_6\text{OS}]^+ = 849.1988$ ). **Solubility:** soluble in dimethyl sulfoxide, dichloromethane, methanol, acetonitrile, acetone, dimethylformamide, tetrahydrofuran.

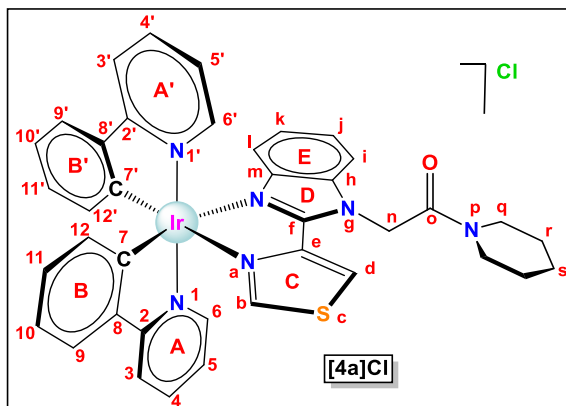
**[Ir(dfppy)<sub>2</sub>(L<sup>3</sup>)]Cl: [3b]Cl**



In a 100 mL Schlenk flask, previously purged with nitrogen, the ancillary ligand L<sup>3</sup> (0.0574 g, 0.165 mmol) was added to a solution of  $[\text{Ir}(\mu\text{-Cl})(\text{dfppy})_2]_2$  (0.1003 g, 0.082 mmol) in a mixture of dichloromethane (8 mL) / methanol (10 mL), and the mixture was stirred at 60 °C for 24 hours under a N<sub>2</sub> atmosphere. The resulting solution was concentrated to half the volume

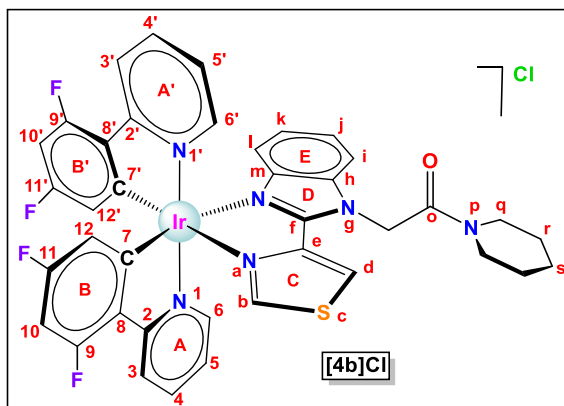
under vacuum and diethyl ether (15 mL) was added to precipitate a crude solid that was isolated by filtration and washed with diethyl ether (2×5 mL). The product was dried under vacuum to produce a yellow powder. Yield: 73 % (0.1144 g, 0.120 mmol). **M<sub>r</sub>** (C<sub>41</sub>H<sub>28</sub>ClF<sub>4</sub>IrN<sub>6</sub>OS) = 956.43 g/mol. **Anal. Calcd for C<sub>41</sub>H<sub>28</sub>ClF<sub>4</sub>IrN<sub>6</sub>OS(CH<sub>2</sub>Cl<sub>2</sub>)<sub>0.25</sub>:** C 50.68; H 2.94; N 8.60; **Found:** C 50.68; H 2.79; N 8.85. **<sup>1</sup>H NMR (400 MHz, DMSO-d<sub>6</sub>, 25 °C)**  $\delta$  9.42 (t, J = 5.5 Hz, 1H, H<sup>p(NH)</sup>), 8.98 (s, 1H, H<sup>d</sup>), 8.72 (s, 1H, H<sup>b</sup>), 8.30 (d, J = 8.3 Hz, 1H, H<sup>3</sup>), 8.24 (d, J = 8.5 Hz, 1H, H<sup>3'</sup>), 8.00 (m, 3H, H<sup>4</sup>, H<sup>4'</sup>, H<sup>i</sup>), 7.81 (d, J = 5.6 Hz, 1H, H<sup>6</sup>), 7.72 (d, J = 5.6 Hz, 1H, H<sup>6'</sup>), 7.44 (t, J = 7.8 Hz, 1H, H<sup>j</sup>), 7.23 (m, 8H, H<sup>5</sup>, H<sup>5'</sup>, H<sup>s</sup>, H<sup>s'</sup>, H<sup>t</sup>, H<sup>t'</sup>, H<sup>u</sup>, H<sup>u'</sup>), 7.03 (t, J<sub>H-F</sub> = 10.4 Hz, 1H, H<sup>10</sup> or H<sup>10'</sup>), 6.97 (t, J<sub>H-F</sub> = 10.4 Hz, 1H, H<sup>10</sup> or H<sup>10'</sup>), 6.21 (d, J = 8.3 Hz, 1H, H<sup>l</sup>), 5.85 – 5.59 (m, 4H, H<sup>12</sup>, H<sup>n</sup>, H<sup>n'</sup>, H<sup>12'</sup>), 4.33 (s, 2H, H<sup>q</sup>, H<sup>q'</sup>) ppm. **<sup>13</sup>C{<sup>1</sup>H} NMR (101 MHz, DMSO-d<sub>6</sub>, 25 °C)**  $\delta$  165.43, 162.90, 159.41, 159.15, 157.29, 153.93, 152.51, 151.63, 149.88, 149.64, 149.18, 142.68, 139.90, 139.80, 138.58, 138.33, 136.20, 128.22, 127.38, 126.97, 126.56, 125.41, 125.02, 124.41, 124.30, 123.13, 122.78, 115.92, 112.53, 109.56, 99.02, 64.91, 47.60, 42.53 ppm. **<sup>19</sup>F NMR (376 MHz, DMSO-d<sub>6</sub>, 25 °C)**  $\delta$  -106.96 (t, J = 6.7 Hz, 2F, F<sup>9</sup>, F<sup>9'</sup>), -109.11 (q, J = 10.4 Hz, 2F, F<sup>11</sup>, F<sup>11'</sup>) ppm. **FT-IR (KBr,  $\text{cm}^{-1}$ ) selected bands:** 3180 (w,  $\nu_{\text{N-H}}$ ), 3029 (w,  $\nu_{\text{C-H}}$ ), 1601-1574 (m,  $\nu_{\text{C=C+C-N}}$ ), 1429 (w,  $\nu_{\text{C=N}}$ ), 1164 (m,  $\nu_{\text{C-C}}$ ), 1066 (m,  $\delta_{\text{C-Hip}}$ ), 756-738 (vs,  $\delta_{\text{C-Hoop}}$ ). **HR ESI+ MS (DCM/DMSO, 4:1):**  $m/z_{\text{exp}} = 921.1612$  ( $m/z_{\text{calcd}} [\text{M}^+] = m/z_{\text{calcd}} [\text{C}_{41}\text{H}_{28}\text{F}_4\text{IrN}_6\text{OS}]^+ = 921.1611$ ). **Solubility:** soluble in dimethyl sulfoxide, dichloromethane, methanol, acetonitrile, acetone, dimethylformamide, tetrahydrofuran.

[Ir(ppy)<sub>2</sub>(L4)]Cl: [4a]Cl



In a 100 mL Schlenk flask, previously purged with nitrogen, the ancillary ligand L<sup>4</sup> (0.0608 g, 0.186 mmol) was added to a solution of [Ir(μ-Cl)(ppy)<sub>2</sub>]<sub>2</sub> (0.1000 g, 0.093 mmol) in a mixture of dichloromethane (8 mL) / methanol (10 mL), and the mixture was stirred at 60 °C for 24 hours under a N<sub>2</sub> atmosphere. The resulting solution was concentrated to half the volume under vacuum and diethyl ether (15 mL) was added to precipitate a crude solid that was

isolated by filtration and washed with diethyl ether (2×5 mL). The product was dried under vacuum to produce a yellow powder. Yield: 78 % (0.1255 g, 0.146 mmol). **M<sub>r</sub>** (C<sub>39</sub>H<sub>34</sub>ClIrN<sub>6</sub>OS) = 862.46 g/mol. **Anal. Calcd for C<sub>39</sub>H<sub>34</sub>ClIrN<sub>6</sub>OS(CH<sub>2</sub>Cl)<sub>0.15</sub>**: C 53.73; H 3.95; N 9.60; **Found**: C 53.76; H 3.92; N 9.59. **<sup>1</sup>H NMR (400 MHz, DMSO-d<sub>6</sub>, 25 °C)** δ 8.74 (s, J = 4.9 Hz, 1H, H<sup>d</sup>), 8.50 (s, 1H, H<sup>b</sup>), 8.27 (d, J = 8.2 Hz, 1H, H<sup>3</sup>), 8.21 (d, J = 8.0 Hz, 1H, H<sup>3'</sup>), 8.04 – 7.83 (m, 5H, H<sup>4</sup>, H<sup>4'</sup>, H<sup>9</sup>, H<sup>9'</sup>, H<sup>i</sup>), 7.71 (d, J = 5.1 Hz, 2H, H<sup>6</sup>, H<sup>6'</sup>), 7.35 (t, J = 7.7 Hz, 1H, H<sup>i</sup>), 7.21 (t, J = 6.6 Hz, 1H, H<sup>5</sup>), 7.16 (t, J = 6.6 Hz, 1H, H<sup>5'</sup>), 7.06 (t, J = 7.4 Hz, 1H, H<sup>10</sup>), 7.01 (t, J = 7.6 Hz, 2H, H<sup>k</sup>, H<sup>10'</sup>), 6.92 (t, J = 7.4 Hz, 1H, H<sup>11</sup>), 6.89 (t, J = 7.4 Hz, 1H, H<sup>11'</sup>), 6.32 (d, J = 7.5 Hz, 1H, H<sup>12</sup>), 6.26 (d, J = 7.4 Hz, 1H, H<sup>12'</sup>), 6.15 (d, J = 8.2 Hz, 1H, H<sup>l</sup>), 5.96 (AB system, 2H, H<sup>n</sup>, H<sup>n</sup>), 3.65 (s, 2H, H<sup>q</sup>, H<sup>q</sup>), 3.54 (s, 2H, H<sup>q</sup>, H<sup>q</sup>), 1.74 (s, 2H, H<sup>r</sup>, H<sup>r</sup>), 1.65 (s, 2H, H<sup>r</sup>, H<sup>r</sup>), 1.46 (s, 2H, H<sup>s</sup>, H<sup>s</sup>) ppm. **<sup>13</sup>C{<sup>1</sup>H} NMR (101 MHz, DMSO-d<sub>6</sub>, 25 °C)** δ 167.14, 167.06, 162.90, 158.52, 149.95, 149.03, 148.82, 148.53, 147.36, 144.57, 144.42, 143.26, 138.59, 138.46, 136.26, 131.76, 131.31, 129.88, 129.55, 126.18, 124.98, 124.89, 124.77, 124.42, 123.66, 122.07, 121.99, 119.90, 119.53, 116.60, 112.26, 46.63, 45.51, 42.87, 25.93, 25.23, 23.87 ppm. **FT-IR (KBr, cm<sup>-1</sup>) selected bands**: 3031 (w, ν<sub>C-H</sub>), 1606-1582 (m, ν<sub>C=C</sub> + ν<sub>C-N</sub>), 1435 (w, ν<sub>C=N</sub>), 1163 (m, ν<sub>C-C</sub>), 1063 (m, δ<sub>C-Hip</sub>), 756-738 (vs, δ<sub>C-Hoop</sub>). **HR ESI+ MS (DCM/DMSO, 4:1)**: m/z<sub>exp</sub> = 827.2145 (m/z<sub>calcd</sub> [M<sup>+</sup>] = m/z<sub>calcd</sub> [C<sub>39</sub>H<sub>34</sub>IrN<sub>6</sub>OS]<sup>+</sup> = 827.2144). **Solubility**: soluble in dimethyl sulfoxide, dichloromethane, methanol, acetonitrile, acetone, dimethylformamide, tetrahydrofuran.

**[Ir(dfppy)<sub>2</sub>(L<sup>4</sup>)]Cl: [4b]Cl**

In a 100 mL Schlenk flask, previously purged with nitrogen, the ancillary ligand L<sup>4</sup> (0.0540 g, 0.165 mmol) was added to a solution of [Ir( $\mu$ -Cl)(dfppy)<sub>2</sub>]<sub>2</sub> (0.1003 g, 0.082 mmol) in a mixture of dichloromethane (8 mL) / methanol (10 mL), and the mixture was stirred at 60 °C for 24 hours under a N<sub>2</sub> atmosphere. The resulting solution was concentrated to half the volume under vacuum and diethyl ether (15 mL) was added to precipitate a crude solid that was

isolated by filtration and washed with diethyl ether (2x5 mL). The product was dried under vacuum to produce a yellow powder. Yield: 51 % (0.0781 g, 0.084 mmol). **M<sub>r</sub>** (C<sub>39</sub>H<sub>30</sub>ClF<sub>4</sub>IrN<sub>6</sub>OS) = 934.42 g/mol. **Anal. Calcd for C<sub>39</sub>H<sub>30</sub>ClF<sub>4</sub>IrN<sub>6</sub>OS(CH<sub>2</sub>Cl<sub>2</sub>)<sub>0.10</sub>**: C 49.81; H 3.23; N 8.91; **Found**: C 49.89; H 3.06; N 8.93. **<sup>1</sup>H NMR (400 MHz, DMSO-d<sub>6</sub>, 25 °C)**  $\delta$  8.78 (s, 1H, H<sup>d</sup>), 8.72 (s, 1H, H<sup>b</sup>), 8.30 (d, J = 8.2 Hz, 1H, H<sup>3</sup>), 8.25 (d, J = 8.1 Hz, 1H, H<sup>3</sup>), 8.04 (t, J = 7.8 Hz, 1H, H<sup>4</sup>), 8.00 (t, J = 7.8 Hz, 1H, H<sup>4</sup>), 7.94 (d, J = 8.1 Hz, 1H, H<sup>i</sup>), 7.77 (s, 2H, H<sup>6</sup>, H<sup>6</sup>), 7.41 (t, J = 7.7 Hz, 1H, H<sup>i</sup>), 7.29 (t, J = 6.1 Hz, 1H, H<sup>5</sup>), 7.26 (t, J = 6.1 Hz, 1H, H<sup>5</sup>), 7.17 (t, J = 7.7 Hz, 1H, H<sup>k</sup>), 7.04 (t, J<sub>H-F</sub> = 10.2 Hz, 1H, H<sup>10</sup> or H<sup>10'</sup>), 6.97 (t, J<sub>H-F</sub> = 10.2 Hz, 1H, H<sup>10</sup> or H<sup>10'</sup>), 6.21 (d, J = 8.2 Hz, 1H, H<sup>i</sup>), 5.95 (AB system, 2H, H<sup>n</sup>, H<sup>n</sup>), 5.76 (d, J<sub>H-F</sub> = 7.5 Hz, 1H, H<sup>12</sup>), 5.68 (d, J<sub>H-F</sub> = 7.3 Hz, 1H, H<sup>12</sup>), 3.65 (s, 2H, H<sup>q</sup>, H<sup>q</sup>), 3.40 (s, 2H, H<sup>q</sup>, H<sup>q</sup>), 1.75 (s, 2H, H<sup>r</sup>, H<sup>r</sup>), 1.65 (s, 2H, H<sup>r</sup>, H<sup>r</sup>), 1.46 (s, 2H, H<sup>s</sup>, H<sup>s</sup>) ppm. **<sup>13</sup>C{<sup>1</sup>H} NMR (101 MHz, DMSO-d<sub>6</sub>, 25 °C)**  $\delta$  162.94, 162.77, 162.23, 161.83, 161.54, 159.46, 153.08, 152.09, 150.42, 150.00, 149.67, 144.54, 142.75, 140.38, 139.96, 138.65, 137.85, 136.66, 135.48, 134.69, 134.59, 128.87, 126.98, 125.69, 125.40, 124.80, 123.80, 123.41, 115.87, 114.12, 112.63, 99.67, 99.19, 46.74, 45.52, 42.90, 25.92, 25.22, 23.85 ppm. **<sup>19</sup>F NMR (376 MHz, DMSO-d<sub>6</sub>, 25 °C)**  $\delta$  -106.84 – -107.07 (m, 2F, F<sup>9</sup>, F<sup>9</sup>), -109.09 (q, J = 10.2 Hz, 2F, F<sup>11</sup>, F<sup>11</sup>) ppm. **FT-IR (KBr, cm<sup>-1</sup>) selected bands**: 3063 (w,  $\nu_{\text{C-H}}$ ), 1602–1573 (m,  $\nu_{\text{C=C+C-N}}$ ), 1429 (w,  $\nu_{\text{C=N}}$ ), 1163 (m,  $\nu_{\text{C-C}}$ ), 1042 (m,  $\delta_{\text{C-Hip}}$ ), 756 (vs,  $\delta_{\text{C-Hoop}}$ ). **HR ESI+ MS (DCM/DMSO, 4:1)**: m/z<sub>exp</sub> = 899.1772 (m/z<sub>calcd</sub> [M<sup>+</sup>] = m/z<sub>calcd</sub> [C<sub>39</sub>H<sub>30</sub>F<sub>4</sub>IrN<sub>6</sub>OS]<sup>+</sup> = 899.1767). **Solubility**: soluble in dimethyl sulfoxide, dichloromethane, methanol, acetonitrile, acetone, dimethylformamide, tetrahydrofuran.

## Bibliography

1. P. Agostinis, K. Berg, K.A. Cengel, T.H. Foster, A.W. Girotti, S.O. Gollnick, S.M. Hahn, M.R. Hamblin, A. Juzeniene, D. Kessel, M. Korbelik, J. Moan, P. Mroz, D. Nowis, J. Piette, B.C. Wilson, and J. Golab, Photodynamic therapy of cancer: An update, *CA. Cancer J. Clin.*, 2011, **61**, 250–281.
2. S. Kwiatkowski, B. Knap, D. Przystupski, J. Saczko, E. Kędzierska, K. Knap-Czop, J. Kotlińska, O. Michel, K. Kotowski, and J. Kulbacka, Photodynamic therapy – mechanisms, photosensitizers and combinations, *Biomed. Pharmacother.*, 2018, **106**, 1098–1107.
3. S. Monro, K.L. Colón, H. Yin, J. Roque, P. Konda, S. Gujar, R.P. Thummel, L. Lilje, C.G. Cameron, and S.A. McFarland, Transition Metal Complexes and Photodynamic Therapy from a Tumor-Centered Approach: Challenges, Opportunities, and Highlights from the Development of TLD1433, *Chem. Rev.*, 2019, **119**, 797–828.
4. T.J. Dougherty, J.E. Kaufman, A. Goldfarb, K.R. Weishaupt, D. Boyle, and A. Mittleman, Photoradiation therapy for the treatment of malignant tumors., *Cancer Res.*, 1978, **38**, 2628–35.
5. V. Novohradsky, A. Rovira, C. Hally, A. Galindo, G. Viguera, A. Gandioso, M. Svitelova, R. Bresolí-Obach, H. Kostrhunova, L. Markova, J. Kasparkova, S. Nonell, J. Ruiz, V. Brabec, and V. Marchán, Towards Novel Photodynamic Anticancer Agents Generating Superoxide Anion Radicals: A Cyclometalated Ir III Complex Conjugated to a Far-Red Emitting Coumarin, *Angew. Chemie Int. Ed.*, 2019, **58**, 6311–6315.
6. V. Novohradsky, L. Markova, H. Kostrhunova, J. Kasparkova, J. Ruiz, V. Marchán, and V. Brabec, A Cyclometalated Ir III Complex Conjugated to a Coumarin Derivative Is a Potent Photodynamic Agent against Prostate Differentiated and Tumorigenic Cancer Stem Cells, *Chem. – A Eur. J.*, 2021, **27**, 8547–8556.
7. C.P. Tan, Y.M. Zhong, L.N. Ji, and Z.W. Mao, Phosphorescent metal complexes as theranostic anticancer agents: combining imaging and therapy in a single molecule, *Chem. Sci.*, 2021, **12**, 2357–2367.
8. L. He, Y. Li, C.-P. Tan, R.-R. Ye, M.-H. Chen, J.-J. Cao, L.-N. Ji, and Z.-W. Mao, Cyclometalated iridium(III) complexes as lysosome-targeted photodynamic anticancer and real-time tracking agents, *Chem. Sci.*, 2015, **6**, 5409–5418.
9. A. Zamora, G. Viguera, V. Rodríguez, M.D. Santana, and J. Ruiz, Cyclometalated iridium(III) luminescent complexes in therapy and phototherapy, *Coord. Chem. Rev.*, 2018, **360**, 34–76.
10. J. Pracharova, G. Viguera, V. Novohradsky, N. Cutillas, C. Janiak, H. Kostrhunova, J. Kasparkova, J. Ruiz, and V. Brabec, Exploring the Effect of Polypyridyl Ligands on the Anticancer Activity of Phosphorescent Iridium(III) Complexes: From Proteosynthesis Inhibitors to Photodynamic Therapy Agents, *Chem. - A Eur. J.*, 2018, **24**, 4607–4619.
11. V. Novohradsky, G. Viguera, J. Pracharova, N. Cutillas, C. Janiak, H. Kostrhunova, V. Brabec, J. Ruiz, and J. Kasparkova, Molecular superoxide radical photogeneration in cancer cells by dipyrrophenazine iridium(III) complexes, *Inorg. Chem. Front.*, 2019, **6**, 2500–2513.
12. C.-S. Tan, N.B. Kumarakulasinghe, Y.-Q. Huang, Y. Li, E. Ang, J. Rou, -En Choo, B.-C. Goh, and R.A. Soo, Third generation EGFR TKIs: current data and future directions, (n.d.).
13. X. Li, J.F. Lovell, J. Yoon, and X. Chen, Clinical development and potential of photothermal and photodynamic therapies for cancer, *Nat. Rev. Clin. Oncol.*, 2020, **17**, 657–674.
14. P. Chinna Ayya Swamy, G. Sivaraman, R.N. Priyanka, S.O. Raja, K. Ponnuvel, J. Shanmugpriya, and A.

Gulyani, Near Infrared (NIR) absorbing dyes as promising photosensitizer for photo dynamic therapy, *Coord. Chem. Rev.*, 2020, **411**, 213233.

15. L.K. McKenzie, I. V. Sazanovich, E. Baggaley, M. Bonneau, V. Guerchais, J.A.G. Williams, J.A. Weinstein, and H.E. Bryant, Metal Complexes for Two-Photon Photodynamic Therapy: A Cyclometallated Iridium Complex Induces Two-Photon Photosensitization of Cancer Cells under Near-IR Light, *Chem. - A Eur. J.*, 2017, **23**, 234–238.

16. P.M. Shah, and H. Gerdes, Endoscopic options for early stage esophageal cancer, *J. Gastrointest. Oncol.*, 2015, **6**, 20–30.

17. C. Huang, C. Liang, T. Sadhukhan, S. Banerjee, Z. Fan, T. Li, Z. Zhu, P. Zhang, K. Raghavachari, and H. Huang, In-vitro and In-vivo Photocatalytic Cancer Therapy with Biocompatible Iridium(III) Photocatalysts, *Angew. Chemie Int. Ed.*, 2021, **60**, 9474–9479.

18. J. Zhao, K. Yan, G. Xu, X. Liu, Q. Zhao, C. Xu, and S. Gou, An Iridium (III) Complex Bearing a Donor–Acceptor–Donor Type Ligand for NIR-Triggered Dual Phototherapy, *Adv. Funct. Mater.*, 2021, **31**, 2008325.

19. H. Yuan, Z. Han, Y. Chen, F. Qi, H. Fang, Z. Guo, S. Zhang, and W. He, Ferroptosis Photoinduced by New Cyclometalated Iridium(III) Complexes and Its Synergism with Apoptosis in Tumor Cell Inhibition, *Angew. Chemie Int. Ed.*, 2021, **60**, 8174–8181.

20. L. Zhang, Y. Geng, L. Li, X. Tong, S. Liu, X. Liu, Z. Su, Z. Xie, D. Zhu, and M.R. Bryce, Rational design of iridium–porphyrin conjugates for novel synergistic photodynamic and photothermal therapy anticancer agents, *Chem. Sci.*, 2021, **12**, 5918–5925.

21. A.P. Castano, T.N. Demidova, and M.R. Hamblin, Mechanisms in photodynamic therapy: part one—photosensitizers, photochemistry and cellular localization, *Photodiagnosis Photodyn. Ther.*, 2004, **1**, 279–293.

22. S. Tornroth-Horsefield, and R. Neutze, Opening and closing the metabolite gate, *Proc. Natl. Acad. Sci.*, 2008, **105** 19565–19566.

23. N.L. Oleinick, R.L. Morris, and I. Belichenko, The role of apoptosis in response to photodynamic therapy: what, where, why, and how, *Photochem. Photobiol. Sci.*, 2002, **1**, 1–21.

24. J. Zielonka, J. Joseph, A. Sikora, M. Hardy, O. Ouari, J. Vasquez-Vivar, G. Cheng, M. Lopez, and B. Kalyanaraman, Mitochondria-Targeted Triphenylphosphonium-Based Compounds: Syntheses, Mechanisms of Action, and Therapeutic and Diagnostic Applications, *Chem. Rev.*, 2017, **117**, 10043–10120.

25. Y. Li, C.-P. Tan, W. Zhang, L. He, L.-N. Ji, and Z.-W. Mao, Phosphorescent iridium(III)-bis-N-heterocyclic carbene complexes as mitochondria-targeted theranostic and photodynamic anticancer agents, *Biomaterials.*, 2015, **39**, 95–104.

26. C. Pérez-Arnaiz, M.I. Acuña, N. Busto, I. Echevarría, M. Martínez-Alonso, G. Espino, B. García, and F. Domínguez, Thiabendazole-based Rh(III) and Ir(III) biscyclometallated complexes with mitochondria-targeted anticancer activity and metal-sensitive photodynamic activity, *Eur. J. Med. Chem.*, 2018, **157**, 279–293.

27. E. Zafón, I. Echevarría, S. Barrabés Vera, B.R. Manzano, F.A. Jalon, A.M. Rodríguez, A. Massaguer, and G. Espino, Photodynamic Therapy with Mitochondria-targeted Biscyclometalated Ir(III) Complexes. Multi-action Mechanism and Strong influence of the Cyclometalating Ligand, *Dalt. Trans.*, 2022, **51**, 111-128.

28. J. Torres, M.C. Carrión, J. Leal, F.A. Jalón, J. V. Cuevas, A.M. Rodríguez, G. Castañeda, and B.R. Manzano, Cationic Bis(cyclometalated) Ir(III) Complexes with Pyridine–Carbene Ligands. Photophysical Properties and Photocatalytic Hydrogen Production from Water, *Inorg. Chem.*, 2018, **57**, 970–984.
29. Y. Chen, L. Qiao, L. Ji, and H. Chao, Phosphorescent iridium(III) complexes as multicolor probes for specific mitochondrial imaging and tracking, *Biomaterials.*, 2014, **35**, 2–13.
30. R.R. Ye, C.P. Tan, L. He, M.H. Chen, L.N. Ji, and Z.W. Mao, Cyclometalated Ir(III) complexes as targeted theranostic anticancer therapeutics: combining HDAC inhibition with photodynamic therapy, *Chem. Commun.*, 2014, **50**, 10945–10948.
31. W.-K. Huang, C.-W. Cheng, S.-M. Chang, Y.-P. Lee, and E.W.-G. Diau, Synthesis and electron-transfer properties of benzimidazole-functionalized ruthenium complexes for highly efficient dye-sensitized solar cells, *Chem. Commun.*, 2010, **46**, 8992.
32. M. Vaquero, N. Busto, N. Fernández-Pampín, G. Espino, and B. García, Appended Aromatic Moieties Determine the Cytotoxicity of Neutral Cyclometalated Platinum(II) Complexes Derived from 2-(2-Pyridyl)benzimidazole, *Inorg. Chem.*, 2020, **59**, 4961–4971.
33. E.C. Constable, M. Neuburger, P. Rösel, G.E. Schneider, J.A. Zampese, C.E. Housecroft, F. Monti, N. Armaroli, R.D. Costa, and E. Ortí, Ligand-Based Charge-Transfer Luminescence in Ionic Cyclometalated Iridium(III) Complexes Bearing a Pyrene-Functionalized Bipyridine Ligand: A Joint Theoretical and Experimental Study, *Inorg. Chem.*, 2013, **52**, 885–897.
34. B.J. Coe, M. Helliwell, J. Raftery, S. Sánchez, M.K. Peers, and N.S. Scrutton, Cyclometalated Ir(III) complexes of deprotonated N-methylbipyridinium ligands: effects of quaternised N centre position on luminescence, *Dalt. Trans.*, 2015, **44**, 20392–20405.
35. C.E. Elgar, H.Y. Otaif, X. Zhang, J. Zhao, P.N. Horton, S.J. Coles, J.M. Beames, and S.J.A. Pope, Iridium(III) Sensitisers and Energy Upconversion: The Influence of Ligand Structure upon TTA-UC Performance, *Chem. – A Eur. J.*, 2011, **27**, 3427–3439.
36. L.K. McKenzie, H.E. Bryant, and J.A. Weinstein, Transition metal complexes as photosensitisers in one- and two-photon photodynamic therapy, *Coord. Chem. Rev.*, 2019, **379**, 2–29.
37. C.D. Sunesh, G. Mathai, and Y. Choe, Constructive Effects of Long Alkyl Chains on the Electroluminescent Properties of Cationic Iridium Complex-Based Light-Emitting Electrochemical Cells, *ACS Appl. Mater. Interfaces.*, 2014, **6**, 17416–17425.
38. R.D.R.D.R.D. Costa, E. Ortí, H.J. Bolink, F. Monti, G. Accorsi, N. Armaroli, E. Orti, H.J. Bolink, F. Monti, G. Accorsi, and N. Armaroli, Luminescent ionic transition-metal complexes for light-emitting electrochemical cells, *Angew. Chemie - Int. Ed.*, 2012, **51**, 8178–8211.
39. J.M. Dąbrowski, B. Pucelik, A. Regiel-Futyra, M. Brindell, O. Mazuryk, A. Kyzioł, G. Stochel, W. Macyk, and L.G. Arnaut, Engineering of relevant photodynamic processes through structural modifications of metallotetrapyrrolic photosensitizers, *Coord. Chem. Rev.*, 2016, **325**, 67–101.
40. A.F. Henwood, A.K. Bansal, D.B. Cordes, A.M.Z. Slawin, I.D.W. Samuel, and E. Zysman-Colman, Solubilised bright blue-emitting iridium complexes for solution processed OLEDs, *J. Mater. Chem. C.*, 2016, **4**, 3726–3737.
41. C. Momblona, C.D. Ertl, A. Pertegás, J.M. Junquera-Hernández, H.J. Bolink, E.C. Constable, M. Sessolo, E. Ortí, C.E. Housecroft, Exploring the effect of the cyclometalating ligand in 2-(pyridine-2-yl)benzo[ d

]thiazole-containing iridium( iii ) complexes for stable light-emitting electrochemical cells, *J. Mater. Chem. C.*, 2018, **6**, 12679–12688.

42. D. Tordera, M. Delgado, E. Ortí, H.J. Bolink, J. Frey, M.K. Nazeeruddin, and E. Baranoff, Stable Green Electroluminescence from an Iridium Tris-Heteroleptic Ionic Complex, *Chem. Mater.*, 2012, **24**, 1896–1903.

43. A.F. Henwood, A.K. Pal, D.B. Cordes, A.M.Z. Slawin, T.W. Rees, C. Momblona, A. Babaei, A. Pertegás, E. Ortí, H.J. Bolink, E. Baranoff, and E. Zysman-Colman, Blue-emitting cationic iridium(III) complexes featuring pyridylpyrimidine ligands and their use in sky-blue electroluminescent devices, *J. Mater. Chem. C.*, 2017, **5**, 9638–9650.

44. N. Demir, M. Karaman, G. Yakali, T. Tugsuz, S. Denizalti, S. Demic, B. Dindar, and M. Can, Structure–Property Relationship in Amber Color Light-Emitting Electrochemical Cell with TFSI Counteranion: Enhancing Device Performance by Different Substituents on N  $\wedge$  N Ligand, *Inorg. Chem.*, 2021, **60**, 4410–4423.

45. M. Martínez-Alonso, J. Cerdá, C. Momblona, A. Pertegás, J.M. Junquera-Hernández, A. Heras, A.M. Rodríguez, G. Espino, H. Bolink, E. Ortí, Highly Stable and Efficient Light-Emitting Electrochemical Cells Based on Cationic Iridium Complexes Bearing Arylazole Ancillary Ligands, *Inorg. Chem.*, 2017, **56**, 10298–10310.

46. H. Iranmanesh, K.S.A. Arachchige, M. Bhadbhade, W.A. Donald, J.Y. Liew, K.T.C. Liu, E.T. Luis, E.G. Moore, J.R. Price, H. Yan, J. Yang, and J.E. Beves, Chiral Ruthenium(II) Complexes as Supramolecular Building Blocks for Heterometallic Self-Assembly, *Inorg. Chem.*, 2016, **55**, 12737–12751.

47. R. Bevernaegie, S.A.M. Wehlin, B. Elias, and L. Troian-Gautier, A Roadmap Towards Visible Light Mediated Electron Transfer Chemistry with Iridium(III) Complexes, *ChemPhotoChem.*, 2021, **5**, 217–234.

48. J.-J. Cao, C.-P. Tan, M.-H. Chen, N. Wu, D.-Y. Yao, X.-G. Liu, L.-N. Ji, and Z.-W. Mao, Targeting cancer cell metabolism with mitochondria-immobilized phosphorescent cyclometalated iridium(III) complexes, *Chem. Sci.*, 2017, **8**, 631–640.

49. S. Takizawa, R. Aboshi, and S. Murata, Photooxidation of 1,5-dihydroxynaphthalene with iridium complexes as singlet oxygen sensitizers, *Photochem. Photobiol. Sci.*, 2011, **10**, 895–903.

50. J. Karges, Clinical Development of Metal Complexes as Photosensitizers for Photodynamic Therapy of Cancer, *Angew. Chemie Int. Ed.*, 2022, **61**.

51. L.N. Lameijer, D. Ernst, S.L. Hopkins, M.S. Meijer, S.H.C. Askes, S.E. Le Dévédec, and S. Bonnet, A Red-Light-Activated Ruthenium-Caged NAMPT Inhibitor Remains Phototoxic in Hypoxic Cancer Cells, *Angew. Chemie Int. Ed.*, 2017, **56**, 11549–11553.

52. P. Avci, A. Gupta, and M. Sadasivam, Low-Level Laser (Light) Therapy (LLLT) in Skin: Stimulating, Healing, Restoring, *Semin Cutan Med Surg.*, 2013, **32**, 41–52.

53. C.D. Ertl, J. Cerdá, J.M. Junquera-Hernández, A. Pertegás, H.J. Bolink, E.C. Constable, M. Neuburger, E. Ortí, and C.E. Housecroft, Colour tuning by the ring roundabout: [Ir(C $\wedge$ N) $_2$ (N $\wedge$ N)] $^+$  emitters with sulfonyl-substituted cyclometalating ligands, *RSC Adv.*, 2015, **5**, 42815–42827.

54. C.D. Ertl, L. Gil-Escrig, J. Cerdá, A. Pertegás, H.J. Bolink, J.M. Junquera-Hernández, A. Prescimone, M. Neuburger, E.C. Constable, E. Ortí, and C.E. Housecroft, Regioisomerism in cationic sulfonyl-substituted [Ir(C $\wedge$ N) $_2$ (N $\wedge$ N)] $^+$  complexes: its influence on photophysical properties and LEC performance, *Dalt. Trans.*, 2016, **45**, 11668–11681.

55. M.-H. Chen, F.-X. Wang, J.-J. Cao, C.-P. Tan, L.-N. Ji, and Z.-W. Mao, Light-Up Mitophagy in Live Cells with Dual-Functional Theranostic Phosphorescent Iridium(III) Complexes, *ACS Appl. Mater. Interfaces.*, 2017, **9**, 13304–13314.
56. P. Coppo, E.A. Plummer, and L. De Cola, Tuning iridium(III) phenylpyridine complexes in the “almost blue” region, *Chem. Commun.*, 2004, **4**, 1774–1775.
57. J. Torres, M.C. Carrión, J. Leal, F.A. Jalón, J. V. Cuevas, A.M. Rodríguez, G. Castañeda, and B.R. Manzano, Cationic Bis(cyclometalated) Ir(III) Complexes with Pyridine–Carbene Ligands. Photophysical Properties and Photocatalytic Hydrogen Production from Water, *Inorg. Chem.*, 2018, **57**, 970–984.
58. H.J. Bolink, E. Coronado, R.D. Costa, N. Lardiés, and E. Ortí, Near-Quantitative Internal Quantum Efficiency in a Light-Emitting Electrochemical Cell, *Inorg. Chem.*, 2008, **47**, 9149–9151.
59. J.S. Nam, M.-G. Kang, J. Kang, S.-Y. Park, S.J.C. Lee, H.-T. Kim, J.K. Seo, O.-H. Kwon, M.H. Lim, H.-W. Rhee, and T.-H. Kwon, Endoplasmic Reticulum-Localized Iridium(III) Complexes as Efficient Photodynamic Therapy Agents via Protein Modifications, *J. Am. Chem. Soc.*, 2016, **138**, 10968–10977.
60. T.C. Motley, L. Troian-Gautier, M.K. Brennaman, and G.J. Meyer, Excited-State Decay Pathways of Tris(bidentate) Cyclometalated Ruthenium(II) Compounds, *Inorg. Chem.*, 2017, **56**, 13579–13592.
61. K.T. Ngo, N.A. Lee, S.D. Pinnace, D.J. Szalda, R.T. Weber, and J. Rochford, Probing the Noninnocent  $\pi$ -Bonding Influence of *N*-Carboxyamidoquinolate Ligands on the Light Harvesting and Redox Properties of Ruthenium Polypyridyl Complexes, *Inorg. Chem.*, 2016, **55**, 2460–2472.
62. C. Yagüe, I. Echevarría, M. Vaquero, J. Fidalgo, A. Carbayo, F.A. Jalón, J.C. Lima, A.J. Moro, B.R. Manzano, and G. Espino, Non-emissive Ru II Polypyridyl Complexes as Efficient and Selective Photosensitizers for the Photooxidation of Benzylamines, *Chem. – A Eur. J.*, 2020, **26**, 12219–12232.
63. O.J. Stacey, and S.J.A. Pope, New avenues in the design and potential application of metal complexes for photodynamic therapy, *RSC Adv.*, 2013, **3**, 25550.
64. M. Li, R. Tian, J. Fan, J. Du, S. Long, and X. Peng, A lysosome-targeted BODIPY as potential NIR photosensitizer for photodynamic therapy, *Dye. Pigment.*, 2017, **147**, 99–105.
65. X.-F. Zhang, and X. Li, The photostability and fluorescence properties of diphenylisobenzofuran, *J. Lumin.*, 2011, **131**, 2263–2266.
66. L. He, K.-N. Wang, Y. Zheng, J.-J. Cao, M.-F. Zhang, C.-P. Tan, L.-N. Ji, and Z.-W. Mao, Cyclometalated iridium(III) complexes induce mitochondria-derived paraptotic cell death and inhibit tumor growth in vivo, *Dalt. Trans.*, 2018, **47**, 6942–6953.
67. J.-J. Cao, Y. Zheng, X.-W. Wu, C.-P. Tan, M.-H. Chen, N. Wu, L.-N. Ji, and Z.-W. Mao, Anticancer Cyclometalated Iridium(III) Complexes with Planar Ligands: Mitochondrial DNA Damage and Metabolism Disturbance, *J. Med. Chem.*, 2019, **62**, 3311–3322.
68. C. Zhang, R. Guan, X. Liao, C. Ouyang, J. Liu, L. Ji, and H. Chao, Mitochondrial DNA targeting and impairment by a dinuclear Ir–Pt complex that overcomes cisplatin resistance, *Inorg. Chem. Front.*, 2020, **7**, 1864–1871.
69. E. Baggaley, J.A. Weinstein, and J.A. a G. Williams, Lighting the way to see inside the live cell with luminescent transition metal complexes, *Coord. Chem. Rev.*, 2012, **256**, 1762–1785.



70. X. Tian, Y. Zhu, M. Zhang, L. Luo, J. Wu, H. Zhou, L. Guan, G. Battaglia, and Y. Tian, Localization matters: a nuclear targeting two-photon absorption iridium complex in photodynamic therapy, *Chem. Commun.*, 2017, **53**, 3303–3306.
71. T. Kirchhausen, E. Macia, and H.E. Pelish, Use of Dynasore, the Small Molecule Inhibitor of Dynamin, in the Regulation of Endocytosis, *Methods Enzymol.*, 2008, 77–93.
72. D. van Straten, V. Mashayekhi, H. de Bruijn, S. Oliveira, and D. Robinson, Oncologic Photodynamic Therapy: Basic Principles, Current Clinical Status and Future Directions, *Cancers (Basel)*, 2017, **9**, 19.
73. J. Zielonka, J. Joseph, A. Sikora, M. Hardy, O. Ouari, J. Vasquez-Vivar, G. Cheng, M. Lopez, and B. Kalyanaraman, Mitochondria-Targeted Triphenylphosphonium-Based Compounds: Syntheses, Mechanisms of Action, and Therapeutic and Diagnostic Applications, *Chem. Rev.*, 2017, **117**, 10043–10120.
74. R. Guan, L. Xie, T.W. Rees, L. Ji, and H. Chao, Metal complexes for mitochondrial bioimaging, *J. Inorg. Biochem.*, 2020, **204**, 110985.
75. C. Caporale, and M. Massi, Cyclometalated iridium(III) complexes for life science, *Coord. Chem. Rev.*, 2018, **363**, 71–91.
76. J.J. Hu, N.-K. Wong, S. Ye, X. Chen, M.-Y. Lu, A.Q. Zhao, Y. Guo, A.C.-H. Ma, A.Y.-H. Leung, J. Shen, and D. Yang, Fluorescent Probe HKSOX-1 for Imaging and Detection of Endogenous Superoxide in Live Cells and In Vivo, *J. Am. Chem. Soc.*, 2015, **137**, 6837–6843.
77. L.D. Zorova, V.A. Popkov, E.Y. Plotnikov, D.N. Silachev, I.B. Pevzner, S.S. Jankauskas, V.A. Babenko, S.D. Zorov, A. V. Balakireva, M. Juhaszova, S.J. Sollott, and D.B. Zorov, Mitochondrial membrane potential, *Anal. Biochem.*, 2018, **552**, 50–59.
78. M. Ouyang, L. Zeng, K. Qiu, Y. Chen, L. Ji, and H. Chao, Cyclometalated Ir III Complexes as Mitochondria-Targeted Photodynamic Anticancer Agents, *Eur. J. Inorg. Chem.*, 2017, 1764–1771.
79. Y. Li, K.N. Wang, L. He, L.N. Ji, and Z.W. Mao, Synthesis, photophysical and anticancer properties of mitochondria-targeted phosphorescent cyclometalated iridium(III) N-heterocyclic carbene complexes, *J. Inorg. Biochem.*, 2020, **205**.
80. O. Haapanen, and V. Sharma, Redox- and protonation-state driven substrate-protein dynamics in respiratory complex I, *Curr. Opin. Electrochem.*, 2021, **29**, 100741.
81. H. Huang, S. Banerjee, K. Qiu, P. Zhang, O. Blacque, T. Malcomson, M.J. Paterson, G.J. Clarkson, M. Staniforth, V.G. Stavros, G. Gasser, H. Chao, and P.J. Sadler, Targeted photoredox catalysis in cancer cells, *Nat. Chem.*, 2019, **11**, 1041–1048.
82. B. Van Houten, V. Woshner, and J.H. Santos, Role of mitochondrial DNA in toxic responses to oxidative stress, *DNA Repair (Amst)*, 2006, **5**, 145–152.
83. A. Kellett, Z. Molphy, C. Slator, V. McKee, and N.P. Farrell, Molecular methods for assessment of non-covalent metallodrug–DNA interactions, *Chem. Soc. Rev.*, 2019, **48**, 971–988.
84. J. Leal, L. Santos, D.M. Fernández-Aroca, J.V. Cuevas, M.A. Martínez, A. Massaguer, F.A. Jalón, M.J. Ruiz-Hidalgo, R. Sánchez-Prieto, A.M. Rodríguez, G. Castañeda, G. Durá, M.C. Carrión, S. Barrabés, and B.R. Manzano, Effect of the aniline fragment in Pt(II) and Pt(IV) complexes as anti-proliferative agents. Standard reduction potential as a more reliable parameter for Pt(IV) compounds than peak reduction potential, *J. Inorg. Biochem.*, 2021, **218**, 111403.

85. J.L. García-Giménez, M. González-Alvarez, M. Liu-González, B. Macías, J. Borrás, and G. Alzuet, Toward the development of metal-based synthetic nucleases: DNA binding and oxidative DNA cleavage of a mixed copper(II) complex with N-(9H-purin-6-yl)benzenesulfonamide and 1,10-phenanthroline. Antitumor activity in human Caco-2 cells and Jurkat T lymphocy, *J. Inorg. Biochem.*, 2009, **103**, 923–934.
86. J.-J. Cao, Y. Zheng, X.-W. Wu, C.-P. Tan, M.-H. Chen, N. Wu, L.-N. Ji, and Z.-W. Mao, Anticancer Cyclometalated Iridium(III) Complexes with Planar Ligands: Mitochondrial DNA Damage and Metabolism Disturbance, *J. Med. Chem.*, 2019, **62**, 3311–3322.
87. Z.H. Siddik, Cisplatin: Mode of cytotoxic action and molecular basis of resistance, *Oncogene.*, 2003, **22**, 7265–7279.
88. M. Kielbik, D. Krzyzanowski, B. Pawlik, and M. Klink, Cisplatin-induced ERK1/2 activity promotes G1 to S phase progression which leads to chemoresistance of ovarian cancer cells, *Oncotarget.*, 2018, **9**, 19847–19860.
89. E. Buytaert, M. Dewaele, and P. Agostinis, Molecular effectors of multiple cell death pathways initiated by photodynamic therapy, *Biochim. Biophys. Acta - Rev. Cancer.*, 2007, **1776**, 86–107.



---

***Part 2. Ru(II) and Ir(III) tris-chelate complexes for photocatalysis***

---

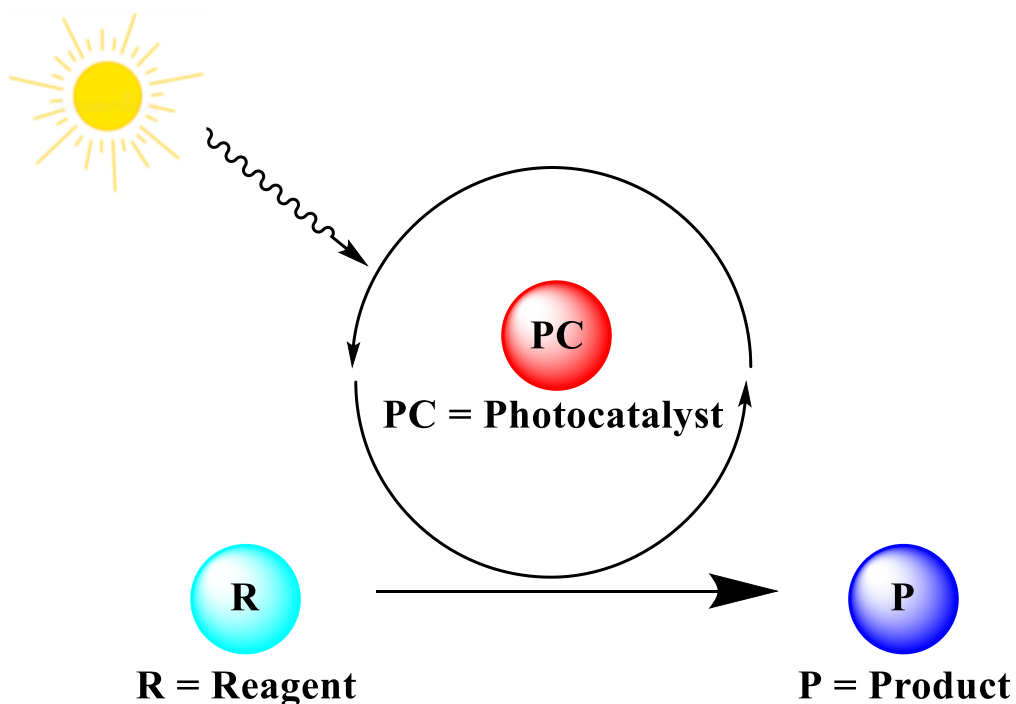




## Objectives

Main Objective: To design and develop new metal-based complexes as potential photocatalysts (PCs) for photocatalysis. This objective can be divided in various secondary objectives:

- To study the relationship between the structure and the photophysical properties of the PSs.
- To study the relationship between the photophysical properties and the photocatalytic performance of the PCs.
- To develop eco-friendly or green procedures to accomplish chemical transformations of potential industrial interest under mild conditions.







---

# *Photocatalysis*

---







# 1. From catalysis to photocatalysis

## 1.1. Catalysis

### 1.1.1. Historical development and definition

Since ancient times, it has been known that the addition of small quantities of some materials could lead to important changes in the composition of other materials. However, there was not a precise explanation for this phenomenon, so it was attributed to philosopher's stone.<sup>1,2</sup> The term catalysis was first used by J. Berzelius in 1835 to describe substances which were able to accelerate a reaction without being consumed during the process. Later, in 1894, W. Ostwald proposed a more precise definition: "Catalysis is the acceleration of a slow chemical process by the presence of a foreign material". This definition also led to a more precise definition of catalyst: "A catalyst is a material that changes the rate of a chemical reaction without appearing in the final products."<sup>2</sup> W. Ostwald did not possess the technical elements required for completely understanding a catalytic process, but his studies in the field led to important advances<sup>3</sup> like the Haber–Bosch process for producing ammonia at industrial scale with an iron catalyst developed by A. Mittasch, (an W. Ostwald's student), which is still in use today,<sup>4</sup> and the industrial production of nitric acid with a platinum catalyst (commonly known as the Ostwald process, which was developed by W. Ostwald and E. Brauer, his son-in-law).<sup>5</sup>

Thus, catalysts are agents that increase the speed of the reactions maintaining their initial state at the end of the process (they participate in a catalytic cycle and are regenerated upon every complete round). It is important to note that catalysts only maintain their initial state ideally; in fact, due to the interactions that they establish, a fraction of the catalyst can fail to recover its initial state completely. So, cycle by cycle they undergo a slight deactivation, eventually needing to be regenerated or substituted.<sup>6,7,8</sup>

### 1.1.2. Main types of catalysis and applications

Catalysis can be classified in two main categories: heterogeneous and homogeneous catalysis.<sup>6</sup> In heterogeneous catalysis, the catalyst and the reagents are in different phases. Most heterogeneous catalysts are solids which act over a liquid or gas mixture. Some frequently used heterogeneous catalysts are transition metal oxides, higher order oxides, zeolites, graphitic carbon, alumina, etc. Heterogeneous catalysts are frequently supported, which means that they are dispersed over a second material that increases its activity and decreases its cost. Sometimes, the supporting material is only used to avoid the aggregation of the catalyst, increasing in this way the surface area of the catalyst, thereby increasing its efficacy. But frequently, the supporting material also interacts with the catalyst, having an effect over the whole process. Supporting

materials or supports are very porous materials, which present a great surface area. Among common supports zeolites, alumina and activated carbon are the most popular. Nevertheless, there are others like titanium and silicon dioxides, barium sulphate and calcium carbonate.<sup>8,9,10,11,12</sup>

Heterogeneous catalysis is the preferred type of catalysis for the industry because of the easiness of removing the catalyst from the reaction mixture after the end of the process. This allows the easy recovery and reuse of the catalyst, and lowers the purifying costs of the product of interest. Common industrial examples of heterogeneous catalysis include synthesis of ammonia (Haber–Bosch process), synthesis of nitric acid (Ostwald process), synthesis of sulfuric acid (Contact process), synthesis of hydrogen cyanide (Andrussov oxidation), synthesis of ethylene oxide, olefin polymerization (Ziegler–Natta polymerization), production of hydrogen by steam reforming and desulfurization of petroleum (hydrodesulfurization).<sup>13,14</sup>

In the case of homogeneous catalysis, the catalyst and the reagents are in the same phase, usually in solution. Some common homogeneous catalysts are transition metals, organocatalysts, organometallic complexes (nowadays these are the preferred and most popular), Bronsted and Lewis acids, etc. Thanks to the homogeneity of the catalyst and the reagents, the interactions between them are favoured, meaning that they are more intense and more probable than in the case of heterogeneous catalysis, which results in a higher selectivity and reactivity, and in milder reaction conditions. Moreover, homogeneous catalysis allows a better control of operating conditions.<sup>6,15,16</sup> Some interesting reactions that can be carried out with homogeneous catalysis are: hydrogenation and related reactions (hydrosilylation and hydrocyanation), carbonylations (the obtention of acetic acid from methanol by the Monsanto and Cativa processes, or hydroformylations conducted with rhodium and cobalt complexes), polymerization and metathesis of alkenes (the obtention of several polyolefins from propylene and ethylene by the Ziegler–Natta catalysis) and oxidations (the production of acetaldehyde from ethane by the Wacker process, the epoxidization of alkenes by the Halcon process, and the dihydroxylation of alkenes by the Sharpless dihydroxylation). However, it is true that many of these transformations can be performed using heterogeneous catalysts, which is the preferred option in industry, but for the synthesis of fine chemicals homogeneous catalysis is the preferred alternative.<sup>16,17</sup>

In addition to heterogeneous and homogeneous catalysis, usually a third type of catalysis is considered: the enzymatic catalysis (also called biocatalysis). It is usually described as a third class even though it can be both heterogeneous or homogeneous depending on the enzyme type: enzymes that are in solution in the cellular media can be considered as homogeneous catalysts, and those which are bounded to a membrane can be considered as heterogeneous catalysts.<sup>6,13,18</sup>

It is worth mentioning that aside the catalytic reactions mentioned above, there are other important types of catalytic reactions like redox catalysis, acid-base catalysis and polyfunctional catalysis.<sup>17</sup> Indeed, catalysis has a great relevance in our society and it will undoubtedly play a critical role in future developments, in several fields such as energy production/storage and food processing, obtention of bulk and fine chemicals, and environmental issues.<sup>19,20</sup> In the energetic sector, petroleum refining uses catalysis for various processes such as alkylation, cracking, and naphtha and steam reforming. Other examples of the use of catalysis within the energy field can be found in the Fischer-Tropsch process, where hydrocarbons are obtained from synthesis gas,<sup>21,22,23</sup> in the production of biofuels,<sup>21,22</sup> in fuel cells<sup>23</sup> and in catalytic heaters.<sup>24</sup> In the food industry, the hydrogenation of fats for the production of margarine is the most common example,<sup>25</sup> but there are other processes, in this case mediated by biocatalytic reactions, as the production of high-fructose corn syrup,<sup>26</sup> beer, wine, cheese, etc.,<sup>27</sup> all of which are of a capital importance. In the case of bulky chemicals, as mentioned before, some important chemicals like sulphuric acid, nitric acid, terephthalic acid, acrylic acid and acrylonitrile are obtained by catalytic oxidations.<sup>28,29</sup> Several polyolefins are obtained from propylene and ethylene by the Ziegler-Natta catalysis.<sup>30</sup> Moreover, carbonylations such as the Monsanto process for the obtainment of acetic acid and hydroformylation require metal catalysts.<sup>31</sup> Furthermore, the obtaining of methanol (starting from carbon monoxide or carbon dioxide) is accomplished with copper-zinc catalysts.<sup>32</sup> In the case of fine chemicals, many of them are prepared via catalytic reactions such as Heck<sup>33</sup> and Friedel–Crafts<sup>34</sup> reactions, or in the case of chiral chemicals, which are very common among the drugs, via enantioselective catalysis.<sup>35</sup> Finally, in environmental related applications, it is remarkable that the exhaust created from the burning of fossil fuels is treated with catalytic converters to reduce their environmental impact.<sup>36</sup> Moreover, the use of catalysts increases intrinsically the efficiency of industrial processes, so the same production volume is accomplished with less wastes and less consume of energy and feedstocks.<sup>37,38</sup>

## 1.2. Photocatalysis

### 1.2.1. Historical development and definition

In 1901, Giacomo Ciamician studied whether light could drive a chemical reaction. For this purpose, he studied the effect of blue and red lights over reactions, observing an effect only when irradiated with blue light. It is worth mentioning, that it was careful enough to discard that the observed effect was not produced by the thermal heating induced by the interaction between light and matter.<sup>39</sup> The first time that the term photocatalysis appeared, was in 1911. The term was used by Eibner to describe the bleaching of Prussian blue using ZnO under irradiation.<sup>40</sup> This work inspired the use of ZnO for other reactions in presence of light, like the reduction of  $\text{Ag}^+$  to Ag,

accomplished in 1924 by Baur and Perret.<sup>41</sup> Back again in 1911, Bruner and Kozak also used the term photocatalysis to describe the degradation of oxalic acid in presence of uranium salts under irradiation.<sup>42</sup> In 1921, the term appeared again, this time in the title of an article published by Baly and co-workers. However, in this article the term was used to describe a reaction which was speeded up by light.<sup>43</sup> So, although photosensitive reactions had been known for a long time, the nature of this phenomenon was unclear.<sup>44</sup>

Apart from these important steps in the development of photocatalysis, prior to them there was another important fact that frequently lies underrated. If it is considered that the main inspiration for photocatalysis lies in natural photosynthesis, it is important to also give the proper credit to Edmond Becquerel, who discovered the photovoltaic effect in 1839, a crucial discovery that prompted the development of photocatalysis and other related areas.<sup>9,45,46</sup>

In 1932, the photocatalytic reduction of  $\text{AgNO}_3$  to Ag and  $\text{AuCl}_3$  to Au driven by  $\text{TiO}_2$  and  $\text{Nb}_2\text{O}_5$  respectively were demonstrated.<sup>47,48</sup> These results led to researching the use of  $\text{TiO}_2$  as a photosensitizer (PS) for bleaching dyes in presence of oxygen, which was accomplished in 1938.<sup>49,50</sup> Then, in 1964, Doerffler and Hauffe published two scientific articles where the description of the term photocatalysis involved the combination of both light and a catalyst, the so-called photocatalyst (PC).<sup>51,52</sup> However, due to the lack of widespread applications, photocatalysis did not acquired relevance until the end of the 1960s and early 1970s. This happened mainly due to the oil crisis, which underscored the need to discover new energy supplies different from fossil fuels.<sup>53</sup> Moreover, because of the growing concern about the environmental impacts caused by the industrial processes and the need of renewable or greener energy sources to lower these impacts.<sup>54</sup> In 1968, Boddy reported for the first time the evolution of  $\text{O}_2$  from  $\text{H}_2\text{O}$  upon UV irradiation in the presence of  $\text{TiO}_2$ .<sup>55</sup> This work led to the event which is considered by most as the real start of the investigation in the field of photocatalysis: the electrochemical water splitting conducted with  $\text{TiO}_2$  under UV light irradiation, published in 1972 by Fujishima and Honda.<sup>56</sup> This work represented a milestone in the area of catalysis. Later, in 1977 Schrauzer and Guth achieved the photocatalytic water splitting without any other energy source than UV light irradiation. Moreover, they accidentally observed the photoreduction of nitrogen to  $\text{NH}_3$  and  $\text{N}_2\text{H}_4$  assisted by  $\text{TiO}_2$ .<sup>57</sup>

After this, studies like the photodecomposition of  $\text{CN}^-$  and  $\text{SO}_3^{2-}$  conducted by  $\text{TiO}_2$ , CdS and  $\text{ZnO}$ ,<sup>58</sup> or the photocatalytic  $\text{CO}_2$  reduction assisted by inorganic semiconductors appeared.<sup>59</sup> A tendency that continued over the 1980s, with the attention mainly focused on  $\text{TiO}_2$  nanoparticles as photocatalysts.<sup>60,61,62</sup> After this,

the attention in the photocatalysis research field has been focused on the understanding of the basic principles, improving the efficiencies of the photocatalytic processes, finding or developing new photocatalysts (specially visible light absorbing PCs), broadening the reaction scope and discovering new applications.<sup>63,64,65</sup>

So, after seeing the historical development of photocatalysis, now it is time to define it. In the scientific literature, the term photocatalysis has been used to describe two different processes.<sup>66</sup> One of them is the use of light energy and a material (a PC) to carry out reactions which are thermodynamically uphill (reactions which possess a positive value of Gibbs free energy). This is not technically precise, and this process should be strictly named as photosynthesis instead of photocatalysis.<sup>67,68</sup> Examples of this kind include the water splitting<sup>69,70</sup> and the CO<sub>2</sub> reduction.<sup>71</sup>

The other process that is described under the name of photocatalysis, and which correctly fits this term, is the use of a PC and light to facilitate chemical reactions which are thermodynamically downhill (negative values of the free energy of Gibbs). In this case, the material does not need to change the thermodynamics of the reaction, only the kinetics by creating new pathways for the reaction after light absorbance. The material which accomplishes this task can be genuinely called photocatalyst.<sup>67,68</sup> An example of this type of processes could be the oxidation of phenol to hydroquinone with oxygen or its complete oxidation to H<sub>2</sub>O and CO<sub>2</sub>.<sup>72,73</sup>

However, it should be mentioned, that IUPAC gives a broader definition for the concepts of photocatalysis and photocatalyst avoiding discussing these technical issues. For the IUPAC, a photocatalyst is a “catalyst able to produce, upon absorption of light, chemical transformations of the reaction partners. The excited state of the photocatalyst repeatedly interacts with the reaction partners forming reaction intermediates and regenerates itself after each cycle of such interactions.” and therefore, photocatalysis is defined as “change in the rate of a chemical reaction or its initiation under the action of ultraviolet, visible or infrared radiation in the presence of a substance—the photocatalyst—that absorbs light and is involved in the chemical transformation of the reaction partners”,<sup>74</sup> which permits to fit the afore-mentioned processes under the term photocatalysis.

### 1.2.2. A brief view inside the mechanism

Most of the PCs used in photocatalytic transformations are essentially semiconductors. Semiconductors possess a band gap, also known as energy gap

( $E_g$ ), which usually has a value between 1.5 and 3 eV, whereas, metals possess a band gap lower than 1 eV, and insulators a band gap higher than 5 eV. The band gap is the energy difference between the valence band (HOMO) and the conduction band (LUMO). Semiconductors work as PCs due to their ability to conduct electricity at room temperature when exposed to light. Thus, when a semiconductor is irradiated with light of an adequate wavelength, a light form with enough energy, an electron of the valence band (VB) is excited or promoted to the conduction band (CB), also generating a hole in the valence band. Consequently, an electron-hole pair is generated in the photocatalyst as a result of light absorption (Fig. 1).<sup>75,76,77</sup>

A PC is able to act efficiently as both an efficient reductant (through valence band holes) and an efficient oxidant (through excited electrons) depending on the relative energy levels of the VB and CB of the PC and the redox potentials of the substrate of interest.<sup>78,79</sup> This leads to 4 different options: the reduction of the substrate when its redox potential is lower than the CB of the PC, the oxidation of the substrate when its redox potential is higher than the VB of the PC, both the reduction and the oxidation of the substrate when its redox potential is lower than the CB and higher than the VB of the PC, and neither the oxidation nor the reduction of the substrate, when its redox potential is higher than the CB and lower than the VB of the PC (Fig. 1).<sup>80,81</sup>

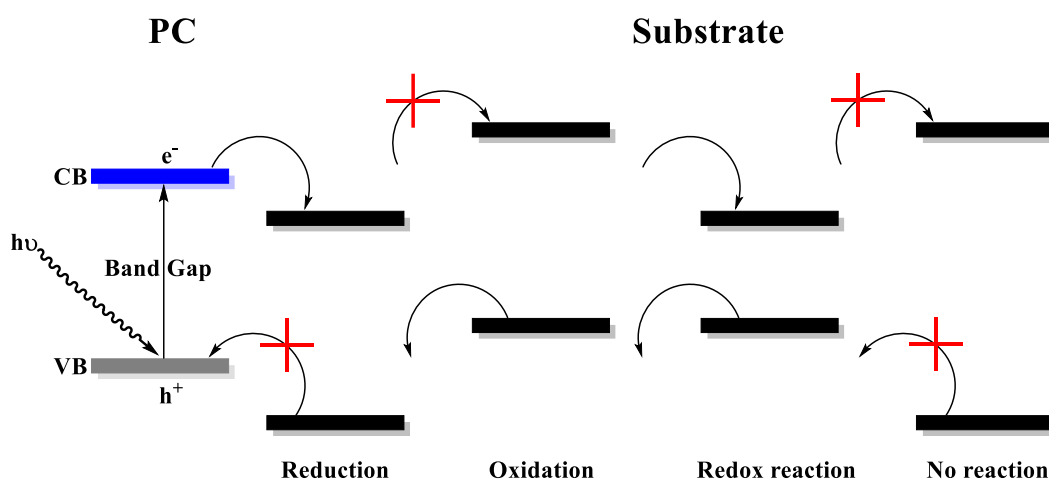


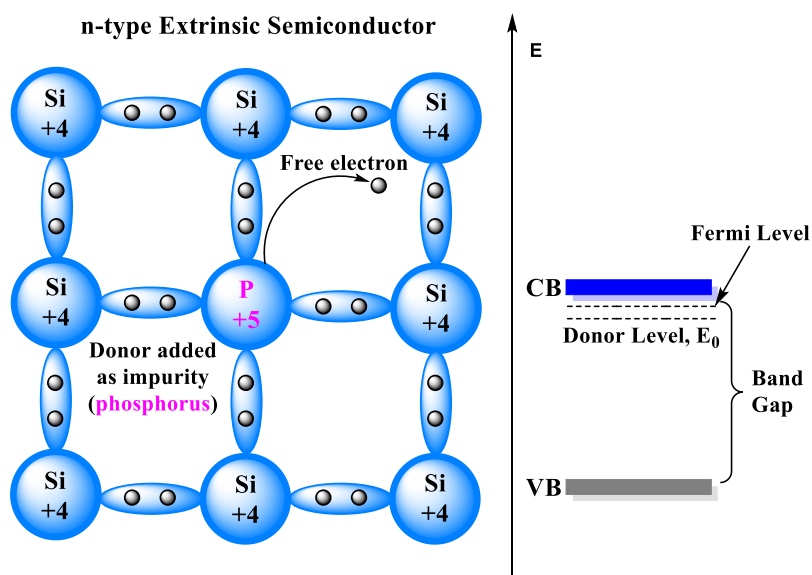
Fig. 1. Different reaction possibilities after irradiating a PC, depending on the relative energy levels of the VB and CB of the PC and the redox potentials of the substrate.

### 1.2.3. Main types of photocatalysis and applications

Photocatalysis is divided in two major classes: heterogeneous and homogeneous. Some common heterogeneous photocatalysts are binary, ternary

and quaternary oxides.<sup>80</sup> Binary oxides, which are the most common, are usually divided in three groups:  $\text{TiO}_2$ ,  $\text{ZnO}$ , and other metal oxides such as  $\text{MoO}_3$ ,  $\text{V}_2\text{O}_5$ ,  $\text{In}_2\text{O}_3$ ,  $\text{WO}_3$ ,  $\text{CeO}_2$ ,  $\text{Fe}_2\text{O}_3$ ,  $\text{CdO}$ ,  $\text{Al}_2\text{O}_3$ .<sup>82</sup> In the case of ternary oxides some examples are  $\text{ZnFe}_2\text{O}_4$ ,<sup>83</sup>  $\text{Sr}_7\text{Fe}_{10}\text{O}_{22}$ , and  $\text{SrFe}_{12}\text{O}_{19}$ ,<sup>84</sup>  $\text{PbCrO}_4$ ,  $\text{PbMoO}_4$ ,  $\text{PbWO}_4$ ,<sup>85</sup> and  $\text{ZnS-Ag}_2\text{S-RGO}$  (reduced graphene oxide) composite.<sup>86</sup> And for quaternary oxides, some common examples are  $\text{Bi}_4\text{Nb}_x\text{Ta}_{1-x}\text{O}_8$ ,<sup>87</sup>  $\text{MnCoTiO}_2$ <sup>88</sup> and  $\text{Pb}_2\text{FeNbO}_6$ .<sup>89</sup>

There are several techniques to improve the performance of heterogeneous PCs: doping, co-doping, coupling PCs (composite), sensitization and substitution, though doping is by far the most widespread strategy. Doping consists in reducing the band gap by adding impurities to the PC, improving in this way the photo-responsiveness of the PC to the visible region of the electromagnetic spectrum.<sup>80</sup> This occurs because the impurities create new energy levels between the VB and the CB. There are two types of impurities, type N or negative dopants and type P or positive dopants. Type N impurities possess more valence electrons than the PC, acting as donors by adding a free electron to the PC and creating in this way a new energy level with electrons below the CB. Type P dopants possess less valence electrons than the PC, acting as acceptors, adding a hole or a vacant to the PC, which leads to the creation of a new energy level with holes above the VB (Fig. 2).<sup>9,90,91,92</sup>



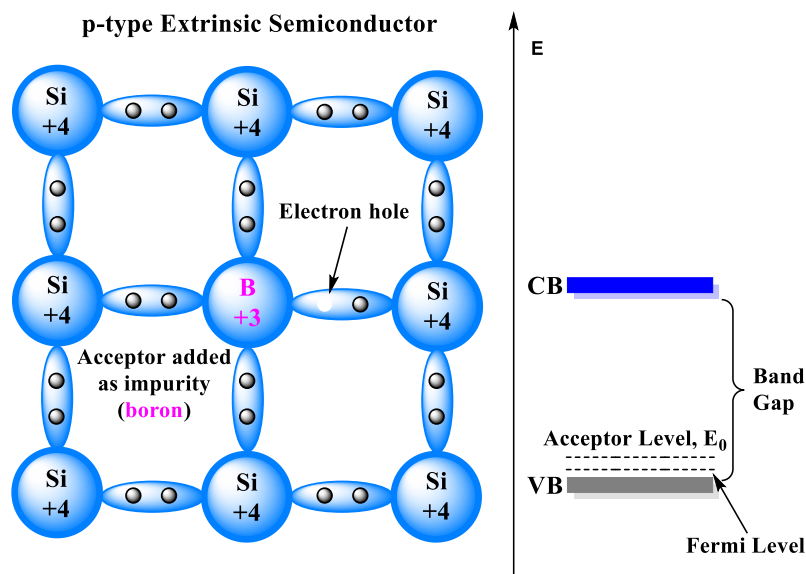


Fig. 2. Schematic representation of n-type and p-type extrinsic semiconductors.

Heterogeneous photocatalysts are the preferred option for industrial applications over homogeneous photocatalysts due to their higher chemical stability, lower cost, commercial availability, non-toxicity and easy separation of PC from reaction products. The most used heterogeneous PCs are TiO<sub>2</sub> and ZnO based composites.<sup>93,94</sup> Heterogeneous photocatalysis is used, among others, for the removal of organic and inorganic pollutants from industrial wastewaters,<sup>95</sup> and also from the air, for disinfecting water<sup>96</sup> and for synthetic purposes, to achieve greener and more sustainable industrial processes.<sup>97</sup>

In homogeneous photocatalysis, the PC and the reagents are in the same phase.<sup>9</sup> Common homogeneous PCs are transition metal complexes like rhenium and ruthenium diimine-carbonyl complexes, nickel and cobalt tetraazamacrocycles, iron, copper and manganese porphyrins, ruthenium polypyridyl complexes, iridium biscyclometalated complexes, polyoxometalates (POMs).<sup>98,99,100</sup> and also some organic dyes like Rose Bengal (RB), Eosin Y (EY) and Methylene Blue (MB).<sup>100</sup> Even though as stated before, heterogeneous photocatalysts are the industrial preferred option, homogeneous photocatalysts possess several applications such as CO<sub>2</sub> reduction,<sup>98,100,101</sup> water oxidation,<sup>98,100</sup> air purification, wastewater treatment, soil decontamination<sup>100</sup>, and specially in organic synthesis, where they are used to produce fine chemicals in a wide variety of reactions like reduction of electron-poor olefins, reductive dehalogenation, nitrogen functional group reductions, functional group oxidations, radical cyclizations, oxidative generation of iminium ions, cycloadditions, photoredox organocatalysis, arylation, alkylation and trifluoromethylation of arenes.<sup>99</sup> A deeper discussion of homogeneous



photocatalysis can be found below (section 2), which is specifically centred in PCs based on iridium(III) and ruthenium(II) trischelate complexes and reactions carried out by them, being this the main goal of this section.

As in the case of catalysis, the enzymes or biocatalysts constitute a third type of photocatalysis. They are also relevant thanks to their ability to catalyze reactions under mild conditions showing high efficiency and selectivity. Because of this, there is a rising interest in creating PCs that imitate their behaviour by designing hybrid PCs with enzymes.<sup>101,102,103</sup>

Photocatalysis has a great impact nowadays, finding applications in very diverse processes. An interesting example is the hydrogen production based on photocatalytic water splitting, that has gained importance due to the fact that its production involves the use of green energy from the sunlight, and because using hydrogen as fuel allows to reduce or to avoid the use of fossil fuels, which is discredited by severe environmental issues.<sup>104</sup> For this purpose, TiO<sub>2</sub> loaded with NiO to increase its efficiency is the main option.<sup>105</sup> The production of self-cleaning glasses is another interesting use of photocatalysis. For this aim, TiO<sub>2</sub> is used, thanks to the free radicals (hydroxyl radicals) photocatalytically generated from water that oxidize organic matter.<sup>106</sup> Solar water disinfection or SODIS is another application for photocatalysis, and more specifically for TiO<sub>2</sub>. The ROS generated under irradiation in its presence, destroy the bacteria present in water, making it safe to drink. Moreover, ROS also destroy undesired organic matter present in water.<sup>107</sup> Other related uses are the self-sterilizing photocatalytic coatings of TiO<sub>2</sub> to prevent the presence of pathogens in surfaces in contact with food and other environments where they usually spread,<sup>108</sup> and the sterilization of health care facilities, which can be easily and cheaply accomplished with a TiO<sub>2</sub> membrane and a UV lamp.<sup>109</sup> It is worth mentioning the applicability of photocatalysis for coping with environmental issues, like decontamination of groundwater by using adsorbents with photoactive catalysts,<sup>110</sup> or the decomposition of waste crude oil (into H<sub>2</sub>O and CO<sub>2</sub>)<sup>111</sup> and polyaromatic hydrocarbons (PAHs),<sup>112</sup> both accomplished by TiO<sub>2</sub>.

## 2. Photocatalysis with Ir(III) and Ru(II) tris-chelate complexes

Ir(III) and Ru(II) tris-chelate complexes own very interesting photophysical properties, making them an attractive option for photocatalysis, more specifically for photoredox catalysis (a type of photocatalytic reactions based on single-electron transfer steps).<sup>113</sup> The key to their excellent photocatalytic activity lies in the fact that this kind of

compounds are both very good oxidants and reductants in their excited state, leading to a rich photoredox chemistry. Moreover, the redox potentials of these complexes can be easily modified by simple changes in their structure, making them a really interesting option to carry out a wide range of photocatalytic reactions.<sup>114</sup>

When the PC is in its excited state (upon light irradiation) the photoredox reactions can take place through two main reaction pathways: the PC can act as an oxidant through a reductive quenching cycle, or it can act as a reductant, taking part in an oxidative quenching cycle, depending on the substrate. The PC which results from the first single electron transfer, suffers a second single electron transfer, being oxidised or reduced, to recover the initial oxidation state (OS) (Fig. 3). Sometimes, there is a third mechanism, which occurs when the PC in its excited state acts as an energy donor instead of taking part in electron transfer steps (Fig. 3). Also, it is worth mentioning that there are non-radiative decay phenomena that compete with both the electron and energy transfer processes.<sup>115,116</sup>

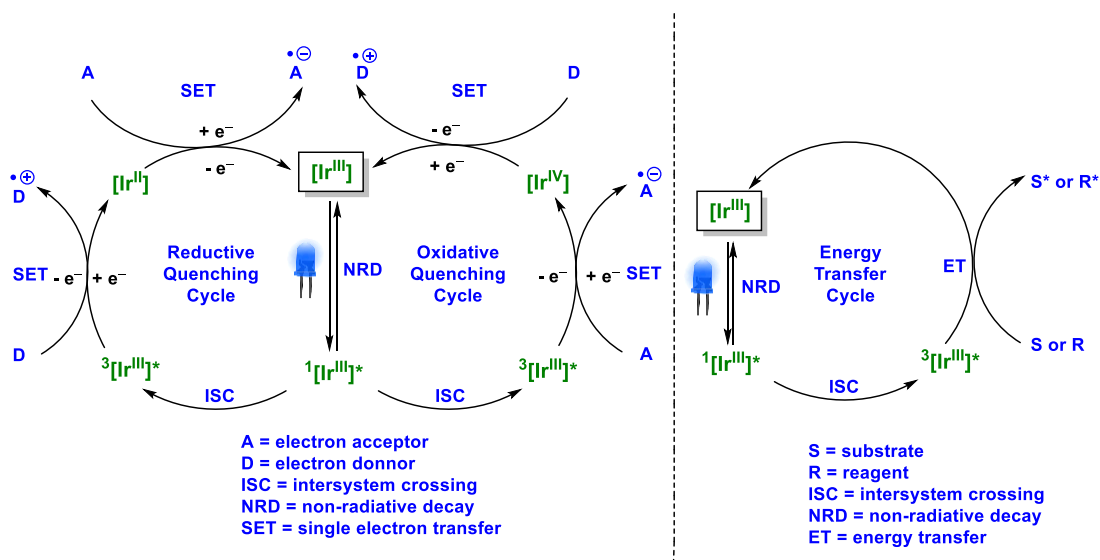


Fig. 3. Main reaction pathways for photoredox catalysis using an Ir(III) PC as example.

There is a wide variety of Ir(III) and Ru(II) tris-chelate complexes that have been used in photocatalysis. Some of the most representative examples, which are commercially available, are summarized in Fig. 4.<sup>117</sup>

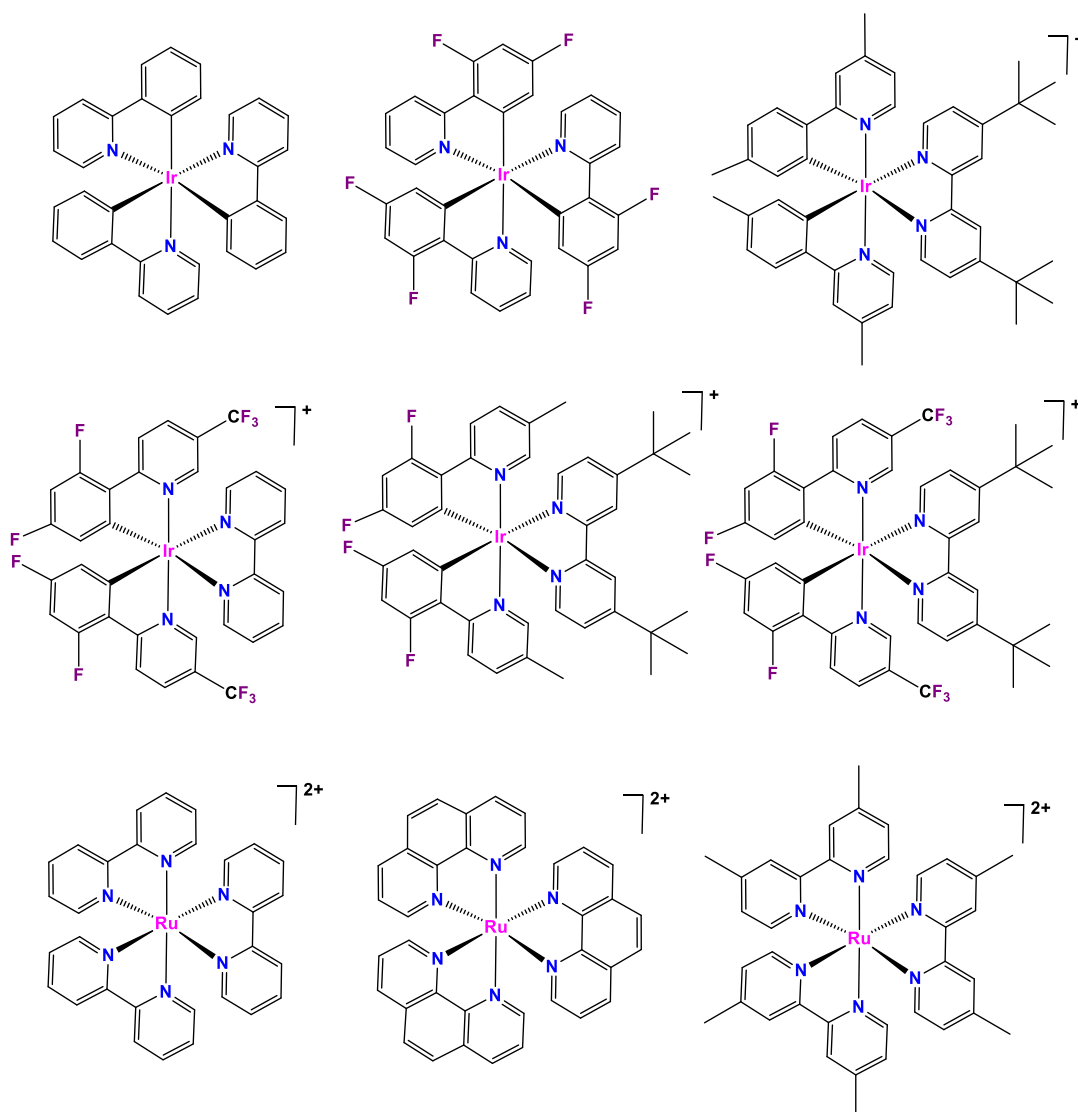


Fig. 4. Some representative Ir(III) and Ru(II) PCs.

The main application of this kind of compounds is related to the development of new synthetic routes in order to obtain fine chemicals. The main types of reactions that can be accomplished with these metal complexes can be classified as: net reductive reactions, net oxidative reactions, redox neutral reactions and energy transfer reactions.<sup>99</sup> The diverse nature of these transformations underscore the huge potential of these compounds in photocatalysis.

The group of net reductive reactions (reactions where an electron donor, also known as sacrificial reductant, is needed to act as a stoichiometric reductant)

includes reactions such as reduction of electron poor olefins, reductive dehalogenations (Fig. 5),<sup>99,118</sup> reductive cleavage of sulfonyl and sulfonium groups, nitrogen functional group reductions (Fig. 6),<sup>99,119,120</sup> radical cyclizations (Fig. 7),<sup>99,121</sup> reductive epoxide and aziridine openings and reactions with reduction-labile protecting groups.<sup>99</sup>

### Reductive dehalogenation of phenacyl bromides

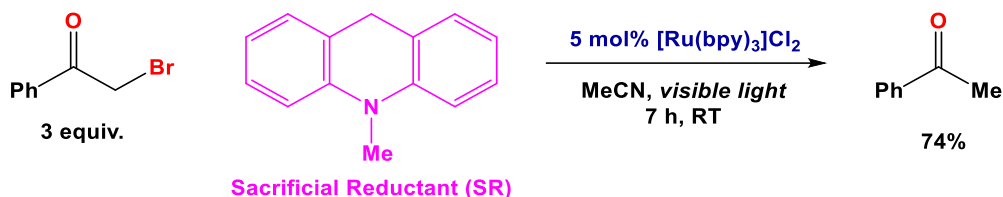


Fig. 5. Reductive dehalogenation phenacyl bromides.

### Nitrogen functional group reductions

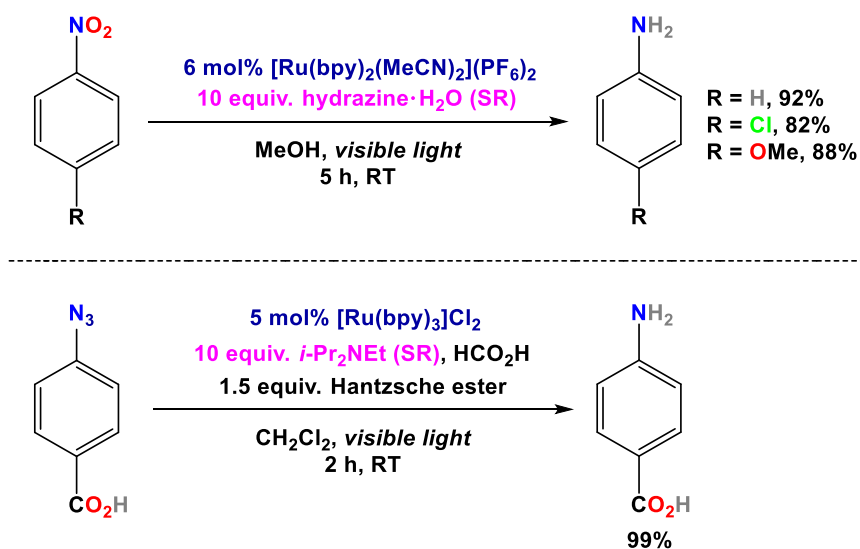


Fig. 6. Nitrogen functional group reductions.

## Radical cyclizations of alkyl, alkenyl and aryl iodides

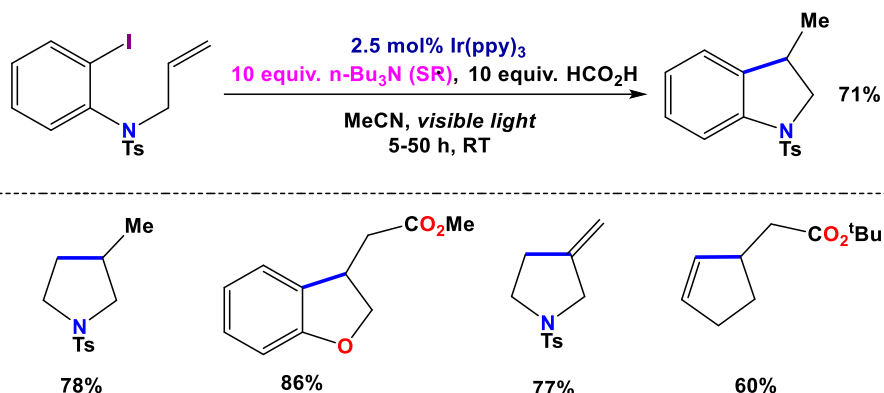


Fig. 7. Radical cyclizations of alkyl, alkenyl and aryl iodides.

The group of net oxidative reactions (reactions where an electron acceptor, also known as sacrificial oxidant, is needed to act as a stoichiometric oxidant) gathers reactions such as functional group oxidations (Fig. 8),<sup>99,122</sup> oxidative removal of the PMB (p-methoxybenzyl) group, oxidative biaryl coupling, oxidative generation of iminium ions, azomethine ylide [3 + 2] cycloadditions (Fig. 9)<sup>99,123,124</sup> and cyclizations of aminium radical cations.<sup>99</sup>

## Aerobic oxidation of benzylic halides

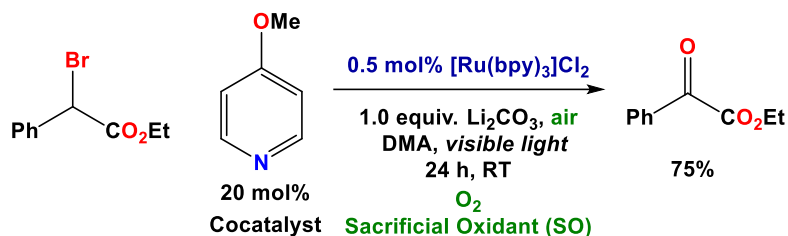


Fig. 8. Aerobic oxidation of benzylic halides.

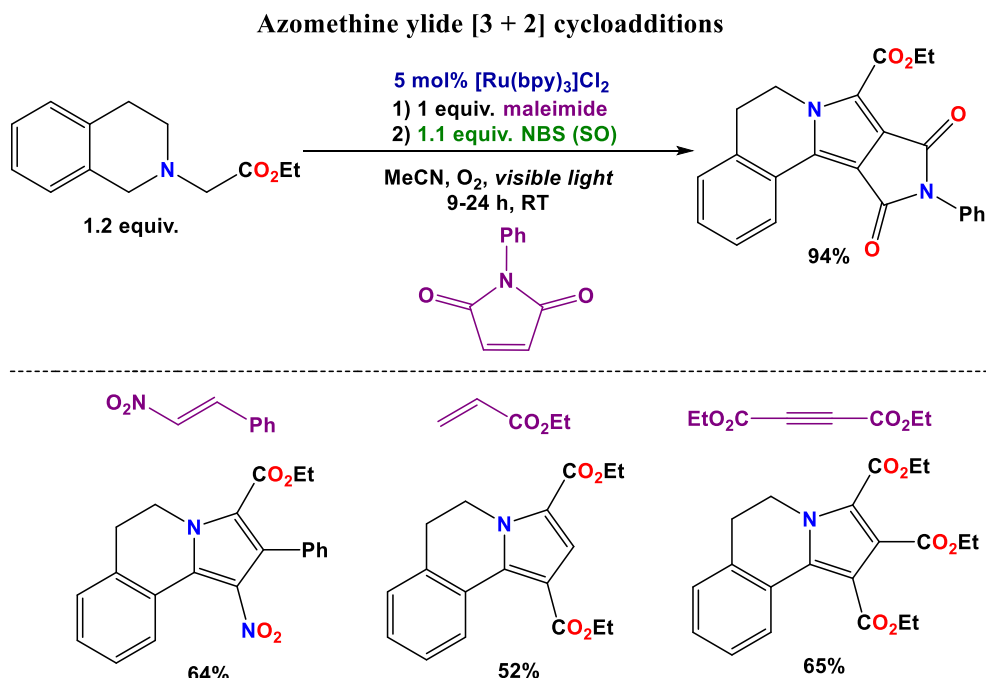
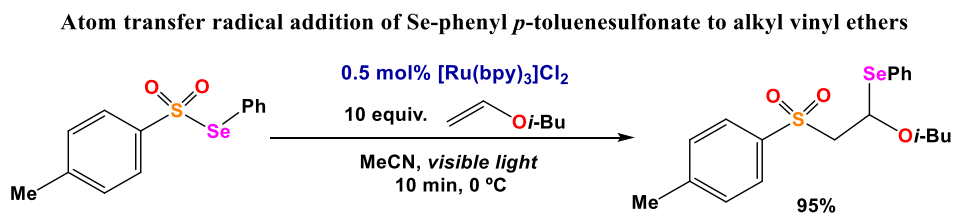


Fig. 9. Azomethine ylide [3 + 2] cycloadditions.

In the group of redox neutral reactions, (a type of reactions that have gained relevance in the last years in which the substrate or substrates suffer both single electron oxidation and reduction at different steps of the cycle, so there is no need of other species to balance the electrons) a wide variety of reactions are included, such as atom transfer radical additions (Fig. 10),<sup>99,125</sup> photoredox organocatalysis, radical additions to arenes (arylation, alkylation, trifluoromethylation (Fig. 11)<sup>99,126</sup> and oxygenation of arenes), radical additions to other  $\pi$  nucleophiles, reactions of enamine radical cations, [2 + 2] cycloadditions, [4 + 2] and [2 + 2 + 2] cycloadditions (Fig. 12),<sup>99,127</sup> [3 + 2] cycloadditions: cyclopropane ring opening, radical conjugate addition reactions,  $\alpha$ -arylation of amines, hydrothiolation (Fig. 13)<sup>99,128</sup> and the generation of the Vilsmeier–Haack reagent (a reagent which is commonly used to perform nucleophilic displacement and formylation reactions).<sup>99</sup>

Fig. 10. Atom transfer radical addition of Se-phenyl *p*-toluenesulfonate to alkyl vinyl ethers.

## Arene and heteroarene trifluoromethylation

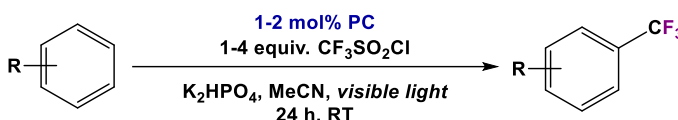
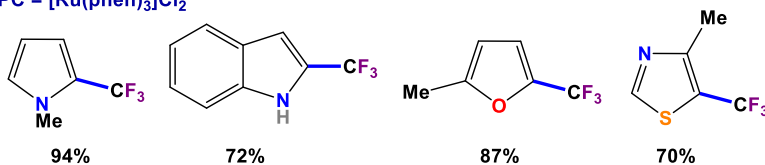
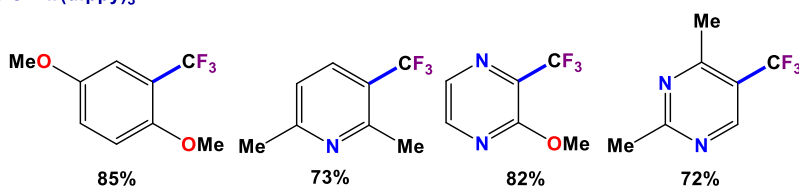
PC =  $[\text{Ru}(\text{phen})_3]\text{Cl}_2$ PC =  $\text{Ir}(\text{dfppy})_3$ 

Fig. 11. Arene and heteroarene trifluoromethylation.

## Synthesis of endoperoxides via [2 + 2 + 2] cycloaddition

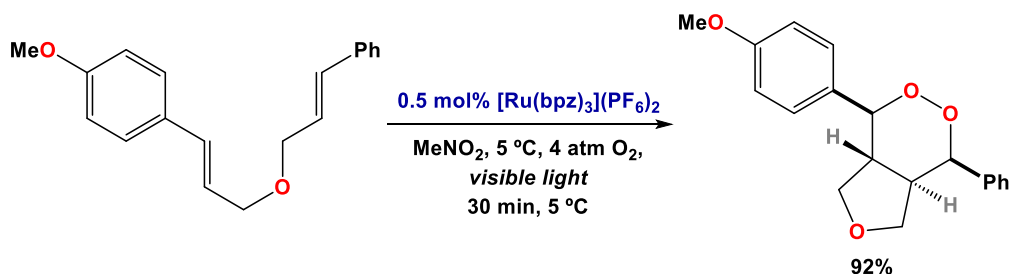


Fig. 12. Synthesis of endoperoxides via [2 + 2 + 2] cycloaddition.

## Hydrothiolation of alkenes via thiyl radicals

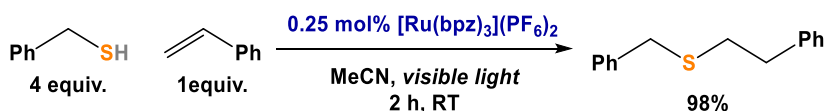


Fig. 13. Hydrothiolation of alkenes via thiyl radicals.

The last group of photocatalytic transformations involves energy transfer steps, the less exploited type of photoreactions so far. In this case, the PC acts like an

energy donor instead of an electron donor or acceptor. Examples of these reactions include [2 + 2] cycloadditions (Fig. 14),<sup>99,129</sup> photo isomerizations<sup>99,130,131</sup> (Fig. 15),<sup>130,131</sup> cyclizations, dearomatizations, transmetalations, reductive eliminations, oxidative additions, cross couplings and homolytic cleavages.<sup>131,132</sup>

**[2 + 2] styrene cycloaddition (via energy transfer)**

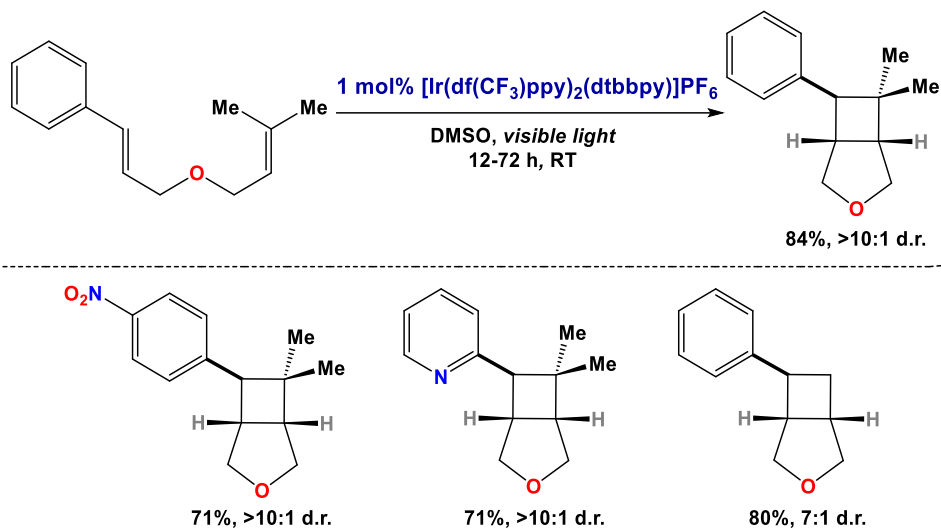


Fig. 14. [2 + 2] styrene cycloaddition.

**E/Z isomerization of styrenyl alkenes (via energy transfer)**

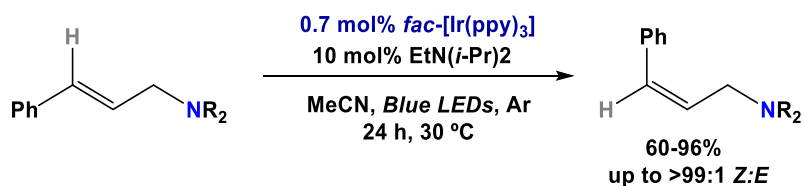


Fig. 15. E/Z isomerization of styrenyl alkenes.



## Bibliography

1. G. Ertl., and T. Gloyna, Katalyse: Vom Stein der Weisen zu Wilhelm Ostwald, *Zeitschrift für physikalische Chemie*, 2003, **217**, 1207-1220.
2. a) G. Ertl, Wilhelm Ostwald: Founder of physical chemistry and Nobel laureate 1909, *Angew. Chem. Int. Ed.*, 2009, **48**, 6600-6606.
3. G. Ertl, Reactions at Surfaces: From Atoms to Complexity (Nobel Lecture), *Angew. Chem. Int. Ed.*, 2008, **47**, 3524-3535.
4. K. H. R. Rouwenhorst, F. Jardali, A. Bogaerts, and L. Lefferts, From the Birkeland–Eyde process towards energy-efficient plasma-based NOX synthesis: a techno-economic analysis, *Energy Environ. Sci.*, 2021, **14**, 2520.
5. C. A. Grande, K. A. Andreassen, J. H. Cavka, David Waller, et al., Process Intensification in Nitric Acid Plants by Catalytic Oxidation of Nitric Oxide, *Ind. Eng. Chem. Res.*, 2018, **57**, 10180–10186.
6. J. Thomas, and R. J. P. Williams, Catalysis: principles, progress, prospects, *Phil. Trans. R. Soc. A*, 2005, **363**, 765–791.
7. E. Roduner, Understanding catalysis, *Chem. Soc. Rev.*, 2014, **43**, 8226.
8. a) V. Augugliaro, G. Palmisano, L. Palmisano, and J. Soria, Heterogeneous photocatalysis and catalysis: an overview of their distinctive features, *Heterogeneous Photocatalysis*, 2019, 1-24. b) H. Knözinger, and K. Kochloefl, Heterogeneous catalysis and solid catalysts. *Ullmann's Encyclopedia of Industrial Chemistry*, 2020.
9. B. A. Bhanvase, S. Sonawane, V. B. Pawade, and A. B. Pandit, *Handbook of Nanomaterials for Wastewater Treatment: Fundamentals and Scale up Issues*, Elsevier, 2021.
10. J. K. Nørskov, F. Studt, F. Abild-Pedersen, T. and Bligaard, *Fundamental concepts in heterogeneous catalysis*, *John Wiley & Sons.*, 2014.
11. L. Liu, and A. Corma, Metal Catalysts for Heterogeneous Catalysis: From Single Atoms to Nanoclusters and Nanoparticles, *Chem. Rev.*, 2018, **118**, 10, 4981–5079.
12. F. Bassani, *Encyclopedia of condensed matter physics*, *Elsevier acad. Press*, 2005.
13. I. Chorkendorff, and J. W. Niemantsverdriet, *Concepts of modern catalysis and kinetics*, *John Wiley & Sons*, 2017.
14. Z. Ma, and F. Zaera, *Heterogeneous catalysis by metals*, *Encyclopedia of Inorganic Chemistry*, 2006.
15. P. W. Van Leeuwen, *Homogeneous catalysis: understanding the art*, *Springer Science & Business Media*, 2006.
16. Y. G. Shelke, A. Yashmeen, A. V. A. Gholap, S. J. Gharpure, and A. R. Kapdi, *Homogeneous Catalysis: A Powerful Technology for the Modification of Important Biomolecules*, *Chem. Asian J.*, 2018, **13**, 2991 – 3013.
17. E. Farnetti, R. Di Monte, and J. Kaspar, *Homogeneous and Heterogeneous Catalysis in 6.100. Inorganic and Bio-inorganic Chemistry*, 2007.

18. A. Zecchina, and E. Groppo, Heterogeneous, homogeneous, and enzymatic catalysis: three branches of the same scientific chapter. Introductory remarks to the "Concepts in catalysis" issue, *Rend. Fis. Acc. Lincei*, 2017, **28**, 1–4.
19. P. Ball, Catalysis: facing the future: —an interview with Gerhard Ertl and Avelino Corma, *Natl. Sci. Rev.*, 2015, **2**, 202–204.
20. J. M. White, and J. Bercaw, Opportunities for Catalysis in The 21st Century, *A report from the Basic Energy Sciences Advisory Committee. DOESC (USDOE Office of Science (SC))*, 2002.
21. Z. Ma, L. Wei, W. Zhou, L. Jia, B. Hou, D. Li, and Y. Zhao, Overview of catalyst application in petroleum refinery for biomass catalytic pyrolysis and bio-oil upgrading, *RSC Adv.*, 2015, **5**, 88287.
22. A. A. Lemonidou, A. A. Lappas, and I. A. Vasalos, Catalysis and Refinery, *Encyclopedia of Life Support Systems (EOLSS)*, 2011, **60**.
23. M. A. Alabdullah, A. Rodriguez, J. Vittenet, A. Bendjeriou-Sedjerari, W. Xu, I. A. Abba, and J. Gascon, A Viewpoint on the Refinery of the Future: Catalyst and Process Challenges, *ACS Catal.*, 2020, **10**, 8131–8140.
24. Catalytic combustion of hydrogen—III. Advantages and disadvantages of a catalytic heater with hydrogen fuel, *Int. J. Hydrog.*, 1982, **7**, 737-740.
25. M. Gupta, Practical guide to vegetable oil processing, *Elsevier*, 2017.
26. A. Zaks, Enzymes in Organic Solvents. In: Dordick J.S. (eds) Biocatalysts for Industry, Topics in Applied Chemistry, *Springer*, 1991, Boston, MA.
27. M. Filice, C. C. Aragon, C. Mateo, and J. M. Palomo, Enzymatic Transformations in Food Chemistry, *Curr. Org. Chem.*, 2017, **21**, 139 – 148.
28. F. Cavani, and J. H. Teles, Sustainability in Catalytic Oxidation: An Alternative Approach or a Structural Evolution?, *ChemSusChem*, 2009, **2**, 508-534.
29. "Chapter 9. Oxidation". Chemical Reaction Technology, Berlin, München, Boston: De Gruyter, 2015, 209-252.
30. A. Shamiri, M. H. Chakrabarti, S. Jahan, M. A. Hussain, et al., The Influence of Ziegler-Natta and Metallocene Catalysts on Polyolefin Structure, Properties, and Processing Ability, *Materials*, 2014, **7**, 5069-5108.
31. C. M. Thomas, and G. Süß-Fink, Ligand effects in the rhodium-catalyzed carbonylation of methanol, *Coord. Chem. Rev.*, 2003, **243**, 125-142.
32. U. J. Etim, Y. Song, and Z. Zhong, Improving the Cu/ZnO-Based Catalysts for Carbon Dioxide Hydrogenation to Methanol, and the Use of Methanol As a Renewable Energy Storage Media, *Front. Energy Res.*, 2020, **8**, 545431.
33. J. G. De Vries, The Heck reaction in the production of fine chemicals, *Can. J. Chem.*, 2001, **79**, 1086-1092.
34. G. Szöllösi, Asymmetric one-pot reactions using heterogeneous chemical catalysis: recent steps towards sustainable processes, *Catal. Sci. Technol.*, 2018, **8**, 389.

35. E. M. da Silva, H. D. A. Vidal, and A. G. Corrêa, Advances on Greener Asymmetric Synthesis of Antiviral Drugs via Organocatalysis, *Pharmaceuticals*, 2021, **14**, 1125.
36. S. Dey, and N.S. Mehta, Automobile pollution control using catalysis, *Res. Environ. Sustain.*, 2020, **2**, 100006.
37. T. Xiao, T. Shirvani, O. Inderwildi, S. Gonzalez-Cortes, H. AlMegren, D. King, and P. P. Edwards, The Catalyst Selectivity Index (CSI): A Framework and Metric to Assess the Impact of Catalyst Efficiency Enhancements upon Energy and CO<sub>2</sub> Footprints, *Top Catal.*, 2015, **58**, 682–695.
38. R. A. Sheldon, E factors, green chemistry and catalysis: an odyssey, *Chem. Comm.*, 2008, **29**, 3352-3365.
39. A. Albini, and M. Fagnoni, 1908: Giacomo Ciamician and the Concept of Green Chemistry, *ChemSusChem*, 2008, **1**, 63-66.
40. A. Eibner, Action of light on pigments I, *Chem.-Ztg.*, 1911, **35**, 753-755.
41. E. Baur, A. Perret, The action of light on dissolved silver salts in the presence of zinc oxide, *Helv. Chim. Acta*, 1924, **7**, 910-915.
42. L. Bruner, and J. Kozak, Information on the photocatalysis I the light reaction in uranium salt plus oxalic acid mixtures, *Z. Elektrochem. Angew. Phys. Chem.*, 1911, **17**, 354-360.
43. 39. E.C.C. Baly, I.M. Heilbron, and W.F. Barker, Photocatalysis Part I. The synthesis of formaldehyde and carbohydrates from carbon dioxide and water, *JCS Trans.*, 1921, **119**, 1025-1035.
44. J. M. Coronado, A historical introduction to photocatalysis. In *Design of Advanced Photocatalytic Materials for Energy and Environmental Applications*, Springer, London 2013.
45. E. Becquerel, Studies of the effect of actinic radiation of sunlight by means of electric currents, *CR Acad. Sci. Paris*, 1839, **9**, 145-159.
46. S. Zhu, and D. Wang, Photocatalysis: Basic Principles, Diverse Forms of Implementations and Emerging Scientific Opportunities, *Advanced Energy Materials*, 2017, **7**, 1700841.
47. C. Renz, Über die Einwirkung von Oxyden auf Silbernitrat und Goldchlorid im Licht, *Helv. Chim. Acta*, 1932, **15**, 1077-1084.
48. A. Fujishima, X. Zhang, and D. A. Tryk, TiO<sub>2</sub> photocatalysis and related surface phenomena, *Surf. Sci. Rep.* 2008, **63**, 515-582.
49. C. Doodeve, and J. Kitchener, Photosensitisation by titanium dioxide, *Trans. Faraday Soc.*, 1938, **34**, 570-579.
50. C. Doodeve, and J. Kitchener, The mechanism of photosensitisation by solids, *Trans. Faraday Soc.*, 1938, **34**, 902-908.
51. W. Doerffler, and K. Hauffe, Heterogeneous photocatalysis I. The influence of oxidizing and reducing gases on the electrical conductivity of dark and illuminated zinc oxide surfaces, *J. Catal.*, 1964, **3**, 156-170.
52. W. Doerffler, and K. Hauffe, Heterogeneous photocatalysis II. The mechanism of the carbon monoxide oxidation at dark and illuminated zinc oxide surfaces, *J. Catal.*, 1964, **3**, 171-178.
53. P. Lotfabadi, Analyzing passive solar strategies in the case of high-rise building, *Renew. Sust. Energ. Rev.*, 2015, **52**, 1340-1353.

54. D. Ravelli, D. Dondi, M. Fagnoni, and A. Albini, Photocatalysis. A multi-faceted concept for green chemistry, *Chem. Soc. Rev.*, 2009, **38**, 1999-2011.
55. P. Boddy, Oxygen evolution on semiconducting TiO<sub>2</sub>, *J. Electrochem. Soc.*, 1968, **115**, 199.
56. A. Fujishima, and K. Honda, Electrochemical photolysis of water at a semiconductor electrode, *Nature*, 1972, **238**, 37-38.
57. G. Schrauzer, and T. Guth, Photolysis of water and photoreduction of nitrogen on titanium dioxide, *J. Am. Chem. Soc.*, 1977, **99**, 7189.
58. S. N. Frank, and A. J. Bard, Heterogeneous photocatalytic oxidation of cyanide and sulfite in aqueous solutions at semiconductor powders, *J. Phys. Chem.*, 1977, **81**, 1484-1488.
59. T. Inoue, A. Fujishima, S. Konishi, and K. Honda, Photoelectrocatalytic reduction of carbon dioxide in aqueous suspensions of semiconductor powders, *Nature*, 1979, **277**, 637-638.
60. G. Blondeel, A. Harriman, and D. Williams, Synergistic effects for the TiO<sub>2</sub>/RuO<sub>2</sub>/Pt photodissociation of water, *Sol. Energy Mater.*, 1983, **9**, 217-227.
61. M. Halmann, M. Ulman, and B. A. Blajeni, Photochemical solar collector for the photoassisted reduction of aqueous carbon dioxide, *Sol. Energy*, 1983, **31**, 429.
62. M. Halmann, V. Katzir, E. Borgarello, and J. Kiwi, Photoassisted carbon dioxide reduction on aqueous suspensions of titanium dioxide, *Sol. Energy Mater.*, 1984, **10**, 85-91.
63. C. Byrne, G. Subramanian, and S. C. Pillai, Recent advances in photocatalysis for environmental applications, *J. Environ. Chem. Eng.*, 2018, **6**, 3531-3555.
64. Y. Wang, X. Ma, H. Li, B. Liu, H. Li, S. Yin, and T. Sato, Recent Advances in Visible-Light Driven Photocatalysis, *Adv. Cat. Mater.*, 2016, **12**, 337.
65. B. Liu, H. Wu, and I. P. Parkin, New Insights into the Fundamental Principle of Semiconductor Photocatalysis, *ACS Omega*, 2020, **5**, **24**, 14847-14856.
66. F. E. Osterloh, Photocatalysis versus Photosynthesis: A Sensitivity Analysis of Devices for Solar Energy Conversion and Chemical Transformations, *ACS Energy Lett.*, 2017, **2**, 445-453.
67. A. J. Nozik, Photochemical Diodes, *Appl. Phys. Lett.*, 1977, **30**, 567-569.
68. A. J. Bard, Photoelectrochemistry and Heterogeneous Photocatalysis at Semiconductors, *J. Photochem.*, 1979, **10**, 59-75.
69. M. G. Walter, E. L. Warren, J. R. McKone, S. W. Boettcher, Q. Mi, E. A. Santori, and N. S. Lewis, Solar Water Splitting Cells, *Chem. Rev.*, 2010, **110**, 6446-6473.
70. S. Chen, T. Takata, and K. Domen, Particulate Photocatalysts for Overall Water Splitting, *Nat. Rev. Mater.*, 2017, **2**, 17050.
71. X. X. Chang, T. Wang, and J. L. Gong, CO<sub>2</sub> Photo-reduction: Insights into CO<sub>2</sub> Activation and Reaction on Surfaces of Photocatalysts, *Energy Environ. Sci.*, 2016, **9**, 2177-2196.
72. J. A. Dean, and N. A. Lange, Lange's Handbook of Chemistry, 15<sup>th</sup> ed., *McGraw-Hill*: New York, 1999.

73. D. R. Lide, CRC Handbook of Chemistry and Physics, 84th ed., *Taylor & Francis*: Boca Raton, FL, USA, 2003.
74. a) A. D. McNaught, A. Wilkinson, and A. D. Jenkins, IUPAC Compendium of Chemical Terminology: The Gold Book, International Union of Pure and Applied Chemistry: Research Triangle Park, NC, USA, 2006. b) G. F. Teixeira, E. S. Junior, R. Vilela, M. A. Zaghete, and F. Colmati, Perovskite Structure Associated with Precious Metals: Influence on Heterogenous Catalytic Process, *Catalysts*, 2019, **9**, 721. c) T. D. Bui, Studies on oxidative decomposition of benzene in liquid phase using titanium dioxide photocatalyst, Osaka University Knowledge Archive, 2010.
75. a) D. Chatterjee, and S. Dasgupta, Visible light induced photocatalytic degradation of organic pollutants, *J. Photochem. Photobiol. C: Photochem. Rev.*, 2005, **6**, 186–205. b) Y. Badr, and M. A. Mahmoud, Photocatalytic degradation of methyl orange by gold silver nano-core/silica nano-shell, *J. Phys. Chem. Solids*, 2007, **68**, 413-419.
76. X. Li, J. Yu, J. Low, Y. Fang, J. Xiaoc, and Xiaobo Chen, Engineering heterogeneous semiconductors for solar water splitting, *Mater. Chem. A*, 2015, **3**, 2485.
77. D. Franchi, and Z. Amara, Applications of Sensitized Semiconductors as Heterogeneous Visible-Light Photocatalysts in Organic Synthesis, *ACS Sustainable Chem. Eng.*, 2020, **8**, 15405–15429.
78. C. K. Prier, D. A. Rankic, and D. W. C. MacMillan, Visible Light Photoredox Catalysis with Transition Metal Complexes: Applications in Organic Synthesis, *Chem Rev.*, 2013, **113**, 5322–5363.
79. R. E. Blankenship, Molecular mechanisms of photosynthesis. John Wiley & Sons, 2021.
80. R. Ameta, M. S. Solanki, S. Benjamin, and S. C. Ameta, Photocatalysis, Chapter 6 - Photocatalysis, *Advanced oxidation processes for waste water treatment*, Academic Press, 2018, 135-175.
81. a) S. Xie, W. Ma, X. Wu, H. Zhang, Q. Zhang, Y. Wang, and Y. Wang, Photocatalytic and electrocatalytic transformations of C1 molecules involving C–C coupling, *Energy Environ. Sci.*, 2021, **14**, 37. b) M. K. Ntobeng, Visible light photocatalytic degradation of pollutants in surface water, Limpopo, South Africa. University of Johannesburg (South Africa), 2021.
82. S. H. S. Chan, T. Y. Wu, J. C. Juan, and C. Y. Teh, Recent developments of metal oxide semiconductors as photocatalysts in advanced oxidation processes (AOPs) for treatment of dye waste-water, *J. Chem. Technol. Biotechnol.*, 2011, **86**, 1130-1158.
83. J. S. Jang, P. H. Borse, J. S. Lee, O. S. Jung, et al., Synthesis of nanocrystalline ZnFe<sub>2</sub>O<sub>4</sub> by polymerized complex method for its visible light photocatalytic application: an efficient photo-oxidant, *Bull. Korean Chem. Soc.*, 2009, **30**, 1738-1742.
84. R. Doma, P.H. Borse, C.R. Chob, J. S. Leec, et al., Synthesis of SrFe<sub>12</sub>O<sub>19</sub> and Sr<sub>7</sub>Fe<sub>10</sub>O<sub>22</sub> systems for visible light photocatalytic studies, *J. Ceram. Proc. Res.*, 2012, **13**, 451-456.
85. A. Kudo, M. Steinberg, A. J. Bard, A. Campion, et al., Photoactivity of ternary lead-group IVB oxides for hydrogen and oxygen evolution, *Catal. Lett.*, 1990, **5**, 61-66.
86. A. D. Reddy, R. Ma, C. M. Yong, and T. K. Kim, Reduced graphene oxide wrapped ZnS-Ag<sub>2</sub>S ternary composites synthesized via hydrothermal method: applications in photocatalyst degradation of organic pollutants, *Appl. Surf. Sci.*, 2015, **324**, 725-735.

87. X. Y. Hu, J. Fan, K. L. Zhang, and J. J. Wang, Photocatalytic removal of organic pollutants in aqueous solution by  $\text{Bi}_4\text{Nb}_x\text{Ta}_{1-x}\text{O}_8$ , *Chemosphere*, 2012, **87**, 1155-1160.
88. G. Kiriakidis, and V. Binas, Metal oxide semiconductors as visible light photocatalysts, *J. Korean Phys. Soc.*, 2014, **65**, 297-302.
89. K. Vijayasankara, N. Y. Hebalkara, H. G. Kimb, and P. H. Borsea, Controlled band energetics in Pb-Fe-Nb-O metal oxide composite system to fabricate efficient visible light photocatalyst, *J. Ceram. Proc. Res.*, 2013, **14**, 557-562.
90. I. Salzmann, and G. Heimel, Toward a comprehensive understanding of molecular doping organic semiconductors (review), *J. Electron Spectrosc. Relat. Phenom.*, 2015, **204**, 208-222.
91. F. Zhang, X. Wang, H. Liu, C. Liu, et al., Recent Advances and Applications of Semiconductor Photocatalytic Technology, *Appl. Sci.*, 2019, **9**, 2489.
92. O. Monfort, and G. Plesch, Bismuth vanadate-based semiconductor photocatalysts: a short critical review on the efficiency and the mechanism of photodegradation of organic pollutants, *Environ. Sci. Pollut. Res.*, 2018, **25**, 19362-19379.
93. S. A. Younis, and K. H. Kim, Heterogeneous Photocatalysis Scalability for Environmental Remediation: Opportunities and Challenges, *Catalysts*, 2020, **10**, 1109.
94. M. B. Tahir, T. Iqbal, M. Rafique, M. S. Rafique, T. Nawaz, and M. Sagir, Nanomaterials for photocatalysis, *Nanotechnology and Photocatalysis for Environmental Applications*, Elsevier, 2020, 65-76.
95. A. F. Caliman, C. Teodosiu, and I. Balasanian, Applications of heterogeneous photocatalysis for industrial wastewater treatment, *Environ. Eng. Manag. J.*, 2002, **1**, 187-196.
96. E. Garcia-Lopez, M. Addamo, A. Di Paola, G. Marci, and L. Palmisano, Preparation in mild conditions of photocatalytically active nanostructured  $\text{TiO}_2$  rutile, *Stud. Surf. Sci. Catal.*, 2006, **162**, 689-696.
97. G. Marci, E. I. García-López, and L. Palmisano, Fine chemistry by  $\text{TiO}_2$  heterogeneous photocatalysis, *Titanium Dioxide (TiO<sub>2</sub>) and Its Applications*, Elsevier, 2021, 609-635.
98. W. C. Hsu, and Y. H. Wang, Homogeneous Water Oxidation Catalyzed by First-Row Transition Metal Complexes: Unveiling the Relationship between Turnover Frequency and Reaction Overpotential, *Chem. Sus. Chem.*, 2022, e202102378.
99. C. K. Prier, D. A. Rankic, and D. W. C. MacMillan, Visible Light Photoredox Catalysis with Transition Metal Complexes: Applications in Organic Synthesis, *Chem. Rev.*, 2013, **10**, 113, 5322-5363.
100. C. H. Mak, X. Han, M. Du, J. J. Kai, et al., Heterogenization of homogeneous photocatalysts utilizing synthetic and natural support materials, *J. Mater. Chem. A*, 2021, **9**, 4454-4504.
101. Kevin D. Dubois, and Gonghu Li, Innovative photocatalysts for solar fuel generation by  $\text{CO}_2$  reduction, *New and Future Developments in Catalysis*, 2013, 219-241.
102. N. Yang, Y. Tian, M. Zhang, X. Peng, et al., Photocatalyst-enzyme hybrid systems for light-driven biotransformation, *Biotechnol. Adv.*, 2022, **54**, 107808.
103. L. Schermund, V. Jurkas, F. F. Özgen, G. D. Barone, et al., Photo-Biocatalysis: Biotransformations in the Presence of Light, *ACS Catal.*, 2019, **9**, 4115-4144.

104. H. Eidsvåg, S. Bentouba, P. Vajeeston, S. Yohi, and D. Velauthapillai, TiO<sub>2</sub> as a Photocatalyst for Water Splitting—An Experimental and Theoretical Review, *Molecules*, 2021, **26**, 1687.
105. N. Banić, J. Krstić, S. Stojadinović, A. Brnović, A. Djordjevic, and B. Abramović, Commercial TiO<sub>2</sub> loaded with NiO for improving photocatalytic hydrogen production in the presence of simulated solar radiation, *Int. J. Energy Res.*, 2020, **44**, 8951–8963.
106. R. J. Isaifan, A. Samara, W. Suwaileh, D. Johnson, W. Yiming, A. A. Abdallah, and B. Aïssa, Improved Self-cleaning Properties of an Efficient and Easy to Scale up TiO<sub>2</sub> Thin Films Prepared by Adsorptive Self-Assembly, *Sci Rep.*, 2017, **7**, 9466.
107. S. Gelover, L. A. Gómez, K. Reyes, and M. T. Leal, A practical demonstration of water disinfection using TiO<sub>2</sub> films and sunlight, *Water Res.*, 2006, **40**, 3274–3280.
108. T. P. T. Cushnie, P. K. J. Robertson, S. Officer, P. M. Pollard, Radhakrishna Prabhu, C. McCullagh, and J. M. C. Robertson, Photobactericidal effects of TiO<sub>2</sub> thin films at low temperatures—A preliminary study, *J. Photochem. Photobiol. A: Chem.*, 2010, **216**, 290–294.
109. H. Shintani, S. Kurosu, A. Miki, F. Hayashi, and S. Kato, Sterilization Efficiency of the Photocatalyst against Environmental Microorganisms in a Health Care Facility, *Biocontrol Sci.*, 2006, **11**, 17–26.
110. J. C. Crittenden, R. P. Suri, D. L. Perram, and D. W. Hand, Decontamination of water using adsorption and photocatalysis, *Water Res.*, 1997, **31**, 411–418.
111. R. L. Ziolli, and W. F. Jardim, Photocatalytic decomposition of seawater-soluble crude-oil fractions using high surface area colloid nanoparticles of TiO<sub>2</sub>, *J. Photochem. Photobiol. A: Chem.*, 2002, **147**, 205–212.
112. A. D. McQueen, M. L. Ballentine, L. R. May, C. H. Laber, A. Das, M. J. Bortner, and A. J. Kennedy, Photocatalytic Degradation of Polycyclic Aromatic Hydrocarbons in Water by 3D Printed TiO<sub>2</sub> Composites, *ACS EST Water*, 2022, **2**, 137–147.
113. N. A. Romero, and D. A. Nicewicz, Organic Photoredox Catalysis, *Chem. Rev.*, 2016, **116**, 10075–10166.
114. Y. You, and W. Nam, Photofunctional triplet excited states of cyclometalated Ir(III) complexes: beyond electroluminescence, *Chem. Soc. Rev.*, 2012, **41**, 7061–7084.
115. K. Kalyanasundaram, Photophysics, photochemistry and solar energy conversion with tris (bipyridyl) ruthenium (II) and its analogues, *Coord. Chem. Rev.*, 1982, **46**, 159–244.
116. N. Kandoth, J. P. Hernández, E. Palomares, and J. Lloret-Fillo, Mechanisms of photoredox catalysts: the role of optical spectroscopy, *Sustain. Energy Fuels*, 2021, **5**, 638.
117. K. Teegardin, J. I. Day, J. Chan, and J. Weaver, Advances in Photocatalysis: A Microreview of Visible Light Mediated Ruthenium and Iridium Catalyzed Organic Transformations, *Org. Process Res. Dev.*, 2016, **20**, 1156–1163.
118. S. Fukuzumi, S. Mochizuki, and T. Tanaka, Photocatalytic reduction of phenacyl halides by 9, 10-dihydro-10-methylacridine: control between the reductive and oxidative quenching pathways of tris (bipyridine) ruthenium complex utilizing an acid catalysis, *J. Phys. Chem.*, 1990, **94**, 722–726.
119. T. Hirao, J. Shiori, and N. Okahata, Ruthenium–bipyridine complex-catalyzed photo-induced reduction of nitrobenzenes with hydrazine, *Bull. Chem. Soc. Jpn.*, 2004, **77**, 1763–1764.

120. Y. Chen, A. S. Kamlet, J. B. Steinman, and D. R. Liu, A biomolecule-compatible visible-light-induced azide reduction from a DNA-encoded reaction-discovery system, *Nat. Chem.*, 2011, **3**, 146-153.
121. J. D. Nguyen, E. M. D'Amato, J. M. R. Narayanam, and C. R. J. Stephenson, Engaging unactivated alkyl, alkenyl and aryl iodides in visible-light-mediated free radical reactions, *Nat. Chem.*, 2021, **4**, 854-859.
122. Y. Su, L. Zhang, and N. Jiao, Utilization of natural sunlight and air in the aerobic oxidation of benzyl halides, *Org. Lett.*, 2011, **13**, 2168-2171.
123. Y. Q. Zou, L. Q. Lu, L. Fu, N. J. Chang, J. Rong, J. R. Chen, and W. J. Xiao, Visible-light-induced oxidation/[3+ 2] cycloaddition/oxidative aromatization sequence: a photocatalytic strategy to construct pyrrolo [2, 1-a] isoquinolines, *Angew. Chem. Int. Ed.*, 2011, **50**, 7171-7175.
124. M. Rueping, D. Leonori, and T. Poisson, Visible light mediated azomethine ylide formation—photoredox catalyzed [3+ 2] cycloadditions, *Chem. Comm.*, 2011, **47**, 9615-9617.
125. a) D. H. Barton, M. A. Csiba, and J. C. Jaszberenyi, Ru (bpy) 3<sup>2+</sup>-mediated addition of Se-phenyl p-tolueneselenosulfonate to electron rich olefins, *Tetrahedron Lett.*, 1994, **35**, 2869-2872. b) F. Teplý, Visible-light photoredox catalysis with [Ru (bpy) 3]<sup>2+</sup>: General principles and the twentieth-century roots, *Phys. Sci. Rev.*, 2020, **5**.
126. D. A. Nagib, and D. W. MacMillan, Trifluoromethylation of arenes and heteroarenes by means of photoredox catalysis, *Nature*, 2011, **480**, 224-228.
127. J. D. Parrish, M. A. Ischay, Z. Lu, S. Guo, N. R. Peters, and T. P. Yoon, Endoperoxide synthesis by photocatalytic aerobic [2+ 2+ 2] cycloadditions, *Org. Lett.*, 2012, **14**, 1640-1643.
128. E. L. Tyson, M. S. Ament, and T. P. Yoon, Transition metal photoredox catalysis of radical thiolene reactions, *J. Org. Chem.*, 2013, **78**, 2046-2050.
129. Z. Lu, and T. P. Yoon, Visible light photocatalysis of [2+ 2] styrene cycloadditions by energy transfer, *Angewandte Chemie*, 2012, **124**, 10475-10478.
130. K. Singh, S. J. Staig, and J. D. Weaver, Facile Synthesis of Z-Alkenes via Uphill Catalysis, *J. Am. Chem. Soc.*, 2014, **136**, 5275-5278.
131. F. Strieth-Kalthoff, M. J. James, M. Teders, L. Pitzer, and F. Glorius, Energy Transfer Catalysis Mediated by Visible Light: Principles, Applications, Directions, *Chem. Soc. Rev.*, 2018, **47**, 7190-7202.
132. F. Strieth-Kalthoff, and F. Glorius, Triplet Energy Transfer Photocatalysis: Unlocking the Next Level, *Chem*, 2020, **6**, 1888-1903.





---

***Chapter 4. Synthesis of  $\alpha$ -Amino  
Nitriles Through One-Pot Selective  
Ru- Photocatalyzed Oxidative  
Cyanation of Amines***

---





This work can be found published as: I. Echevarría, M. Vaquero, R. Quesada, and G. Espino, Synthesis of  $\alpha$ -amino nitriles through one-pot selective Ru-photocatalyzed oxidative cyanation of amines, *Inorg. Chem. Front.*, 2020, **7**, 3092-3105.

## 0. Abstract

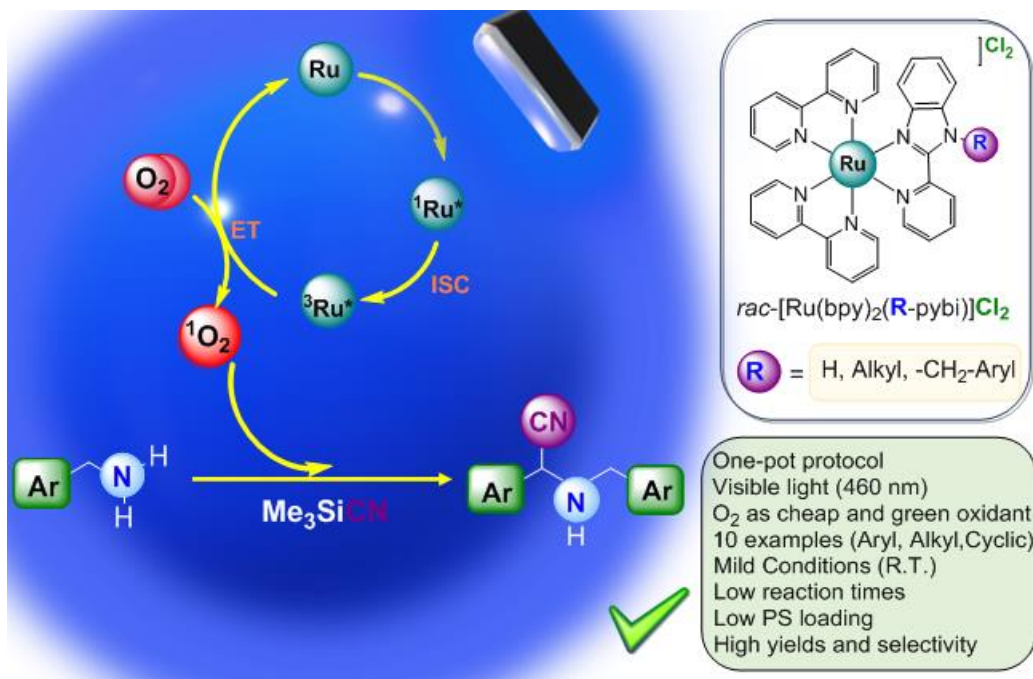


Fig.1. Schematic representation of the photocatalytic synthesis of  $\alpha$ -amino nitriles.

Photocatalysis is an expanding tool designed to synthesize organic molecules in a very efficient and selective way, using mild and environmentally friendly conditions. Thus, the development of new photosensitizers and photocatalytic protocols can further boost the applicability of photocatalysis in preparative chemistry. In this paper, we have conceived a family of Ru(II) polypyridyl complexes of general formula [Ru(bpy)<sub>2</sub>(N<sup>^</sup>N<sup>'</sup>)]Cl<sub>2</sub> (bpy = 2,2'-bipyridine) bearing the 2-pyridylbenzimidazole (Hpybim) scaffold in the ancillary ligands (N<sup>^</sup>N<sup>'</sup> = R-pybim). Moreover, using these Ru(II) derivatives as photosensitizers we have described a protocol for the synthesis of imines from primary and secondary amines and also a simple, efficient and selective methodology for the one-pot preparation of  $\alpha$ -amino nitriles from primary and secondary amines involving the consecutive photooxidation of the amine substrate and the cyanation of the imine intermediate. In addition, we have formulated a mechanism for the afore-mentioned transformations based on the participation of singlet oxygen.

## 1. Introduction

Imines are useful intermediates in the preparation of a variety of N-containing organic molecules with applications as ligands, fine chemicals and pharmaceuticals.<sup>1,2</sup> Traditionally, they have been prepared by condensation of amines with aldehydes or ketones and subsequently used as electrophiles to afford amines,<sup>3,4</sup>  $\alpha$ -amino nitriles<sup>5</sup> or N-containing heterocycles.<sup>6</sup> More recently, highly efficient methods based on the catalytic oxidation or photooxidation of primary<sup>7</sup> and secondary<sup>8</sup> amines have been developed as a very attractive alternative for the synthesis of imines.

$\alpha$ -Amino nitriles are bifunctional compounds bearing both an amino group and a nitrile group on the same carbon atom. The  $\alpha$ -amino nitrile motif is found in a variety of drugs. For instance, Vildagliptin, Saxagliptin and Anagliptin are used as oral anti-diabetic pharmaceuticals (hypoglycemic agents, see Fig. 2).<sup>9</sup> The natural product Saframycin A and its synthetic derivative Phthalascidin display interesting antitumor properties,<sup>10</sup> while Odanacatib was studied for the treatment of osteoporosis and bone metastasis, but finally abandoned due to increased risk of stroke (Fig. 2).<sup>11</sup>

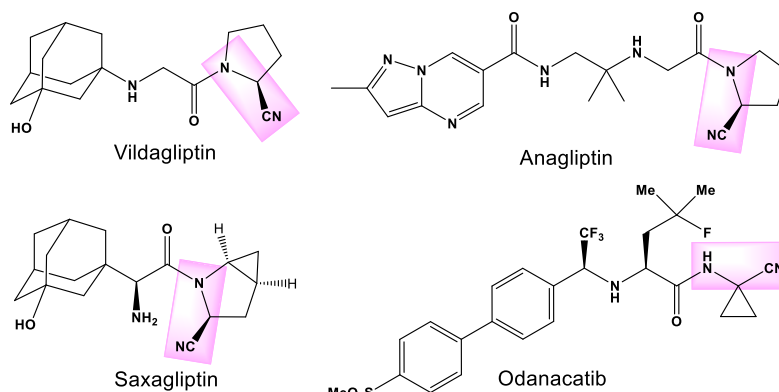


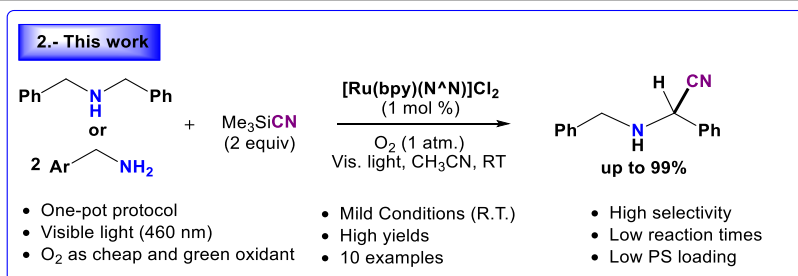
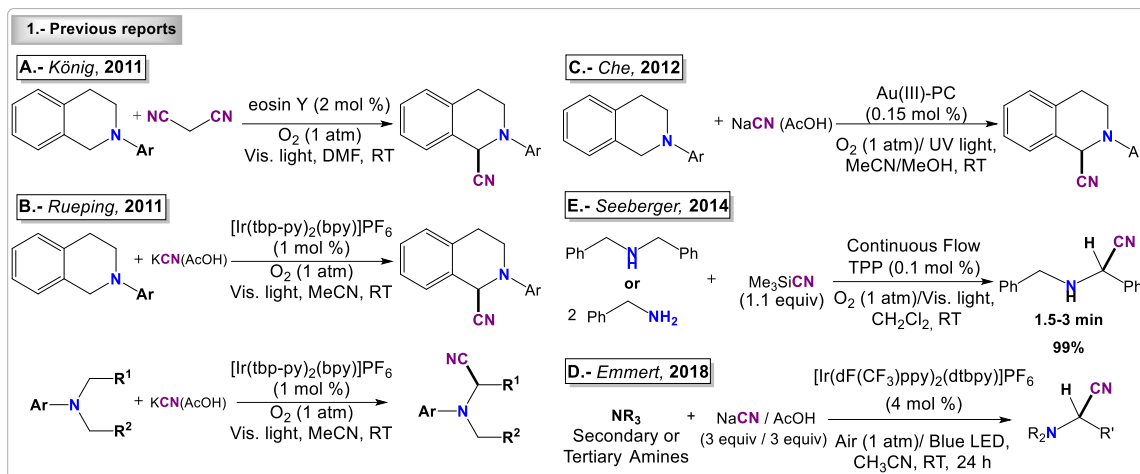
Fig. 2.  $\alpha$ -Aminonitriles with biological activity.

In addition,  $\alpha$ -amino nitriles are key and versatile intermediates in the synthesis of a wide variety of organic chemicals and drugs. More specifically, they can be used to produce  $\alpha$ -amino acids *via* hydrolysis of the  $\text{--C}\equiv\text{N}$  functional group. They can generate amines, enamines and ketones through loss of the cyanide anion followed by nucleophilic additions, deprotonation or hydrolysis. They can afford  $\alpha$ -hydroxy ketones,  $\alpha$ -amino ketones and 1,2-amino alcohols *via* deprotonation of the  $\alpha$ -C and subsequent reaction with electrophiles.<sup>10</sup> Moreover, they can also be employed to prepare N-heterocycles<sup>12</sup> and can be reduced to yield 1,2-diamines.<sup>13</sup>

Consequently, the development of efficient and sustainable methods for the preparation of these organic products (imines and  $\alpha$ -amino nitriles) is an attractive goal. In line with this ambition, the use of visible-light as the energetic driving force and oxygen as the oxidant agent in photocatalytic oxidation reactions, could render the synthesis of these chemicals cleaner, safer and easy-to-handle in comparison to traditional synthetic protocols, which use high temperatures or corrosive oxidants, such as  $t$ BuOOH.<sup>14,15,16</sup>

During the last decade the groups of König,<sup>17</sup> Rueping,<sup>13</sup> Che<sup>18</sup> and Emmert<sup>19</sup> have reported different homogeneous photocatalytic systems for the oxidative cyanation of *N*-aryl tetrahydroisoquinolines, acyclic tertiary anilines and aliphatic secondary and tertiary amines using different cyanide sources and solvents and either eosin Y, Ir(III) or Au(III) complexes as the photosensitizers. Moreover, in 2014, Seeberger developed a continuous-flow LED-photoreactor for the rapid and efficient preparation of  $\alpha$ -amino nitriles through the oxidative cyanation of primary and secondary amines using trimethylsilyl cyanide as the *in situ* cyanide donor and tetraphenylporphyrin as the photosensitizer (Scheme 1).<sup>20</sup> More recently, Opatz employed functionalized TiO<sub>2</sub> nanoparticles in the oxidative photocyanation of tertiary amines.<sup>21</sup> Nevertheless, some of the reported protocols use undesirable solvents, such as dichloromethane<sup>20</sup> or *N,N*-dimethylformamide<sup>17</sup> and others employ hazardous combinations of cyanide sources and acidic additives, such as KCN and AcOH.<sup>13</sup> Therefore, optimization of this type of methodology is still possible.

We have recently reported different Ir- and Ru-based photocatalytic systems for the oxidation of sulfides<sup>22</sup> and benzylamines,<sup>23</sup> respectively. Herein, we have developed an efficient and selective one-pot procedure for the preparation of  $\alpha$ -amino nitriles from primary and secondary amines (benzylamines, tetrahydroisoquinolines and alkylamines). The transformation involves the consecutive Ru(II)-photocatalyzed oxidation of the amine substrate and the cyanation of the resultant imine intermediate and it takes place at room temperature, using blue light as the energy source and oxygen as a green oxidant.



Scheme 1. Photocatalytic systems described for the oxidative cyanation of *N*-aryl tetrahydroisoquinolines, acyclic tertiary anilines and primary and secondary benzylamines, and our new photocatalytic protocol developed to synthesize  $\alpha$ -amino nitriles from primary and secondary amines. The amino nitriles are obtained as racemic mixtures in all the cases.

## 2. Results and discussion

### 2.1. Synthesis of ligands and ruthenium(II) complexes

With the goal of developing new photocatalysts we decided to prepare a family of Ru(II) polypyridyl complexes bearing the 2-pyridylbenzimidazole scaffold in the ancillary ligands. Indeed, 2-(2-pyridyl)benzimidazole (Hpybim = **L1**) is a commercial ligand. However, its *N*-alkyl derivatives (**L2–L5**) were prepared by reacting **L1** with the appropriate alkyl halide in the presence of K<sub>2</sub>CO<sub>3</sub>, using DMF as the solvent at room temperature, according to a methodology adapted from the literature (see Fig. 3).<sup>24,25,26</sup>

The corresponding Ru(II) dicationic complexes, [**Ru1**]**Cl**<sub>2</sub>–[**Ru5**]**Cl**<sub>2</sub>, were obtained by refluxing the starting material *rac-cis*-[Ru(bpy)<sub>2</sub>Cl<sub>2</sub>]**·**2H<sub>2</sub>O<sup>27</sup> with the ligands **L1–L5** in ethanol (Fig. 3, Section 4 and SI). The synthesis of different salts of complexes [**Ru1**]<sup>2+</sup>, [**Ru2**]<sup>2+</sup> and [**Ru5**]<sup>2+</sup> had been previously reported, but as far as we know their photocatalytic properties had not been studied.<sup>26,28,29</sup>

These Ru(II) dicationic complexes were isolated in the form of chloride salts as dark red solids, consisting of racemic mixtures of the  $\Delta$  and  $\Lambda$  enantiomers with good yields and purities according to analytical and spectroscopic data. Moreover, they are moisture and air-stable solids soluble in common organic solvents such as DMSO, DMF, acetone, CH<sub>3</sub>CN, MeOH, EtOH, CHCl<sub>3</sub>, CH<sub>2</sub>Cl<sub>2</sub> as well as in water, and partially soluble in THF.

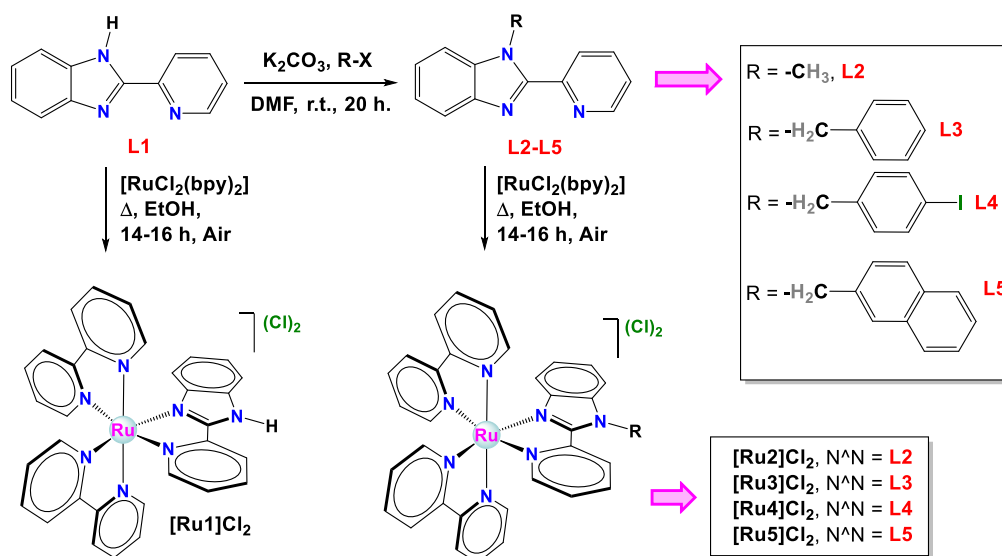


Fig. 3. Synthesis and molecular structures of ligands L1–L5 and complexes [Ru1]Cl<sub>2</sub> – [Ru5]Cl<sub>2</sub>.

## 2.2. Characterization of the Ru(II)-complexes

The ruthenium derivatives were fully characterized by multinuclear NMR and IR spectroscopy and ESI mass spectrometry as well as by elemental analysis. The <sup>1</sup>H and <sup>13</sup>C{<sup>1</sup>H} NMR spectra of complexes [Ru1]Cl<sub>2</sub>–[Ru5]Cl<sub>2</sub> in DMSO-d<sub>6</sub> (Section 4.1. and SI Fig. 1–5) displayed peaks for both the ancillary (N<sup>^N</sup>) and the bpy ligands with the following significant features: (1) Two different sets of resonances were observed for the two non-equivalent bpy ligands of every complex due to the asymmetric nature of [Ru1]Cl<sub>2</sub>–[Ru5]Cl<sub>2</sub> (C<sub>1</sub>-symmetry); (2) a broad singlet at 16.21 ppm was detected for the N–H proton of [Ru1]Cl<sub>2</sub>; (3) a narrow singlet at 4.47 ppm was observed for the N–Me group of [Ru2]Cl<sub>2</sub> in the corresponding <sup>1</sup>H NMR; (4) Two mutually coupled doublets (<sup>2</sup>J<sub>H–H</sub> ≈ 18 Hz), appearing as an AB pseudo-quartet, were detected between 6.52 and 6.24 ppm for the diastereotopic protons of the –CH<sub>2</sub> groups in the <sup>1</sup>H NMR spectra of [Ru3]Cl<sub>2</sub>–[Ru5]Cl<sub>2</sub> owing to the helical chirality implicit in tris-chelate octahedral complexes, while free ligands L2–L5 (achiral) exhibit one singlet integrating as two protons for the –CH<sub>2</sub> group; (5) The <sup>13</sup>C{<sup>1</sup>H} NMR spectra of

complexes **[Ru3]Cl<sub>2</sub>** to **[Ru5]Cl<sub>2</sub>** featured a singlet at around 48 ppm for the methylene group.

The HR-MS (ESI+) spectra of the Ru(II) complexes display peaks whose *m/z* values and patterns of isotopic distribution are fully consistent with those calculated for the dicationic species of general formula  $[\text{Ru}(\text{bpy})_2(\text{N}^{\wedge}\text{N}')^{2+}]^{2+}$  ( $\text{N}^{\wedge}\text{N}' = \text{L1-L5}$ ). For instance, we found a peak at 304.5612 Da for **[Ru1]<sup>2+</sup>**, consistent with the calculated *m/z* = 304.5602 for  $[\text{C}_{32}\text{H}_{25}\text{N}_7\text{Ru}]^{2+}$ . All the spectra also show a common peak at 608.1140 Da attributed to the monocationic fragment  $[\text{Ru}(\text{bpy})_2(\text{pybim})]^+$ , which results from the loss of the -R groups (R = H, Me, -CH<sub>2</sub>-Ar) in every case (see characterization in Section 4.1.).

### 2.3. Crystal structure by X-ray diffraction

Attempts to obtain single crystals of the chloride salts of the new Ru(II) complexes were fruitless. Nonetheless, we obtained single crystals of *rac*-**[Ru3](PF<sub>6</sub>)<sub>2</sub>** suitable for X-ray diffraction analysis by slow diffusion of a saturated aqueous solution of NH<sub>4</sub>PF<sub>6</sub> into a solution of **[Ru3]Cl<sub>2</sub>** in methanol. The complex crystallizes in the monoclinic P2<sub>1</sub>/c space group. The ORTEP diagram for the (Λ)-**[Ru3]<sup>2+</sup>** enantiomer is shown in Fig. 4. Selected bond distances and angles with estimated standard deviations are compiled in Table 1, and the crystallographic parameters are given in SI Table 1.

The unit cell consists of two pairs of enantiomeric molecular cations (Λ and Δ) along with eight PF<sub>6</sub><sup>-</sup> counteranions. The coordination environment for the Ru(II) centre features a slightly distorted octahedral coordination geometry. The bond distances and the angles of the coordination polyhedron are standard in comparison with those of similar compounds.<sup>30</sup> Interestingly, the Ru-N<sub>bpy</sub> distances (2.048-2.065 Å) are slightly shorter than the Ru-N<sub>pybim</sub> distances (2.080-2.095 Å). The 3D crystal structure of this complex is brought together by weak hydrogen bonding interactions, resulting in motifs where every metal complex is surrounded by eight PF<sub>6</sub><sup>-</sup> counterions which act as hydrogen bonding acceptors (SI Fig. 6). Anion-π and π-π interactions are also observed (SI Fig. 7).



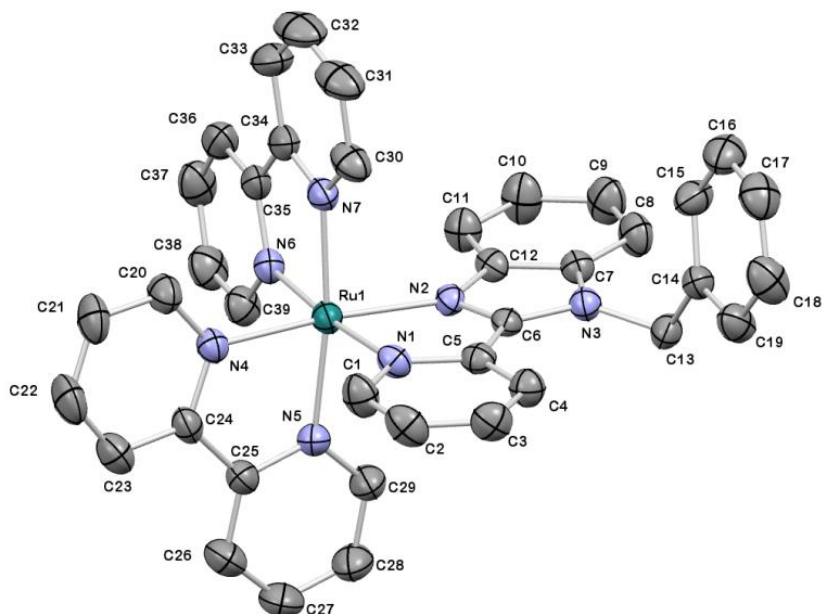


Fig. 4. ORTEP diagram for the molecular structure of  $(\Lambda)$ - $[\text{Ru}3]^{2+}$ . Thermal ellipsoids are shown at the 30% probability level. Hydrogen atoms and  $\text{PF}_6^-$  counterions have been omitted for the sake of clarity.

Table 1. Selected bond lengths ( $\text{\AA}$ ) and angles ( $^\circ$ ) for  $[\text{Ru}3](\text{PF}_6)_2$ .

Distances ( $\text{\AA}$ )		Angles ( $^\circ$ )	
Ru(1)-N(1)	2.095(5)	N(2)-Ru(1)-N(1)	77.57(19)
Ru(1)-N(2)	2.080(5)	N(6)-Ru(1)-N(7)	78.4(2)
Ru(1)-N(4)	2.051(5)	N(4)-Ru(1)-N(5)	78.9(2)
Ru(1)-N(5)	2.065(5)	N(5)-Ru(1)-N(1)	87.7(2)
Ru(1)-N(6)	2.048(5)	N(6)-Ru(1)-N(4)	89.0(2)
Ru(1)-N(7)	2.055(5)	N(7)-Ru(1)-N(2)	88.58(18)

## 2.4. Photostability experiments

The photostability of the new Ru(II)-complexes and the reference complex  $[\text{Ru}(\text{bpy})_3]\text{Cl}_2$  (hereafter denoted as **[1]Cl<sub>2</sub>**) was studied by monitoring the evolution of their  $^1\text{H}$  NMR spectra in deuterated acetonitrile ( $1.4 \times 10^{-2}$  M) over a period of 24 h under air and irradiation with blue light, ( $\lambda_{\text{irr}} = 460$  nm, 24 W) at room temperature (see SI Fig. 9–14). Interestingly, complex **[Ru1]Cl<sub>2</sub>** showed a remarkable stability under these conditions (no photodegradation after 24 h), whereas all the *N*-functionalized derivatives and **[1]Cl<sub>2</sub>** displayed symptoms of photodegradation even after 6 h of irradiation compatible with the dissociation of the ancillary ligand (10 % for **[Ru2]Cl<sub>2</sub>**, 12 % for **[Ru3]Cl<sub>2</sub>**, 25 % for **[Ru4]Cl<sub>2</sub>**, 18 % for **[Ru5]Cl<sub>2</sub>** and 12 % for **[1]Cl<sub>2</sub>**).

## 2.5. Theoretical calculations

Density functional theory (DFT) calculations were performed on the cation complexes  $[\text{Ru}\mathbf{1}]^{2+}$ – $[\text{Ru}\mathbf{3}]^{2+}$ , as representatives of the family, and also on  $[\text{Ru}(\text{bpy})_3]^{2+}$  ( $[\mathbf{1}]^{2+}$ ) to get an in-depth understanding of the electrochemical and photophysical properties discussed below. Calculations were carried out at the B3LYP/(6-31G(d,p)+LANL2DZ) level including solvent effects ( $\text{CH}_3\text{CN}$ ) (see description in SI Section 5 and SI Tables 2 and 3). Calculations predict a near-octahedral structure for the four complex cations in their ground electronic state ( $S_0$ ), in harmony with the molecular structure determined experimentally by X-ray diffraction for  $[\text{Ru}\mathbf{3}](\text{PF}_6)_2$ . Fig. 5 features the isovalue contour plots calculated for the molecular orbitals (MOs), HOMO–2 to LUMO+2, of  $[\mathbf{1}]^{2+}$  and  $[\text{Ru}\mathbf{3}]^{2+}$  at their electronic ground state ( $S_0$ ). The topologies of these MOs for  $[\text{Ru}\mathbf{1}]^{2+}$ ,  $[\text{Ru}\mathbf{2}]^{2+}$  are very similar to those of  $[\text{Ru}\mathbf{3}]^{2+}$  and are shown in SI Table 3. As previously reported, the filled HOMO and filled degenerate HOMO–1 and HOMO–2 of  $[\mathbf{1}]^{2+}$  are mostly dominated by Ru  $d$  orbitals and exhibit a non-bonding character between the Ru and the bpy ligands. The LUMO of  $[\mathbf{1}]^{2+}$  is located in the bpy ligands and features a M–L non-bonding nature, while the degenerate LUMO+1 and LUMO+2 are predominantly distributed in the bpy ligands but exhibit small participations from  $d$  orbitals of the Ru center, which gives an antibonding character to the Ru–N interfaces. Hence, the Ru–N interactions in  $[\mathbf{1}]^{2+}$  exhibit mainly a  $\sigma$ -bonding character (coming from non-shown low energy MO) with negligible  $\pi$ -bonding nature between the Ru(II) and the ligand set.<sup>31</sup> Similarly, for  $[\text{Ru}\mathbf{1}]^{2+}$ – $[\text{Ru}\mathbf{3}]^{2+}$ , the filled HOMO–1 and HOMO–2 are metal-based orbitals with insignificant contributions of the ligands and, therefore, exhibit a non-bonding nature, although the orbital degeneracy is lost due to the  $C_1$  symmetry. The HOMO, on the contrary, displays a hybrid topology with a major contribution of the metal centre and a minor contribution of the imidazolyl ring, and is endowed with an anti-bonding character at the Ru–N<sub>im</sub> interface. Thus, for  $[\text{Ru}\mathbf{3}]^{2+}$ , the resulting Ru( $d\pi$ )–L3( $\pi$ ) overlap suggests a modest  $\pi$  interaction and impart a moderate destabilization (0.12 eV) to the HOMO of  $[\text{Ru}\mathbf{3}]^{2+}$  relative to the HOMO of  $[\mathbf{1}]^{2+}$ , consistent with the higher  $\pi$ -donor character of the imidazole ring compared to that of the pyridine ring. The LUMO of  $[\text{Ru}\mathbf{3}]^{2+}$  is formed essentially by a combination of MO from the two bpy ligands and **L3** and is very slightly destabilized relative to the LUMO of  $[\mathbf{1}]^{2+}$ , (0.03 eV), in agreement with the coincidental  $E^{\text{red}}$  values determined for these two complexes (see Table 3). Consequently, the HOMO–LUMO band gap is narrower for  $[\text{Ru}\mathbf{3}]^{2+}$  than for  $[\mathbf{1}]^{2+}$  (3.47 vs. 3.56 eV, Fig.5) in consonance with the tendency in the electrochemical band gaps (2.55 vs. 2.62 V, see  $\Delta E_{1/2}$  in Table 3). On the other hand, the participation of the benzyl group (alkyl groups in general for the other Ru congeners) in the frontier orbitals is non-existent and hence

the effect of the N-substitution on the energies of the frontier orbitals is expected to be only inductive in character. This implies that the effect is similar in both the HOMO and LUMO and very small on the energyband gap among the present series of Ru complexes (SI Fig. 15).

Phosphorescent emission in complexes of the type  $[\text{Ru}(\text{bpy})_2(\text{N}^{\wedge}\text{N}')^{2+}]^{2+}$  is originated from the lowest-lying triplet state,  $T_1$  ( $^3\text{MLCT}$ ), which actually displays a singlet–triplet mixed nature due to strong spin–orbit coupling.<sup>32,33</sup> Therefore, the low lying excited states of complexes  $[\text{Ru}1]^{2+}$ – $[\text{Ru}3]^{2+}$ , and  $[\mathbf{1}]^{2+}$  were calculated at the optimized geometries of the ground state ( $S_0$ ) by mean of the time-dependent DFT (TD-DFT) approach. SI Table 2 summarizes the vertical excitation energies calculated for the first three singlets and first three triplets, together with their molecular orbital description and electronic nature.

A summary of these results is graphically illustrated in Fig. 6. The three first triplet excited states of  $[\mathbf{1}]^{2+}$  are originated from HOMO  $\rightarrow$  LUMO+1, HOMO  $\rightarrow$  LUMO+2 and HOMO  $\rightarrow$  LUMO excitations, respectively, and all of them display  $^3\text{MLCT}$  character. On the contrary, the three first triplet states of  $[\text{Ru}1]^{2+}$ – $[\text{Ru}2]^{2+}$ , come from combinations of H  $\rightarrow$  L+1 and H  $\rightarrow$  L+2 ( $T_1$  and  $T_2$ ) and H  $\rightarrow$  L ( $T_3$ ), while for  $[\text{Ru}3]^{2+}$  the first three triplets result from H  $\rightarrow$  L+1 ( $T_1$ ), H  $\rightarrow$  L+2 ( $T_2$ ) and H  $\rightarrow$  L ( $T_3$ ).

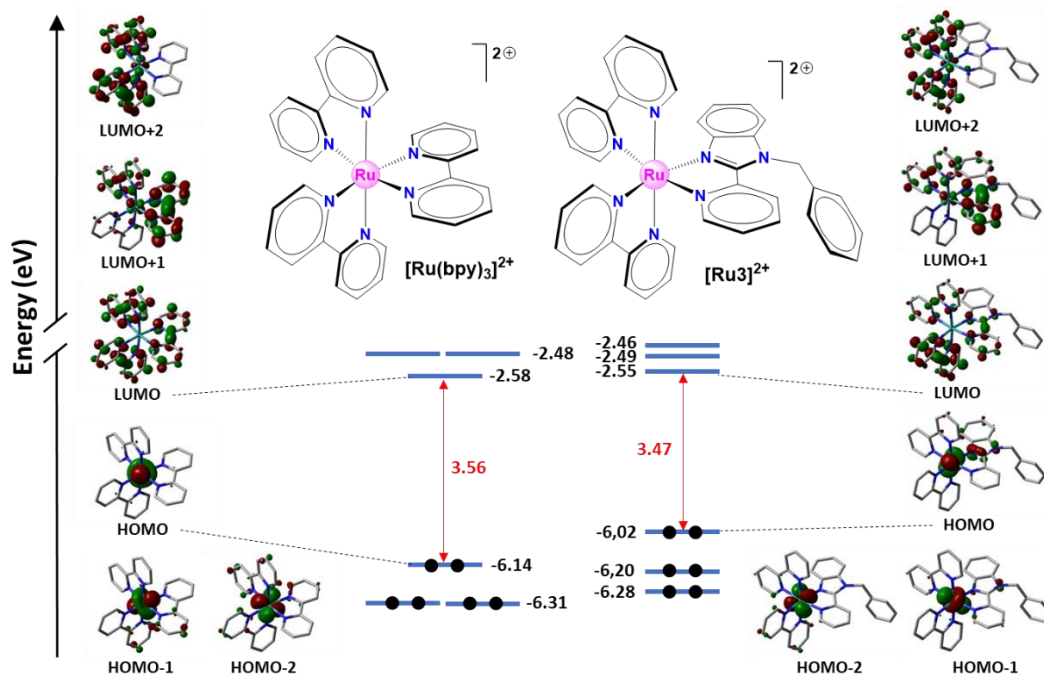


Fig. 5. Schematic representation showing the energies and the isovalue contour plots calculated for the frontier molecular orbitals of  $[\mathbf{1}]^{2+}$  and  $[\text{Ru}3]^{2+}$ .

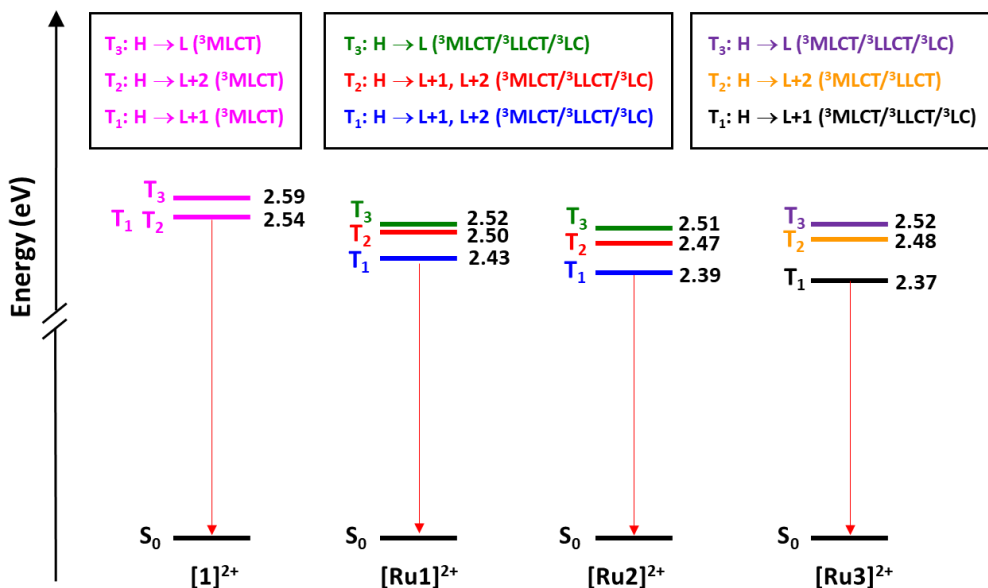


Fig. 6. Energy diagram showing the energy values calculated for the lowest-energy triplet excited states ( $T_n$ ) of complexes  $[\text{Ru}1]^{2+}$ – $[\text{Ru}3]^{2+}$  and  $[1]^{2+}$ . Different colours are used to display the different electronic nature of the  $T_n$  states according to the key in the boxes.

Due to the hybrid nature of the HOMO in  $[\text{Ru}1]^{2+}$ – $[\text{Ru}3]^{2+}$ , the transitions exhibit a combination of  ${}^3\text{MLCT}$ ,  ${}^3\text{LLCT}$  and  ${}^3\text{LC}$  character.

In all the cases, the three first triplet excited states are very close in energy, within intervals of 0.09 ( $[\text{Ru}1]^{2+}$ ), 0.12 ( $[\text{Ru}2]^{2+}$ ) and 0.15 eV ( $[\text{Ru}3]^{2+}$ ). The calculated emission energies of the new dyes, estimated as the vertical energy difference between  $T_1$  and  $S_0$ , predict very similar emission maxima for  $[\text{Ru}1]^{2+}$ – $[\text{Ru}3]^{2+}$ , and a moderate bathochromic shift relative to  $[1]^{2+}$  as determined experimentally (see below).

## 2.6. Photophysical properties

**UV-Vis absorption spectra.** The UV-Vis absorption spectra of complexes  $[\text{Ru}1]\text{Cl}_2$ – $[\text{Ru}5]\text{Cl}_2$  and  $[1]\text{Cl}_2$  were recorded in acetonitrile solutions ( $10^{-5}$  M) at 25 °C (see Fig. 7). The spectra of complexes  $[\text{Ru}1]\text{Cl}_2$ – $[\text{Ru}5]\text{Cl}_2$  feature one medium and one strong absorption band between 200 and 300 nm, which are attributed to singlet spin-allowed ligand centred ( ${}^1\text{LC}$ ) transitions taking place in both the bpy and the N<sup>^N</sup> ancillary ligands. Complex  $[\text{Ru}5]\text{Cl}_2$  displays an additional very intense absorption band at 220 nm, likely associated to the naphthyl group. Furthermore, weak bands are also observed with maxima around 315 and 452 nm, approximately. These bands are assigned to mixed spin-allowed  ${}^1\text{MLCT}$  (singlet to singlet  $d_\pi(\text{Ru}) \rightarrow \pi^*(\text{bpy})$ ),  ${}^1\text{LLCT}$  (singlet to singlet,

$^1\pi(\text{N}^{\wedge}\text{N}) \rightarrow \pi^*\text{bpy}$ ) and  $^1\text{LC}$  (singlet to singlet  $^1\pi \rightarrow \pi^*$ ) transitions.<sup>31</sup> Compared to the archetypal complex **[1]Cl<sub>2</sub>**, the Ru(II) complexes with 2-pyridylbenzimidazole based ligands exhibit slightly broader and red-shifted absorption profiles, which overlap efficiently with the emission band of the blue light used in the photocatalytic experiments as shown in Fig. 7.

**Emission spectra.** The complexes **[RuL1]Cl<sub>2</sub>**–**[RuL5]Cl<sub>2</sub>** show photoluminescence in the red hue, as shown visually under irradiation with an UV lamp ( $\lambda_{\text{irr}} = 365$  nm). The corresponding emission spectra were recorded under excitation at 450 nm for  $10^{-5}$  M solutions of the complexes in dry and deoxygenated acetonitrile at 25 °C (see Fig. 7 and Table 2). All the spectra are virtually identical and show a broad band with an absolute maximum between  $\lambda_{\text{em}} = 649$ – $657$  nm, showing that the substitution of the N-H hydrogen atom with different alkyl groups exerts a modest influence on the  $T_1 \rightarrow S_0$  energy gap. Moreover, the  $\lambda_{\text{max}}$  of these complexes is red shifted (28–36 nm) relative to that of **[1]Cl<sub>2</sub>** ( $\lambda_{\text{em}} = 621$  nm), as anticipated theoretically by the energy difference between  $T_1$  and  $S_0$  (see theoretical calculations).

The photoluminescent quantum yields (PLQY,  $\phi_{\text{PL}}$ ), determined in deoxygenated acetonitrile, are moderate and very similar for all the derivatives, that is, between 13–15 % and hence higher than that ascertained for **[1]Cl<sub>2</sub>** in similar conditions (9.4 %).<sup>34</sup> The excited states lifetimes ( $\tau$ ) are 231 ns for **[Ru1]Cl<sub>2</sub>** and between 457 and 617 ns for the substituted derivatives, revealing that the replacement of the N-H hydrogen with bulky alkyl groups increases the stability of the excited state. Indeed, it has been suggested that the N-H group of imidazole can facilitate the fast deactivation of the excited state through vibrational dissipation of the excitation energy to the solvent medium.<sup>35</sup> Nonetheless, the excited state lifetimes of **[Ru2]Cl<sub>2</sub>**–**[Ru5]Cl<sub>2</sub>** are lower than that determined for **[1]Cl<sub>2</sub>**, which is 1100 ns.<sup>36</sup>

In addition, the quenching effect of O<sub>2</sub> on the emission of **[Ru3]Cl<sub>2</sub>** was proved by recording the respective spectrum for a deoxygenated acetonitrile solution of this derivative and then additional spectra every 4 minutes upon air exposure. A sustained and dramatic drop in intensity was observed, until almost complete quenching after 24 h (see SI Fig. 17).

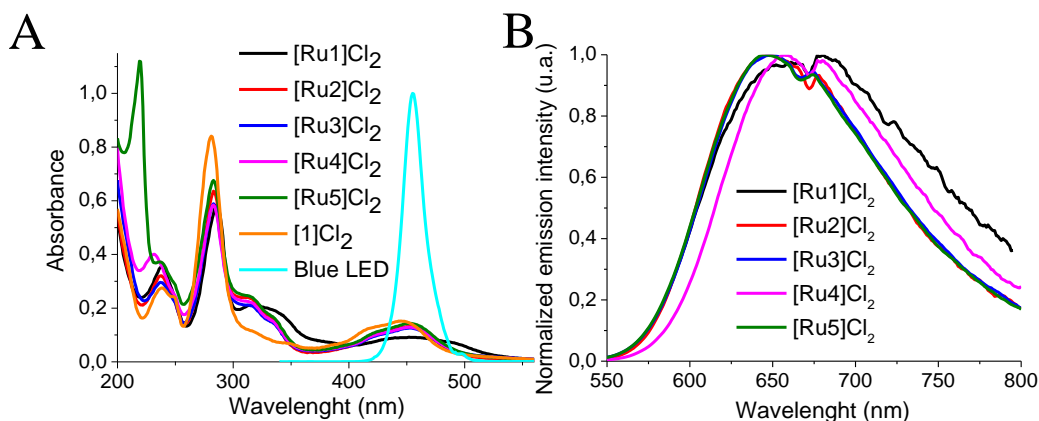


Fig. 7. Overlaid UV-Vis absorption spectra of complexes  $[\text{Ru}1]\text{Cl}_2$ – $[\text{Ru}5]\text{Cl}_2$  and  $[1]\text{Cl}_2$  ( $10^{-5}$  M) in  $\text{CH}_3\text{CN}$  at 25 °C along with the emission spectrum of the blue light used in the photocatalytic assays (left). Overlaid emission spectra of complexes of  $[\text{Ru}1]\text{Cl}_2$ – $[\text{Ru}5]\text{Cl}_2$  in deoxygenated acetonitrile ( $10^{-5}$  M) at 25 °C (right).

Table 2. Photophysical properties for complexes  $[\text{Ru}1]\text{Cl}_2$ – $[\text{Ru}5]\text{Cl}_2$  and  $[1]\text{Cl}_2$  ( $10^{-5}$  M) in  $\text{CH}_3\text{CN}$  at 25 °C under  $\lambda_{\text{ex}} = 450$  nm.

Complex	$\lambda_{\text{abs}}$ (nm)	$\epsilon$ [ $\text{M}^{-1} \text{cm}^{-1}$ ]	$\lambda_{\text{em}}$ (nm)	$\phi_{\text{PL}}$ (%)	$\tau$ (ns)	$\phi_{\Delta}^{\text{PC}}$ (%)
$^a[1]\text{Cl}_2$	238, 282, 445	27500, 83800, 15200	621	9.4	1100	56
$[\text{Ru}1]\text{Cl}_2$	239, 286, 316, 452	35500, 58500, 21300, 9200	649	15	231	36
$[\text{Ru}2]\text{Cl}_2$	238, 283, 313, 452	32100, 63600, 24000, 13200	647	15	457	64
$[\text{Ru}3]\text{Cl}_2$	237, 283, 313, 452	29600, 58900, 21200, 12600	656	14	487	52
$[\text{Ru}4]\text{Cl}_2$	232, 283, 315, 451	40100, 58400, 22200, 12900	657	15	617	42
$[\text{Ru}5]\text{Cl}_2$	219, 236, 283, 316, 453	112000, 37200, 67600, 24100, 14300	650	13	527	39

<sup>a</sup> Data for  $[1]\text{Cl}_2$  are retrieved from the literature.<sup>34,36,37</sup>

## 2.7. Determination of singlet oxygen quantum yields

The  $^1\text{O}_2$  quantum yields ( $\phi_{\Delta}^{\text{PC}}$ ) of  $[\text{Ru}1]\text{Cl}_2$ – $[\text{Ru}5]\text{Cl}_2$  were experimentally determined, by monitoring the photooxidation of 1,3-diphenylisobenzofuran (DPBF)<sup>38,39,40</sup> in the presence of these photosensitizers relative to  $[1]\text{Cl}_2$  (see experimental procedure in SI, SI Fig. 16 and data in Table 2).<sup>37</sup> This parameter is regarded as a measure of the number of absorbed photons which are efficiently used to generate  $^1\text{O}_2$ . The experimentally determined  $\phi_{\Delta}^{\text{PC}}$  values increased in the order:  $[\text{Ru}1]\text{Cl}_2 < [\text{Ru}5]\text{Cl}_2 < [\text{Ru}4]\text{Cl}_2 < [\text{Ru}3]\text{Cl}_2 < [1]\text{Cl}_2 < [\text{Ru}2]\text{Cl}_2$ . Interestingly, K. Kam-Wing Lo *et al.* established a direct correlation between  $\phi_{\Delta}^{\text{PC}}$  and  $\tau$  among a series of photosensitizers.<sup>40</sup> This correspondence is well-founded since longer-lived excited states should increase the chances of efficient collisional triplet-triplet energy transfer from  $^3\text{PC}^*$  to  $^3\text{O}_2$ . However, in the present family of Ru(II) complexes other factors seem to influence on the  $\phi_{\Delta}^{\text{PC}}$ ,

since although **[Ru1]Cl<sub>2</sub>** exhibits the lowest values for both  $\phi_{\Delta}^{\text{PC}}$  and  $\tau$  (36 %, 231 ns, Table 2), **[Ru2]Cl<sub>2</sub>** is the most efficient <sup>1</sup>O<sub>2</sub> photosensitizer with a modest  $\tau$  compared to some of its congeners (64 %, 457 ns, Table 2). In any event, the ability of these complexes as <sup>1</sup>O<sub>2</sub> photosensitizers could be useful in Photodynamic Therapy (PDT). Indeed, a related Ru(II) polypyridyl complex (TLD1433)<sup>41</sup> has successfully completed phase Ib clinical trials and our group is involved in the development of metal-based <sup>1</sup>O<sub>2</sub> photosensitizers with potential activity in this field.<sup>42,43</sup>

## 2.8. Electrochemical properties

In order to study the electrochemical stability of the Ru(II) complexes and the ability of their excited states as oxidants and reductants, the redox potentials of complexes **[Ru1]Cl<sub>2</sub>**–**[Ru5]Cl<sub>2</sub>** were experimentally determined in deoxygenated acetonitrile solutions ( $5 \times 10^{-4}$  M) by cyclic voltammetry (CV) using [*n*Bu<sub>4</sub>N][PF<sub>6</sub>] (0.1 M) as supporting electrolyte and glassy carbon as working electrode (see SI Fig. 18). Argon was bubbled through the solutions to displace oxygen. Potentials are referred to the ferrocenium/ferrocene (Fc<sup>+</sup>/Fc) couple and representative cyclic voltammograms are depicted in Fig. 8. The anodic region of the corresponding voltammograms show two peaks: (a) an irreversible peak between +0.59 and +0.63 V (see Table 3 and Fig. 8) which is ascribed to the oxidation of the Cl<sup>-</sup> counteranion (Cl<sup>-</sup>/Cl<sub>2</sub> redox couple) and (b) a reversible one-electron oxidation peak in the range +0.78 to +0.83 V, attributed to the Ru(II)-imidazolyl environment according to the topology of the HOMO. Consequently, the oxidized species should be better described by the combination of two canonical structures (see Fig. 8). These values reveal a shift to less anodic potentials relative to the reference compound **[1]<sup>2+</sup>** (+0.90 V vs Fc<sup>+</sup>/Fc), which was measured for comparative purposes, in agreement with the predicted destabilization of the HOMO for complexes **[Ru1]<sup>2+</sup>**–**[Ru3]<sup>2+</sup>** compared to **[1]<sup>2+</sup>**. Indeed, this fact reflects an increase in the electron density on the Ru(II)-imidazolyl environment due to the higher electron-donating ability of the benzimidazole entity compared to the pyridyl ring in **[1]<sup>2+</sup>**.<sup>44,45</sup>

In the cathodic region, complexes **[Ru2]Cl<sub>2</sub>**–**[Ru5]Cl<sub>2</sub>** display three reversible one-electron waves ranging from –1.72 to –1.75 V ( $E^{\text{red}1}_{1/2}$ ), from –1.91 to –1.95 V ( $E^{\text{red}2}_{1/2}$ ) and from –2.16 to –2.19 V ( $E^{\text{red}3}_{1/2}$ ) vs Fc<sup>+</sup>/Fc. According to the topology of the LUMO and LUMO+1, these peaks are ascribed to stepwise ligand-centered reversible reductions (see cathodic species in Fig. 8). Assuming that bpy is a better  $\pi$ -acceptor than 2-pyridylbenzimidazole-based ligands,  $E^{\text{red}1}_{1/2}$  and  $E^{\text{red}2}_{1/2}$  are likely due to bpy-centred processes and  $E^{\text{red}3}_{1/2}$  is probably due to **L2**–**L5** centred electron transfers.<sup>26,35</sup> The respective values are very similar to those of

**[1]<sup>2+</sup>** in consonance with the energies predicted theoretically for the respective LUMO and LUMO+1 (see SI Tables 2 and 3). On the other side, complex **[Ru1]Cl<sub>2</sub>** shows only two reversible one-electron peaks at -1.87 and -2.1 V presumably due to bpy reductions, as previously reported.<sup>35</sup> Similarly to the reference complex **[1]<sup>2+</sup>**,<sup>36</sup> the excited-state of every of these complexes is both a much stronger reductant and a much stronger oxidant than the respective ground state (See SI Table 4).

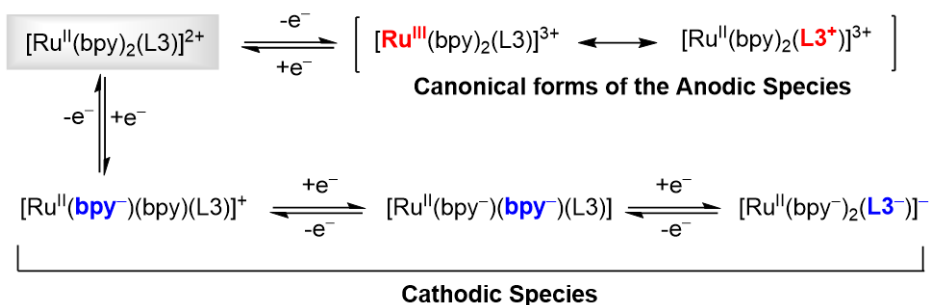
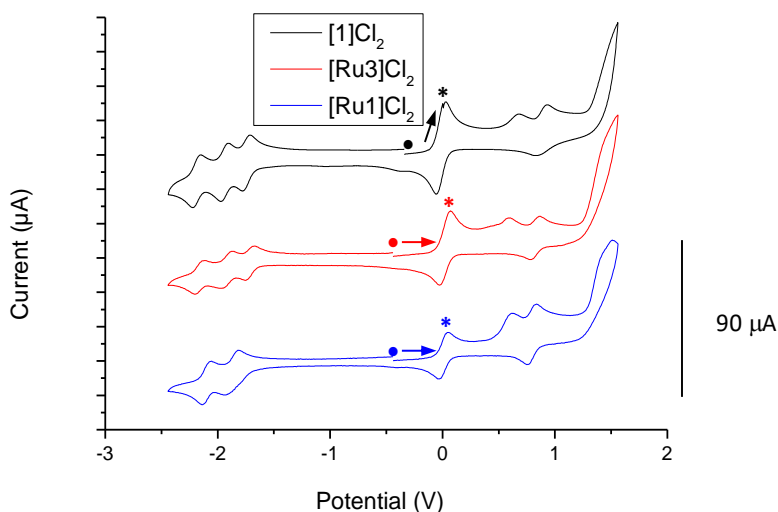


Fig. 8. Cyclic voltammograms of selected complexes, **[Ru1]Cl<sub>2</sub>**, **[Ru3]Cl<sub>2</sub>** and **[1]Cl<sub>2</sub>**, in acetonitrile solution ( $5 \times 10^{-4}$  M), using 0.1 M  $[\text{nBu}_4\text{N}][\text{PF}_6]$  as supporting electrolyte and recorded with scan rate of  $0.10 \text{ V}\cdot\text{s}^{-1}$ . The starting and final potentials ( $E_i$ ,  $E_f$ ) are indicated by (•) and the sense of the scan is indicated by the arrow (clockwise). The symbol (\*) refers to the  $\text{Fc}^+/\text{Fc}$  peak used as reference. Anodic and cathodic species formed in the electrochemical experiments are shown as well.



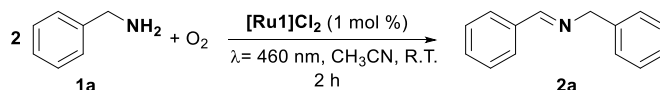
Table 3. Redox potentials recorded by cyclic voltammetry referenced to  $Fc^+/Fc$  in deoxygenated acetonitrile solutions.<sup>[a]</sup>

Complex	$E^{ox1}_{1/2}$ (V)	$E^{ox2}_{1/2}$ (V)	$E^{red1}_{1/2}$ (V)	$E^{red2}_{1/2}$ (V)	$E^{red3}_{1/2}$ (V)	$\Delta E_{1/2}$ (V)
[1]Cl <sub>2</sub>	+0.68 (irr)	+0.90 (rev)	-1.72 (rev)	-1.92 (rev)	-2.17 (rev)	2.62
[Ru1]Cl <sub>2</sub>	+0.63 (irr)	+0.80 (rev)	-1.87 (rev)	-2.1 (rev)	-	2.67
[Ru2]Cl <sub>2</sub>	+0.60 (irr)	+0.78 (rev)	-1.75 (rev)	-1.95 (rev)	-2.19 (rev)	2.53
[Ru3]Cl <sub>2</sub>	+0.60 (irr)	+0.83 (rev)	-1.72 (rev)	-1.91 (rev)	-2.16 (rev)	2.55
[Ru4]Cl <sub>2</sub>	+0.59 (irr)	+0.81 (rev)	-1.72 (rev)	-1.92 (rev)	-2.17 (rev)	2.53
[Ru5]Cl <sub>2</sub>	+0.59 (irr)	+0.80 (rev)	-1.74 (rev)	-1.92 (rev)	-2.17 (rev)	2.54

<sup>[a]</sup>Voltammograms recorded in acetonitrile solution ( $5 \times 10^{-4}$  M), using 0.1 M  $[nBu_4N][PF_6]$  as supporting electrolyte and recorded with scan rate of  $0.10 \text{ V}\cdot\text{s}^{-1}$  and referenced to  $Fc^+/Fc$ .

## 2.9. Photooxidation of amines

The synthesized Ru(II) derivatives were evaluated as photocatalysts in two different processes: the photooxidation of primary and secondary alkylamines and the one-pot synthesis of  $\alpha$ -amino nitriles from primary and secondary amines.

Table 4. Photocatalytic oxidative coupling of benzylamine **1a** with [Ru1]Cl<sub>2</sub> and control experiments.<sup>[a]</sup>

Entry	Conditions	Yield (%)
1	PC, O <sub>2</sub> , light	>99
2	PC, O <sub>2</sub> , no light	1
3	No PC, O <sub>2</sub> , light	< 1
4	PC, N <sub>2</sub> , light	4
5	PC, O <sub>2</sub> , light, DABCO <sup>[b]</sup>	< 1
6	PC, O <sub>2</sub> , light, TEMPO <sup>[c]</sup>	>99%
7	PC, air, light	78

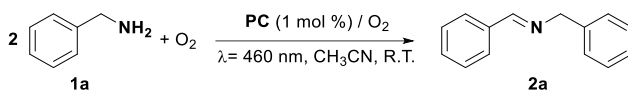
<sup>[a]</sup> Reaction conditions: Benzylamine **1a** (10 mM), [Ru1]Cl<sub>2</sub> ( $10^{-1}$  mM, 1 mol %), CH<sub>3</sub>CN (0.5 mL) at room temperature, under a saturated atmosphere of either O<sub>2</sub> or N<sub>2</sub> (1 atm) and under irradiation with blue light (LED,  $\lambda_{irr} = 460 \text{ nm}$ , 24 W) during 2 hours in a septum-capped tube. Yields of **2a** were determined by <sup>1</sup>H NMR analysis of the crude mixture as average values of at least two independent experiments. Overoxidation and/or hydrolysis products were not detected in any case. <sup>[b]</sup>DABCO (11 mM). <sup>[c]</sup>TEMPO (11 mM).

First, we selected the photooxidation of benzylamine in the presence of O<sub>2</sub> (1 atm, pure oxygen balloon) as the model reaction. Thus, initially we examined the photocatalytic activity of [Ru1]Cl<sub>2</sub> using a catalyst loading of 1 mol % under irradiation with blue LED light ( $\lambda_{irr} = 460 \text{ nm}$ ) at room temperature in acetonitrile. Satisfyingly, the analysis of the reaction crude by <sup>1</sup>H NMR showed that the substrate **1a**

was oxidized to the corresponding E-secondary aldimine, **2a**, with a high yield (>99%) and with an excellent selectivity in 2 hours (see entry 1 in Table 4). Indeed, we could not observe the products corresponding to either hydrolysis (benzaldehyde)<sup>46</sup> or overoxidation reactions (benzonitrile,<sup>47</sup> benzamide,<sup>48</sup> N-benzylbenzamide,<sup>49</sup> N-benzylhydroxylamine,<sup>50</sup> benzaldehyde oxime,<sup>47</sup> N-benzylidene-benzylamine N-oxide (nitron).<sup>51</sup>

Then, we performed control experiments to confirm the photocatalytic nature of this chemical reaction and the active role of O<sub>2</sub>. Conclusively, the reaction did not work in the absence of light, photocatalyst (**PC**) or oxygen, confirming that these three actors play essential roles to accomplish the transformation (entries 2-4, Table 4). Moreover, when the photooxidation of benzylamine was tested in the presence of a <sup>1</sup>O<sub>2</sub> quencher, DABCO, the yield of **2a** was very low (< 1%), suggesting that this species is the actual oxidant agent (entry 5, Table 4). However, when the reaction was tried in the presence of TEMPO (O<sub>2</sub><sup>•-</sup> scavenger) the expected product was obtained in a quantitative manner, which rules out the participation of the radical superoxide in the process (entry 6, Table 4). In addition, when we used air instead of O<sub>2</sub> the yield of **2a** was 78 % after 2 h., revealing that the reaction is also possible in air but sensitive to the O<sub>2</sub> concentration (entry 7, Table 4).

Moreover, we performed a screening of the Ru(II) photosensitizers **[Ru1]Cl<sub>2</sub>**–**[Ru5]Cl<sub>2</sub>** in the model reaction under the afore-mentioned conditions and concurrently we optimized the reaction time (see Table 5). Thus, we determined that complexes **[Ru2]Cl<sub>2</sub>**–**[Ru5]Cl<sub>2</sub>** with alkyl substituents on the N of the ancillary ligand seem to be more efficient as PCs than the parent complex, **[Ru1]Cl<sub>2</sub>**. Thus quantitative yields for **2a** after 60 min and also after 30 min were obtained using **[Ru2]Cl<sub>2</sub>**–**[Ru5]Cl<sub>2</sub>**, while **[Ru1]Cl<sub>2</sub>** gave only 95 % of **2a** after 1h (Table 5). These observations could be rationalized due to the lower excited state lifetime ( $\tau$ ) and quantum yield for the generation of <sup>1</sup>O<sub>2</sub> ( $\phi_{\Delta}^{PC}$ ) of **[Ru1]Cl<sub>2</sub>** relative to its functionalized congeners.

Table 5. Photocatalysts screening in the photooxidative coupling of **1a**.<sup>[a]</sup>

Entry	Complex	Yield (%)			
		120 min	60 min	30 min	15 min
1	[Ru1]Cl <sub>2</sub>	100	95	-	-
2	[Ru2]Cl <sub>2</sub>	100	100	100	-
3	[Ru3]Cl <sub>2</sub>	100	100	100	98
4	[Ru4]Cl <sub>2</sub>	100	100	100	-
5	[Ru5]Cl <sub>2</sub>	100	100	100	-
6	[Ru3]Cl <sub>2</sub> <sup>[b]</sup>	100 <sup>[b]</sup>	-	39 <sup>[b]</sup>	-

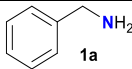
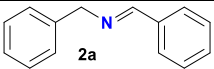
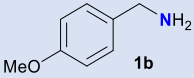
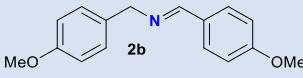
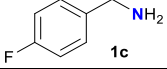
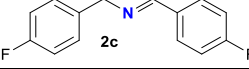
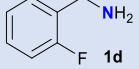
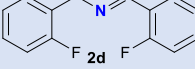
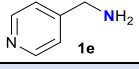
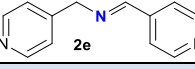
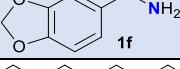
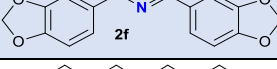
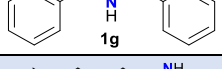
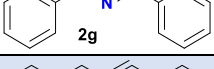
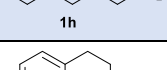
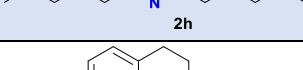
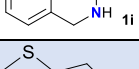
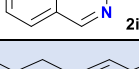
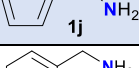
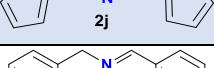
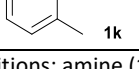
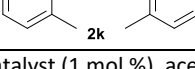
<sup>[a]</sup> **Reaction conditions:** Amine (10 mM), **PC** (1 mol %), acetonitrile (0.5 mL), O<sub>2</sub> (balloon, 1 atm), blue light (LED, λ<sub>irr</sub> = 460 nm, 24 W), room temperature for the above-mentioned time (min). Yields of **2a** were experimentally determined from <sup>1</sup>H NMR integration of the corresponding reaction crudes. <sup>[b]</sup> **PC** (0.1 mol %).

In additional experiments we demonstrated that it is possible to accomplish this transformation using even lower reaction times (98 % after 15 min) with **[Ru3]Cl<sub>2</sub>**, or lower catalyst loadings (0.1 mol %), although in this case the reaction time needed to achieve full conversion is longer (2 h, entry 6, Table 5 and SI Fig. 37).

The application of the afore-mentioned conditions was proved in the photooxidation of different primary and secondary alkyl amines with both electron-withdrawing and electron-donating groups. The corresponding secondary aldimines were obtained with high yields and excellent selectivities in all the cases, *via* photooxidative self-coupling when using primary amines (**1a-1f**, **1j**, **1k**) as substrates and *via* photooxidation of a -CH<sub>2</sub>-NHR bond when using the secondary amines **1g** and **1i** (Table 6). It is worth mentioning that 1-hexylamine, **1h**, was also fully converted to the expected product **2h** (Table 6), even though the α-H atoms are non-activated in the absence of an aryl group. In addition, 1,2,3,4-tetrahydroisoquinoline (**1i**) was regioselectively oxidized to imine **2i**. Overall, these results are remarkable compared to previously reported protocols for the aerobic photooxidation of alkylamines in the presence of homogeneous or heterogenous PCs. Although conditions are not always the same, in general, reported protocols require longer reaction times and higher temperatures.<sup>52,53,54,55,56</sup>

Table 6. Substrate Scope for the photooxidation of primary and secondary amines<sup>[a]</sup>

$$2 \text{ R-CH}_2\text{-NH}_2 + \text{O}_2 \xrightarrow[\text{CH}_3\text{CN, RT, } \lambda = 460 \text{ nm}]{[\text{Ru3}]\text{Cl}_2 \text{ (1 mol \%)} } \text{R-CH}_2\text{-N=CH-R}$$
  
 1x (1 atm) 2x

Entry	Substrate	Product	Yield (%) [Time (min)]
1			>99 [30]
2			>99 [30]
3			>99 [60]
4			>99 [90]
5			>99 [30]
6			>99 [90]
7			>99 [30]
8			>99 [30]
9			>99 [30]
10			>99 [60]
11			>99 [30]

<sup>[a]</sup>Reaction Conditions: amine (10 mM), photocatalyst (1 mol %), acetonitrile (0.5 mL), O<sub>2</sub> (balloon, 1 atm), blue LED light (460 nm), room temperature for the above-mentioned time. The yields (parenthesis) were experimentally determined from <sup>1</sup>H NMR integration of the corresponding reaction crudes (see Supporting information). Reaction times between brackets.

## 2.10. One-Pot Photocatalytic Cyanation of Amines to produce $\alpha$ -amino nitriles

Then, we envisioned and developed a one-pot protocol for the synthesis of secondary  $\alpha$ -amino nitriles from the afore-mentioned primary and secondary amines. This one-pot protocol is based on the Strecker reaction<sup>5</sup> and consists of two consecutive transformations: (a) Photooxidation of the amine to the corresponding secondary aldimine and (b) Cyanation of the aldimine to the expected secondary  $\alpha$ -amino nitrile. We assayed our idea applying the optimized photocatalytic conditions for the achievement of the imines, but in

the presence of  $\text{Me}_3\text{SiCN}$  (TMSCN, 2 equiv) from the beginning and extending the reaction time for a second stirring period in the absence of light (Fig. 9). The choice of TMSCN as the cyanation agent instead NaCN/KCN, is based on its higher solubility in  $\text{CH}_3\text{CN}$ , its safer nature and the fact that it avoids the harsh conditions typical of NaCN/KCN (very alkaline pH when used alone, or very acidic pH when combined with AcOH).<sup>5</sup> Pleasantly, we probed that the new protocol is efficient and selective for the formation of the expected  $\alpha$ -amino nitriles **3x** (Fig. 9). Indeed, it was successfully implemented for eight different amines with excellent selectivities and outstanding (**3a–3c**, **3f**, **3g**, **3h** and **3k**, between 85–99%) or moderate (**3i**, 67%) yields for the respective  $\alpha$ -amino nitriles, which were obtained in the form of racemic mixtures. On the contrary,  $\alpha$ -amino nitriles **3d** and **3j** were obtained in low yields (30–36%) and the product **3e** was not observed. Afterwards, our methodology was successfully scaled up to twenty-fold and some of the products were purified and isolated (yields in red in Fig. 9, <sup>1</sup>H NMR of crudes and of isolated products and characterization data in SI Fig. 19-32). To further demonstrate the advantages of this one-pot protocol over a two-step procedure, we performed an experiment in which TMSCN was added to the reaction mixture for the photooxidative cyanation of **1a** after a period of 30 min under the typical photooxidation conditions. As a result of such an experiment we obtained 89% of  $\alpha$ -amino nitrile **3a**, and 11% of the respective imine, **2a**, whereas the yield obtained for **3a** in the one-pot reaction was >99%. This result demonstrates that the presence of the cyanide source from the very beginning is beneficial for the conversion of benzylamines into  $\alpha$ -amino nitriles, since the imine intermediate can be trapped by the cyanide as soon as it is formed. Furthermore, the one-pot protocol is more convenient from an operational point of view. Finally, we carried out this transformation using 200 mg (1.87 mmol) of **1a** in the presence of  $[\text{Ru3}]\text{Cl}_2$  (1 mol %); that means an additional 10-fold increase in the scale of the reaction, to conclude that the protocol is equally efficient (96% yield of  $\alpha$ -amino nitrile **3a** was obtained). However, some modifications were applied to guarantee the efficiency (the irradiation was kept during the whole period of stirring, that is 6 h, and the concentration of all the reactants was doubled).

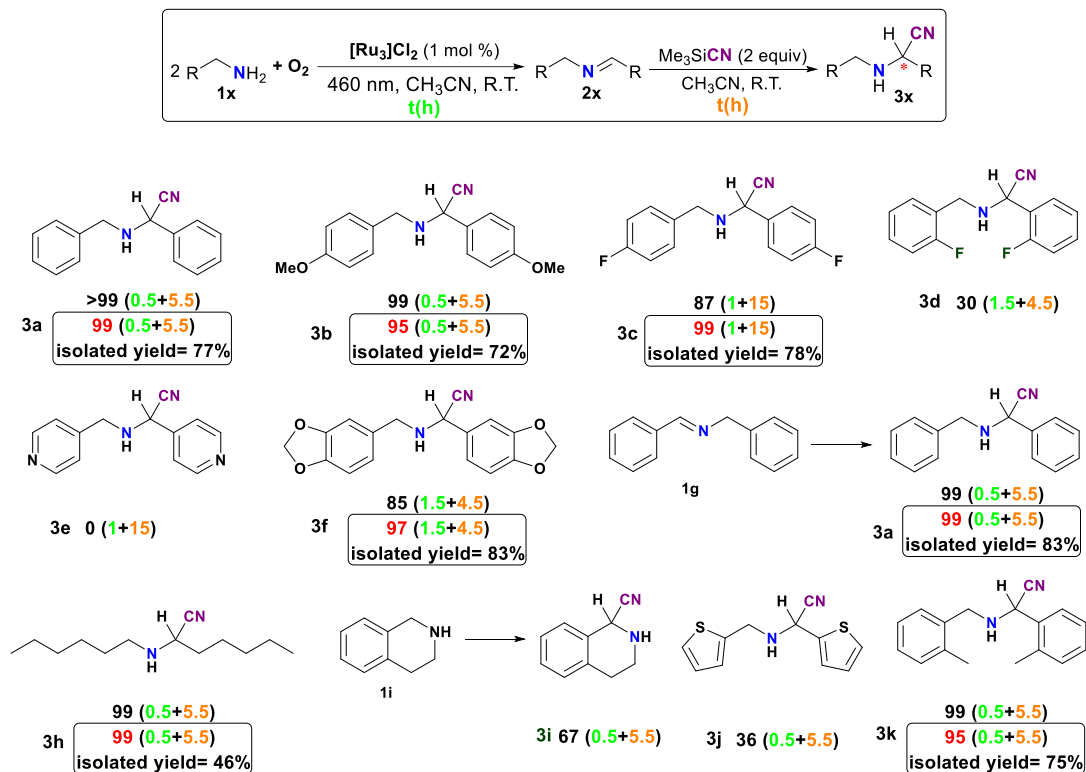


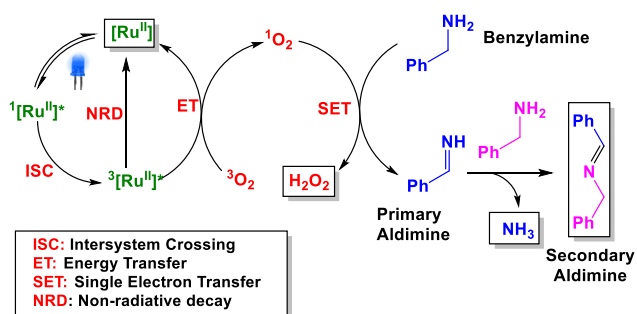
Fig. 9. Substrate scope for the one-pot photocatalytic oxidative cyanation of primary and secondary amines to produce  $\alpha$ -aminonitriles. Reaction conditions: amine (10 mM), TMSCN (2 equiv),  $[\text{Ru}_3]\text{Cl}_2$  (1 mol %), acetonitrile (0.5 mL),  $\text{O}_2$  (balloon, 1 atm), blue LED light (460 nm), bold (conversion yield %), reaction times between parenthesis. Reaction conditions for isolated products: amine (20 mM), TMSCN (2 equiv),  $[\text{Ru}_3]\text{Cl}_2$  (1 mol %), acetonitrile (5 mL),  $\text{O}_2$  (balloon, 1 atm), blue LED light (460 nm). Yields in red, reaction times between parenthesis.

## 2.11. Mechanism

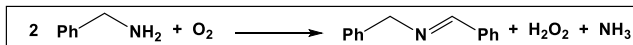
Based on our experimental data and the literature reports<sup>5</sup> on similar reactions we propose the mechanism summarized in Fig. 10. It consists of five different processes: (a) Photoexcitation of the Ru(II) photocatalyst with visible light to generate a singlet excited state and then a long-lived triplet excited state; (b) photosensitization of  $^3\text{O}_2$  to  $^1\text{O}_2$ ; (c) oxidation of benzylamine to the respective primary aldimine; (d) coupling between the primary aldimine and a second molecule of benzylamine to give the secondary aldimine and (e) addition of the cyanide anion to the electrophilic imine carbon to generate the  $\alpha$ -amino nitrile. We speculate that in the last step, TMSCN undergoes hydrolysis due to water traces present in wet  $\text{CH}_3\text{CN}$ ,<sup>5</sup> which generates HCN and  $\text{Me}_3\text{SiOH}$ . Then, HCN activates the imine by proton transfer and the cyanide anion is added to the electrophilic carbon of the iminium intermediate (Fig. 10(b)). Hence, the cyanide addition step involves the participation of one molecule of water which

facilitates the release of the cyanide anion and provides the proton required for the formation of the final product. As a matter of fact, the by-product of the photooxidation step,  $\text{H}_2\text{O}_2$ , was noticed in the crudes of the photocatalytic experiments by  $^1\text{H}$  NMR (see SI Fig. 33 and 34) and was also detected with a peroxide stick test in the crude obtained for the photooxidation of **1a** (SI Fig. 35).

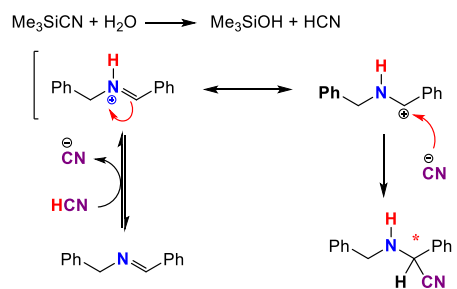
(a) Mechanism for the photooxidative coupling of benzylamines



Global Chemical Equation for the photooxidative coupling of benzylamines



(b) Mechanism for the cyanation step



Global Chemical Equation for the cyanation step

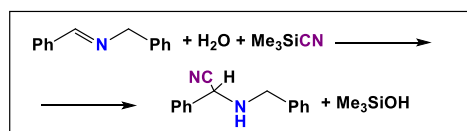


Fig. 10. Mechanism of the photocatalytic one-pot preparation of  $\alpha$ -aminonitriles from primary benzylamines: a) Mechanism for the photooxidative coupling of benzylamines; b) Mechanism for the cyanation step.

### 3. Conclusions

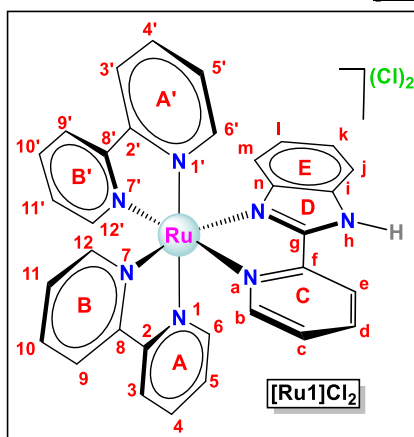
In conclusion, we have prepared and characterized a series of dicationic Ru(II) polypyridyl complexes with general formula  $[\text{Ru}(\text{bpy})_2(\text{N}^{\wedge}\text{N}')]\text{Cl}_2$ , bearing 2-(pyridyl)benzimidazole or its N-alkylated derivatives as the ancillary ligands ( $\text{N}^{\wedge}\text{N}'$ ). Theoretical calculations estimate a moderate destabilization of the HOMO for the new derivatives relative to the prototype complex  $[\text{Ru}(\text{bpy})_3]^{2+}$ ,  $[\mathbf{1}]^{2+}$ , in agreement with their photophysical and electrochemical features. Indeed, this series of complexes exhibit moderate or excellent photostability under visible light irradiation, efficient light absorption in the visible range and photoluminescence with  $\lambda_{\text{em}}$  longer than that recorded for  $[\mathbf{1}]\text{Cl}_2$ . Moreover, our Ru(II) photosensitizers display better PLQY (between 13 and 15 %) than  $[\mathbf{1}]\text{Cl}_2$  (9 %) and half lifetimes for their excited states in the range 231-617 ns. Interestingly, we have demonstrated that the emission of these Ru(II) complexes is quenched by  $\text{O}_2$ , which concurrently generates singlet oxygen with moderate or good  $\phi_{\Delta}$  (e. g., 64 % for  $[\text{Ru}2]\text{Cl}_2$ ). All these features suggest that

phosphorescence is the most likely emission mechanism for these dyes. Electrochemical measurements have confirmed that the excited state of these Ru(II) complexes is a good oxidant and an excellent reductant. Consequently, the photophysical and electrochemical features of these dyes make them suitable triplet photosensitizers and excellent photoredox catalysts. Indeed, we have proved that they promote the photooxidation of primary and secondary amines to produce the corresponding imines in an efficient and selective manner. More importantly, we have applied them to the one-pot photooxidative cyanation of the afore-mentioned amines to produce  $\alpha$ -amino nitriles (10 examples). This transformation proceeds selectively with excellent or moderate yields, under mild and eco-friendly conditions, that is, room temperature, visible light, O<sub>2</sub> as a green oxidant, low PC loading and acetonitrile as solvent. At the same time, we have revealed that complexes [Ru2]Cl<sub>2</sub>-[Ru5]Cl<sub>2</sub> are slightly more active PCs than their parent compound [Ru1]Cl<sub>2</sub>. Therefore, the functionalization of the N<sup>A</sup>N' ligand with alkyl groups is beneficial in terms of photocatalytic activity, likely due to the higher  $\tau$  and  $\phi_{\Delta}^{PC}$  of [Ru2]Cl<sub>2</sub>-[Ru5]Cl<sub>2</sub> relative to [Ru1]Cl<sub>2</sub>. Further to this, we have plotted a mechanism for the studied one-pot photooxidative cyanation of amines which involves the participation of <sup>1</sup>O<sub>2</sub> as the actual oxidant. In brief, we have developed a new family of accessible Ru(II) PCs and we have demonstrated their excellent performance in the efficient and eco-friendly one-pot preparation of  $\alpha$ -amino nitriles.

## 4. Synthesis and characterization

### 4.1. Ru(II)-complexes

#### [Ru(bpy)<sub>2</sub>(L1)]Cl<sub>2</sub>: [Ru1]Cl<sub>2</sub>



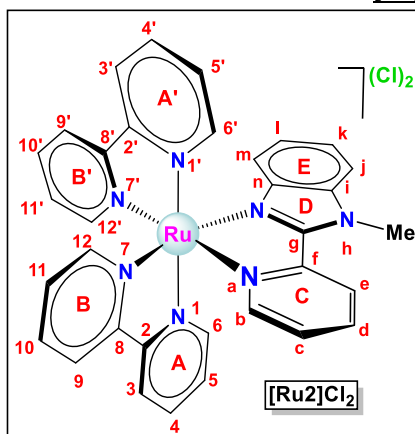
In a 100 mL Schlenk flask, the ancillary ligand **L1** (0.037 g, 0.193 mmol) was added to a solution of RuCl<sub>2</sub>(bpy)<sub>2</sub>·2H<sub>2</sub>O (0.100 g, 0.193 mmol) in EtOH (19 mL), and the mixture was stirred at 90 °C for 16 h. Then, the volume was reduced to the half under vacuum and Et<sub>2</sub>O (15 mL) was added to precipitate a dark red solid that was isolated by filtration and washed with Et<sub>2</sub>O (5 mL). Then, the solid was dried under vacuum at 80 °C for 6 h. Dark red powder. Yield: 0.081 g (0.119 mmol, 62%). **M<sub>r</sub>** (C<sub>32</sub>H<sub>25</sub>Cl<sub>2</sub>N<sub>7</sub>Ru) = 679.56 g/mol. **Anal. Calcd for C<sub>32</sub>H<sub>25</sub>Cl<sub>2</sub>N<sub>7</sub>Ru(H<sub>2</sub>O)<sub>0.35</sub>**: C 56.04; H 3.78; N 14.29; **Found**: C 56.25; H 4.01; N 14.25. <sup>1</sup>H NMR (400 MHz, DMSO-d<sub>6</sub>, 25 °C)  $\delta$  16.20 (s,

1H; H<sup>N-H</sup>), 9.06 (d,  $J_{H-H}$  = 7.7 Hz, 1H; H<sup>e</sup>), 8.88 (dd,  $J_{H-H}$  = 8.1, 4.1 Hz, 3H; H<sup>9</sup>, H<sup>9'</sup>, H<sup>3</sup>), 8.80 (d,  $J_{H-H}$  = 8.1 Hz, 1H; H<sup>3'</sup>), 8.24 (t,  $J_{H-H}$  = 7.9 Hz, 2H; H<sup>d</sup>, H<sup>4</sup>), 8.15 (dt,  $J_{H-H}$  = 10.6, 7.6 Hz, 2H; H<sup>10</sup>, H<sup>10'</sup>), 8.08



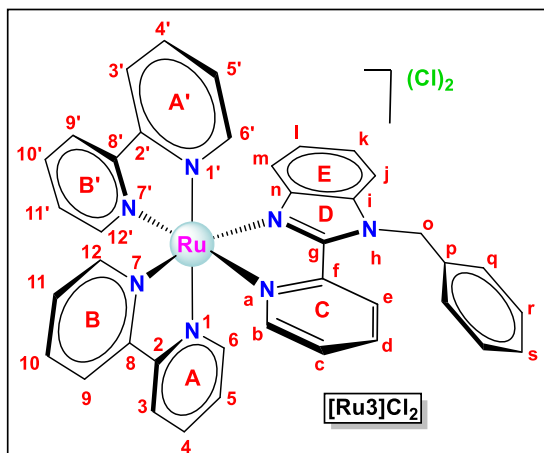
(t,  $J_{H-H} = 7.5$  Hz, 1H;  $H^4$ ), 7.96 (d,  $J_{H-H} = 5.7$  Hz, 1H;  $H^6$ ), 7.85 (d,  $J_{H-H} = 5.7$  Hz, 1H;  $H^{12'}$ ), 7.82 – 7.76 (m, 2H,  $H^{12}$ ,  $H^6$ ), 7.74 (d,  $J = 8.3$  Hz, 1H,  $H^b$ ), 7.70 (d,  $J = 5.6$  Hz, 1H,  $H^l$ ), 7.63 – 7.57 (m, 1H,  $H^c$ ), 7.52 (dq,  $J = 13.5, 6.6$  Hz, 4H,  $H^5$ ,  $H^{11}$ ,  $H^{11'}$ ,  $H^{5'}$ ), 7.36 (t,  $J = 7.7$  Hz, 1H,  $H^k$ ), 7.02 (t,  $J = 7.8$  Hz, 1H,  $H^l$ ), 5.65 (d,  $J = 8.3$  Hz, 1H,  $H^m$ ) ppm.  $^{13}\text{C}\{^1\text{H}\}$  NMR spectra data is not available due to decomposition signs observed in DMSO- $d_6$ . **FT-IR (ATR) selected bands:** 3376 (w,  $\nu_{N-H}$ ), 3012 (w,  $\nu_{C-H}$ ), 1602-1541 (m,  $\nu_{C=C+C-N}$ ), 1419 (w,  $\nu_{C=N}$ ), 1151 (m,  $\nu_{C-C}$ ), 1065-1023 (m,  $\delta_{C-Hip}$ ), 764-730 (vs,  $\delta_{C-Hoop}$ ). **HR-MS ESI(+)(DCM/DMSO, 4:1):**  $[\text{M}-\text{H}^+]^+$  calcd. for  $[\text{C}_{32}\text{H}_{24}\text{N}_7\text{Ru}]^+$  608.1137; found 608.1145;  $[\text{M}]^{2+}$  calcd. for  $[\text{C}_{32}\text{H}_{25}\text{N}_7\text{Ru}]^{2+}$  304.5602 found 304.5612 Da. **Anal. Calcd for  $\text{C}_{32}\text{H}_{25}\text{Cl}_2\text{N}_7\text{Ru}(\text{H}_2\text{O})_{0.35}$ :** C 56.04; H 3.78; N 14.29; **Found:** C 56.25; H 4.01; N 14.25.

**[Ru(bpy)<sub>2</sub>(L2)]Cl<sub>2</sub>, [Ru<sub>2</sub>]Cl<sub>2</sub>**



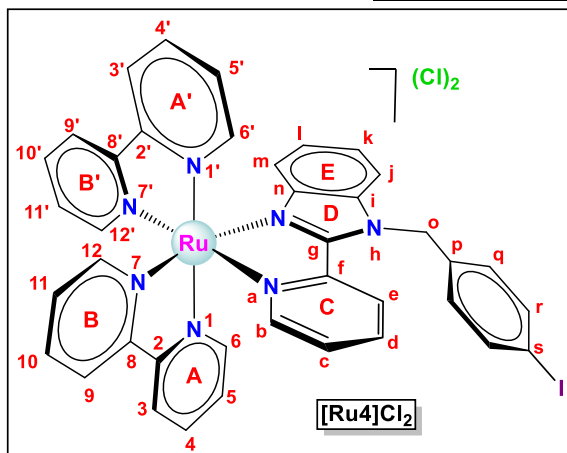
In a 100 mL Schlenk flask, the ancillary ligand **L2** (0.040 g, 0.192 mmol) was added to a solution of  $\text{RuCl}_2(\text{bpy})_2 \cdot 2\text{H}_2\text{O}$  (0.100 g, 0.192 mmol) in ethanol (19 mL), and the mixture was stirred at 90 °C for 16 h. Then, the volume was reduced to the half under vacuum and diethyl ether (15 mL) was added to precipitate a crude solid that was isolated by filtration and washed with diethyl ether (5 mL). The solid was dissolved in methanol/acetone 1:1 (0.75 mL:0.75 mL) and placed in the freezer for 2 days to precipitate the excess of precursor. Then the solution was filtered, the solvent was removed under vacuum and the resulting solid was washed with  $\text{Et}_2\text{O}$  (5 mL), and dried under vacuum

at 80 °C for 6 h. Dark Red solid. Yield: 0.041 g (0.059 mmol, 31%).  $M_r(\text{C}_{33}\text{H}_{27}\text{Cl}_2\text{N}_7\text{Ru}) = 693.59$  g/mol. **Anal. Calcd for  $\text{C}_{33}\text{H}_{27}\text{Cl}_2\text{N}_7\text{Ru}(\text{H}_2\text{O})_{0.32}$ :** C 56.67; H 3.98; N 14.02; **Found:** C 56.80; H 4.13; N 14.29.  $^1\text{H}$  NMR (400 MHz, DMSO- $d_6$ , 25 °C)  $\delta$  8.91 (d,  $J_{H-H} = 8.2$  Hz, 3H;  $H^3$ ,  $H^9$ ,  $H^9$ ), 8.81 (dd,  $J_{H-H} = 8.2, 4.3$  Hz, 2H;  $H^3$ ,  $H^e$ ), 8.24 (m, 2H;  $H^4$ ,  $H^{10}$ ), 8.15 (m, 2H;  $H^{10'}$ ,  $H^4$ ), 8.09 (td,  $J_{H-H} = 7.9, 1.2$  Hz, 1H;  $H^d$ ), 8.01 (d,  $J_{H-H} = 8.5$  Hz, 1H;  $H^j$ ), 7.91 (d,  $J_{H-H} = 5.0$  Hz, 1H;  $H^6$ ), 7.82 (d,  $J_{H-H} = 5.5$  Hz, 1H;  $H^6$ ), 7.79 (d,  $J_{H-H} = 5.57$  Hz, 2H;  $H^b$  or  $H^{12'}$ ), 7.77 (d,  $J_{H-H} = 5.2$  Hz, 2H;  $H^b$  or  $H^{12'}$ ), 7.73 (d,  $J_{H-H} = 5.1$  Hz, 1H;  $H^{12}$ ), 7.57 (m, 4H;  $H^5$ ,  $H^{5'}$ ,  $H^{11}$ ,  $H^{11'}$ ), 7.46 (m, 2H;  $H^c$ ,  $H^k$ ), 7.08 (t,  $J_{H-H} = 7.8$  Hz, 1H;  $H^l$ ), 5.68 (d,  $J_{H-H} = 8.4$  Hz, 1H;  $H^m$ ), 4.47 (s, 3H;  $H^{\text{N-Me}}$ ) ppm.  $^{13}\text{C}\{^1\text{H}\}$  NMR spectra data is not available due to decomposition signs observed in DMSO- $d_6$ . **FT-IR (ATR) selected bands:** 3063 (w,  $\nu_{C-H}$ ), 1601-1565 (m,  $\nu_{C=C+C-N}$ ), 1420 (w,  $\nu_{C=N}$ ), 1162 (m,  $\nu_{C-C}$ ), 1025 (m,  $\delta_{C-Hip}$ ), 806 (w,  $\delta_{C-C}$ ), 745-731 (vs,  $\delta_{C-Hoop}$ ). **HR-MS ESI(+)(DCM/DMSO, 4:1):**  $m/z$   $[\text{M}-\text{Me}]^+$  calcd. for  $[\text{C}_{32}\text{H}_{24}\text{N}_7\text{Ru}]^+$  608.1131 found 608.1140 Da;  $[\text{M}-\text{L}_2+\text{Cl}]^+$  calcd. for  $[\text{C}_{20}\text{H}_{16}\text{N}_4\text{RuCl}]^+$  449.0102; found 449.0106 Da;  $[\text{M}]^{2+}$  calcd. for  $[\text{C}_{33}\text{H}_{27}\text{N}_7\text{Ru}]^{2+}$  311.5680; found 311.5693. **Anal. Calcd for  $\text{C}_{33}\text{H}_{27}\text{Cl}_2\text{N}_7\text{Ru}(\text{H}_2\text{O})_{0.32}$ :** C 56.67; H 3.98; N 14.02; **Found:** C 56.80; H 4.13; N 14.29.

**[Ru(bpy)<sub>2</sub>(L3)]Cl<sub>2</sub>, [Ru<sub>3</sub>Cl<sub>2</sub>]**

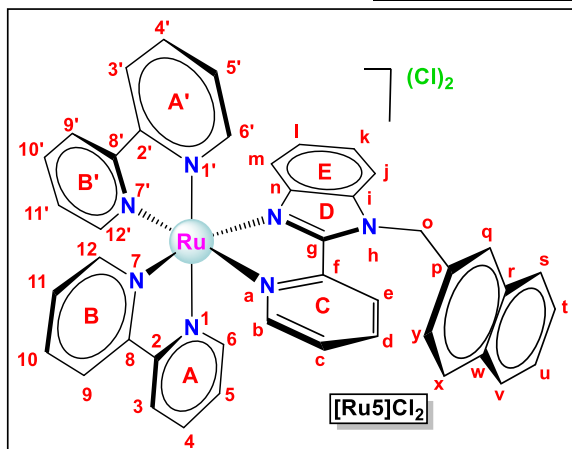
In a 100 mL Schlenk flask, the ancillary ligand **L3** (0.055 g, 0.193 mmol) was added to a solution of RuCl<sub>2</sub>(bpy)<sub>2</sub>·2H<sub>2</sub>O (0.100 g, 0.192 mmol) in ethanol (19 mL), and the mixture was stirred at 90 °C for 24 h. Then, the volume was reduced to the half under vacuum and diethyl ether (15 mL) was added to precipitate a crude solid that was isolated by filtration and washed with diethyl ether (5 mL). The solid was dissolved in water, filtered and dried under vacuum. The solid was washed with diethyl ether (5 mL) and dried under vacuum at 80 °C for 6 h. Dark red solid.

Yield: 0.083 g (0.107 mmol, 56%). **M<sub>r</sub>** (C<sub>39</sub>H<sub>31</sub>Cl<sub>2</sub>N<sub>7</sub>Ru) = 769.69 g/mol. **Anal. Calcd for C<sub>39</sub>H<sub>31</sub>Cl<sub>2</sub>N<sub>7</sub>Ru(H<sub>2</sub>O)<sub>0.85</sub>**: C 59.67; H 4.20; N 12.49; **Found**: C 59.79; H 4.35; N 12.70. **<sup>1</sup>H NMR (400 MHz, DMSO-d<sub>6</sub>, 25 °C)** δ 8.93 (br s, 3H; H<sup>3</sup>, H<sup>9</sup>, H<sup>9'</sup>), 8.85 (d, *J*<sub>H-H</sub> = 8.3 Hz; 1H, H<sup>3'</sup>), 8.53 (d, *J*<sub>H-H</sub> = 8.3 Hz, 1H; H<sup>6</sup>), 8.27 (t, *J*<sub>H-H</sub> = 7.9 Hz, 1H; H<sup>4</sup>), 8.17 (m, 2H; H<sup>10</sup>, H<sup>10'</sup>), 8.11 (d, *J*<sub>H-H</sub> = 8.3 Hz, 1H; H<sup>6</sup>), 8.06 (m, 2H; H<sup>d</sup>, H<sup>4'</sup>), 7.97 (d, *J*<sub>H-H</sub> = 5.4 Hz, 1H; H<sup>6</sup>), 7.88 (d, *J*<sub>H-H</sub> = 5.4 Hz, 1H; H<sup>6'</sup>), 7.77 (m, 2H; H<sup>12'</sup>, H<sup>12</sup>), 7.68 (d, *J*<sub>H-H</sub> = 5.4 Hz, 1H; H<sup>l</sup>), 7.63 (m, 1H; H<sup>5</sup>), 7.50 (m, 5H; H<sup>11</sup>, H<sup>11'</sup>, H<sup>5'</sup>, H<sup>c</sup>, H<sup>k</sup>), 7.33 (m, 3H; H<sup>r</sup>, H<sup>r</sup>, H<sup>s</sup>), 7.14 (m, 1H; H<sup>l</sup>), 7.05 (s, H<sup>q</sup>), 7.03 (s, H<sup>q</sup>), 6.37 (d, *J*<sub>H-H</sub> = 17.9 Hz, 1H; H<sup>o</sup>), 6.29 (d, *J*<sub>H-H</sub> = 17.9 Hz, 1H, H<sup>o</sup>), 5.76 (d, *J* = 8.3 Hz, 1H; H<sup>m</sup>) ppm. **<sup>13</sup>C{<sup>1</sup>H} NMR (101 MHz, DMSO-d<sub>6</sub>, 25 °C)** δ 157.33, 156.91, 156.46, 152.44, 151.62, 151.20, 151.00, 150.55, 147.73, 139.77, 137.93, 137.72, 137.59, 137.54, 137.41, 136.64, 135.09, 128.95, 127.77, 127.74, 127.63, 127.59, 127.55, 127.43, 126.13, 125.59, 125.38, 125.14, 124.50, 124.37, 124.22, 123.98, 114.87, 112.85, 47.98 ppm. **FT-IR (ATR) selected bands**: 3065 (w, ν<sub>C-H</sub>), 1601-1565 (m, ν<sub>C=C + C-N</sub>), 1420 (w, ν<sub>C=N</sub>), 1157 (m, ν<sub>C-C</sub>), 1062-1015 (m, δ<sub>C-Hip</sub>), 773 (vs, δ<sub>C-Hoop</sub>). **HR-MS ESI(+)(DCM/DMSO, 4:1)**: *m/z* [M-Bn]<sup>+</sup> calcd. for [C<sub>32</sub>H<sub>24</sub>N<sub>7</sub>Ru]<sup>+</sup> 608.1131; found 608.1138 Da; [M]<sup>2+</sup> calcd. for [C<sub>39</sub>H<sub>31</sub>N<sub>7</sub>Ru]<sup>2+</sup> 349.5837; found 349.5850 Da. **Anal. Calcd for C<sub>39</sub>H<sub>31</sub>Cl<sub>2</sub>N<sub>7</sub>Ru(H<sub>2</sub>O)<sub>0.85</sub>**: C 59.67; H 4.20; N 12.49; **Found**: C 59.79; H 4.35; N 12.70

**[Ru(bpy)<sub>2</sub>(L4)]Cl<sub>2</sub>, [Ru4]Cl<sub>2</sub>**

In a 100 mL Schlenk flask, the ancillary ligand **L4** (0.079 g, 0.192 mmol) was added to a solution of RuCl<sub>2</sub>(bpy)<sub>2</sub>·2H<sub>2</sub>O (0.100 g, 0.192 mmol) in ethanol (19 mL), and the mixture was stirred at 90 °C for 16 h. Then, the volume was reduced to the half under vacuum and diethyl ether (15 mL) was added to precipitate a crude solid that was isolated by filtration and washed with diethyl ether (5 mL). The solid was dissolved in methanol/acetone 1:1 (0.75/0.75 mL) and placed in the freezer for 2 days. Then the solution was

filtered, dried under vacuum, washed with diethyl ether (5 mL) and finally, dried under vacuum at 80 °C for 6h. Dark red solid. Yield: 0.09 g (0.101 mmol, 53%). **M<sub>r</sub>** (C<sub>39</sub>H<sub>30</sub>Cl<sub>2</sub>I<sub>1</sub>N<sub>7</sub>Ru) = 895.58 g/mol. **Anal. Calcd for C<sub>39</sub>H<sub>30</sub>Cl<sub>2</sub>I<sub>1</sub>N<sub>7</sub>Ru(H<sub>2</sub>O)<sub>0.64</sub>**: C 51.64; H 3.48; N 10.81; **Found**: C 51.69; H 3.60; N 11.03. **<sup>1</sup>H NMR (400 MHz, DMSO-d<sub>6</sub>, 25 °C)** δ 8.90 (m, 3H; H<sup>3</sup>, H<sup>9</sup>, H<sup>9'</sup>), 8.82 (d, *J*<sub>H-H</sub> = 8.0 Hz, 1H; H<sup>3'</sup>), 8.46 (d, *J*<sub>H-H</sub> = 8.4 Hz, 1H; H<sup>6</sup>), 8.27 (t, *J*<sub>H-H</sub> = 7.9 Hz, 1H; H<sup>4</sup>), 8.17 (q, *J*<sub>H-H</sub> = 7.9 Hz, 2H; H<sup>10</sup>, H<sup>10'</sup>), 8.09 (m, 2H; H<sup>4'</sup>, H<sup>d</sup>), 8.01 (d, *J*<sub>H-H</sub> = 8.5 Hz, 1H; H<sup>j</sup>), 7.96 (d, *J*<sub>H-H</sub> = 5.3 Hz, 1H; H<sup>6</sup>), 7.85 (d, *J*<sub>H-H</sub> = 5.3 Hz, 1H; H<sup>12'</sup>), 7.79 (d, *J*<sub>H-H</sub> = 5.2 Hz, 1H; H<sup>12</sup>), 7.75 (d, *J*<sub>H-H</sub> = 5.4 Hz, 1H; H<sup>6'</sup>), 7.72 (s, 1H; H<sup>b</sup>), 7.62 (m, 2H; H<sup>r</sup>, H<sup>r'</sup>), 7.62 (m, 1H; H<sup>5</sup>), 7.51 (m, 5; H<sup>11</sup>, H<sup>11'</sup>, H<sup>5</sup>, H<sup>c</sup>, H<sup>k</sup>), 7.13 (t, *J*<sub>H-H</sub> = 7.8 Hz, 1H; H<sup>l</sup>), 6.89 (s, 1H; H<sup>q</sup>), 6.86 (s, 1H; H<sup>q</sup>), 6.32 (d, *J*<sub>H-H</sub> = 18.1 Hz, 1H; H<sup>o</sup>), 6.24 (d, *J*<sub>H-H</sub> = 18.1 Hz, 1H; H<sup>o</sup>), 5.75 (d, *J* = 8.4 Hz, 1H, H<sup>m</sup>) ppm. **<sup>13</sup>C{<sup>1</sup>H} NMR (101 MHz, DMSO-d<sub>6</sub>, 25 °C)** δ 157.54, 157.13, 156.66, 156.64, 152.67, 151.78, 151.34, 150.68, 147.83, 139.99, 138.12, 137.84, 137.77, 137.66, 136.72, 135.10, 128.11, 127.84, 126.42, 125.49, 125.39, 124.66, 124.54, 124.13, 115.08, 113.00, 94.23, 47.80 ppm. **FT-IR (ATR) selected bands**: 3066 (w, ν<sub>C=CH</sub>), 1601-1572 (m, ν<sub>C=C + C-N</sub>), 1439 (w, ν<sub>C=N</sub>), 1159 (m, ν<sub>C-C</sub>), 1060 (m, δ<sub>C-Hip</sub>), 762-746 (vs, δ<sub>C-Hoop</sub>). **HR-MS ESI(+)(DCM/DMSO, 4:1)**: m/z [M-(4-I-Bn)]<sup>+</sup> calcd. for [C<sub>32</sub>H<sub>24</sub>N<sub>7</sub>Ru]<sup>+</sup> 608.1131; found 608.1143; [M]<sup>2+</sup> calcd. for 412.5320; found 412.5329. **Anal. Calcd for C<sub>39</sub>H<sub>30</sub>Cl<sub>2</sub>I<sub>1</sub>N<sub>7</sub>Ru(H<sub>2</sub>O)<sub>0.64</sub>**: C 51.64; H 3.48; N 10.81; **Found**: C 51.69; H 3.60; N 11.03.

**[Ru(bpy)<sub>2</sub>(L5)]Cl<sub>2</sub>, [Ru5]Cl<sub>2</sub>**

In a 100 mL Schlenk flask, the ancillary ligand **L5** (0.065 g, 0.193 mmol) was added to a solution of RuCl<sub>2</sub>(bpy)<sub>2</sub>·2H<sub>2</sub>O (0.100 g, 0.192 mmol) in ethanol (19 mL), and the mixture was stirred at 90 °C for 16 h. Then, the volume was reduced to the half under vacuum and diethyl ether (15 mL) was added to precipitate a crude solid that was isolated by filtration and washed with diethyl ether (5 mL). The solid was dissolved in ethanol/Acetone 1:1 (0.75/0.75 mL) and placed in the

freezer for 3 days. Then the solution is filtered, dried under vacuum, washed with diethyl ether (5 mL) and dried under vacuum at 80 °C for 6 h. Dark red solid. Yield: 0.081 g (0.099 mmol, 51%). **M<sub>r</sub>** (C<sub>43</sub>H<sub>33</sub>Cl<sub>2</sub>N<sub>7</sub>Ru) = 819.75 g/mol. **Anal. Calcd for C<sub>43</sub>H<sub>33</sub>Cl<sub>2</sub>N<sub>7</sub>Ru(H<sub>2</sub>O)<sub>0.75</sub>**: C 61.98; H 4.17; N 11.77; **Found**: C 61.90; H 4.32; N 12.01. **<sup>1</sup>H NMR (400 MHz, DMSO-d<sub>6</sub>, 25 °C)** δ 8.92 (m, 3H; H<sup>3</sup>, H<sup>9</sup>, H<sup>9'</sup>), 8.86 (d, *J*<sub>H-H</sub> = 7.9 Hz, 1H; H<sup>3'</sup>), 8.50 (d, *J*<sub>H-H</sub> = 8.3 Hz, 1H; H<sup>e</sup>), 8.28 (t, *J*<sub>H-H</sub> = 7.7 Hz, 1H; H<sup>4</sup>), 8.17 (m, 3H; H<sup>10</sup>, H<sup>10'</sup>, H<sup>4'</sup>), 8.09 (d, *J*<sub>H-H</sub> = 8.4 Hz, 1H), 8.03 (m, 1H; H<sup>d</sup>), 7.97 (m; 3H), 7.91 (m, 1H), 7.74 (m; 4H), 7.64 (m, 1H; H<sup>5</sup>), 7.51 (m, 8H; H<sup>11</sup>, H<sup>11'</sup>, H<sup>5'</sup>, H<sup>c</sup>, H<sup>k</sup>, 3H<sub>arom</sub>), 7.29 (d, *J*<sub>H-H</sub> = 8.7 Hz, 1H), 7.16 (t, *J*<sub>H-H</sub> = 7.7 Hz, 1H; H<sup>l</sup>), 6.52 (d, *J*<sub>H-H</sub> = 18.1 Hz, 1H; H<sup>o</sup>), 6.42 (d, *J*<sub>H-H</sub> = 18.1 Hz, 1H; H<sup>o</sup>), 5.79 (d, *J*<sub>H-H</sub> = 8.2 Hz, 1H; H<sup>m</sup>) ppm. **<sup>13</sup>C{<sup>1</sup>H} NMR (101 MHz, DMSO-d<sub>6</sub>, 25 °C)** δ 157.58, 157.13, 156.69, 152.64, 151.93, 151.84, 151.37, 151.32, 150.81, 147.91, 140.08, 138.13, 137.91, 137.82, 137.75, 137.60, 136.91, 132.96, 132.75, 132.37, 131.45, 129.01, 127.95, 127.87, 127.80, 127.72, 127.67, 127.64, 126.76, 126.44, 126.37, 126.33, 125.55, 125.38, 124.68, 124.55, 124.43, 124.22, 124.15, 123.93, 115.14, 113.12, 48.45 ppm. **FT-IR (ATR) selected bands**: 3065 (w, ν<sub>C-H</sub>), 1601-1576 (m, ν<sub>C=C + C-N</sub>), 1421 (w, ν<sub>C=N</sub>), 1157 (m, ν<sub>C-C</sub>), 1062-1013 (m, δ<sub>C-Hip</sub>), 763-746 (vs, δ<sub>C-Hoop</sub>). **HR-MS ESI(+)(DCM/DMSO, 4:1)**: m/z [M-(CH<sub>2</sub>-Naphtyl)]<sup>+</sup> calcd. for [C<sub>32</sub>H<sub>24</sub>N<sub>7</sub>Ru]<sup>+</sup> 608.1131; found 608.1130; [M]<sup>2+</sup> calcd. for [C<sub>43</sub>H<sub>33</sub>N<sub>7</sub>Ru]<sup>2+</sup> 374.5915; found 374.5924. **Anal. Calcd for C<sub>43</sub>H<sub>33</sub>Cl<sub>2</sub>N<sub>7</sub>Ru(H<sub>2</sub>O)<sub>0.75</sub>**: C 61.98; H 4.17; N 11.77; **Found**: C 61.90; H 4.32; N 12.01.

## Bibliography

1. S.-I. Murahashi, Synthetic Aspects of Metal-Catalyzed Oxidations of Amines and Related Reactions,

- Angew. Chem. Int. Ed. Engl.*, 1995, **34**, 2443–2465.
2. S. Kobayashi, and H. Ishitani, Catalytic Enantioselective Addition to Imines, *Chem. Rev.*, 1999, **99**, 1069–1094.
  3. K. Yamada, and K. Tomioka, Copper-Catalyzed Asymmetric Alkylation of Imines with Dialkylzinc and Related Reactions, *Chem. Rev.*, 2008, **108**, 2874–2886.
  4. T. Sonobe, K. Oisaki, and M. Kanai, Catalytic aerobic production of imines en route to mild, green, and concise derivatizations of amines, *Chem. Sci.*, 2012, **3**, 3249.
  5. V. V. Kouznetsov, and C. E. P. Galvis, Strecker reaction and  $\alpha$ -amino nitriles: Recent advances in their chemistry, synthesis, and biological properties, *Tetrahedron*, 2018, **74**, 773–810.
  6. R. W. Layer, The Chemistry of Imines., *Chem. Rev.*, 1963, **63**, 489–510.
  7. M. LARGERON, Protocols for the Catalytic Oxidation of Primary Amines to Imines, *European J. Org. Chem.*, 2013, **2013**, 5225–5235.
  8. F. Stanek, R. Pawlowski, P. Morawska, R. Bujok, and M. Stodulski, Dehydrogenation and  $\alpha$ -functionalization of secondary amines by visible-light-mediated catalysis, *Org. Biomol. Chem.*, 2020, **18**, 2103–2112.
  9. F. F. Fleming, L. Yao, P. C. Ravikumar, L. Funk, and B. C. Shook, Nitrile-Containing Pharmaceuticals: Efficacious Roles of the Nitrile Pharmacophore, *J. Med. Chem.*, 2010, **53**, 7902–7917.
  10. D. Enders, and J. P. Shillock, Some recent applications of  $\alpha$ -amino nitrile chemistry, *Chem. Soc. Rev.*, 2000, **29**, 359–373.
  11. F. Le Vaillant, M. D. Wodrich, and J. Waser, Room temperature decarboxylative cyanation of carboxylic acids using photoredox catalysis and cyanobenziodoxolones: a divergent mechanism compared to alkynylation, *Chem. Sci.*, 2017, **8**, 1790–1800.
  12. N. Otto, and T. Opatz, Heterocycles from  $\alpha$ -Aminonitriles, *Chem. - A Eur. J.*, 2014, **20**, 13064–13077.
  13. M. Rueping, S. Zhu, and R. M. Koenigs, Visible-light photoredox catalyzed oxidative Strecker reaction, *Chem. Commun.*, 2011, **47**, 12709–12711.
  14. M. Zheng, J. Shi, T. Yuan, and X. Wang, Metal-Free Dehydrogenation of N-Heterocycles by Ternary h-BCN Nanosheets with Visible Light, *Angew. Chem. Int. Ed. Engl.*, 2018, **57**, 5487–5491.
  15. P.-Y. Liu, C. Zhang, S.-C. Zhao, F. Yu, F. Li, and Y.-P. He, Metal-Free Aerobic Oxidative Cyanation of Tertiary Amines: Azobis(isobutyronitrile) (AIBN) as a Sole Cyanide Source, *J. Org. Chem.*, 2017, **82**, 12786–12790.
  16. M. Huang, Q. Deng, Q. Gao, J. Shi, X. Zhang, and Y. Xiong, Iron-Sulfate-Catalyzed Direct Dehydrogenative Coupling Cyanation of Secondary Phenylamines, *Asian J. Org. Chem.*, 2018, **7**, 404–410.
  17. D. P. Hari, and B. König, Eosin Y Catalyzed Visible Light Oxidative C–C and C–P bond Formation, *Org. Lett.*, 2011, **13**, 3852–3855.
  18. W. P. To, G. S. M. Tong, W. Lu, C. Ma, J. Liu, A. L. F. Chow, and C. M. Che, Luminescent organogold(III) complexes with long-lived triplet excited states for light-induced oxidative C–H bond functionalization and hydrogen production, *Angew. Chem. Int. Ed. Engl.*, 2012, **51**, 2654–2657.

19. O. Yilmaz, M. S. Oderinde, and M. H. Emmert, Photoredox-Catalyzed C  $\alpha$ -H Cyanation of Unactivated Secondary and Tertiary Aliphatic Amines: Late-Stage Functionalization and Mechanistic Studies, *J. Org. Chem.*, 2018, **83**, 11089–11100.
20. D. B. Ushakov, K. Gilmore, D. Kopetzki, D. T. McQuade, and P. H. Seeberger, Continuous-Flow Oxidative Cyanation of Primary and Secondary Amines Using Singlet Oxygen, *Angew. Chem. Int. Ed. Engl.*, 2014, **53**, 557–561.
21. A. M. Nauth, E. Schechtel, R. Dören, W. Tremel, and T. Opatz, TiO<sub>2</sub> Nanoparticles Functionalized with Non-innocent Ligands Allow Oxidative Photocyanation of Amines with Visible/Near-Infrared Photons, *J. Am. Chem. Soc.*, 2018, **140**, 14169–14177.
22. M. Vaquero, A. Ruiz-Riaguas, M. Martínez-Alonso, F. A. Jalón, B. R. Manzano, A. M. Rodríguez, G. García-Herbosa, A. Carbayo, B. García, and G. Espino, Selective Photooxidation of Sulfides Catalyzed by Bis-cyclometalated Ir(III) Photosensitizers Bearing 2,2'-Dipyridylamine-Based Ligands, *Chem. - A Eur. J.*, 2018, **24**, 10662–10671.
23. C. Yagüe, I. Echevarría, M. Vaquero, J. Fidalgo, A. Carbayo, F. A. Jalón, J. Lima, A. Moro, B. R. Manzano, and G. Espino, Non-emissive Ru(II) polypyridyl complexes as efficient and selective photosensitizers for the photooxidation of benzylamines, *Chem. - A Eur. J.*, 2020, **26**, 12219–12232.
24. W.-K. Huang, C.-W. Cheng, S.-M. Chang, Y.-P. Lee, and E. W.-G. Diau, Synthesis and electron-transfer properties of benzimidazole-functionalized ruthenium complexes for highly efficient dye-sensitized solar cells, *Chem. Commun.*, 2010, **46**, 8992.
25. M. Vaquero, N. Busto, N. Fernández-Pampín, G. Espino, and B. García, Appended Aromatic Moieties Determine the Cytotoxicity of Neutral Cyclometalated Platinum(II) Complexes Derived from 2-(2-Pyridyl)benzimidazole, *Inorg. Chem.*, 2020, **59**, 4961–4971.
26. N. M. Shavaleev, Z. R. Bell, T. L. Easun, R. Rutkaite, L. Swanson, and M. D. Ward, Complexes of substituted derivatives of 2-(2-pyridyl)benzimidazole with Re(I), Ru(II) and Pt(II): structures, redox and luminescence properties, *Dalton Trans.*, 2004, 3678.
27. B. P. Sullivan, D. J. Salmon, and T. J. Meyer, Mixed phosphine 2,2'-bipyridine complexes of ruthenium, *Inorg. Chem.*, 1978, **17**, 3334–3341.
28. J. Wu, H.-Y. Li, L.-C. Kang, D.-P. Li, Q.-L. Xu, Y.-C. Zhu, Y.-M. Tao, Y.-X. Zheng, J.-L. Zuo, and X.-Z. You, Ruthenium(II) polypyridyl complexes based on bipyridine and two novel diimine ligands with carrier-transporting unit: synthesis, photoluminescence and redox properties, *J. Organomet. Chem.*, 2010, **695**, 2048–2056.
29. A. Begum, and P. G. Pickup, Electrocatalysis of CO<sub>2</sub> reduction by ruthenium benzothiazole and bithiazole complexes, *Electrochem. commun.*, 2007, **9**, 2525–2528.
30. R. Gobetto, G. Caputo, C. Garino, S. Ghiani, C. Nervi, L. Salassa, E. Rosenberg, J. B. A. Ross, G. Viscardi, G. Martra, I. Miletto, and M. Milanesio, Synthesis, Electrochemical and Electrogenerated Chemiluminescence Studies of Ruthenium(II) Bis(2,2'-bipyridyl){2-(4-methylpyridin-2-yl)benzo[d]-X-azole} Complexes, *Eur. J. Inorg. Chem.*, 2006, **2006**, 2839–2849.
31. K. T. Ngo, N. A. Lee, S. D. Pinnace, D. J. Szalda, R. T. Weber, and J. Rochford, Probing the Noninnocent  $\pi$ -Bonding Influence of N-Carboxyamidoquinolate Ligands on the Light Harvesting and Redox Properties of Ruthenium Polypyridyl Complexes, *Inorg. Chem.*, 2016, **55**, 2460–2472.

32. K. Nakamaru, Synthesis, Luminescence Quantum Yields, and Lifetimes of Trischelated Ruthenium(II) Mixed-ligand Complexes Including 3,3'-Dimethyl-2,2'-bipyridyl, *Bull. Chem. Soc. Jpn.*, 1982, **55**, 2697–2705.
33. A. Juris, V. Balzani, F. Barigelletti, S. Campagna, P. Belser, and A. von Zelewsky, Ru(II) polypyridine complexes: photophysics, photochemistry, electrochemistry, and chemiluminescence, *Coord. Chem. Rev.*, 1988, **84**, 85–277.
34. K. Suzuki, A. Kobayashi, S. Kaneko, K. Takehira, T. Yoshihara, H. Ishida, Y. Shiina, S. Oishi, and S. Tobita, Reevaluation of absolute luminescence quantum yields of standard solutions using a spectrometer with an integrating sphere and a back-thinned CCD detector, *Phys. Chem. Chem. Phys.*, 2009, **11**, 9850.
35. M.-A. Haga, Synthesis, and electrochemical properties of mononuclear and binuclear ruthenium complexes containing 2,2'-bibenzimidazole, *Inorganica Chim. Acta*, 1980, **45**, L183–L184.
36. C. K. Prier, D. A. Rankic, and D. W. C. MacMillan, Visible Light Photoredox Catalysis with Transition Metal Complexes: Applications in Organic Synthesis, *Chem. Rev.*, 2013, **113**, 5322–5363.
37. Y. Lu, R. Conway-Kenny, J. Wang, X. Cui, J. Zhao, and S. M. Draper, Exploiting coumarin-6 as ancillary ligands in 1,10-phenanthroline Ir(III) complexes: generating triplet photosensitisers with high upconversion capabilities, *Dalton Trans.*, 2018, **47**, 8585–8589.
38. N. Adarsh, R. R. Avirah, and D. Ramaiah, Tuning Photosensitized Singlet Oxygen Generation Efficiency of Novel Aza-BODIPY Dyes, *Org. Lett.*, 2010, **12**, 5720–5723.
39. P. Majumdar, X. Yuan, S. Li, B. Le Guennic, J. Ma, C. Zhang, D. Jacquemin, and J. Zhao, Cyclometalated Ir(III) complexes with styryl-BODIPY ligands showing near IR absorption/emission: preparation, study of photophysical properties and application as photodynamic/luminescence imaging materials, *J. Mater. Chem. B*, 2014, **2**, 2838–2854.
40. S. P.-Y. Li, C. T.-S. Lau, M.-W. Louie, Y.-W. Lam, S. H. Cheng, and K. K.-W. Lo, Mitochondria-targeting cyclometalated iridium(III)-PEG complexes with tunable photodynamic activity, *Biomaterials*, 2013, **34**, 7519–7532.
41. S. Monro, K. L. Colón, H. Yin, J. Roque, P. Konda, S. Gujar, R. P. Thummel, L. Lilge, C. G. Cameron, and S. A. McFarland, Transition Metal Complexes and Photodynamic Therapy from a Tumor-Centered Approach: Challenges, Opportunities, and Highlights from the Development of TLD1433, *Chem. Rev.*, 2019, **119**, 797–828.
42. M. Martínez-Alonso, N. Busto, L. D. Aguirre, L. Berlanga, M. C. Carrión, J. V. Cuevas, A. M. Rodríguez, A. Carbayo, B. R. Manzano, E. Ortí, F. A. Jalón, B. García, and G. Espino, Strong Influence of the Ancillary Ligand over the Photodynamic Anticancer Properties of Neutral Biscyclometalated Ir III Complexes Bearing 2-Benzoazole-Phenolates, *Chem. - A Eur. J.*, 2018, **24**, 17523–17537.
43. C. Pérez-Arnaiz, M. I. Acuña, N. Busto, I. Echevarría, M. Martínez-Alonso, G. Espino, B. García, and F. Domínguez, Thiabendazole-based Rh(III) and Ir(III) biscyclometalated complexes with mitochondria-targeted anticancer activity and metal-sensitive photodynamic activity, *Eur. J. Med. Chem.*, 2018, **157**, 279–293.
44. H. Iranmanesh, K. S. A. Arachchige, M. Bhadbhade, W. A. Donald, J. Y. Liew, K. T. C. Liu, E. T. Luis, E. G. Moore, J. R. Price, H. Yan, J. Yang, and J. E. Beves, Chiral Ruthenium(II) Complexes as Supramolecular Building Blocks for Heterometallic Self-Assembly, *Inorg. Chem.*, 2016, **55**, 12737–12751.
45. M. Martínez-Alonso, J. Cerdá, C. Momblona, A. Pertegás, J. M. Junquera-Hernández, A. Heras, A. M.

Rodríguez, G. Espino, H. Bolink, and E. Ortí, Highly Stable and Efficient Light-Emitting Electrochemical Cells Based on Cationic Iridium Complexes Bearing Arylazole Ancillary Ligands, *Inorg. Chem.*, 2017, **56**, 10298–10310.

46. R. Lechner, and B. König, Oxidation and Deprotection of Primary Benzylamines by Visible Light Flavin Photocatalysis, *Synthesis*, 2010, **2010**, 1712–1718.

47. V. V. Patil, E. M. Gayakwad, and G. S. Shankarling, m-CPBA Mediated Metal Free, Rapid Oxidation of Aliphatic Amines to Oximes, *J. Org. Chem.*, 2016, **81**, 781–786.

48. H. Wang, L. Wang, S. Wang, X. Dong, J. Zhang, and F. Xiao, Aerobic Activation of C-H Bond in Amines Over a Nanorod Manganese Oxide Catalyst, *ChemCatChem*, 2019, **11**, 401–406.

49. G. F. P. de Souza, T. W. von Zuben, and A. G. Salles, “On Water” Metal-Catalyst-Free Oxidative Coupling–Amidation of Amines To Access Imines and Amides, *ACS Sustain. Chem. Eng.*, 2017, **5**, 8439–8446.

50. M. Sheykhani, Z. Rashidi Ranjbar, A. Morsali, and A. Heydari, Minimisation of E-Factor in the synthesis of N-hydroxylamines: the role of silver(I)-based coordination polymers, *Green Chem.*, 2012, **14**, 1971.

51. A. Primo, M. Puche, O. D. Pavel, B. Cojocaru, A. Tirsoaga, V. Parvulescu, and H. García, Graphene oxide as a metal-free catalyst for oxidation of primary amines to nitriles by hypochlorite, *Chem. Commun.*, 2016, **52**, 1839–1842.

52. C. Su, R. Tandiana, B. Tian, A. Sengupta, W. Tang, J. Su, and K. P. Loh, Visible-Light Photocatalysis of Aerobic Oxidation Reactions Using Carbazolic Conjugated Microporous Polymers, *ACS Catal.*, 2016, **6**, 3594–3599.

53. M. Rueping, C. Vila, A. Szadkowska, R. M. Koenigs, and J. Fronert, Photoredox Catalysis as an Efficient Tool for the Aerobic Oxidation of Amines and Alcohols: Bioinspired Demethylations and Condensations, *ACS Catal.*, 2012, **2**, 2810–2815.

54. Y. R. Girish, R. Biswas, and M. De, Mixed-Phase 2D-MoS<sub>2</sub> as an Effective Photocatalyst for Selective Aerobic Oxidative Coupling of Amines under Visible-Light Irradiation, *Chem. - A Eur. J.*, 2018, **24**, 13871–13878.

55. A. Kumar, A. M. Sadanandhan, and S. L. Jain, Silver doped reduced graphene oxide as a promising plasmonic photocatalyst for oxidative coupling of benzylamines under visible light irradiation, *New J. Chem.*, 2019, **43**, 9116–9122.

56. J. Jin, C. Yang, B. Zhang, and K. Deng, Selective oxidation of amines using O<sub>2</sub> catalyzed by cobalt thiophorphrazine under visible light, *J. Catal.*, 2018, **361**, 33–39.





---

***Chapter 5. Photocatalytic Aerobic  
Dehydrogenation of N-Heterocycles  
with Ir(III) Photosensitizers Bearing  
the 2(2'-Pyridyl)benzimidazole  
Scaffold***

---





This work can be found published as: I. Echevarría, M. Vaquero, B. R. Manzano, F. A. Jalón, R. Quesada, and G. Espino, Photocatalytic Aerobic Dehydrogenation of N-Heterocycles with Ir (III) Photosensitizers Bearing the 2 (2'-Pyridyl) benzimidazole Scaffold, *Inorg. Chem.*, 2022, **61**, 6193-6208.

## 0. Abstract

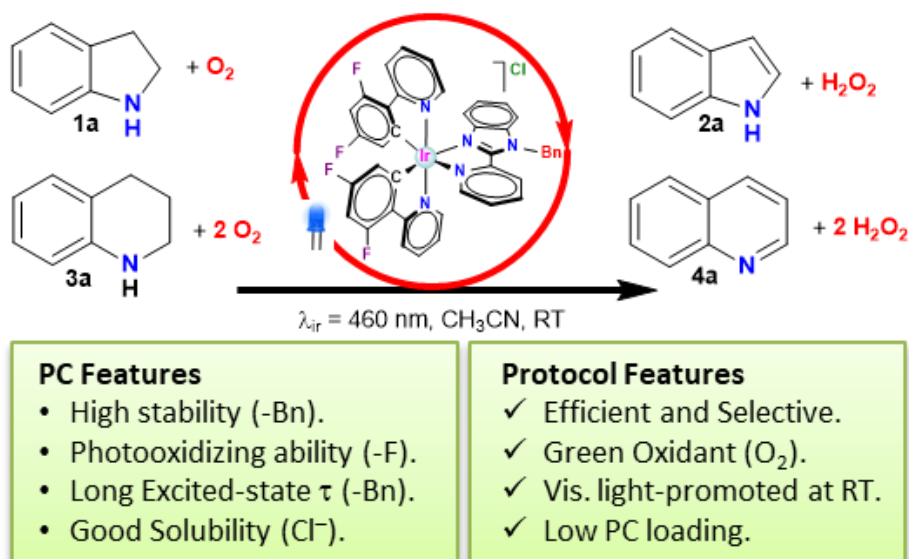


Fig. 1. Scheme of the photocatalytic dehydrogenation of N-heterocycles and highlights of its main features.

Photoredox catalysis constitutes a very powerful tool in organic synthesis, due to its versatility, efficiency, and the mild conditions required by photoinduced transformations. In this paper, we present an efficient and selective photocatalytic procedure for the aerobic oxidative dehydrogenation of partially saturated N-heterocycles to afford the respective N-heteroarenes (indoles, quinolines, acridines, and quinoxalines). The protocol involves the use of new Ir(III) biscyclometalated photocatalysts of general formula  $[\text{Ir}(\text{C}^{\wedge}\text{N})_2(\text{N}^{\wedge}\text{N}')]\text{Cl}$ , where the  $\text{C}^{\wedge}\text{N}$  ligand is 2-(2,4-difluorophenyl)pyridinate, and  $\text{N}^{\wedge}\text{N}'$  are different ligands based on the 2-(2'-pyridyl)benzimidazole scaffold. In-depth electrochemical and photophysical studies as well as DFT calculations have allowed us to establish structure–activity relationships, which provide insights for the rational design of efficient metal-based dyes in photocatalytic oxidation reactions. In addition, we have formulated a dual mechanism, mediated by the radical anion superoxide, for the above-mentioned transformations.

## 1. Introduction

N-heterocycles are pivotal scaffolds in the pharmaceutical industry due to their biological activity and medicinal applications.<sup>1</sup> In particular, indoles,<sup>2</sup> quinolines,<sup>3,4</sup> acridines,<sup>5,6</sup> and quinoxalines<sup>7</sup> display anticancer, antibiotic, antibacterial, antifungal, and anti-inflammatory properties. Moreover, the redox couples formed by 1,2,3,4-tetrahydroquinolines (THQ) and the corresponding quinolines have been proposed as potential hydrogen-storage material systems for fuel cell applications, since the catalytic hydrogenation of quinolines takes place under mild reaction conditions and can be reverted through catalytic dehydrogenation protocols.<sup>8</sup>

Traditional procedures for preparing N-containing aromatic molecules from partially saturated N-heterocycles involve harsh reaction conditions (high temperatures), the use of stoichiometric toxic or corrosive oxidants (2,3-dichloro-5,6-dicyano-1,4-benzoquinone (DDQ), sulfur, or metal oxides), as well as the generation of undesirable waste.<sup>9</sup>

More recently, several groups have described methodologies to prepare different aromatic N-heterocycles (N-heteroarenes) from partially saturated precursors through either catalytic oxidative dehydrogenation using O<sub>2</sub><sup>10</sup> or catalytic acceptorless dehydrogenation.<sup>11,12</sup> Nevertheless, both strategies require high temperatures and/or harsh reaction conditions and, in some cases, harmful solvents and high catalyst loadings.

The synthesis of N-heteroarenes can also be accomplished through photocatalytic approaches such as the acceptorless dehydrogenation (ADH) of THQs, indolines and similar heterocycles. Different photocatalytic systems have been successfully used to prove this methodology, namely, combinations of a Ru-photocatalyst (PC) and a Co catalyst,<sup>8,13</sup> or an acridinium PC and a Pd metal catalyst,<sup>14</sup> and also heterogeneous PCs, that is, hexagonal boron carbon nitride nanosheets<sup>15</sup> or Rh-photodeposited TiO<sub>2</sub> nanoparticles.<sup>16</sup> This transformation produces molecular hydrogen as the only byproduct, but it must be managed through expensive procedures when operating at high scale.

Alternatively, it is possible to access N-heteroarenes through oxidative dehydrogenation (ODH) of partially saturated precursors under aerobic photocatalytic conditions, which implies the use of O<sub>2</sub> as the hydrogen acceptor (green oxidant), visible light, and a photosensitizer. In particular, the synthesis of a variety of N-heteroarenes (quinolines, quinoxalines, quinazolines, acridines, and indoles) has been performed using this type of strategy in the presence of different photocatalytic systems: [Ru(bpy)<sub>3</sub>]Cl<sub>2</sub>,<sup>17</sup> Rose Bengal,<sup>9</sup> TiO<sub>2</sub> grafted with Ni(II) ions in the presence of 4-amino-TEMPO,<sup>18</sup> and a cobalt-phthalocyanine photoredox catalyst in a biphasic

medium.<sup>19</sup> Nevertheless, there is still scope to explore new photosensitizers with the goal of increasing product yields, reducing reaction times and employing solvents with low boiling points. What is more, additional studies should be done for a better understanding of the reaction mechanism entailed in this type of transformations.

In a previous work, we have designed a family of new Ir(III) biscyclometalated complexes with  $\beta$ -carbolines as efficient photocatalysts for the one-pot oxidative thiocyanation of indolines, which produces the respective 3-thiocyanate indoles.<sup>20</sup> We have also reported on a protocol to prepare  $\alpha$ -amino nitriles through the Ru-photosensitized oxidative cyanation of amines.<sup>21</sup>

In this work, we present the synthesis of new Ir(III) biscyclometalated complexes of general formula  $[\text{Ir}(\text{C}^{\wedge}\text{N})_2(\text{N}^{\wedge}\text{N}')]\text{Cl}$ , where  $\text{C}^{\wedge}\text{N} = 2$ -(2,4-difluorophenyl)pyridinate (dfppy) and  $\text{N}^{\wedge}\text{N}'$  stands for different N,N-donor ligands containing the 2-(2'-pyridyl)benzimidazole scaffold. The ligand dfppy was chosen to obtain enhanced photoluminescent quantum yields and higher excited-state lifetimes, since this behaviour is usually expected from the presence of electron-withdrawing groups, such as the -F atoms on the  $\text{C}^{\wedge}\text{N}$  ligands in this type of complexes.<sup>22,23</sup> 2-(2'-pyridyl)benzimidazole was selected as the scaffold for the  $\text{N}^{\wedge}\text{N}'$  ligands due to both its commercial availability and the presence of the imidazole N-H, which allows easy functionalization with a variety of alkyl groups. This, in turn, allows to explore the impact of different functional groups on the photophysical and electrochemical properties of the resulting complexes (see below). In addition, we describe the evaluation of these complexes as photosensitizers in oxidative dehydrogenation processes. Furthermore, relationships between the photosensitizing abilities of these complexes and their electrochemical and photophysical properties are established. In particular, the effect of using dfppy as the  $\text{C}^{\wedge}\text{N}$  ligand and the influence of the different functional groups of the  $\text{N}^{\wedge}\text{N}'$  ligands on the photocatalytic performance of our dyes are emphasized.

## 2. Results and discussion

### 2.1. Synthesis of Ligands and Iridium(III) Complexes

We have synthesized a family of Ir(III) biscyclometalated compounds of general formula  $\text{rac}[\text{Ir}(\text{C}^{\wedge}\text{N})_2(\text{N}^{\wedge}\text{N}')]\text{Cl}$  with the aim of developing new efficient photocatalysts. In this series of compounds, we have furnished the iridium center with two units of the anionic  $\text{C}^{\wedge}\text{N}$  donor 2-(2,4-difluorophenyl)pyridinate (dfppy) and one N,N-ligand, that is the 2-(2'-pyridyl)benzimidazole scaffold (Hpybim = **L1**) or its N-alkylated derivatives (**L2-L5**). The ligand 2-(2'-pyridyl)benzimidazole (**L1**) is commercially available, and its N-functionalized derivatives (**L2-L5**) were prepared by reacting **L1** with MeI, for **L2**, or the

appropriate alkyl bromide (R-Br), for **L3–L5**, at room temperature in the presence of  $K_2CO_3$  and using DMF as solvent (see Fig. 2).<sup>24–26</sup> The incorporation of diverse alkyl groups into the N^A N' ligand aimed to reduce intermolecular interactions and to assess different effects on the photophysical and photocatalytic properties of the resulting Ir derivatives. Thus, the methyl and benzyl groups (**L2**, **L3**, and **L4**) were chosen to protect the respective complexes from either self-quenching or N–H reactivity. The naphthalenylmethyl group (**L5**) was used to evaluate the potential beneficial effect of a  $\pi$ -extended system on the absorption profile of its Ir derivative.

The Ir(III) compounds **[Ir1]Cl–[Ir5]Cl** were obtained by refluxing the iridium dimer  $[Ir(\mu\text{-Cl})(dfppy)_2]_2$  (dfppy = 2-(2,4-difluorophenyl)pyridinate) in the presence of ligands **L1–L5** (1:2 molar ratio) in a dichloromethane-methanol mixture (1:1.25; v/v) (Fig. 2). The products were isolated in the form of bright yellow solids, as chloride salts of racemic mixtures corresponding to the  $\Delta$  and  $\Lambda$  cationic complexes (helical chirality).

The synthesis of the  $PF_6^-$  salts of complexes **[Ir1]<sup>+</sup>** and **[Ir2]<sup>+</sup>** has been previously described, but to the best of our knowledge, their photocatalytic activity has not been studied so far.<sup>27,28</sup>

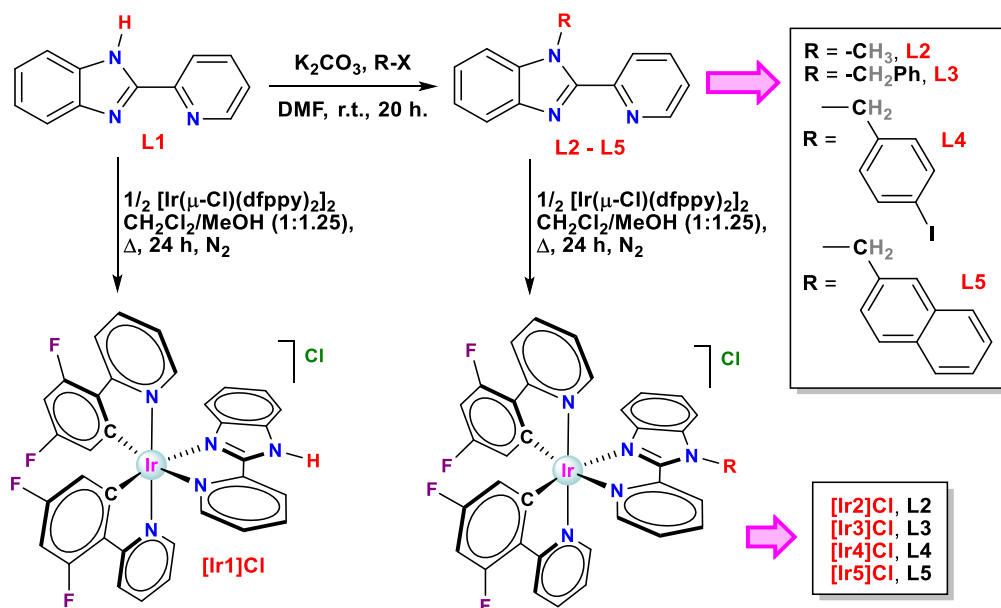


Fig. 2. Synthesis route and molecular structures of ligands **L1–L5** and complexes **[Ir1]Cl–[Ir5]Cl**. Complexes were obtained as racemic mixtures but only  $\Lambda$  enantiomers are shown.

## 2.2. Characterization of the Ir(III) Complexes

The iridium derivatives were unequivocally characterized by multinuclear NMR, mass spectrometry, elemental analysis, and IR spectroscopy. In addition, the crystal structures of **[Ir1]Cl** and the PF<sub>6</sub><sup>-</sup> salts of **[Ir3]<sup>+</sup>**, **[Ir4]<sup>+</sup>**, and **[Ir5]<sup>+</sup>** were determined by X-ray diffraction.

The <sup>1</sup>H and <sup>13</sup>C{<sup>1</sup>H} spectra of complexes **[Ir1]Cl–[Ir5]Cl** were recorded in DMSO-d<sub>6</sub> (SI Fig. 1–15) and show the following distinctive attributes: (1) The non-equivalent dfppy ligands exhibit two sets of peaks, due to the asymmetry of the complexes (C<sub>1</sub> symmetry group); (2) **[Ir1]Cl** displays a strongly deshielded broad singlet (δ = 15.91 ppm) due to the N–H proton which is likely involved in a hydrogen bond with the Cl<sup>-</sup> counterion,<sup>29</sup> while **[Ir2]Cl** features a narrow singlet at 4.48 ppm belonging to the N-Me group; (3) for complexes **[Ir3]Cl–[Ir5]Cl**, two reciprocally coupled doublets (<sup>2</sup>J<sub>H–H</sub> ≈ 18 Hz), emerging as an AB pseudo-quartet, were found in the range 6.52–6.24 ppm and are attributed to the diastereotopic protons of the –CH<sub>2</sub> group as a result of the helical chirality typical of tris-chelate octahedral complexes, while for the achiral free ligands **L3–L5**, the –CH<sub>2</sub> group appears as a singlet integrating for 2H; (4) complexes **[Ir3]Cl–[Ir5]Cl** exhibit a singlet around 48 ppm for the –CH<sub>2</sub> group in their <sup>13</sup>C{<sup>1</sup>H} NMR spectra.

The <sup>19</sup>F NMR spectra of all the derivatives feature two quartets in the range between –106.5 and –107 ppm (F<sup>11</sup> and F<sup>11'</sup>) and two triplets at about –109 ppm (F<sup>9</sup> and F<sup>9'</sup>), for the two non-equivalent dfppy (see atom numbering in Section 4.1. and SI).

The HR-MS (ESI+) spectra of the Ir(III) complexes present peaks where the *m/z* values and the isotopic patterns match unambiguously with those calculated for the monocationic species of general formula [Ir(dfppy)<sub>2</sub>(N<sup>^</sup>N')]<sup>+</sup> (N<sup>^</sup>N' = **L1–L5**). We also detected for all the compounds a peak corresponding to the monocationic fragment [C<sub>22</sub>H<sub>12</sub>F<sub>4</sub>IrN<sub>2</sub>]<sup>+</sup> = [Ir(dfppy)<sub>2</sub>]<sup>+</sup>, which corresponds to the loss of the N<sup>^</sup>N' ligand.

## 2.3. Crystal Structure by X-ray Diffraction

The crystal structures of *rac*-**[Ir1]Cl**, *rac*-**[Ir3]PF<sub>6</sub>**, *rac*-**[Ir4]PF<sub>6</sub>**, and *rac*-**[Ir5]PF<sub>6</sub>** were resolved by single-crystal X-ray diffraction. Single crystals were isolated either by slow evaporation of a methanolic solution of **[Ir1]Cl** or by slow diffusion of a saturated NH<sub>4</sub>PF<sub>6</sub> aqueous solution into solutions of **[Ir3]Cl**, **[Ir4]Cl**, and **[Ir5]Cl** in methanol/dichloromethane. The complexes crystallize in either the monoclinic *P*2<sub>1/c</sub> or *P*2<sub>1/n</sub>, or triclinic *P*-1 space groups. The ORTEP diagrams for the corresponding  $\Lambda$  enantiomers are shown in Fig. 3. Selected bond distances and angles along with standard deviations are collected in Table 1, and relevant crystallographic parameters are included in SI Table 1.

The molecular structures of these complexes display a pseudo-octahedral geometry with the well-known *trans*-N,N and *cis*-C,C arrangement for the C<sup>^</sup>N ligands (Fig. 3). In all the derivatives, the Ir–N bond distances for the C<sup>^</sup>N ligands (1.963(12)–2.074(12) Å) are shorter than for the N<sup>^</sup>N' ligands (2.119(6)–2.181(7) Å) as a consequence of the strong *trans* influence exerted by the coordinated phenyl rings.<sup>30,31,32,33</sup> Besides, the Ir–N<sub>bim</sub> length is shorter than the Ir–N<sub>py</sub> in the N<sup>^</sup>N' ligand of every complex, likely due to the bigger  $\pi$ -electron density on the benzimidazole (bim) fragment relative to the pyridine (py) ring and therefore the higher  $\pi$ -donor ability of bim versus py. The Ir–C bond distances are standard (1.995(13)–2.020(6) Å).<sup>34,35</sup> The torsion angles for the C<sup>^</sup>N and the N<sup>^</sup>N' ligands, C–C–N (–0.02 to –6.22°) and N–C–N (1.57 to –18.99°), are small, which in practice underlines the virtual coplanarity of the metallacycles.

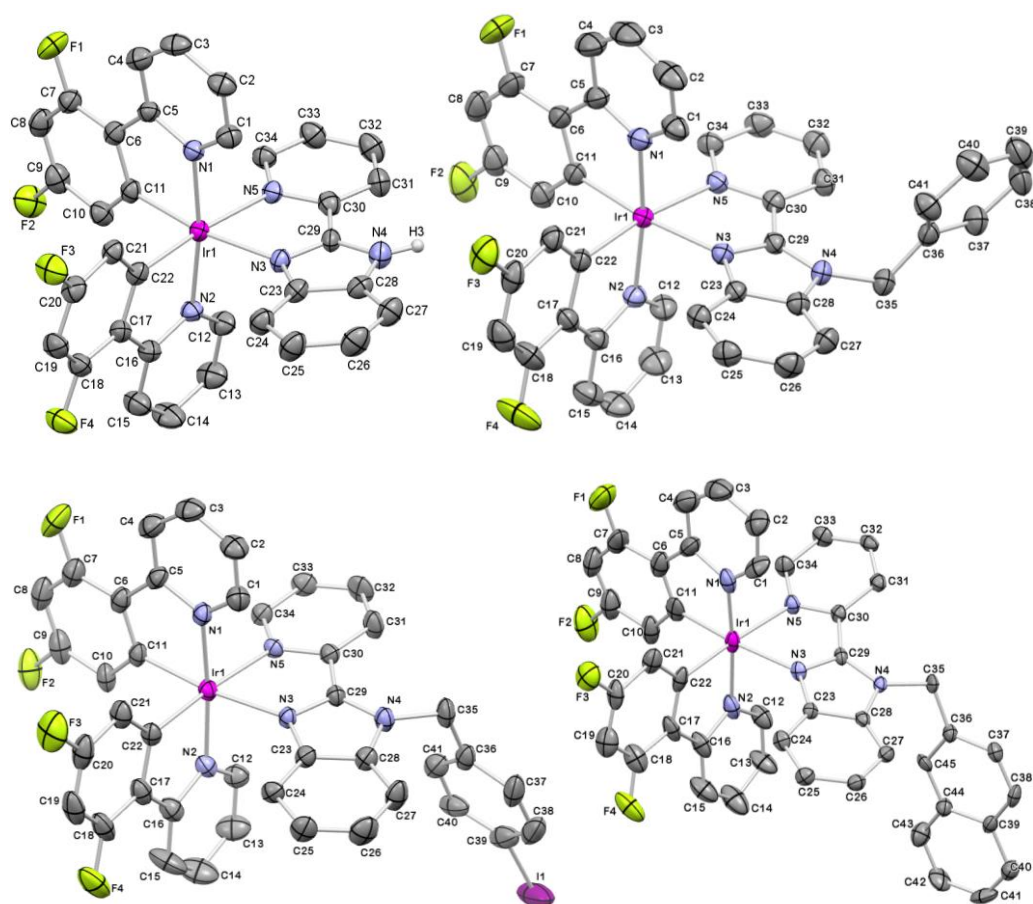


Fig. 3. ORTEP diagrams for the molecular structures of ( $\Lambda$ )-[Ir1]<sup>+</sup>, ( $\Lambda$ )-[Ir3]<sup>+</sup>, ( $\Lambda$ )-[Ir4]<sup>+</sup> and ( $\Lambda$ )-[Ir5]<sup>+</sup> obtained by X-ray diffraction. Thermal ellipsoids are shown at the 30% probability level. The  $\Delta$  enantiomers, the H atoms, the Cl<sup>-</sup> or PF<sub>6</sub><sup>-</sup> counterions, and the solvent molecules (MeOH for rac-[Ir1]Cl) have been omitted for the sake of clarity.



Table 1. Selected Bond Lengths (Å) for [Ir1]Cl·MeOH, [Ir3]PF<sub>6</sub>, [Ir4]PF<sub>6</sub>, and [Ir5]PF<sub>6</sub>.

[Ir1]Cl·MeOH		[Ir3]PF <sub>6</sub>		[Ir4]PF <sub>6</sub>		[Ir5]PF <sub>6</sub>			
Ir(1)-N(1)	2.054(5)	Ir(1)-N(1)	2.042(4)	Ir(1)-N(1)	2.059(7)	Ir(1)-N(1)	1.963(12)	Ir(2)-N(7)	2.046(8)
Ir(1)-N(2)	2.058(5)	Ir(1)-N(2)	2.054(4)	Ir(1)-N(2)	2.043(7)	Ir(1)-N(2)	2.074(12)	Ir(2)-N(6)	2.032(8)
Ir(1)-N(3)	2.138(5)	Ir(1)-N(3)	2.142(4)	Ir(1)-N(3)	2.119(6)	Ir(1)-N(3)	2.131(8)	Ir(2)-N(9)	2.119(8)
Ir(1)-N(5)	2.179(5)	Ir(1)-N(5)	2.153(4)	Ir(1)-N(5)	2.158(6)	Ir(1)-N(5)	2.163(8)	Ir(2)-N(8)	2.181(7)
Ir(1)-C(11)	2.020(6)	Ir(1)-C(11)	2.019(5)	Ir(1)-C(11)	2.013(8)	Ir(1)-C(11)	1.995(13)	Ir(2)-C(67)	2.000(10)
Ir(1)-C(22)	2.018(6)	Ir(1)-C(22)	2.005(5)	Ir(1)-C(22)	2.002(7)	Ir(1)-C(22)	2.015(11)	Ir(2)-C(56)	2.003(9)

## 2.4. Photostability Experiments

In order to verify the photostability in solution of the new Ir(III)-complexes and the standard photocatalysts [Ir(ppy)<sub>2</sub>(bpy)]Cl and [Ir(dfppy)<sub>2</sub>(bpy)]Cl (denoted as **[1]Cl** and **[2]Cl**), we monitored their evolution in acetonitrile under air by <sup>1</sup>H NMR spectroscopy ( $1.4 \times 10^{-2}$  M, CD<sub>3</sub>CN) over a period of 24 h under irradiation with blue light ( $\lambda_{ir} = 460$  nm, 24 W) at room temperature (SI Fig. 16–22). All the complexes including **[1]Cl** and **[2]Cl** are remarkably stable over the 24 h irradiation period. Indeed, no degradation was observed for **[Ir1]Cl**–**[Ir4]Cl**, and just 3% photodegradation was experimentally determined for **[Ir5]Cl**. An in-depth analysis of the spectrum, recorded for this PC upon 24 h under light exposure, allowed us to speculate that it undergoes photocleavage of the –CH<sub>2</sub>-naphthyl group.

## 2.5. Theoretical Calculations

Density functional theory (DFT) calculations were performed on the cation complexes **[Ir1]<sup>+</sup>**–**[Ir5]<sup>+</sup>** and also on the reference photosensitizers [Ir(ppy)<sub>2</sub>(bpy)]<sup>+</sup>, **[1]<sup>+</sup>**, and [Ir(dfppy)<sub>2</sub>(bpy)]<sup>+</sup>, **[2]<sup>+</sup>**, for a deeper comprehension of the photophysical and electrochemical properties of the synthesized compounds and to rationalize the observed trends among them and relative to **[1]<sup>+</sup>** and **[2]<sup>+</sup>**. Calculations were executed at the B3LYP/(6-31GDP+LANL2DZ) level including solvent effects (CH<sub>3</sub>CN) (see procedure in the SI and SI Tables 2a, 2b, and 3).

In agreement with the molecular structure determined by X-ray diffraction for **[Ir1]Cl**, **[Ir3]PF<sub>6</sub>**, **[Ir4]PF<sub>6</sub>**, and **[Ir5]PF<sub>6</sub>**, our calculations provide structures with a pseudo-octahedral geometry for **[Ir1]<sup>+</sup>**–**[Ir5]<sup>+</sup>**, **[1]<sup>+</sup>**, and **[2]<sup>+</sup>** in their ground electronic state (*S*<sub>0</sub>). Fig. 4 shows the isovalue contour pictures for the molecular orbitals, from HOMO–2 (or HOMO–3) to LUMO+2, of **[Ir3]<sup>+</sup>** and **[2]<sup>+</sup>** at their electronic ground state (*S*<sub>0</sub>). A similar sketch is shown in SI Fig. 23b for **[Ir3]<sup>+</sup>** and **[1]<sup>+</sup>**. The topologies of the MOs for **[Ir1]<sup>+</sup>**, **[Ir2]<sup>+</sup>** and **[Ir4]<sup>+</sup>** are very similar to those of **[Ir3]<sup>+</sup>**. By contrast, the MO of **[Ir5]<sup>+</sup>** exhibit some differences that will be discussed later. The MOs of all the compounds are gathered in SI Tables 2a and 2b.

The HOMOs calculated for **[1]<sup>+</sup>**, **[2]<sup>+</sup>**, and the new derivatives are formed by a combination of Ir orbitals ( $d_{\pi}$ ) and C<sup>N</sup> orbitals ( $\pi$  of ppy<sup>-</sup> or dfppy<sup>-</sup>) as described elsewhere for this type of complexes.<sup>20,36,37</sup> Hence, the HOMOs are located on the Ir metal centre and the phenyl rings of the C<sup>N</sup> ligands, although they exhibit a  $\pi$ -antibonding nature at the Ir-C<sub>phenyl</sub> interfaces. On the contrary, the LUMOs are distributed mainly over the N<sup>N'</sup> ligands (bpy or 2-(2'-pyridyl)benzimidazole scaffold of **L1–L5**) in all the cases,<sup>37,38</sup> with a very small contribution of the Ir  $d_{\pi}$  orbitals. Interestingly, the alkyl substituents installed on the N<sup>N'</sup> ligands of **[Ir2]<sup>+</sup>–[Ir4]<sup>+</sup>** do not participate in the respective frontier orbitals, while the naphthyl group of **[Ir5]<sup>+</sup>** contributes predominantly to HOMO–1 and LUMO+4. Hence, we assume that the alkyl groups of **[Ir2]<sup>+</sup>–[Ir4]<sup>+</sup>** are not involved in photophysical processes, that is, absorption or emission of photons, and therefore these moieties act as protecting shields for the PC emitting excited states against decay processes.<sup>39</sup>

The energies calculated for the HOMOs of **[Ir1]<sup>+</sup>–[Ir5]<sup>+</sup>** and **[2]<sup>+</sup>** are in a very small range (from –5.93 to –5.97 eV, Fig. 4 and SI Fig. 23a), but are noticeably lower than the energy obtained for the HOMO of **[1]<sup>+</sup>** (–5.65 eV). This effect is ascribed to the electron-withdrawing ability of the –F atoms in dfppy, which leads to a remarkable stabilization of the HOMO in **[Ir1]<sup>+</sup>–[Ir5]<sup>+</sup>** and **[2]<sup>+</sup>** relative to **[1]<sup>+</sup>**.<sup>28,40</sup>

The energies calculated for the LUMOs of **[Ir1]<sup>+</sup>–[Ir5]<sup>+</sup>** and **[2]<sup>+</sup>** are also very similar (from –2.45 to –2.49 eV, Fig. 4 and SI Fig. 23) and slightly lower than that estimated for the LUMO of **[1]<sup>+</sup>** (–2.41 eV). These energies show a negligible influence of either the replacement of a pyridine ring with a benzimidazole unit or the installation of different substituents on the N atom of **L1–L5**. Consequently, the HOMO–LUMO band gaps for **[Ir1]<sup>+</sup>–[Ir5]<sup>+</sup>** and **[2]<sup>+</sup>** (3.45–3.49 eV) are in a narrow range, but they are significantly higher than that corresponding to **[1]<sup>+</sup>** (3.23 eV). These tendencies are in agreement with those observed experimentally for the electrochemical band gaps (*vide infra*).

The nature of the emitting excited states and the emission energies for the new compounds ( $T_1 - S_0$ ) were calculated using the time-dependent DFT (TD-DFT) method (Fig. 5). The obtained values predict very similar emission  $\lambda_{\max}$  for **[Ir1]<sup>+</sup>–[Ir5]<sup>+</sup>** and **[2]<sup>+</sup>**, although a blue-shift relative to the respective  $\lambda_{\max}$  for **[1]<sup>+</sup>** is also predicted. All these estimations are consistent with the emission energies determined experimentally (see next section) and establish that the presence of the electron-withdrawing –F atoms on the C<sup>N</sup> ligands is the main factor affecting the emission energies.

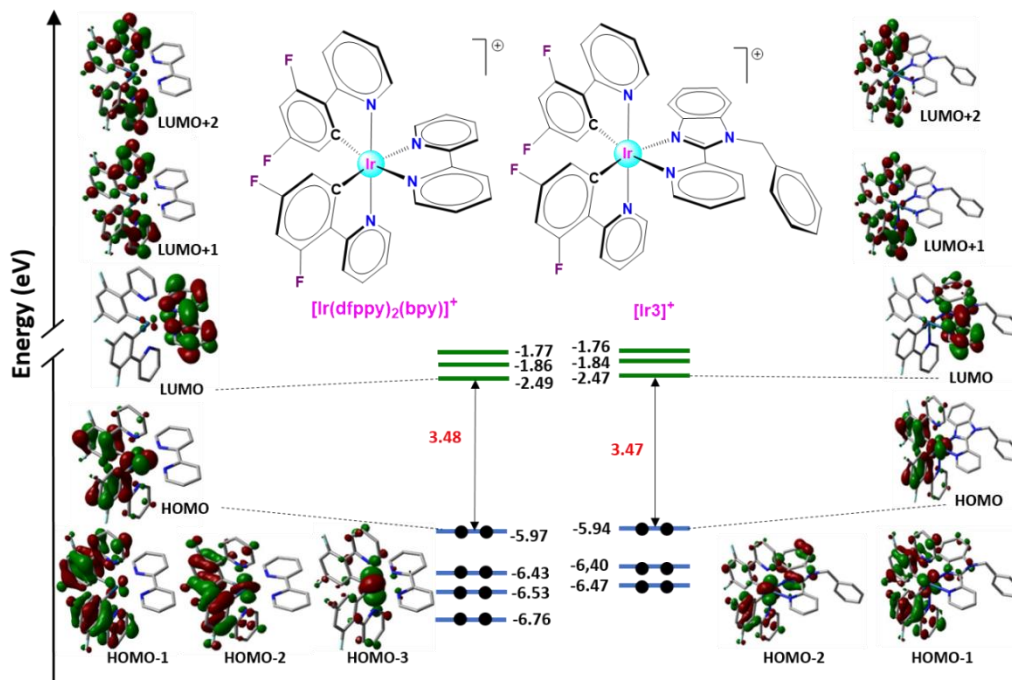


Fig. 4. Schematic representation of the energies and the isovalue contour pictures calculated for the frontier molecular orbitals of  $[\text{Ir}(\text{dfppy})_2(\text{bpy})]^+$ ,  $[2]^+$ , and  $[\text{Ir}3]^+$ .

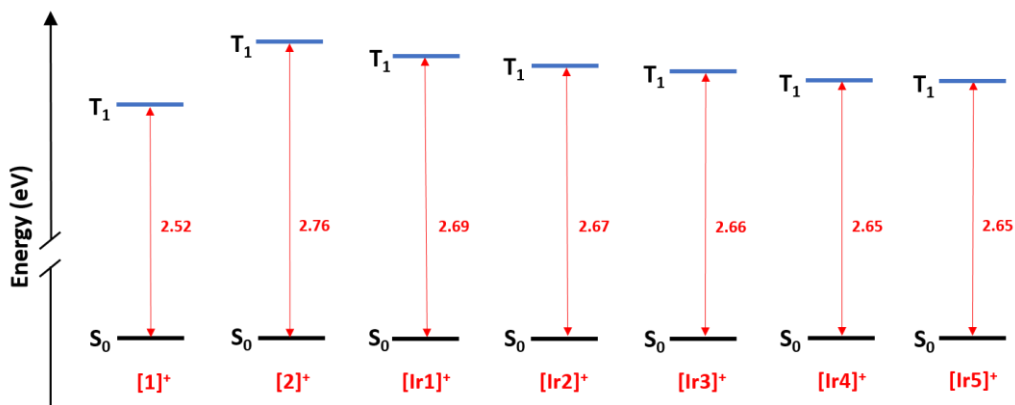


Fig. 5. Energy diagram showing the calculated energy difference values between the lowest triplet excited state ( $T_1$ ) and the singlet ground state ( $S_0$ ), keeping the geometry of the respective triplet for complexes  $[1]^+$ ,  $[2]^+$ , and  $[\text{Ir}1]^+$ – $[\text{Ir}5]^+$ .

## 2.6. Photophysical Properties

**UV-vis Absorption Spectra.** The UV-vis spectra of complexes **[Ir1]Cl–[Ir5]Cl** were recorded in acetonitrile solutions ( $10^{-5}$  M) at 25 °C (Fig. 6(A)). The absorption spectra of complexes **[Ir1]Cl–[Ir5]Cl** show one intense absorption band centred at around 250 nm, which corresponds to singlet spin-allowed ligand centred transitions ( $^1LC$ ,  $\pi \rightarrow \pi^*$ ) occurring in both types of ligands, the C<sup>^</sup>N (dfppy) and the N<sup>^</sup>N'. Additional bands are observed at around 313 nm for **[Ir2]Cl–[Ir5]Cl** and 348 nm for **[Ir1]Cl**. These bands are attributed to mixed spin-allowed  $^1MLCT$  and  $^1LLCT$  transitions. The weak absorption tails entering in the visible region come from spin-forbidden  $^3MLCT$  and  $^3LC$  transitions.<sup>41,42,43</sup> In general, the absorption bands of **[Ir5]Cl** are more intense and are more extended in the range between 420 and 500 nm, and hence overlap better with the emission band of the light source used in photocatalytic assays (Fig. 6(A)). This is likely due to the higher  $\pi$ -conjugation of the naphthyl group.

**Emission Spectra.** The emission spectra of complexes **[Ir1]Cl–[Ir5]Cl** were recorded in solutions of dry and deoxygenated acetonitrile ( $10^{-5}$  M) at 25 °C under excitation at 405 nm (see Fig. 6(B)). All the spectra are alike, featuring a broad unstructured emission band, typical of a high charge transfer character.<sup>40</sup> These bands have an absolute maximum between 522 and 546 nm for **[Ir1]Cl–[Ir5]Cl** (Table 2), which resembles the value reported for **[2]PF<sub>6</sub>** ( $\lambda_{em} = 534$  nm). Nevertheless, the emission of all these complexes is blue-shifted relative to that of the archetypal photosensitizer **[1]PF<sub>6</sub>** (602 nm), as anticipated by DFT calculations.

The photoluminescence quantum yields (PLQY,  $\Phi_{PL}$ ) were also determined in deoxygenated acetonitrile solutions ( $10^{-5}$  M). **[Ir1]Cl** and **[Ir3]Cl** display very good quantum yields of 78% and 63%, respectively (Table 2). On the other hand, **[Ir2]Cl** and **[Ir4]Cl** feature moderate quantum yields of 36% and 46%, respectively, while **[Ir5]Cl** shows a low quantum yield (9%) equal to that of **[1]PF<sub>6</sub>** (9%) and lower than that for **[2]PF<sub>6</sub>** (18%). We speculate that the lower  $\Phi_{PL}$  values determined for **[Ir2]Cl–[Ir5]Cl** versus **[Ir1]Cl** are mainly due to the intramolecular rotation of the N-alkyl groups in solution, which favours the dissipation of energy by non-radiative channels for these complexes.<sup>44,45</sup> In addition, the very low PLQY of **[Ir5]Cl** could be the result of an extra factor, that is, the thermal population of a ligand-centred ( $^3LC$ ,  $\pi_{L5} \rightarrow \pi^*_{L5}$ ) excited state, ( $T_2$ , 2.70 eV) close in energy to the emissive lowest excited state ( $T_1$ , 2.65 eV) (SI Table 3). This feature provides a non-radiative decay pathway to **[Ir5]Cl**, since the non-participation of the metal centre in  $T_2$  hampers the intersystem crossing process, and hence a low PLQY is observed.<sup>46</sup> Therefore, we conclude that the functional group on the N<sup>^</sup>N' ligand exerts an important influence in the efficiency of the emission process.

The excited-state lifetimes ( $\tau$ ) are excellent for the substituted derivatives **[Ir2]Cl–[Ir5]Cl**, between 1012 and 2066 ns and much longer than that reported for

**[1]PF<sub>6</sub>**, whereas for the non-functionalized compound, **[Ir1]Cl**,  $\tau$  is much shorter, 59 ns (Table 2). Hence, the functionalization of the imidazolyl nitrogen has also an important effect on the lifetimes of the excited states. In particular, we speculate that the presence of the N–H group in **[Ir1]Cl** could accelerate the radiative deactivation of the excited state relative to its functionalized counterparts **[Ir2]Cl–[Ir5]Cl**. The rationale for this could be that the ground state ( $S_0$ ) of **[Ir1]<sup>+</sup>** is stabilized in acetonitrile solution through either N–H---Cl<sup>-</sup> or N–H---N≡C–Me hydrogen bonding interactions. By contrast, in the excited state, which exhibits partial <sup>3</sup>MLCT nature, the charge transfer from the metal centre to the  $\pi^*$  orbital of the N<sup>^</sup>N' ligand decreases the polarization of the N–H bond and therefore the strength of the interaction with either the Cl<sup>-</sup> counterion or the solvent molecules, shortening the lifetime of the triplet excited state ( $T_1$ ). In **[Ir2]Cl–[Ir5]Cl**, the presence of bulky apolar alkyl groups impedes hydrogen-bonding interactions and therefore avoids the differential stabilization of  $S_0$  relative to  $T_1$ . This would explain the longer lifetimes observed for the excited states of **[Ir2]Cl–[Ir5]Cl** vs **[Ir1]Cl**.

The radiative and non-radiative deactivation rate constants,  $k_r$  and  $k_{nr}$ , were calculated from  $\Phi_{PL}$  and  $\tau$  and are summarized in Table 2. It is worth noting that **[Ir1]Cl** has a  $k_r < k_{nr}$ , while **[Ir2]Cl–[Ir4]Cl** exhibit similar values for  $k_r$  and  $k_{nr}$  and **[Ir5]Cl** features a  $k_{nr}$  one order of magnitude higher than  $k_r$ .

Overall, the photophysical properties of our photosensitizers are in general superior to those reported for **[1]PF<sub>6</sub>**<sup>47</sup> and **[2]PF<sub>6</sub>**, and *a priori* the long lifetimes of **[Ir2]Cl–[Ir5]Cl** could favour their interaction with O<sub>2</sub> to generate ROS.

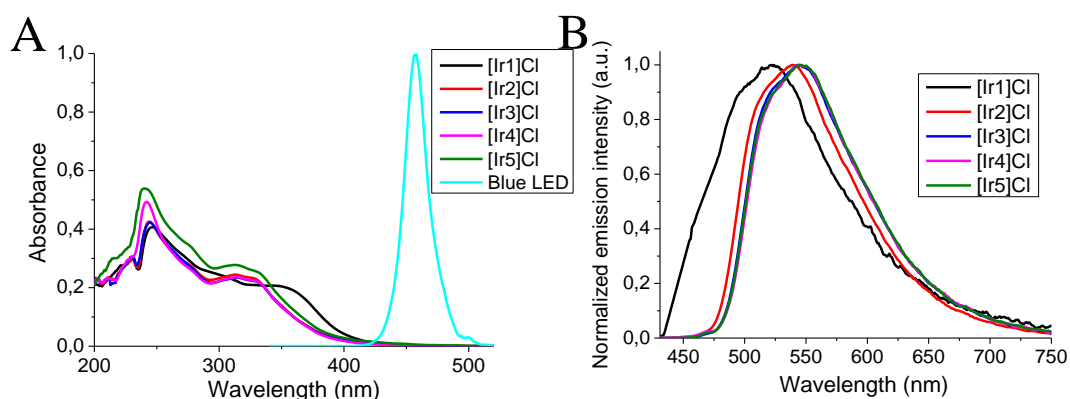


Fig. 6. (A) Overlaid UV-vis absorption spectra of **[Ir1]Cl–[Ir5]Cl** ( $10^{-5}$  M) in  $CH_3CN$  at 25 °C along with the emission spectrum of the blue light used in the photocatalytic assays. (B) Overlaid emission spectra of **[Ir1]Cl–[Ir5]Cl** ( $10^{-5}$  M) in deoxygenated  $CH_3CN$  at 25 °C upon excitation with  $\lambda_{ex} = 405$  nm (right).

Table 2. Photophysical Properties for Complexes [Ir1]Cl–[Ir5]Cl ( $10^{-5}$  M) in  $\text{CH}_3\text{CN}$  at 25 °C under  $\lambda_{\text{ex}} = 405$  nm.<sup>[a]</sup>

Complex	$\lambda_{\text{abs}}$ (nm)	$\epsilon$ [ $\text{M}^{-1} \text{cm}^{-1}$ ]	$\lambda_{\text{em}}$ (nm)	$\Phi_{\text{PL}}$ (%)	$\tau$ (ns)	$k_r$ ( $\text{s}^{-1}$ ) <sup>[b]</sup>	$k_{\text{nr}}$ ( $\text{s}^{-1}$ ) <sup>[c]</sup>
[Ir(ppy) <sub>2</sub> (bpy)] <sup>+</sup>	265, 310, 375, 420	-	602	9	275	$3.38 \times 10^5$	$33 \times 10^5$
[Ir(dfppy) <sub>2</sub> (bpy)] <sup>+</sup>	250, 305	-	534	18	1500	$1.20 \times 10^5$	$5.47 \times 10^5$
[Ir1]Cl	233, 246, 348	0.303, 0.408, 0.206	522	78	59	$132 \times 10^5$	$37.3 \times 10^5$
[Ir2]Cl	238, 244, 319, 331	0.348, 0.428, 0.239, 0.226	539	36	2066	$1.74 \times 10^5$	$3.10 \times 10^5$
[Ir3]Cl	237, 244, 320, 333	0.328, 0.426, 0.229, 0.215	544	63	1321	$4.77 \times 10^5$	$2.80 \times 10^5$
[Ir4]Cl	244, 322, 334	0.487, 0.228, 0.213	544	46	1510	$3.05 \times 10^5$	$3.58 \times 10^5$
[Ir5]Cl	244, 321, 333	0.533, 0.268, 0.249	546	9	1012	$0.89 \times 10^5$	$8.99 \times 10^5$

<sup>[a]</sup>Data for [1]PF<sub>6</sub> and [2]PF<sub>6</sub> reported by E. Zysman-Colman<sup>47,49</sup> and De Cola,<sup>48</sup> respectively. <sup>[b]</sup>Radiative deactivation rate constant:  $k_r = \Phi_{\text{PL}} \times \tau^{-1}$ . <sup>[c]</sup>Non-radiative deactivation rate constant:  $k_{\text{nr}} = \tau^{-1} - k_r$  (assuming unitary intersystem crossing efficiency).

## 2.7. Electrochemical Properties

The redox potentials of [Ir1]Cl–[Ir5]Cl were experimentally ascertained by cyclic voltammetry (CV) in deoxygenated  $\text{CH}_3\text{CN}$  solutions ( $5 \times 10^{-4}$  M), in order to establish the oxidative and reductive abilities of the corresponding ground and excited states, as well as the redox stability of our complexes. Potentials are referred to the ferrocenium/ferrocene ( $\text{Fc}^+/\text{Fc}$ ) couple.

The cyclic voltammograms (CV) of these compounds are presented in Fig. 7. The anodic region of every CV shows two peaks: (a) an irreversible peak between +0.56 and +0.63 V (Table 3 and Fig. 7) attributed to the oxidation of the chloride counteranion ( $2 \text{Cl}^- \rightarrow \text{Cl}_2 + 2 \text{e}^-$ ) and (b) a reversible one electron oxidation peak in the range +1.19 to +1.22 V, ascribed to an oxidation process affecting the Ir(III) center along with the difluorophenyl rings of C<sup>N</sup> ligands,<sup>28</sup> as disclosed by the topology of the respective HOMO.

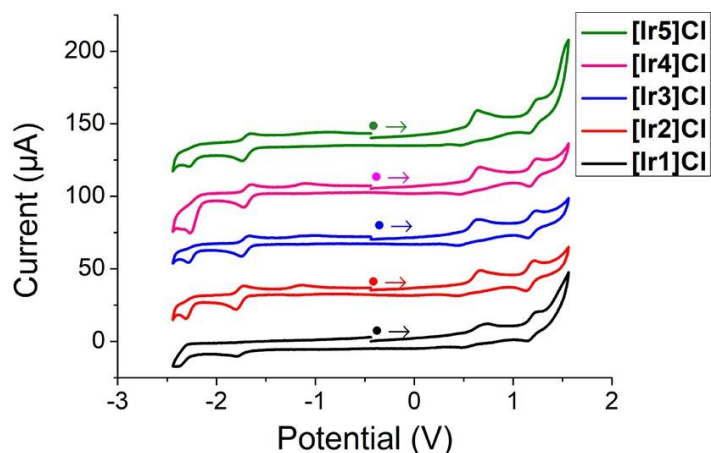


Fig. 7. Cyclic voltammograms of complexes **[Ir1]Cl–[Ir5]Cl** in acetonitrile solution ( $5 \times 10^{-4}$  M), using 0.1 M  $[n\text{Bu}_4\text{N}][\text{PF}_6]$  as supporting electrolyte and recorded with a scan rate of  $0.10 \text{ V}\cdot\text{s}^{-1}$ .

In the cathodic region, **[Ir1]Cl** exhibits two irreversible peaks ( $E^{\text{red}1}_{1/2} = -1.79 \text{ V}$ ,  $E^{\text{red}2}_{1/2} = -2.33 \text{ V}$ ). Nonetheless, complexes **[Ir2]Cl–[Ir5]Cl** display one pseudo-reversible one-electron peak and one irreversible one-electron peak in the ranges from  $-1.67$  to  $-1.76 \text{ V}$  ( $E^{\text{red}1}_{1/2}$ ) and from  $-2.21$  to  $-2.27 \text{ V}$  ( $E^{\text{red}2}_{1/2}$ ), respectively. These waves are attributed to stepwise reductions centred in the respective  $\text{N}^{\wedge}\text{N}'$  ligands, as suggested by the topology of the calculated LUMO for these compounds. Interestingly, the pseudo-reversible nature of  $E^{\text{red}1}_{1/2}$  observed for **[Ir2]Cl–[Ir5]Cl**, compared to the irreversible character of  $E^{\text{red}1}_{1/2}$  obtained for **[Ir1]Cl**, underlines the stabilizing effect of the alkyl groups attached to the  $\text{N}^{\wedge}\text{N}'$  ligands on the redox behaviour of these dyes. Moreover, a low intensity irreversible wave is observed for complexes **[Ir2]Cl–[Ir4]Cl** between  $-1.00$  and  $-1.11 \text{ V}$ . This peak is imputed to the oxidation of a species formed *in situ* by chemical decomposition during the CV experiment, as it can only be seen in the return scan. The experimental electrochemical band gaps have been calculated as the difference between  $E^{\text{ox}2}_{1/2}$  and  $E^{\text{red}1}_{1/2}$ . They are in a very narrow range for complexes **[Ir1]Cl–[Ir5]Cl** and are very similar to the value reported for **[2]PF<sub>6</sub>**, although are higher than the respective value for **[1]PF<sub>6</sub>** in agreement with the trends predicted theoretically for the HOMO–LUMO band gaps. Paradoxically, the excited states of this type of Ir(III) derivatives exhibit a versatile and outstanding redox behavior,<sup>50,51,52</sup> Indeed, our dyes show a high excited-state redox power as oxidants,  $E_{1/2}(\text{Ir}^{\text{III}*}/\text{Ir}^{\text{II}})$  ranges from  $+0.54$  to  $+0.61 \text{ V}$ , and also as reductants,  $E_{1/2}(\text{Ir}^{\text{IV}}/\text{Ir}^{\text{III}*})$  ranges from  $-1.16$  to  $-1.05 \text{ V}$  (Fig. 8 and SI Table 4), and they are meaningfully better excited-state oxidants than the standard photosensitizer **[1](PF<sub>6</sub>)** ( $E_{1/2}(\text{Ir}^{\text{III}*}/\text{Ir}^{\text{II}}) = +0.28 \text{ V}$ ).<sup>53</sup> These facts underscore their potential as photocatalysts in single electron transfer (SET) processes.

Table 3. Redox potentials for complexes [Ir1Cl]–[Ir5Cl] referenced to Fc<sup>+</sup>/Fc and recorded by CV in acetonitrile solution.<sup>[a]</sup>

Complex	E <sup>ox1</sup> <sub>1/2</sub> (V)	E <sup>ox2</sup> <sub>1/2</sub> (V)	E <sup>red1</sup> <sub>1/2</sub> (V)	E <sup>red2</sup> <sub>1/2</sub> (V)	ΔE <sub>1/2</sub> (V) <sup>[b]</sup>	E <sub>1/2</sub> (Ir <sup>IV</sup> /Ir <sup>III*</sup> ) <sup>[d]</sup>	E <sub>1/2</sub> (Ir <sup>III*</sup> /Ir <sup>II</sup> ) <sup>[d]</sup>
[1]PF <sub>6</sub> <sup>[c]</sup>	-	+0.87	-1.78 (qr)	-	2.65	-1.19	+0.28
[2]PF <sub>6</sub> <sup>[c]</sup>	-	+1.22	-1.65	-	2.87	-1.10	+0.67
[Ir1]Cl	+0.63 (ir)	+1.22 (qr)	-1.79 (ir)	-2.33 (ir)	3.01	-1.16	+0.59
[Ir2]Cl	+0.58 (ir)	+1.19 (qr)	-1.76 (qr)	-2.27 (ir)	2.95	-1.11	+0.54
[Ir3]Cl	+0.56 (ir)	+1.21 (qr)	-1.69 (qr)	-2.22 (ir)	2.90	-1.07	+0.59
[Ir4]Cl	+0.59 (ir)	+1.22 (qr)	-1.67 (qr)	-2.21 (ir)	2.89	-1.06	+0.61
[Ir5]Cl	+0.59 (ir)	+1.22 (qr)	-1.69 (qr)	-2.23 (ir)	2.91	-1.05	+0.58

<sup>[a]</sup>Data for [1]PF<sub>6</sub> and [2]PF<sub>6</sub> reported by McCusker<sup>53</sup> and Ko,<sup>54</sup> respectively. Voltammograms recorded in acetonitrile solution (5 × 10<sup>-4</sup> M), using 0.1 M [nBu<sub>4</sub>N][PF<sub>6</sub>] as supporting electrolyte with scan rate of 0.10 V·s<sup>-1</sup> and referenced to Fc<sup>+</sup>/Fc (qr = quasi-reversible, ir = irreversible) <sup>[b]</sup>ΔE<sub>1/2</sub> = E<sup>ox2</sup><sub>1/2</sub> – E<sup>red1</sup><sub>1/2</sub>. <sup>[c]</sup>Data for [1]PF<sub>6</sub> and [2]PF<sub>6</sub> are given in acetonitrile vs Fc<sup>+</sup>/Fc (calculated from the original works using the equation: V(Fc<sup>+</sup>/Fc) = V(SCE) – 0.404). <sup>[d]</sup>E<sub>1/2</sub>(Ir<sup>IV</sup>/Ir<sup>III\*</sup>) and E<sub>1/2</sub>(Ir<sup>III\*</sup>/Ir<sup>II</sup>) are calculated as explained in Table S4.

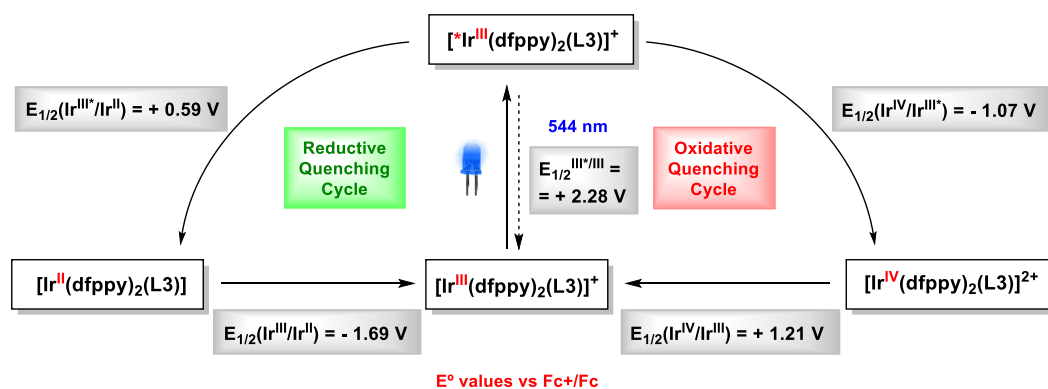


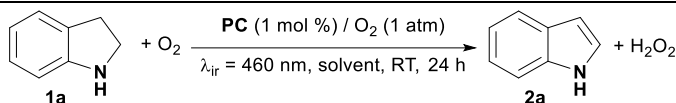
Fig. 8. Latimer diagram for [Ir3]Cl, with redox potentials determined by CV and the emission energy calculated from the photoluminescence spectrum. The redox potentials for [Ir3]<sup>+</sup> and its excited state [Ir3\*]<sup>+</sup> are given in V versus Fc<sup>+</sup>/Fc. E<sub>1/2</sub>(Ir<sup>IV</sup>/Ir<sup>III\*</sup>) = E<sub>1/2</sub>(Ir<sup>IV</sup>/Ir<sup>III</sup>) – E<sub>1/2</sub>(Ir<sup>III\*</sup>/Ir<sup>III</sup>) and E<sub>1/2</sub>(Ir<sup>III\*</sup>/Ir<sup>II</sup>) = E<sub>1/2</sub>(Ir<sup>III</sup>/Ir<sup>II</sup>) + E<sub>1/2</sub>(Ir<sup>III\*</sup>/Ir<sup>III</sup>). All the potential values are given as reduction potentials regardless the sense of the arrows for the quenching cycles.

## 2.8. Photocatalytic Activity in the Oxidation of Heterocycles

The new iridium complexes were tested as photocatalysts in the dehydrogenation of different partially saturated heterocycles (indolines, quinolines, isoquinolines, etc.). First, we chose indoline (**1a**) as the model substrate and irradiated it with blue light (460 nm) in the presence of [Ir1]Cl (1 mol %) under O<sub>2</sub> (1 atm, pure oxygen balloon) at room temperature for 24 h, using three different solvents, i.e.: acetonitrile, dichloromethane, and ethanol.

Thus, we could determine that acetonitrile is the best solvent choice, since it provides a quantitative yield (>99%) for indole (**2a**), whereas lower yields were obtained using dichloromethane and ethanol (Table 4) under analogous conditions.

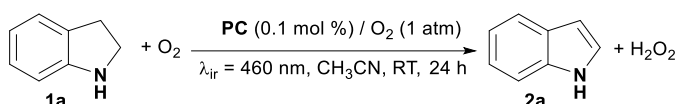


Table 4. Solvent screening in the photooxidation of indoline **1a**.<sup>[a]</sup>

Entry	Solvent	Yield (%)
1	CH <sub>3</sub> CN	100
2	CH <sub>2</sub> Cl <sub>2</sub>	65
3	EtOH	48

<sup>[a]</sup> Reaction conditions: indoline **1a** (10 mM), PC ([Ir1]Cl, 1 mol %), solvent (0.5 mL), O<sub>2</sub> (balloon, 1 atm), blue light (LED, λ<sub>irr</sub> = 460 nm, 24 W), room temperature, for 24 hours. Yields of **2a** were experimentally determined by <sup>1</sup>H NMR integration of the corresponding reaction crudes. The yield values were calculated as the mean of three independent experiments.

It is noteworthy that the transformation is selective for **2a**, since no overoxidation products such as isatin were observed.<sup>55,56</sup> Then, we performed a catalyst screening for the photooxidation of indoline (**1a**) using acetonitrile as solvent and a catalyst loading of 0.1 % for [Ir1]Cl–[Ir5]Cl and also for the standard PSs [1]Cl and [2]Cl. Consequently, we found out that [Ir3]Cl is the most efficient catalyst for the oxidative dehydrogenation of indoline (**1a**), whereas [Ir1]Cl provided a very low yield for **2a** (entries 1 and 3, Table 5). We tentatively explain the poor yield obtained with the non-alkylated luminophore [Ir1]Cl owing to the irreversible nature of its reduction [Ir<sup>III</sup>] → [Ir<sup>II</sup>] and also to its short excited-state lifetime, as seen in Fig. 7 and discussed in the Mechanism section.

Table 5. Photocatalysts screening in the photooxidation of indoline **1a**.<sup>[a]</sup>

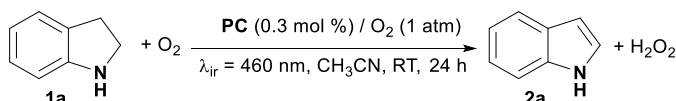
Entry	Complex	Yield (%)
1	[1]Cl	54
2	[2]Cl	55
3	[Ir1]Cl	20
4	[Ir2]Cl	42
5	[Ir3]Cl	62
6	[Ir4]Cl	58
7	[Ir5]Cl	57

<sup>[a]</sup> Reaction conditions: indoline **1a** (10 mM), PC (0.1 mol %), acetonitrile (0.5 mL), O<sub>2</sub> (balloon, 1 atm), blue light (LED, λ<sub>irr</sub> = 460 nm, 24 W), room temperature, for 24 hours. Yields of **2a** were experimentally determined by <sup>1</sup>H NMR integration of the corresponding reaction crudes. The yield values were calculated as the mean of three independent experiments.

By contrast, it is worth remarking that the alkylated derivatives, **[Ir3]Cl**–**[Ir5]Cl**, provide better yields than the standard PSs, **[1]Cl** and **[2]Cl**, as a result of a balanced combination of favourable photophysical and electrochemical properties.

Next, we performed a set of control experiments to verify the photocatalytic essence of this transformation and the role of O<sub>2</sub>. Indeed, we realized that in the absence of light, PC, or O<sub>2</sub> (N<sub>2</sub> atmosphere), the reaction did not proceed or was dramatically impeded, and thus we concluded that this transformation is light-driven in the presence of a PC and that oxygen is involved in the oxidation (Table 6). It is worth mentioning that the detection of a small percentage of **2a** under a N<sub>2</sub> atmosphere (entry 4, Table 6) could be due to the presence of O<sub>2</sub> traces in the solvent (incomplete deoxygenation). Moreover, we carried out additional control experiments in the presence of DABCO (O<sub>2</sub> quencher),<sup>57</sup> TEMPO (radical scavenger),<sup>58</sup> and 1,4-benzoquinone (BQ, O<sub>2</sub><sup>•-</sup> scavenger)<sup>56,59</sup> to elucidate the actual oxidant. The presence of DABCO decreases the yield slightly (84%), while TEMPO and BQ cause a dramatic and significant drop of the yield, respectively. These results suggest that superoxide has a major contribution in this reaction, while singlet oxygen plays just a minor role (Table 6).

Table 6. Control experiments for the photooxidation of indoline **1a**.<sup>[a]</sup>



Entry	Conditions	Yield (%)
1	PC, O <sub>2</sub> , light	100
2	PC, O <sub>2</sub> , no light	0
3	No PC, O <sub>2</sub> , light	0
4	PC, N <sub>2</sub> , light	10
5	PC, O <sub>2</sub> , light, DABCO <sup>[b]</sup>	84
6	PC, O <sub>2</sub> , light, TEMPO <sup>[c]</sup>	15
7	PC, O <sub>2</sub> , light, BQ <sup>[d]</sup>	45

<sup>[a]</sup> Reaction conditions: indoline **1a** (10 mM), PC (**[Ir3]Cl**, 0.3 mol %), CH<sub>3</sub>CN (0.5 mL) at room temperature, under a saturated atmosphere of either O<sub>2</sub> or N<sub>2</sub> (1 atm) and under irradiation with blue light (LED, λ<sub>irr</sub> = 460 nm, 24 W) during 24 hours in a septum-capped tube. Yields of **2a** were determined by <sup>1</sup>H NMR integration of the corresponding reaction crudes. <sup>[b]</sup>DABCO (3 eq). <sup>[c]</sup>TEMPO (3 eq). <sup>[d]</sup>BQ (3 eq). The yield values were calculated as the mean of three independent experiments.

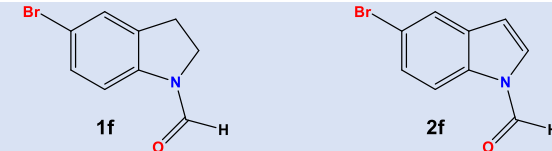

Then, we tested the substrate scope using the optimized conditions on a variety of indolines bearing different functional groups (Table 7). Most of the desired indoles were obtained in high yields and with excellent selectivity. However, the oxidation of 1-acetyl-5-bromoindoline (**1f**) was ineffective. This failure is likely due to the electron-withdrawing and steric effects attributed to the N-acetyl group, which inhibit the oxidation step.<sup>8,16,18</sup> Indeed, according to our general mechanistic proposal, we presume

that the reductive quenching of the triplet excited state of the PC,  $^3[\text{Ir}^{\text{III}}]^*$ , in the presence of **1f** would give rise to an unstable radical cation intermediate due to the remarkable electron-withdrawing effect attributed to the formyl substituent on the N atom. Moreover, the oxidative dehydrogenation of 5-nitroindoline (**1c**) and 6-nitroindoline (**1g**) were also precluded (0 and 20% of respective indoles), which is likely related to the strong electron-withdrawing ability of the  $-\text{NO}_2$  group.<sup>18</sup> Indeed, it is well-known that electron-poor nitro-aromatic substrates can undergo a photoinduced electron donation from the triplet excited state of different photosensitizers, which competes with the photoinduced reductive quenching proposed as one of the steps in the mechanism of this reaction.<sup>60,61</sup>

To validate the applicability of this protocol, we decided to scale the reaction up to 1 g (gram scale) of indoline (**1a**) in the presence of  $[\text{Ir3}]\text{Cl}$  (0.3 mol %). Thus, it was possible to obtain **2a** in 95 % yield by increasing the reaction time from 24 to 75 h. (see  $^1\text{H}$  and  $^{13}\text{C}$  NMR and characterization of isolated products in SI Fig. 40 and 41).

Table 7. Substrate Scope for the photooxidation of indolines<sup>[a]</sup>

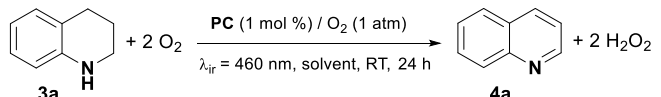
Entry	Substrate	Product	Yield (%) / [Photocatalyst (mol%)]
1			100 [0.3]
2			62 [1]
3			0 [1.5]
4			94 [1]
5			100 [0.3]

6		0 [1.5]
7		20 [1.5]

<sup>[a]</sup> Reaction conditions: indoline (10 mM), PC ([Ir3]Cl; 0.1 – 1.5 mol %), CH<sub>3</sub>CN (0.5 mL) at room temperature, under a saturated atmosphere of O<sub>2</sub> (1 atm) and under irradiation with blue light (LED, λ<sub>irr</sub> = 460 nm, 24 W) during 24 hours in a septum-capped tube. Yields were determined by <sup>1</sup>H NMR integration of the corresponding reaction crudes. The yield values were calculated as the mean of three independent experiments.

Next, we assayed the stepwise oxidative dehydrogenation of 1,2,3,4-tetrahydroquinolines to produce the respective quinolines. First, we selected 1,2,3,4-tetrahydroquinoline (THQ, **3a**) as the model substrate and applied the standard conditions using [Ir1]Cl as the photocatalyst (1 mol %) for 24 h in three different solvents, that is, acetonitrile, dichloromethane, and ethanol (Table 8).

Table 8. Solvent screening in the photooxidation of 1,2,3,4-tetrahydroquinoline **3a**.<sup>[a]</sup>



Entry	Solvent	Yield (%)
1	CH <sub>3</sub> CN	20
2	CH <sub>2</sub> Cl <sub>2</sub>	13
3	EtOH	7

<sup>[a]</sup> Reaction conditions: 1,2,3,4-tetrahydroquinoline **3a** (10 mM), PC ([Ir1]Cl, 1 mol %), solvent (0.5 mL), O<sub>2</sub> (balloon, 1 atm), blue light (LED, λ<sub>irr</sub> = 460 nm, 24 W), room temperature for 24 hours. Yields of **4a** were experimentally determined by <sup>1</sup>H NMR integration of the corresponding reaction crudes. The yield values were calculated as the mean of three independent experiments.

Again, acetonitrile provided the best yield for quinoline, **4a**, (20%) and was chosen as the solvent for additional experiments. Partial dehydrogenation products such as 3,4-dihydroquinoline were not detected, making this protocol selective.<sup>62</sup> A PCs screening including complexes [Ir1]Cl–[Ir5]Cl and also [1]Cl and [2]Cl was performed using a catalyst loading of 1 mol %. Unlike [Ir1]Cl, the functionalized PCs, [Ir2]Cl–[Ir5]Cl, promoted full conversions of **3a** to **4a** under these conditions. Hence, in order to discriminate the most active PC, we examined the photocatalytic activity of these complexes one more time, decreasing the catalyst loading down to 0.1 mol % (Table 9). In short, [Ir4]Cl turned out to be the most efficient PC (70 % yield of **4a**), and again, the non-alkylated complex, [Ir1]Cl, was by far the less efficient PC. Besides, complexes

**[Ir3]Cl**–**[Ir5]Cl** exhibited better performances than the archetypal photosensitizer **[1]Cl**, and **[Ir4]Cl**–**[Ir5]Cl** are even more active than the fluorinated standard PS **[2]Cl**. We theorize that the good performance of **[Ir5]Cl**, despite its low  $\Phi_{\text{PL}}$ , could be ascribed to its better absorptivity in the visible range.

Table 9. Photocatalysts screening in the photooxidation of 1,2,3,4-tetrahydroquinoline **3a**.<sup>[a]</sup>

C1CNc2ccccc12 + 2 O<sub>2</sub>  $\xrightarrow[\lambda_{\text{irr}} = 460 \text{ nm, CH}_3\text{CN, RT, 24 h}]{\text{PC (0.1 mol \%)} / \text{O}_2 (1 \text{ atm})}$  C1CN=Cc2ccccc12 + 2 H<sub>2</sub>O<sub>2</sub>

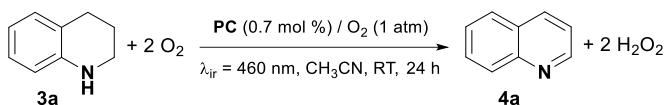
Entry	Complex	Yield (%)
1	<b>[1]Cl</b>	45
2	<b>[2]Cl</b>	62
3	<b>[Ir1]Cl</b>	0
4	<b>[Ir2]Cl</b>	27
5	<b>[Ir3]Cl</b>	56
6	<b>[Ir4]Cl</b>	70
7	<b>[Ir5]Cl</b>	68

<sup>[a]</sup> **Reaction conditions:** 1,2,3,4-tetrahydroquinoline **3a** (10 mM), **PC** (0.1 mol %), acetonitrile (0.5 mL), O<sub>2</sub> (balloon, 1 atm), blue light (LED,  $\lambda_{\text{irr}} = 460 \text{ nm}$ , 24 W), room temperature for 24 hours. Yields of **4a** were experimentally determined from <sup>1</sup>H NMR integration of the corresponding reaction crudes. The yield values were calculated as the mean of three independent experiments.

The usual control experiments were done to gain insight into the mechanism of this transformation. In particular, we observed no conversion without light or PC as well as a drastic decrease in the yield in the absence of O<sub>2</sub> (4% of **4a**, under a N<sub>2</sub> atmosphere) (Table 10). The use of the ROS scavengers DABCO, TEMPO, and BQ revealed similar behaviours to those established for the photooxidation of indoline, that is, a slight drop in the yield of **4a** in the presence of DABCO (87%), but a severe inhibition of the transformation in the presence of TEMPO (7%) and BQ (17%) relative to the standard conditions (entries 1 and 5–7 in Table 10). In conclusion, we propose that both singlet oxygen and superoxide take part in the dehydrogenation reaction of 1,2,3,4-tetrahydroquinoline, although the main role would correspond to the radical anion superoxide (O<sub>2</sub><sup>•-</sup>). To gain additional insight into the reaction mechanism, we performed emission quenching Stern–Volmer experiments. Thus, we could determine that phosphorescence of **[Ir4]Cl** was strongly quenched in the presence of increasing concentrations of **3a** under nitrogen, and consequently we proved that reductive quenching can be rationally proposed as the first step in the mechanism of this transformation. In other words, we concluded that **3a** can be efficiently oxidized by **[Ir4]<sup>•+</sup>** with a quenching constant,  $K_{\text{sv}} = 29.728 \times 10^3 \text{ M}^{-1}$ .<sup>63,64,65</sup> However, we also demonstrated that the emission of **[Ir4]Cl** is quenched upon exposure to open air (SI

Fig. 47). Hence, oxidative quenching of **[Ir4]\*** mediated by O<sub>2</sub> can operate as the first step in the mechanism of this reaction as well. See a detailed discussion below.

Table 10. Control experiments for the photooxidation of 1,2,3,4-tetrahydroquinoline **3a**.<sup>[a]</sup>



Entry	Conditions	Yield (%)
1	PC, O <sub>2</sub> , light	100
2	PC, O <sub>2</sub> , no light	0
3	No PC, O <sub>2</sub> , light	0
4	PC, N <sub>2</sub> , light	4
5	PC, O <sub>2</sub> , light, DABCO <sup>[b]</sup>	86
6	PC, O <sub>2</sub> , light, TEMPO <sup>[c]</sup>	7
7	PC, O <sub>2</sub> , light, BQ <sup>[d]</sup>	17

<sup>[a]</sup> **Reaction conditions:** 1,2,3,4-tetrahydroquinoline **3a** (10 mM), PC (**[Ir4]Cl**; 0.7 mol %), CH<sub>3</sub>CN (0.5 mL) at room temperature, under a saturated atmosphere of either O<sub>2</sub> or N<sub>2</sub> (1 atm) and under irradiation with blue light (LED, λ<sub>irr</sub> = 460 nm, 24 W) during 24 hours in a septum-capped tube. Yields of **4a** were determined by <sup>1</sup>H NMR integration of the corresponding reaction crudes. <sup>[b]</sup>DABCO (3 eq). <sup>[c]</sup>TEMPO (3 eq). <sup>[d]</sup>1,4-Benzoquinone (3 eq). The yield values were calculated as the mean of three independent experiments.

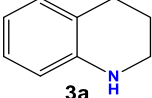
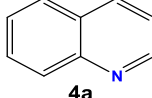
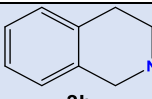
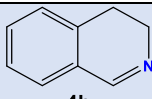
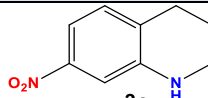
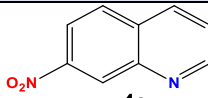
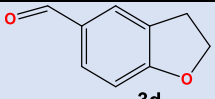
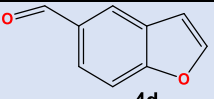
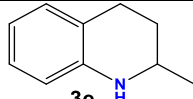
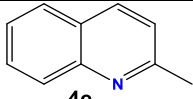
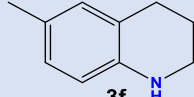
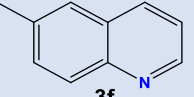
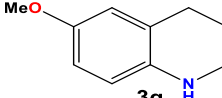
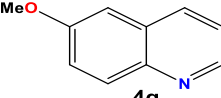
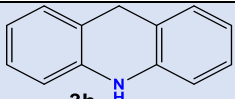
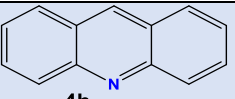
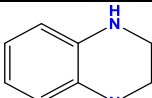
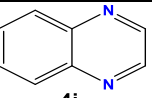
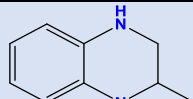
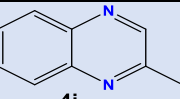
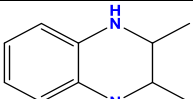
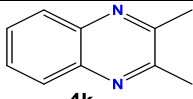
To complete this study, we extended the above-mentioned protocol to a selection of tetrahydroquinolines and analogues, such as 1,2,3,4-tetrahydroisoquinoline, 9,10-dihydroacridine and several 1,2,3,4-tetrahydroquinoxalines (Table 11).

In general, we obtained high yields and excellent selectivity for most of the expected products (**4b**, **4c**, and **4e–4h**). In a previous photocatalytic protocol, Bahnemann et al. obtained a mixture between the partially dehydrogenated product **4b** and the fully dehydrogenated product, when using the tetrahydroisoquinoline **3b**.<sup>18</sup> However, the yields for the quinoxalines, **4i–4k**, and 6-methyl-quinoline, **4f**, were only moderate, in the range between 52 and 62%. On the other hand, 2,3-dihydrobenzofuran-5-carboxaldehyde (**3d**) was not oxidized to its dehydrogenated derivative. It is noteworthy that the oxidation of 7-nitro-1,2,3,4-tetrahydroquinoline (**3c**) was achieved albeit with a low yield, since, as aforementioned, the nitro substituent usually behaves as a quencher for the excited state of PCs. Moreover, the yield for **4c** could be improved by prolonging the reaction time and increasing the catalyst loading (>99% yield, with 5 mol % PC, 48 h).

After this, we successfully scaled our methodology up to 1 g (gram scale) of **3a** in the presence of **[Ir4]Cl** (0.7 mol %) to obtain **4a** with a yield of 88%, albeit it was necessary to extend the reaction time from 24 to 75 h (see <sup>1</sup>H and <sup>13</sup>C NMR spectra and characterization of isolated products in SI Fig. 42 and 43).

Table 11. Substrate Scope for the photooxidation of tetrahydroquinolines<sup>[a]</sup>

$$3 + \text{O}_2 \xrightarrow[\lambda_{\text{ir}} = 460 \text{ nm, CH}_3\text{CN, RT, 24 h}]{\text{PC (0.7-5 mol \%)} / \text{O}_2 (1 \text{ atm})} 4 + \text{H}_2\text{O}_2$$

Entry	Substrate	Product	Yield (%) / [PC (mol %)]
1	 3a	 4a	100 [0.7]
2	 3b	 4b	100 [0.7]
3	 3c	 4c	40 / >99 <sup>[b]</sup> [5]
4	 3d	 4d	0 [5]
5	 3e	 4e	100 [0.7]
6	 3f	 3f	61 [1.5]
7	 3g	 4g	94 [1.5]
8	 3h	 4h	100 [0.7]
9	 3i	 4i	52 [1.5]
10	 3j	 4j	54 [3]
11	 3k	 4k	62 [5]

<sup>[a]</sup> **Reaction conditions:** substrate (10 mM), PC (**[Ir4]Cl**; 0.1 - 5 mol %), CH<sub>3</sub>CN (0.5 mL) at room temperature, under a saturated atmosphere of O<sub>2</sub> (1 atm) and under irradiation with blue light (LED,  $\lambda_{\text{irr}} = 460 \text{ nm}$ , 24 W) during 24 hours in a septum-capped tube. Yields were determined by <sup>1</sup>H NMR integration of the corresponding reaction crudes. <sup>[b]</sup> Reaction time of 48 hours. The yield values were calculated as the mean of three independent experiments.

## 2.9. Mechanism

Based on the experimental results summarized in Table 12 along with the bibliographic background,<sup>17</sup> we propose a dual mechanism for the aerobic photooxidative dehydrogenation of 1,2,3,4-tetrahydroquinoline based on both a reductive quenching cycle (pathway A) and simultaneously on an oxidative quenching cycle (pathway B). In both cases, the reaction is mediated by the radical anion superoxide (O<sub>2</sub><sup>•-</sup>), and we postulate that both mechanisms could operate concurrently (Fig. 10).

Table 12. Experimental evidences supporting both the reductive and the oxidative quenching cycles as well as the participation of O<sub>2</sub><sup>•-</sup> in the afore-mentioned photocatalytic reactions.

Evidence	Experiment
<ul style="list-style-type: none"> <li>Strong inhibition of photocatalytic oxidation in the presence of TEMPO and BQ (radical and O<sub>2</sub><sup>•-</sup> scavengers).</li> </ul>	Control experiments performed in Tables 6 and 10.
<ul style="list-style-type: none"> <li>Low photocatalytic activity obtained for <b>[Ir1]Cl</b>, due to irreversible reductive quenching.</li> </ul>	Screening of photocatalysts (Tables 5 and 9) and Redox Potentials (Table 3).
<ul style="list-style-type: none"> <li>Low dehydrogenation for <b>1c</b>, <b>1g</b> and <b>3c</b>, due to the presence of -NO<sub>2</sub> groups which induce oxidative quenching on PS and inhibit the photocatalytic quenching steps.</li> </ul>	Substrate scope experiments. See Table 7 and 11.
<ul style="list-style-type: none"> <li>Suitable redox potentials for sustaining both a reductive quenching cycle and an oxidative quenching cycle.</li> </ul>	See text in this section, Table 3 and SI Table 4.
<ul style="list-style-type: none"> <li>Detection of H<sub>2</sub>O<sub>2</sub>.</li> </ul>	<sup>1</sup> H NMR of crudes and peroxide test sticks.
<ul style="list-style-type: none"> <li>Evidence of both reductive quenching of *PC in the presence of THQ and oxidative quenching in the presence of O<sub>2</sub>.</li> </ul>	Stern–Volmer Experiments in Fig. 9 and SI Fig. 47.

**Pathway A.** First, the model Ir(III) photosensitizer, **[Ir3]Cl**, is promoted to the singlet excited state under irradiation with blue light and then is converted to the respective triplet excited state through intersystem crossing. This species, <sup>3</sup>[Ir<sup>III</sup>]\*, exhibits a high oxidation ability and therefore is capable of generating the radical cation intermediate species **A** (THQ<sup>+</sup>), through a SET, which entails a reductive quenching of the excited state. The redox potential of the couple THQ/THQ<sup>+</sup> was determined by CV, E(THQ/THQ<sup>+</sup>) = -0.16 V vs Fc<sup>+</sup>/Fc (SI Fig. 24) and compared to E(Ir<sup>III</sup>\*/Ir<sup>II</sup>) = +0.59 V to demonstrate the feasibility of this step. Concurrently, the reduced form of the PC, [Ir<sup>II</sup>], is formed, and then, [Ir<sup>II</sup>] reduces O<sub>2</sub> to produce O<sub>2</sub><sup>•-</sup>. Next, two protons and one additional electron are transferred from intermediate **A** to O<sub>2</sub><sup>•-</sup>, resulting in



intermediate **B** plus one molecule of hydrogen peroxide ( $\text{H}_2\text{O}_2$ ). It is noteworthy that  $\text{H}_2\text{O}_2$  has been detected by both  $^1\text{H}$  NMR and using Quantofix peroxide sticks in the crude solutions of photocatalytic assays (see SI). Subsequently, imine-enamine tautomerization facilitates the second oxidation process, yielding the aromatic heterocycle.

**Pathway B.** Alternatively,  $^3[\text{Ir}^{\text{III}}]^*$  can undergo oxidative quenching upon reaction with  $\text{O}_2$  to produce  $\text{O}_2^{\bullet-}$  and concomitantly the oxidized intermediate  $[\text{Ir}^{\text{IV}}]$  (Fig. 10). Both the emission quenching of **[Ir4]Cl** in the presence of  $\text{O}_2$  and the corresponding redox potentials,  $E([\text{Ir}^{\text{III}}]^*/[\text{Ir}^{\text{IV}}]) = 1.06 \text{ V}$  and  $E(\text{O}_2/\text{O}_2^{\bullet-}) = -0.95 \text{ V}$  versus  $\text{Fc}^+/\text{Fc}$  support this step. Subsequently,  $[\text{Ir}^{\text{IV}}]$  oxidizes THQ to generate the species **A** ( $\text{THQ}^+$ ), returning to its ground state  $[\text{Ir}^{\text{III}}]$ . Then,  $\text{O}_2^{\bullet-}$  and species **A** react with each other to give **B** and **C**, as explained above for **pathway A**. A similar mechanism could operate for the photocatalytic aerobic dehydrogenation of indolines, etc.

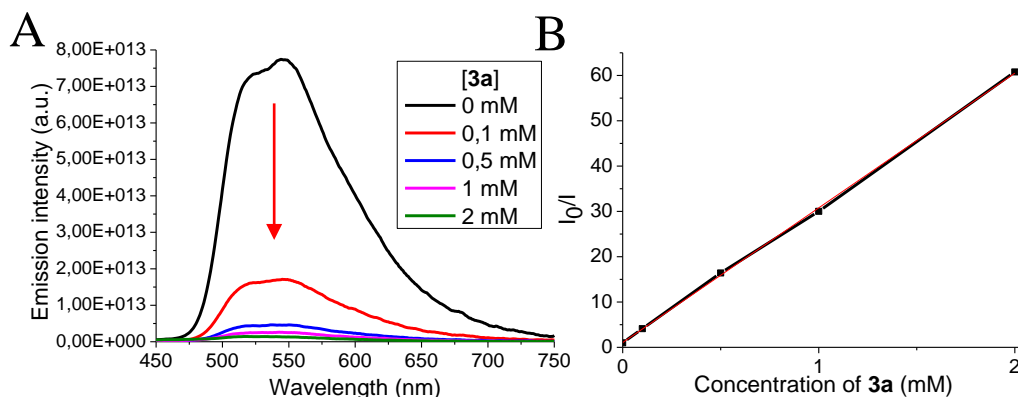


Fig. 9. (A) Stern–Volmer quenching experiments. Emission quenching of **[Ir4]Cl** (0.07 mM in  $\text{CH}_3\text{CN}$ ,  $25^\circ\text{C}$ ) upon incremental addition of substrate **3a** ( $0.1\text{--}2 \text{ mM}$ ) under  $\text{N}_2$  and  $\lambda_{\text{ir}} = 405 \text{ nm}$  (left). (B) Stern–Volmer quenching plot, where  $I_0$  = PL intensity of **[Ir4]Cl** at **[3a]** = 0 mM;  $I$  = PL intensity of **[Ir4]Cl** at different **[3a]**;  $I_0/I = 29.728 \times [\text{3a}] + 1.0544$ ;  $R^2 = 0.9996$  (right).

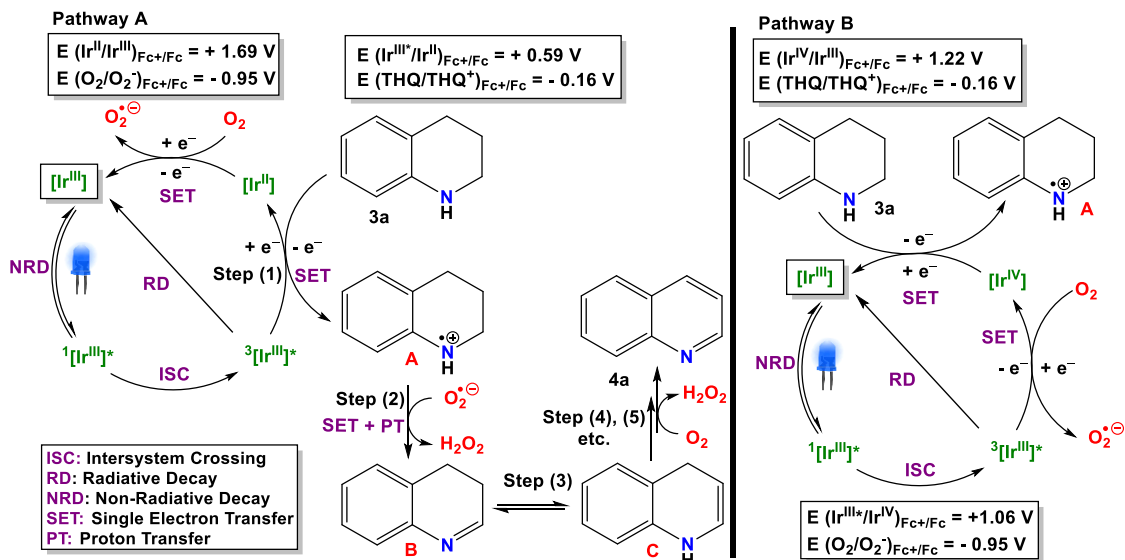


Fig. 10. Pathways A and B for the oxidative dehydrogenation of **3a** in the presence of the new Ir(III) PCs. Steps (2), (3) and (4), (5) etc. from species A are common for both pathways.

### 3. Conclusions

In conclusion, we have designed and prepared a new family of Ir(III) photosensitizers of general formula  $[\text{Ir}(\text{C}^{\wedge}\text{N})_2(\text{N}^{\wedge}\text{N}')]\text{Cl}$ , where  $\text{C}^{\wedge}\text{N} = 2\text{-(2,4-difluorophenyl)pyridinate}$  and  $\text{N}^{\wedge}\text{N}' = 2\text{-(2'-pyridyl)benzimidazole (L1)}$  or its N-alkylated derivatives **L2-L5**. We have ascertained that these complexes are notably stable under irradiation with blue light for a period of 24 h. Moreover, we have demonstrated that they absorb weakly in the visible light region and can be excited with blue light. Indeed, all of them are emissive in the range between 522 and 546 nm ( $\lambda_{\text{ex}} = 405 \text{ nm}$ ). In particular, the N-functionalized derivatives, **[Ir2]Cl**–**[Ir5]Cl**, exhibit moderate or high PLQYs (9–63%) and very long excited-state lifetimes (1012–2066 ns). On the contrary, the non-alkylated compound, **[Ir1]Cl**, features an excellent PLQY (78%) but a very short excited-state lifetime (59 ns). This divergent behaviour suggests that the N–H group speeds up the radiative deactivation of the excited state for **[Ir1]Cl**, by stabilization of the ground state through hydrogen bonds with counterion/solvent molecules, whereas the replacement of the N–H with apolar N-alkyl groups prevents this effect on the ground state and lengthens the lifetime of the respective excited states in acetonitrile. Regarding their electrochemical properties, all the Ir complexes display a similar redox behaviour, with electrochemical band-gaps higher than that determined for the standard photosensitizer  $[\text{Ir}(\text{ppy})_2(\text{bpy})]\text{PF}_6$ , **[1]PF<sub>6</sub>**. This is due to the strong stabilization of the HOMO, associated with the presence of electro-withdrawing –F atoms in the  $\text{C}^{\wedge}\text{N}$

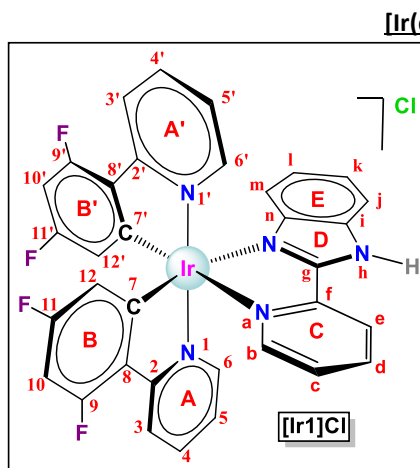
ligands of our PS, as revealed by theoretical calculations. Nevertheless, **[Ir1]Cl** features an irreversible  $E^{\text{red}1}_{1/2}$  in contrast to the reversible  $E^{\text{red}1}_{1/2}$  of its derivatives.

Upon excitation with blue light, these compounds exhibit highly efficient and selective photocatalytic activities in the preparation of a wide variety of aromatic N-heterocyclic products through oxidative dehydrogenation of partially saturated substrates such as different indolines, 1,2,3,4-tetrahydroquinolines, 1,2,3,4-tetrahydroisoquinoline, 9,10-dihydroacridine, and 1,2,3,4-tetrahydroquinoxalines. More specifically, the performance of the N-alkylated derivatives is better than that of **[Ir1]Cl** in these transformations, which seems to be linked to either the irreversible  $E^{\text{red}1}_{1/2}$  of **[Ir1]Cl** compared to the reversible  $E^{\text{red}1}_{1/2}$  of **[Ir2]Cl**–**[Ir5]Cl** or the low excited-state lifetime of **[Ir1]Cl**. We have proved the efficiency of this methodology on a gram scale for the synthesis of **2a** and **4a**. It is worth mentioning that this protocol satisfies most of the requirements of green chemistry, since it makes use of  $O_2$  as a green oxidant, acetonitrile as a low boiling point solvent, visible light as the energy source, and very low PC loadings.<sup>66</sup> Furthermore, we propose that these Ir-photosensitized transformations occur through a dual mechanism based on both a reductive quenching cycle (**pathway A**) and an oxidative quenching cycle (**pathway B**) which operate simultaneously and are mediated by the radical anion superoxide ( $O_2^{\bullet-}$ ).

To summarize, we have shown that the easy N-alkylation of 2-(2'-pyridyl)benzimidazole affords ligands suitable for the assembly of Ir(III) photosensitizers, **[Ir2]Cl**–**[Ir5]Cl**, which feature ideal properties to be used in photoredox catalysis. Indeed, these PSs exhibit highly efficient and selective photocatalytic activities in the preparation of a wide variety of N-heterocyclic products through oxidative dehydrogenation of partially saturated substrates. The above-mentioned results provide insights and tools for the rational design of efficient photocatalysts.

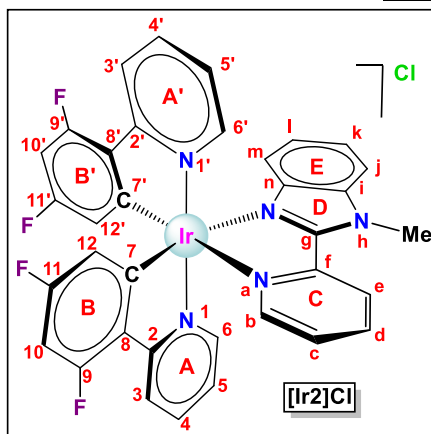
## 4. Synthesis and characterization

### 4.1. Ir(III)-complexes



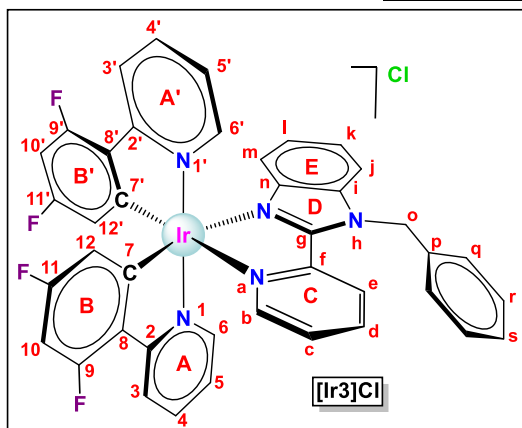
In a 100 mL Schlenk flask, previously purged with nitrogen, the ancillary ligand **L1** (0.0323 g, 0.165 mmol) was added to a solution of  $[\text{Ir}(\mu\text{-Cl})(\text{dfppy})_2]_2$  (0.1003 g, 0.082 mmol) in a mixture of dichloromethane (8 mL) / methanol (10 mL), and the mixture was stirred at 60 °C for 24 hours under a  $\text{N}_2$  atmosphere. The resulting solution was concentrated to half the volume under vacuum and diethyl ether (15 mL) was added to precipitate a crude solid that was isolated by filtration and washed with diethyl ether (2×5 mL). The product was dried under vacuum to produce a yellow powder. Yield: 0.0940 g (0.117

mmol, 71%). **M<sub>r</sub>** ( $\text{C}_{34}\text{H}_{21}\text{ClF}_4\text{IrN}_5$ ) = 803.23 g/mol. **Anal. Calcd for  $\text{C}_{34}\text{H}_{21}\text{ClF}_4\text{IrN}_5(\text{CH}_2\text{Cl}_2)_{0.15}$ :** C 50.27; H 2.63; N 8.58; **Found:** C 50.55; H 2.59; N 8.24. **<sup>1</sup>H NMR (400 MHz, DMSO-*d*<sub>6</sub>, 25 °C)** δ 15.91 (bs, 1H, NH), 9.06 (d, J = 7.4 Hz, 1H, H<sup>e</sup>), 8.38 (t, J = 7.8 Hz, 1H, H<sup>d</sup>), 8.25 (dd, J = 21.6, 8.3 Hz, 2H, H<sup>3</sup>, H<sup>3'</sup>), 8.07 – 7.85 (m, 3H, H<sup>4</sup>, H<sup>4'</sup>, H<sup>b</sup>), 7.83 – 7.64 (m, 4H, H<sup>i</sup>, H<sup>6</sup>, H<sup>6'</sup>, H<sup>c</sup>), 7.39 (t, J = 7.7 Hz, 1H, H<sup>k</sup>), 7.22 (q, J = 5.9 Hz, 2H, H<sup>5</sup>, H<sup>5'</sup>), 7.13 (t, J = 7.7 Hz, 1H, H<sup>l</sup>), 7.08 – 6.87 (m, 2H, H<sup>10</sup>, H<sup>10'</sup>), 6.21 (d, J = 8.3 Hz, 1H, H<sup>m</sup>), 5.76 (d, J = 7.1 Hz, 1H, H<sup>12</sup>), 5.67 (d, J = 7.4 Hz, 1H, H<sup>12'</sup>) ppm. **<sup>19</sup>F NMR (376 MHz, DMSO-*d*<sub>6</sub>, 25 °C)** δ -106.68 (q, J = 9.7 Hz, 1F, F<sup>11</sup>), -107.11 (q, J = 9.2 Hz, 1F, F<sup>11'</sup>), -108.83 (t, J = 11.5 Hz, 1F, F<sup>9</sup>), -109.31 (t, J = 11.8 Hz, 1F, F<sup>9'</sup>) ppm. **<sup>13</sup>C{<sup>1</sup>H} NMR (101 MHz, DMSO-*d*<sub>6</sub>, 25 °C)** δ 163.38, 162.69, 161.53, 160.84, 158.94, 155.06, 153.29, 151.27, 150.54, 149.93, 149.84, 149.73, 149.64, 146.94, 140.20, 139.61, 139.38, 134.51, 128.80, 128.16, 127.78, 125.36, 124.71, 124.30, 123.09, 122.90, 122.60, 115.56, 114.04, 113.97, 113.47, 112.90, 98.71, 98.55 ppm. **FT-IR (KBr, cm<sup>-1</sup>) selected bands:** 3333 (w, ν<sub>N-H</sub>), 3017 (w, ν<sub>C-H</sub>), 1602-1571 (m, ν<sub>C=C</sub> + ν<sub>C-N</sub>), 1429 (w, ν<sub>C=N</sub>), 1165 (m, ν<sub>C-C</sub>), 1042 (m, δ<sub>C-Hip</sub>), 750-739 (vs, δ<sub>C-Hoop</sub>). **HR ESI+ MS (DCM/DMSO, 4:1):** m/z<sub>exp</sub> = 768.1368 (m/z<sub>calcd</sub> [M<sup>+</sup>] = m/z<sub>calcd</sub> [C<sub>34</sub>H<sub>21</sub>F<sub>4</sub>IrN<sub>5</sub>]<sup>+</sup> = 768.1362); 573.0560 (m/z<sub>calcd</sub> [M<sup>+</sup>-L1] = m/z<sub>calcd</sub> [C<sub>22</sub>H<sub>12</sub>F<sub>4</sub>IrN<sub>2</sub>]<sup>+</sup> = 573.0566). **Solubility:** soluble in dimethyl sulfoxide, dichloromethane, methanol, acetone, acetonitrile, dimethylformamide, tetrahydrofuran.

**[Ir(dfppy)<sub>2</sub>(L2)]Cl: [Ir<sub>2</sub>]Cl**

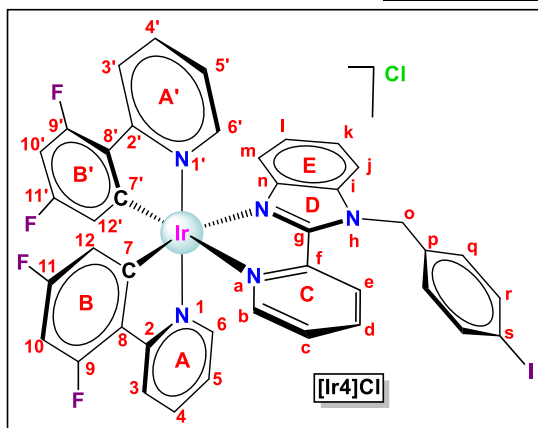
In a 100 mL Schlenk flask, previously purged with nitrogen, the ancillary ligand **L2** (0.0387 g, 0.185 mmol) was added to a solution of  $[\text{Ir}(\mu\text{-Cl})(\text{dfppy})_2]_2$  (0.1001 g, 0.082 mmol) in a mixture of dichloromethane (8 mL) / methanol (10 mL), and the mixture was stirred at 60 °C for 24 hours under a N<sub>2</sub> atmosphere. The resulting solution was concentrated to half the volume under vacuum and diethyl ether (15 mL) was added to precipitate a crude solid that was isolated by filtration and washed with diethyl ether (2×5 mL). The product was dried under vacuum to produce a yellow powder. Yield: 0.0896 g (0.110 mmol, 67%). **M<sub>r</sub>** (C<sub>35</sub>H<sub>23</sub>ClF<sub>4</sub>IrN<sub>5</sub>) =

817.25 g/mol. **Anal. Calcd for C<sub>35</sub>H<sub>23</sub>ClF<sub>4</sub>IrN<sub>5</sub>(CH<sub>2</sub>Cl)<sub>0.88</sub>**: C 48.31; H 2.80; N 7.85; **Found**: C 48.35; H 2.85; N 8.19. **<sup>1</sup>H NMR (400 MHz, DMSO-d<sub>6</sub>, 25 °C)** δ 8.85 (d, J = 8.4 Hz, 1H, H<sup>e</sup>), 8.36 (t, J = 8.0 Hz, 1H, H<sup>d</sup>), 8.30 (d, J = 8.7 Hz, 1H, H<sup>3</sup>), 8.23 (d, J = 8.6 Hz, 1H, H<sup>3'</sup>), 8.05 – 7.94 (m, 4H, H<sup>4</sup>, H<sup>4'</sup>, H<sup>j</sup>, H<sup>b</sup>), 7.80 (d, J = 5.9 Hz, 1H, H<sup>6</sup>), 7.77 – 7.68 (m, 2H, H<sup>6'</sup>, H<sup>c</sup>), 7.48 (t, J = 7.8 Hz, 1H, H<sup>k</sup>), 7.27 – 7.14 (m, 3H, H<sup>5</sup>, H<sup>5'</sup>, H<sup>l</sup>), 7.08 – 6.93 (m, 2H, H<sup>10</sup>, H<sup>10'</sup>), 6.24 (d, J = 8.3 Hz, 1H, H<sup>m</sup>), 5.72 (d, J = 8.4 Hz, 1H, H<sup>12</sup>), 5.63 (d, J = 8.4 Hz, 1H, H<sup>12'</sup>), 4.48 (s, 3H, H<sup>N-Me</sup>) ppm. **<sup>13</sup>C{<sup>1</sup>H} NMR (101 MHz, DMSO-d<sub>6</sub>, 25 °C)** δ 162.74, 159.36, 159.01, 155.65, 155.08, 152.83, 151.90, 151.42, 151.32, 150.19, 149.35, 148.02, 146.67, 145.18, 139.82, 138.32, 136.51, 134.23, 133.13, 130.81, 130.11, 127.82, 126.48, 125.10, 124.37, 124.26, 123.34, 120.46, 120.10, 113.76, 112.93, 98.78, 33.52 ppm. **<sup>19</sup>F NMR (376 MHz, DMSO-d<sub>6</sub>, 25 °C)** δ -106.57 (q, J = 9.6 Hz, 1F), -107.01 (q, J = 8.9 Hz, 1F), -108.75 (t, J = 11.2 Hz, 1F), -109.21 (t, J = 11.2 Hz, 1F) ppm. **FT-IR (KBr, cm<sup>-1</sup>) selected bands**: 3064 (w, ν<sub>C-H</sub>), 1601-1571 (m, ν<sub>C=C + C-N</sub>), 1428 (w, ν<sub>C=N</sub>), 1162 (m, ν<sub>C-C</sub>), 1042 (m, δ<sub>C-Hip</sub>), 746 (vs, δ<sub>C-Hoop</sub>). **HR ESI+ MS (DCM/DMSO, 4:1)**: m/z<sub>exp</sub> = 782.1520 (m/z<sub>calcd</sub> [M<sup>+</sup>] = m/z<sub>calcd</sub> [C<sub>35</sub>H<sub>23</sub>F<sub>4</sub>IrN<sub>5</sub>]<sup>+</sup> = 782.1519); 573.0558 (m/z<sub>calcd</sub> [M<sup>+</sup>-L2] = m/z<sub>calcd</sub> [C<sub>22</sub>H<sub>12</sub>F<sub>4</sub>IrN<sub>2</sub>]<sup>+</sup> = 573.0566). **Solubility**: soluble in dimethyl sulfoxide, dichloromethane, methanol, acetone, acetonitrile, dimethylformamide, tetrahydrofuran.

**[Ir(dfppy)<sub>2</sub>(L3)]Cl: [Ir3]Cl**

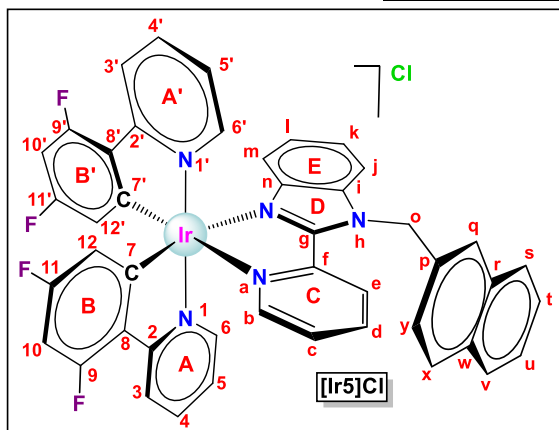
In a 100 mL Schlenk flask, previously purged with nitrogen, the ancillary ligand **L3** (0.0530 g, 0.186 mmol) was added to a solution of  $[\text{Ir}(\mu\text{-Cl})(\text{dfppy})_2]_2$  (0.1003 g, 0.082 mmol) in a mixture of dichloromethane (8 mL) / methanol (10 mL), and the mixture was stirred at 60 °C for 24 hours under a N<sub>2</sub> atmosphere. The resulting solution was concentrated to half the volume under vacuum and diethyl ether (15 mL) was added to precipitate a crude solid that was isolated by filtration and washed with

diethyl ether (2×5 mL). The product was dried under vacuum to produce a yellow powder. Yield: 0.1216 g (0.136 mmol, 83%). **M<sub>r</sub>** (C<sub>41</sub>H<sub>27</sub>ClF<sub>4</sub>IrN<sub>5</sub>) = 893.35 g/mol. **Anal. Calcd for C<sub>41</sub>H<sub>27</sub>ClF<sub>4</sub>IrN<sub>5</sub>·(CH<sub>2</sub>Cl<sub>2</sub>)<sub>1.2</sub>**: C 50.93; H 2.98; N 7.04; **Found**: C 50.97; H 3.24; N 7.35. **<sup>1</sup>H NMR (400 MHz, DMSO-d<sub>6</sub>, 25 °C)** δ 8.54 (d, J = 8.4 Hz, 1H, H<sup>e</sup>), 8.31 (d, J = 8.6 Hz, 1H, H<sup>3</sup>), 8.27 – 8.17 (m, 2H, H<sup>3'</sup>, H<sup>d</sup>), 8.01 (td, J = 14.6, 14.1, 6.8 Hz, 4H, H<sup>4</sup>, H<sup>4'</sup>, H<sup>j</sup>, H<sup>b</sup>), 7.91 (d, J = 5.9 Hz, 1H, H<sup>6</sup>), 7.71 – 7.62 (m, 2H, H<sup>6'</sup>, H<sup>c</sup>), 7.53 – 7.44 (m, 1H, H<sup>k</sup>), 7.29 (ddt, J = 28.6, 12.8, 6.9 Hz, 6H, H<sup>f</sup>, H<sup>f'</sup>, H<sup>5</sup>, H<sup>5'</sup>, H<sup>l</sup>), 7.13 – 6.94 (m, 4H, H<sup>q</sup>, H<sup>q</sup>, H<sup>10</sup>, H<sup>10'</sup>), 6.41 – 6.23 (m, 3H, H<sup>o</sup>, H<sup>o</sup>, H<sup>m</sup>), 5.77 (dd, J = 8.4, 2.1 Hz, 1H, H<sup>12</sup>), 5.64 (dd, J = 8.4, 2.1 Hz, 1H, H<sup>12'</sup>) ppm. **<sup>19</sup>F NMR (376 MHz, DMSO-d<sub>6</sub>, 25 °C)** δ -106.51 (q, J = 9.6 Hz, 1F), -106.89 (q, J = 9.2, 8.6 Hz, 1F), -108.63 (t, J = 11.9 Hz, 1F), -109.13 (t, J = 11.6 Hz, 1F) ppm. **<sup>13</sup>C{<sup>1</sup>H} NMR (101 MHz, DMSO-d<sub>6</sub>, 25 °C)** δ 162.77, 155.17, 152.52, 152.48, 151.71, 150.20, 149.66, 145.70, 140.30, 139.98, 139.89, 138.44, 136.69, 135.17, 135.13, 129.25, 129.16, 129.12, 128.02, 126.39, 125.87, 124.54, 124.36, 123.19, 116.36, 113.87, 113.65, 113.25, 113.02, 99.07, 98.90, 48.36 ppm. **FT-IR (KBr, cm<sup>-1</sup>) selected bands**: 3063 (w, ν<sub>C-H</sub>), 1602-1569 (m, ν<sub>C=C + C-N</sub>), 1429 (w, ν<sub>C=N</sub>), 1165 (m, ν<sub>C-C</sub>), 1067-1024-1013 (m, δ<sub>C-Hip</sub>), 741 (vs, δ<sub>C-Hoop</sub>). **HR ESI+ MS (DCM/DMSO, 4:1)**: m/z<sub>exp</sub> = 858.1830 (m/z<sub>calcd</sub> [M<sup>+</sup>] = m/z<sub>calcd</sub> [C<sub>41</sub>H<sub>27</sub>F<sub>4</sub>IrN<sub>5</sub>]<sup>+</sup> = 858.1831); 573.0554 (m/z<sub>calcd</sub> [M<sup>+</sup>-L<sup>3</sup>] = m/z<sub>calcd</sub> [C<sub>22</sub>H<sub>12</sub>F<sub>4</sub>IrN<sub>2</sub>]<sup>+</sup> = 573.0566). **Solubility**: soluble in dimethyl sulfoxide, dichloromethane, methanol, acetone, acetonitrile, dimethylformamide, tetrahydrofuran.

**[Ir(dfppy)<sub>2</sub>(L4)]Cl: [Ir4]Cl**

In a 100 mL Schlenk flask, previously purged with nitrogen, the ancillary ligand **L4** (0.0758 g, 0.184 mmol) was added to a solution of  $[\text{Ir}(\mu\text{-Cl})(\text{dfppy})_2]_2$  (0.1005 g, 0.083 mmol) in a mixture of dichloromethane (8 mL) / methanol (10 mL), and the mixture was stirred at 60 °C for 24 hours under a  $\text{N}_2$  atmosphere. The resulting solution was concentrated to half the volume under vacuum and diethyl ether (15 mL) was added to precipitate a crude solid that was isolated by filtration and washed with diethyl ether (2x5 mL).

The product was dried under vacuum to produce a yellow powder. Yield: 0.1308 g (0.128 mmol, 78%). **Mr** ( $\text{C}_{41}\text{H}_{26}\text{ClF}_4\text{IrN}_5$ ) = 1019.25 g/mol. **Anal. Calcd for  $\text{C}_{41}\text{H}_{26}\text{ClF}_4\text{IrN}_5$ :** C 48.32; H 2.57; N 6.87; **Found:** C 48.34; H 2.60; N 6.54.  **$^1\text{H}$  NMR (400 MHz, DMSO- $d_6$ , 25 °C)**  $\delta$  8.48 (d,  $J$  = 8.2 Hz, 1H,  $\text{H}^e$ ), 8.30 (d,  $J$  = 8.8 Hz, 1H,  $\text{H}^3$ ), 8.27 – 8.19 (m, 2H,  $\text{H}^{3'}$ ,  $\text{H}^d$ ), 8.01 (dd,  $J$  = 16.4, 8.0 Hz, 4H,  $\text{H}^4$ ,  $\text{H}^4$ ,  $\text{H}^j$ ,  $\text{H}^b$ ), 7.89 (d,  $J$  = 5.9 Hz, 1H,  $\text{H}^6$ ), 7.74 – 7.65 (m, 4H,  $\text{H}^6$ ,  $\text{H}^r$ ,  $\text{H}^r$ ,  $\text{H}^c$ ), 7.49 (t,  $J$  = 7.7 Hz, 1H,  $\text{H}^k$ ), 7.25 (dt,  $J$  = 14.0, 7.3 Hz, 3H,  $\text{H}^5$ ,  $\text{H}^{5'}$ ,  $\text{H}^l$ ), 7.10 – 7.02 (m, 1H,  $\text{H}^{10}$ ), 7.02 – 6.95 (m, 1H,  $\text{H}^{10}$ ), 6.92 (d,  $J$  = 7.0 Hz, 2H,  $\text{H}^q$ ,  $\text{H}^q$ ), 6.36 – 6.19 (m, 3H,  $\text{H}^o$ ,  $\text{H}^o$ ,  $\text{H}^m$ ), 5.76 (d,  $J$  = 8.4 Hz, 1H,  $\text{H}^{12}$ ), 5.63 (d,  $J$  = 8.4 Hz, 1H,  $\text{H}^{12}$ ) ppm.  **$^{19}\text{F}$  NMR (376 MHz, DMSO- $d_6$ , 25 °C)**  $\delta$  -106.50 (q,  $J$  = 9.9, 9.3 Hz, 1F), -106.90 (q,  $J$  = 9.6 Hz, 1F), -108.63 (t,  $J$  = 11.6 Hz, 1F), -109.13 (t,  $J$  = 11.6 Hz, 1F) ppm.  **$^{13}\text{C}\{^1\text{H}\}$  NMR (101 MHz, DMSO- $d_6$ , 25 °C)**  $\delta$  164.05, 163.64, 162.75, 161.63, 161.51, 161.10, 159.37, 159.11, 155.14, 153.39, 152.44, 151.72, 151.65, 145.59, 140.37, 139.99, 139.89, 138.46, 137.78, 136.60, 134.96, 129.28, 128.33, 128.19, 127.80, 126.46, 125.92, 125.72, 124.54, 124.40, 123.45, 123.25, 122.92, 116.34, 113.22, 112.96, 112.75, 99.07, 98.65, 94.29, 47.98 ppm. **FT-IR (KBr,  $\text{cm}^{-1}$ ) selected bands:** 3011 (w,  $\nu_{\text{C}=\text{H}}$ ), 1600-1571 (m,  $\nu_{\text{C}=\text{C} + \text{C}=\text{N}}$ ), 1441 (w,  $\nu_{\text{C}=\text{N}}$ ), 1162 (m,  $\nu_{\text{C}-\text{C}}$ ), 1061 (m,  $\delta_{\text{C}-\text{H}_{\text{ip}}}$ ), 755-745 (vs,  $\delta_{\text{C}-\text{H}_{\text{oop}}}$ ). **HR ESI+ MS (DCM/DMSO, 4:1):**  $m/z_{\text{exp}} = 984.0792$  ( $m/z_{\text{calcd}} [\text{M}^+] = m/z_{\text{calcd}} [\text{C}_{41}\text{H}_{26}\text{F}_4\text{IrN}_5]^+ = 984.0798$ );  $573.0553$  ( $m/z_{\text{calcd}} [\text{M}^+ - \text{L}^4] = m/z_{\text{calcd}} [\text{C}_{22}\text{H}_{12}\text{F}_4\text{IrN}_2]^+ = 573.0566$ ). **Solubility:** soluble in dimethyl sulfoxide, dichloromethane, methanol, acetone, acetonitrile, dimethylformamide, tetrahydrofuran.

**[Ir(dfppy)<sub>2</sub>(L5)]Cl: [Ir5]Cl**

In a 100 mL Schlenk flask, previously purged with nitrogen, the ancillary ligand **L5** (0.0620 g, 0.185 mmol) was added to a solution of  $[\text{Ir}(\mu\text{-Cl})(\text{dfppy})_2]_2$  (0.1003 g, 0.082 mmol) in a mixture of dichloromethane (8 mL) / methanol (10 mL), and the mixture was stirred at 60 °C for 24 hours under a N<sub>2</sub> atmosphere. The resulting solution was concentrated to half the volume under vacuum and diethyl ether (15 mL) was added to precipitate a crude solid that was

isolated by filtration and washed with diethyl ether (2×5 mL). The product was dried under vacuum to produce a yellow-orange powder. Yield: 0.1206 g (0.128 mmol, 77%). **M<sub>r</sub>** (C<sub>45</sub>H<sub>29</sub>ClF<sub>4</sub>IrN<sub>5</sub>) = 943.41g/mol. **Anal. Calcd for C<sub>45</sub>H<sub>29</sub>ClF<sub>4</sub>IrN<sub>5</sub>(CH<sub>2</sub>Cl<sub>2</sub>)<sub>0.85</sub>**: C 54.22; H 3.05; N 6.90; **Found**: C 54.25; H 3.05; N 7.22. **<sup>1</sup>H NMR (400 MHz, DMSO-d<sub>6</sub>, 25 °C)** δ 8.52 (d, J = 8.2 Hz, 1H, H<sup>6</sup>), 8.29 (t, J = 9.1 Hz, 2H, H<sup>3</sup>, H<sup>3'</sup>), 8.18 (t, J = 8.0 Hz, 1H, H<sup>d</sup>), 8.05 (t, J = 7.6 Hz, 3H, H<sup>4</sup>, H<sup>4'</sup>, H<sup>j</sup>), 8.00 (d, J = 5.7 Hz, 1H), 7.96 (d, J = 9.0 Hz, 2H, H<sup>b</sup>), 7.91 (dd, J = 6.0, 3.3 Hz, 1H), 7.78 – 7.73 (m, 1H), 7.71 (d, J = 5.7 Hz, 1H, H<sup>6'</sup>), 7.68 – 7.61 (m, 1H, H<sup>c</sup>), 7.58 – 7.46 (m, 4H, H<sup>k</sup>, H<sup>6</sup>), 7.35 (d, J = 8.6 Hz, 1H), 7.34 – 7.29 (m, 1H, H<sup>5</sup>), 7.29 – 7.20 (m, 2H, H<sup>5'</sup>, H<sup>l</sup>), 7.07 (t, J = 10.9 Hz, 1H, H<sup>10</sup>), 6.98 (t, J = 11.1 Hz, 1H, H<sup>10'</sup>), 6.49 (q, J = 18.1 Hz, 2H, H<sup>o</sup>, H<sup>o'</sup>), 6.36 (d, J = 8.4 Hz, 1H, H<sup>m</sup>), 5.79 (d, J = 8.2 Hz, 1H, H<sup>12</sup>), 5.64 (d, J = 8.3 Hz, 1H, H<sup>12'</sup>) ppm. **<sup>19</sup>F NMR (376 MHz, DMSO-d<sub>6</sub>, 25 °C)** δ -106.49 (q, J = 9.6 Hz, 1F), -106.92 (q, J = 9.6 Hz, 1F), -108.62 (t, J = 11.6 Hz, 1F), -109.11 (t, J = 11.2 Hz, 1F) ppm. **<sup>13</sup>C{<sup>1</sup>H} NMR (101 MHz, DMSO-d<sub>6</sub>, 25 °C)** δ 162.80, 161.12, 159.14, 153.87, 153.52, 152.53, 151.69, 150.28, 149.82, 145.66, 140.78, 140.29, 139.99, 139.85, 138.57, 137.32, 136.77, 136.23, 132.80, 132.78, 132.38, 131.62, 130.38, 129.22, 129.00, 127.70, 127.65, 126.71, 126.42, 125.96, 125.70, 124.56, 124.39, 124.18, 124.01, 122.95, 122.18, 116.41, 113.84, 113.05, 111.41, 98.91, 48.61 ppm. **FT-IR (KBr, cm<sup>-1</sup>) selected bands**: 3016 (w, ν<sub>C-H</sub>), 1601-1575 (m, ν<sub>C=C</sub> + ν<sub>C-N</sub>), 1427 (w, ν<sub>C=N</sub>), 1160 (m, ν<sub>C-C</sub>), 1065 (m, δ<sub>C-Hip</sub>), 756 (vs, δ<sub>C-Hoop</sub>). **HR ESI+ MS (DCM/DMSO, 4:1)**: m/z<sub>exp</sub> = 908.1986 (m/z<sub>calcd</sub> [M<sup>+</sup>] = m/z<sub>calcd</sub> [C<sub>45</sub>H<sub>29</sub>F<sub>4</sub>IrN<sub>5</sub>]<sup>+</sup> = 908.1988); 573.0553 (m/z<sub>calcd</sub> [M<sup>+</sup>-L<sup>5</sup>] = m/z<sub>calcd</sub> [C<sub>22</sub>H<sub>12</sub>F<sub>4</sub>IrN<sub>2</sub>]<sup>+</sup> = 573.0566). **Solubility**: soluble in dimethyl sulfoxide, dichloromethane, methanol, acetone, acetonitrile, dimethylformamide, tetrahydrofuran.



## Bibliography

1. E. Vitaku, D. T. Smith, and J. T. Njardarson, Analysis of the Structural Diversity, Substitution Patterns, and Frequency of Nitrogen Heterocycles among U.S. FDA Approved Pharmaceuticals, *J. Med. Chem.* 2014, **57**, 10257–10274.
2. N. K. Kaushik, N. Kaushik, P. Attri, N. Kumar, C. Kim, A. Verma, and E. Choi, Biomedical Importance of Indoles, *Molecules*, 2013, **18**, 6620–6662.
3. N. C. Desai, G. M. Kotadiya, and A. R. Trivedi, Studies on Molecular Properties Prediction, Antitubercular and Antimicrobial Activities of Novel Quinoline Based Pyrimidine Motifs, *Bioorg. Med. Chem. Lett.*, 2014, **24**, 3126–3130.
4. R.-J. Man, N. Jeelani, C. Zhou, and Y.-S. Yang, Recent Progress in the Development of Quinoline Derivatives for the Exploitation of Anti-Cancer Agents, *Anticancer. Agents Med. Chem.*, 2021, **21**, 825–838.
5. M. Fonte, N. Tassi, P. Gomes, and C. Teixeira, Acridine-Based Antimalarials—From the Very First Synthetic Antimalarial to Recent Developments, *Molecules*, 2021, **26**, 600.
6. I. Gabriel, 'Acridines' as New Horizons in Antifungal Treatment, *Molecules*, 2020, **25**, 1480.
7. H. Khatoon, and E. Abdulmalek, Novel Synthetic Routes to Prepare Biologically Active Quinoxalines and Their Derivatives: A Synthetic Review for the Last Two Decades, *Molecules*, 2021, **26**, 1055.
8. K.-H. He, F.-F. Tan, C.-Z. Zhou, G.-J. Zhou, X.-L. Yang, and Y. Li, Acceptorless Dehydrogenation of N-Heterocycles by Merging Visible-Light Photoredox Catalysis and Cobalt Catalysis, *Angew. Chemie Int. Ed.*, 2017, **56**, 3080–3084.
9. M. K. Sahoo, G. Jaiswal, J. Rana, and E. Balaraman, Organo-Photoredox Catalyzed Oxidative Dehydrogenation of N-Heterocycles, *Chem. - A Eur. J.*, 2017, **23**, 14167–14172.
10. S. Bera, A. Bera, and D. Banerjee, Nickel-Catalyzed Dehydrogenation of N-Heterocycles Using Molecular Oxygen., *Org. Lett.*, 2020, **22**, 6458–6463.
11. J. Wu, D. Talwar, S. Johnston, M. Yan, and J. Xiao, Acceptorless Dehydrogenation of Nitrogen Heterocycles with a Versatile Iridium Catalyst, *Angew. Chemie Int. Ed.*, 2013, **52**, 6983–6987.
12. K. Fujita, Y. Tanaka, M. Kobayashi, and R. Yamaguchi, Homogeneous Perdehydrogenation and Perhydrogenation of Fused Bicyclic N-Heterocycles Catalyzed by Iridium Complexes Bearing a Functional Bipyridonate Ligand, *J. Am. Chem. Soc.*, 2014, **136**, 4829–4832.
13. M. K. Sahoo, and E. Balaraman, Room Temperature Catalytic Dehydrogenation of Cyclic Amines with the Liberation of H<sub>2</sub> Using Water as a Solvent, *Green Chem.*, 2019, **21**, 2119–2128.
14. S. Kato, Y. Saga, M. Kojima, H. Fuse, S. Matsunaga, A. Fukatsu, M. Kondo, S. Masaoka, and M. Kanai, Hybrid Catalysis Enabling Room-Temperature Hydrogen Gas Release from N-Heterocycles and Tetrahydronaphthalenes, *J. Am. Chem. Soc.*, 2017, **139**, 2204–2207.
15. M. Zheng, J. Shi, T. Yuan, and X. Wang, Metal-Free Dehydrogenation of N-Heterocycles by Ternary h-BCN Nanosheets with Visible Light, *Angew. Chemie Int. Ed.*, 2018, **57**, 5487–5491.
16. N. O. Balayeva, Z. Mamiyev, R. Dillert, N. Zheng, and D. W. Bahnemann, Rh/TiO<sub>2</sub> -Photocatalyzed Acceptorless Dehydrogenation of N-Heterocycles upon Visible-Light Illumination, *ACS Catal.*, 2020, **10**, 5542–5553.

17. S. Chen, Q. Wan, and A. K. Badu-Tawiah, Picomole-Scale Real-Time Photoreaction Screening: Discovery of the Visible-Light-Promoted Dehydrogenation of Tetrahydroquinolines under Ambient Conditions, *Angew. Chemie Int. Ed.*, 2016, **55**, 9345–9349.
18. N. O. Balayeva, N. Zheng, R. Dillert, and D. W. Bahnemann, Visible-Light-Mediated Photocatalytic Aerobic Dehydrogenation of N-Heterocycles by Surface-Grafted TiO<sub>2</sub> and 4-Amino-TEMPO, *ACS Catal.*, 2019, **9**, 10694–10704.
19. S. Srinath, R. Abinaya, A. Prasanth, M. Mariappan, R. Sridhar, and B. Baskar, Reusable, Homogeneous Water Soluble Photoredox Catalyzed Oxidative Dehydrogenation of N-Heterocycles in a Biphasic System: Application to the Synthesis of Biologically Active Natural Products, *Green Chem.*, 2020, **22**, 2575–2587.
20. J. Sanz-Villafrauela, C. Martínez-Alonso, I. Echevarría, M. Vaquero, A. Carbayo, J. Fidalgo, A. M. Rodríguez, J. V. Cuevas-Vicario, J. C. Lima, A. J. Moro, et al., One-Pot Photocatalytic Transformation of Indolines into 3-Thiocyanate Indoles with New Ir(III) Photosensitizers Bearing  $\beta$ -Carbolines, *Inorg. Chem. Front.*, 2021, **8**, 1253–1270.
21. I. Echevarría, M. Vaquero, R. Quesada, and G. Espino, Synthesis of  $\alpha$ -Amino Nitriles through One-Pot Selective Ru-Photocatalyzed Oxidative Cyanation of Amines, *Inorg. Chem. Front.*, 2020, **7**, 3092–3105.
22. Y. Chen, L. Qiao, L. Ji, and H. Chao, Phosphorescent Iridium(III) Complexes as Multicolor Probes for Specific Mitochondrial Imaging and Tracking, *Biomaterials*, 2014, **35**, 2–13.
23. J. Torres, M. C. Carrión, J. Leal, F. A. Jalón, J. V. Cuevas, A. M. Rodríguez, G. Castañeda, and B. R. Manzano, Cationic Bis(Cyclometalated) Ir(III) Complexes with Pyridine–Carbene Ligands. Photophysical Properties and Photocatalytic Hydrogen Production from Water, *Inorg. Chem.*, 2018, **57**, 970–984.
24. W.-K. Huang, C.-W. Cheng, S.-M. Chang, Y.-P. Lee, and E. W.-G. Diau, Synthesis and Electron-Transfer Properties of Benzimidazole-Functionalized Ruthenium Complexes for Highly Efficient Dye-Sensitized Solar Cells, *Chem. Commun.*, 2010, **46**, 8992.
25. M. Vaquero, N. Busto, N. Fernández-Pampín, G. Espino, and B. García, Appended Aromatic Moieties Determine the Cytotoxicity of Neutral Cyclometalated Platinum(II) Complexes Derived from 2-(2-Pyridyl)Benzimidazole, *Inorg. Chem.*, 2020, **59**, 4961–4971.
26. N. M. Shavaleev, Z. R. Bell, T. L. Easun, R. Rutkaite, L. Swanson, and M. D. Ward, Complexes of Substituted Derivatives of 2-(2-Pyridyl)Benzimidazole with Re(I), Ru(II) and Pt(II): Structures, Redox and Luminescence Properties, *Dalt. Trans.*, 2004, **21**, 3678.
27. C. D. Sunesh, and Y. Choe, Synthesis and Characterization of Cationic Iridium Complexes for the Fabrication of Green and Yellow Light-Emitting Devices, *Mater. Chem. Phys.*, 2015, **156**, 206–213.
28. C. D. Sunesh, G. Mathai, and Y. Choe, Constructive Effects of Long Alkyl Chains on the Electroluminescent Properties of Cationic Iridium Complex-Based Light-Emitting Electrochemical Cells, *ACS Appl. Mater. Interfaces*, 2014, **6**, 17416–17425.
29. H. Sun, S. Liu, W. Lin, K. Y. Zhang, W. Lv, X. Huang, F. Huo, H. Yang, G. Jenkins, Q. Zhao, et al., Smart Responsive Phosphorescent Materials for Data Recording and Security Protection, *Nat. Commun.*, 2014, **5**, 4601/1-4601/9.
30. F. Gärtner, S. Denurra, S. Losse, A. Neubauer, A. Boddien, A. Gopinathan, A. Spannenberg, H. Junge, S. Lochbrunner, M. Blug, et al., Synthesis and Characterization of New Iridium Photosensitizers for Catalytic Hydrogen Generation from Water, *Chem. - A Eur. J.*, 2012, **18**, 3220–3225.

31. W. Lin, Q. Zhao, H. Sun, K. Y. Zhang, H. Yang, Q. Yu, X. Zhou, S. Guo, S. Liu, and W. Huang, An Electrochromic Phosphorescent Iridium(III) Complex for Information Recording, Encryption, and Decryption, *Adv. Opt. Mater.*, 2015, **3**, 368–375.
32. H. Cao, H. Sun, Y. Yin, X. Wen, G. Shan, Z. Su, R. Zhong, W. Xie, P. Li, and D. Zhu, Iridium(III) Complexes Adopting 1,2-Diphenyl-1H-Benzimidazole Ligands for Highly Efficient Organic Light-Emitting Diodes with Low Efficiency Roll-off and Non-Doped Feature, *J. Mater. Chem. C*, 2014, **2**, 2150–2159.
33. C. Pérez-Arnaiz, M. I. Acuña, N. Busto, I. Echevarría, M. Martínez-Alonso, G. Espino, B. García, and F. Domínguez, Thiabendazole-Based Rh(III) and Ir(III) Biscyclometallated Complexes with Mitochondria-Targeted Anticancer Activity and Metal-Sensitive Photodynamic Activity, *Eur. J. Med. Chem.*, 2018, **157**, 279–293.
34. E. Baranoff, B. F. E. Curchod, F. Monti, F. Steimer, G. Accorsi, I. Tavernelli, U. Rothlisberger, R. Scopelliti, M. Grätzel, and M. K. Nazeeruddin, Influence of Halogen Atoms on a Homologous Series of Bis-Cyclometallated Iridium(III) Complexes, *Inorg. Chem.*, 2012, **51**, 799–811.
35. A. Maity, L. Q. Le, Z. Zhu, J. Bao, and T. S. Teets, Steric and Electronic Influence of Aryl Isocyanides on the Properties of Iridium(III) Cyclometalates, *Inorg. Chem.*, 2016, **55**, 2299–2308.
36. A. F. Henwood, A. K. Pal, D. B. Cordes, A. M. Z. Slawin, T. W. Rees, C. Momblona, A. Babaei, A. Pertegás, E. Ortí, H. J. Bolink, et al., Blue-Emitting Cationic Iridium(III) Complexes Featuring Pyridylpyrimidine Ligands and Their Use in Sky-Blue Electroluminescent Devices, *J. Mater. Chem. C*, 2017, **5**, 9638–9650.
37. C. D. Ertl, C. Momblona, A. Pertegás, J. M. Junquera-Hernández, M.-G. La-Placa, A. Prescimone, E. Ortí, C. E. Housecroft, E. C. Constable, and H. J. Bolink, Highly Stable Red-Light-Emitting Electrochemical Cells, *J. Am. Chem. Soc.*, 2017, **139**, 3237–3248.
38. G. E. Schneider, A. Pertegás, E. C. Constable, C. E. Housecroft, N. Hostettler, C. D. Morris, J. A. Zampese, H. J. Bolink, J. M. Junquera-Hernández, E. Ortí, et al., Bright and Stable Light-Emitting Electrochemical Cells Based on an Intramolecularly  $\pi$ -Stacked, 2-Naphthyl-Substituted Iridium Complex, *J. Mater. Chem. C*, 2014, **2**, 7047–7055.
39. W. He, D. Zu, D. Liu, and R. Cheng, A Series of Iridium Complexes Equipped with Inert Shields: Highly Efficient Bluish Green Emitters with Reduced Self-Quenching Effect in Solid State, *Inorganica Chim. Acta*, 2011, **365**, 78–84.
40. R. D. Costa, E. Ortí, H. J. Bolink, F. Monti, G. Accorsi, N. Armaroli, E. Ortí, H. J. Bolink, F. Monti, G. Accorsi, et al., Luminescent Ionic Transition-Metal Complexes for Light-Emitting Electrochemical Cells, *Angew. Chemie - Int. Ed.*, 2012, **51**, 8178–8211.
41. R. Bevernaegie, S. A. M. Wehlin, B. Elias, and L. A. Troian-Gautier, Roadmap Towards Visible Light Mediated Electron Transfer Chemistry with Iridium(III) Complexes, *ChemPhotoChem*, 2021, **5**, 217–234.
42. J.-J. Cao, C.-P. Tan, M.-H. Chen, N. Wu, D.-Y. Yao, X.-G. Liu, L.-N. Ji, and Z.-W. Mao, Targeting Cancer Cell Metabolism with Mitochondria-Immobilized Phosphorescent Cyclometallated Iridium(III) Complexes, *Chem. Sci.*, 2017, **8**, 631–640.
43. S. Takizawa, R. Aboshi, and S. Murata, Photooxidation of 1,5-Dihydroxynaphthalene with Iridium Complexes as Singlet Oxygen Sensitizers, *Photochem. Photobiol. Sci.*, 2011, **10**, 895–903.
44. L. Huang, D. Qing, S. Zhao, X. Wu, K. Yang, X. Ren, X. Zheng, M. Lan, J. Ye, L. Zeng, et al., Acceptor-

Donor-Acceptor Structured Deep-Red AIE Photosensitizer: Lysosome-Specific Targeting, in Vivo Long-Term Imaging, and Effective Photodynamic Therapy, *Chem. Eng. J.*, 2022, **430**, 132638.

45. K. S. Bejoymohandas, T. M. George, S. Bhattacharya, S. Natarajan, and M. L. P. Reddy, AIPE-Active Green Phosphorescent Iridium(III) Complex Impregnated Test Strips for the Vapor-Phase Detection of 2,4,6-Trinitrotoluene (TNT), *J. Mater. Chem. C*, 2014, **2**, 515–523.

46. M. Martínez-Alonso, J. Cerdá, C. Momblona, A. Pertegás, J. M. Junquera-Hernández, A. Heras, A. M. Rodríguez, G. Espino, H. Bolink, and E. Ortí, Highly Stable and Efficient Light-Emitting Electrochemical Cells Based on Cationic Iridium Complexes Bearing Arylazole Ancillary Ligands, *Inorg. Chem.*, 2017, **56**, 10298–10310.

47. S. Ladouceur, D. Fortin, and E. Zysman-DE , Enhanced Luminescent Iridium(III) Complexes Bearing Aryltriazole Cyclometallated Ligands, *Inorg. Chem.*, 2011, **50**, 11514–11526.

48. F. Lafolet, S. Welter, Z. Popović, and L. De. Cola, Iridium Complexes Containing P-Phenylene Units. The Influence of the Conjugation on the Excited State Properties, *J. Mater. Chem.*, 2005, **15**, 2820–2828.

49. S. Ladouceur, and E. Zysman-Colman, A Comprehensive Survey of Cationic Iridium(III) Complexes Bearing Nontraditional Ligand Chelation Motifs, *Eur. J. Inorg. Chem.*, 2013, **2013**, 2985–3007.

50. C. K. Prier, D. A. Rankic, and D. W. C. MacMillan, Visible Light Photoredox Catalysis with Transition Metal Complexes: Applications in Organic Synthesis, *Chem. Rev.*, 2013, **113**, 5322–5363.

51. J. Twilton, C. C. Le, P. Zhang, M. H. Shaw, R. W. Evans, and D. W. C. MacMillan, The Merger of Transition Metal and Photocatalysis, *Nat. Rev. Chem.*, 2017, **1**, 0052.

52. M. H. Shaw, J. Twilton, D. W. C. MacMillan, Photoredox Catalysis in Organic Chemistry, *J. Org. Chem.*, 2016, **81**, 6898–6926.

53. D. M. Arias-Rotondo, and J. K. McCusker, The Photophysics of Photoredox Catalysis: A Roadmap for Catalyst Design, *Chem. Soc. Rev.*, 2016, **45**, 5803–5820.

54. Y. Xiao, Y.-K. Chun, S.-C. Cheng, C.-O. Ng, M.-K. Tse, N.-Y. Lei, R. Liu, and C.-C. Ko, Photocatalytic Amidation and Esterification with Perfluoroalkyl Iodide, *Catal. Sci. Technol.*, 2021, **11**, 556–562.

55. C. Zhang, S. Li, F. Bureš, R. Lee, X. Ye, and Z. Jiang, Visible Light Photocatalytic Aerobic Oxygenation of Indoles and PH as a Chemoselective Switch, *ACS Catal.*, 2016, **6**, 6853–6860.

56. W. Schilling, Y. Zhang, D. Riemer, and S. Das, Visible-Light-Mediated Dearomatisation of Indoles and Pyrroles to Pharmaceuticals and Pesticides, *Chem. – A Eur. J.*, 2020, **26**, 390–395.

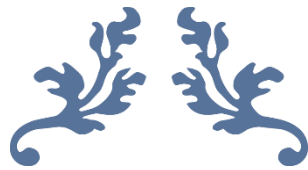
57. S. M. Bonesi, I. Manet, M. Freccero, M. Fagnoni, and A. Albini, Photosensitized Oxidation of Sulfides: Discriminating between the Singlet-Oxygen Mechanism and Electron Transfer Involving Superoxide Anion or Molecular Oxygen, *Chem. - A Eur. J.*, 2006, **12**, 4844–4857.

58. Z. Li, S. Han, C. Li, P. Shao, H. Xia, H. Li, X. Chen, X. Feng, and X. Liu, Screening Metal-Free Photocatalysts from Isomorphous Covalent Organic Frameworks for the C-3 Functionalization of Indoles, *J. Mater. Chem. A*, 2020, **8**, 8706–8715.

59. H. Yu, J. Wang, Y. Zhai, M. Zhang, S. Ru, S. Han, and Y. Wei, Visible-Light-Driven Photocatalytic Oxidation of Organic Chlorides Using Air and an Inorganic-Ligand Supported Nickel-Catalyst Without Photosensitizers, *ChemCatChem*, 2018, **10**, 4274–4279.

60. W. Dong, Q. Ma, Z. Ma, Q. Duan, X. Lü, N. Qiu, T. Fei, and Z. Su, Phosphorescent Iridium(III) Complex Based Photoluminescence Sensor for Sensitive and Selective Detection of Picric Acid, *Dye. Pigment.*, 2020, **172**, 107799.
61. X. Sun, Y. Wang, and Y. Lei, Fluorescence Based Explosive Detection: From Mechanisms to Sensory Materials, *Chem. Soc. Rev.*, 2015, **44**, 8019–8061.
62. A. Kamal, V. Devaiah, K. L. Reddy, and N. Shankaraiah, Conversion of Amines to Imines Employing Polymer-Supported Sulfoxide (PSS) and Polymer-Supported Perruthenate (PSP): Synthesis of Pyrrolo[2,1-c][1,4]Benzodiazepines, *Adv. Synth. Catal.*, 2006, **348**, 249–254.
63. K. Aganda, B. Hong, and A. Lee, Aerobic A-Oxidation of N-Substituted Tetrahydroisoquinolines to Dihydroisoquinolones via Organo-photocatalysis, *Adv. Synth. Catal.*, 2018, **361**, adsc.201801301.
64. P.-F. Yuan, Q.-B. Zhang, X.-L. Jin, W.-L. Lei, L.-Z. Wu, and Q. Liu, Visible-Light-Promoted Aerobic Metal-Free Aminothiocyation of Activated Ketones, *Green Chem.*, 2018, **20**, 5464–5468.
65. A. Guerrero-Corella, A. María Martínez-Gualda, F. Ahmadi, E. Ming, A. Fraile, and J. Alemán, Thiol–Ene/Oxidation Tandem Reaction under Visible Light Photocatalysis: Synthesis of Alkyl Sulfoxides, *Chem. Commun.*, 2017, **53**, 10463–10466.
66. H. C. Erythropel, J. B. Zimmerman, T. M. de Winter, L. Petitjean, F. Melnikov, C. H. Lam, A. W. Lounsbury, K. E. Mellor, N. Z. Janković, Q. Tu, et al., The Green ChemisTREE: 20 Years after Taking Root with the 12 Principles, *Green Chem.*, 2018, **20**, 1929–1961.





---

## ***Final conclusions***

---







### Chapter 1. Thiabendazole-based Rh(III) and Ir(III) Biscyclometalated Complexes with Mitochondria-Targeted Anticancer Activity and Metal-Sensitive Photodynamic Activity.

1. Ir(III) and Rh(III) tris-chelate complexes with general formula  $[M(C^AN)_2(N^AN')]X$  ( $M = Rh, Ir$ ;  $N^AN' =$  thiabendazole and its N-benzylated derivative) display significant cytotoxicity in the dark against cancer cells A549 and SW480
2. In the case of the Ir(III) derivatives their cytotoxic activity is enhanced upon blue light irradiation (PI of 15.8 for **[Ir a]Cl** and 3.6 for **[Ir-b]Cl** for A549 cells), whereas the Rh analogues do not show photo-enhancement of their activity due to lack of absorption in the blue range.
3. These complexes are accumulated in the mitochondria and cause cell death by apoptosis and among the Ir PSs, the N-benzyl derivative exhibits better cellular uptake and is the most cytotoxic.
4. Moreover, we have proved that the Ir(III) complexes exhibit photocatalytic activity in the photo-oxidation of sulphur-containing amino acids through the generation of singlet oxygen, suggesting that their mechanism of action could be related with the damage of proteins and the inhibition of their enzymatic or structural functions.

### Chapter 2. Photodynamic Therapy with Mitochondria-targeted Biscyclometalated Ir(III) Complexes. Multi-action Mechanism and Strong influence of the Cyclometalating Ligand.

1. Two pairs of Ir(III) tris-chelate complexes with general formula  $[Ir(C^AN)_2(N^AN')]X$  ( $C^AN = ppy, dfppy$ ;  $N^AN' =$  thiabendazole and 2-pyridylbenzimidazole moieties functionalized with an alkylamide on the imidazolic N atom) show a moderate cytotoxicity in the dark.
2. The complexes with  $C^AN = ppy$  can be activated efficiently with blue light (PI of 20.8 for **[1a]Cl** and PI of 17.3 for **[2a]Cl** in PC-3 cells), whereas the analogue PSs with  $C^AN = dfppy$  do not show significant photo-enhancement of their activity due to lack (or low) absorption in the blue range.
3. The photoactivable complexes **[1a]Cl** and **[2a]Cl** are very active against PC-3 and SK-MEL-28 cells upon light irradiation, with a high degree of selectivity for the SK-MEL-28 cells with respect to non-malignant cells.
4. These compounds are internalized by endocytosis, are accumulated preferentially in the mitochondria and cause cell death by apoptosis (thanks to their ability to generate ROS).

5. It is worth mentioning, that they do not alter the cell cycle progression, which can make them an interesting option for cancers with resistance against cisplatin.

### **Chapter 3. Rational Design of Mitochondria Targeted Thiabendazole-based Ir(III) Biscyclometalated Complexes for a Multimodal Photodynamic Therapy of Cancer.**

1. Photocytotoxicity of two series of Ir(III) tris-chelate complexes with general formula  $[\text{Ir}(\text{C}^{\wedge}\text{N})_2(\text{N}^{\wedge}\text{N}')]\text{X}$  ( $\text{C}^{\wedge}\text{N}$  = ppy, dfppy;  $\text{N}^{\wedge}\text{N}'$  = thiabendazole derivatives with acetophenone and various alkylamides on the imidazolic N atom) was determined and only complexes bearing ppy show an appreciable cytotoxicity enhancement under blue light irradiation.
2. Interestingly, complexes **[1a]Cl** and **[3a]Cl** show promising PIs for SK-MEL-28 melanoma cells (PI = 23.4 for **[1a]Cl** and PI = 21.4 for **[3a]Cl**) and a certain degree of selectivity relative to non-tumoral cells.
3. Upon light irradiation, they cause cell death (by both necrosis and apoptosis) through ROS generation causing a multi-target effect involving mitochondrial membrane depolarization and severe cleavage on mtDNA resulting in the inhibition of the transcriptional process, which is an interesting result for the treatment of cancer resistant to conventional drugs.

### **Chapter 4. Synthesis of $\alpha$ -amino nitriles through one-pot selective Ru-photocatalyzed oxidative cyanation of amines.**

1. Ru(II) tris-chelate complexes with general formula  $[\text{Ru}(\text{N}^{\wedge}\text{N})_2(\text{N}^{\wedge}\text{N}')]\text{X}_2$  ( $\text{N}^{\wedge}\text{N}$  = bpy;  $\text{N}^{\wedge}\text{N}'$  = 2-(2-pyridyl)benzimidazole and its alkylated derivatives) are very active PCs for the photooxidation of primary and secondary amines to produce the corresponding imines.
2. N-alkylated derivatives possess better photophysical properties than the parent PC with 2-(2-pyridyl)benzimidazole and some of them even better than the reference compound  $[\text{Ru}(\text{bpy})_3]\text{Cl}_2$ .
3. A scalable protocol for the one-pot photooxidative cyanation of the amines to produce  $\alpha$ -amino nitriles in a selective way under mild and eco-friendly conditions was developed.

---

**Chapter 5. Photocatalytic Aerobic Dehydrogenation of N-Heterocycles with Ir(III) Photosensitizers Bearing the 2(2'-Pyridyl)benzimidazole Scaffold.**

1. Ir(III) tris-chelate complexes with general formula  $[\text{Ir}(\text{C}^{\wedge}\text{N})_2(\text{N}^{\wedge}\text{N}')]\text{X}$  ( $\text{C}^{\wedge}\text{N}$  = dfppy;  $\text{N}^{\wedge}\text{N}'$  = 2-(2-pyridyl)benzimidazole or different alkylated derivatives) are active PCs in the oxidative dehydrogenation of partially saturated substrates such as indolines, 1,2,3,4-tetrahydroquinolines and others, giving aromatic N-heterocyclic products with high yields and selectivity for most of the tested substrates.
2. These compounds offer improved activities compared to model PCs like  $[\text{Ir}(\text{ppy})_2(\text{bpy})]\text{PF}_6$  and  $[\text{Ir}(\text{dfppy})_2(\text{bpy})]\text{PF}_6$ .
3. It is possible to scale up this green protocol up to one gram satisfactorily.